AAAS

Science

20 NOVEMBER 2025

The grisly demise of Europe's first farmers **p. 776**

Recognizing scientific distinctions between coca and cocaine **p. 782**

Calcium waves in the developing fly eye **pp. 787 & 807**

SOFT 3D TRANSISTORS

Hydrogel semiconductors for biologically compatible electronics **p. 824**

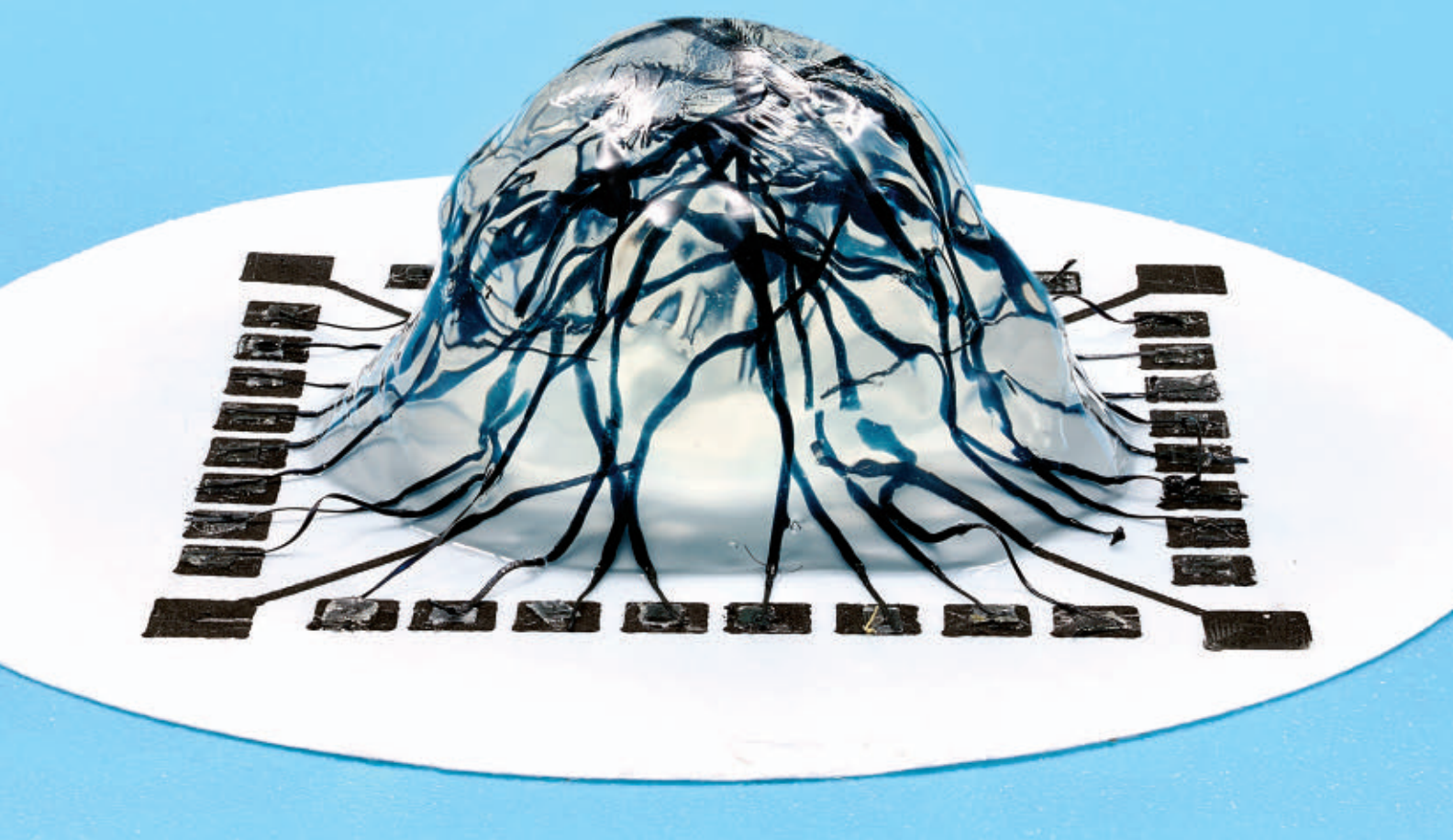

The Chen Institute and *Science* launched the "Chen Institute and *Science* Prize for AI Accelerated Research" in August 2024. This initiative aims to drive advancements in artificial intelligence that can expand scientific research. Young scientists from around the world are invited to submit AI-driven projects that demonstrate significant potential to improve research and lives.

The competition will award a Grand Prize of $30,000, with the winner's essay published in *Science* and an accompanying five-year AAAS membership. Additionally, up to two runners-up will receive $10,000 each, with their essays published on *Science* Online and the same membership benefits, promoting sustained engagement with scientific progress.

Apply at

cheninstitute.org/prize

CONTENTS

20 NOVEMBER 2025
VOLUME 390
ISSUE 6775

776 What happened to Europe's first farmers? Headless burials deepen the mystery.

PHOTO: VRÁBLE EXCAVATION TEAM

EDITORIAL

767 A megadam test for China and South Asia
—R. J. P. Schmitt and B. Eyler

NEWS

768 High-resolution climate model forecasts a wet future
With details as fine as short-term weather forecasts, model achieves newfound accuracy —P. Voosen

769 Make the census voluntary? Bad idea, say statisticians
Pending bills in U.S. Congress could degrade data from national surveys —J. Mervis

771 'A sigh of relief': New malaria drug succeeds in clinical trial as existing treatments falter
Ganaplacide, developed by Novartis, eases worries about drug resistance—but hard choices loom on how to use it —K. Kupferschmidt

773 As neural organoids advance, ethics races to keep pace
Scientists, ethicists, and patient advocates mull biology's latest provocative technology —M. Leslie

774 Startup pioneers subscription service for space telescope
Blue Skies Space will sell data from its tiny, low-cost UV observatory —D. Clery

FEATURES

776 A headless mystery
Archaeologists find evidence that a wave of mass brutality accompanied the collapse of the first pan-European culture —A. Curry
PODCAST

COMMENTARY

POLICY FORUM

782 Scientific distinctions between coca and cocaine support policy reform
Ongoing review of international drug policy should correct long-standing, misguided, and harmful conflation —D. M. White *et al.*

PERSPECTIVES

786 Engineering chromosome number in plants
Chromosome engineering produces a reduced eight-chromosome karyotype in *Arabidopsis thaliana* —F. Zhang and R. K. Dawe
RESEARCH ARTICLE p. 843

787 The retina's rhythm
Calcium waves facilitate the emergence of sight —J. P. Kumar
RESEARCH SUMMARY p. 807

789 A bacterial toxin disarms gut defenses against inflammation
Macrophage-toxic bacteria from patients with ulcerative colitis worsen gut inflammation in mice —S. Modilevsky and S. Bel
RESEARCH SUMMARY p. 805

790 Tracking magma with earthquakes
Linking stress in Earth's crust and magma flow could help forecast eruptions and associated hazards —V. Pinel
RESEARCH SUMMARY p. 806

BOOKS ET AL.

792 An ode to change
A historian confronts the transformative nature of metamorphosis —V. Callier

793 In defense of the know-it-all
A scholar probes the scorn provoked by the intellectual elite across the ages —J. Wai

CALL FOR PAPERS

SPJ
SCIENCE PARTNER JOURNALS

Ocean-Land-Atmosphere Research

Ocean-Land-Atmosphere Research (OLAR) is an online-only, Open Access journal published in affiliation with **Southern Marine Science and Engineering Guangdong Laboratory (Zhuhai) (SML-ZHUHAI)** and distributed by the **American Association for the Advancement of Science (AAAS)**. With an emphasis on ocean-related sciences, *OLAR* provides an international platform for researchers engaged in marine, terrestrial, and atmospheric studies and the interactions among them. The journal welcomes relevant fundamental research in physics, chemistry, biology and geology as well as emerging applied research in ocean observation, environment protection, and resources utilization. Manuscripts featuring cutting-edge science, innovative technology, and interdisciplinary studies within the journal's scope are particularly welcome.

Submit your research to *OLAR* today!

Learn more at **spj.science.org/olar**

The Science Partner Journal (SPJ) program was established by the American Association for the Advancement of Science (AAAS), the nonprofit publisher of the *Science* family of journals. The SPJ program features high-quality, online-only, Open Access publications produced in collaboration with international research institutions, foundations, funders, and societies. Through these collaborations, AAAS furthers its mission to communicate science broadly and for the benefit of all people by providing top-tier international research organizations with the technology, visibility, and publishing expertise that AAAS is uniquely positioned to offer as the world's largest general science membership society.

Visit us at **spj.science.org**

@SPJournals **@SPJournals** **@SPJournals**

OPEN ACCESS

ARTICLE PROCESSING CHARGES WAIVED THROUGH DECEMBER 2025

LETTERS

794 Brazil's credibility at stake with drilling
—F. do Rocio Lacerda *et al*.

794 Brazil's hypocrisy at COP30 —J. A. Reis-Filho *et al*.

795 Bolivia's political transition and COP30
—F. M. Benítez Romero and P. M. Fearnside

REVIEWS

REVIEW SUMMARY

797 Origins of language
What enables human language? A biocultural framework
—I. Arnon *et al*.

RESEARCH

HIGHLIGHTS

798 From *Science* and other journals

RESEARCH SUMMARIES

801 Signal transduction
Noncanonical agonist-dependent and -independent arrestin recruitment of GPR1 —H. Cai *et al.*

802 Immunology
Rebalancing viral and immune damage versus repair prevents death from lethal influenza infection
—H. Ichise *et al.*

803 Genetic code
An archaeal genetic code with all TAG codons as pyrrolysine
—V. Kivenson *et al.*

804 Neuroscience
The synaptic ectokinase VLK triggers the EphB2–NMDAR interaction to drive injury-induced pain —K. D. Srikanth *et al.*

805 Immunology
An *Aeromonas* variant that produces aerolysin promotes susceptibility to ulcerative colitis —Z. Jiang *et al.*
PERSPECTIVE p. 789

An artist's impression of the giant impact between proto-Earth and Theia, with the Sun in the background. Debris from this collision formed the Moon.

ILLUSTRATION: MPS/MARK A. GARLICK

806 Volcanology
The 2025 Santorini unrest unveiled: Rebounding magmatic dike intrusion with triggered seismicity
—A. Lomax *et al.*
PERSPECTIVE p. 790

807 Neurodevelopment
Retinal calcium waves coordinate uniform tissue patterning of the *Drosophila* eye
—B. J. Choi *et al.*
PERSPECTIVE p. 787

RESEARCH ARTICLES

808 Gas adsorption
Multigas adsorption with single-site cooperativity in a metal–organic framework —K. M. Carsch *et al.*

813 Device technology
Atomic layer bonding contacts in two-dimensional semiconductors
—L. Gao *et al.*

819 Cosmochemistry
The Moon-forming impactor Theia originated from the inner Solar System —T. Hopp *et al.*

824 Organic electronics
Increasing the dimensionality of transistors with hydrogels
—D. Liu *et al.*

831 Organic chemistry
An anion-binding approach to enantioselective photoredox catalysis —P. Vojáčková and E. N. Jacobsen

837 Solar cells
A cross-linked molecular contact for stable operation of perovskite/silicon tandem solar cells
—B. Zhang *et al.*

843 Plant science
CRISPR-Cas–mediated heritable chromosome fusions in *Arabidopsis* —M. Rönspies *et al.*
PERSPECTIVE p. 786

849 Quantum simulation
Realization of a Rydberg-dressed extended Bose-Hubbard model
—P. Weckesser *et al.*

ON THE COVER

Bulky hydrogels are used as structured supports for tissue engineering because of their high water content and soft mechanical properties, but they lack semiconducting properties. This image shows three-dimensional, millimeter-thick, and cell-embeddable semiconducting hydrogel fibers. These fibers can be used to construct interwoven living transistors that mimic real neuronal connections in the brain, redefining the boundary between technology and life. See page 824. Credit: The WISE Research Group (Wearable, Intelligent, Soft Electronics) at the University of Hong Kong

ON THE PODCAST

A headless mystery, and a deep dive on dog research

WORKING LIFE

858 Time to laugh
—L. S. Taillie

766 *Science* Staff
854 *Science* Careers

Science **serves as a forum for discussion of important issues related to the advancement of science by publishing material on which a consensus has been reached as well as including the presentation of minority or conflicting points of view. Accordingly, all articles published in *Science*—including editorials, news, commentary, and book reviews—are signed and reflect the individual views of the authors and not official points of view adopted by AAAS or the institutions with which the authors are affiliated.** *Science* (ISSN 0036-8075) is published weekly on Thursday, except last week in December, by the American Association for the Advancement of Science, 1200 New York Avenue, NW, Washington, DC 20005. Periodicals mail postage (publication No. 484460) paid at Washington, DC, and additional mailing offices. Copyright © 2025 by the American Association for the Advancement of Science. The title *Science* is a registered trademark of the AAAS. Domestic individual membership, including subscription (12 months): $165 ($74 allocated to subscription). Domestic institutional subscription (51 issues): $2865; Foreign postage extra: Air assist delivery: $135. First class, airmail, student, and emeritus rates on request. Canadian rates with GST available upon request, GST #125488122. Publications Mail Agreement Number 1069624. **Printed in the U.S.A. Change of address:** Allow 4 weeks, giving old and new addresses and 8-digit account number. **Postmaster:** Send change of address to AAAS, P.O. Box 96178, Washington, DC 20090–6178. **Single-copy sales:** $15 each plus shipping and handling available from backissues.science.org; bulk rate on request. **Authorization to reproduce** material for internal or personal use under circumstances not falling within the fair use provisions of the Copyright Act can be obtained through the Copyright Clearance Center (CCC), www.copyright.com. The identification code for *Science* is 0036-8075. *Science* is indexed in the *Reader's Guide to Periodical Literature* and in several specialized indexes.

Science AAAS

EDITOR-IN-CHIEF Holden Thorp, hthorp@aaas.org

EXECUTIVE EDITOR Valda Vinson

EDITORS, RESEARCH Sacha Vignieri, Jake S. Yeston **EDITOR, COMMENTARY** Lisa D. Chong

DEPUTY EXECUTIVE EDITOR Lauren Kmec

DEPUTY EDITORS Stella M. Hurtley (UK), Phillip D. Szuromi **SENIOR EDITORS** Caroline Ash (UK), Michael A. Funk, Angela Hessler, Di Jiang, Priscilla N. Kelly, Marc S. Lavine (Canada), Sarah Lempriere (UK), Mattia Maroso, Yevgeniya Nusinovich, Ian S. Osborne (UK), Joana Osório (UK), L. Bryan Ray, H. Jesse Smith, Keith T. Smith (UK), Jelena Stajic, Peter Stern (UK), Yury V. Suleymanov, Valerie B. Thompson, Brad Wible **ASSOCIATE EDITORS** Jack Huang, Sumin Jin, Bianca Lopez, Sarah Ross (UK), Madeleine Seale (UK), Corinne Simonti, Ekeoma Uzogara **SENIOR LETTERS EDITOR** Jennifer Sills **NEWSLETTER EDITOR** Christie Wilcox **RESEARCH & DATA ANALYST** Jessica L. Slater **LEAD CONTENT PRODUCTION EDITORS** Chris Filiatreau, Harry Jach **SR. CONTENT PRODUCTION EDITOR** Amelia Beyna **CONTENT PRODUCTION EDITORS** Anne Abraham, Robert French, Julia Haber-Katris, Nida Masiulis, Abigail Shashikanth, Suzanne M. White **SENIOR PROGRAM ASSOCIATE** Maryrose Madrid **EDITORIAL MANAGER** Joi S. Granger **EDITORIAL ASSOCIATES** Aneera Dobbins, Lisa Johnson, Jerry Richardson, Anita Wynn **SENIOR EDITORIAL COORDINATORS** Alexander Kief, Ronmel Navas, Isabel Schnaidt, Alice Whaley (UK), Brian White **EDITORIAL COORDINATORS** Samuel Bates, Clair Goodhead (UK), Kat Kirkman, Daniel Young **ADMINISTRATIVE COORDINATOR** Karalee P. Rogers **ASI DIRECTOR, OPERATIONS** Janet Clements (UK) **ASI OFFICE MANAGER** Carly Hayward (UK) **ASI SR. OFFICE ADMINISTRATORS** Simon Brignell (UK), Jessica Waldock (UK) **COMMUNICATIONS DIRECTOR** Meagan Phelan **DEPUTY DIRECTOR** Matthew Wright **SENIOR WRITERS** Walter Beckwith, Joseph Cariz, Abigail Eisenstadt **WRITER** Mahathi Ramaswamy **SENIOR COMMUNICATIONS ASSOCIATES** Zachary Graber, Sarah Woods **COMMUNICATIONS ASSOCIATES** Kiara Brooks, Haley Riley, Mackenzie Williams

NEWS EDITOR Tim Appenzeller

NEWS MANAGING EDITOR John Travis **INTERNATIONAL EDITOR** David Malakoff **DEPUTY NEWS EDITORS** Rachel Bernstein, Martin Enserink, David Grimm, Eric Hand, Michael Price, Kelly Servick, Matt Warren (Europe) **SENIOR CORRESPONDENTS** Daniel Clery (UK), Jon Cohen, Jeffrey Mervis **ASSOCIATE EDITORS** Michael Greshko, Katie Langin **NEWS REPORTERS** Jeffrey Brainard, Adrian Cho, Phie Jacobs, Jocelyn Kaiser, Robert F. Service, Jennie Erin Smith, Erik Stokstad, Paul Voosen **CONSULTING EDITOR** Elizabeth Culotta **CONTRIBUTING CORRESPONDENTS** Vaishnavi Chandrashekhar, Dan Charles, Warren Cornwall, Andrew Curry (Berlin), Ann Gibbons, Kai Kupferschmidt (Berlin), Andrew Lawler, Mitch Leslie, Virginia Morell, Dennis Normile (Tokyo), Catherine Offord, Cathleen O'Grady, Elisabeth Pain (Careers), Charles Piller, Zack Savitsky, Richard Stone (Senior Asia Correspondent), Gretchen Vogel (Berlin), Lizzie Wade (Mexico City) **INTERNS** Celina Zhao **COPY EDITORS** Julia Cole (Senior Copy Editor), Hannah Knighton, Cyra Master (Copy Chief) **ADMINISTRATIVE SUPPORT** Meagan Weiland

CREATIVE DIRECTOR Beth Rakouskas

DESIGN MANAGING EDITOR Chrystal Smith **GRAPHICS MANAGING EDITOR** Chris Bickel **PHOTOGRAPHY MANAGING EDITOR** Emily Petersen **MULTIMEDIA MANAGING PRODUCER** Kevin McLean **DIGITAL DIRECTOR** Kara Estelle-Powers **DESIGN EDITOR** Marcy Atarod **DESIGNER** Noelle Jessup **SENIOR SCIENTIFIC ILLUSTRATOR** Noelle Burgess **SCIENTIFIC ILLUSTRATORS** Austin Fisher, Kellie Holoski, Ashley Mastin **SENIOR GRAPHICS EDITOR** Monica Hersher **GRAPHICS EDITOR** Veronica Penney **SENIOR PHOTO EDITOR** Charles Borst **PHOTO EDITOR** Elizabeth Billman **SENIOR PODCAST PRODUCER** Sarah Crespi **SENIOR VIDEO PRODUCER** Meagan Cantwell **SOCIAL MEDIA STRATEGIST** Jessica Hubbard **SOCIAL MEDIA PRODUCER** Sabrina Jenkins **WEB DESIGNER** Jennie Pajerowski

CHIEF EXECUTIVE OFFICER AND EXECUTIVE PUBLISHER

Sudip Parikh

PUBLISHER, SCIENCE FAMILY OF JOURNALS Bill Moran

DIRECTOR, BUSINESS OPERATIONS & ANALYSIS Eric Knott **MANAGER, BUSINESS OPERATIONS** Jessica Tierney **SENIOR MANAGER, BUSINESS ANALYSIS** Cory Lipman **BUSINESS ANALYSTS** Kurt Ennis, Maggie Clark, Isacco Fusi **BUSINESS OPERATIONS ADMINISTRATOR** Taylor Fisher **DIGITAL SPECIALIST** Marissa Zuckerman **SENIOR PRODUCTION MANAGER** Jason Hillman **SENIOR MANAGER, PUBLISHING AND CONTENT SYSTEMS** Marcus Spiegler **CONTENT OPERATIONS MANAGER** Rebecca Doshi **PUBLISHING PLATFORM MANAGER** Jessica Loayza **PUBLISHING SYSTEMS SPECIALIST, PROJECT COORDINATOR** Jacob Hedrick **SENIOR PRODUCTION SPECIALIST** Kristin Wowk **PRODUCTION SPECIALISTS** Kelsey Cartelli, Audrey Diggs **SPECIAL PROJECTS ASSOCIATE** Shantel Agnew

MARKETING DIRECTOR Sharice Collins **ASSOCIATE DIRECTOR, MARKETING** Justin Sawyers **GLOBAL MARKETING MANAGER** Allison Pritchard **ASSOCIATE DIRECTOR, MARKETING SYSTEMS & STRATEGY** Aimee Aponte **SENIOR MARKETING MANAGER** Shawana Arnold **MARKETING MANAGER** Ashley Evans **MARKETING ASSOCIATES** Hugues Beaulieu, Ashley Hylton, Lorena Chirinos Rodriguez, Jenna Voris **MARKETING ASSISTANT** Courtney Ford **SENIOR DESIGNER** Kim Huynh

DIRECTOR AND SENIOR EDITOR, CUSTOM PUBLISHING Erika Gebel Berg **ADVERTISING PRODUCTION OPERATIONS MANAGER** Deborah Tompkins **DESIGNER, CUSTOM PUBLISHING** Jeremy Huntsinger **SENIOR TRAFFIC ASSOCIATE** Christine Hall

DIRECTOR, PRODUCT MANAGEMENT Kris Bishop **PRODUCT DEVELOPMENT MANAGER** Scott Chernoff **ASSOCIATE DIRECTOR, PUBLISHING INTELLIGENCE** Rasmus Andersen **SR. PRODUCT ASSOCIATE** Robert Koepke **PRODUCT ASSOCIATES** Caroline Breul, Anne Mason

ASSOCIATE DIRECTOR, INSTITUTIONAL LICENSING MARKETING Kess Knight **ASSOCIATE DIRECTOR, INSTITUTIONAL LICENSING SALES** Ryan Rexroth **INSTITUTIONAL LICENSING MANAGER** Nazim Mohammedi, Claudia Paulsen-Young **SENIOR MANAGER, INSTITUTIONAL LICENSING OPERATIONS** Judy Lillibridge **MANAGER, RENEWAL & RETENTION** Lana Guz **SYSTEMS & OPERATIONS ANALYST** Ben Teincuff **FULFILLMENT ANALYST** Aminta Reyes

ASSOCIATE DIRECTOR, INTERNATIONAL Roger Goncalves **ASSOCIATE DIRECTOR, US ADVERTISING** Stephanie O'Connor **US MID WEST, MID ATLANTIC AND SOUTH EAST SALES MANAGER** Chris Hoag **DIRECTOR, OUTREACH AND STRATEGIC PARTNERSHIPS, ASIA** Shoupeng Liu **SALES REP, ROW** Sarah Lelarge **SALES ADMIN ASSISTANT, ROW** Victoria Glasbey **DIRECTOR OF GLOBAL COLLABORATION AND ACADEMIC PUBLISHING RELATIONS, ASIA** Xiaoying Chu **ASSOCIATE DIRECTOR, INTERNATIONAL COLLABORATION** Grace Yao **SALES MANAGER** Danny Zhao **MARKETING MANAGER** Kilo Lan **ASCA CORPORATION, JAPAN** Rie Rambelli (Tokyo), Miyuki Tani (Osaka)

DIRECTOR, COPYRIGHT, LICENSING AND SPECIAL PROJECTS Emilie David **RIGHTS AND PERMISSIONS ASSOCIATE** Elizabeth Sandler **LICENSING ASSOCIATE** Virginia Warren **RIGHTS AND LICENSING COORDINATOR** Dana James **CONTRACT SUPPORT SPECIALIST** Michael Wheeler

EDITORIAL
science_editors@aaas.org

NEWS
science_news@aaas.org

INFORMATION FOR AUTHORS
science.org/authors/
science-information-authors

REPRINTS AND PERMISSIONS
science.org/help/
reprints-and-permissions

MULTIMEDIA CONTACTS
SciencePodcast@aaas.org
ScienceVideo@aaas.org

MEDIA CONTACTS
scipak@aaas.org

PRODUCT ADVERTISING & CUSTOM PUBLISHING
advertising.science.org
science_advertising@aaas.org

CLASSIFIED ADVERTISING
advertising.science.org/
science-careers
advertise@sciencecareers.org

JOB POSTING CUSTOMER SERVICE
employers.sciencecareers.org
support@sciencecareers.org

MEMBERSHIP AND INDIVIDUAL SUBSCRIPTIONS
science.org/subscriptions

MEMBER BENEFITS
aaas.org/membership/
benefits

INSTITUTIONAL SALES AND SITE LICENSES
science.org/librarian

AAAS BOARD OF DIRECTORS

CHAIR Joseph S. Francisco

IMMEDIATE PAST PRESIDENT
Willie E. May

PRESIDENT
Theresa A. Maldonado

PRESIDENT-ELECT
Marina Picciotto

TREASURER Carolyn N. Ainslie

COUNCIL CHAIR
Ichiro Nishimura

CHIEF EXECUTIVE OFFICER
Sudip Parikh

BOARD
Mark Dingfield
Morton Ann Gernsbacher
Kathleen Hall Jamieson
Jane Maienschein
Babak Parviz
Gabriela Popescu
Juan S. Ramírez Lugo
Susan M. Rosenberg
Vassiliki Betty Smocovitis
Roger Wakimoto

BOARD OF REVIEWING EDITORS (Statistics board members indicated with **S**)

Erin Adams, *U. of Chicago*
Takuzo Aida, *U. of Tokyo*
Leslie Aiello, *Wenner-Gren Fdn.*
Anastassia Alexandrova, *UCLA*
Mohammed AlQuraishi, *Columbia U.*
James Analytis, *UC Berkeley*
Paola Arlotta, *Harvard U.*
Madan Babu, *St. Jude*
Jennifer Balch, *U. of Colorado*
Nenad Ban, *ETH Zürich*
Carolina Barillas-Mury, *NIH, NIAID*
Christopher Barratt, *U. of Dundee*
François Barthelat, *U. of Colorado Boulder*
Franz Bauer, *Universidad de Tarapacá*
Andreas Baumler, *UC Davis*
Carlo Beenakker, *Leiden U.*
Sarah Bergbreiter, *Carnegie Mellon U.*
Kiros T. Berhane, *Columbia U.*
Aude Bernheim, *Inst. Pasteur*
Joseph J. Berry, *NREL*
Aditi Bhargav, *UCSF*
Dominique Bonnet, *Francis Crick Inst.*
Chris Bowler, *École Normale Supérieure*
Ian Boyd, *U. of St. Andrews*
Malcolm Brenner, *Baylor Coll. of Med.*
Ron Brookmeyer, *UCLA* (**S**)
Christian Büchel, *UKE Hamburg*
Johannes Buchner, *TUM*
Dennis Burton, *Scripps Res.*
Carter Tribley Butts, *UC Irvine*
György Buzsáki, *NYU School of Med.*
Annmarie Carlton, *UC Irvine*
Jane Carlton, *Johns Hopkins U.*
Pedro Carvalho, *U. of Oxford*
Simon Cauchemez, *Inst. Pasteur*
Ling-Ling Chen, *SIBCB, CAS*
Hilde Cheroutre, *La Jolla Inst.*
Wendy Cho, *UIUC*
Ib Chorkendorff, *Denmark TU*
Chunaram Choudhary, *Københavns U.*
Karlene Cimprich, *Stanford U.*
Laura Colgin, *UT Austin*
James J. Collins, *MIT*
Robert Cook-Deegan, *Arizona State U.*
Carolyn Coyne, *Duke U.*
Roberta Croce, *VU Amsterdam*
Ismaila Dabo, *Penn State U.*
Nicolas Dauphas, *U. of Chicago*
Claude Desplan, *NYU*
Sandra Díaz, *U. Nacional de Córdoba*
Samuel Díaz-Muñoz, *UC Davis*
Ulrike Diebold, *TU Wien*
Stefanie Dimmeler, *Goethe-U. Frankfurt*
Hong Ding, *Inst. of Physics, CAS*
Dennis Discher, *UPenn*
Jennifer A. Doudna, *UC Berkeley*
Ruth Drdla-Schutting, *Med. U. Vienna*
Raissa M. D'Souza, *UC Davis*
Bruce Dunn, *UCLA*
William Dunphy, *Caltech*
Scott Edwards, *Harvard U.*
Todd A. Ehlers, *U. of Glasgow*
Tobias Erb, *MPS, MPI Terrestrial Microbiology*
Beate Escher, *UFZ & U. of Tübingen*
Barry Everitt, *U. of Cambridge*
Vanessa Ezenwa, *U. of Georgia*
Toren Finkel, *U. of Pitt. Med. Ctr.*
Natascha Förster Schreiber, *MPI Extraterrestrial Phys.*
Serita Frey, *U. of New Hampshire*
Elaine Fuchs, *Rockefeller U.*
Caixia Gao, *Inst. of Genetics and Developmental Bio., CAS*
Daniel Geschwind, *UCLA*
Lindsey Gillson, *U. of Cape Town*
Alemu Gonsamo Gosa, *McMaster U.*
Simon Greenhill, *U. of Auckland*
Gillian Griffiths, *U. of Cambridge*
Nicolas Gruber, *ETH Zürich*
Hua Guo, *U. of New Mexico*
Taekjip Ha, *Johns Hopkins U.*
Daniel Haber, *Mass. General Hos..*
Hamida Hammad, *VIB IRC*
Brian Hare, *Duke U.*
Kelley Harris, *U. of Wash*
Carl-Philipp Heisenberg, *IST Austria*
Emiel Hensen, *TU Eindhoven*
Christoph Hess, *U. of Basel & U. of Cambridge*
Brian Hie, *Stanford U.*
Heather Hickman, *NIAID, NIH*
Janneke Hille Ris Lambers, *ETH Zürich*
Kai-Uwe Hinrichs, *U. of Bremen*
Pinshane Huang, *UIUC*
Christina Hulbe, *U. of Otago, New Zealand*
Gwyneth Ingram, *ENS Lyon*
Darrell Irvine, *Scripps Res.*
Erich Jarvis, *Rockefeller U.*
Peter Jonas, *IST Austria*
Sheena Josselyn, *U. of Toronto*
Matt Kaeberlein, *U. of Wash.*
Daniel Kammen, *UC Berkeley*
Kisuk Kang, *Seoul Nat. U.*
Vedika Khemani, *Stanford U.*
V. Narry Kim, *Seoul Nat. U.*
Nancy Knowlton, *Smithsonian*
Etienne Koechlin, *École Normale Supérieure*
LaShanda Korley, *U. of Delaware*
Paul Kubes, *U. of Calgary*
Deborah Kurrasch, *U of Calgary*
Laura Lackner, *Northwestern U.*
Mitchell A. Lazar, *UPenn*
Hedwig Lee, *Duke U.*
Fei Li, *Xi'an Jiaotong U.*
Jianyu Li, *McGill U.*
Ryan Lively, *Georgia Tech*
Luis Liz-Marzán, *CIC biomaGUNE*
Omar Lizardo, *UCLA*
Jonathan Losos, *WUSTL*
Ke Lu, *Inst. of Metal Res., CAS*
Christian Lüscher, *U. of Geneva*
Jean Lynch-Stieglitz, *Georgia Tech*
David Lyons, *U. of Edinburgh*
Fabienne Mackay, *QIMR Berghofer*
Vidya Madhavan, *UIUC*
Anne Magurran, *U. of St. Andrews*
Oscar Marín, *King's Coll. London*
Matthew Marinella, *Arizona State U.*
Charles Marshall, *UC Berkeley*
Christopher Marx, *U. of Idaho*
Geraldine Masson, *CNRS*
Jennifer McElwain, *Trinity College Dublin*
Scott McIntosh, *NCAR*
Rodrigo Medellín, *U. Nacional Autónoma de México*
Mayank Mehta, *UCLA*
C. Jessica Metcalf, *Princeton U.*
Tom Misteli, *NCI, NIH*
Jeffery Molkentin, *Cincinnati Children's Hospital Medical Center*
Alison Motsinger-Reif, *NIEHS, NIH* (**S**)
Rosa Moysés, *U. of São Paulo School of Medicine*
Carey Nadell, *Dartmouth College*
Thi Hoang Duong Nguyen, *MRC LMB*
Pilar Ossorio, *U. of Wisconsin*
Andrew Oswald, *U. of Warwick*
Isabella Pagano, *Istituto Nazionale di Astrofisica*
Giovanni Parmigiani, *Dana-Farber* (**S**)
Zak Page, *UT Austin*
Pierre Paoletti, *Ecole Normale Supérieure, Paris*
Sergiu Pasca, *Stanford U.*
Julie Pfeiffer, *UT Southwestern Med. Ctr.*
Philip Phillips, *UIUC*
Matthieu Piel, *Inst. Curie*
Kathrin Plath, *UCLA*
Martin Plenio, *Ulm U.*
Katherine Pollard, *UCSF*
Elvira Poloczanska, *Alfred-Wegener-Inst.*
Julia Pongratz, *Ludwig Maximilians U.*
Philippe Poulin, *CNRS*
Suzie Pun, *U. of Wash*
Lei Stanley Qi, *Stanford U.*
Simona Radutoiu, *Aarhus U.*
Maanasa Raghavan, *U. of Chicago*
Trevor Robbins, *U. of Cambridge*
Adrienne Roeder, *Cornell U.*
Joeri Rogelj, *Imperial Coll. London*
John Rubenstein, *SickKids*
Sylvie Roke, *École Polytechnique Fédérale de Lausanne*
Yvette Running Horse Collin, *Toulouse U.*
Mike Ryan, *UT Austin*
Alberto Salleo, *Stanford U.*
Miquel Salmeron, *Lawrence Berkeley Nat. Lab*
Nitin Samarth, *Penn State U.*
Erica Ollmann Saphire, *La Jolla Inst.*
Joachim Saur, *U. zu Köln*
Alexander Schier, *Harvard U.*
Susannah Scott, *UC Santa Barbara*
Anuj Shah, *U. of Chicago*
Vladimir Shalaev, *Purdue U.*
Jie Shan, *Cornell U.*
Jay Shendure, *U. of Wash.*
Steve Sherwood, *U. of New South Wales*
Ken Shirasu, *RIKEN CSRS*
Robert Siliciano, *JHU School of Med.*
Emma Slack, *ETH Zürich & U. of Oxford*
Richard Smith, *UNC* (**S**)
Ivan Soltesz, *Stanford U.*
John Speakman, *U. of Aberdeen*
Allan C. Spradling, *Carnegie Institution for Sci.*
V. S. Subrahmanian, *Northwestern U.*
Sandip Sukhtankar, *U. of Virginia*
Tavneet Suri, *MIT*
Naomi Tague, *UC Santa Barbara*
A. Alec Talin, *Sandia Natl. Labs*
Patrick Tan, *Duke-NUS Med. School*
Sarah Teichmann, *Wellcome Sanger Inst.*
Dörthe Tetzlaff, *Leibniz Institute of Freshwater Ecology and Inland Fisheries*
Amanda Thomas, *UC Davis*
Rocio Titiunik, *Princeton U.*
Shubha Tole, *Tata Inst. of Fundamental Res.*
Maria-Elena Torres Padilla, *Helmholtz Zentrum München*
Kimani Toussaint, *Brown U.*
Barbara Treutlein, *ETH Zürich*
Li-Huei Tsai, *MIT*
Jason Tylianakis, *U. of Canterbury*
Matthew Vander Heiden, *MIT*
Jo Van Ginderachter, *VIB, U. of Ghent*
Ivo Vankelecom, *KU Leuven*
Henrique Veiga-Fernandes, *Champalimaud Fdn.*
Elizabeth Villa, *UC San Diego*
Bert Vogelstein, *Johns Hopkins U.*
David Wallach, *Weizmann Inst.*
Jane-Ling Wang, *UC Davis* (**S**)
Jessica Ware, *Amer. Mus. of Natural Hist.*
David Waxman, *Fudan U.*
Alex Webb, *U. of Cambridge*
Chris Wikle, *U. of Missouri* (**S**)
Ian A. Wilson, *Scripps Res.* (**S**)
Marjorie Weber, *U. of Michigan*
Sylvia Wirth, *ISC Marc Jeanneroд*
Hao Wu, *Harvard U.*
Amir Yacoby, *Harvard U.*
Benjamin Youngblood, *St. Jude*
Kenneth Zaret, *UPenn School of Med.*
Lidong Zhao, *Beihang U.*
Bing Zhu, *Inst. of Biophysics, CAS*
Xiaowei Zhuang, *Harvard U.*
Maria Zuber, *MIT*

A megadam test for China and South Asia

Rafael J. P. Schmitt and **Brian Eyler**

China has begun construction on what may become the world's most ambitious effort to harness mighty rivers to generate electricity. The 60-gigawatt Lower Yarlung Tsangpo Hydropower Project portends a new frontier in renewable energy but also reopens long-standing questions about managing rivers that cross national borders and the unintended impacts of hydropower megaprojects on people and ecosystems depending on rivers.

In the remote southeastern corner of Tibet, the Yarlung Tsangpo River carves one of the world's deepest canyons before emerging in India as the Brahmaputra River. Here, vast flows of water and sediment descend from the Tibetan Plateau to sustain ecosystems and livelihoods across its floodplains in India and Bangladesh. In this environment, the project is designed to divert up to 3000 cubic meters of water per second through tunnels that cut through the Himalayan bedrock and several underground power stations, exploiting a vertical drop of more than 2000 m. The water will be returned downstream of the canyon and a few kilometers before the China-India border. The unmatched combination of high flow and vertical drop will enable the generation of up to 300 terawatt-hours of electricity annually, three times the output of the world's largest hydropower project, the Three Gorges Dam in central China. This engineering endeavor could thus benefit China's economy and global climate targets alike.

Hydropower is critical for China's clean energy transition. China leads the installation of wind and solar photovoltaics worldwide, but their variable output poses persistent challenges to the electrical grid. Hydropower can instead satisfy a steady baseload and has the capacity to quickly ramp up to meet peak demands. With an output comparable to that of the entire electrical generation of the United Kingdom or Spain, the new project could provide China's grid operators with a backstop to reliably deliver low-carbon electricity.

However, firming up China's energy transition comes with environmental and geopolitical trade-offs. The Brahmaputra river system is among the most dynamic on Earth, with estimates indicating that 300 to 400 million tons of sediment, around 40% of the Brahmaputra's total sediment, originate within or just downstream of the Yarlung Tsangpo Canyon. Altering river flows and trapping some of the river's sediment could affect the processes that sustain communities and ecosystems far downstream. In other transboundary rivers, China has promoted dams as mutually beneficial, providing hydropower for China and "flow regulation" for downstream countries. Yet, the natural pulse of rivers is critical for maintaining ecosystems, as exemplified by the impact of dam projects in the Mekong River, where upstream dams trap sediments, reduce life-giving flood peaks, and drown downstream forests with increased dry-season flows. In addition, the power generated by the Lower Yarlung Tsangpo Hydropower Project will be carried away to China's sprawling industrial centers, while local Tibetan communities might face resettlement and construction-related impacts.

Details of the Lower Yarlung Tsangpo project remain scarce, and official statements follow a familiar pattern of emphasizing hydropower's benefits while offering little acknowledgment of potential harm. The project is often framed as a "run-of-river," implying no storage reservoirs that trap sediment, immediate return of turbined water, and thus minimal disruption to the river. But this notion obscures that the project will divert a large share of the river's flow, partially dewatering nearly 200 km of China's Yarlung Tsangpo Canyon. Moreover, at least one sizable reservoir seems to be part of the project, designed to buffer the river's variable discharge and to help realize the project's full generating potential.

...opacity risks undermining trust and regional cooperation.

Given the sheer size of the Brahmaputra River with its multiple sources of water and sediment, the project's impacts might ultimately prove modest compared with its climate contributions. Still, little is known about the analyses that must have preceded construction. Engineers must have assessed flow and sediment regimes and evaluated how climate change affects future dam operations. They also would have considered hazards, from earthquakes as well as from mountains and glaciers that crumble as they thaw in a warming climate, and designed release rules to sustain downstream ecosystems. Without disclosure of any engineering plans and environmental assessments, downstream countries, India and Bangladesh, are left uncertain about the effects. In a region already marked by political sensitivity, this opacity risks undermining trust and regional cooperation.

Transparent environmental assessments, data sharing during construction and operation, and cooperative governance are essential to ensure that China's energy ambitions do not come at the expense of India and Bangladesh. □

Rafael J. P. Schmitt is an assistant professor in the Environmental Studies Program at the University of California Santa Barbara, Santa Barbara, CA, USA and a nonresident fellow at the Stimson Center, Washington, DC, USA. rschmitt@ucsb.edu **Brian Eyler** is director of the Southeast Asia Program and the Energy, Water, and Sustainability Program at the Stimson Center, Washington, DC, USA. beyler@stimson.org

10.1126/science.aed9275

PHOTO: BRETT COMER/*HOUSTON CHRONICLE* VIA GETTY IMAGES

CLIMATE CHANGE

High-resolution climate model forecasts a wet future

With details as fine as short-term weather forecasts, model achieves newfound accuracy **PAUL VOOSEN**

In 2019, Tropical Storm Imelda inundated Patton Village, Texas. Downpours will be more common along the Gulf Coast, according to a new, detailed climate model.

For all their usefulness in forecasting global warming, climate models tend to paint the future in the broad strokes of an Impressionist artist. This is by necessity: To simulate hundreds of years in a manageable amount of computer time, the models divide the atmosphere into the equivalent of coarse pixels, 100 kilometers across, before solving the equations of fluid dynamics for each one. But the coarseness leads to inaccuracies in the predictions, especially when it comes to patchy phenomena such as heat waves and downpours, which are heavily influenced by what happens at a finer scale.

Now, a new high-resolution modeling project called MESACLIP, run at great computational expense over the past 5 years, is putting Earth's future into sharper focus by simulating the churning of the atmosphere and ocean at a level of detail similar to the scale of weather forecasts. The project reveals heightened risks for regions like the Gulf Coast and coastal California, where extreme rainfall could occur far more often than traditionally projected. The trends, published this week in *Nature Geoscience*, show the benefit of high-resolution models, which better capture shifts in wind patterns that lead to the downpours.

"It's becoming clear now that the [traditional] models are not producing the true impacts of climate change," says Doug Smith, a climate scientist at the United Kingdom's Met Office who has warned that gaps in forecasting wind patterns could lead to surprises. MESACLIP could start to close those gaps, he adds. "Their results are extremely interesting. They're starting to verify what we're thinking."

MESACLIP divides the atmosphere into 25-kilometer boxes and the upper layer of the ocean into a 10-kilometer grid. Resolution that fine is not new. But earlier efforts tended to focus on a limited region or a limited amount of time, just years or decades into the future, and they usually repeated the computation-heavy runs just a few times. MESACLIP distinguished itself by running global simulations that began in 1900 and looked ahead to 2100 for multiple greenhouse gas emission scenarios. For several of those scenarios, it repeated the simulations 10 times with slightly different initial conditions, to create an "ensemble" forecast that better captures natural variations.

The end result, the product of 900 days of computing time on machines including Derecho, the newest supercomputer at the National Center for Atmospheric Research (NCAR), was 4500 years of simulation that produced 6 petabytes of data. That feat will be hard to match, says Jennifer Kay, an atmospheric scientist at the University of Colorado Boulder. "High resolution is a hard argument still because it's so expensive."

MESACLIP does a better job than most other simulations at re-creating the changes the world has seen over

the past century. The results match the historic records of ocean and air temperature, which many climate models have long struggled to do. They also better capture cold tongues of upwelling water and swirling eddies in the ocean, which are thought to play an important role in modulating wind patterns. And they mimic the extreme rainfall events observed today far more accurately. "We're right for the right reasons," says Ping Chang, an oceanographer at Texas A&M University who helped lead the effort.

That fidelity in reproducing the past gives MESACLIP scientists more confidence in the model's future predictions—and some of them are alarming. For a pessimistic scenario, in which carbon emissions peak in 2080, daily extreme precipitation over land could increase by 37% by 2100. Warmer air holds more moisture, but that trend can't fully explain the soaking. Much of the increase, the team found, was driven by shifts in wind patterns that created chains of severe thunderstorms hundreds of kilometers long, which traditional models fail to capture, Chang says.

MESACLIP also re-created hurricanes and the long ocean-fed cloud bands called atmospheric rivers. The results could bolster efforts to attribute these extreme weather events to global warming, says Davide Faranda, a climate scientist at the Pierre-Simon Laplace Institute. "I think we have to go for this kind of scale," he says.

Projections of regional climate change should also benefit. Those projections have often relied on high-resolution models applied to relatively small regions—an area the size of Europe, or Texas. They, too, suggested the future will bring more extreme rainfall. But their forecasts faced skepticism because the models were fed information at their boundaries from the coarser global models, says Flavio Lehner, a climate scientist at Cornell University. "This is different."

The impetus for MESACLIP came nearly a decade ago, when Chang wanted to explore how ocean eddies could influence the development of atmospheric rivers. Early on, he and his colleagues decided to use a variant of the first version of the Community Earth System Model (CESM) developed at NCAR. The CESM variant had low computational demands, which enabled Chang and his colleagues to run it at much higher resolution, bringing in colleagues from China who had access to spare time on Chinese supercomputers.

But after a few years and promising first results, Texas A&M terminated the project because of national security concerns, cutting off Chang's Chinese collaborators. So Chang and his fellow lead, Gokhan Danabasoglu, an oceanographer at NCAR, turned to the Gulf Research Program, funded by BP after the *Deepwater Horizon* oil spill and operated by the National Academies of Sciences, Engineering, and Medicine. The program wanted high-resolution simulations to predict sea-level rise along the Gulf Coast, and the grant paid for the huge amounts of computing time that MESACLIP required.

Other climate scientists are lining up for the project's data, despite the challenges posed by the sheer size of the data set. They are eager to explore other lessons about Earth's future that may lurk within it. For example, unlike regular climate models, several runs of MESACLIP have reproduced a puzzling cooling observed in the Southern Ocean and eastern Pacific Ocean over the past few decades. The model suggests it is tied to the ozone hole above Antarctica, which cooled the stratosphere and intensified the howling winds around the Southern Ocean. The resulting ocean cooling could ultimately extend all the way to the tropics.

The model also seems to better capture the rapid warming of the Arctic, probably because it properly renders flows of warm water through the Bering Strait, the critical chokepoint between the Pacific and Arctic oceans, Chang says. And it delivers reassuring news about the Atlantic Meridional Overturning Circulation, the conveyor belt of currents that warm Europe and sequester carbon into the abyss, which some lower resolution models forecast could collapse as the world warms. MESACLIP suggests the conveyor belt is more resilient, Danabasoglu says.

The results are so promising that NCAR has now made it a priority to run its newest and third version of its flagship model, CESM3, at similarly high resolutions. But Danabasoglu says it is crucial to replicate runs at this resolution with the climate models developed by other centers. Only then will he and his colleagues start to know whether their improved forecast is a one-off anomaly—or reality. □

DEMOGRAPHY

Make the census voluntary? Bad idea, say statisticians

Pending bills in U.S. Congress could degrade data from national surveys

JEFFREY MERVIS

Representative Greg Steube (R–FL) appears to understand why local businesses, school officials, social service agencies, and others might want statistics about housing, health, and employment in his area. His official website helpfully includes a link to demographic data from the annual American Community Survey (ACS) conducted by the U.S. Census Bureau.

But in July, Steube introduced legislation that would undermine the accuracy of those data. Demographers say it's part of a broader assault by congressional Republicans on the nation's premier statistical agency.

Steube's bill, the Freedom from Government Surveys Act, would remove potential criminal penalties for not answering the seven-page survey, in effect making the ACS voluntary. Senator James Risch (R–ID) introduced an identical bill in the Senate earlier in the year. Language in a pending 2026 spending bill written by the Republican-led U.S. House of Representatives goes further. It would make both the ACS and the 10-year census voluntary, and would also prohibit the agency from reaching out more than once to anyone who doesn't initially respond to any of its more than 100 surveys.

Risch and Steube say they are simply protecting constituents "from unreasonable inquiries … into their private lives" and allowing them to "exercise their right to privacy." But demographers and statisticians warn that the legislation, if enacted, would have a devastating impact on the agency's ability to do its job.

"It's hard to imagine an ACS that is voluntary and allows only two contacts," says Christa Jones, who served as chief of staff to the deputy Census director before taking an early buyout in the spring. "It becomes almost a poll rather than an actual survey."

The ACS, an offshoot of the decennial census, contains roughly 70 questions on housing, employment, education, health, military service, and other demographic details. Each question has been ordered by Congress or requested by an agency to carry out its mission. "But some of them are pretty invasive," says a spokesperson for

Steube, citing questions about when someone begins their daily commute to work and whether they have difficulty getting dressed. The data are used for myriad purposes, including by companies deciding where to build a new factory and officials planning recovery efforts after a natural disaster.

Before the Census Bureau launched the ACS in 2005, Congress asked it to test the idea of making the survey voluntary. But the agency found it would cost more (because it required more follow-up) and would be less accurate (because it was unrepresentative). A subsequent analysis of the results showed a voluntary survey would yield "unacceptable" data affecting nearly two-thirds of the U.S. population—some 208 million people. In contrast, a mandatory ACS yielded problematic numbers for just 15 million people.

Limiting surveys to one follow-up visit would compound the impact, demographers say. Those visits are critical to the decennial census, which spends most of its budget—$13 billion in 2020—on what's called the nonresponse follow-up, in which hundreds of thousands of temporary Census employees go door to door to connect with stragglers. The follow-up limit would have forced the Census Bureau to end the 2020 head count, for example, after only 28% of households had responded.

A voluntary survey is also likely to provide a distorted picture of the population being surveyed. It tends to underreport immigrants; younger, poorer, and rural residents; and those in greater need of government services—as Canada found out in 2011 when it switched to voluntary participation in its 5-year census.

The result was a demographic nightmare, says Rosemary Bender, a former senior administrator at Statistics Canada. "We could only publish data for 75% of our cities—and the percentage was as low as 57% for some provinces." In 2016, Canada reinstated a mandatory census after businesses, local and provincial officials, researchers, and other users complained about the dearth of data.

So far neither the Senate nor the House have taken up Risch's and Steube's bills. But Congress must ultimately approve the 2026 spending bill. Census advocates hope Congress will remove the restrictive language before any bill is enacted. But Mark Calabria, who in July was appointed chief U.S. statistician within the White House Office of Management and Budget, says many lawmakers may not appreciate what is at stake. They tend to ignore statistics if they don't reinforce existing beliefs, says Calabria, who served as chief economist to former Vice President Mike Pence during President Donald Trump's first administration.

"I can tell you that asking, 'What do the data tell us?' is a minority view in this town," Calabria said at a 6 November forum on the value of federal statistics for economic security hosted by the Center for Strategic and International Studies, a think tank. "The average member just doesn't see a lot of value in collecting [federal] data."

But census advocates aren't giving up. They have defused previous Republican attempts to undermine the ACS by showing legislators how much a voluntary ACS would distort data that their local and regional businesses rely on to make decisions, says Howard Fienberg of the Census Project. He and his colleagues are making similar arguments this year.

As Bender notes, "The only reliable [data] source is a mandatory survey, done properly." □

IN FOCUS

Giant telescope gets cozy with Spain

The Thirty Meter Telescope (TMT), one of two U.S.-led projects aiming to build the next generation of giant telescopes, last week announced it is considering a €400 million offer from Spain that would see it abandon its preferred site of Mauna Kea in Hawaii in favor of the Spanish island of La Palma, home to the Roque de los Muchachos Observatory (pictured). Spain made the offer in July, after the U.S. National Science Foundation announced it could not afford to fund the TMT as well as the Giant Magellan Telescope being built in Chile. The project has long held a move to Spain as a backup plan: Since 2014, TMT protesters have blocked efforts to begin construction on Mauna Kea, which many Native Hawaiians consider sacred. The TMT has not officially given up on Hawaii, and the project's executive director, Robert Kirshner, says a final decision may come in the next few months. —Daniel Clery

PHOTO: TMT INTERNATIONAL OBSERVATORY

‘A sigh of relief’: New malaria drug succeeds in clinical trial as existing treatments falter

Ganaplacide, developed by Novartis, eases worries about drug resistance—but hard choices loom on how to use it **KAI KUPFERSCHMIDT**, in Toronto

For almost a quarter-century, malaria treatment has relied on a single group of drugs. Artemisinin-based combination therapies (ACTs), which combine artemisinin or one of its derivatives with a “partner drug,” have been very effective, but *Plasmodium falciparum*, the parasite that causes the most severe form of malaria, is becoming increasingly resistant to artemisinin. Now, the world may have a fresh new weapon against one of its deadliest diseases.

In a large clinical trial in Africa, a new drug combination produced by Novartis and known as KLU156 has proved just as efficacious against malaria as the most widely used ACT. “This is a very important development,” says Dyann Wirth, a malaria researcher at the Harvard T. H. Chan School of Public Health who was not involved in the work. “We’ve been looking for this for a long time.”

But researchers say difficult discussions are ahead about when to start using the new drug: when ACTs really start failing, or earlier, to keep that from happening.

Artemisinin was isolated from a plant, sweet wormwood, that has long been used in traditional Chinese medicine. (Its discovery garnered Chinese pharmacologist Youyou Tu a Nobel Prize in 2015.) The World Health Organization began to recommend ACTs as the front-line treatment for malaria in 2001 in countries facing resistance to older drugs, and globally in 2006.

The new drug has a very different origin story: Its key component, ganaplacide, was developed by researchers at Novartis after screening more than 2 million compounds for antimalaria activity in the lab. Ganaplacide kills malaria parasites very effectively, apparently by interfering with the organism’s ability to make proteins, but exactly how it does so is still unclear, says Thierry Diagana, head of global health biomedical research at Novartis, whose surname inspired the compound’s name.

KLU156 combines ganaplacide with lumefantrine, an older antimalarial that is also the partner drug in the world’s most widely used ACT, known by the brand name Coartem.

The new study enrolled more than 1600 malaria patients across 12 African countries who were treated for 3 days with either KLU156 or Coartem. On 12 November, researchers reported at the annual meeting of the American Society of Tropical Medicine and Hygiene here that 99.2% of those treated with the new combination were cured, compared with 96.7% of patients who received the artemisinin combination.

“Having a new compound that is not artemisinin-based, and that is that effective and safe, is really music to my ears,” study team member Abdoulaye Djimdé, a malaria researcher at the University of Sciences, Techniques, and Technologies of Bamako, said at a press conference. Africa bears the heaviest burden from malaria, with an estimated 246 million cases and 569,000 deaths, most of them children, in 2023.

The drug was also faster than Coartem at killing gametocytes, the sexual stages of the parasite that mosquitoes pick up from human blood when they bite, notes David Fidock, a malaria researcher at Columbia University who was not involved in the study. “I think that is a huge added bonus,” Fidock says, because it may mean KLU156 is better at reducing transmission. But this needs more research.

A Tanzanian child is treated for malaria with an artemisinin-based combination therapy. Malaria parasites are increasingly resistant to such drugs, and scientists have been looking for alternatives.

PHOTO: FREDERIC COURBET/PANOS PICTURES/REDUX

KLU156 performed far worse than Coartem in one respect: Almost 20% of patients who received it reported vomiting, compared with less than 5% in the Coartem group. And more than 10 times as many patients broke off their treatment with the new drug. But that problem was most pronounced in the early stages of the trial, says Cornelis Winnips, malaria program clinical head at Novartis. The bitter-tasting powder needs to be given with a liquid, and over the course of the trial participating sites learned how best to do that, Winnips says. “We think it can be managed by proper instructions quite easily, and we’re also looking at options to mask the taste.”

Worries about the future of ACTs began in 2009, when researchers

found that malaria patients in the border region between Thailand and Cambodia were taking longer to clear infections because parasites were developing resistance to artemisinin. The resistance, conferred by mutations in a protein named K13, soon started to spread across the region. Later, different mutations in K13 emerged and spread in Africa.

ACTs are essentially one-two punches, with the fast-acting artemisinin knocking down the malaria parasites first—and being quickly cleared from the body—and the longer lasting partner drug killing off remaining parasites. The partner drug still works, but with artemisinin resistance spreading, malaria parasites are staying in some patients' bodies longer and at higher numbers, increasing the risk that they will develop resistance to the partner drug as well. "We could lose partner drug efficacy, and then we would have [drug] failure, and that would be catastrophic," Wirth says.

KLU156 may help prevent this scenario from happening. In the trial, it cleared parasites carrying the K13 mutation much faster than Coartem did, which likely reduces the risk of resistance against lumefantrine.

How best to use the new therapy is likely to be hotly debated. One idea is to keep it on the shelf until current treatments no longer work, the way some new antibiotics are kept in reserve. But because lumefantrine is the partner drug in both KLU156 and existing ACTs like Coartem, waiting until resistance to lumefantrine has emerged could put the new drug at a disadvantage from the start. "We really need to protect lumefantrine from failing," says Fitsum Tadesse, a molecular biologist at the Armauer Hansen Research Institute.

One way to reduce that risk is to roll out the drug as soon as possible in areas where K13 mutations are already very common. Or the drugs could be alternated, using ACTs one year and KLU156 the next. KLU156's cost will also affect the strategy. Novartis has not yet announced a price but has said it aims to deliver the drug largely on a not-for-profit basis.

Novartis aims to seek regulatory approval for KLU156 as soon as possible. "We hope to see it within a year, year and a half, in the hands of countries, and eventually patients," says George Jagoe of the nonprofit Medicines for Malaria Venture, which helped develop the drug. "Public health–wise, it's like a sigh of relief." □

IN FOCUS

Mammoths yield oldest RNA yet found

Scientists have sequenced RNA from woolly mammoths preserved for up to 50,000 years in the Siberian permafrost. The molecule, widely thought to be too fragile to survive for long, could open a new window into extinct animals' biology. The researchers analyzed tissue samples from 10 mammoth mummies, using enzymes to convert any surviving RNA molecules into short strands of DNA and reverse-engineering the corresponding RNA sequence. Three mammoth samples yielded ancient RNA, the team reported last week in *Cell*, most of it fragmentary. But the RNA from one mammoth, nicknamed Yuka (pictured), showed extraordinary detail, with sequences containing instructions for building and maintaining muscle tissue. Because RNA contains information about where and when genes are expressed, it can provide insight into the traits of extinct species that cannot be gleaned from DNA alone. —Michael Price

PHOTO: PICHI CHUANG/REUTERS

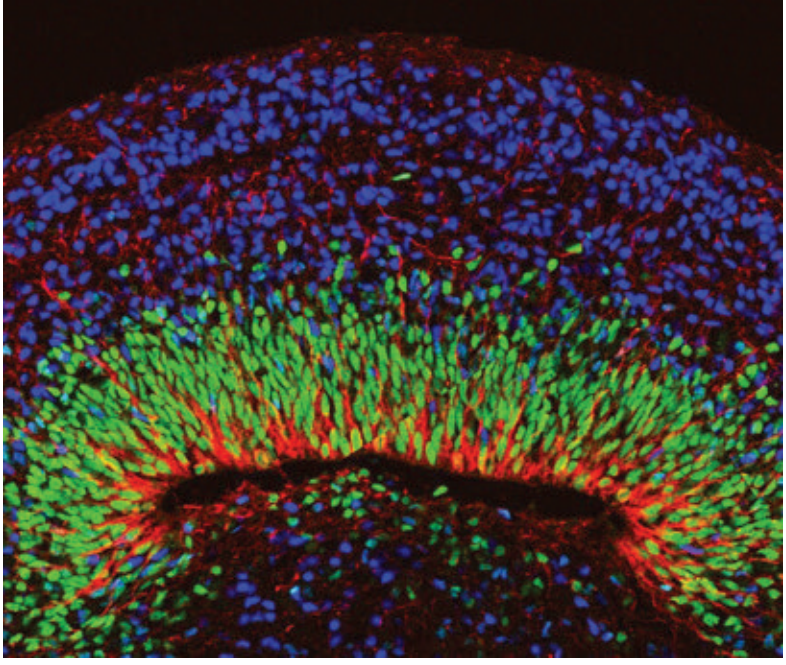

Neural organoids made from human stem cells can mimic the natural layers of the brain and help model diseases.

IMAGE: UNIVERSITY OF CALIFORNIA, LOS ANGELES BROAD STEM CELL RESEARCH CENTER; *NATURE NEUROSCIENCE*

NEUROSCIENCE

As neural organoids advance, ethics races to keep pace

Scientists, ethicists, and patient advocates mull biology's latest provocative technology **MITCH LESLIE**, in Pacific Grove, California

Pop a few human stem cells into culture, provide the right molecular signals, and before long a mock cerebral cortex or a cerebellum knockoff could be floating in the medium. These neural, or brain, organoids, typically just a few millimeters across, are not "brains in a dish," as some journalists have described them. But they are becoming ever more sophisticated and true to life, capturing more of the brain's cellular and structural intricacy. "It's surprising how far this [area] has advanced in the last year," says John Evans, a sociologist at the University of California San Diego who follows the research and public opinions on it. "It's really striking."

That progress has allowed researchers to delve deeper into how the human brain develops, functions, and goes awry in diseases, but it has also sharpened ethical questions. Could these globules of human neurons and other cell types feel pain, exhibit intelligence, become conscious, or even dream—and how would we know whether they did? Is it OK to transplant the blobs into the brains of animals—or into people? Could they challenge what it means to be human?

Last week at the Asilomar Conference Grounds, a rustic former YWCA camp near Monterey, California, a group of scientists, ethicists, patient advocates, and other participants tackled these and other vexing questions. They chose a site with historical resonance—50 years ago a famous meeting here hashed out the first guidelines for genetic engineering. This time around, the attendees didn't aim to set new rules, says conference co-organizer Henry Greely, a law professor at Stanford University who works on bioethics.

Instead, the meeting reviewed the rapidly expanding science of organoids and mulled whether a new organization or an existing body such as the International Society for Stem Cell Research, which has already issued recommendations on editing human embryos and other matters, should track the advances and provide guidance and oversight when necessary. The attendees also discussed ways to involve the public in discussions about organoid ethics, a step they agreed was imperative.

The conference didn't settle on any prescriptions, and its organizers don't thinks organoids will be transplanted into people anytime soon. Alta Charo, professor emerita of law and bioethics at the University of Wisconsin–Madison and one of the conference participants, says researchers still have time to come up with the right approach. "I can't say there's anything we need to do differently" right away, she says.

Some of the work described at the conference underscored the power of these cellular constructs for understanding brain disorders. Neuroscientist Guo-Li Ming of the University of Pennsylvania related how she and colleagues have harnessed organoids to explore how certain viruses harm the brain. They had previously showed that the Zika virus invades progenitor cells in the organoids and inhibits their division, suggesting hampered brain growth could explain why some babies born to mothers infected by the virus have abnormally small heads. This year, she and her team reported in a preprint that the Oropouche virus, a pathogen that is expanding rapidly in Latin America and appears to have the same effect on a baby's head size, also targets brain progenitor cells.

Other work highlighted the ethical questions. By combining organoids to form so-called assembloids, for example, scientists can boost their complexity. Earlier this year, researchers led by Stanford neuroscientist Sergiu Pasca, the conference's other organizer, reported in *Nature* they had produced four neural organoids that represent different parts of the brain and spinal cord. When the scientists linked the organoids in sequence and then chemically prodded one end, the organoid at the opposite end of the chain responded, indicating the structures had formed a sensory pathway that could detect stimuli and share information.

That finding raised the question of whether the assembloids felt pain. They did react to the tongue-scorching chemical that gives chili powder its kick. But Pasca notes that two pathways are necessary to feel pain, one that detects the harmful stimulus and a second that induces the unpleasant sensation. The assembloids lack this second pathway.

Another of Pasca's studies could deliver some of the first practical pay-

> **"It's surprising how far this [area] has advanced.**
>
> **John Evans**
> University of California San Diego

offs of brain organoids. His team is seeking a treatment for Timothy syndrome, a rare genetic disorder in which patients develop often fatal heart arrhythmias along with autism, epilepsy, and other neural symptoms. The cause is a faulty protein that forms part of a channel for letting calcium into cells, and scientists have been growing heart and neural organoids from patient stem cells with the responsible mutation. In a 2024 *Nature* paper, Pasca and colleagues reported they had identified short chains of nucleotides, known as antisense oligonucleotides, that cut levels of the defective protein in the disease-mimicking neural organoids. Because there wasn't an animal model of the syndrome in which to test this potential treatment, the researchers created one by implanting the human organoids into the brains of rats. The antisense oligonucleotides also worked in the rodents, they found.

Experiments that insert human cells into animal brains have sparked unease in the past. And Evans has performed surveys of attitudes toward brain organoid work, which show much of the public views implanting organoids into other species as objectionable because it breaches the boundary between humans and animals. But the desire for new medical treatments may outweigh that concern, or so an oversight body could conclude.

Pasca says early next year his team plans to submit an application to begin a clinical trial seeing whether one of the rodent-tested antisense oligonucleotides helps with the cognitive symptoms of Timothy syndrome. The drug would be the first potential treatment for a psychiatric disease developed through research on neural organoids, he says.

Patients and their families are counting on organoids to yield new therapies, says Alison Singer, president of the Autism Science Foundation, which is funding such research. "I want to light a spark under the scientists." She hopes they'll quickly decide on some ground rules. "These types of conversations are important, but real action has to emerge."

Bioethicist Ben Hurlbut of Arizona State University, on the other hand, worries scientists will shut out other viewpoints. In *Science* earlier this year, he slammed the "science first, ethics second" approach taken by such Asilomar meetings. In his view, after experts convene to evaluate the risks of a particular technology, they typically set standards on their own, presenting them to the public as a fait accompli and foreclosing debate. He attended last week's conference and says that although the participants "are asking the right questions," they also fell into the same trap. "It's a bad habit."

Evans, however, says he found the meeting illuminating and useful. But he acknowledges that ensuring that neural organoids don't cross ethical lines is still very much a work in progress. The big question, he says, is "what we are going to do next, and that's not clear." □

ASTRONOMY

Startup pioneers subscription service for space telescope

Blue Skies Space will sell data from its tiny, low-cost UV observatory **DANIEL CLERY**

This month, a diminutive telescope called Mauve will take to space. Unusually, a government space agency is not the owner. Rather, Mauve was built by a startup company that will sell astronomical data to researchers by subscription. With a 13-centimeter telescope squeezed into a satellite smaller than a microwave oven, Mauve is squarely in the little league of astronomical missions. But its creators hope it will set a precedent.

"It's a new way of doing astronomy," says Emma Whelan, an astronomer at Maynooth University and one of Mauve's first subscribers. Mauve aims to supply optical-ultraviolet observations of tempestuous young stars that larger instruments, such as the oversubscribed Hubble Space Telescope, only offer to the select few. But whether enough researchers will sign up to make Mauve sustainable remains to be seen.

> **Having more assets in space funded through different mechanisms is a win-win.**
>
> **Jon Morse**
> AstronetX

With launch costs falling and telescope components getting cheaper, private missions backed by companies or philanthropies are "definitely something that will be more common in the future, and we'll see how ambitious they can really be," says Jon Morse. The former head of astrophysics at NASA and current president of AstronetX, a for-profit public benefit corporation that provides data services for space science missions, Morse attempted a decade ago to launch a philanthropy-funded telescope to look for exoplanets around nearby stars.

Major flagship missions such as Hubble cost billions of dollars and often take a decade or more to get to the launchpad. Yet even now, 35 years since its launch, demand for time on Hubble exceeds the hours available by six to one. That thirst for data has prompted some academic groups to build their own pint-size space telescopes using CubeSats. These 10-centimeter cubes can be bolted together into cheap spacecraft containing standardized electronics, thrusters, solar arrays, and communication systems. They can hitch rides on rockets carrying larger satellites, giving astronomers a miniature observatory for a few million dollars.

In 2021, for example, the NASA-funded Colorado Ultraviolet Transit Experiment was launched to observe how stellar winds erode the atmospheres of giant exoplanets. The six-unit CubeSat is still going years later. "We demonstrated that you could conduct meaningful scientific investigations in this small package," says principal investigator Kevin France of the University of Colorado Boulder.

Mauve, a 16-unit CubeSat built by Blue Skies Space, a startup spun out of University College London, aims to go a step further, by selling its astronomical data. Because Earth's atmosphere blocks most ultraviolet light, and because demand on Hubble—one of the few space telescopes capable of observing in the UV—is so high, the company saw an opportunity. "We knew about the interest that scientists have in monitoring stars in the UV," says Blue Skies CEO Marcell Tessenyi.

The development of the satellite, which was set to ride into space as soon as 19 November on a SpaceX Falcon 9 rocket, was funded by a €1.2 million grant from the Euro-

Blue Skies Space's Mauve telescope will observe young, tempestuous stars in a package smaller than a microwave oven.

PHOTO: C3S LLC/BLUE SKIES SPACE

pean Union, combined with prelaunch subscriptions, grants, and investors. An annual subscription, which provides researchers with access to all of Mauve's data, costs the rough equivalent of a year's salary for a Ph.D. student. Nine research groups have signed up already, Tessenyi says, and the company hopes more will join once Mauve is in orbit and functioning. If the model works and makes a profit, Blue Skies will put that toward its next project, a 0.5-meter telescope called Twinkle to study exoplanets. "I think there's a little bit of a wait and see" going on, says Vanderbilt University astronomer Keivan Stassun, another early subscriber who plans to study how eruptions of hot plasma from young stars affect the atmospheres of nearby planets.

Whelan signed up after seeing a Blue Skies presentation. "I thought it would be something very exciting to get involved with," she says. She won funding from Research Ireland to pay for the subscription and to hire two Ph.D. students and a postdoc. Whelan aims to study turbulent young stars that vary drastically in brightness, which could confirm theories that such stars brighten when they're accreting matter and dim when clumps of material—embryonic planets—eclipse them. Mauve will let her observe such a system every day for months, tweaking the observations on the fly, unlike a larger telescope, she says. "It's a bit of an adventure, we don't know what we're going to find."

Morse believes more private space missions are coming. Privately owned facilities are already common in ground-based astronomy, he notes. Las Cumbres Observatory, for example, is a nonprofit that runs 25 small, automated telescopes at sites around the world that researchers can pay to use as needed. "We astronomers have been doing it for decades," Morse says. "It's normal and it's not a surprise that this would carry over into space telescopes."

Mass production of communication satellites is making space hardware ever cheaper, and some astronomers are starting to think independently funded space telescopes could move beyond CubeSats. A report last month from the Keck Institute for Space Studies offers a blueprint for a philanthropy-funded effort to design a mini-Hubble with a 1-meter mirror that could be repeatedly built and launched at reasonable cost.

Each iteration of this compact observatory could carry workhorse instruments as well as experimental sensors from academic groups. If the cost of development and launches could be covered by donations, subscriptions and other user fees could pay for operations. Morse, who contributed to the report, says, "Having more assets in space funded through different mechanisms is a win-win, especially in these challenging fiscal times." □

IN OTHER NEWS

U.S. TO LOWER PROTECTION OF STREAMS AND WETLANDS

In a win for farmers and property developers, the U.S. Environmental Protection Agency (EPA) and the U.S. Army Corps of Engineers proposed this week to narrow the scope of environmental protections under the Clean Water Act. The key change is a more limited definition of federally protected "waters of the United States" conforming to a 2023 Supreme Court ruling that EPA's jurisdiction only includes land on which surface water is continuously connected, above ground, to a "relatively permanent" water body that leads to "traditional navigable water." Legal scholars expect the change will leave most nontidal wetlands unprotected (*Science*, 27 September 2024, p. 1414). "This is one of the most significant setbacks to clean water protections in half a century," Betsy Southerland, former director of the Office of Science and Technology in EPA's Office of Water, said in a statement. The draft rule is open for public comment for 45 days. —Erik Stokstad

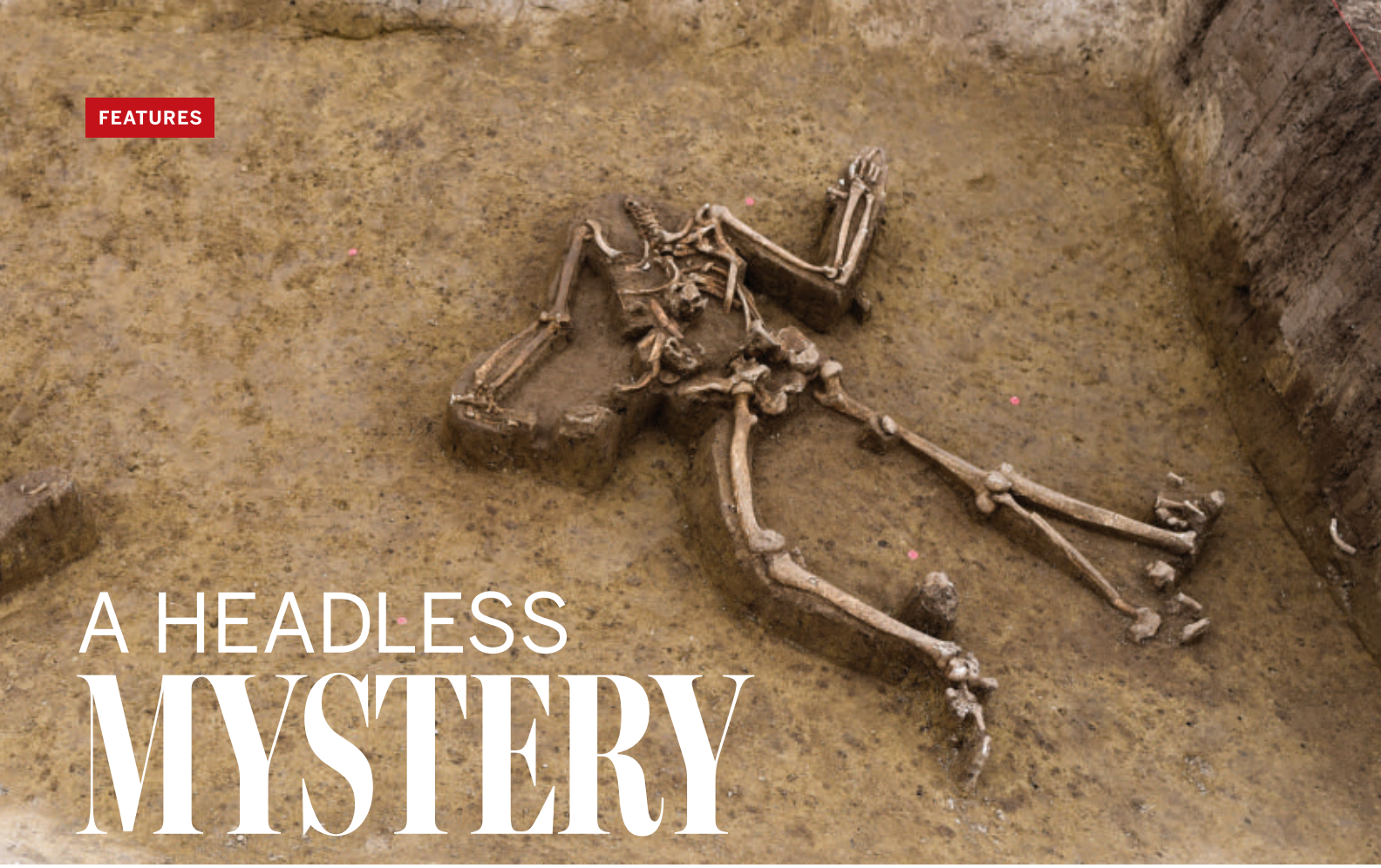

A HEADLESS MYSTERY

Archaeologists find evidence that a wave of mass brutality accompanied the collapse of the first pan-European culture

ANDREW CURRY

In 2017, archaeologists digging in the middle of a Slovak wheat field uncovered four headless skeletons. The burials, in a ditch dug on the edge of a settlement more than 7000 years ago, belonged to one of Europe's first farming communities. Burying people in or near settlements wasn't unusual at the time—but burying them without heads was.

Year after year, the researchers have returned to find more and more headless skeletons on the outskirts of Vráble, a small village 100 kilometers east of Bratislava. "Everywhere we started to dig, we found bones. Everywhere we were sitting or standing, there were bones," says Katharina Fuchs, a biological anthropologist at Kiel University (KU) who has excavated in Vráble every summer since 2021. In the summer of 2022, she and colleagues from KU and Constantine the Philosopher University in Nitra recovered the skeletal remains of 34 people, piled on top of each other two or three deep in a space about the size of a parking spot. With the exception of one child, none of them had heads.

Each year the team expects to reach the mass grave's edge. Instead, it finds more bodies. "Every time we think we have a clue, the site shows differently," Fuchs says. "It's not stopping. We now have a skeleton layer 45 meters long."

Vráble's headless bodies are more than a ghoulish curiosity. They could help answer a decades-old question: What happened to central Europe's first farmers?

Known as the Linear Pottery culture (or LBK, after their German name, Linearbandkeramik), these early agriculturalists were direct descendants of the people who began to domesticate plants and animals in the hills of Anatolia around 9000 B.C.E. By 5500 B.C.E., they had reached today's Hungary. Then they spread westward, farther into Europe. The LBK farmers flourished for more than 400 years, eventually occupying a 1500-kilometer belt of fertile land stretching as far west as the Paris Basin.

Then something went terribly wrong. Vráble and other other mass graves across Europe attest to a wave of brutality around 5000 B.C.E., about the same time as hundreds of LBK settlements across the continent abruptly vanished. In the aftermath, parts of the continent remained empty for centuries. Other settlements transitioned peacefully into something else, with people living in the same place and continuing to farm, but building houses and decorating their ceramics in a different way. "The LBK were the first farmers, the first large pan-European culture, and the first time we see these repeated finds of violence," says paleopathologist Christian Meyer, an independent osteoarchaeologist who has studied human remains from multiple LBK mass graves.

The finds at Vráble and other LBK sites challenge a long-held notion that prehistory was more or less peaceful, with isolated cases of interpersonal violence but no large-scale conflicts or wars. It may also shed light on one of prehistory's great vanishing acts. "It's one of the most interesting questions in history," Fuchs says. "What led to the disappearance of an entire culture?"

A FEW HUNDRED METERS away from a small river, the Vráble site has been productive farmland since the dawn of agriculture in the Neolithic period. Like people all across the LBK, farmers here favored land covered by a type of loose, stone-free soil called loess. Burnt grains in the soil show that at Vráble, they grew early forms of wheat called emmer and einkorn. Piles of cattle, pig, sheep, and goat bones found at the site show meat was on the menu, too.

The bountiful harvest fueled a centurieslong demographic boom. Wherever these pioneers appear, within a few generations "every valley seems to fill up," says Martin Furholt, an archaeologist at KU who leads the work at Vráble.

Perhaps thanks to its rapid expansion, LBK society remained remarkably uniform across an estimated 700,000 square kilometers of Europe, judging from artifacts and, more recently, ancient DNA. Extracted from LBK skeletons, the DNA shows these pioneers were directly descended from early Anatolian farmers, and mostly avoided mingling with local hunter-gatherers they may

In a 7000-year-old mass grave belonging to some of Europe's first farmers, dozens of bodies were buried without their heads (opposite page, top). In 2022, researchers found more than 30 in a space barely 10 meters square (opposite page, bottom). Biological anthropologist Katharina Fuchs has also unearthed individuals buried nearby with their heads attached (left).

PHOTOS: VRÁBLE EXCAVATION TEAM

Europe's first farmers

About 7500 years ago, farmers who traced their ancestry to Anatolia began spreading across Europe, clearing forests and founding small settlements. Known as the Linear Pottery culture (LBK), they were stunningly successful: In the space of just a few centuries, they expanded across a 1500-kilometer belt of fertile, easily tilled land.

Uneasy neighbors

Excavations and ground-penetrating radar have shown that the Vráble settlement had three distinct neighborhoods. Centuries after the settlement was founded, one of the neighborhoods was walled off from the others.

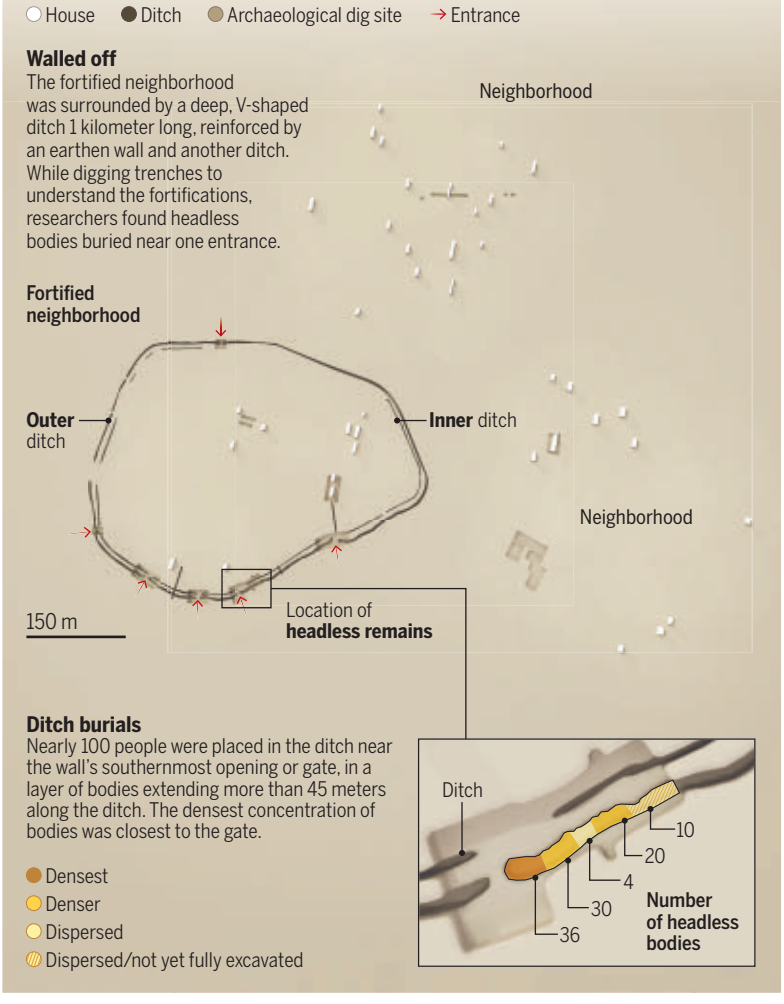

have encountered as they spread across Europe.

When well-preserved, LBK settlements and cemeteries are easy for modern-day archaeologists to identify. Postholes found by the thousands across Europe suggest these farmers built wooden longhouses with wattle-and-daub walls big enough to house an extended family and their livestock. They typically buried their dead lying on their left sides in a fetal position, and fired pottery decorated with distinctive incised lines.

Archaeologists long believed the LBK era was a sort of early Eden. There are few signs of inequality or competition for resources. People lived on small family farms without social hierarchy or accumulated wealth, using stone axes to clear forests and wood or bone implements to plow fields. The sword wouldn't be invented for 2000 years. "When you see an agrarian society with no specialized weapons," Furholt says, "it's easy to imagine it's peaceful."

THAT IDYLLIC VISION began to crumble in the 1980s, when archaeologists in southern Germany excavated a grave containing the skeletons of 34 people, most of them children. The victims' fractured skulls showed many had been killed with blows to the head. Now known as the Talheim Death Pit, the grave was radiocarbon dated to 5000 B.C.E., coinciding with the very end of the LBK period.

In the decades since, archaeologists have found many more mass graves across Europe, all dating to roughly the same time. Many, like Talheim, looked at first like the results of small-scale raiding or local conflicts.

But as more burials emerged, those easy explanations faded. If conflict was a regular part of LBK life, the graves should appear throughout the culture's 400-year span instead of only at the very end. And each new LBK massacre site seems to have its own distinct character and particular details that suggest some mysterious constellation of brutal practices, not competition for land or mates. "What we see is different from anything we see before. It's an indication of an end phase, where people turn to rituals and odd beliefs," says Leibniz Center for Archaeology archaeologist Detlef Gronenborn. "Then it breaks out in an orgy of violence. Then it stops, but it's too late."

At a site in southwestern Germany called Kilianstädten, for example, the 26 victims included 10 children under age 6. As at Talheim, many of the skulls had been smashed, but the assailants had systematically shattered their targets' shins, too, either as a form of torture or as a symbolic postmortem maiming. "It was a statement by the perpetrators," says Meyer, who examined the bones. "They did this on purpose."

Another site that Meyer helped excavate in Germany revealed violence reminiscent of the Neolithic version of gangland killings. Eight of the nine people tossed in the mass grave were young men. They had fractures on the backs of their head, invariably on the right-hand side—suggesting they had been forced to kneel for a killing blow from behind. "These people were held prisoner and executed," Meyer says.

At a site in Austria called Asparn-Schletz, archaeologists found the remains of about 200 women, children, and men of all ages in a deep ditch outside a large LBK settlement. At first it looked as though an entire village had been slaughtered at once, presumably wiped out by rivals in an early act of organized warfare. In that

CREDITS: (GRAPHICS, TOP TO BOTTOM) V. PENNEY/*SCIENCE*; A. MASTIN/*SCIENCE*; (DATA, TOP TO BOTTOM) J. LÜNING *ET AL.*, *GERMANIA*, **67**, 2 (1989); VRÁBLE EXCAVATION TEAM

The excavation site outside Vráble, Slovakia, has been productive farmland for millennia. Early farmers planted grains such as emmer and einkorn and raised pigs, sheep, cows, and goats.

PHOTO: VRÁBLE EXCAVATION TEAM

scenario, the dead should include many biological relatives. But a study of ancient DNA from Asparn-Schletz published this year showed only two of the people in the ditch were close genetic kin, indicating something far stranger had occurred there.

Perhaps the most bizarre LBK massacre site is a grim spot called Herxheim, now mostly buried beneath an industrial park near Germany's border with France. The sheer scale of the slaughter is stunning. Between 1996 and 2010, archaeologists excavated more than 80,000 pieces of human bone, including the skull caps of more than 500 people, mostly older children and young adults. Cut marks on the bones indicate they were purposefully dismembered, and shards of pottery and animal bones from feasts are interspersed with the remains. "People at Herxheim definitely didn't die normal deaths," says Andrea Zeeb-Lanz, an archaeologist at the Rhineland-Palatinate General Directorate for Cultural Heritage who directs research on the site. "These are special activities, not just villages on the warpath."

Isotopes of strontium, oxygen, and nitrogen from the teeth, which can reveal geographic origin, show the victims weren't local. Zeeb-Lanz is convinced they were brought to the site and killed as part of ceremonies that lasted for weeks and included feasting, digging the deep ditches, and even firing high-quality pottery destined to be thrown in the pits days later, along with smashed human bone. "It's not done in a ritual fury," she says. "It's a processing which is done with great care."

AT VRÁBLE, archaeologists hope to trace the forces that drove these curious acts of violence. Sending a drone into the clear sky, KU archaeologist Nils Müller-Scheeßel points out where ground-penetrating radar surveys found three massive "neighborhoods" occupied simultaneously at Vráble between 5250 and 5050 B.C.E. Each one is 400 meters across and had 15 to 20 longhouses at any given time, each housing an extended family. Together they amounted to a metropolis by LBK standards, with up to 1000 inhabitants. But each neighborhood maintained its own identity. Different concentrations of animal bones suggest the three neighborhoods specialized in raising sheep, pigs, and cattle, respectively. They even featured slightly different pottery styles and tools.

Previous excavations had shown that around 5100 B.C.E., more than 2 centuries after Vráble was founded, a deep, V-shaped ditch was dug around one of the three neighborhoods and reinforced with an earthen berm. A second, inner ditch completed the structure. The effort required would have been immense. "A double ditch 1.3 kilometers long, with the tools they had back then? It's crazy," Fuchs says.

Müller-Scheeßel thinks the village's size makes the earthworks unlikely to be fortifications against some outside threat. "It's the largest settlement in the region, so you'd need an army to attack them," he says.

Instead, the ditch may be a sign that social relationships were splintering inside Vráble itself. The wall had five gates, all facing away from the settlement's other two neighborhoods. "The entrances cut off other neighborhoods," Furholt says. "It's quite a hostile act." He notes that the three neighborhoods had been distinctive from the start. "We have very individual farms, with strong autonomy, living together as a village," Furholt

Grim reapers

Over the past century, archaeologists have excavated hundreds of Linear Pottery culture (LBK) settlements, tracing the rapid expansion and often violent end of these first European farmers. Population numbers at Vráble, one of the largest known settlements, followed the same overall pattern.

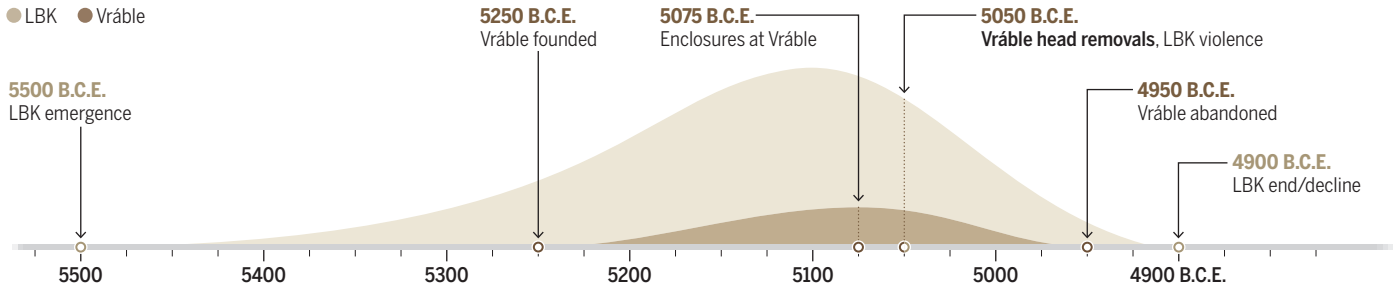

says. "You could see how this is a setup that falls apart at some point."

Then came the killings and decapitations. The bodies were all thrown in the ditch around one of the gates and along the adjacent ditch. And within a few decades, radiocarbon dating shows, the surrounding settlement emptied out and was never reoccupied. "It lasted another one or two generations at most," Furholt says. "I can see why all these people without heads wouldn't be good for a community, and might be a cause for abandonment."

BY LATE AUGUST, the team at Vráble has been in the field for 5 weeks, working under a white party tent that sheltered them from both blazing sunshine and rain that turned the surrounding fields to gluey mud. Standing on the edge of a trench 2 meters deep and about 10 meters long, Müller-Scheeßel gestures at the intermingled bones: "It just doesn't end."

So far, the team has identified the headless skeletons of at least 85 men, women, and children. In six seasons of excavation, they've found just one head. "Why did they cut off the heads?" Meyer asks. "And what did they do with them?"

The team is now tracing how the massacre unfolded. On one of the excavation's last days, Fuchs and a team of students crouch among bones they've carefully uncovered over the past few weeks, some wearing only socks to avoid damaging the fragile skeletons. They carefully clean soil away from individual bones with brushes and trowels. Exposed for the first time in 7000 years, the remains must be kept moist using spray bottles or they'll start to crumble. Each individual is placed in a paper bag and stowed in a labeled box. Later, the team will be able to reconstruct the grave digitally, using the hundreds of photos taken during the excavation to locate each body in the pit.

When they found the first headless skeletons, Fuchs and her colleagues weren't sure whether the bodies had been deliberately decapitated. Neolithic societies sometimes disinterred people and rearranged their bones long after death. Perhaps, they thought, the bodies were allowed to decay after dying naturally, and then the loosened skulls were removed as part of some unknown ritual.

But as more bodies have emerged, it's become obvious they were deliberately removed around the time of death. The skeletons are mostly intact and in anatomical order, down to small bones like fingers and toes—a sign the bodies were not left out for scavengers to pick at, or buried and then moved again after decaying. "They seem to have been covered quite fast," Furholt says. "This is one mass deposition event, or several in a short period." And in the Stone Age equivalent of a smoking gun, many of the neck vertebrae bear cut marks. Dozens of people were decapitated using just flint or obsidian knives the length of a finger, in what must have been a messy, strenuous operation.

Over the next 3 years, osteologists will examine each bone for clues to how old the people in the pit were when they died, their sex, and any signs of prior trauma or injury. Forensic examination of any cut marks, meanwhile, could indicate whether they were the handiwork of multiple people or a single perpetrator. "Something very special happened here," Fuchs says. "Understanding how they did it could tell us who did it and why they did it."

For the researchers, "not having the skull is very difficult," Fuchs says. To suss out a skeleton's geographic origin, they need isotopes in teeth. Ancient DNA, which can point to kinship and deeper ancestry, is best preserved in teeth and a bone in the inner ear. And estimates for bodies' ages at death are often based on the way the skull knits together over time, or whether wisdom teeth have emerged.

Still, analysis of the bones in the field has yielded some impressions. Both men and women were buried in the trench—along with teens—but young children are underrepresented. And so far, the bones of the people buried appear robust, suggesting a highly active lifestyle.

The Vráble burial has other odd features, such as the fist-size river pebbles found scattered among the

The Linear Pottery culture is easily recognized by its distinctively patterned pots.

CREDITS: (GRAPHIC) A. MASTIN/*SCIENCE*; (PHOTO) GDKE RHINELAND-PALATINATE/FABIAN HAACK

Signs of violence appear across Europe around 5000 B.C.E. At a site called Herxheim in western Germany, researchers found the smashed skeletons of nearly 1000 people, including about 500 carefully removed skull caps.

PHOTO: GDKE RHINELAND-PALATINATE/FABIAN HAACK

bones. The site's loess soil is free of rocks, so the pebbles must have been brought from the nearby river and tossed in on purpose. Other artifacts—including a dozen human teeth with holes drilled through them, likely worn as necklaces—and fragments of pottery dot the bottom of the ditch.

ALL ARE CLUES to a mystery yet to be solved. Why did violence break out all across the LBK at the same time, and with such lasting consequences? Since the discovery of the Talheim Death Pit, archaeologists have been searching for a convincing explanation. "Are these strange manipulations a reaction to a crisis," Zeeb-Lanz asks, "or an effort not to let a crisis happen?"

Archaeologists often invoke overpopulation and climate change to explain ancient turmoil. But so far, none of the bones from massacre sites have shown evidence of famine or malnutrition. And even if there was a shift in the region's climate, "I'm hesitant to point to climate change as a single driver," says Rick Schulting, an archaeologist at the University of Oxford. "There are all kind of cases where the climate changes and people do not start killing each other in large numbers."

To him the evidence points to "something of a cultural collapse." From a demographic point of view, the LBK was a stunning success story. What started as a small core group of pioneering farmers spread and expanded across vast territories in just a few centuries, a population boom with few parallels in human history. But perhaps that growth was unsustainable. "As LBK people multiply, communication becomes more and more difficult, and society breaks apart," Gronenborn says.

Zeeb-Lanz thinks sites like Herxheim were ways to reinforce cultural connections in an increasingly unfamiliar world, perhaps through human sacrifices or some other Stone Age bonding rites. "We're looking at a change in ideology over a generation or two. Social ideas and cohesion aren't working well," Zeeb-Lanz says. "And ritualistic violence is a very strong way to bring cohesion in a community."

Penny Bickle, an archaeologist at the University of York, suggests a culture accustomed to constant expansion might have simply run out of room. Around 5100 B.C.E., the furious pace of the LBK's territorial expansion slows, then stops, as it reaches the edges of the fertile loess zone. "Maybe the society reaches the limits of the landscape where expansion makes sense. Moving on and making new settlements doesn't work as a social system anymore, so they start to look inwards," Bickle says. "There's a shift in how people are relating to each other."

Whatever its cause, the LBK's end has forced archaeologists to grapple with the fact that human beings have always had the capacity to brutalize others. "It's a basic human thing," Meyer says. "If there are problems, people try to find a scapegoat."

Yet Schulting warns against ignoring the centuries when the LBK was a peaceful, flourishing culture, or the many settlements that transitioned into a different way of life without obvious signs of bloodshed. "Vráble and these other sites show violence is always in the repertoire of human behavior. But that doesn't mean it's inevitable." □

COMMENTARY

Leandra Lagos harvests coca leaves from a farm outside her community of Encuentro in La Convención Province, Peru, on 16 February 2024.

PHOTO: FAISAL TISNÉS

POLICY FORUM

DRUG POLICY

Scientific distinctions between coca and cocaine support policy reform

Ongoing review of international drug policy should correct long-standing, misguided, and harmful conflation

Dawson M. White[1], Ricardo Soberón Garrido[2], Caroline S. Conzelman[3], Wade Davis[4], Claude Guislain[5], Anthony Henman[6], Orlando Adolfo Jara-Muñoz[7], Martin Jelsma[8], Susana Mejía[9], Daniel Montoya-Cataño[9,10], Oscar Alejandro Pérez-Escobar[11], David Alfonso Restrepo[12], Yenny Alejandra Saavedra-Rojas[13], Imika Tariru[14]

The coca bush, a sacred South American crop plant, is classified alongside cocaine and heroin as a Schedule I controlled substance under international law. This scheduling, and the myriad effects of prohibition, have fostered a general perception that coca and its purified alkaloid cocaine are one and the same. Yet this conflation obscures a striking contrast: Whereas cocaine's 165-year history is marked by health risks and social disruption, the use of coca leaf has played a positive role in Andean and Amazonian societies for thousands of years. Studies across the biological and social sciences corroborate coca leaf as a benign, nonaddictive stimulant and a culturally vital plant, profoundly different from its purified derivative. The World Health Organization (WHO)'s Expert Committee on Drug Dependence (ECDD) is now reviewing the health effects of coca (*1*), offering a rare opportunity to correct this misclassification and align international drug policy with scientific evidence and social reality.

Under the 1961 United Nations (UN) Single Convention on Narcotic Drugs, coca crops and their wild relatives are legally treated as Schedule I narcotics and prohibited from use and cultivation. The convention defines "coca" as all members of the genus *Erythroxylum*, a group of around 285 plant species closely related to red mangroves that grow in tropical forests across the globe. This sweeping legal framework criminalizes more than 11 million primarily Indigenous and mixed-Indigenous (mestizo) South American peoples whose lifeways are intertwined with traditional coca farming and use while also restricting scientific research on one of the world's most culturally important and pharmacologically intriguing plant groups. Coca policy has targeted specific peoples and cultural practices, a distinction that enables the engagement of international frameworks such as the UN Declaration on the Rights of Indigenous Peoples (UNDRIP), the International Labour Organization's Indigenous and Tribal Peoples Convention, 1989 (ILO Convention 169), and the Nagoya Protocol to the Convention on Biological Diversity, which affirm Indigenous rights to territory, traditional knowledge, and biocultural heritage.

The ECDD's forthcoming recommendation to the UN Commission on Narcotic Drugs, expected at the end of November 2025, considers five established criteria: chemistry, pharmacology, toxicology, therapeutic and/or traditional use, and epidemiology (*1*). Among these, the criterion of traditional use offers a particularly appropriate and underutilized lens for evaluating coca on its own scientific and cultural terms. We offer a synthesis of scientific evidence and practical considerations to support the descheduling of coca leaf and the implementation of more informed and equitable policy.

ANCIENT ORIGINS, MULTIFACETED USES, AND ENDURING VALUE

Understanding the diversity and geographical distribution of coca, an ancient and complex crop embedded in diverse histories of plant-human interaction, is fundamental to understanding its long traditional use in South America. Coca comprises four distinct taxonomic varieties, each associated with specific regions and cultural histories: Yungas coca (*Erythroxylum coca* var. *coca*) of the eastern Andean foothills of Bolivia and Peru, Amazonian coca (*E. coca* var. *ipadu*), Colombian coca (*Eythroxylum novogranatense* var. *novogranatense*), and Trujillo coca (*E. novogranatense* var. *truxillense*) of northern Peru and western Ecuador, which is the natural flavoring of Coca-Cola (*2*). Each of these taxonomic varieties is, in turn, represented by regional landraces, often with many local names.

Coca is a dynamic and versatile resource. As a mild daily stimulant similar to tea or coffee, chewing coca leaf offers a subtle sense of clarity and well-being, though first-time users often feel nothing at all (*3*). Yet across many cultures, its true uility emerges within ritual and relational contexts grounded in local knowledge systems. Learning when, why, and how to use coca—and when not to—turns it into a medium that reaffirms shared values, worldviews, and the interdependence of self, community, and the wider ecological networks.

In this framework, coca is frequently used in communicative activities. It formalizes community gatherings and serves as a bridge between elders and younger adult generations, with coming of age often marking access to coca—transmitting instructional narratives and reinforcing communal bonds. Through these exchanges, coca sustains the intergenerational transmission of knowledge and collective identity (*4*).

Beyond personal and ceremonial exchange, coca also structures systems of reciprocity and governance. It supports collective labor and mutual obligation through practices such as *ayni*, where coca accompanies agricultural work as both stimulant and symbolic offering. In these settings, coca fosters social cohesion and exchange, organizing relationships of trust, authority, and cooperation. It mediates interactions among people and between communities and their landscapes, linking ecoregions through systems of trade, reciprocity, and shared stewardship (*4*).

The importance of these human-plant relationships is deepened by coca's extraordinary antiquity. Archaeological evidence, including artwork, burial offerings, plant remains, and chewing paraphernalia, confirms coca use across the past five millennia in most regions of its cultivation (*2*). The recent discovery of 8000-year-old *E. novogranatense* leaves in northern Peru (*5*) places coca among the oldest cultivated plants in the Americas, alongside such transformative crops as squash and common bean.

This long history of use is matched by considerable evolutionary complexity. Recent phylogenomic research has shown that the cultivated coca varieties originated from at least two, and likely three, independent domestication events of distinct populations of the wild species *Erythroxylum gracilipes* (*6*). This suggests that different Holocene societies across South America independently recognized coca's value and adapted it to their ecological and cultural needs. Other plants known to have been domesticated multiple times include amaranth, barley, common bean, and rice, plants that, like coca, rank among humanity's most enduring and useful crops.

Coca's repeated domestications and deep timescale of use as a daily stimulant, medicine, and ritual element, reflected in its ongoing role across more than 100 living cultures (comunidades.khokaproject.com), now position interdisciplinary ethnobotanical research to investigate the distinct evolutionary and cultural trajectories of each crop variety, with pharmacology offering especially revealing insights into the plant's uses and health effects.

A COMPLEX CHEMICAL AND PHARMACOLOGICAL PROFILE

Cocaine is the most abundant alkaloid in coca leaves, typically making up 0.2 to 0.8% of dry weight. Concentrations vary with environmental conditions (up to 1.2% in experimental manipulations; see table S1) and among varieties, with Amazonian coca generally producing less cocaine than the three Andean varieties. The wild progenitor, *E. gracilipes*, is also within this range (0.1 to 0.3%; table S1), pointing the role of cocaine as a chemical defense against herbivory. Sixty other wild *Erythroxylum* species have been found to not produce cocaine, and another 25 to 30 have very low concentrations (<0.001%), but most of these assays were performed on degraded herbarium specimens and not recently collected tissues. The "new" coca cultigens cultivated for cocaine production in Colombia and Mexico have not been shown to exceed the range of concentrations observed in traditional coca varieties (table S1), despite selective pressures to increase yields. Yet despite such lack of support by available data, the ECDD Critical Review Report states the common misconception that new cultigens have been bred for higher leaf cocaine content (*7*).

Beyond cocaine, coca's pharmacological activity is shaped by more than 30 additional alkaloids, plus flavonoids and other bioactive compounds. This chemical diversity varies both within and among the four taxonomic varieties (*8*). Coca's phytochemical complexity helps explain why chewing the leaves produces subtle yet effective stimulant effects, supporting mental clarity and physical stamina without the pronounced euphoria or overstimulation associated with purified cocaine (*9*). Traditional chewing results in slow absorption and markedly lower plasma cocaine concentrations than purified cocaine (*10*), with clinical and ethnographic studies reporting no evidence of dependence or long-term harm among habitual users (*3*, *10*). Coca chewing produces mild stimulant, antihypertensive, vasodilatory, and metabolic effects—such as transient increases in blood glucose and free fatty acids—that may support sustained physical activity. The leaf also exhibits antioxidant, anti-inflammatory, and antimicrobial properties (*7*). Among Aymara communities in Bolivia, preferences for regional coca cultigens are not correlated with variation in cocaine content but may reflect differences in texture and flavor that are possibly influenced by flavonoids or

essential oils. Unlike other chewed, psychoactive plants such as tobacco, studies of coca chewing show no consistent evidence of carcinogenic potential. Some oral irritation and cytotoxic changes have been observed, perhaps owing to the use of alkaline additives while chewing, as detailed in the ECDD Critical Review Report (*7*).

Beyond its value as a stimulant, coca has been used to treat gastrointestinal discomfort, motion sickness, toothache, oral lesions, and altitude sickness, as well as to suppress hunger and fatigue (*3*, *9*). It has also been suggested for testing as a substitute for caffeine and, in therapeutic contexts, as a mild antidepressant and potential aid in the treatment of cocaine- and amphetamine-use disorders. In addition, it shows promise for regulating blood sugar in diabetes and supporting liver function (*3*, *7*). Although its nutritional contribution remains uncertain, coca contains a full protein profile, along with calcium, potassium, phosphorus, iron, and vitamins B1, B2, C, and E (*11*).

Descheduling coca would correct a long-standing scientific and legal misclassification...

Taken together, the chemical, therapeutic, and nutritional properties of coca, combined with its demonstrated safety and absence of harm in traditional and modern contexts, help explain its parallel evolution and enduring cultural importance throughout South America, even as global policy continues to criminalize its use and undermine the communities that depend on it.

SUPPORTING SOCIAL JUSTICE AND HUMAN RIGHTS

International coca prohibition has long conflicted with the cultural autonomy and territorial rights of coca-growing peoples—Indigenous, mestizo, and rural communities—across the Andes and Amazon. The 1961 UN Single Convention on Narcotic Drugs effectively criminalized their traditional coca practices, which are rooted in health, labor, ritual, and governance, and has facilitated decades of marginalization and colonial exploitation (*12*). In Ecuador, colonial suppression and modern drug-policy enforcement have effectively extinguished at least five millennia of coca biocultural practices across the Amazon, Andean highlands, and coastal regions [see (*2*)]. These plant-human interactions are characterized today by escalating levels of narcotrafficking and associated violence.

Coca's international prohibition under the 1961 UN Single Convention on Narcotic Drugs stems from the WHO's 1952 assessment of its health effects—a process marked by racial bias, scientific disregard, and the exclusion of local knowledge—in which coca was wrongly blamed for poverty, malnutrition, and even violence in Andean communities (*1*, *12*). The persistence of this flawed judgment reflects more than error: It was reinforced by the institutional momentum of the international drug-control system, the entrenched conflation of coca with cocaine, and the oft-cited "ease of convertibility" of coca leaves into cocaine. These arguments have sustained prohibition even as advocacy, ethnography, and science have repeatedly exposed the biases and inaccuracies of the WHO's consensus through the decades, and even as Andean nations, beginning in the 1950s, established rules permitting Indigenous coca use under national law. The 1988 UN Convention against Illicit Traffic in Narcotic Drugs and Psychotropic Substances acknowledged respect for traditional uses, providing a back door for Peru and Bolivia to evade mandates for eradication.

The present ECDD Critical Review process (*1*) offers a historic opportunity to finally and formally recommend the descheduling of the coca leaf. Such action would lay the foundation for sound, evidence-based policy centered on coca-growing communities. This review was catalyzed by decades of advocacy, led largely by movements by Aymara and Quechua peoples in Peru and Bolivia, who represent the vast majority of South America's coca-using population. These Andean groups have long treated coca as both a commodity, which has been integrated into trade and labor systems since at least the 16th century (*13*), and as a sacred plant governed by systems of reciprocity, protocol, and meaning. Their call for descheduling centers on dissociating coca with cocaine and reclaiming cultural sovereignty, thereby liberating the sacred leaf from the black market and restoring its rightful role as a symbol of heritage, health, and identity (*14*).

Yet no single perspective defines the way forward if coca is to be successfully descheduled. Views on coca reform are mostly positive but reflect distinct histories and complex legacies of armed conflict, political fragmentation, and the harms of the illicit economy. Among some Amazonian communities who actively or have only recently faced the social and territorial impacts of illicit coca production, concerns center on tensions between protecting coca's sacred uses and opening it to commercial markets. For them, governance over coca must include not only who cultivates, transforms, and sells the plant but also who teaches its proper use, and on what epistemological grounds. For instance, some view the mixing of coca with sugars, flours, and fats as harmful and culturally inappropriate, warning that such combinations cause illness, dependency, and violate traditional values–theories that are supported by their own evidence base rooted in observation and cultural practice.

Yet there is broad agreement that the use and sharing of coca should be accompanied by instruction based in ancestral knowledge systems. Policy must create space for respectful, intercultural dialogue and agreements that uphold traditional governance. Safeguards will be needed to ensure that market pressures do not incentivize smallholders to abandon cultural practices or divert household coca away from its vital social and ceremonial roles. Effective regulation must affirm the plant's plural uses and the rights of the diverse communities who steward it.

Social organization and existing legal frameworks can accommodate these worldviews and roles involving coca. Indeed, governments as well as producer and consumer communities are already stating their directives (*14*). To build on this, producer countries could strengthen inclusive, state-supported deliberative processes on coca's cultivation, use, industrialization, and commercialization. Such processes would provide a forum for producer and consumer communities to organize, articulate priorities, and exercise their rights to self-determination while protecting cultural practices rooted in the ancestral transmission of knowledge and the stewardship of plant genetic resources. In alignment with international legal frameworks such as UNDRIP, ILO Convention 169, and the Nagoya Protocol on Access and Benefit-Sharing, decision-making authority over coca's future should rest with these communities so that they can defend and direct their own actions and future.

Ultimately, this is not only about Indigenous sovereignty but also a matter of human rights and social justice. Driven by massive production in Colombia, where nearly 3000 metric tons of cocaine are processed annually from more than 250,000 ha of coca farms, global output is now at a historic high. This increase is characterized by larger areas of coca production and increased cocaine yield per hectare arising from improved agricultural processing practices (*15*).

Despite known problems with traceability, estimates comparing total coca leaf production in Peru with the amount reported for legal whole-leaf or industrial consumption suggest that about 90% of production is diverted to the illicit cocaine market, a statistic frequently extrapolated to the global level. Yet under international law, the remaining 10%, which is used in traditional, nutritional, and medicinal contexts, is treated as equally criminal. Addressing this will require more than just descheduling coca. It requires creating

space for community-led, culturally informed, and legally protected uses of the plant to thriv under frameworks of equity and recognition of the plant's historic and cultural contexts.

COMMERCIAL MARKETS AND CONVERTIBILITY

There have been consistent critiques of the conflation of coca and cocaine by the 1961 UN Single Convention on Narcotic Drugs since its adoption, and its rigid framework has begun to fracture. Argentina legalized coca leaf in the 1980s in response to its widespread use and safe cultural integration across socioeconomic classes in the mestizo populations of the Salta and Jujuy provinces. In the northern Andean countries, coca leaf chewing is increasing, and markets are growing for powdered Amazonian coca (or *mambe*), coca flour, energy drinks, fertilizers, herbal infusions, and wellness products. Coca-producing communities are building supply chains for domestic and international markets. However, without a change in coca's scheduling, these efforts remain largely unsupported by public policy and unrecognized by international regulators.

Descheduling would open policy space for producer countries and coca-growing communities to transition illicit cultivation into legal, locally governed enterprises. Such a shift would diversify rural economies, generate employment, and strengthen household incomes through taxation, value-added production, and trade, contributing to sustainable rural development. A legal framework would also allow communities to retain control over the cultural and ecological integrity of their crops while benefiting from new domestic and export opportunities for coca-based foods, nutraceuticals, and herbal products.

Globally, interest in coca-based markets is growing. Canada has authorized the import and commercial use of decocainized coca extracts for food, beverage, and wellness products, marking one of the first legal nonnarcotic applications of the plant outside of South America or Coca-Cola. Cocaine is being legally isolated from coca leaves by South American and international pharmaceutical companies for medical use, primarily as a local anesthetic in nasal, ophthalmic, and throat surgeries.

Concerns that descheduling might increase illicit cocaine production under the ease-of-convertibility argument—long cited as a secondary justification for coca's prohibition—are not justifiable. Illegality presently restricts lawful commercialization, leaving the illicit market as the dominant outlet for a cash crop. Descheduling would enable regulated markets that channel coca leaves into legal, traceable uses. Because producing 1 kg of cocaine requires about 860 kg of fresh leaf (*15*), diversion from legal commercial products into the illicit market is economically impractical (*10*). Expanding lawful options would therefore likely reduce, not expand, the dominance of the illicit economy while supporting equitable, community-led development in coca-growing regions. Even if coca is taken out of the UN schedules, other treaty articles remain in place that prohibit coca cultivation or the use of coca leaves for the purpose of illicit cocaine production.

TOWARD EVIDENCE-BASED AND EQUITABLE POLICY

We call for an international policy that clearly distinguishes between coca and cocaine. Coca's long record of safe use, cultural importance, and pharmacological distinctiveness, alongside its nutritional and therapeutic potential, supports a wide range of legitimate applications. Yet global policy and public perception continue to conflate the leaf with the drug, obstructing research and innovation while criminalizing and demonizing an ancient and sacred plant central to the cultural life of Andean and Amazonian peoples.

The ECDD's role is limited to reviewing evidence and recommending coca's scheduling status; it does not determine who cultivates, governs, or trades the plant. However, descheduling would open policy space for national governments and social organizations to define governance frameworks that center Indigenous and coca consumer and producer community leadership while engaging broader stakeholders in market regulation. These frameworks could support the growth of lawful, transparent, and culturally grounded coca economies, thereby redirecting production from illicit channels toward sustainable and equitable development.

Descheduling coca would correct a long-standing scientific and legal misclassification, uphold the rights of Indigenous and other coca-growing communities, and enable evidence-based regulation informed by traditional knowledge. It would also unlock medical research into coca's many bioactive compounds and create new economic opportunities within sustainable rural development. The ECDD Critical Review (*1*) offers a rare and timely opportunity to align international drug policy with science, justice, and social reality so that people everywhere may understand and benefit from this plant with respect and responsibility. □

REFERENCES AND NOTES

1. M. Jelsma, J. Walsh, "The UN coca leaf review and Indigenous Peoples' rights: Can the WHO meet the moment?" (Transnational Institute, 2025).
2. T. Plowman, *Pap. Peabody Mus. Archaeol. Ethnogr.* **76**, 125 (1984).
3. A. T. Weil, *J. Ethnopharmacol.* **3**, 367 (1981).
4. C. J. Allen, *The Hold Life Has: Coca and Cultural Identity in an Andean Community* (Smithsonian Books, 2012).
5. T. D. Dillehay *et al.*, *Antiquity* **84**, 939 (2010).
6. D. M. White *et al.*, *Syst. Biol.* **70**, 1 (2021).
7. World Health Organization, "Critical Review Report: Coca leaf" (World Health Organization, 2025).
8. D. A. Restrepo *et al.*, *Molecules* **24**, 3788 (2019).
9. A. Henman, *Drugs Habits Soc. Policy* **26**, 51 (2025).
10. I. Bauer, *Trop. Dis. Travel Med. Vaccines* **5**, 20 (2019).
11. M. E. Penny *et al.*, *Food Nutr. Bull.* **30**, 205 (2009).
12. W. Davis, "The secret history of coca," *Rolling Stone*, 6 April 2025.
13. P. Gootenberg, *Andean Cocaine: The Making of a Global Drug* (Univ. North Carolina Press, 2008).
14. C. Quispe Zúñiga, C. L. Ochoa Huamantica, R. Soberón Garrido, Pronunciamiento de los productores y consumidores tradicionales de hoja de coca ante la Organización Mundial de la Salud (OMS), Version 2. Zenodo (2025); https://zenodo.org/records/17281859.
15. United Nations Office on Drugs and Crime (UNODC), Integrated Illicit Crops Monitoring System (SIMCI), Eds., "Colombia-Monitoring of territories with presence of coca crops, 2023" (UNODC-SIMCI, 2025).

SUPPLEMENTARY MATERIALS

science.org/doi/10.1126/science.aeb2948

ACKNOWLEDGMENTS

A Spanish-language translation of this piece is available in the supplementary materials. D.M.W. and R.S.G. conceptualized the article and invited other authors based on their contributions to investigative knowledge on coca and policy. We acknowledge the expertise of traditional knowledge holders, including the farmers, artisans, and community members from whom we have learned about coca use. We thank the McKenna Academy for bringing many authors together at the "Wisdom of the Leaf" summit. We thank three anonymous reviewers for their constructive comments and note that we used ChatGPT with privacy protections to help condense the drafted text. D.M.W. is supported by a Harvard University Herbaria Research Fellowship. D.A.R. serves on the advisory board of Federación de Cocacultores de Colombia. C.G. is a consultant for The International Center for Ethnobotanical Education, Research, and Service. M.J. is affiliated with Swansea University and is a research associate at the Global Drug Policy Observatory. Many authors have received honoraria for speaking about coca but declare no conflicts of interest.

Published online 15 October 2025
10.1126/science.aeb2948

[1]Harvard University Herbaria, Harvard University, Cambridge, MA, USA. [2]Centro de Investigación de Drogas y Derechos Humanos, Lima, Peru. [3]College of Arts and Sciences, University of Colorado, Boulder, CO, USA. [4]E.O. Wilson Biodiversity Foundation, Durham, NC, USA. [5]Indigenous Medicine Conservation Fund, Santa Rosa, CA, USA. [6]Editorial de la Universidad del Cauca, Popayán, Colombia. [7]Instituto de Ciencias Naturales, Universidad Nacional de Colombia, Bogotá D.C., Colombia. [8]Transnational Institute, Amsterdam, Netherlands. [9]Khoka Project, Medellín, Colombia. [10]Facultad de Ciencias Humanas y Económicas, Universidad Nacional de Colombia, Medellín, Colombia. [11]Lankester Botanic Garden, Cartago, Costa Rica. [12]Centro de Estudios sobre Seguridad y Drogas, Universidad de Los Andes, Bogotá D.C., Colombia. [13]Faculty of Agricultural Sciences, University of La Salle, Bogotá D.C., Colombia. [14]Nación Tubu Hummurimassa, Mitú, Colombia.
Email: dawson.white@gmail.com; drogasyddhh@gmail.com

GENETICS

Engineering chromosome number in plants

Chromosome engineering produces a reduced eight-chromosome karyotype in *Arabidopsis thaliana*

Feng Zhang[1,2] and **R. Kelly Dawe**[3,4]

Genomic DNA is organized into chromosomes, and different species have different numbers of chromosomes. For example, humans have 23 pairs, whereas the model plant *Arabidopsis thaliana* only has 5 pairs. Chromosome number is one of the defining features of a species, yet, in most cases, it is not known why the chromosome number is what it is or what the consequences might be if the chromosome number was altered. On page 843 of this issue, Rönspies *et al.* (*1*) report directed chromosome fusion in *A. thaliana*. The authors used CRISPR technology to create fertile plants with a reduced, eight-chromosome karyotype. Their work demonstrates that plant genomes are resilient to large-scale architectural changes and establishes groundwork for experimentally manipulating plant karyotypes in both basic science and applied contexts.

Each chromosome has a centromere that the cell recognizes and binds to during cell division, ensuring that it is safely delivered to daughter cells. Therefore, the number of centromeres is equal to the number of chromosomes. Chromosome fusion has been performed in yeast and in mice, resulting in offspring with a reduced chromosome number (*2*–*4*). In plants, chromosome fission has been achieved in maize by installing a synthetic centromere on a chromosome arm, dividing the chromosome in two and producing stable lines with an increased number of chromosomes (*5*).

Manipulating chromosome number

Chromosome fusion can be achieved through precise end-joining of targeted breakpoints induced by CRISPR, producing a reduced karyotype ($n - 1$) when a minichromosome is lost. Chromosome fission increases chromosome number ($n + 1$) by introducing a synthetic centromere at a targeted site. These complementary approaches provide a framework for both basic and applied research.

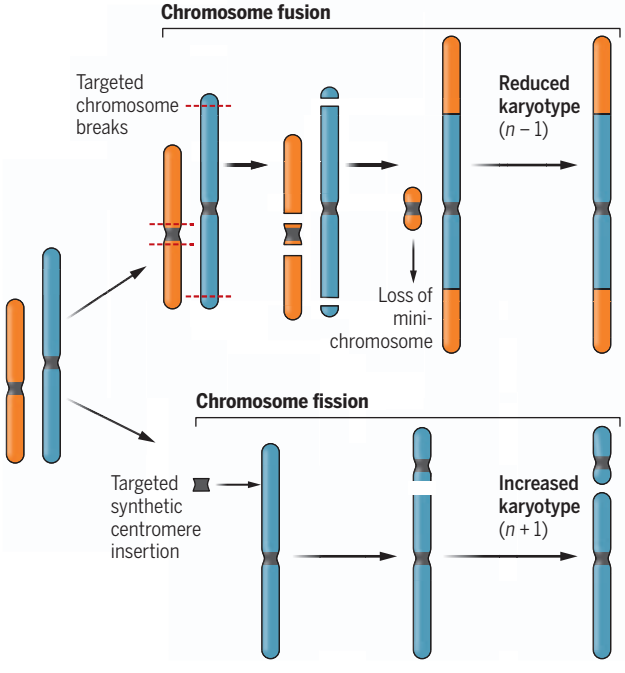

GRAPHIC: K. HOLOSKI/*SCIENCE*

In their study, Rönspies *et al.* used a CRISPR method that they had previously used to create chromosomal translocations and a large inversion in *A. thaliana* (*6*, *7*). CRISPR is a process that precisely cuts DNA at defined sites using an RNA guide and a DNA-cutting enzyme. The authors used this method to induce targeted double-strand breaks (DSBs) in DNA to remove each arm of a donor chromosome (chromosome 3) and join them to a recipient chromosome (chromosome 1 or 5). The likelihood of obtaining fusion chromosomes by this method ranged from 0.04 to 0.2% of the progeny screened, which is comparable to that of the prior translocation and inversion experiments. The chromosome fusion events were validated by fluorescence in situ hybridization and long-read sequencing, confirming the successful generation of two independent, stable lines of plants with eight chromosomes. A minichromosome derived from the centromeric region of chromosome 3 was produced as a by-product but was rapidly lost in subsequent generations (see the figure).

Despite the drastic changes to chromosome number and architecture, the engineered eight-chromosome plants were phenotypically indistinguishable from those with a wild-type background. No differences in growth rate, leaf shape, root length, or seed characteristics were detected. Transcriptome profiling showed that fewer than 0.5% of genes exhibited significant differential expression in the engineered plants compared with that in wild-type plants, with no enrichment for DNA repair or stress-response pathways and no changes in gene expression near the fusion junctions. By contrast, reductions in chromosome number in yeast trigger the up-regulation of replication stress-response genes and measurable growth defects under challenging conditions (*1*, *2*). In mice, chromosome fusions result in abnormal behavior, postnatal overgrowth, and decreased fecundity (*3*). The absence of such effects in *A. thaliana* suggests that plants may be more tolerant of large-scale karyotype changes than animals or yeast, perhaps reflecting an inherent genomic flexibility shaped by repeated cycles of whole-genome duplication and subsequent gene loss (*8*).

Although the engineered plants appeared normal by most measures, the patterns of meiotic recombination (where DNA is exchanged between maternal and paternal chromosomes) were altered. Crossover events are normally suppressed near centromeres and heterochromatic regions (densely packed, transcriptionally inactive areas of the genome) and enriched along the distal arms (*9*). However, following chromosome restructuring, crossovers were consistently lower near fusion junctions and higher toward chromosome ends, independent of the original recombination profile. The data demonstrate a compensatory phenomenon whereby structural rearrangements that reduce recombination in one region of a chromosome often result in increases elsewhere on the chromosome (*10*). Engineered chromosomes may provide a valuable model for understanding how and where recombination events are redistributed following structural rearrangement and could be used to enhance breeding outcomes for traits encoded within low-recombination regions.

Parallels to the types of genome alterations engineered by Rönspies *et al.* are also prevalent in nature, where such rearrangements can limit the flow of genetic information among populations and ultimately contribute to the generation of new species (*11*). Changes in chromosome

structure and number not only alter recombination landscapes but also disrupt chromosome pairing during meiosis, which is required to produce functional gametes. Mules, for example, are healthy hybrids, but the mismatched chromosome numbers from their parents (horse and donkey) make them sterile (*12*). Rönspies *et al.* crossed structurally altered *A. thaliana* to karyotypically normal plants and observed a 60 to 75% reduction in fertility relative to that of wild-type crosses. Additional alterations would likely lead to complete sterility of the hybrids. This property could be useful to provide a means to restrict gene flow between genetically modified crops and their wild relatives, providing a potential strategy for biocontainment.

Although the efficiency of generating structural alterations with conventional CRISPR methods remains relatively low, the work of Rönspies *et al.* provides a crucial proof of concept. Advances in genome engineering tools are likely to make large-scale chromosome manipulation increasingly feasible. Achieving further progress will depend on precise and efficient control of DSBs. Recent studies reported the insertion of recombination sites, such as *loxP* or *FRT* sequences, which are recognized by Cre and Flp recombinases (enzymes that catalyze precise DNA rearrangements between these sites), respectively, into chromosomes using a modified form of CRISPR editing. This enabled efficient manipulation of large chromosomal rearrangements with unprecedented precision in rice (*13*). An emerging system based on bridge RNA–guided DNA recombinases offers an alternative approach by coupling programmable RNA guides with recombinase enzymes. This method can enable recombination between specific genomic loci in human cell lines without relying on preinserted recognition sites, thereby expanding the opportunities for large-scale chromosome reorganization with high precision (*14*).

Building on these advances, future efforts will likely move toward deliberate chromosome design. For example, chromosome engineering could be used to explore the minimal chromosome size compatible with stable transmission through mitosis and meiosis and provide insight into the principles that govern chromosome organization. Such experiments would also lay the groundwork for creating artificial chromosomes that maintain centromere function, replication origins, and other essential elements while carrying tailored genetic payloads. This will likely require a combination of CRISPR, recombinases, synthetic centromeres, and advanced DNA synthesis and assembly methods (*15*). □

REFERENCES AND NOTES

1. M. Rönspies *et al.*, *Science* **390**, 843 (2025).
2. J. Luo, X. Sun, B. P. Cormack, J. D. Boeke, *Nature* **560**, 392 (2018).
3. Y. Shao *et al.*, *Nature* **560**, 331 (2018).
4. L.-B. Wang *et al.*, *Science* **377**, 967 (2022).
5. Y. Zeng, M. Wang, J. I. Gent, R. K. Dawe, *Sci. Adv.* **11**, eadw3433 (2025).
6. N. Beying *et al.*, *Nat. Plants* **6**, 638 (2020).
7. M. Rönspies *et al.*, *Nat. Plants* **8**, 1153 (2022).
8. J. F. Wendel, D. Lisch, G. Hu, A. S. Mason, *Curr. Opin. Genet. Dev.* **49**, 1 (2018).
9. P. A. Salomé *et al.*, *Heredity* **108**, 447 (2012).
10. A. Ederveen *et al.*, *BMC Genomics* **16**, 89 (2015).
11. L. H. Rieseberg, *Trends Ecol. Evol.* **16**, 351 (2001).
12. A. C. Chandley *et al.*, *Cytogenet. Genome Res.* **13**, 330 (1974).
13. C. Sun *et al.*, *Nat. Biotechnol.* **42**, 316 (2024).
14. N. T. Perry *et al.*, *Science* **VOL**, eadz0276 (2025).
15. F. Du, J. Dai, Y. Jiao, *New Phytol.* **244**, 46 (2024).

ACKNOWLEDGMENTS

The authors acknowledge support from National Science Foundation (grant IOS-2040218). F.Z. holds stock options and is a founding adviser to Vireo AG Inc.

10.1126/science.aec7902

[1]Department of Plant and Microbial Biology, University of Minnesota, Saint Paul, MN, USA. [2]Center for Precision Plant Genomics, University of Minnesota, Saint Paul, MN, USA. [3]Department of Genetics, University of Georgia, Athens, GA, USA. [4]Department of Plant Biology, University of Georgia, Athens, GA, USA. Email: zhangumn@umn.edu (F.Z.); kdawe@uga.edu (R.K.D.)

CELL BIOLOGY

The retina's rhythm

Calcium waves facilitate the emergence of sight

Justin P. Kumar

Compound eyes, which are found in most arthropods such as insects and crustaceans, are simple nervous systems consisting of hundreds to thousands of unit eyes called ommatidia. Proper vision and high visual acuity depend on several structural and optical factors that include the number and density of ommatidia and the precise patterning of both neuronal and non-neuronal cells within and between the ommatidia (*1*). Although the mechanisms by which cells in the eye acquire their identity are well understood, how they adopt their final positions and shapes is less clear. On page 807 of this issue, Choi *et al.* (*2*) describe the unexpected finding that during the pupal phase of development, spontaneous calcium waves within the compound eye of the fruit fly (*Drosophila melanogaster*) ensure that each ommatidium has a precise hexagonal shape and that the honeycomb-like lattice is patterned uniformly across the entire retina.

Each of the approximately 750 unit eyes within the *D. melanogaster* eye contains eight photoreceptor neurons. Just above the photoreceptors lie four non-neuronal cone cells and two primary pigment cells. Together these surround the pseudocone (a fluid-filled cavity that focuses light) and lens. This ommatidial core is surrounded by a sheath of secondary and tertiary pigment cells and mechanosensory bristles (*3*). These ensheathing cells optically insulate one unit eye from another and create the honeycomb-like arrangement of the ommatidial lattice. This mosaic pattern is established during the early stages of pupal development when waves of signals that activate epidermal growth factor receptors (EGFRs) and the notch pathway emanate from the cone cells and trigger the stepwise specification of primary, secondary, and tertiary pigment cells (*4*). Excess cells between unit eyes are removed by programmed cell death (*5*), and the surviving cone and pigment cells undergo substantial cellular rearrangements and shape changes so that a perfect hexagonal lattice is created. Mediating these changes in cell fate, contacts, arrangement, and shape is a gene regulatory network that is still being discovered. So far, this network comprises transcription factors, signaling pathways, and cell adhesion molecules (*6*).

Choi *et al.* report that spontaneous waves of calcium ensure that each ommatidium has a perfect hexagonal shape. The authors show that as the arrangement of cone and pigment cells is being finalized, activation of tyrosine kinase receptor Cad96Ca triggers phospholipase C–γ (PLC-γ)–mediated calcium release within a single cone cell per ommatidium. This initial burst of calcium turns into a small ripple as additional bursts initiate within the remaining non-neuronal cells of the ommatidium. The wave of calcium then spreads to the cone and pigment cells of neighboring ommatidia. The propagation of calcium waves across the retina is mediated by innexin proteins that function as gatekeepers of gap junctions (protein-lined channels that connect the cytoplasm of adjacent cells) between non-neuronal cone and pigment cells. These calcium waves ultimately trigger remodeling of the apical profiles of secondary and tertiary pigment cells that is driven by myosin II (a molecular motor

Ripples of calcium define eye structure

The compound eyes of the fruit fly (*Drosophila melanogaster*) contain hundreds of thousands of unit eyes called ommatidia. Each ommatidium contains eight photoreceptor neurons, above which lie four non-neuronal cone cells and two primary pigment cells. These cells hold the pseudocone and are surrounded by a layer of secondary and tertiary pigment cells. Proper vision depends on the precise patterning of neuronal and non-neuronal cells, which is finalized ~40 hours after pupal formation (APF).

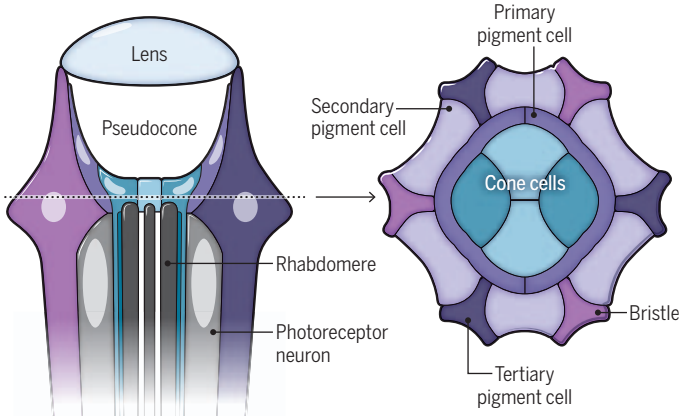

Early calcium waves

During early pupal development, spontaneous waves of calcium release trigger remodeling of the apical profiles of secondary and tertiary pigment cells to ensure that each ommatidium has a precise hexagonal shape. These waves are triggered by activation of tyrosine kinase receptor Cad96Ca, begin in the cone cells (**1**, **2**), and spread out to interommatidial cells (**3**, **4**).

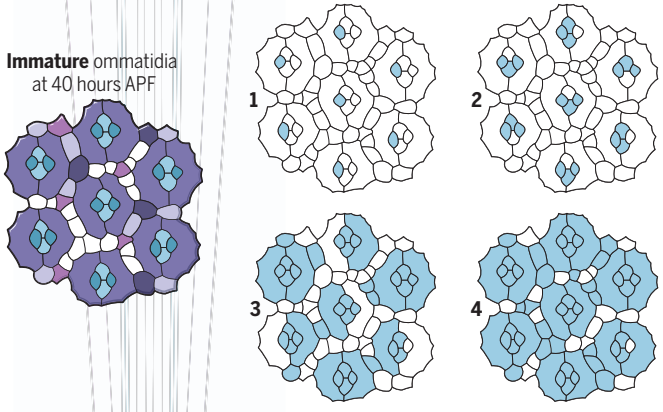

Late calcium waves

During late pupal development and early adulthood, calcium waves initiate the contraction of actin fibers at the base of the interommatidial cells to form the convex shape of the eye. These waves originate in the secondary pigment cells, tertiary pigment cells, and bristles (**1**, **2**) before spreading to the primary pigment cells (**3**, **4**). They do not affect the cone cells.

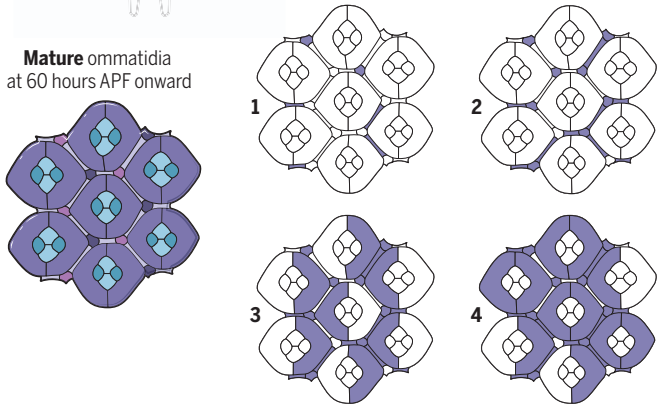

GRAPHIC: A. FISHER/*SCIENCE*

that interacts with actin filaments)—and this sets the final hexagonal shape of each unit eye. It should be noted that these calcium waves do not drive the specification of individual cell types or the initial arrangement of pigment cells. Instead, these waves are important for the final refinement of cell shape.

An underappreciated aspect of compound eyes is that not all ommatidia are of the same size—ventral ommatidia are larger, and this helps to maximize light sensitivity so that certain insects like *D. melanogaster* can detect objects that are in low-light conditions and below the visual horizon. Choi *et al.* demonstrate that the calcium waves in the larger ventral ommatidia are scaled to ensure that irrespective of the size of the facet, the precise hexagonal shape and packing are maintained across the entire retina.

These findings complement those from a previous study in which calcium waves were shown to be essential for generating the overall curvature of the *D. melanogaster* eye (*7*). These waves force the contraction of actin stress fibers at the base of interommatidial cells, and this turns a flat sheet of cells into a convex eye. Some notable differences exist between the two studies. The waves described by Choi *et al.* take place early in pupal development, whereas the ones that generate eye curvature take place during late pupal stages and persist into adulthood for several days. Furthermore, the early calcium waves initiate within the cone cells and propagate through the pigment cell lattice, whereas the later waves start and spread through the interommatidial cells without including the cone cells (see the figure).

Several spontaneous waves are initiated in the vertebrate retina as well. These waves are mainly composed of bursts of action potentials that originate and propagate through neuronal populations—primarily retinal ganglion, amacrine, and bipolar cells (*8*). These waves are critical for the establishment and organization of connections between the retina and visual processing centers in the brain. Interestingly, waves of calcium (similar to those seen in *D. melanogaster* interommatidial cells) radiate through non-neuronal Müller glia cells in the retina of mice and rats (*9*–*12*) and are thought to change the activity and synaptic strength of adjacent neurons. The retinal waves observed in vertebrate eye are not yet implicated in fine-tuning retinal structure. However, as insect and vertebrate retinas share extensive structural homologies (*13*), it is exciting to consider the possibility that calcium waves in the Müller glia could organize the packing of cells within the vertebrate retina in a manner similar to that of the *D. melanogaster* eye. It also remains to be seen how much of an impact the calcium waves have on visual behavior in both systems. It is clear, however, that calcium signaling is a fundamental property of non-neuronal cells in the invertebrate and vertebrate retinas. □

REFERENCES AND NOTES

1. M. F. Land, *Annu. Rev. Entomol.* **42**, 147 (1997).
2. B. J. Choi *et al.*, *Science* **390**, eady5541 (2025).
3. T. Wolff, D. F. Ready, "Pattern formation in the *Drosophila* retina" in *The Development of Drosophila melanogaster*, M. Bate, A. Martinez Arias, Eds. (Cold Spring Harbor Laboratory Press, 1993), pp. 1277.
4. R. W. Carthew, *Curr. Opin. Genet. Dev.* **17**, 309 (2007).
5. T. Wolff, D. F. Ready, *Development* **113**, 825 (1991).
6. R. L. Johnson, *Molecular Genetics of Axial Patterning, Growth and Disease in Drosophila Eye*, A. Singh, M. Kango-Singh, Eds. (Springer, 2020), pp. 189.
7. D. F. Ready, H. C. Chang, *Development* **148**, dev199700 (2021).
8. B. J. Choi, Y. D. Chen, C. Desplan, *Genes Dev.* **35**, 677 (2021).
9. J. M. Rosa *et al.*, *eLife* **4**, e09590 (2015).
10. R. W. Zhang, W. J. Du, D. A. Prober, J. L. Du, *Cell Rep.* **27**, 2871 (2019).
11. J. M. Tworig, C. J. Coate, M. B. Feller, *eLife* **10**, e73202 (2021).
12. Z. L. Kurth-Nelson, A. Mishra, E. A. Newman, *J. Neurosci.* **29**, 11339 (2009).
13. J. R. Sanes, S. L. Zipursky, *Neuron* **66**, 15 (2010).

ACKNOWLEDGMENTS

J.P.K. acknowledges support from the National Eye Institute (grant R01EY030847).

10.1126/science.aec6302

Department of Biology, Indiana University, Bloomington, IN, USA. Email: jkumar@iu.edu

A bacterial toxin disarms gut defenses against inflammation

Macrophage-toxic bacteria from patients with ulcerative colitis worsen gut inflammation in mice

Sonia Modilevsky and **Shai Bel**

Koch's postulates, formulated in 1884 by Robert Koch and Friedrich Loeffler, state that a microorganism causes a disease if it is found in all disease cases, can be isolated and grown in culture, causes the disease when introduced into a healthy host, and can be reisolated from that host (*1*). These criteria have been revised to account for "unculturable" microbes, such as viruses, and to recognize microbial genes as disease agents rather than the microbes themselves (*1*, *2*). No microorganism that fits Koch's revised postulates has been identified as the cause of ulcerative colitis (*3*). On page 805 of this issue, Jiang *et al.* (*4*) report that a bacterial strain isolated from patients with ulcerative colitis drives gut inflammation in mice by producing aerolysin, which is toxic to protective immune cells. The findings suggest a previously unidentified mechanism by which a microbe might contribute to the progression of ulcerative colitis.

Aerolysin was present in the mucosa of all patients with ulcerative colitis but not in that of healthy individuals.

Inflammatory bowel disease (IBD) is an umbrella term for a group of chronic conditions in which the body's immune system attacks the digestive tract, causing inflammation and symptoms such as abdominal pain, diarrhea, and fatigue. The most common types of IBD are Crohn's disease and ulcerative colitis. Ulcerative colitis specifically affects the lining of the colon and rectum, leading to ulcers and bleeding (*3*). Early attempts to cultivate bacteria from patients with ulcerative colitis did not identify a microbe specifically associated with the disease (unlike similar approaches that uncovered the infectious agents, such as *Salmonella*, that cause other diarrheal diseases). Genomic sequencing approaches were equally unsuccessful, although they revealed that the composition of the gut microbial community (microbiota) was altered in patients with ulcerative colitis. In parallel, epidemiological observations linking the prevalence of ulcerative colitis to urbanization and modern lifestyles suggested that this disease has environmental causes (*5*).

Jiang *et al.* studied biopsies of tissue from the colons of patients with ulcerative colitis using histology and analysis of immune cell populations. The authors observed that tissue-resident macrophages—a type of immune cell that surveys mucosal tissues to detect infections or damage—were nearly absent from the subepithelial mucosa (the layer of tissue beneath the epithelial layer) in the colons of these patients. Chemical or genetic depletion of these gut-resident macrophages in mice revealed that these cells were crucial to protect the colon from chemically induced inflammation.

Jiang *et al.* hypothesized that an agent produced by the gut microbiota might be responsible for the depletion of mucosal-resident macrophages in patients with ulcerative colitis. They found that fecal matter from these patients, but not that from healthy donors, contained aerolysin, a substance secreted by bacteria from the *Aeromonas* genus. Aerolysin forms pores in target cells, which leads to cell death. Experiments in cultured mouse and human cells showed that aerolysin is highly toxic to macrophages but not to intestinal epithelial cells. The authors dubbed the aerolysin-producing bacterial strain *Aeromonas* sp. macrophage-toxic bacteria (MTB).

To assess the effects of MTB on gut tissue, Jiang *et al.* used mouse models of colonic inflammation. Infection with MTB worsened clinical

Aerolysin makes the colon susceptible to inflammation

Aeromonas sp. macrophage-toxic bacteria (MTB) isolated from patients with ulcerative colitis produce aerolysin, which is toxic to gut macrophages. Loss of macrophages leads to inflammation and accumulation of B cells and other components of the immune system, which weakens the colon's defenses. Anti-aerolysin (α-aerolysin) antibodies restore the gut mucosa to a healthy state.

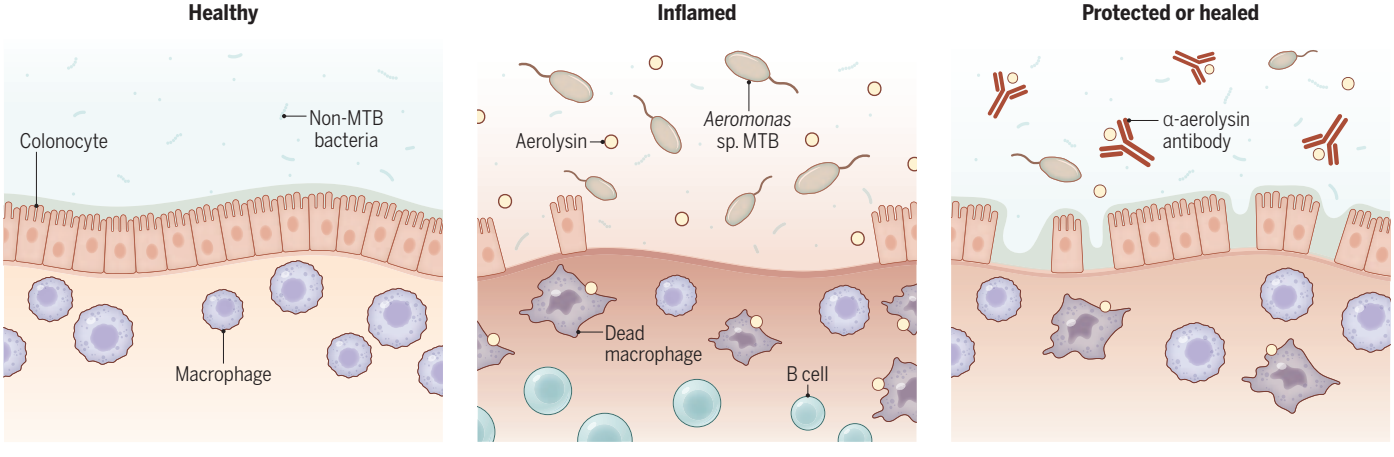

GRAPHIC: A. MASTIN/*SCIENCE*

symptoms of colonic inflammation, such as weight loss, rectal bleeding, and colonic ulcerations, in these animals. Genetically engineered microbes lacking the gene encoding aerolysin did not have a proinflammatory effect when they were orally given to mice. Notably, MTB did not aggravate colitis in mice chemically treated to lack gut-resident macrophages. Furthermore, administering antibodies targeting aerolysin into the abdominal cavities of MTB-infected mice relieved signs of colonic inflammation. Thus, MTB infection renders the colon susceptible to inflammation by destroying gut-resident macrophages with aerolysin (see the figure).

Jiang *et al.* also assessed whether MTB and aerolysin were present in fecal samples and colonic biopsies from a cohort of 117 patients with IBD and 430 healthy controls across 12 provinces in China. The authors detected aerolysin-producing MTB in more than 70% of patients with ulcerative colitis, whereas these microbes were only present in ~12% of healthy individuals. Aerolysin was present in the mucosa of all patients with ulcerative colitis but not in that of healthy individuals. Notably, only 1 of the 38 patients with Crohn's disease had MTB.

Why are MTB found in patients with ulcerative colitis but not in healthy individuals or in patients with other forms of IBD? Jiang *et al.* observed that MTB do not colonize the colons of healthy mice to a detectable concentration. However, oral pretreatment with a mix of antibiotics that depleted competing gut bacteria or the induction of colonic inflammation with a chemical agent enabled persistent colonization of mice by MTB. Notably, MTB could persist in mice 2 months after infection, even if they could not be detected, as antibiotic treatment restored the MTB population to detectable levels. This is an important observation because antibiotic use, a hallmark of a modern lifestyle, is a major risk factor for the development of IBD (*6*–*8*).

It is unlikely that Koch's postulates will ever be fulfilled for IBD. Mice do not develop these diseases, which limits the ability to experimentally prove that a proposed causative agent initiates disease in healthy animals. Although not fulfilling these postulates, the findings of Jiang *et al.* do establish a causative link between *Aeromonas* sp. MTB and the worsening of gut inflammation in mice as well as a correlative link between aerolysin-producing MTB and ulcerative colitis in humans.

It is also unlikely that a single agent can produce an array of disease presentations, as seen in IBD, which are complex ailments that develop over decades (*3*). However, it is possible that various microbes directly target gut-resident immune cells, which could impede the host's ability to preserve gut homeostasis. Directly targeting these microbes and their toxins could be a promising avenue for treating IBD without inhibiting patients' immune systems with biologics, such as antibodies, and steroid drugs. □

REFERENCES AND NOTES

1. S. Falkow, *Rev. Infect. Dis.* **10**, S274 (1988).
2. D. N. Fredericks, D. A. Relman, *Clin. Microbiol. Rev.* **9**, 18 (1996).
3. J. T. Chang, *N. Engl. J. Med.* **383**, 2652 (2020).
4. Z. Jiang *et al.*, *Science* **390**, eadz4712 (2025).
5. T. Kobayashi *et al.*, *Nat. Rev. Dis. Primers* **6**, 74 (2020).
6. A. S. Faye *et al.*, *Gut* **72**, 663 (2023).
7. L. H. Nguyen *et al.*, *Lancet Gastroenterol. Hepatol.* **5**, 986 (2020).
8. J. Sawaed *et al.*, *Sci. Adv.* **10**, eadp4119 (2024).

10.1126/science.aec7924

Azrieli Faculty of Medicine, Bar-Ilan University, Safed, Israel. Email: shai.bel@biu.ac.il

VOLCANOLOGY

Tracking magma with earthquakes

Linking stress in Earth's crust and magma flow could help forecast eruptions and associated hazards

Virginie Pinel

According to classical thinking, magma—a mixture of molten rocks, crystals, and gas—rises vertically from a deep reservoir to feed eruptions at the center of a volcanic system. By contrast, magma may propagate horizontally over tens of kilometers beneath Earth's surface under the effect of extensional stress, which can cause hazardous eruptions away from a volcanic center (*1*–*3*). As magma moves, it can displace preexisting fractures in Earth's crust, called faults, or create new ones, resulting in seismic activity. Nonetheless, the magmatic origin of this induced seismicity is not always clearly identified. On page 806 of this issue, Lomax *et al.* (*4*) report that the early 2025 earthquakes near the Greek island of Santorini were caused by a vertical fault, which was filled with laterally propagating magma. Such observations will improve models of magma transport within Earth's crust and help in hazard assessment and forecasting eruptions.

Magma flows into dikes, which are blade-shaped structures that propagate by fracturing rocks and open by deforming Earth's crust (*5*). This diking process is the primary way by which magma moves from a deep reservoir to the surface to feed volcanic eruptions. Modeling magma propagation requires consideration of the physical properties of both magma and the surrounding rocks. However, magma is a multiphase fluid that exhibits spatiotemporal evolution of density and viscosity because of the crystallization of the melt (molten rock) and the associated gas release. These processes occur when temperature and pressure of the magma decreases as it rises. Moreover, the surrounding rocks have heterogeneous structures and composition, complicating their stress state and deformation behavior under stress. Thus, complex concepts of fracture mechanics and fluid dynamics are needed for magma-transport models. Consequently, existing models (*6*, *7*) cannot encompass the full complexity of magma propagation in three dimensions. Furthermore, model validation relies solely on indirect observations of displacements of Earth's surface and magma propagation–driven seismicity.

Lomax *et al.* located tens of thousands of earthquakes that were recorded in January and February 2025 in the Aegean Sea, between the Greek islands of Santorini and Amorgos. The spatiotemporal distribution of seismicity along a 50-km section that extends along a southwest-northeast direction and covers a depth of 20 km from Earth's surface was used as a stress indicator. This provided information on the origin of earthquakes by reconstructing the shape of the magma-filled fracture over time.

Previous studies analyzed sparse measurements of ground deformation to infer the position and geometry of the magma fracture (*8*). Lomax *et al.* interpreted the back-and-forth migration of seismicity to track changes in the

Lateral magma flow within Earth's crust

Instead of a vertical eruption, magma can flow horizontally into a dike from a deep reservoir that is located underneath a volcanic center. The diking process creates a pumping system in which alternating cycles of contraction and expansion of the dike promote magma to travel laterally underneath Earth's surface. This creates a potential hazard for unexpected eruption and associated seismicity.

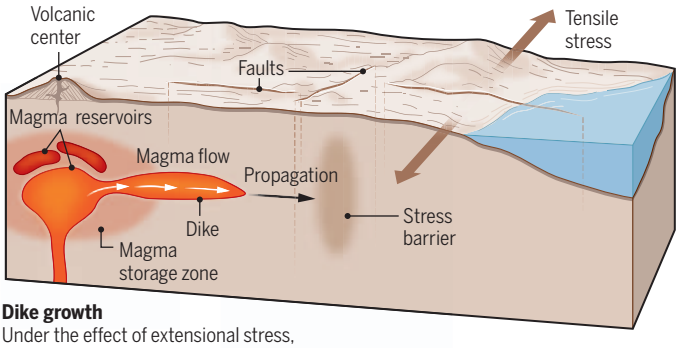

Dike growth
Under the effect of extensional stress, magma flows horizontally into a dike from a reservoir.

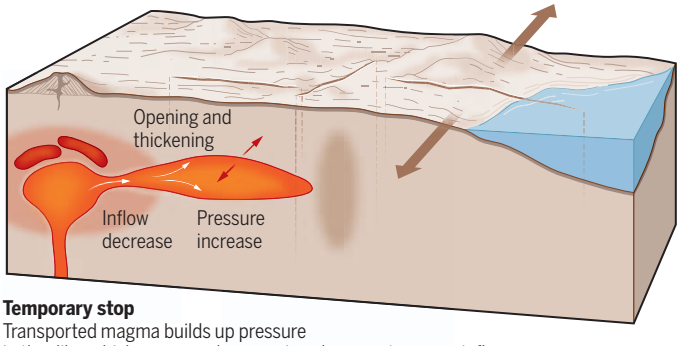

Temporary stop
Transported magma builds up pressure in the dike, which causes a decrease in subsequent magma inflow.

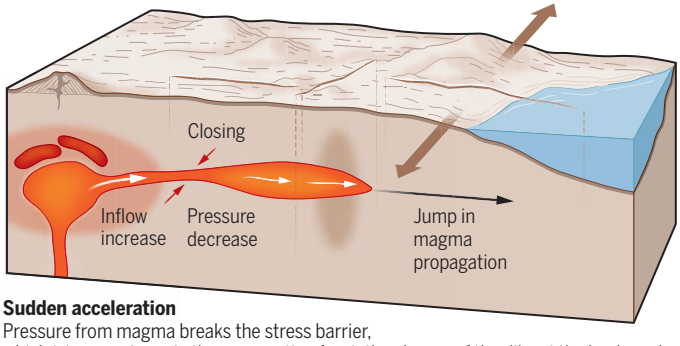

Sudden acceleration
Pressure from magma breaks the stress barrier, which triggers a jump in the propagation front, the closure of the dike at the back, and an increase in magma inflow.

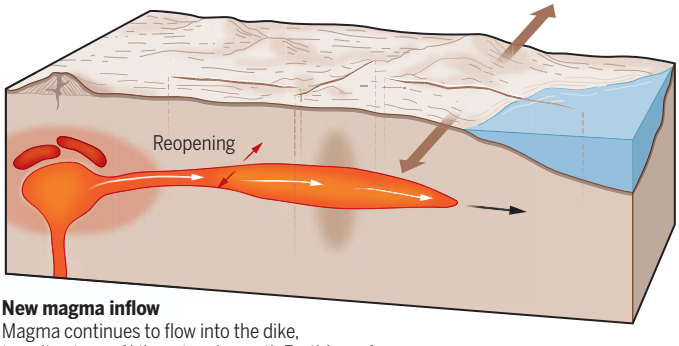

New magma inflow
Magma continues to flow into the dike, traveling tens of kilometers beneath Earth's surface.

GRAPHIC: K. HOLOSKI/*SCIENCE*

opening of the dike. This provided detailed information about the evolution of pressure that is driven by magmatic propagation (see the figure). When a stress barrier was broken by the increase in magma pressure, a jump in the front propagation of magma was observed followed by a dynamic pressure change along the entire length of the dike. This process affected the inflow of magma into the dike from the reservoir. The alternating phases of contraction and expansion of the dike after the sudden acceleration of magmatic flow acted as a pumping system. This description was lacking in previous studies in which the closure of dikes was generally dismissed.

The island of Santorini experienced one of the largest volcanic events of the Holocene (the present geological epoch) in 1600 BCE (*9*), and recent episodes of magmatic recharge in the shallow plumbing system (*10*) raise concerns about explosive volcanic activity on the island. The study of Lomax *et al.* suggests a different scenario of cascading risks in which a diking event caused by magmatic recharge could trigger a distant underwater eruption or a sudden destabilization of major faults in a highly active tectonic zone that is prone to tsunami formation (*11*). In addition, the risk posed by magma reaching the surface several dozen kilometers from a volcanic center complicates hazard assessment. An eruption can potentially affect densely populated areas, as in the emblematic case of Lake Kivu in East Africa (*12*). In this case, magma propagated beneath the gas-rich lake located about 17 km south of the volcanic center, increasing the risk of a sudden release of toxic gases that could kill millions of people. Such a societal impact could be a strong motivation for improving the modeling of magma transport combined with detailed field observations.

The study of Lomax *et al.* could lead to new dynamic models of magma transport that account for spatial variations in the fracture resistance of surrounding rocks. Beyond tracking magma flow at depth, the findings could be used to understand the state and evolution of the crustal stress field (*13*). For example, lateral magma propagation may be driven by an increase in extensional stress with depth, which counterbalances the buoyancy of magma (*14*). Magma flow may also depend strongly on its interaction with preexisting faults (*15*). Integrating advanced seismicity information into numerical models could enable better characterization of the crustal stress field, particularly in areas where lateral magma propagation prevails. Furthermore, combining real-time observations and dynamic models could predict the location and timing of eruptions by using advanced data assimilation or machine-learning techniques. □

REFERENCES AND NOTES

1. C. A. Neal *et al.*, *Science* **363**, 367 (2019).
2. F. Sigmundsson *et al.*, *Science* **383**, 1228 (2024).
3. N. Feuillet *et al.*, *Nat. Geosci.* **14**, 787 (2021).
4. A. Lomax, V. Anagnostou, V. Karakostas, S. P. Hicks, E. Papadimitriou, *Science* **390**, eadz8538 (2025).
5. E. Rivalta, B. Taisne, A. P. Bunger, R. F. Katz, *Tectonophysics* **638**, 1 (2015).
6. S. Furst *et al.*, *J. Geophys. Res.* **128**, e2022JB025697 (2023).
7. L. A. Blackstone, B. E. Grossman-Ponemon, E. R. Heimisson, A. J. Lew, P. Segall, *Bull. Volcanol.* **86**, 52 (2024).
8. M. P. Isken *et al.*, *Nature* **645**, 939 (2025).
9. J. Karstens *et al.*, *Nat. Commun.* **14**, 2497 (2023).
10. M. M. Parks *et al.*, *J. Geophys. Res. Solid Earth* **120**, 1309 (2015).
11. F. Leclerc *et al.*, *Commun. Earth Environ.* **5**, 663 (2024).
12. D. Smittarello *et al.*, *Nature* **609**, 83 (2022).
13. E. Rivalta *et al.*, *Sci. Adv.* **5**, eaau9784 (2019).
14. V. Pinel, C. Mériaux, *J. Afr. Earth Sci.* **226**, 105569 (2025).
15. F. Maccaferri, E. Rivalta, L. Passarelli, Y. Aoki, *Earth Planet. Sci. Lett.* **434**, 64 (2016).

ACKNOWLEDGMENTS

The author acknowledges support from the E-DOORs project funded by the Institut de Recherche pour le Développement.

10.1126/science.aec7912

Université Grenoble Alpes, Université Savoie Mont Blanc, CNRS, IRD, Université Gustave Eiffel, ISTerre, Grenoble, France. Email: virginie.pinel@univ-smb.fr

BOOKS ET AL.

BIOLOGY

An ode to change

A historian confronts the transformative nature of metamorphosis **Viviane Callier**

Oren Harman
Basic Books, 2025.
400 pp.

METAMORPHOSIS | In *Metamorphosis: A Natural and Human History*, historian of science Oren Harman offers a meditation on transformation writ large. His focus is not only on the remarkable transformations seen in nature—as when a caterpillar becomes a butterfly, a tadpole a frog, or a polyp a jellyfish—but also on transformations we humans experience over the course of our lives as we encounter new people, ideas, and experiences. The book is a mosaic of short essays, written with a "spirit of loose-jointedness" that explores the biological phenomenon of metamorphosis.

Per the fossil record, Harman tells readers, insect metamorphosis evolved about 280 million years ago, but it was the evolution of flowering plants 150 million years later that drove a coevolutionary process that "made complete metamorphosis a stunning success" and led to the diversification of many insect species.

Insects that undergo complete metamorphosis (holometabolous insects) hatch from an egg to become a caterpillar, which then becomes a pupa. The animal then emerges from the pupa as an adult. In contrast, insects that undergo incomplete metamorphosis, such as grasshoppers and cicadas, start out as pronymphs, then hatch into nymphs that resemble adults, and eventually molt into adults. But it was unclear for some time how these stages corresponded to one another.

One hypothesis, proposed by the Paduan entomologist Antonio Berlese and disseminated by British scientist Augustus Daniel Imms at the turn of the 20th century, was that the larval stage of holometabolous insects corresponded to a pronymph that had hatched prematurely. But another English scientist, Howard Hinton, suggested a different idea: that the larvae of holometabolous insects were equivalent to the nymphs of incompletely metamorphosing creatures.

There are many advantages to having drastically different life stages.

However complete metamorphosis came about, there is no question that it was a big evolutionary success. Scientists generally agree that there are advantages to having juvenile and adult stages that are completely different: It avoids within-species competition for the same resources, and each stage can be adapted to a specific job (growing versus reproducing).

A highlight from part 1 of the book, titled "Where Do We Come From?," is the story of the 17th-century German naturalist Maria Sibylla Merian, who documented observations about the life cycle of insects and published several illustrated books about them. She even traveled with her daughter Dorothea Maria to the South American Dutch colony of Suriname to study tropical insects and carefully described the process of insect metamorphosis—an ambitious undertaking for two women at that time. Harman's warm, empathetic recounting of Merian's extraordinary life is wonderful and brings to light not only her scientific contributions but also her humanity and courage.

In part 2, "Where Are We Going?," Harman explores the history of evolutionary thinking from the 18th century to today. Here, again, his writing brings to life the stories of scientists and naturalists of the time, such as Ernst Haeckel, Johann Wolfgang von Goethe, and Charles Darwin. Harman artfully places ideas espoused by these and other scholars into historical context, weaving together their theories with a sense of who they were as people.

And in the third and final section of the book, Harman recounts the story of contemporary entomologists Lynn Riddiford and Jim Truman, who have dedicated their careers to studying the physiology and genetics of insect metamorphosis. This section traces an arc from the early studies conducted by Vincent Wigglesworth, a British entomologist known as the father of insect physiology, to the advances in evolutionary developmental biology and genetics that allowed Riddiford and Truman to identify key genes associated with insect metamorphosis.

Nature's transformations also inspire self-reflection, as Harman contemplates becoming a father for the third time. "Many things change us: ideas, travels, dreams," he writes. "But nothing more than the people who depart from us, and the ones we bring to life." For all of his explorations about how we change and grow throughout our lifetimes, however, I did not come away with a clear sense of how Harman had changed or been changed by the arrival of his third child.

I also wished that Harman had explored in greater detail the bittersweetness of change and transformation. Becoming something new almost always requires some kind of loss: the shedding of an old identity. The vulnerable pupal stage of insect metamorphosis, for example, feels like an apt metaphor for the human experience of shedding an old identity while remaining uncertain of when or how we will emerge into something new.

In a world that is increasingly unstable and uncertain, where things around us feel as though they are changing faster than ever before, each of us will need to transform at some point or another. The radical transformations of creatures all around us offer lessons in how to navigate these changes. □

ACKNOWLEDGEMENTS

The views in this article are the author's own and do not represent the opinions of Leidos Biomedical Research, Inc., or its parent company.

10.1126/science.aed0043

The reviewer is at Leidos Biomedical Research, Inc., Frederick, MD, USA. Email: vcallier@gmail.com

PHOTO: OLI SCARFF/GETTY IMAGES

SCIENCE AND SOCIETY

In defense of the know-it-all

A scholar probes the scorn provoked by the intellectual elite across the ages

Jonathan Wai

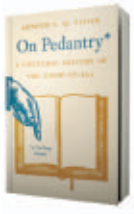

Arnoud S. Q. Visser
Princeton University Press, 2025.
344 pp.

ON PEDANTRY | Growing up as a verbally precocious young child in a rural part of the Netherlands, Arnoud Visser was often told "What expensive words you use." Over time, he realized that this was not meant as a compliment. His new book, *On Pedantry*, seeks to help readers understand the contempt he encountered when he flexed his knowledge as a gifted youth and places recent trends toward anti-intellectualism into broader historical and cultural context.

Visser's book covers a period of 25 centuries, arguing that "What all pedants across the ages share…is the tendency to arouse antipathy toward know-it-all behavior." From the intellectual elites of ancient China, who were selected for civil service through grueling examinations; to Socrates, who—despite the wisdom he offered the world—was not especially liked in his day; "to today's interrupting mansplainers and grammar police," pedants have earned scorn throughout history, often more for their behavior than for their ideas.

The Sophists, for example, provoked ire, because they "bypassed the traditional structure for elite male training, which in turn provoked resentment and distrust," writes Visser. In a chapter on ancient philosophers, he argues that "The criticism of philosophers as wise guys without substance was a product of a fiercely competitive intellectual culture in which representatives of different types of learning and wisdom vied for authority." One needn't look far to see similar competition among the intellectual elite today. Visser argues that conflicts within the academic and intellectual communities are "inevitable features of a competitive field" and that a core criticism of the pedant relies on replaying a cultural script that "regulates the acceptable use of brainpower according to prevailing social norms."

PHOTO: LIGHTFIELD STUDIOS/ALAMY STOCK PHOTO

Scholars have faced resentment throughout history—not all of it unwarrented.

In a chapter on "Foolish Humanists," Visser introduces readers to the 15th-century German humanist Sebastian Brant's famous satirical work *Das Narrenschiff* (*The Ship of Fools*), which features a bespectacled fool who dusts but does not read his large collection of books. ("Of splendid books I own no end, but few that I can comprehend / I cherish books from various ages / and keep the flies from off the pages.") The Italian humanist Leon Battista Alberti, Brant's contemporary, had his own take on the pedant's preferred resource: "Books make the scholar feel guilty about any other form of amusement, and they affect one's rest, health, even one's life expectancy, and offer only slim chances for worldly success."

Visser notes that an argument broke out among the "ancients" and the "moderns" in 1687 in which both camps accused the other of pedantry as a means of discrediting their opponents' positions. (The ancients believed in the superiority of the classics, whereas the moderns championed a critical approach to literature, philosophy, and science.) Meanwhile, the 17th-century Dutch political philosopher Ulrik Huber wrote the first academic analysis of pedantry, with a working definition of the offense as "learning that is corrupted by arrogance, feigned virtue, and impertinent judgement." Pedants, he maintained, were to be found among teachers, scholars, physicians, lawyers, ministers, senators, noblemen, kings, and rulers. "Arrogance arises…when learned people consider themselves superior to others and do not tolerate contradiction," he argued.

In a chapter entitled "Effete Elitists," Visser reflects on the rejection of intellectualism that spread throughout religious organizations in the 18th century. "To be successful in some way, religious missionaries had to adapt to the culture of the settler communities, including its anti-authoritarian and anti-intellectual sentiments," he observes. "Larnin isn't religion, and eddication don't give a man the power of the Spirit…St. Peter was a fisherman—do you think he ever went to Yale College?" one preacher of the era is reported to have argued. Such criticisms likely arose because education held high cultural prestige and threatened the authority of the church.

Visser argues that the pedant is useful in his or her capacity to offer honest feedback and to defend the intellectual record. He hopes that his book helps those seeking to understand the cycle of historical sentiment toward intellectuals across the ages as well as contemporary know-it-alls. The anecdotes and examples the book offers, he maintains, "can help the pedants of this age to become more acutely aware of the history of which they are part. And awareness will enable them to make the benefits they offer more effective." □

10.1126/science.aec6383

The reviewer is at the Department of Education Reform and Department of Psychology, University of Arkansas, Fayetteville, AR, USA. Email: jwai@uark.edu

LETTERS

Edited by **Jennifer Sills**

Expanding fossil fuel exploration near the Amazon River threatens the environment as well as the global transition to clean energy .

PHOTO: CHIEN LEE/MINDEN PICTURES

Brazil's credibility at stake with drilling

As the 30th Conference of the Parties to the United Nations Framework Convention on Climate Change (COP30) convenes in Brazil this week, the country's recent actions raise questions about its commitments to the environment and climate. On 20 October, the Brazilian Institute of Environment and Renewable Natural Resources granted the government-run company Petrobras a license to explore for oil at the mouth of the Amazon River. Despite opposition from minister of the environment and climate change Marina Silva, intense political pressure compelled the approval. This included a strong endorsement by Brazil's president Luiz Inácio Lula da Silva for economic reasons (*1*). The decision undermines Brazil's credibility as a global climate leader, contradicting its commitments to an energy transition toward sustainable sources and threatening a highly biodiverse and sensitive region.

The Amazon region contributes up to 50% of regional rainfall and supplies atmospheric moisture that regulates climate across South America (*2*). Home to Earth's greatest diversity of life (*3*), the region comprises interlinked ecosystems, including the planet's largest estuary, deep-water reefs, and broad expanses of mangroves (*4*). The mangroves not only contribute substantially to carbon storage and coastal resilience (*5*) but also shelter extraordinary biodiversity and sustain ecosystem functions that support coastal populations (*6*).

More than 27 others drilling licenses for drilling at the mouth of the Amazon River await approval (*7*). Expanding fossil fuel exploration increases the risk of pollution, habitat degradation, and severe damage from oil extraction and potential spills--impacts already documented elsewhere in the world (*8*, *9*). Conserving the Amazon River and region is a global priority to halt climate collapse and biodiversity loss (*10*).

Brazil cannot both support the phasing out of fossil fuels and allow drilling for oil. There is no justification for oil exploration near the Amazon, and President Lula da Silva's claim that profits from fossil fuel operations will finance a transition to clean energy (*11*) is absurd. Brazil is already the world's eighth largest producer of oil in the world (*12*). Brazil must reverse course on fossil fuels and demonstrate its commitment to addressing the climate crisis and to preserving the Amazon River and region. Leaders at COP30 should urge Brazil to strengthen its policies for environmental protection and shift investment priorities to sustainable and renewable energy. The Amazon should not become a new global oil frontier.

Fabiele do Rocio Lacerda[1,2], Ana Paula dos Santos Bertoncin[1,2,3], Renata Ruaro[1,2]

[1]Graduate Program in Environmental Science and Technology, Federal Technological University of Paraná, Curitiba, PR, Brazil. [2]Laboratory of Biomonitoring and Applied Ecology, Department of Chemistry and Biology, Federal Technological University of Paraná, Curitiba, PR, Brazil. [3]Department of General Biology, State University of Ponta Grossa, Campus Uvaranas, Ponta Grossa, PR, Brazil. Email: renataruaro@utfpr.edu.br

REFERENCES AND NOTES

1. F. Cardoso, E. Simões, *Reuters*, 12 February 2025; https://www.reuters.com/world/americas/brazils-lula-meet-with-environment-agency-petrobras-bid-drill-near-mouth-amazon-2025-02-12.
2. A. Staal *et al.*, *Nat. Clim. Change* **8**, 539 (2018).
3. J. M. Guayasamin *et al.*, *Acta Amazonica* **54**, e54bc21360 (2024).
4. R. B. Francini-Filho *et al.*, *Front. Mar. Sci.* **5**, 142 (2018).
5. A. F. Bernardino *et al.*, *Nat. Commun.* **15**, 1549 (2024).
6. M. Owuor *et al.*, *Front. Environ. Sci.* **12**, 1329006 (2024).
7. C Antunes, R. Moro Martins, *SUMAÚMA*, 20 October 2025; https://sumauma.com/en/foz-do-amazonas-governo-lula-autoriza-a-exploracao-de-petroleo-e-enfraquece-a-cop30.
8. M. G. Barron *et al.*, *Environ. Sci. Technol.* **54**, 6456 (2020).
9. J. Beyer *et al.*, *Mar. Pollut. Bull.* **110**, 28 (2016).
10. C. Lorenz *et al.*, *Sci. Total Environ.* **783**, 147090 (2021).
11. O. Bois von Kursk, J. Roth, R. J. Fujii, C. Schiavo, L. H. Verazaín, E. Erhan, "Brazil at a crossroads: rethinking Petrobras oil and gas expansion" (Winnipeg: International Institute for Sustainable Development, 2025); https://www.iisd.org/system/files/2025-06/brazil-petrobras-oil-gas-expansion.pdf.
12. Empresa de Pesquisa Energética (EPE), "Decarbonization Scenarios for E&P" (Ministry of Mines and Energy, 2025); https://www.epe.gov.br/sites-en/publicacoes-dados-abertos/publicacoes/PublicacoesArquivos/publicacao-272/2025_Final%20Report_RCNPE%208-2024.pdf.

10.1126/science.aed3752

Brazil's hypocrisy at COP30

The Brazilian government's 20 October authorization of oil drilling in the mouth of the Amazon River stands in stark contrast to Brazil's role as host this week of the 30th Conference of the Parties to the United Nations Framework Convention on Climate Change (COP30) (*1*). This decision undermines the credibility of Brazil's climate commitments and the message the country seeks to convey on a global stage.

The project allows the government-run company Petrobas to conduct exploratory oil drilling in an offshore area near the mouth of the Amazon River. This runs counter to the International Energy Agency's position (Net Zero by 2050) that no new oil and gas fields should be developed anywhere in the world (*2*). The project is estimated to take

roughly 5 years before commercial production of oil could begin, followed by another 5 years to recover the initial investment. After that, investors would be unlikely to halt operations at zero profit, meaning that extraction would continue.

The depth of water at the drilling site is twice that of the site of the 2010 Gulf of Mexico oil spill, which took 5 months to contain. A spill at the Amazon site might not be contained for many months, which could lead to an unprecedented disaster for biodiversity (*3*). The area is ecologically diverse (*4*, *5*), including coral reefs and coastal mangroves (*6*, *7*). The livelihoods of Indigenous peoples and traditional fishing communities would be threatened by such a disaster (*3*).

Brazil's dual stance—proclaiming global environmental stewardship while expanding hydrocarbon frontiers—reveals a dangerous incoherence between rhetoric and reality. Just before COP30, Brazil and other Amazonian nations signed the Declaration of Bogota, a commitment to lead climate diplomacy as a unified front (*8*). Amazonian nations have an opportunity to present a strong, shared position at COP30 and act as a leader in climate negotiations. If these countries seek to lead by example at COP30, then Brazil must reconcile its development strategies with the ecological and ethical imperatives it publicly upholds (*9*). Leadership will not arise from extracting the last drop of oil but from embracing a future anchored in ecological integrity, justice, and genuine commitment to the post–carbon energy transition.

José Amorim Reis-Filho[1,2,3,4], Tommaso Giarrizzo[3], Friedrich Wolfgang Keppeler[2], Eurico Noleto-Filho[5], Marcelo Oliveira Soares[3], Valter M. Azevedo-Santos[6,7], Guilherme O. Longo[8], Mariana Bender[9], Rafael A. Magris[10], Philip M. Fearnside[11]

[1]Graduate Program in Ecology: Theory, Application and Values, Federal University of Bahia (UFBA), Salvador, BA, Brazil. [2]Aquatic Ecology Group and Aquatic Ecology Center, Federal University of Pará, Belém, PA, Brazil. [3]Institute of Marine Science (LABOMAR), Federal University of Ceará, CA, Brazil. [4]Marine Spatial Planning Northeast (PEM NE), Universidade Federal do Rio Grande do Norte (UFRN), Comissão Interministerial para os Recursos do Mar (CIRM), DF, Brazil. [5]Geophysical Institute, University of Bergen, Bergen, Norway. [6]Centro Universitário Eduvale, Avaré, SP, Brazil. [7]Programa de Pós-Graduação em Biodiversidade, Ecologia e Conservação (PPGBEC), Federal University of Tocantins, Porto Nacional, TO, Brazil. [8]Marine Ecology Laboratory, Department of Oceanography and Limnology, Universidade Federal do Rio Grande do Norte, Natal, RN, Brazil. [9]Marine Macroecology and Conservation Lab, Federal University of Santa Maria, Santa Maria, RS, Brazil. [10]Instituto Chico Mendes de Conservação da Biodiversidade, Brasília, DF, Brazil. [11]National Institute for Research in Amazonia (INPA), Manaus, AM, Brazil. E-mail: amorim_agua@yahoo.com.br

REFERENCES AND NOTES

1. B. De Freitas Moura, *Agência Brasil*, 20 October 2025; https://agenciabrasil.ebc.com.br/en/geral/noticia/2025-10/petrobras-granted-environmental-license-explore-equatorial-margin.
2. International Energy Agency (IEA), *Net Zero by 2050: A Roadmap for the Global Energy Sector* (IEA, 2021); https://iea.blob.core.windows.net/assets/ad0d4830-bd7e-47b6-838c-40d115733c13/NetZeroby2050-ARoadmapfortheGlobalEnergySector.pdf.
3. H. O. B. Duarte *et al. Nat. Sustain.* **8**, 1105 (2025).
4. A. P. Marceniuk *et al. Estuar. Coast Shelf Sci.* **305**, 108847 (2024).
5. A. G. C. M. Klautau *et al., Sci. Rep.* **15**, 26681 (2025).
6. R. B. Francini-Filho *et al.*, *Front. Mar. Sci.* **5** (2018.
7. T. N. S. Banha *et al. Front. Mar. Sci.* **9** (2022).
8. P. R. Vilela, *Agência Brasil*, 25 August 2025; https://agencia-brasil.ebc.com.br/en/meio-ambiente/noticia/2025-08/bogota-declaration-advances-coordination-falls-short-targets.
9. P. M. Fearnside, W. Leal Filho, *Science* **387**, 1237 (2025).

10.1126/science.aed3748

Bolivia's political transition and COP30

Bolivia's new president, Rodrigo Paz Pereira, took office on 8 November 2025. He has promised to prioritize bridging regional, political, and social divisions to build a long-term vision for the country. This political transition is timely in that it also adds a new dimension to Bolivia's position at the 30th Conference of the Parties to the United Nations Framework Convention on Climate Change (COP30), which takes place this week in Brazil (*1*).

At COP30, Bolivia will discuss its updated Nationally Determined Contribution (2026–2035) (*2*), which was submitted in September 2025 (*3*). The plan sets ambitious climate targets across the country's forest, energy, water, agriculture, and waste sectors. However, achieving its goals is highly dependent on international cooperation and financing (*2*). Involvement of the Indigenous Native Peasant Autonomous Governments would help to implement nonmarket cooperative mechanisms under the Paris Agreement, in which developed nations provide grant-based financial support, technology transfer, and capacity-building rather than carbon-credit trading. This could be channeled through the Green Climate Fund, the Adaptation Fund, and bilateral partnerships with parties such as Germany and the European Union, which have already supported reforestation and integrated water-management projects in the Amazon region (*4*).

Rural communities, including Indigenous peoples, are the main stewards of Bolivia's ecosystems. By increasing consultation with, for example, Bolivia's Indigenous Native Peasant Autonomous Governments, improvements in managing local forest resources, community water systems, and fire-prevention networks could be achieved, reinforcing ecosystem resilience and food security at the local level. Unfortunately, rural residents are often ignored or even penalized when it comes to land-use issues. For example, some communities have been sanctioned (*5*) for opening small subsistence plots ("chacos") of 1 to 3 ha, which are essential for food security (*6*). This is in stark contrast to large forest concession holders, who each control between 50,000 and 200,000 ha (*7*). The vast majority have not conducted the legally required forest management audits since 1996 (*3*, *4*).

Notably, nearly 70% of Bolivia's land area is part of the Amazon Basin, the source of rivers that flow to the Amazon River, and about 7% of the Amazon rainforest lies in Bolivia (*8*). This setting reinforces Bolivia's constitutionally mandated defense of the Law of the Rights of Mother Earth, which was established in 2010. Bolivia's new leadership must reconcile that although this law is central to the updated Nationally Determined Contribution plan, the country has allowed increases in mining activities, large hydroelectricity projects, oil and gas exploitation, and large-scale agriculture.

As Bolivia begins a political transition, the country is poised to strengthen its climate policies. It can begin by committing to the Amazonian agenda set forth at COP30.

Flora Magdaline Benítez Romero[1,2] and Philip M. Fearnside[2]

[1]Universidad Amazónica de Pando, Cobija, Pando, Bolivia. [2]National Institute for Amazonian Research (INPA), Manaus, AM, Brazil. Email: pmfearn@inpa.gov.br

REFERENCES AND NOTES

1. Estado Plurinacional de Bolivia, "Nationally Determined Contribution (NDC) of the Plurinational State of Bolivia" [United Nations Framework Convention on Climate Change (UNFCCC), 2022]; https://unfccc.int/sites/default/files/NDC/2022-06/NDC_Bolivia-2021-2030_UNFCCC_en.pdf.
2. Estado Plurinacional de Bolivia, "Contribución Determinada a Nivel Nacional (CND 3.0" (UNFCCC, 2024); https://unfccc.int/sites/default/files/2025-09/Bolivia_NDC3.0_2026-2035%20final%2029.09.2024.pdf.
3. UNFCCC, Nationally Determined Contributions Registry (29 September 2025); https://unfccc.int/NDCREG.
4. UNFCCC, "Article 6.8: Non-market approaches" (UNFCCC, 2015); https://unfccc.int/process-and-meetings/the-paris-agreement/article-6/article-68.
5. L. E. Andersen *et al.*, "Deforestation and property rights in Bolivia" [Sustainable Development Solutions Network (SDSN) Bolivia, 2023]; https://sdsnbolivia.org/en/deforestation-and-property-rights-in-bolivia.
6. Forest Trends, Illegal Deforestation and Associated Trade (IDAT) Risk—Bolivia; https://www.forest-trends.org/idat_countries/bolivia.
7. Forest Policy, Forest Governance Risk Tool—Bolivia; https://forestpolicy.org/risk-tool/country/bolivia
8. F. Argandoña, S. C. Sunagua, ."Deforestation in Bolivia's Amazon rainforest" (SDSN Bolivia, 2023); https://sdsnbolivia.org/en/deforestation-in-bolivias-amazon-rainforest.

10.1126/science.aed3936

Science Webinars
AAAS

Science Webinars help you keep pace with emerging scientific fields!

Stay informed about scientific breakthroughs and discoveries.
Get insight into current research from top scientists.
Take the opportunity to ask questions during live broadcasts.
Get alerted to upcoming webinars.

Sign up at: scim.ag/wcfp2023

REVIEW SUMMARY

ORIGINS OF LANGUAGE

What enables human language? A biocultural framework

Inbal Arnon*, Liran Carmel, Nicolas Claidière, W. Tecumseh Fitch, Susan Goldin-Meadow, Simon Kirby, Kazuo Okanoya, Limor Raviv, Lucie Wolters, Simon E. Fisher*

Full article and list of author affiliations: https://doi.org/10.1126/science.adq8303

BACKGROUND: Explaining the origins of language is a key challenge in understanding ourselves as a species. We present an empirical framework that draws on synergies across scientific disciplines to facilitate robust studies of language evolution. The approach is multifaceted, seeing language emergence as dependent on convergence of multiple capacities, each with their own evolutionary trajectories. It is explicitly biocultural, recognizing and incorporating the importance of both biological preparedness and cultural transmission as well as interactions between them. Biocultural and multifaceted perspectives are increasingly appreciated, but there remains a need to integrate them within a unified framework and demonstrate how this advances understanding. We do so in this paper through three case studies examining the evolution of different facets of human language (vocal production learning, linguistic structure, and social underpinnings), each synthesizing the latest findings from multiple fields to generate valuable insights and setting a new agenda for future research.

ADVANCES: Case study 1 considers vocal production learning, an organism's capacity to enlarge and modify its repertoire of vocalizations based on auditory experience. This ability is crucial for learning spoken language and limited in nonhuman primates but has emerged in other branches of the evolutionary tree, including subsets of birds, bats, elephants, cetaceans, and pinnipeds. Bringing together data from molecular investigations of speech and language disorders, genetic manipulations in animal models, and studies of ancient DNA, this case study demonstrates how ancient genetic and neural infrastructures may have been modified and recombined to enable distinctive human capacities. Case study 2 examines the emergence of linguistic structure, a defining property of human language, using data from real-world cases of emergence (e.g., homesign and emerging sign languages); experiments recreating cultural evolution in the lab; and comparative studies of nonhuman animals, including songbirds and primates. This case study highlights the importance of transmission and interaction, suggesting that emergence of structure involves a combination of biological, cognitive, and cultural conditions: Although some (or all) traits are shared with other species, their combination may be specific to humans. Case study 3 focuses on the social underpinnings of communication across species. Social interaction contributes to language learning in humans and learned behaviors in other species with culturally transmitted communication systems, such as songbirds. But humans also demonstrate a strong internal drive to socially share information, which is rarely observed in nonhuman animals.

OUTLOOK: Drawing on diverse data, the case studies show how modification and recombination of abilities present in nonhumans, combined with intra- and intergenerational cultural transmission, may yield linguistic capacities in our own species. This perspective increases the range of species relevant for understanding language origins, as different abilities may be present across different branches of the evolutionary tree. The case studies also demonstrate the value of explicit biocultural framing, where both biological preparedness and cultural evolution shape language emergence. Language evolution is impacted by three distinct but interacting timescales: the individual (language learning), the community (cultural evolution), and the species (biological evolution). Understanding how the timescales interact and constrain one another requires synergies of data, methods, and fields. A recurring theme and avenue for future research is the role of biological reward systems in language evolution, including the motivation to communicate and endogenous and exogenous rewards for successful imitation and communication. Our integrative framework shows how research across disciplines and methods can advance understanding of a fundamental question in human evolution. □

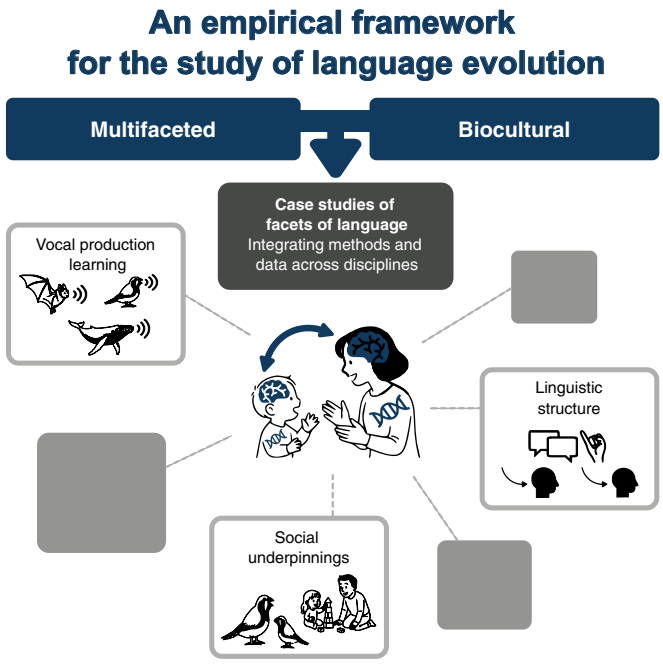

Our framework is both multifaceted and explicitly biocultural and is grounded in empirical investigations spanning a diverse array of fields and benefiting from major advances in methods, analyses, and theory. We demonstrate the potential of this integrated framework through three example case studies, each focused on a different facet with its own distinctive evolutionary history (other facets relevant to language, not discussed in the present paper, could be similarly investigated under this framework; these facets are represented by the empty gray boxes). Drawing on data from multiple disciplines and several species, including humans, primates, and songbirds, the case studies highlight the importance of both biological preparedness and cultural processes, as well as the interactions between them, in the emergence of language.

*Corresponding author. Email: inbal.arnon@mail.huji.ac.il (I.A.); simon.fisher@mpi.nl (S.E.F.) Cite this article as I. Arnon *et al.*, *Science* **390**, eadq8303 (2025). DOI: 10.1126/science.adq8303

ORIGINS OF LANGUAGE

What enables human language? A biocultural framework

Inbal Arnon[1]*, Liran Carmel[2], Nicolas Claidière[3,4,5], W. Tecumseh Fitch[6], Susan Goldin-Meadow[7], Simon Kirby[8], Kazuo Okanoya[9], Limor Raviv[10,11], Lucie Wolters[12], Simon E. Fisher[13,14]*

Explaining the origins of language is a key challenge in understanding ourselves as a species. We present an empirical framework that draws on synergies across fields to facilitate robust studies of language evolution. The approach is multifaceted, seeing language emergence as dependent on the convergence of multiple capacities, each with their own evolutionary trajectories. It is explicitly biocultural, recognizing and incorporating the importance of both biological preparedness and cultural transmission as well as interactions between them. We demonstrate this approach through three case studies that examine the evolution of different facets involved in human language (vocal production learning, linguistic structure, and social underpinnings).

Human language is a distinctive trait of our species, yet its origins are still not understood (*1*, *2*). The lack of any fossil record of the first language(s) together with many unknowns about human evolution and animal communication have led some to conclude that this question is scientifically intractable (*3*). We propose instead that studying language evolution lies well within the scope of scientific enquiry when new sources of data and theoretical perspectives are incorporated. We present an empirical biocultural framework for research on language evolution, applying it to three case studies, each examining a different facet involved in human language. Our aim is neither to comprehensively review the many existing theories nor to advocate for our own special one but to set an agenda for future interdisciplinary research, highlighting promising avenues.

This approach is multifaceted in seeing language emergence as dependent on convergence of multiple capacities (physical, cognitive, social, and cultural), each with its own developmental and evolutionary trajectories [see (*4*, *5*)]. Proposed facets include those related to production and perception of signals (e.g., vocal learning), systematic organization of language (e.g., linguistic structure), and communicative motivations (e.g., aspects of social behavior). A facet does not have to be specific to humans or language to offer explanatory value: Similar to the evolution of other complex biological systems (e.g., the eye), the emergence of language can be explained by modifications and recombination of ancestral infrastructures and exaptation of existing structures (*6*, *7*). This reflects a move away from "silver bullet" views of language evolution [e.g., (*8*, *9*)], where human distinctiveness is defined by just one explanatory factor (e.g., a single genetic mutation). Although such accounts have been historically prolific, persisting in some academic discourse and popular science writing, they are untenable in light of modern biology. Considerable evidence from multiple sources indicates that no one thing itself was enough to "give us language" or "make us human" (*10*–*12*). The multifaceted perspective calls for empirical investigations of larger historical windows. Although common wisdom was that language is specific to anatomically modern humans, appearing on the *Homo sapiens* lineage within the past 50 to 150 thousand years (kyr) [e.g., (*8*, *9*)], contemporary data suggest that deeper evolutionary timescales, those of hundreds of thousands (perhaps millions) of years, are more plausible (*10*, *13*). Even if the language system as we know it in present-day humans only emerged recently, then different facets may have evolved over longer timescales, under different selective pressures.

Our approach is also biocultural, recognizing and incorporating biological preparedness, cultural processes, and the interactions between them as key factors in language emergence. Understanding biological preparedness, including innate learning mechanisms and biases, is necessary to explain the distinctiveness of human language and helps guide comparative research on nonhuman species. However, no human infant develops a fully structured language in isolation; such languages arise only after extended social and communicative interaction [e.g., (*14*, *15*)]. Over generations, learners progressively systematize language through communication and cultural transmission (*16*–*18*), processes shaped by properties of the individual and the community (*19*, *20*). Computational simulations, experiments, and real-world cases of emergence identified specific cultural processes necessary for structured language to emerge. One reason nonhuman species lack human-like language may be their limited biological capacity to support these cultural processes. Notably, biology and culture can interact in complex nonintuitive ways. For example, the emergence of more complex communication systems can increase selective pressure on the cognitive mechanisms required to learn and produce complex signals. This could result in virtuous cycles of gene-culture coevolution (Fig. 1), making iterated biocultural processes central to understanding language emergence. Crucially, both classes of phenomena, biological and cultural, along with their interactions, can be empirically investigated in humans, nonhuman animals, and simulated or artificial agents (*21*).

Biocultural and multifaceted perspectives are increasingly appreciated in discussions of language evolution, but there is a need to integrate them in a unifying framework and show concrete examples of how that advances understanding. We demonstrate application of an integrated framework through three case studies, targeting different facets important for language emergence: (i) Vocal production learning: the ability to modify vocalizations based on experience, critical for acquiring spoken language; (ii) language structure: the systematic ways in which linguistic elements relate to one another, underlying the productivity of human language; and (iii) social underpinnings: behaviors and processes that facilitate social interaction, enabling cultural transmission of language. These are not claimed as the sole or primary facets relevant to language evolution but are used to demostrate the value of a biocultural framework.

Case study 1: Vocal production learning

Human language is inherently multimodal, expressible through speech, sign, writing, or touch (*22*, *23*). However, when available, speech is the primary modality across societies. Its acquisition depends on auditory-guided vocal production learning (VPL): the ability of an organism to flexibly enlarge and modify its repertoire of vocalizations based on auditory experiences (*24*). VPL is critical for learning the sounds and

[1]Department of Psychology, The Hebrew University of Jerusalem, Jerusalem, Israel. [2]Department of Genetics, The Alexander Silberman Institute of Life Sciences, The Hebrew University of Jerusalem, Jerusalem, Israel. [3]Centre de recherche en psychologie et neurosciences, UMR7077, Université Aix-Marseille/CNRS, Marseille, France. [4]Station de Primatologie-Celphedia, CNRS UAR846, Rousset, France. [5]Institute for Language, Communication and the Brain, Université Aix-Marseille, CNRS, Aix-en-Provence, France. [6]Department of Behavioral and Cognitive Biology, University of Vienna, Vienna, Austria. [7]Departments of Psychology and Comparative Human Development, University of Chicago, Chicago, IL, USA. [8]Centre for Language Evolution, University of Edinburgh, Edinburgh, UK. [9]Advanced Comprehensive Research Organization, Teikyo University, Tokyo, Japan. [10]LEADS group, Max Planck Institute for Psycholinguistics, Nijmegen, Netherlands. [11]Donders Center for Cognition, Radboud University, Nijmegen, Netherlands. [12]Department of Cognitive and Brain Sciences, The Hebrew University of Jerusalem, Jerusalem, Israel. [13]Language and Genetics Department, Max Planck Institute for Psycholinguistics, Nijmegen, Netherlands. [14]Donders Institute for Brain, Cognition, and Behaviour, Radboud University, Nijmegen, Netherlands. ***Corresponding author. Email: inbal.arnon@mail.huji.ac.il (I.A.); simon.fisher@mpi.nl (S.E.F.)**

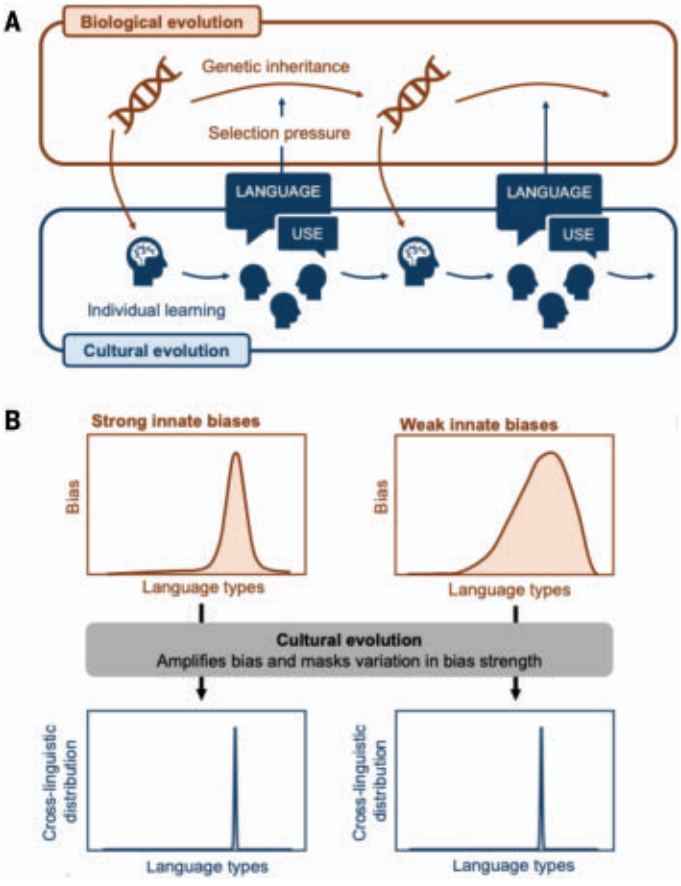

Fig. 1. Gene-culture coevolution model. Interacting processes operating on different timescales, from milliseconds to millennia, shape language emergence. (**A**) Processes of language use operate at the shortest timescale, as individuals comprehend and produce utterances in ongoing conversation. Learning to form these utterances (learning sounds, words, and rules) happens over a lifetime of exposure to the language of the community. Zooming out further, the structure of a specific language emerges and changes through cultural evolution, as knowledge of language is passed from one generation to the next. Lastly, the cognitive and anatomical machinery that allows humans to learn and use language has been subject to genetic evolution over the course of human evolution. The processes of biological and cultural evolution interact to produce a dual-inheritance system (*154*). Features of languages are inherited culturally, and the mechanisms that support such cultural inheritance are themselves inherited genetically. These processes may interact in complex and interesting ways, studied using mathematical and computational models that include all three timescales: individual learning and use, cultural evolution, and biological evolution. (**B**) One prominent approach, iterated Bayesian learning (*155*), treats learning as a process of inductive inference, combining utterances that the learner observes with a prior bias favoring particular types of languages. Cultural evolution is modeled as a process in which the languages inferred by one generation provide data observed by the next generation of learners. Iterated Bayesian learning allows us to compute expected results of cultural evolution for any hypothesized prior bias learners might have along with a model of how language is used for communication (*19*). This approach has been extended to the full dual-inheritance model by assuming that priors for learners are shaped by their genes, and these genes are selected based on communicative effectiveness of the individuals in the population (*156*). One notable finding is that the existence of cultural evolution tends to weaken inductive biases in language learning (*156*). Cultural evolution amplifies weak biases in individual learners, such that weak biases have the same outcome at the population level as strong constraints would. If strong biases are costly to maintain (e.g., by being more subject to mutation pressure), then weak biases are the inevitable consequence. This is surprising given previous work on the evolution of learning, which suggests the opposite: that learning can make evolution of innate constraints more likely (*157*).

open-ended vocabulary of language. Nonhuman primates appear much more limited than humans in their capacity to produce new vocalizations, but these abilities have emerged in other species, including subsets of birds, bats, cetaceans, pinnipeds, and elephants (*24*). There is increasing evidence that the independent appearance of VPL on different branches of the evolutionary tree involves deep homology (*25*, *26*), a phenomenon where convergently evolved traits recruit similar underlying genetic regulatory mechanisms across species (*27*). This aligns with the idea that some facets of language rely on ancient genetic and neural infrastructures, modified and recombined to enable more complex systems or abilities. The relevance of deep homology for understanding VPL is exemplified by studies of the *FOXP2* gene.

FOXP2 was originally discovered by using human genetics tools (Table 1) to investigate the biological bases of developmental speech and language disorders (*28*). Given adequate exposure to spoken language (and in the absence of sensory disorders), most children become proficient language users within the first years of life. However, there are unusual cases where this process goes awry. Before the advent of molecular methods, studies comparing identical and nonidentical twins and documenting recurrence of cases within families suggested that genetic factors play a role in these otherwise unexplained disorders without pinpointing the genes involved. In 2001, a rare pathogenic DNA variation in *FOXP2* was found to disturb development of the coordinated sequencing of mouth and face movements underlying proficient speech (childhood apraxia of speech) in a large family known as the "KE family" (*29*) (Fig. 2A). Multiple independent cases of people carrying *FOXP2* disruptions have since been reported, with developmental speech deficits being the most consistent consequence (*30*).

Once *FOXP2* was identified in humans, researchers looked for versions of the gene in other species, retracing its evolutionary history. Cross-species DNA comparisons (Fig. 2B) revealed that *FOXP2* is not specific to humans but is evolutionarily ancient, with similar versions in disparate vertebrates, including mammals, birds, reptiles, fish, and amphibians (*26*, *31*). There is high species-wide concordance in the places where this gene is active in the developing or adult central nervous system, including in subsets of neurons in the cortex or pallium, basal ganglia, thalamus, and cerebellum. These findings suggested that contributions of *FOXP2* to human speech may be built on ancient evolutionary pathways involved in motor-skill learning and vocal behaviors (*32*). Such deep evolutionary conservation means that genetic manipulations of versions of *FOXP2* in nonhuman species can help elucidate its functions and how these influence brain plasticity and behavior (*33*–*38*).

For example, though mice have very limited VPL capacities (*39*), valuable insights were gained from mouse models engineered to carry *FOXP2* disruptions known to cause speech disorders in humans (Fig. 2C). Mice carrying the pathogenic variant of the KE family show motor skill learning deficits and altered neuronal properties in basal ganglia and cortex (*33*–*36*), among other findings. Investigating nonhuman animals that are vocal learners, such as songbirds, is even more revealing (Fig. 2D). Male zebra finches sing structured songs comprising vocal elements (syllables) arranged in a stereotyped sequence, which they learn as juveniles by listening to adult males (*37*). During this developmental period of plasticity, *FoxP2* (the avian version of *FOXP2*) has elevated activity in Area X, a basal ganglia structure that is crucial for VPL (*37*). Experimentally reducing *FoxP2* Area X activity interferes with song learning and variability, potentially mediated by disturbed dopaminergic signaling (*37*, *38*). Thus, impacts of this gene on brain plasticity linked to sensorimotor functions and motor skill learning may have been independently recruited toward VPL in disparate species (i.e., supporting speech in humans and song in zebra finches). Most recently, genome-wide investigations of >200 mammals with different vocal-learning capacities pinpointed multiple additional genetic loci as candidates for cross-species involvement in VPL (*40*).

Table 1: Identifying genetic links to language through genomic studies in modern humans. Researchers can investigate genetics of relevant pathologies (childhood apraxia of speech, developmental language disorders, etc.) by identifying genetic correlates of individual differences in language-related skills in the general population, exploiting advances in molecular methods and analytic approaches.

Type of DNA variation	Biological impact	Molecular methods	Typical study designs	Examples from the literature	Linking to evolution
Rare gene disruptions	Rarely, a change at a single genetic locus can be sufficient to substantially derail language development.	Advances in next-generation sequencing now allow rapid reading of almost all of a person's genome at high resolution at a fraction of the cost of classical methods.	Pathogenic variants can be identified by analyzing DNA of relatives in multigenerational families where multiple individuals have a developmental speech and/or language disorder.	The first rare gene variants in childhood apraxia of speech were discovered by studying a three-generation family before the advent of next-generation sequencing (*29*).	The evolutionary history of genes implicated in speech and/or language disorders can be retraced by comparing to versions found in extinct archaic hominins and extant apes and testing for evidence of Darwinian selection at these genomic loci on the lineage leading to *H. sapiens* (*177*).
			A complementary approach investigates de novo cases of disorder (where parents or siblings are unaffected) to identify pathogenic DNA variants that are only present in the affected child.	Whole-genome sequencing in speech apraxia has since identified pathogenic de novo disruptions of multiple candidate genes, with regulatory roles in early brain development (*178*).	
Common variation	Many studies focus on single-nucleotide polymorphisms (SNPs) found at >1% frequency in the general population. Any one SNP by itself has little impact, but combinations of many such variants across the genome may jointly explain a significant proportion of trait variance.	High-throughput low-cost genotyping technologies, such as DNA microarrays, make it possible to capture allelic variation at millions of SNPs in large samples. These technologies fueled the rise of genome-wide association studies (GWASs) that systematically screen vast numbers of SNPs, testing each for a relationship with a trait of interest.	One GWAS design is a case or control study assessing contributions of common DNA variation to a disorder (or categorical trait). GWAS designs can also identify associations of SNPs with individual differences in quantitative traits. Because the effect size of one SNP may be tiny, cohorts of tens (even hundreds) of thousands of people are needed to give adequate power while adjusting for substantial multiple testing.	In a multicohort GWAS study of individual differences in quantitatively assessed reading- and language-related skills involving <34,000 participants, researchers could capture up to 26% of trait variability with common DNA variation (*179*).	Findings on genetic contributions to individual differences in language-related skills and/or neural infrastructure in living humans can be integrated with information about evolutionary signatures across the genome over a range of different timescales in primate and hominin history. For example, a UK Biobank study used this approach to uncover effects of human-gained regulatory elements on left-hemisphere brain regions related to speech, among other findings (*180*).
			Studies of genetic associations with language-related traits can be extended to individual differences in brain structure and function, assessed with neuroimaging. Effect sizes of individual SNPs are small even for traits measured with magnetic resonance imaging (*181*). With availability of neuroimaging and DNA data in large biobanking resources, it is now possible to carry out GWAS studies of neural circuits involved in language processing.	GWAS investigations of structural and functional connectivity in the brains of ~30,000 to 32,000 participants in the UK Biobank have given new insights into how genetic variants contribute to language-related circuits in the human brain [e.g. (*182*)].	

Identifying genes contributing to VPL across species allows researchers to use a transformative new data source to test hypotheses about language evolution: ancient DNA. In the past 15 years, it became possible to obtain high-quality sequence information from nuclear genomes of Neanderthals and Denisovans, extinct hominins that shared with modern humans a most recent common ancestor ~600 kyr ago (*41*). These archaic hominins existed until a few tens of thousands of years ago, temporarily overlapping with *H. sapiens* at sites across Eurasia (*42*). Analyzing ancient genomes enables detection of DNA variants that arose in modern humans after our split from Neanderthals and Denisovans (*43*). It also enables detection of variants that we share with archaic hominins, but that are distinct from those in extant nonhuman apes. These more ancient variants arose after our split from the common ancestor of chimpanzees and bonobos ~6 million years (Myr) ago but before the split between modern and archaic humans (*44*). Applied to *FOXP2*, this approach identified two amino acid changes in the protein that it encodes, both arising on the *Homo* lineage during the 6 Myr to 600 kyr time window (*45*). Researchers used genetic manipulations to introduce the hominin amino acid substitutions into mice, observing varied effects on vocal behaviors and basal ganglia functions (*46*–*49*) (Fig. 2E). Thus, by identifying evolutionary variants in genes implicated in facets of language and introducing them into nonhuman animals, we can investigate whether these variants affect brains and behavior in ways that might be relevant to language emergence. Despite this promise, we stress that no single genetic change is, by itself, sufficient to yield a vocal-learning brain (*50*).

Evolution acts not only through genetically specified changes to protein structure and function but also by modifying where and when

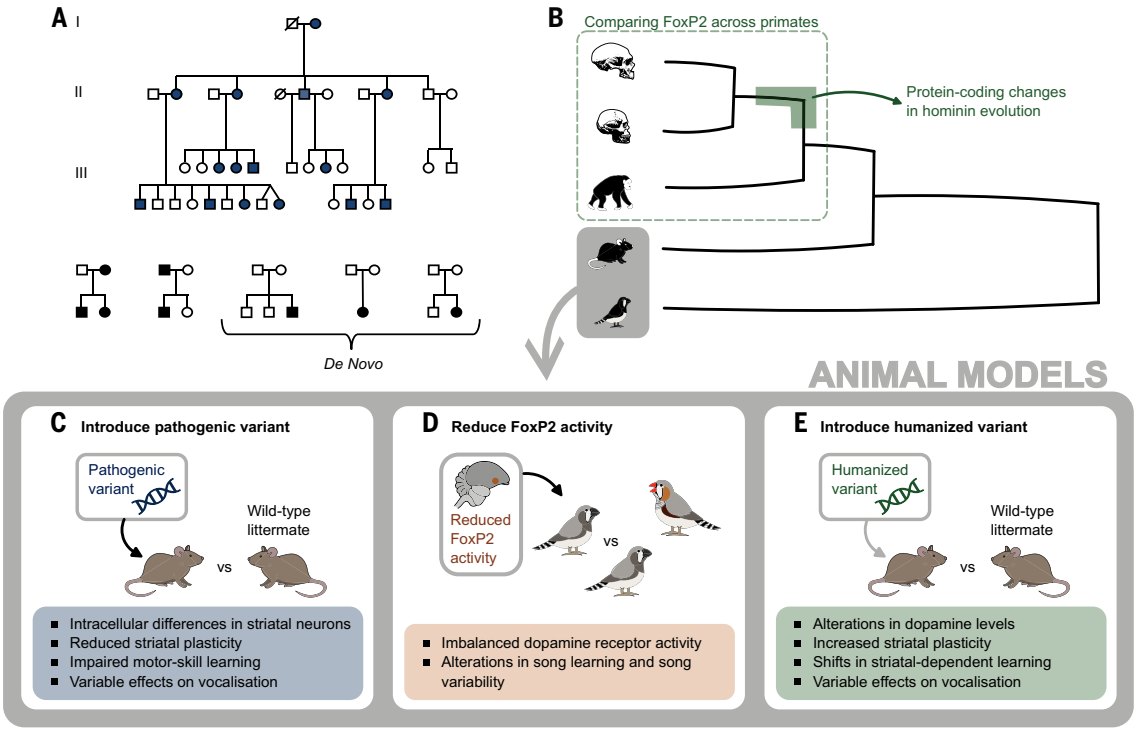

Fig. 2. Investigating evolution of vocal production learning with tools of molecular genetics: *FOXP2* as an example. (**A**) The starting point was a three-generation family, the KE family, in which half of the relatives (shaded symbols) were affected by a neurodevelopmental disorder primarily involving childhood apraxia of speech, accompanied by expressive and receptive language deficits (top). The affected relatives carried a change of one DNA letter (nucleotide) in the *FOXP2* gene (*29*). This small change in DNA alters the amino acid sequence and, hence, the shape of a key part of the regulatory protein that *FOXP2* encodes, stopping it from functioning in its normal way. Advances in DNA sequencing led to identification of >28 additional individuals (from 17 families) carrying different pathogenic single-nucleotide variants of *FOXP2*, with problems in speech development being the most common feature found in these cases (*30*). As shown in the bottom of the panel, although pathogenic variants were sometimes inherited from affected parents, in many of the cases, they arose de novo in children with unaffected parents. (**B**) Comparisons of DNA sequences across different species (comparative genomics) identified versions of *FOXP2* in distantly related vertebrates, including mammals, birds, reptiles, fish, and amphibians (*26*,*31*), showing that the gene has a deep evolutionary history. Against this background, integration of findings from extant apes and extinct archaic hominins revealed that changes in the amino acid sequence of the encoded protein occurred on the *Homo* lineage after splitting from the common ancestor of chimpanzees and bonobos (*45*). (**C**) Researchers engineered mouse models that carry the same pathogenic variant that causes speech problems in the KE family. Investigations of these mice reported motor skill learning deficits (*33*), reduced plasticity in the striatum (part of the basal ganglia) (*34*), disturbed intracellular "protein motors" in striatal neurons (*35*), and loss of neuronal homeostasis in deep-layer cortical neurons (*36*), among other findings. (**D**) Moving to songbirds, lentivirus-mediated RNA interference has been used to reduce activity of *FoxP2* (the avian equivalent of *FOXP2*) in Area X, a key nucleus in the basal ganglia of male zebra finches. Such studies uncovered effects of the gene on song learning and the control of song variability, potentially mediated by changes in dopaminergic signaling (*37*,*38*). (**E**) When researchers used genetic manipulations to introduce hominin amino acid substitutions of *FOXP2* into mice, they observed regional changes in dopamine levels and increased plasticity in the striatum (*46*). Motor skill learning and vocal behaviors of adult male mice were unaffected according to one study (*47*), but later investigations of female and male vocalizations in social contexts found that the partially "humanized" mice used higher frequencies and more complex syllable types (*48*). Another study of these mice uncovered different patterns of striatal-dependent stimulus-response association learning (*49*). Overall, this suite of human and animal model studies shows how genes involved in VPL can be empirically investigated across species to give new insights into evolutionary pathways.

genes or proteins are active in development and adulthood (*51*). These effects are mediated by a wide variety of regulatory elements in the genome. Many of the DNA variants distinguishing us from other extant apes and extinct hominins may lie within such elements. For example, among primates, *FOXP2* shows human-specific expression in microglia, the primary immune cells of the brain, although the regulatory elements responsible for this specificity are not yet described (*52*). Moreover, innovations in paleoepigenetics take advantage of degradation processes in ancient DNA to reconstruct patterns of methylation, a chemical modification that helps mediate changes in gene activity without changing DNA sequence itself. This approach revealed changes in gene regulation differentiating Neanderthals and/or Denisovans from modern humans (*53*). Several of the identified modern human-specific gene expression changes are associated with genes that affect the face and voice and may underlie characteristics that are specific to modern humans (*54*).

Additional insights into VPL evolution come from considering developmental processes. Take babbling, an early, self-initiated form of vocal production in infants that starts as simple and repetitive verbal "play" but gradually approaches a mature form. Babbling-like behaviors have been documented in humans, songbirds, parrots (*55*, *56*), and vocal-learning bats (*57*) but are not common in species lacking VPL. Manual "babbling" is seen in hearing and deaf human babies exposed to signed language from birth (*58*), illustrating both the multimodality of language and the role of babbling in language acquisition. Deaf babies also babble vocally, but this babbling does not progress normally when appropriate input models are inaccessible (*59*), demonstrating how biological preparedness and environmental input interact in language learning.

Babbling (termed "subsong" in birds) is self-generated and self-rewarding, occurring without immediate environmental triggers or exogenous rewards. Thus, part of the biological preparedness for VPL

includes an endogenous reward system, making vocal play enjoyable to the young organism without feedback from parents or others. Although little is known about the underlying circuity in humans, recent evidence implicates endogenous reward in songbird vocal behaviors. Avian song learning begins with a sensory learning period in which the bird stores auditory templates of exemplars of its species' song. This involves an endogenously rewarding listening process: Juveniles selectively attend to and memorize songs of their own species, indicating that hearing them is intrinsically rewarding (*60*). Endogenous reward is key during the subsequent sensory-motor learning period, when spontaneous subsong is gradually adjusted, without external feedback, to approach stored adult template(s) (*61*–*64*). Vocal practice correlates temporally with neural expression of opioid markers and increased activity in reward systems (*61*), and blocking dopamine receptors in the basal ganglia in young zebra finches impairs song copying (*63*). Later in development, both infant babbling and bird subsong are impacted by social reinforcement (see case study 3), but the early self-reinforcing stages are required to provide raw material for later, exogenously directed, learning. Evolution of VPL may therefore depend both on changes to neural circuits involved in learning and on those underlying endogenous reward.

Case study 2: The emergence of linguistic structure

Human language shows systematic structure at multiple levels and of multiple kinds. Elements can be combined in productive ways, with the meaning of larger units composed of the meanings of their parts (e.g., "cat," "cats," "big cats"). There is ongoing debate on how to define and quantify this systematicity. In this case study, we classify a behavior as systematic when it can be described more concisely as a set than as a collection of individual instances. "Grammars" in linguistics (in the most theory-neutral use of that term) refer to these shorter descriptions and are possible because language is systematic. For example, it is more concise to describe formation of the regular English plural using the rule "add -s to the singular form" than to list all plural forms. Although prevalent in human language, systematicity is rare in the vast majority of communication systems in nature. An extensive literature investigates neural correlates of systematic language structure [see (*23*, *65*)]; comparing those circuits across humans and nonhuman primates offers ways to study their evolution [e.g., (*66*–*68*)]. Though illuminating, current literature leaves open how linguistic structure first came about.

Over the past 25 years, various experimental and computational methods have been developed to study origins of systematic linguistic structure (*17*, *69*–*71*) and ask how that structure is shaped by cognitive and communicative pressures. Specifically, language must serve the communicative needs of interacting language users and be learnable by subsequent generations of language users. Because language is culturally transmitted (passed on by being repeatedly learned and used by multiple generations), its structure is impacted by the interplay of communicative and cognitive forces. To demonstrate, we here focus on one feature: combinatoriality, the fact that language has units that can be recombined, at multiple levels of linguistic analysis (*19*, *72*, *73*). For example, sounds can be combined into words, and words can be combined to form sentences.

How did this combinatoriality emerge? We have no access to or record of hominin communication systems preceding modern human languages. However, insights can come from real-world cases of emergence (*74*) and lab-based studies recreating evolutionary processes in miniature (*20*, *75*, *76*). Two real-world settings illuminate the pressures and biases impacting the emergence of linguistic structure in modern-day humans. One is homesign, gesture systems created by individuals whose hearing loss prevented them from accessing spoken language and who were not exposed to sign language (*77*). Another is emerging sign languages, where new signed languages develop in communities with a high proportion of deaf individuals, lacking access to an established signed language. An influential example is Nicaraguan Sign Language (NSL), which spontaneously emerged when homesigners were first brought together in the mid-1980s (*78*). Examining how linguistic structure in such systems changes over time demonstrates how individual learning and cultural transmission impact the emergence of structure.

Researchers have documented and compared linguistic structure in solo language creators (homesign), homesigners who came together and formed the first NSL cohort (NSL1), and subsequent cohorts of signers who entered the community after the language began and were thus exposed to a language model (NSL2, NSL3, etc.). Some linguistic structural properties are observed in solo creators, irrespective of the specific cultural environment they were raised in. Child homesigners in the US, China, Turkey, and Nicaragua use gestures to refer to objects, actions, and attributes and combine them into strings characterized by consistent word order. For example, gestures for the object of an action appear before gestures for the action, yielding "grape-eat" as opposed to "eat-grape" (*77*, *79*) (Fig. 3). These same properties appear across societies, without exposure to linguistic input, indicating shared human cognitive biases [e.g., hierarchical structure (*80*)]. Other properties emerge only after homesigners came together to form NSL1 [e.g., a stable lexicon (*79*)], highlighting the importance of communication with others in shaping linguistic structure. Still other linguistic properties are not produced by homesigners or in NSL1 but tend to appear only after the emerging sign languages are transmitted to new learners. For example, spatial modulations are rare in NSL1 but commonly used to indicate shared reference in NSL2 (*14*).

A well-studied feature of NSL, relevant to combinatoriality, involves how complex motion events are conveyed. Consider a ball bouncing down a hill. In early NSL cohorts, both the ball's path (downwards) and its movement manner (bouncing) are typically conveyed simultaneously [(*78*) but see (*81*)]. However, later cohorts typically segment path and manner into separate parts, yielding a more combinatorial flexible system. Thus, transmission from one cohort to another seems important for building and enhancing combinatoriality. In an experimental analog of the homesign situation, nonsigning participants are asked to convey meanings with gesture and no speech (*82*). When presented with complex motion events possessing manner and path components, participants prefer to convey both aspects simultaneously even if expressed separately in their spoken language (*83*). However, gestures and vocalizations beginning as holistic (e.g., simultaneously expressing motion and speed) become more segmented and linearized during ongoing dyadic communication (*84*, *85*).

Experiments can recreate processes of cultural evolution using a paradigm called iterated learning. In these studies, a participant learns from the output of a previous participant in the experiment, creating multiple simulated "generations" (*17*). When silent gestures get transmitted in this way, there is a learning-driven preference for segmented manner and path. This preference is amplified over generations [as in NSL2 (*78*)] so that more systematic and combinatorial behaviors emerge (*84*, *85*). More generally, productive units emerge during dyadic and group communication paradigms (*20*, *86*, *87*), a process enhanced by learning and transmission (*88*). The combined findings demonstrate that systems starting as a collection of wholes are gradually segmented and analyzed into productive parts, consistent with evolutionary approaches that propose a holistic origin for language (*89*, *90*). Further evidence for the role of whole-to-part learning comes from first language acquisition (*91*) and homesign creation (*92*), where learners discover parts from unanalyzed wholes [e.g., "Ididit" > "I did it" (*93*)] in ways that facilitate the mastery and emergence of systematic structure (Fig. 3) (*94*, *95*).

Real-world language emergence and lab-based studies necessarily involve humans with modern brains but are nevertheless informative. Linguistic features evident in homesign provide insights into products of biological evolution. Properties that homesigners fail to develop but

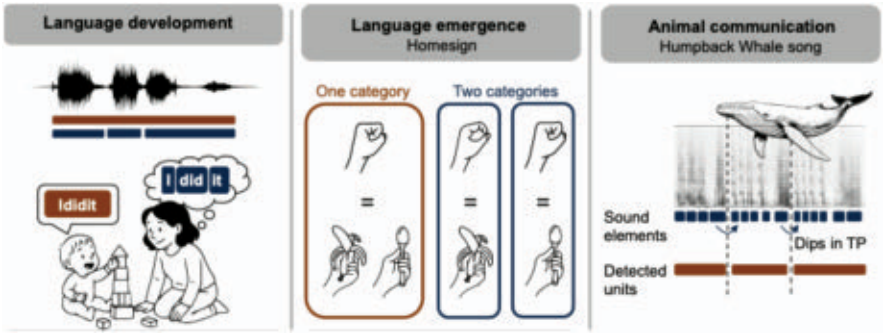

Fig. 3. Finding the right units. One of the challenges in studying communication in children and nonhuman animals is zeroing in on the right unit of analysis. This is challenging because the units we use to code data are influenced by hypotheses [explicit or implicit (*158*)], often based on our own categories. For example, when we describe early child language, we typically attribute individuated words to the child (left). But we might be wrong; a child might use a larger unit, treating several words as a single "chunk" (*91*,*159*). Infants extract single word units from the speech they hear, but they also extract larger units containing more than one lexical word (*91*,*93*). In fact, starting from larger units plays an important role in learning linguistic structure, particularly in learning grammatical relations between words (*91, 94, 95*), and in creating linguistic structure (*92*). One way to validate the categories we use is to find systematic patterns based on those categories, providing indirect evidence for the categories and also for their level of representation. For example, using semantic roles (patient, act, recipient, etc.) to categorize homesigners' gestures results in systematic orderings (patient-act, patient-recipient, and act-recipient), which validates coding at this level (*160*). But sometimes our coding system fails to produce systematic patterns. This may be the time to scrap the system and start again, coding at a level smaller than the one previously used (middle). For example, homesigners could vary thumb-to-finger distance so that the handshape in the gesture for banana grasping is distinct from that in the gesture for spoon grasping (as they are when these objects are actually grasped). Alternatively, homesigners could use the same handshape in both gestures, introducing one larger category for grasping objects <1 inch in diameter. To discover the homesigner's categories, we need to code in units that are smaller than the units on which those categories are based; otherwise, the categories may be created by us, not the child (*161*). When we seek the right units in nonhuman communication [e.g., gestures in great apes (*162*)], the challenge is greater because we have limited insight into the categories relevant to nonhuman animals (*163*) and must validate the categories in the animal itself [e.g., by using playback experiments, (*164*)]. Nonetheless, the approach of seeking out coherent patterns can also help reveal units in animal communication (right). For example, using transitional probabilities (TP) between syllables to segment humpback whale song [a cue used by human infants to segment speech (*113*)] uncovered statistically coherent subsequences whose frequency distribution followed a particular power law also found in all human languages (*165*). This points to a notable similarity between two evolutionarily distant species (whales and humans), united by having culturally transmitted communication systems. Debates about how to detect the appropriate units continue (*166*), with new perspectives coming from machine learning (*167*). In general, allowing for units at multiple levels of representation provides insight into structure in child language, homesign, and animal communication (*168*).

are found in emerging sign languages are good candidates for ones that require cultural evolution to emerge (*15*). With lab-based studies, researchers can manipulate communicative and cognitive pressures in ways that cannot be done in the real world to assess effects on emerging systems. Moreover, computational simulations, not yet discussed [but see Fig. 1 and (*96*, *97*)], allow investigation of learning biases that may differ from those of modern humans. Notably, it is still an open question of which, if any, capabilities underlying language structure are distinctly enhanced in humans. One component hypothesized as highly developed in humans and weak or absent in other species is "dendrophilia," a domain-general proclivity to infer tree structures from data whenever possible (*98*) (Fig. 4).

So far, we have demonstrated impacts of learning, communication, and cultural transmission in creating combinatorial structure in humans who are already biologically prepared for language. Roles of biological evolution can be investigated by using animal models. In this case, researchers control preparedness through the choice of species while experimentally manipulating social pressures and rewards. Two relevant models are songbirds and baboons, who differ from humans and each other in important ways. As introduced in case study 1, songbirds are vocal production learners with culturally transmitted song (*99*, *100*). Songbirds are also among the few nonhuman animals whose signaling exhibits combinatorial structure. Songs are constructed from individual elements that are repeated and recombined (*101*). Despite their "instinct to learn" a species-typical song (*102*), isolated songbirds deprived of appropriate input sing only a harsh, atonal "isolate song" (*101*). When isolate songs are transmitted to successive generations of learners through iterated learning, zebra finches converge within a few generations on a new (albeit well-formed and species-typical) song exhibiting combinatorial structure (*103*). Even if this developmental process is limited to one bird hearing its own songs played back after a delay, a more species-typical song results (*104*). Transmission over generations or iterations seems crucial for the emergence of elaborated species-typical structure, whether the starting point is isolate song in vocal-learning birds or homesign in humans.

Songbirds are biologically prepared to learn and transmit songs. By contrast, despite powerful learning abilities (*105*), nonhuman primates largely lack culturally transmitted communication systems, and the combinatoriality of their gestural signaling is not as productive or widespread as in humans or songbirds (*106*). Recent evidence indicates a degree of combinatoriality in vocalizations of some ape or primate species [e.g., (*107*, *108*)], though it is unclear whether they are used communicatively. Experiments with captive baboons suggest that systematically structured behavior can emerge in animals lacking it if cultural transmission is supported externally (*109*). In these studies, baboons are given exogenous rewards for reproducing randomly generated visual patterns. Cultural transmission is experimentally simulated by providing patterns from one baboon as input to another, creating an iterated learning design. Notably, systematically structured patterns emerge over iterations: although baboons lack biological preparedness for cultural transmission, when transmission is supported externally, structured patterns emerge. These experiments demonstrate that adding exogenous rewards for copying behavior (present endogenously in humans and songbirds) facilitates the emergence of systematicity.

Case study 3: Social underpinnings of language

Social interactions are key for first language acquisition, with individual learning typically occurring within interactive contexts (*110*, *111*). These interactions provide children with valuable linguistic input, facilitating learning in various ways (*112*). Although infants can learn in noncommunicative settings and do so in experimental contexts (*113*, *114*), many aspects of language learning are facilitated by social interaction (*112*). For example, contingent maternal responses yield more mature vocalizations in human infants (*115*). Similarly, learning of non-native phonetic sounds in infancy is enhanced by social interaction (*116*). Both homesign and emerging sign languages (case study 2) are motivated by the need and desire for social communication [although in homesign, the communications systems themselves are not shared with others (*117*)]. Later in development, there is evidence of bidirectional links between language abilities and aspects of

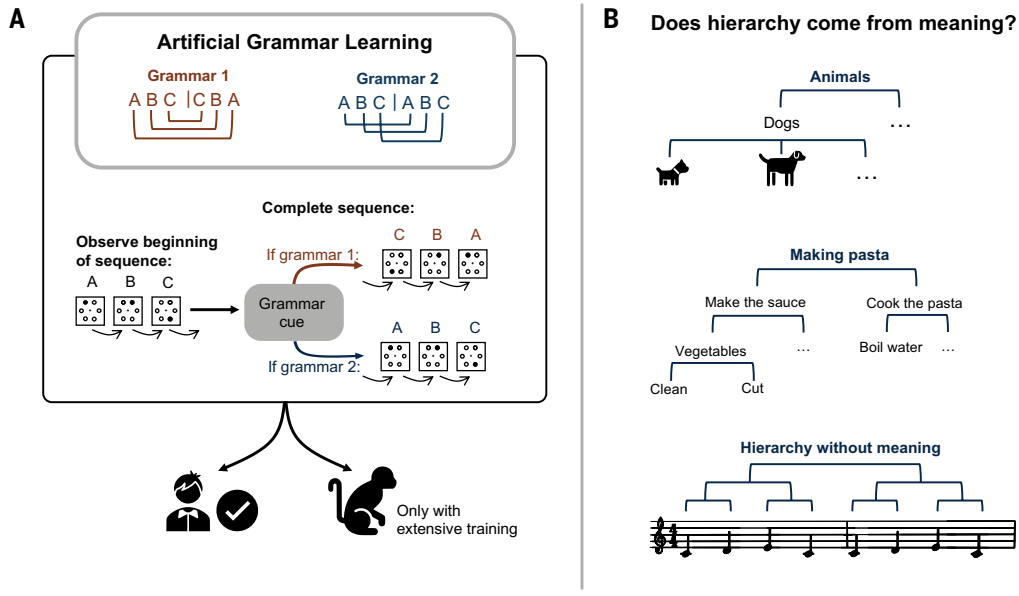

Fig. 4. The origins of hierarchical structure: Dendrophilia or semantics? An open question for the field concerns which, if any, capabilities underlying language are specifically enhanced in humans. One component hypothesized as highly developed in humans and weak or absent in other species is "dendrophilia," a domain-general proclivity to infer tree structures from data whenever possible (*98*). Dendrophilia combines a domain-general capacity to perceive hierarchical structures in stimuli with a strong preference to encode data into hierarchical structures. (**A**) This preference is often studied using Artificial Grammar Learning (AGL) experiments, where learners are exposed to sequences of stimuli whose appearance is governed by an underlying hierarchical grammar. If learners deduced the grammar, then they should be able to complete sequences in a way that conforms to it. Considerable experimental evidence from cross-species AGL research supports dendrophilia as being both highly developed and biologically canalized in humans and reduced or absent in other species studied to date (*4*,*169*,*170*). For example, a recent study found that, with adequate time and a consistent exogenous reward structure, macaque monkeys can learn hierarchical structures based on meaningless spatial or motor sequences, but learning required many months and tens of thousands of rewarded trials. By contrast, preschool children learn these same systems rapidly, in as few as six trials, with few or no errors (*170*). The presence of some hierarchical structure in homesign (case study 2) offers further evidence of biological preparedness for dendrophilia in our species (*80*). However, the finding that linguistic structure emerges gradually over generations indicates that cultural transmission is important for explaining hierarchical structure in fully developed languages (as for birdsong). Some precursor(s) of dendrophilia may be present in the motor and/or social domain in other primates, such as the perception and processing of complex dominance hierarchies, as shown in baboons and other socially complex species (*171*,*172*). (**B**) The problem of acquiring and using treelike structures may be greatly reduced in contexts involving signal or meaning pairs (as in human language). If semantics already possess hierarchical structure and signals are mapped onto this hierarchical meaning space, then it may strongly bias the learner to impose or perceive tree structure in the signals themselves. Notably, the existence of hierarchical structure in human music [e.g., (*173*)] or similar systems, such as bird or whale song [e.g., (*174*)], where signals do not map onto highly structured meanings, suggests that compositional semantic mappings are not necessary (or solely responsible) for hierarchical structure to emerge. Similarly, in AGL experiments, humans readily perceive hierarchical structure in meaningless visual strings (*175*,*176*). Better understanding of the neural mechanisms involved in structural learning and innovative new methods to "tweak" reward structures in animals can shed light on origins of hierarchical structure not just in language but also other domains, such as music and art.

social cognition or interaction (*118*–*120*). Gains in prosocial behaviors in early childhood (age 3 to 5 years) are significantly associated with later gains in verbal ability (age 5 to 11 years), and vice versa (*121*). Better language skills facilitate children's social–emotional competence, allowing formation of more prosocial, cooperative relationships (*121*–*124*). Conversely, language difficulties often associate with increased difficulty with social interactions (*125*, *126*).

Social interaction contributes to individual learning in other species with culturally transmitted communication systems. Although we stress the importance of endogenous reward during early birdsong acquisition, exogenous reinforcement from social partners is crucial in later learning, maintenance, and modification of song (*127*, *128*). Female cowbirds provide behavioral feedback (wing flaps) to courting males, influencing later use of particular syllables or syllable sequences (*127*). When parent zebra finches give behavioral feedback, juveniles develop more accurate copies of tutor song (*128*). Exogenous reward of vocal learning involves dopaminergic systems (*129*, *130*). Socially tutored zebra finches show higher activity of dopaminergic neurons in the ventral tegmental area compared with that of birds who passively heard songs or untutored controls (*129*), and optogenetically blocking dopaminergic input to song circuits during social tutoring impairs song learning (*64*).

Beyond social underpinnings, which enable cultural transmission of language, humans have a strong, unparalleled internal drive to socially share information, including about inner states, emotions, and ideas using language ["Mitteilungsbedürfnis" (*2*)]. Sharing for sharing's sake is prevalent in humans but rare in nonhuman primates. Even language-trained apes, who master aspects of human sign language, show limited interest in using this to express things other than direct requests (*131*, *132*). By contrast, our drive to share thoughts and feelings with others is so strong that humans create a communication system de novo even if one is not available (case study 2).

The social context together with our "mitteilungsbedürfnis" make language learning and use rewarding for humans. How might the evolution of reward mechanisms relate to emergence of communication systems? One evolutionary pathway of potential relevance is the process of domestication. The Bengalese finch, a domesticated variant of a wild songbird, the white-rumped munia (*133*–*136*), offers an example of relationships between changes in reward and communication systems. As in many domesticates, stress hormone levels are significantly lower in Bengalese finches compared with that in munias (*135*), and the former display less aggression (*134*) and explore new environments faster than their wild counterparts (*136*). Notably, Bengalese finches produce songs with greater phonological and syntactic complexity than those of munias (*137*). They are capable of learning munia songs, whereas munias struggle to master Bengalese songs (*133*). Domesticated Bengalese show higher concentrations of cerebral oxytocin than their wild ancestors (*138*, *139*); oxytocin and dopaminergic reward systems are known to be closely interconnected (*140*, *141*).

Did humans follow evolutionary pathways similar to those underlying animal domestication, where less aggressive individuals that were more prone to cooperatively interact had a greater likelihood to survive and/or reproduce? According to the human self-domestication hypothesis, such processes enhanced social learning and cultural transmission in humans (*142*–*144*). This could generate virtuous cycles at the

community level: Increased social reward for communication favors emergence of more advanced forms of communication, enabling larger in-groups and more interaction with nonkin, which results in even richer social interaction. Some support for links between greater communicative complexity and greater social complexity (operationalized by larger group sizes, more dense networks, etc.) comes from multispecies comparative research, from bats to primates (*145*, *146*). Human experimental data provide suggestive evidence: Artificial languages evolving in larger microsocieties of interacting participants show more systematic compositional structures, emerging faster and more consistently than in smaller groups (*20*).

Discussion

Our case studies include diverse data sources (behavioral, neural, genetic, and developmental) and adopt broad comparative perspectives, with particular focus on humans, primates, and songbirds. They demonstrate how facets involved in language emergence can be insightfully studied in nonhumans. No single method, tool, or model holds all the answers, and investigations of different facets may require different approaches. A common thread is that exaptation and recombination of abilities present in nonhumans, combined with intra- and intergenerational cultural transmission, can yield linguistic capacities in our own species. VPL, crucial for acquiring spoken language in humans, is a capacity that humans share with other species, appearing in diverse branches of the vertebrate evolutionary tree. Social underpinnings needed for human language transmission are documented in other species with culturally transmitted systems, but humans also demonstrate communicative tendencies rarely observed in nonhuman animals (e.g., our "mitteilungsbedürfnis"). Emergence of linguistic structure, a defining property of human language, involves a combination of biological, cognitive, and cultural conditions: Although some (or all) conditions are shared with various nonhuman species, the combination may be specific to humans.

The case studies demonstrate the value of explicit biocultural framing, showing how language emerges dynamically at three distinct but interacting levels: the individual (language acquisition and use), the community (cultural evolution and historical language change), and the species (biological evolution). The human ability to acquire and use language as well as languages themselves result from multiple interactions over time and among these levels, making all three important for understanding language emergence. Biological evolution generates the biological preparedness to acquire language shared by all human infants. Through individual learning in a social setting, the child acquires the language(s) of their community, which themselves develop through dynamic processes of cultural evolution. The ways in which these distinct levels interact, constrain, and structure one another can be nonintuitive. Understanding them requires combinations of data, models, and experiments.

A recurring theme and promising avenue for future research is the role of biological reward systems in language evolution. These systems include the motivation to communicate and both endogenous and exogenous reward for successful imitation and communication during language acquisition, use, and transmission. Although it is currently impossible to "insert" endogenous rewards for babbling into species that lack them, we can experimentally block such rewards, as shown for songbirds [case study 1 (*63*)]. Further, we can experimentally introduce exogenous rewards to trigger learning in species that lack endogenous reward systems for the learned behavior; potentially "unmasking" cognitive capabilities that were previously unexpressed in that species, as in baboon studies [case study 2 (*147*)]. These experiments can empirically circumvent the common criticism that investigating modern humans, who are already biologically prepared to acquire language, reveals nothing about how key facets evolved.

An open issue concerns modality. Like many researchers, we see language as inherently multimodal (*22*), and our case studies consider both spoken and signed languages. However, we have not discussed possibilities that the use of visual and auditory modalities may emphasize different types of structure. Because gestural capabilities of apes greatly exceed their vocal flexibility, some researchers have suggested that human language origins may be found in gesture and/or sign ("gestural protolanguage") rather than speech (*148*, *149*), whereas others vehemently deny this (*150*, *151*). The multifaceted biocultural framework combined with data showing that, like humans, primates are multimodal communicators (*152*, *153*) strongly suggest that gesture coexisted with vocal communication, and eventually language, all along. Furthermore, vocal-learning abilities might have already been enhanced in archaic hominins, such as Neanderthals (case study 1), although they likely lacked fully modern language. Thus, asking whether sign or speech came first is the wrong question. Productive future debate should center on how gesture and speech support one another and why language (unlike, say, birdsong) is flexible enough to be conveyed by radically different sensory systems.

REFERENCES AND NOTES

1. M. H. Christiansen, S. Kirby, "Language evolution: The Hardest Problem in Science?" in *Language Evolution*, M. H. Christiansen, S. Kirby, Eds. (OUP Oxford, 2003), pp. 1–15. doi: 10.1093/acprof:oso/9780199244843.003.0001
2. W. T. Fitch, *The Evolution of Language* (Cambridge University Press, 2010). doi: 10.1017/CBO9780511817779
3. M. D. Hauser *et al.*, The mystery of language evolution. *Front. Psychol.* **5**, 401 (2014). doi: 10.3389/fpsyg.2014.00401; pmid: 24847300
4. W. T. Fitch, Empirical approaches to the study of language evolution. *Psychon. Bull. Rev.* **24**, 3–33 (2017). doi: 10.3758/s13423-017-1236-5; pmid: 28150125
5. E. H. Lenneberg, *Biological Foundations of Language* (Wiley, 1967). doi: 10.1080/21548331.1967.11707799
6. S. J. Gould, E. S. Vrba, Exaptation-A Missing Term in the Science of Form. *Paleobiology* **8**, 4–15 (1982). doi: 10.1017/S0094837300004310
7. S. E. Fisher, G. F. Marcus, The eloquent ape: Genes, brains and the evolution of language. *Nat. Rev. Genet.* **7**, 9–20 (2006). doi: 10.1038/nrg1747; pmid: 16369568
8. R. G. Klein, *The Dawn of Human Culture* (Turner Publishing Company, 2007).
9. T. J. Crow, Schizophrenia as the price that homo sapiens pays for language: A resolution of the central paradox in the origin of the species. *Brain Res. Brain Res. Rev.* **31**, 118–129 (2000). doi: 10.1016/S0165-0173(99)00029-6; pmid: 10719140
10. A. Bergström, C. Stringer, M. Hajdinjak, E. M. L. Scerri, P. Skoglund, Origins of modern human ancestry. *Nature* **590**, 229–237 (2021). doi: 10.1038/s41586-021-03244-5; pmid: 33568824
11. K. Laland, A. Seed, Understanding Human Cognitive Uniqueness. *Annu. Rev. Psychol.* **72**, 689–716 (2021). doi: 10.1146/annurev-psych-062220-051256; pmid: 33400565
12. J. R. Hurford, *The Origins of Grammar: Language in the Light of Evolution II* (OUP Oxford, 2012).
13. P. Skoglund, I. Mathieson, Ancient Genomics of Modern Humans: The First Decade. *Annu. Rev. Genomics Hum. Genet.* **19**, 381–404 (2018). doi: 10.1146/annurev-genom-083117-021749; pmid: 29709204
14. A. Senghas, M. Coppola, Children creating language: How Nicaraguan sign language acquired a spatial grammar. *Psychol. Sci.* **12**, 323–328 (2001). doi: 10.1111/1467-9280.00359; pmid: 11476100
15. S. Goldin-Meadow, What the hands can tell us about language emergence. *Psychon. Bull. Rev.* **24**, 213–218 (2017).
16. L. Raviv, A. Meyer, S. Lev-Ari, Compositional structure can emerge without generational transmission. *Cognition* **182**, 151–164 (2019). doi: 10.1016/j.cognition.2018.09.010; pmid: 30267952
17. S. Kirby, H. Cornish, K. Smith, Cumulative cultural evolution in the laboratory: An experimental approach to the origins of structure in human language. *Proc. Natl. Acad. Sci. U.S.A.* **105**, 10681–10686 (2008). doi: 10.1073/pnas.0707835105; pmid: 18667697
18. Y. Motamedi, M. Schouwstra, K. Smith, J. Culbertson, S. Kirby, Evolving artificial sign languages in the lab: From improvised gesture to systematic sign. *Cognition* **192**, 103964 (2019). doi: 10.1016/j.cognition.2019.05.001; pmid: 31302362
19. S. Kirby, M. Tamariz, Cumulative cultural evolution, population structure and the origin of combinatoriality in human language. *Philos. Trans. R. Soc. Lond. B Biol. Sci.* **377**, 20200319 (2022). doi: 10.1098/rstb.2020.0319; pmid: 34894728
20. L. Raviv, A. Meyer, S. Lev-Ari, Larger communities create more systematic languages. *Proc. Biol. Sci.* **286**, 20191262 (2019). doi: 10.1098/rspb.2019.1262; pmid: 31311478
21. K. Smith, How Culture and Biology Interact to Shape Language and the Language Faculty, How Culture and Biology Interact to Shape Language and the Language Faculty. *Top. Cogn. Sci.* **12**, 690–712 (2020). doi: 10.1111/tops.12377; pmid: 30182526
22. P. Hagoort, A. Özyürek, Extending the Architecture of Language From a Multimodal Perspective. *Top. Cogn. Sci.* **17**, 877–887 (2025). doi: 10.1111/tops.12728; pmid: 38493475

23. P. Hagoort, The core and beyond in the language-ready brain. *Neurosci. Biobehav. Rev.* **81** (Pt B), 194–204 (2017). doi: 10.1016/j.neubiorev.2017.01.048; pmid: 28193452
24. S. C. Vernes, V. M. Janik, W. T. Fitch, P. J. B. Slater, Vocal learning in animals and humans. *Philos. Trans. R. Soc. Lond. B Biol. Sci.* **376**, 20200234 (2021). doi: 10.1098/rstb.2020.0234; pmid: 34482718
25. W. T. Fitch, "The Biology and Evolution of Language: 'Deep Homology' and the Evolution of Innovation" in *Cogn. Neurosci. Michael Gazzaniga* (The MIT Press, 2009), pp. 873–883. doi: 10.7551/mitpress/8029.003.0075
26. C. Scharff, J. Petri, Evo-devo, deep homology and FoxP2: Implications for the evolution of speech and language. *Philos. Trans. R. Soc. Lond. B Biol. Sci.* **366**, 2124–2140 (2011). doi: 10.1098/rstb.2011.0001; pmid: 21690130
27. N. Shubin, C. Tabin, S. Carroll, Deep homology and the origins of evolutionary novelty. *Nature* **457**, 818–823 (2009). doi: 10.1038/nature07891; pmid: 19212399
28. J. den Hoed, S. E. Fisher, Genetic pathways involved in human speech disorders. *Curr. Opin. Genet. Dev.* **65**, 103–111 (2020). doi: 10.1016/j.gde.2020.05.012; pmid: 32622339
29. C. S. Lai, S. E. Fisher, J. A. Hurst, F. Vargha-Khadem, A. P. Monaco, A forkhead-domain gene is mutated in a severe speech and language disorder. *Nature* **413**, 519–523 (2001). doi: 10.1038/35097076; pmid: 11586359
30. L. D. Morison *et al.*, In-depth characterisation of a cohort of individuals with missense and loss-of-function variants disrupting *FOXP2*. *J. Med. Genet.* **60**, 597–607 (2023). doi: 10.1136/jmg-2022-108734; pmid: 36328423
31. S. E. Fisher, C. Scharff, FOXP2 as a molecular window into speech and language. *Trends Genet.* **25**, 166–177 (2009). doi: 10.1016/j.tig.2009.03.002; pmid: 19304338
32. S. E. Fisher, Evolution of language: Lessons from the genome. *Psychon. Bull. Rev.* **24**, 34–40 (2017). doi: 10.3758/s13423-016-1112-8; pmid: 27432000
33. M. Groszer *et al.*, Impaired synaptic plasticity and motor learning in mice with a point mutation implicated in human speech deficits. *Curr. Biol.* **18**, 354–362 (2008). doi: 10.1016/j.cub.2008.01.060; pmid: 18328704
34. C. A. French *et al.*, An aetiological Foxp2 mutation causes aberrant striatal activity and alters plasticity during skill learning. *Mol. Psychiatry* **17**, 1077–1085 (2012). doi: 10.1038/mp.2011.105; pmid: 21876543
35. H.-Y. Kuo *et al.*, Speech- and language-linked FOXP2 mutation targets protein motors in striatal neurons. *Brain* **146**, 3542–3557 (2023). doi: 10.1093/brain/awad090; pmid: 37137515
36. M. Druart, M. Groszer, C. Le Magueresse, An Etiological Foxp2 Mutation Impairs Neuronal Gain in Layer VI Cortico-Thalamic Cells through Increased $GABA_B$/GIRK Signaling. *J. Neurosci.* **40**, 8543–8555 (2020). doi: 10.1523/JNEUROSCI.2615-19.2020; pmid: 33020214
37. P. Norton, P. Barschke, C. Scharff, E. Mendoza, Differential Song Deficits after Lentivirus-Mediated Knockdown of FoxP1, FoxP2, or FoxP4 in Area X of Juvenile Zebra Finches. *J. Neurosci.* **39**, 9782–9796 (2019). doi: 10.1523/JNEUROSCI.1250-19.2019; pmid: 31641053
38. L. Xiao *et al.*, Expression of FoxP2 in the basal ganglia regulates vocal motor sequences in the adult songbird. *Nat. Commun.* **12**, 2617 (2021). doi: 10.1038/s41467-021-22918-2; pmid: 33976169
39. V. M. Janik, M. Knörnschild, Vocal production learning in mammals revisited. *Philos. Trans. R. Soc. Lond. B Biol. Sci.* **376**, 20200244 (2021). doi: 10.1098/rstb.2020.0244; pmid: 34482736
40. M. E. Wirthlin *et al.*, Vocal learning-associated convergent evolution in mammalian proteins and regulatory elements. *Science* **383**, eabn3263 (2024). doi: 10.1126/science.abn3263; pmid: 38422184
41. V. Slon *et al.*, The genome of the offspring of a Neanderthal mother and a Denisovan father. *Nature* **561**, 113–116 (2018). doi: 10.1038/s41586-018-0455-x; pmid: 30135579
42. T. Higham *et al.*, The timing and spatiotemporal patterning of Neanderthal disappearance. *Nature* **512**, 306–309 (2014). doi: 10.1038/nature13621; pmid: 25143113
43. M. Kuhlwilm, C. Boeckx, A catalog of single nucleotide changes distinguishing modern humans from archaic hominins. *Sci. Rep.* **9**, 8463 (2019). doi: 10.1038/s41598-019-44877-x; pmid: 31186485
44. Z. N. Kronenberg *et al.*, High-resolution comparative analysis of great ape genomes. *Science* **360**, eaar6343 (2018). doi: 10.1126/science.aar6343; pmid: 29880660
45. J. Krause *et al.*, The derived FOXP2 variant of modern humans was shared with Neandertals. *Curr. Biol.* **17**, 1908–1912 (2007). doi: 10.1016/j.cub.2007.10.008; pmid: 17949978
46. W. Enard, The Molecular Basis of Human Brain Evolution. *Curr. Biol.* **26**, R1109–R1117 (2016). doi: 10.1016/j.cub.2016.09.030; pmid: 27780052
47. K. Hammerschmidt *et al.*, A humanized version of Foxp2 does not affect ultrasonic vocalization in adult mice. *Genes Brain Behav.* **14**, 583–590 (2015). doi: 10.1111/gbb.12237; pmid: 26250064
48. S. von Merten, C. Pfeifle, S. Künzel, S. Hoier, D. Tautz, A humanized version of Foxp2 affects ultrasonic vocalization in adult female and male mice. *Genes Brain Behav.* **20**, e12764 (2021). doi: 10.1111/gbb.12764; pmid: 34342113
49. C. Schreiweis *et al.*, Humanized Foxp2 accelerates learning by enhancing transitions from declarative to procedural performance. *Proc. Natl. Acad. Sci. U.S.A.* **111**, 14253–14258 (2014). doi: 10.1073/pnas.1414542111; pmid: 25225386
50. S. E. Fisher, Human Genetics: The Evolving Story of FOXP2. *Curr. Biol.* **29**, R65–R67 (2019). doi: 10.1016/j.cub.2018.11.047; pmid: 30668952
51. S. B. Carroll, Evolution at two levels: On genes and form. *PLOS Biol.* **3**, e245 (2005). doi: 10.1371/journal.pbio.0030245; pmid: 16000021
52. S. Ma *et al.*, Molecular and cellular evolution of the primate dorsolateral prefrontal cortex. *Science* **377**, eabo7257 (2022). doi: 10.1126/science.abo7257; pmid: 36007006
53. D. Gokhman *et al.*, Reconstructing the DNA methylation maps of the Neandertal and the Denisovan. *Science* **344**, 523–527 (2014). doi: 10.1126/science.1250368; pmid: 24786081
54. D. Gokhman *et al.*, Differential DNA methylation of vocal and facial anatomy genes in modern humans. *Nat. Commun.* **11**, 1189 (2020). doi: 10.1038/s41467-020-15020-6; pmid: 32132541
55. P. Marler, Birdsong and speech development: Could there be parallels? *Am. Sci.* **58**, 669–673 (1970). pmid: 5480089
56. I. Pepperberg, K. J. Brese, B. J. Harris, Solitary sound play during acquisition of English vocalizations by an African Grey parrot (Psittacus erithacus): Possible parallels with children's monologue speech. *Appl. Psycholinguist.* **12**, 151–178 (1991). doi: 10.1017/S0142716400009127
57. A. A. Fernandez, L. S. Burchardt, M. Nagy, M. Knörnschild, Babbling in a vocal learning bat resembles human infant babbling. *Science* **373**, 923–926 (2021). doi: 10.1126/science.abf9279; pmid: 34413237
58. L. A. Petitto, S. Holowka, L. E. Sergio, B. Levy, D. J. Ostry, Baby hands that move to the rhythm of language: Hearing babies acquiring sign languages babble silently on the hands. *Cognition* **93**, 43–73 (2004). doi: 10.1016/j.cognition.2003.10.007; pmid: 15110725
59. D. K. Oller, R. E. Eilers, D. H. Bull, A. E. Carney, Prespeech vocalizations of a deaf infant: A comparison with normal metaphonological development. *J. Speech Hear. Res.* **28**, 47–63 (1985). doi: 10.1044/jshr.2801.47; pmid: 3981997
60. P. Adret, Operant conditioning, song learning and imprinting to taped song in the zebra finch. *Anim. Behav.* **46**, 149–159 (1993). doi: 10.1006/anbe.1993.1170
61. L. V. Riters, J. A. Spool, D. P. Merullo, A. H. Hahn, Song practice as a rewarding form of play in songbirds. *Behav. Processes* **163**, 91–98 (2019). doi: 10.1016/j.beproc.2017.10.002; pmid: 29031813
62. Y. Kim, S. Kwon, R. Rajan, C. Mori, S. Kojima, Intrinsic motivation for singing in songbirds is enhanced by temporary singing suppression and regulated by dopamine. *Sci. Rep.* **11**, 20350 (2021). doi: 10.1038/s41598-021-99456-w; pmid: 34645903
63. E. Hisey, M. G. Kearney, R. Mooney, A common neural circuit mechanism for internally guided and externally reinforced forms of motor learning. *Nat. Neurosci.* **21**, 589–597 (2018). doi: 10.1038/s41593-018-0092-6; pmid: 29483664
64. M. Tanaka, F. Sun, Y. Li, R. Mooney, A mesocortical dopamine circuit enables the cultural transmission of vocal behaviour. *Nature* **563**, 117–120 (2018). doi: 10.1038/s41586-018-0636-7; pmid: 30333629
65. E. Fedorenko, A. A. Ivanova, T. I. Regev, The language network as a natural kind within the broader landscape of the human brain. *Nat. Rev. Neurosci.* **25**, 289–312 (2024). doi: 10.1038/s41583-024-00802-4; pmid: 38609551
66. Y. Becker *et al.*, Long arcuate fascicle in wild and captive chimpanzees as a potential structural precursor of the language network. *Nat. Commun.* **16**, 4485 (2025). doi: 10.1038/s41467-025-59254-8; pmid: 40374618
67. J. Sierpowska *et al.*, Comparing human and chimpanzee temporal lobe neuroanatomy reveals modifications to human language hubs beyond the frontotemporal arcuate fasciculus. *Proc. Natl. Acad. Sci. U.S.A.* **119**, e2118295119 (2022). doi: 10.1073/pnas.2118295119; pmid: 35787056
68. G. Gallardo *et al.*, Morphological evolution of language-relevant brain areas. *PLOS Biol.* **21**, e3002266 (2023). doi: 10.1371/journal.pbio.3002266; pmid: 37656748
69. S. Kirby, Spontaneous evolution of linguistic structure-an iterated learning model of the emergence of regularity and irregularity. *IEEE Trans. Evol. Comput.* **5**, 102–110 (2001). doi: 10.1109/4235.918430
70. C. Kemp, Y. Xu, T. Regier, Semantic Typology and Efficient Communication. *Annu. Rev. Linguist.* **4**, 109–128 (2018). doi: 10.1146/annurev-linguistics-011817-045406
71. E. Gibson *et al.*, How Efficiency Shapes Human Language. *Trends Cogn. Sci.* **23**, 389–407 (2019). doi: 10.1016/j.tics.2019.02.003; pmid: 31006626
72. B. de Boer, W. Sandler, S. Kirby, New perspectives on duality of patterning: Introduction to the special issue. *Lang. Cogn.* **4**, 251–259 (2012). doi: 10.1515/langcog-2012-0014; pmid: 24587833
73. H. Little, K. Eryılmaz, B. de Boer, Signal dimensionality and the emergence of combinatorial structure. *Cognition* **168**, 1–15 (2017). doi: 10.1016/j.cognition.2017.06.011; pmid: 28641078
74. W. Sandler, C. Padden, M. Aronoff, Emerging Sign Languages. *Languages (Basel)* **7**, 284 (2022). doi: 10.3390/languages7040284
75. T. C. Scott-Phillips, S. Kirby, Language evolution in the laboratory. *Trends Cogn. Sci.* **14**, 411–417 (2010). doi: 10.1016/j.tics.2010.06.006; pmid: 20675183
76. M. Tamariz, Experimental Studies on the Cultural Evolution of Language. *Annu. Rev. Linguist.* **3**, 389–407 (2017). doi: 10.1146/annurev-linguistics-011516-033807
77. S. Goldin-Meadow, C. Mylander, Spontaneous sign systems created by deaf children in two cultures. *Nature* **391**, 279–281 (1998). doi: 10.1038/34646; pmid: 9440690
78. A. Senghas, S. Kita, A. Ozyürek, Children creating core properties of language: Evidence from an emerging sign language in Nicaragua. *Science* **305**, 1779–1782 (2004). doi: 10.1126/science.1100199; pmid: 15375269
79. S. Goldin-Meadow, D. Brentari, M. Coppola, L. Horton, A. Senghas, Watching language grow in the manual modality: Nominals, predicates, and handshapes. *Cognition* **136**, 381–395 (2015). doi: 10.1016/j.cognition.2014.11.029; pmid: 25546342

80. D. Hunsicker, S. Goldin-Meadow, Hierarchical structure in a self-created communication system: Building nominal constituents in homesign. *Language* **88**, 732–763 (2012). doi: 10.1353/lan.2012.0092; pmid: 23626381
81. A. Senghas, A. Özyürek, S. Goldin-Meadow, "Homesign as a way-station between co-speech gesture and sign language: The evolution of segmenting and sequencing" in *Evol. Emergence Lang. Evid. Inference*, R. Botha, M. Everaert, Eds. (OUP Oxford, 2013), pp. 62–76. doi: 10.1093/acprof:oso/9780199654840.003.0004
82. S. Goldin-Meadow, W. C. So, A. Ozyürek, C. Mylander, The natural order of events: How speakers of different languages represent events nonverbally. *Proc. Natl. Acad. Sci. U.S.A.* **105**, 9163–9168 (2008). doi: 10.1073/pnas.0710060105; pmid: 18599445
83. Ş. Özçalışkan, C. Lucero, S. Goldin-Meadow, Does language shape silent gesture? *Cognition* **148**, 10–18 (2016). doi: 10.1016/j.cognition.2015.12.001; pmid: 26707427
84. Y. Motamedi, M. Schouwstra, S. Kirby, An evolutionary approach to sign language emergence: From *state* to *process*. *Behav. Brain Sci.* **40**, e65 (2017). doi: 10.1017/S0140525X15003003; pmid: 29342521
85. S. Kirby, Y. Motamedi, L. Wolters, K. Smith, Compositionality Arises From Iterated Learning Despite a Preference for Holistic Signals: An Experimental Model of Sign Language Emergence. *Proceedings of the Joint Conference on Language Evolution (JCoLE)* (2022), pp. 402–404.
86. J. Nölle, M. Staib, R. Fusaroli, K. Tylén, The emergence of systematicity: How environmental and communicative factors shape a novel communication system. *Cognition* **181**, 93–104 (2018). doi: 10.1016/j.cognition.2018.08.014; pmid: 30173106
87. R. Selten, M. Warglien, The emergence of simple languages in an experimental coordination game. *Proc. Natl. Acad. Sci. U.S.A.* **104**, 7361–7366 (2007). doi: 10.1073/pnas.0702077104; pmid: 17449635
88. S. Kirby, M. Tamariz, H. Cornish, K. Smith, Compression and communication in the cultural evolution of linguistic structure. *Cognition* **141**, 87–102 (2015). doi: 10.1016/j.cognition.2015.03.016; pmid: 25966840
89. A. Wray, Protolanguage as a holistic system for social interaction. *Lang. Commun.* **18**, 47–67 (1998). doi: 10.1016/S0271-5309(97)00033-5
90. S. Kirby, "Syntax without natural selection: How compositionality emerges from vocabulary in a population of learners" in *The Evolutionary Emergence of Language* (Cambridge Univ. Press, 2000), pp. 303–323. doi: 10.1017/CBO9780511606441.019
91. I. Arnon, The Starting Big approach to language learning. *J. Child Lang.* **48**, 937–958 (2021). doi: 10.1017/S0305000921000386; pmid: 34219627
92. S. Goldin-Meadow, I. Arnon, Whole-to-part development in language creation. *Trends Cogn. Sci.* **29**, 12–14 (2025). doi: 10.1016/j.tics.2024.09.015; pmid: 39472231
93. B. Skarabela, M. Ota, R. O'Connor, I. Arnon, 'Clap your hands' or 'take your hands'? One-year-olds distinguish between frequent and infrequent multiword phrases. *Cognition* **211**, 104612 (2021). doi: 10.1016/j.cognition.2021.104612; pmid: 33578095
94. I. Arnon, M. Ramscar, Granularity and the acquisition of grammatical gender: How order-of-acquisition affects what gets learned. *Cognition* **122**, 292–305 (2012). doi: 10.1016/j.cognition.2011.10.009; pmid: 22169657
95. N. Siegelman, I. Arnon, The advantage of starting big: Learning from unsegmented input facilitates mastery of grammatical gender in an artificial language. *J. Mem. Lang.* **85**, 60–75 (2015). doi: 10.1016/j.jml.2015.07.003
96. S. Kirby, T. Griffiths, K. Smith, Iterated learning and the evolution of language. *Curr. Opin. Neurobiol.* **28**, 108–114 (2014). doi: 10.1016/j.conb.2014.07.014; pmid: 25062470
97. A. Cangelosi, D. Parisi, *Simulating the Evolution of Language* (Springer Science & Business Media, 2012).
98. W. T. Fitch, Toward a computational framework for cognitive biology: Unifying approaches from cognitive neuroscience and comparative cognition. *Phys. Life Rev.* **11**, 329–364 (2014). doi: 10.1016/j.plrev.2014.04.005; pmid: 24969660
99. J. Hyland Bruno, E. D. Jarvis, M. Liberman, O. Tchernichovski, Birdsong Learning and Culture: Analogies with Human Spoken Language. *Annu. Rev. Linguist.* **7**, 449–472 (2021). doi: 10.1146/annurev-linguistics-090420-121034
100. H. Williams, R. F. Lachlan, Evidence for cumulative cultural evolution in bird song. *Philos. Trans. R. Soc. Lond. B Biol. Sci.* **377**, 20200322 (2022). doi: 10.1098/rstb.2020.0322; pmid: 34894731
101. W. H. Thorpe, *Bird-song: the biology of vocal communication and expression in birds* (Cambridge Univ. Press, 1961).
102. P. Marler, "The instinct to learn" in *Epigenesis Mind Essays Biol. Cogn* (Psychology Press, 2014), pp. 37–66.
103. O. Fehér, H. Wang, S. Saar, P. P. Mitra, O. Tchernichovski, De novo establishment of wild-type song culture in the zebra finch. *Nature* **459**, 564–568 (2009). doi: 10.1038/nature07994; pmid: 19412161
104. O. Fehér, I. Ljubičić, K. Suzuki, K. Okanoya, O. Tchernichovski, Statistical learning in songbirds: From self-tutoring to song culture. *Philos. Trans. R. Soc. Lond. B Biol. Sci.* **372**, 20160053 (2017). doi: 10.1098/rstb.2016.0053; pmid: 27872371
105. C. I. Petkov, C. Ten Cate, Structured Sequence Learning: Animal Abilities, Cognitive Operations, and Language Evolution. *Top. Cogn. Sci.* **12**, 828–842 (2020). doi: 10.1111/tops.12444; pmid: 31359600
106. K. Zuberbühler, Combinatorial capacities in primates. *Curr. Opin. Behav. Sci.* **21**, 161–169 (2018). doi: 10.1016/j.cobeha.2018.03.015
107. C. Girard-Buttoz *et al.*, Versatile use of chimpanzee call combinations promotes meaning expansion. *Sci. Adv.* **11**, eadq2879 (2025). doi: 10.1126/sciadv.adq2879; pmid: 40344055
108. Q. Gallot, C. Depriester, S. Moran, K. Zuberbühler, A nonhuman primate combinatorial system for long-distance communication. *iScience* **27**, 111172 (2024). doi: 10.1016/j.isci.2024.111172; pmid: 39559758
109. N. Claidière, K. Smith, S. Kirby, J. Fagot, Cultural evolution of systematically structured behaviour in a nonhuman primate. *Proceedings of the Royal Society B: Biological Sciences* **281**, 2014.1541 (2014).
110. E. V. Clark, "Language is Acquired in Interaction" in *Algebraic Structures in Natural Language* (CRC Press, 2022). doi: 10.1201/9781003205388-4
111. M. Tomasello, The social bases of language acquisition. *Soc. Dev.* **1**, 67–87 (1992). doi: 10.1111/j.1467-9507.1992.tb00135.x
112. S. R. Lytle, P. K. Kuhl, "Social Interaction and Language Acquisition" in *The Handbook of Psycholinguistics* (John Wiley & Sons, Ltd, 2017), pp. 615–634, doi: 10.1002/9781118829516.ch27
113. J. R. Saffran, R. N. Aslin, E. L. Newport, Statistical learning by 8-month-old infants. *Science* **274**, 1926–1928 (1996). doi: 10.1126/science.274.5294.1926; pmid: 8943209
114. M. Babineau, R. Shi, A. Christophe, 14-month-olds exploit verbs' syntactic contexts to build expectations about novel words. *Infancy* **25**, 719–733 (2020). doi: 10.1111/infa.12354; pmid: 32857439
115. M. H. Goldstein, A. P. King, M. J. West, Social interaction shapes babbling: Testing parallels between birdsong and speech. *Proc. Natl. Acad. Sci. U.S.A.* **100**, 8030–8035 (2003). doi: 10.1073/pnas.1332441100; pmid: 12808137
116. P. K. Kuhl, F.-M. Tsao, H.-M. Liu, Foreign-language experience in infancy: Effects of short-term exposure and social interaction on phonetic learning. *Proc. Natl. Acad. Sci. U.S.A.* **100**, 9096–9101 (2003). doi: 10.1073/pnas.1532872100; pmid: 12861072
117. S. Goldin-Meadow, *Thinking with Your Hands: The Surprising Science Behind How Gestures Shape Our Thoughts* (Hachette, 2023).
118. E. V. Clark, Conversational Repair and the Acquisition of Language. *Discourse Process.* **57**, 441–459 (2020). doi: 10.1080/0163853X.2020.1719795
119. W. T. Fitch, L. Huber, T. Bugnyar, Social cognition and the evolution of language: Constructing cognitive phylogenies. *Neuron* **65**, 795–814 (2010). doi: 10.1016/j.neuron.2010.03.011; pmid: 20346756
120. S. C. Levinson, "Interactional Foundations of Language: The Interaction Engine Hypothesis" in *Human Language*, P. Hagoort, Ed. (The MIT Press, 2019), pp. 189–200. doi: 10.7551/mitpress/10841.003.0018
121. D. I. Tsomokos, L. Raviv, A bidirectional association between language development and prosocial behavior in childhood: Evidence from a longitudinal birth cohort in the United Kingdom. *Dev. Psychol.* (2024). doi: 10.1037/dev0001875; pmid: 39531699
122. R. Ensor, D. Spencer, C. Hughes, 'You Feel Sad?' Emotion Understanding Mediates Effects of Verbal Ability and Mother–Child Mutuality on Prosocial Behaviors: Findings from 2 Years to 4 Years. *Soc. Dev.* **20**, 93–110 (2011). doi: 10.1111/j.1467-9507.2009.00572.x
123. E. Longobardi, P. Spataro, C. Rossi-Arnaud, Direct and Indirect Associations of Empathy, Theory of Mind, and Language with Prosocial Behavior: Gender Differences in Primary School Children. *J. Genet. Psychol.* **180**, 266–279 (2019). doi: 10.1080/00221325.2019.1653817; pmid: 31456504
124. V. Ornaghi, A. Pepe, I. Grazzani, False-Belief Understanding and Language Ability Mediate the Relationship between Emotion Comprehension and Prosocial Orientation in Preschoolers. *Front. Psychol.* **7**, 1534 (2016). doi: 10.3389/fpsyg.2016.01534; pmid: 27774075
125. N. P. van den Bedem, J. E. Dockrell, P. M. van Alphen, S. V. Kalicharan, C. Rieffe, Victimization, Bullying, and Emotional Competence: Longitudinal Associations in (Pre)Adolescents With and Without Developmental Language Disorder. *J. Speech Lang. Hear. Res.* **61**, 2028–2044 (2018). doi: 10.1044/2018_JSLHR-L-17-0429; pmid: 29998317
126. C. L. Forrest, J. L. Gibson, S. L. Halligan, M. C. St Clair, A longitudinal analysis of early language difficulty and peer problems on later emotional difficulties in adolescence: Evidence from the Millennium Cohort Study. *Autism Dev. Lang. Impair.* **3**, 2396941518795392 (2018). doi: 10.1177/2396941518795392
127. M. J. West, A. P. King, Female visual displays affect the development of male song in the cowbird. *Nature* **334**, 244–246 (1988). doi: 10.1038/334244a0; pmid: 3398921
128. S. Carouso-Peck, O. Menyhart, T. J. DeVoogd, M. H. Goldstein, Contingent parental responses are naturally associated with zebra finch song learning. *Anim. Behav.* **165**, 123–132 (2020). doi: 10.1016/j.anbehav.2020.04.019
129. Y. Chen, L. E. Matheson, J. T. Sakata, Mechanisms underlying the social enhancement of vocal learning in songbirds. *Proc. Natl. Acad. Sci. U.S.A.* **113**, 6641–6646 (2016). doi: 10.1073/pnas.1522306113; pmid: 27247385
130. S. Yanagihara, Y. Yazaki-Sugiyama, Social interaction with a tutor modulates responsiveness of specific auditory neurons in juvenile zebra finches. *Behav. Processes* **163**, 32–36 (2019). doi: 10.1016/j.beproc.2018.04.003; pmid: 29656094
131. P. M. Greenfield, E. S. Savage-Rumbaugh, Comparing communicative competence in child and chimp: The pragmatics of repetition. *J. Child Lang.* **20**, 1–26 (1993). doi: 10.1017/S0305000900009090; pmid: 7681067
132. C. Yang, Ontogeny and phylogeny of language. *Proc. Natl. Acad. Sci. U.S.A.* **110**, 6324–6327 (2013). doi: 10.1073/pnas.1216803110; pmid: 23576720
133. M. Takahasi, K. Okanoya, Song Learning in Wild and Domesticated Strains of White-Rumped Munia, Lonchura striata, Compared by Cross-Fostering Procedures: Domestication Increases Song Variability by Decreasing Strain-Specific Bias. *Ethology* **116**, 396–405 (2010). doi: 10.1111/j.1439-0310.2010.01761.x

134. K. Suzuki, K. Okanoya, Domestication effects on aggressiveness: Comparison of biting motivation and bite force between wild and domesticated finches. *Behav. Processes* **193**, 104503 (2021). doi: 10.1016/j.beproc.2021.104503; pmid: 34537267
135. K. Suzuki, H. Yamada, T. Kobayashi, K. Okanoya, Decreased fecal corticosterone levels due to domestication: A comparison between the white-backed Munia (Lonchura striata) and its domesticated strain, the Bengalese finch (Lonchura striata var. domestica) with a suggestion for complex song evolution. *J. Exp. Zool. Part A. Ecol. Genet. Physiol.* **317**, 561–570 (2012). doi: 10.1002/jez.1748; pmid: 22927235
136. K. Suzuki, M. Ikebuchi, H. Kagawa, T. Koike, K. Okanoya, Effects of domestication on neophobia: A comparison between the domesticated Bengalese finch (Lonchura striata var. domestica) and its wild ancestor, the white-rumped munia (Lonchura striata). *Behav. Processes* **193**, 104502 (2021). doi: 10.1016/j.beproc.2021.104502; pmid: 34530107
137. E. Honda, K. Okanoya, Acoustical and Syntactical Comparisons between Songs of the White-backed Munia (Lonchura striata) and Its Domesticated Strain, the Bengalese Finch (Lonchura striata var. domestica). *Zool. Sci.* **16**, 319–326 (1999). doi: 10.2108/zsj.16.319
138. Y. Tobari *et al.*, Oxytocin variation and brain region-specific gene expression in a domesticated avian species. *Genes Brain Behav.* **21**, e12780 (2022). doi: 10.1111/gbb.12780; pmid: 34854547
139. T. O'Rourke *et al.*, Capturing the Effects of Domestication on Vocal Learning Complexity. *Trends Cogn. Sci.* **25**, 462–474 (2021). doi: 10.1016/j.tics.2021.03.007; pmid: 33810982
140. K. M. Kendrick, The neurobiology of social bonds. *J. Neuroendocrinol.* **16**, 1007–1008 (2004). doi: 10.1111/j.1365-2826.2004.01262.x; pmid: 15667456
141. T. M. Love, Oxytocin, motivation and the role of dopamine. *Pharmacol. Biochem. Behav.* **119**, 49–60 (2014). doi: 10.1016/j.pbb.2013.06.011; pmid: 23850525
142. B. Hare, Survival of the Friendliest: Homo sapiens Evolved via Selection for Prosociality. *Annu. Rev. Psychol.* **68**, 155–186 (2017). doi: 10.1146/annurev-psych-010416-044201; pmid: 27732802
143. L. Progovac, A. Benítez-Burraco, From Physical Aggression to Verbal Behavior: Language Evolution and Self-Domestication Feedback Loop. *Front. Psychol.* **10**, 2807 (2019). doi: 10.3389/fpsyg.2019.02807; pmid: 31920850
144. J. Thomas, S. Kirby, Self domestication and the evolution of language. *Biol. Philos.* **33**, 9 (2018). doi: 10.1007/s10539-018-9612-8; pmid: 29606782
145. T. M. Freeberg, R. I. M. Dunbar, T. J. Ord, Social complexity as a proximate and ultimate factor in communicative complexity. *Philos. Trans. R. Soc. Lond. B Biol. Sci.* **367**, 1785–1801 (2012). doi: 10.1098/rstb.2011.0213; pmid: 22641818
146. L. Raviv, L. R. Peckre, C. Boeckx, What is simple is actually quite complex: A critical note on terminology in the domain of language and communication. *J. Comp. Psychol.* **136**, 215–220 (2022). doi: 10.1037/com0000328; pmid: 36222620
147. A. Formaux, D. Sperber, J. Fagot, N. Claidière, Guinea baboons are strategic cooperators. *Sci. Adv.* **9**, eadi5282 (2023). doi: 10.1126/sciadv.adi5282; pmid: 37889969
148. M. C. Corballis, From mouth to hand: Gesture, speech, and the evolution of right-handedness. *Behav. Brain Sci.* **26**, 199–208, discussion 208–260 (2003). doi: 10.1017/S0140525X03000062; pmid: 14621511
149. M. A. Arbib, From monkey-like action recognition to human language: An evolutionary framework for neurolinguistics. *Behav. Brain Sci.* **28**, 105–124, discussion 125–167 (2005). doi: 10.1017/S0140525X05000038; pmid: 16201457
150. D. McNeill, *How Language Began: Gesture and Speech in Human Evolution* (Cambridge University Press, 2012). doi: 10.1017/CBO9781139108669
151. P. F. MacNeilage, B. L. Davis, The Frame/Content theory of evolution of speech: A comparison with a gestural-origins alternative. *Interact. Stud.* **6**, 173–199 (2005). doi: 10.1075/is.6.2.03mac
152. M. Fröhlich, C. Sievers, S. W. Townsend, T. Gruber, C. P. van Schaik, Multimodal communication and language origins: integrating gestures and vocalizations. *Biol. Rev. Camb. Philos. Soc.* **94**, 1809–1829 (2019). doi: 10.1111/brv.1253; pmid: 31250542
153. M. A. Arbib, K. Liebal, S. Pika, Primate vocalization, gesture, and the evolution of human language. *Curr. Anthropol.* **49**, 1053–1063, discussion 1063–1076 (2008). doi: 10.1086/593015; pmid: 19391445
154. P. J. Richerson, R. Boyd, A dual inheritance model of the human evolutionary process I: Basic postulates and a simple model. *J. Soc. Biol. Struct.* **1**, 127–154 (1978). doi: 10.1016/S0140-1750(78)80002-5
155. S. Kirby, M. Dowman, T. L. Griffiths, Innateness and culture in the evolution of language. *Proc. Natl. Acad. Sci. U.S.A.* **104**, 5241–5245 (2007). doi: 10.1073/pnas.0608222104; pmid: 17360393
156. B. Thompson, S. Kirby, K. Smith, Culture shapes the evolution of cognition. *Proc. Natl. Acad. Sci. U.S.A.* **113**, 4530–4535 (2016). doi: 10.1073/pnas.1523631113; pmid: 27044094
157. G. E. Hinton, S. J. Nowlan, How Learning Can Guide Evolution. *Complex Syst.* **I**, 495–502 (1987).
158. E. Ochs, "Transcription as theory" in *Dev. Pragmat*, E. Ochs, B. Schieffelin, Eds. (Academic Press, 1979), pp. 43–72.
159. A. M. Peters, *The Units of Language Acquisition* (Cambridge Univ. Press, 1983).
160. S. Goldin-Meadow, *The resilience of language: What gesture creation in deaf children can tell us about how all children learn language* (Psychology Press, 2003).
161. S. Goldin-Meadow, C. Mylander, C. Butcher, The resilience of combinatorial structure at the word level: Morphology in self-styled gesture systems. *Cognition* **56**, 195–262 (1995). doi: 10.1016/0010-0277(95)00662-I; pmid: 7554795
162. C. Grund, G. Badihi, K. E. Graham, A. Safryghin, C. Hobaiter, GesturalOrigins: A bottom-up framework for establishing systematic gesture data across ape species. *Behav. Res. Methods* **56**, 986–1001 (2024). doi: 10.3758/s13428-023-02082-9; pmid: 36922450
163. Y. Prat, Animals Have No Language, and Humans Are Animals Too. *Perspect. Psychol. Sci.* **14**, 885–893 (2019). doi: 10.1177/1745691619858402; pmid: 31398084
164. D. L. Cheney, R. M. Seyfarth, *Baboon Metaphysics: The Evolution of a Social Mind* (Univ. of Chicago Press, 2008). doi: 10.7208/9780226102429
165. I. Arnon *et al.*, Whale song shows language-like statistical structure. *Science* **387**, 649–653 (2025). doi: 10.1126/science.adq7055; pmid: 39913578
166. Y. Yovel, O. Rechavi, AI and the Doctor Dolittle challenge. *Curr. Biol.* **33**, R783–R787 (2023). doi: 10.1016/j.cub.2023.06.063; pmid: 37552937
167. C. Rutz *et al.*, Using machine learning to decode animal communication. *Science* **381**, 152–155 (2023). doi: 10.1126/science.adg7314; pmid: 37440653
168. C. Hobaiter, K. E. Graham, R. W. Byrne, Are ape gestures like words? Outstanding issues in detecting similarities and differences between human language and ape gesture. *Philos. Trans. R. Soc. Lond. B Biol. Sci.* **377**, 20210301 (2022). doi: 10.1098/rstb.2021.0301; pmid: 35934962
169. S. Ferrigno, S. J. Cheyette, S. T. Piantadosi, J. F. Cantlon, Recursive sequence generation in monkeys, children, U.S. adults, and native Amazonians. *Sci. Adv.* **6**, eaaz1002 (2020). doi: 10.1126/sciadv.aaz1002; pmid: 32637593
170. X. Jiang *et al.*, Production of Supra-regular Spatial Sequences by Macaque Monkeys. *Curr. Biol.* **28**, 1851–1859.e4 (2018). doi: 10.1016/j.cub.2018.04.047; pmid: 29887304
171. T. J. Bergman, J. C. Beehner, D. L. Cheney, R. M. Seyfarth, Hierarchical classification by rank and kinship in baboons. *Science* **302**, 1234–1236 (2003). doi: 10.1126/science.1087513; pmid: 14615544
172. O. Mascaro *et al.*, Human and animal dominance hierarchies show a pyramidal structure guiding adult and infant social inferences. *Nat. Hum. Behav.* **7**, 1294–1306 (2023). doi: 10.1038/s41562-023-01634-5; pmid: 37386104
173. A. D. Patel, Language, music, syntax and the brain. *Nat. Neurosci.* **6**, 674–681 (2003). doi: 10.1038/nn1082; pmid: 12830158
174. E. C. Garland, P. K. McGregor, Cultural Transmission, Evolution, and Revolution in Vocal Displays: Insights From Bird and Whale Song. *Front. Psychol.* **11**, 544929 (2020). doi: 10.3389/fpsyg.2020.544929; pmid: 33132953
175. Mde. J. Martins, Z. Muršič, J. Oh, W. T. Fitch, Representing visual recursion does not require verbal or motor resources. *Cogn. Psychol.* **77**, 20–41 (2015). doi: 10.1016/j.cogpsych.2015.01.004; pmid: 25743443
176. G. Westphal-Fitch, B. Giustolisi, C. Cecchetto, J. S. Martin, W. T. Fitch, Artificial Grammar Learning Capabilities in an Abstract Visual Task Match Requirements for Linguistic Syntax. *Front. Psychol.* **9**, 1210 (2018). doi: 10.3389/fpsyg.2018.01210; pmid: 30087630
177. E. G. Atkinson *et al.*, No Evidence for Recent Selection at FOXP2 among Diverse Human Populations. *Cell* **174**, 1424–1435.e15 (2018). doi: 10.1016/j.cell.2018.06.048; pmid: 30078708
178. E. Eising *et al.*, A set of regulatory genes co-expressed in embryonic human brain is implicated in disrupted speech development. *Mol. Psychiatry* **24**, 1065–1078 (2019). doi: 10.1038/s41380-018-0020-x; pmid: 29463886
179. E. Eising *et al.*, Genome-wide analyses of individual differences in quantitatively assessed reading- and language-related skills in up to 34,000 people. *Proc. Natl. Acad. Sci. U.S.A.* **119**, e2202764119 (2022). doi: 10.1073/pnas.2202764119; pmid: 35998220
180. G. Alagöz *et al.*, Using neuroimaging genomics to investigate the evolution of human brain structure. *Proc. Natl. Acad. Sci. U.S.A.* **119**, e2200638119 (2022). doi: 10.1073/pnas.2200638119; pmid: 36161899
181. J. Uddén *et al.*, Toward Robust Functional Neuroimaging Genetics of Cognition. *J. Neurosci.* **39**, 8778–8787 (2019). doi: 10.1523/JNEUROSCI.0888-19.2019; pmid: 31570534
182. J. S. Amelink *et al.*, Imaging genetics of language network functional connectivity reveals links with language-related abilities, dyslexia and handedness. *Commun. Biol.* **7**, 1209 (2024). doi: 10.1038/s42003-024-06890-3; pmid: 39342056

ACKNOWLEDGMENTS

We thank the Israel Institute for Advanced Studies for providing the funds that allowed us to convene this research group and for creating a truly unique space for deep and intense intellectual exploration. We thank the participants of the 2023 workshop on "The Origins of human language: a multidisciplinary perspective" for stimulating and insightful discussions. (https://iias.huji.ac.il/event/origins-language-multidisciplinary-perspective-research-group-conference). All remaining mistakes are our own. **Funding:** Israel Institute for Advanced Studies research group fellowship (all authors); Israel Science Foundation grant 445/20 (I.A.); Institute for Language Communication and the Brain (ILCB) through the Agence Nationale de la Recherche grant ANR-16-CONV-0002 (N.C.); ANR TECHNICION grant ANR-21-CE28-0023-02 (N.C.); SCALUP grant ANR-21-CE28-0016-02 (N.C.); Japan Society for the Promotion of Sciences and Ministry of Education grant JP23H05428 (K.O.); Ministry of Education, Culture, Sports, Science and Technology grant #4903 (K.O.); Max Planck Society (L.R., S.E.F.); NIDCD grant R01 DC00491 (S.G.-M.). **Author contributions:** Conceptualization: All authors; Visualization: L.W., S.K., N.C., L.C., S.E.F.; Funding acquisition: I.A. and L.C. secured the funds for the research fellowship that led to the development of the paper; Project administration: I.A., S.E.F.; Writing – original draft: I.A. and S.E.F. created the first draft of the paper structure and led the introduction. Case studies were drafted by S.E.F. and W.T.F. (vocal production learning); S.K. and I.A. (emergence of structure); and L.R., K.O., and N.C. (prosociality). W.T.F. led the writing of the discussion. Figures were drafted by L.W. with S.K. (Fig. 1), S.E.F. (Fig. 2), S.G.-M. (Fig. 3), and W.T.F. (Fig. 4). The table was drafted by S.E.F. Writing – review & editing: Led by I.A. and S.E.F.; all authors contributed. **Competing interests:** The authors declare that they have no competing interests. **License information:** Copyright © 2025 the authors, some rights reserved; exclusive licensee American Association for the Advancement of Science. No claim to original US government works. https://www.science.org/about/science-licenses-journal-article-reuse

Submitted 5 July 2024; resubmitted 12 February 2025; accepted 23 September 2025

10.1126/science.adq8303

Science
JOURNALS AAAS

Publish your research in the *Science* family of journals

The *Science* family of journals (*Science, Science Advances, Science Immunology, Science Robotics, Science Signaling*, and *Science Translational Medicine)* are among the most highly-regarded journals in the world for quality and selectivity. Our peer-reviewed journals are committed to publishing cutting-edge research, incisive scientific commentary, and insights on what's important to the scientific world at the highest standards.

Submit your research today!

Learn more at **Science.org/journals**

RESEARCH

IN *SCIENCE* JOURNALS

Edited by **Michael Funk**

GAS ADSORPTION

Binding on the double

Terminal cobalt(II)–methyl sites in a porous metal–organic framework can bind two carbon monoxide (CO) molecules, which leads to high adsorption capacities at ambient temperatures and pressures. Carsch *et al*. showed that the binding of the first CO molecule triggers a spin transition. Binding of the second CO molecule causes the first to insert into the cobalt-methyl bond to form an acetyl group. Sigmoidal adsorption isotherms are indicative of a cooperative process driven by the stronger binding in the second CO adsorption step. —Phil Szuromi

Science p. 808, 10.1126/science.ady2607

ORGANIC ELECTRONICS

Hydrogel-modulated transistors

With the development of organic bioelectronics, there has been interest in making stretchable semiconductors with acceptable performance. Most approaches to date rely on blending a semiconductor with an elastomer and perform well electronically, but they have a modulus much higher than biological tissue and cannot be modulated through the insertion of ions. Liu *et al*. created a secondary hydrogel network that facilitated the formation of a continuous phase of a primary redox-active polymer. This composition makes it possible to produce millimeter-thick semiconducting layers with biological compatibility. By controlling the hydrogel's porosity, the researchers optimized ionic and electronic mobility and demonstrated electrochemical transistors with a high on/off switching ratio. —Marc S. Lavine

Science p. 824, 10.1126/science.adx4514

DEVICE TECHNOLOGY

Making good contact to MoS_2

Electrical contact between two-dimensional semiconductors and metals is usually weak because of weak band coupling and low bond strength. Gao *et al*. created a strong electrical contact between a gold electrode and molybdenum disulfide (MoS_2) by using an ultrasoft argon plasma to etch away the topmost layer of sulfur to expose the molybdenum atoms. The researchers used this approach to fabricate MoS_2 transistors that had contact resistances as low as 70 ohm·micrometer and were stable to temperatures as high as 400°C. —Phil Szuromi

Science p. 813, 10.1126/science.adz2405

ORGANIC CHEMISTRY

An ion binder steers photocatalysis

Photoredox catalysis relies on light-absorbing compounds to activate reactants by charge transfer. Because the reactants are typically neutral, the intermediates become charged, and recent studies have introduced chiral counterions to steer their reactivity toward one of two mirror-image products. Vojáčková and Jacobsen now report an alternate, flexible method in which the chiral agent is neutral but can bind to a variety of counterions by hydrogen bonding. The authors demonstrated the selectivity of this approach in the preparation of a range of three-, four-, and five-membered ring products. —Jake S. Yeston

Science p. 831, 10.1126/science.adz3362

IMAGE: JACOB KEGERREIS/NASA AMES AND DURHAM UNIVERSITY/INSTITUTE FOR COMPUTATIONAL COSMOLOGY/SWIFT/DIRAC

COSMOCHEMISTRY

Giant impactor Theia formed nearby

In the early Solar System, a small planet known as Theia collided with proto-Earth. The debris from that giant impact formed the Moon, with material from Theia incorporated into both the Moon and Earth. Hopp *et al.* measured iron isotopes in lunar samples, Earth samples, and meteorites. They then combined these results with previous measurements of other elements with different geochemical behaviors. By simultaneously calculating the contributions of Theia material to each of those elements in both bodies, the authors concluded that Theia formed in the inner Solar System, nearby to Earth but possibly slightly closer to the Sun. —Keith T. Smith *Science* p. 819, 10.1126/science.ado0623

Computational simulation of the impact between a proto-Earth and the small planet Theia

QUANTUM SIMULATION

Extending interactions

Ultracold atoms in optical lattices have been used extensively to simulate the behavior of the Hubbard model, which describes the physics of interacting particles on a lattice. However, past studies focused largely on on-site interactions, which are easier to implement experimentally. Weckesser *et al*. used the so-called Rydberg dressing technique to create extended-range interactions between rubidium atoms residing in a one-dimensional optical lattice. The researchers used a stroboscopic dressing sequence to control the losses that plagued prior implementations and studied both equilibrium and nonequilibrium behavior of the resulting extended Hubbard model. —Jelena Stajic

Science p. 849, 10.1126/science.adq7082

STEM CELLS

The healing effects of radiation

Salivary gland damage is a detrimental side effect of radiotherapy for head and neck cancers. Cinat *et al*. compared the effects of photon and proton irradiation in mouse salivary gland organoids (see the Focus by Sato and Yu). Both types of radiation elicited similar amounts of DNA damage and type I interferon (IFN-I) signaling early after irradiation. At later time points, proton irradiation caused greater derepression of transposable elements and increased IFN-I responses, leading to enhanced stem cell proliferation and self-renewal. IFN-β treatment increased salivary gland stem cell activity in photon-irradiated mice, suggesting a potential strategy to improve salivary gland recovery after conventional photon radiotherapy. —Annalisa VanHook

Sci. Signal. (2025) 10.1126/scisignal.ady0398; see also 10.1126/scisignal.aeb6151

MACROPHAGES

Macrophages preserve pancreatic function

Resident macrophages perform tissue-specific functions to support organ development and homeostasis. Using single-cell transcriptomics, Grosjean *et al.* found that islet-resident macrophages (IRMs) displayed increased proinflammatory, metabolic, and antioxidant activity compared with macrophages from pancreatic exocrine tissue in mice. The cysteine-glutamate antiporter SLC7A11 drove this program, which protected IRMs from ferroptosis and supported β cell homeostasis. Human islet macrophages displayed a similar antioxidant profile, particularly in patients with type 2 diabetes. —Claire Olingy

Sci. Immunol. (2025) 10.1126/scitranslmed.adz5181

COLON CANCER

Lighting up tumors for removal

Endoscopic resection offers a minimally invasive approach for early colorectal cancer treatment, but accurately identifying tumor margins and eliminating residual microlesions are major challenges. Li *et al.* developed orally delivered, aptamer-decorated nanoparticles that serve as colon-targeted Raman probes based on a stacking-induced, charge transfer–enhanced Raman scattering mechanism. Validated in orthotopic and spontaneous tumor models, this oral platform integrates molecular imaging and therapy, advancing safer, patient-friendly precision endoscopic interventions for colorectal cancer. —Ruirui Qiao

Sci. Adv. (2025) 10.1126/sciadv.adx5246

IN OTHER JOURNALS

Edited by **Corinne Simonti** and **Jesse Smith**

PSYCHOLOGY

Spotting workplace stress in the brain

Feelings of burnout or disengagement can be common in the workplace but are difficult to talk about for fear of judgement or perceived social norms. Goldstein *et al*. used functional near-infrared spectroscopy, a noninvasive neuroimaging technique, to study brain activity in a group of 68 business executives while they watched a video about work. Specific patterns of changes in activity at the temporoparietal junction and the dorsomedial prefrontal cortex were associated with feeling overwhelmed or needing a new challenge, respectively. The findings provide preliminary insights into how these two regions might support different psychological functions and could eventually have applications in the workplace, although the authors emphasize that robust ethical guardrails would be needed to prevent misuse. —Sarah Lemprière

Proc. Natl. Acad. Sci. U.S.A. (2025) 10.1073/pnas.2504382122

EVOLUTION

On the origin of mimetic butterflies

Many butterflies have evolved wing patterns that mimic those of toxic species, which helps them evade predators. The switch between mimetic and nonmimetic wing patterns in *Papilio* swallowtail butterflies is controlled by the *doublesex* supergene, a DNA region encompassing the *dsx* gene and other genetic elements. VanKuren *et al.* identified six new regulatory elements in the mimetic version of the *doublesex* supergene in two species of *Papilio* butterflies. These regulatory elements and the *dsx* gene have been linked together by an inversion in the chromosome that contains them, which may have prevented further DNA rearrangements. —Joana Osório

Proc. Natl. Acad. Sci. U.S.A. (2025) 10.1073/pnas.2509864122

POLLUTION

PFAS in blubber

Per- and polyfluoralkyl substances (PFAS) generated from the production and use of chemicals have known negative health impacts on humans and wildlife. These compounds bioaccumulate in the liver and blood of marine mammals, occurring mostly through binding to proteins or partitioning to phospholipids. Lauria *et al.* followed up on an unidentified organoflourine in a killer whale, looking at four other individuals from Greenland and Sweden. They found fluorinated PFAS in the blubber rather than in the liver and blood, suggesting previously unidentified PFAS threats. Lipid bioaccumulation is especially worrying given that blubber makes up a large proportion of tissue in many marine mammals. —Sacha Vignieri

Environ. Sci. Technol. Lett. (2025) 10.1021/acs.estlett.5c00516

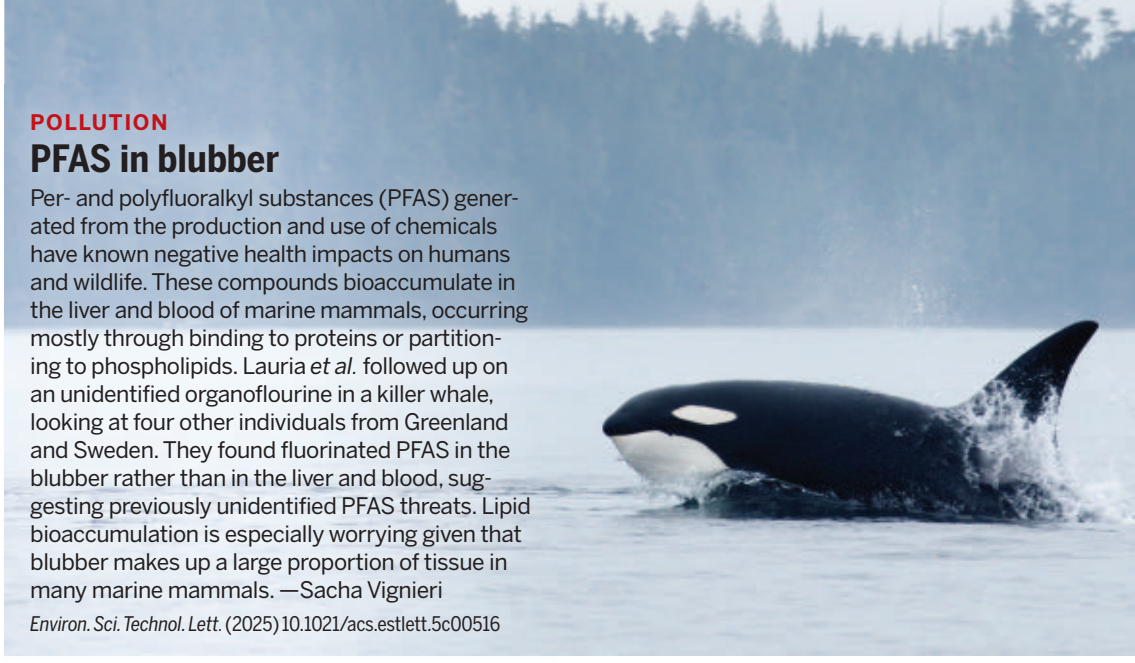

PFAS, the so-called forever chemicals, may bioaccumulate in whale blubber, raising concerns about marine health.

ICE CORES

Frozen

Antarctic ice cores provide a continuous climate record of the past 800,000 years, supplying important details about temperature, atmospheric composition, and a raft of other environmental variables over that time interval. Much effort has gone into identifying older samples, but older ice is discontinuous and difficult to find. Shackleton *et al.* report the discovery of the oldest Antarctic ice to date: more than 6 million years old. This finding makes possible directly determining climate conditions during the Pliocene, when Earth was warmer and sea level was higher. —Jesse Smith

Proc. Nat. Acad. Sci. U.S.A. (2025) 10.1073/pnas.2502681122

MITOCHONDRIAL IMPORT

Problematic PINK1 processing

Mitochondria import many nuclear-encoded proteins from the cytosol. Among these is PINK1, a membrane protein kinase that helps sense and respond to mitochondrial dysfunction. Bayne *et al.* investigated how PINK1 is processed by mitochondrial membrane proteases, which are key players in regulating its function. They found that in vitro proteolysis measurements did not necessarily match what happened in cells, and PINK1 could be degraded by the membrane protease PARL independently of prior cleavage of its mitochondrial targeting sequence. These results help to clarify how PINK1 is processed, providing basic insights into a pathway important for the clearance of unhealthy mitochondria. —Michael A. Funk

J. Biol. Chem. (2025) 10.1016/j.jbc.2025.110860

ADAPTATION

Fungal adaptation in cheese caves

Fungi play vital roles in food production and ecosystems, but we rarely observe their evolution in real time. Louw *et al.* followed a population of the mold *Penicillium solitum* growing in a Vermont cheese cave over 8 years. They observed a striking change from green to white colonies caused by mutations in the melanin-producing gene *alb1*. These white strains made less pigment and fewer spores but grew better than green ones in the dark cave environment. These findings reveal how fungi can quickly adapt to human-made habitats with relaxed selection for traits such as pigmentation. Such local adaptation represents an early stage of fungal domestication and could inspire the development of new molds for cheese and fermented foods. —Di Jiang

Curr. Biol. (2025) 10.1016/j.cub.2025.08.053

HYDROGELS

Aligned at the interface

Most natural hydrogels such as collagen and cellulose have anisotropic structures in which ordered networks of polymer chains produce direction-dependent properties. Similar anisotropy has been achieved in synthetic hydrogels, primarily by introducing additives or complicated processes. Takahashi *et al.* report that bonding two blocks of hydrogels creates a gel-to-gel interface in which polymer networks spontaneously align perpendicular to the boundary. This ordering, which was driven by swelling and fixation of cross-linked polymers, could be further tuned by using a photoinitiator, establishing a universal approach for synthesizing anisotropic hydrogels with desired orientations of polymer networks. —Sumin Jin

Adv. Mater. (2025) 10.1002/adma.202505268

PHOTO: ASCENTXMEDIA/ISTOCK PHOTO

Edited by **Michael Funk**

ORIGINS OF LANGUAGE

A biological and biocultural framework

For nearly as long as humans have had an understanding of language, we have been interested in understanding its origins. Although human language is unique in many ways, recent research has made clear that language per se is not unique to humans. Arnon *et al*. describe a framework for understanding language evolution that incorporates both culture and biological preparedness. The authors then demonstrate the value of this framework in case studies of three aspects of language evolution. —Sacha Vignieri

Science p. 797, 10.1126/science.adq8303

SIGNAL TRANSDUCTION

Unusual arrestin-GPCR structures

G protein–coupled receptor 1 (GPR1) is a receptor for chemerin, a protein made in adipocytes. It is unusual in that it signals primarily through the β-arrestin 1 or β-arrestin 2 proteins rather than through G proteins. Cai *et al*. describe cryo–electron microscopy structures of the receptor with the arrestins in the presence or absence of chimerin. The structures reveal unusual binding conformations and the presence of a sterol and fatty acid that may contribute to the receptor's role in metabolic regulation in adipose tissue. —L. Bryan Ray

Science p. 801, 10.1126/science.adt8794

IMMUNOLOGY

Salvaging lung function after infection

Severe lung infection can become fatal because of the extensive tissue damage that impairs organ function. People generally seek treatment several days after infection, but this is often too late for therapies to be effective. Ichise *et al*. used a mouse model of influenza infection to identify two regimens of currently available therapeutic approaches combining immunomodulatory agents with a drug blocking viral replication, which could be administered 4 days after infection and overcame the damage that led to lethality. Although achieved in different ways, both treatments promoted the integrity of the lung epithelial cell barrier to sustain lung function in infected mice. —Sarah H. Ross

Science p. 802, 10.1126/science.adr4635

GENETIC CODE

TAG for pyrrolysine

The universal triple-nucleotide genetic code is common to all living organisms on Earth, but it varies in small and subtle ways across the tree of life. Kivenson *et al*. explored the reassignment of TAG codons from stop to pyrrolysine (Pyl) among diverse archaea and showed that this is not a rare event restricted to a few proteins; rather, it appears to represent a distinct genetic code that arose multiple independent times in different lineages. Proteomics data support the incorporation of Pyl into many proteins, and engineering experiments successfully assimilated it into *Escherichia coli* proteins. TAG occurs sporadically across the Archaea and seems to be more easily gained than lost, suggesting that a mobile element may have been instrumental in its evolution. —Caroline Ash

Science p. 803, 10.1126/science.adu2404

NEUROSCIENCE

Extracellular pain signaling

In the brain, extracellular kinases are responsible for phosphorylating the extracellular domain of proteins involved in synaptic transmission. Srikanth *et al*. focused on the mechanism of action of the synaptic kinase VLK (vertebrate lonesome linase) in sensory neurons. VLK is released from presynaptic sites and phosphorylates the extracellular domain of ephrin-B receptor kinases, thereby promoting the clustering of *N*-methyl-D-aspartic acid receptors (NMDARs) at synapses. Furthermore, VLK appears indispensable for neuronal viability and plays a crucial role in NMDAR-dependent injury-induced pain. These results suggest that VLK-mediated signaling might be targeted for managing NMDAR-dependent pain. —Mattia Maroso

Science p. 804, 10.1126/science.adp1007

IMMUNOLOGY

Bacterial toxins promote inflammation

Ulcerative colitis (UC) is a debilitating inflammatory bowel disease linked to dysfunction of cells within the large intestine. Jiang *et al*. hypothesized that toxins produced by microbiota might impair macrophages in the gut and contribute to the pathology of UC (see the Perspective by Modilevsky and Bel). Stool samples from UC patients contained a species of bacteria, a variant of the *Aeromonas* genus, that released a toxin called aerolysin. Under pathological conditions, this *Aeromonas* variant could colonize mouse intestines, deplete macrophages, and increase the sensitivity of mice to gut inflammation. These effects were linked to the ability of aerolysin to kill macrophages directly. Administration of anti-aerolysin antibodies provided protection against colitis in mice that were exposed to the *Aeromonas* variant. —Sarah H. Ross

Science p. 805, 10.1126/science.adz4712; see also p. 789, 10.1126/science.aec7924

VOLCANOLOGY

Wave-like opening of magma dikes

Early in 2025, an intense seismic swarm near the volcanic island of Santorini forced thousands of people to evacuate. To understand the cause of the unrest, Lomax *et al*. used data from seismic stations on Santorini and surrounding islands to locate about 25,000 earthquakes over an 8-week period (see the Perspective by Pinel). Their machine learning–derived maps provide an unusually detailed picture of the seismicity, including episodic tremor bursts just a few hours long. Changes in failure stress indicators suggest that the unrest was caused by pump-like intrusions of magma into newly opened dikes 12 kilometers below the seafloor. —Angela Hessler

Science p. 806, 10.1126/science.adz8538; see also p. 790, 10.1126/science.aec7912

NEURODEVELOPMENT

Calcium waves orchestrate eye development

Achieving precise structural and functional specialization requires coordination between multiple cell types during the development of the central nervous system. Studying retinal morphogenesis in the developing eye of fruit flies (*Drosophila melanogaster*), Choi *et al*. identified

spontaneous calcium waves originating from non-neuronal cells responsible for orchestrating tissue architecture in the developing nervous system (see the Perspective by Kumar). Initiation of these waves involved a receptor tyrosine kinase inducing phospholipase Cγ–mediated calcium release from the endoplasmic reticulum. After initiation, wave propagation followed a defined gap junction pathway across three distinct types of non-neuronal retinal cells. The results uncover a calcium-dependent mechanism in non-neuronal cells coordinating the development of the nervous system in *Drosophila*. —Mattia Maroso

Science p. 807, 10.1126/science.ady5541
see also p. 787, 10.1126/science.aec6302

SOLAR CELLS

Polymeric hole contacts for tandem cells

Polymerizing phosphonic acid hole transporters through Schiff-base chemistry was shown to enhance the operational stability of perovskite-silicon tandem solar cells at elevated temperatures. Zhang *et al*. reduced the thermal degradation of these self-assembled layers by derivatizing the molecules with primary amines that were cross-linked with aldehyde-functionalized bipyridine molecules. One-square-centimeter tandem solar cells achieved power conversion efficiencies exceeding 34% and lost less than 4% of their initial performance after about 1200 hours of maximum power point tracking at 65°C. —Phil Szuromi

Science p. 837, 10.1126/science.ady6874

PLANT SCIENCE

Plant chromosome reduction

Restructuring chromosomes alters inheritance patterns of genetic information. In plants, chromosomal rearrangements can reproductively isolate engineered plants from wild relatives or can change the inheritance of desirable agronomic traits. Rönspies *et al*. used the model plant *Arabidopsis thaliana* as a testbed to implement CRISPR-Cas technology to fuse chromosomes together (see the Perspective by Zhang and Dawe). The researchers generated plants with eight chromosomes instead of 10, which appeared to be phenotypically normal and were self-fertile. Altered recombination patterns illustrated the changes to genetic inheritance rules. This work opens avenues for large-scale chromosomal changes in plants and provides insights into the plasticity of plant genomes. —Madeleine Seale

Science p. 843, 10.1126/science.adz8505;
see also p. 786, 10.1126/science.aec7902

VIRAL INFECTIONS

Evading a viral Fc receptor

Herpes simplex virus (HSV) encodes two glycoproteins, gE and gI, that together form a viral Fc receptor (vFcR) capable of binding most human immunoglobulin G antibodies. Slein *et al*. sought to determine whether binding to vFcR altered the protection afforded by monoclonal antibodies against HSV. The authors found that antibodies engineered to lack binding to the vFcR were superior at HSV neutralization in vitro, which translated into enhanced protection in neonatal mice in vivo. This improvement in protection extended across antibody allotypes and specificities and across strains of HSV, including to clinical isolates. These data demonstrate that HSV-targeting monoclonal antibodies benefit from engineering to prevent binding to the vFcR, an important finding toward therapeutic antibody development. —Courtney Malo

Sci. Transl. Med. (2025)
10.1126/scitranslmed.adu8579

BLOOD DISEASE

A hammer to straighten the sickle

About half a million babies are born each year with sickle cell disease, a genetic condition that produces misshaped red blood cells due to alterations in hemoglobin structure. Sickle cell disease is responsible for high mortality rates, particularly in children, and leads to serious complications such as vascular occlusion, deficient tissue oxygenation, acute and chronic pain, anemia, susceptibility to infections, and pregnancy complications. Hara *et al*. identified a molecular pathway that reactivated fetal hemoglobin genes, thereby generating a fresh supply of functional hemoglobin that rescued the morphology of red blood cells from patients and alleviated disease symptoms in a mouse model. This pathway can be targeted with drugs already tested in humans, which paves the way for future clinical trials. —Miguel Torres

Sci. Adv. (2025)
10.1126/sciadv.adx1144

RESEARCH ARTICLE SUMMARY

SIGNAL TRANSDUCTION

Noncanonical agonist-dependent and -independent arrestin recruitment of GPR1

Heng Cai†, Xiaowen Lin†, Lechen Zhao†, Maozhou He†, Jie Yu†, Bingjie Zhang†, Yuandi Ma†, Xiaohua Chang, Yuxuan Tang, Tianyu Luo, Jie Jiang, Mengna Ma, Wenqi Song, Limin Ma, Xiaojing Chu, Cuiying Yi, Kun Chen, Shuo Han, Cen Xie*, Wenqing Shui*, Qiang Zhao*, Ya Zhu*, Beili Wu*

Full article and list of author affiliations: https://doi.org/10.1126/science.adt8794

INTRODUCTION: Atypical G protein (heterotrimeric guanine nucleotide–binding protein)–coupled receptors (GPCRs) govern important physiological processes, such as immune responses, cell migration, and tissue homeostasis, through arrestin-biased pathways, but the molecular mechanisms underlying the arrestin-mediated modulations of these receptors remain elusive. GPR1, an atypical GPCR, is activated by the chemokine-like protein chemerin and is involved in inflammation, adipogenesis, and metabolism. Unlike another chemerin receptor chemokine-like receptor 1 (CMKLR1)—a classical class A GPCR that activates G protein and promotes β-arrestin recruitment—GPR1 undergoes agonist-dependent and -independent β-arrestin internalization but induces weak G protein signaling. Thus, GPR1 is believed to serve as a decoy receptor to scavenge chemerin, which may attenuate pathologic signaling that results from excessive chemerin production.

RATIONALE: To extend our knowledge about the arrestin-associated regulations of GPR1, we combined cryo–electron microscopy (cryo-EM) single-particle analysis, mass spectrometry analysis, and functional assays of β-arrestin recruitment and internalization to investigate the binding modes between GPR1 and different β-arrestin subtypes—β-arrestin 1 and β-arrestin 2, which have distinct signaling patterns with this receptor—in both chemerin-bound and ligand-free states. Additionally, we measured lipid accumulation in lipid-overloaded adipocytes to explore the functionalities of GPR1 and CMKLR1 in adipocyte metabolism and lipid homeostasis, which further highlights the importance of GPR1-arrestin interaction in defining chemerin-mediated physiological functions.

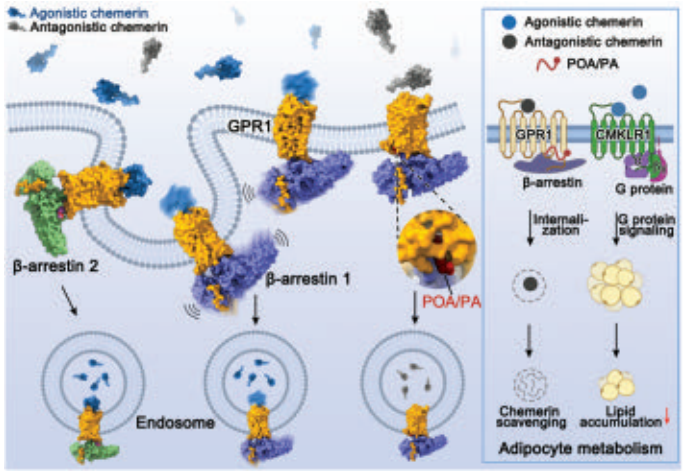

Chemerin scavenging of GPR1 through β-arrestin–mediated internalization. (Left) Agonistic chemerin isoforms induce GPR1 to recruit β-arrestin 1 and β-arrestin 2 in distinct interaction patterns, which leads to internalization into endosomes. Aided by palmitoleic acid (POA) or palmitic acid (PA), GPR1 scavenges antagonistic chemerin. (Right) Under lipid-overloaded conditions, GPR1 scavenges antagonistic chemerin and allows CMKLR1 to activate G proteins, thereby reducing lipid accumulation and modulating adipocyte metabolism.

RESULTS: The cryo-EM structures of chemerin–GPR1–β-arrestin 1 and chemerin–GPR1–β-arrestin 2 complexes reveal that β-arrestin 1 adopts four distinct noncanonical binding poses, showing plasticity of its finger loop and C-edge, which align with a dynamic swing model of arrestin recruitment that is beneficial to receptor internalization; by contrast, β-arrestin 2 binds to GPR1 in a more stable manner, with only one binding conformation that may facilitate receptor signaling. In the absence of ligand, GPR1 exhibits an inactive conformation that accommodates β-arrestin 1 in an interaction mode distinct from those upon chemerin stimulation. These findings indicate that GPR1 internalizes both agonistic and antagonistic isoforms of chemerin by adopting distinct conformations to recruit the β-arrestins, which allows the receptor to scavenge ligands with broader specificity. Supported by mass spectrometry analysis and functional data, the constitutive phosphorylation in the C terminus of GPR1 accounts for the constitutive β-arrestin recruitment and internalization of this receptor, which are further facilitated by two fatty acids, palmitoleic acid and palmitic acid, that couple to the receptor-arrestin binding interface to strengthen the interaction. The fatty acid–mediated complex assembly between the inactive GPR1 and β-arrestin aligns with the fact that in adipocytes overexpressing GPR1, triglyceride accumulation was decreased on stimulation with high concentrations of palmitate and oleate, which may promote scavenging of antagonistic chemerin isoforms produced by adipose tissue to allow more CMKLR1 molecules to be activated to mediate lipolysis.

CONCLUSION: Our work provides a full picture of GPR1-arrestin engagement in distinct functional states. The diverse arrestin binding modes not only provide a basis for differential cellular effects mediated by different β-arrestin subtypes for GPR1 but also offer diversity to ligand scavenging of this receptor, which is key for modulating the physiological functions of the chemerin-receptor system. □

*Corresponding author. Email: xiecen@simm.ac.cn (C.X.); shuiwq@shanghaitech.edu.cn (W.S.); zhaoq@simm.ac.cn (Q.Z.); ya.zhu@lglab.ac.cn (Y.Z.); beiliwu@simm.ac.cn (B.W.)
†These authors contributed equally to this work. **Cite this article as H. Cai *et al.*, *Science* 390, eadt8794 (2025). DOI: 10.1126/science.adt8794**

SIGNAL TRANSDUCTION

Noncanonical agonist-dependent and -independent arrestin recruitment of GPR1

Heng Cai[1,2,3,4]†, Xiaowen Lin[1,2,5]†, Lechen Zhao[1,5]†, Maozhou He[1,5]†, Jie Yu[4,5,6]†, Bingjie Zhang[6]†, Yuandi Ma[2,5]†, Xiaohua Chang[1,5], Yuxuan Tang[1,5], Tianyu Luo[1,5], Jie Jiang[2,5], Mengna Ma[6], Wenqi Song[1,5], Limin Ma[2], Xiaojing Chu[2], Cuiying Yi[2], Kun Chen[7], Shuo Han[2,5], Cen Xie[2,5]*, Wenqing Shui[4,6]*, Qiang Zhao[2,5,7]*, Ya Zhu[3,4]*, Beili Wu[1,2,4,5,8]*

G protein (heterotrimeric guanine nucleotide–binding protein)–coupled receptors have diverse signaling properties with differential preferences for downstream pathways. Certain receptors, such as the chemerin receptor GPR1, undergo arrestin-mediated internalization but weak G protein signaling. However, the mechanisms of this unusual signaling pattern and its physiological relevance are unclear. We report the structures of GPR1 bound to chemerin and β-arrestin 1 or β-arrestin 2 and an agonist-free GPR1–β-arrestin 1 complex. Upon agonist stimulation, the receptor binds the two arrestins in distinct interaction patterns, which may account for their differential cellular responses. Agonist-independent internalization was mediated by an inactive, constitutively phosphorylated GPR1 that accommodates β-arrestin 1 in an unconventional pocket together with a fatty acid, which potentially provides a basis for GPR1 modulating lipid accumulation in lipid-overloaded adipocytes.

Atypical G protein (heterotrimeric guanine nucleotide –binding protein)–coupled receptors (GPCRs), such as atypical chemokine receptors (ACKRs), complement C5a receptor 2, and the chemerin receptor GPR1, exert their functions mainly through the β-arrestin pathways with limited G protein activation (*1*–*3*). However, the molecular details that define the arrestin-dependent regulation of these receptors are largely unknown. Chemerin is a chemokine-like protein that exhibits characteristics of both chemoattractant protein and adipokine (*4*, *5*) and has been considered as a key biomarker of numerous metabolic and inflammatory diseases (*6*, *7*). Chemerin exerts most of its known functions by acting on the chemokine-like receptor 1 (CMKLR1), a classical class A GPCR that activates G proteins and promotes β-arrestin recruitment (*3*, *5*, *8*). Despite high sequence similarity with CMKLR1 (35%), GPR1 undergoes constitutive and chemerin-stimulated β-arrestin internalization but induces weak G protein signaling (*3*, *9*). Thus, GPR1 may modulate chemerin activity through arrestin-biased signaling and serve as a decoy receptor by scavenging chemerin, which could be beneficial to attenuating inappropriate immune responses, disrupted glucose homeostasis, and pathologic signaling that result from excessive chemerin production in obesity (*6*, *9*). These findings imply a role of GPR1 in chemerin-mediated physiological and pathological processes, but the underlying molecular mechanism remains poorly understood.

GPR1 binds β-arrestin 1 (βarr1) and β-arrestin 2 (βarr2) with similar potencies; however, the two β-arrestins differentially contribute to the signaling and cellular responses of the receptor (*3*, *10*). This supports that these two arrestins are not functionally redundant and aligns with previous studies that have implied the differential roles of the two arrestins in defining physiological functions of numerous receptors (*11*–*13*). However, there is no GPCR-βarr2 structure available, which limits our understanding of the arrestin-mediated regulation for not only GPR1 but also for the entire GPCR superfamily. Furthermore, in addition to agonist-stimulated internalization, a number of GPCRs, including GPR1, undergo constitutive internalization, and this may affect receptor localization and functions (*9*, *14*–*16*).

To extend our knowledge about GPCR regulation by different arrestins and uncover molecular mechanisms of the chemerin scavenging of GPR1, we determined the structures of modified forms of this receptor in complex with chemerin and βarr1 or βarr2 as well as the ligand-free structure of the GPR1-βarr1 complex. Combined with functional data and phosphorylation analysis, these structures provide insight into arrestin binding to a single GPCR with molecular details that define receptor interactions with different β-arrestin subtypes and constitutive internalization, adding to our understanding of the functional modulation of the chemerin-receptor system.

Structure determination of the GPR1-arrestin complexes

To improve protein quality of arrestin-bound GPR1 complexes, we exchanged the C-terminal region of the receptor for the C-terminal residues in the vasopressin type 2 receptor (V_2R) (fig. S1, A and B). Using a bioluminescence resonance energy transfer (BRET) assay, it was confirmed that adding the V_2R tail has little effect on the chemerin-induced βarr1 binding to GPR1 (table S1). Aiming to optimize protein quality of the ligand-free GPR1-βarr1 complex, a disulfide bridge between the receptor and arrestin [GPR1, Val^{143}→Cys (V143C); βarr1, Y249C] was further introduced based on cysteine cross-linking data (fig. S1C). The chemerin-bound and ligand-free GPR1-βarr1 complexes and chemerin-GPR1-βarr2 complex were prepared using modified βarr1 and βarr2, respectively (fig. S1, A and B; see Materials and methods for details), and subjected to cryo–electron microscopy (cryo-EM) single-particle analysis, yielding four maps of the chemerin-GPR1-βarr1 complex with different βarr1 binding poses (referred to conformations 1 to 4), a map of the GPR1-βarr1 complex, and a map of the βarr2-bound complex (Fig. 1; fig. S1, D to O; fig. S2; and table S2).

The maps allowed modeling of most of the residues in the receptor, βarr1, and βarr2 (Fig. 1 and fig. S3). In the βarr2-bound GPR1 structure, full-length chemerin was defined and adopted a binding pose similar to that in our recently determined structure of GPR1 bound to chemerin and G_{i1} protein (*17*) (Fig. 1, C and D, and figs. S3E and S4A). By contrast, densities were only observed for the C terminus of the agonist in the maps of chemerin-GPR1-βarr1 (Fig. 1, A and B, and fig. S3, A to D), which suggests a higher degree of conformational dynamics of chemerin in this complex. The receptor in the chemerin-GPR1-βarr complexes is structurally similar to that in the chemerin-GPR1-G_{i1} complex [Cα root mean square deviation (RMSD) of transmembrane helical bundle, 0.6 to 1.4 Å]. In comparison, the ligand-free GPR1-βarr1 displays a larger deviation (Cα RMSD of transmembrane helical bundle, 1.9 Å), which suggests different conformational states of the βarr1-bound receptor upon chemerin stimulation and in the basal state.

Dynamic binding between GPR1 and βarr1

A multistep process has been proposed for GPCRs recruiting arrestins by adopting distinct interaction patterns at different stages (*18*, *19*). However, the molecular mechanism underlying the dynamics of the

[1]School of Pharmaceutical Science and Technology, Hangzhou Institute for Advanced Study, University of Chinese Academy of Sciences, Hangzhou, China. [2]State Key Laboratory of Drug Research, State Key Laboratory of Chemical Biology, Shanghai Institute of Materia Medica, Chinese Academy of Sciences, Shanghai, China. [3]Lingang Laboratory, Shanghai, China. [4]School of Life Science and Technology, ShanghaiTech University, Shanghai, China. [5]University of Chinese Academy of Sciences, Beijing, China. [6]iHuman Institute, ShanghaiTech University, Shanghai, China. [7]Zhongshan Institute for Drug Discovery, Shanghai Institute of Materia Medica, Chinese Academy of Sciences, Zhongshan, China. [8]Shanghai Academy of Natural Sciences (SANS), Shanghai Institute of Materia Medica, Chinese Academy of Sciences, Shanghai, China. ***Corresponding author. Email: xiecen@simm.ac.cn (C.X.); shuiwq@shanghaitech.edu.cn (W.S.); zhaoq@simm.ac.cn (Q.Z.); ya.zhu@lglab.ac.cn (Y.Z.); beiliwu@simm.ac.cn (B.W.)** †These authors contributed equally to this work.

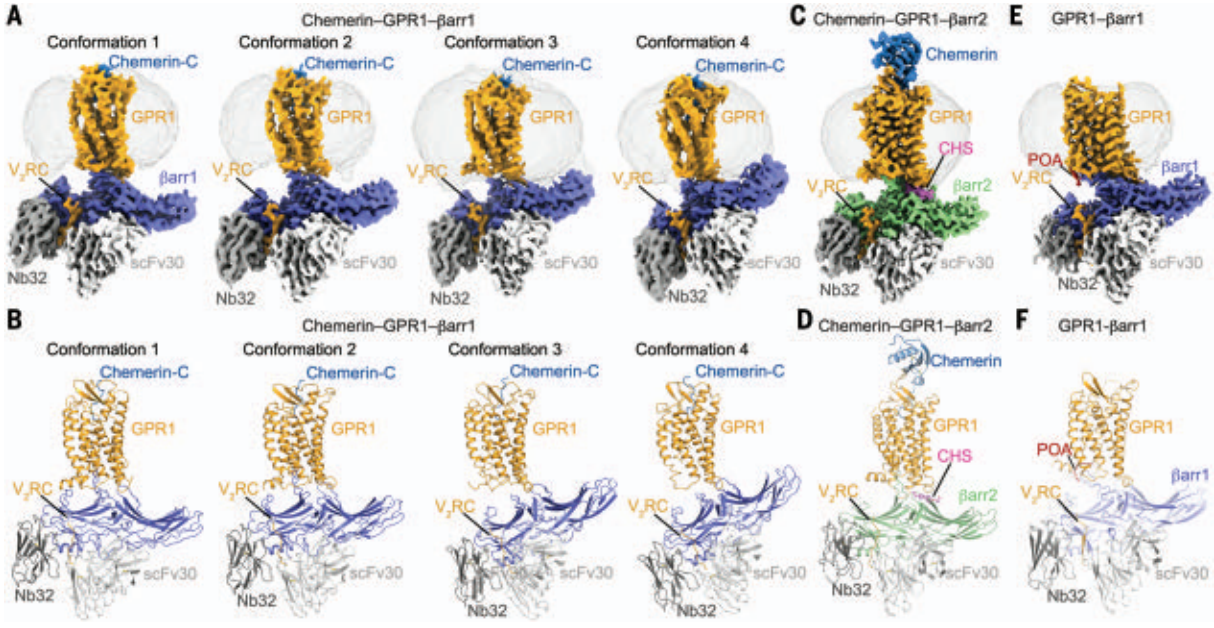

Fig. 1. Cryo-EM maps and structures of the GPR1-βarr complexes. The maps and structures are colored according to chains. (**A** and **B**) Cryo-EM maps (A) and structures (B) of the conformations 1 to 4 of the chemerin-GPR1-βarr1 complex. Nb32 (nanobody 32), a nanobody that stabilizes the active conformation of arrestin. (**C** and **D**) Cryo-EM map (C) and structure (D) of the chemerin-GPR1-βarr2 complex. (**E** and **F**) Cryo-EM map (E) and structure (F) of the ligand-free GPR1-βarr1 complex.

arrestin recruitment is poorly understood. In previously reported class A GPCR–arrestin structures, arrestin adopts a tilted binding pose with its finger loop inserted into the receptor transmembrane core and the C-edge attached to the detergent micelles or nanodiscs (*20*–*27*) (fig. S4B). These structural studies yielded one single, well-defined arrestin binding pose for each receptor, despite rocking motions of arrestin reported (*23*). By contrast, the chemerin-GPR1-βarr1 complex exhibited four different binding poses of βarr1 (conformations 1 to 4) that formed distinct angles with the membrane plane, ranging from 10° to 40°, which may reflect a dynamic process of arrestin recruitment that engages multiple conformational states (Fig. 1B, Fig. 2A, fig. S2A, and movie S1).

In conformations 1 and 2, which are slightly different in the relative orientation between the receptor and arrestin, the C-edge of βarr1 does not make any contact with detergent micelles, resulting in a relatively horizontal binding pose of the arrestin (Fig. 2, A and B, and fig. S4B). In these two conformations, the finger loop of βarr1 binds to the canonical intracellular pocket of GPR1 mainly through a hydrophobic interaction core formed by the residues V70 to L73 in its turn region and multiple receptor residues in helices II, III, V, VI, and VII (Fig. 2C). These interactions are not conserved in most class A GPCR–arrestin structures owing to a shallower binding site for the arrestin finger loop in those receptors, except for β_1 adrenergic receptor (β_1AR) (fig. S4C). The binding site of the βarr1 finger loop in GPR1 is largely overlapped with that of α5 helix in the α subunit of G_{i1} protein (fig. S4A), which ensures efficient desensitization of G protein signaling upon arrestin binding. In addition to the finger loop, the C-loop of βarr1 also contributes to the GPR1-βarr1 binding in conformations 1 and 2, with the residue F244 approaching the third intracellular loop (ICL3) of the receptor to form hydrophobic contacts with $I238^{ICL3}$ and $L239^{ICL3}$ and the residue Y249 interacting with the segment $H141^{ICL2}$ to $V143^{ICL2}$ in the second intracellular loop (ICL2) of GPR1 (Fig. 2D).

In contrast to the horizontal binding poses of βarr1 in conformations 1 and 2, conformations 3 and 4 showed a swing of βarr1 toward the cell membrane, which allows the C-edge to interact with the micelles and leads to a largely tilted binding conformation (Fig. 2, A and E, and fig. S4B). The finger loop of βarr1, which binds deep to the receptor intracellular pocket in all class A GPCR–arrestin structures, failed to form any stable interaction with the receptor and loosely attached to the helical bundle in conformations 3 and 4 (Fig. 2E). This is supported by the absence of densities for the turn of the finger loop (residues R65 to T74) and the relatively poor densities for the intracellular regions of helices VI and VII in the cryo-EM maps (fig. S3, C and D). In these two conformations, the C-loop and lariat loop of βarr1, rather than the finger loop, make up the primary binding interface for GPR1 by forming a binding groove for the segment $H141^{ICL2}$ to $R149^{ICL2}$ in the receptor (Fig. 2F). Although the interaction pattern may vary, similar binding modes between the receptor ICL2 and the C-loop and lariat loop of the arrestin were also observed in most other class A GPCR–arrestin structures (fig. S4D).

During the early stages of arrestin recruitment, the receptor and arrestin are thought to form a "precomplex" that is mainly mediated by interactions between the phosphorylated C terminus of the receptor and the arrestin N domain and is stabilized by a membrane anchor through the C-edge of the arrestin (*19*, *28*). In later stages, the finger loop of the arrestin tightly binds to the receptor core to form a high-affinity complex with the receptor (*18*, *19*). This model aligns with our observation of the multiple binding poses of βarr1 in GPR1. Particularly, conformations 3 and 4 may represent the precomplex in an early stage with the membrane anchoring of the arrestin C-edge but a loose binding of the finger loop to the receptor, whereas conformations 1 and 2 may function in later stages with tight receptor-arrestin binding. The exposed C-edge potentially facilitates internalization and endocytosis because the C-edge of βarr1 is required for binding to the endocytic protein clathrin to mediate recruitment of the active receptor to the clathrin-coated pits at the membrane (*29*, *30*) (Fig. 2G).

The phosphorylation pattern in the C terminus of a GPCR is thought to be a key determinant of arrestin binding conformation and subsequent functional outcomes, which is referred to as the phospho barcode hypothesis (*31*, *32*). We mapped the phosphorylation sites in the C-terminal region of GPR1 by mass spectrometry analysis of the chemerin-GPR1-βarr1 complex, which identified eight phosphorylation

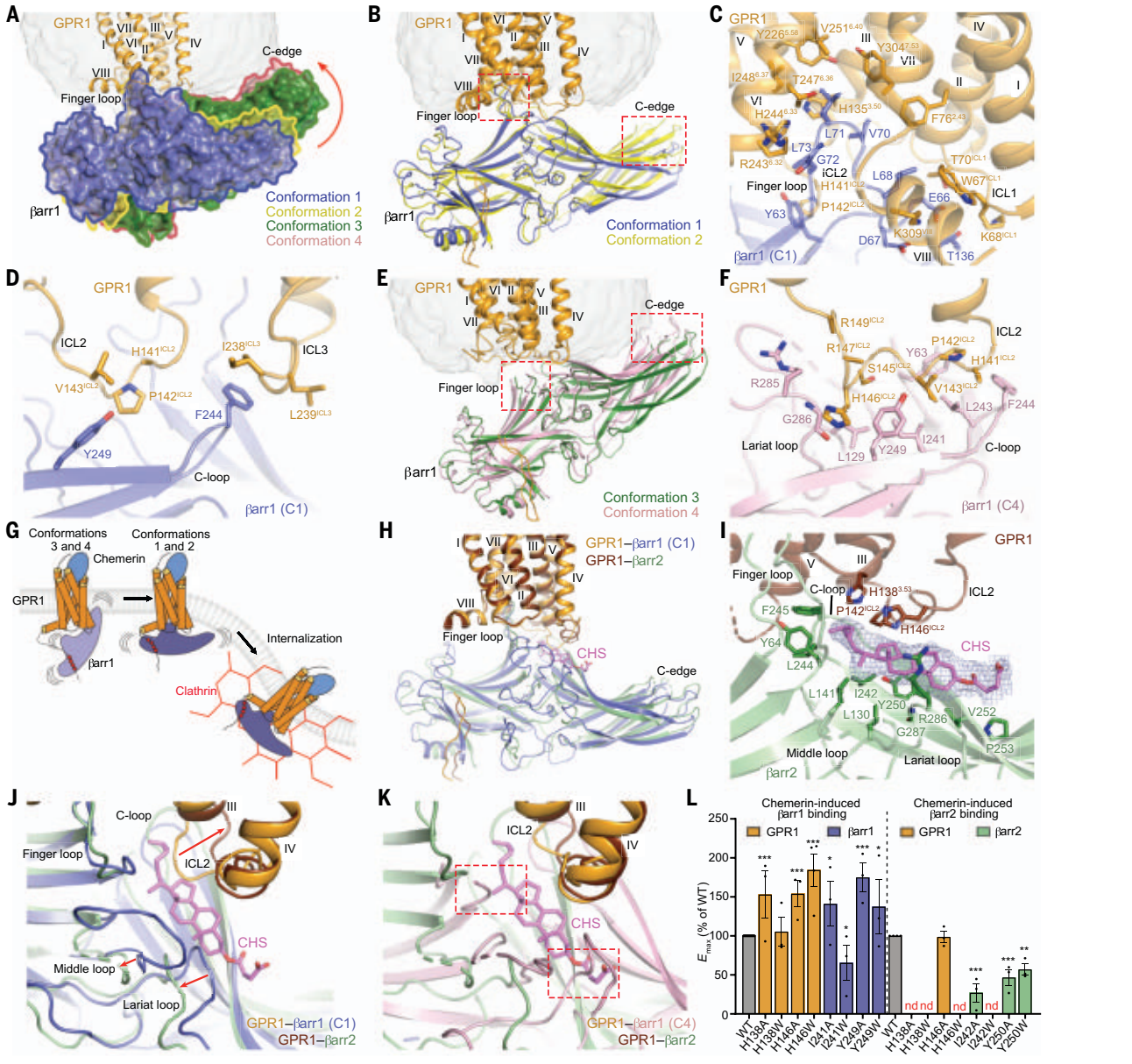

Fig. 2. Chemerin-induced βarr1 and βarr2 recruitment of GPR1. (**A**) Alignment of the four binding conformations of chemerin-GPR1-βarr1. The arrestin is shown in surface representation. (**B**) Comparison of conformations 1 and 2 of chemerin-GPR1-βarr1. The structures are aligned at the transmembrane helical bundle of the receptor. (**C** and **D**) Interactions between GPR1 and βarr1 in conformation 1 (C1) of chemerin-GPR1-βarr1. The side chain of $H141^{ICL2}$ was not modeled owing to lack of densities in the cryo-EM map. (**E**) Comparison of conformations 3 and 4 of chemerin-GPR1-βarr1. (**F**) Interactions between GPR1 and βarr1 in conformation 4 (C4) of chemerin-GPR1-βarr1. The side chains of $H141^{ICL2}$, $R147^{ICL2}$, and $R149^{ICL2}$ were not modeled owing to lack of densities in the cryo-EM map. (**G**) Schematic representation of the swing model of the chemerin-induced βarr1 recruitment and internalization of GPR1. (**H**) Structural comparison between the chemerin-GPR1-βarr1 (C1) and chemerin-GPR1-βarr2 complexes. (**I**) The binding mode of CHS in the chemerin-GPR1-βarr2 structure. The electron densities for the lipid are colored light blue. (**J**) Comparison between the chemerin-GPR1-βarr1 (C1) and chemerin-GPR1-βarr2 complexes in the lipid binding site. The shifts of the receptor ICL2 and the middle and lariat loops of the arrestin in the chemerin-GPR1-βarr2 structure relative to the βarr1-bound structure are indicated by red arrows. (**K**) Comparison between the chemerin-GPR1-βarr1 (C4) and chemerin-GPR1-βarr2 complexes in the lipid binding site. The clashes between the lipid and βarr1 are highlighted by red dashed boxes. (**L**) Chemerin-induced βarr1 and βarr2 binding of the wild-type (WT) GPR1 and mutants measured by BRET assays. The E_{max} are represented by bars. Data are shown as means ± SEMs from at least three independent experiments performed in technical duplicate. nd, not determined; $*P < 0.05$; $**P < 0.001$; $***P < 0.0001$ [one-way analysis of variance (ANOVA) followed by Dunnett's post hoc test, compared with the response of wild type]. Table S1 provides detailed independent experiment numbers (*n*), statistical evaluation, and expression levels. Single-letter abbreviations for the amino acid residues are as follows: A, Ala; C, Cys; D, Asp; E, Glu; F, Phe; G, Gly; H, His; I, Ile; K, Lys; L, Leu; M, Met; N, Asn; P, Pro; Q, Gln; R, Arg; S, Ser; T, Thr; V, Val; W, Trp; and Y, Tyr.

sites, S317, S318, T326, S331, S333, T335, S337, and S343 (fig. S5, A to G, and table S3). This suggests that binding occurs between the GPR1 C terminus and arrestin. Indeed, removing the phosphorylated residues impaired chemerin-induced recruitment of βarr1 as monitored by the BRET assay (fig. S6A and table S1). Furthermore, substituting the C-terminal region in GPR1 (residues L323 to Q355) with the C terminus of CMKLR1 (residues L338 to L373) [GPR1(CMKLR1-C)], which has a distinct distribution of serine, threonine, and acidic residues compared with that of the GPR1 C terminus (fig. S7A), resulted in a 75% drop of the maximal amount of chemerin-induced βarr1 binding

(fig. S6A and table S1). These data indicate a vital role of the C terminus of GPR1 in agonist-dependent arrestin engagement. In our chemerin-GPR1-βarr1 structures, the receptor C terminus was replaced with the C-terminal tail of V_2R, which occupies the canonical phosphorylated peptide binding groove in the βarr1 N-lobe (*21*–*27*) (Fig. 1A). The C-terminal segments of GPR1 and V_2R share a similar pattern of arrestin recognition elements, such as serine, threonine, and acidic residues, including PxxP and PxPP motifs (where P is a phosphorylated S or T or acidic residue and x can be any residue) (*33*, *34*) (fig. S7A). Furthermore, spacing between the arrestin recognition site (PxxP motif) and receptor helical bundle is also similar in the wild-type GPR1 and GPR1-V_2RC chimera (GPR1, 18 residues; GPR1-V_2RC, 19 residues). These similarities minimize the impact of the introduced V_2R tail on the binding conformations of βarr1.

Lipid-mediated interaction between GPR1 and βarr2

The contribution of βarr2, but not βarr1, to the GPR1-mediated phosphorylation of extracellular signal–regulated kinases 1 and 2 (ERK1 and ERK2) indicates distinct signaling patterns of these two arrestins with this receptor (*3*). Consistent with this finding, our chemerin-GPR1-βarr structures revealed different interaction modes of GPR1 binding to βarr1 and βarr2. In contrast to the multiple binding poses of βarr1, only a single binding conformation was observed for βarr2, although the same receptor modification was used to determine the structures (fig. S2B). This conformation is similar to the conformations 1 and 2 of βarr1, with the finger loop interacting with the receptor transmembrane core and the C-edge not making any contact with detergent micelles (Fig. 2H). The absence of membrane anchoring is likely associated with a shortened loop in the βarr2 C-edge (residues V329 to D335), of which the corresponding loop in βarr1 is eight residues longer and interacts with detergent micelles or nanodiscs in the conformations 3 and 4 of chemerin-GPR1-βarr1 and reported GPCR-βarr1 structures (figs. S4B and S7B). This binding mode of GPR1-βarr2 potentially enables an efficient coupling between βarr2 and ERK, given that the C-edge of βarr2 is a putative interaction site for ERK2 (*35*) and may provide a molecular basis for the βarr2-dependent phosphorylation of ERKs. However, this does not rule out the possibility that the C-edge forms transient contacts with the cell membrane in the early stage of recruitment because preassociation of arrestin with the lipid bilayer is important for its interactions with the receptor and subsequent activation (*36*).

Another difference between the βarr1- and βarr2-bound structures of GPR1 is that a lipid molecule binds to the arrestin interaction interface in the chemerin-GPR1-βarr2 complex but not in the βarr1-bound structures (Fig. 1, A to D, and Fig. 2H). The cryo-EM map allowed modeling of a cholesterol hemisuccinate (CHS) molecule (Fig. 2I and fig. S3E), which was included in the protein purification buffers to stabilize the protein. Thus, it is possible that cholesterol, an essential component of the cell membrane, may contribute to GPR1-βarr2 interaction under physiological conditions. CHS engages in extensive hydrophobic interactions with the residues $H138^{3.53}$ [superscript represents residue numbering using the Ballesteros-Weinstein nomenclature (*37*)], $P142^{ICL2}$, and $H146^{ICL2}$ in GPR1 and multiple hydrophobic residues in the central loops of βarr2 to strengthen receptor-arrestin binding (Fig. 2I). To allow lipid binding, the receptor ICL2 as well as the middle and lariat loops of βarr2 move outward, generating a larger cavity in the βarr2-bound complex compared with that in the βarr1-bound structures (Fig. 2J). This finding indicates that there may be binding specificity of cholesterol to the chemerin-GPR1-βarr2 complex. Our BRET data show that replacing some key residues in this lipid binding site (GPR1, $H138^{3.53}$ and $H146^{ICL2}$; βarr2, I242 and Y250) with alanine to break the receptor-lipid interaction or with tryptophan to introduce spatial hindrances have large effects on the chemerin-induced βarr2 binding of GPR1 with more than 40% reduction of the maximal response (E_{max}), despite wild-type amounts of cell-surface expression (Fig. 2L; fig. S6, B and C; and table S1). The only exception is $H146^{ICL2}$A that displays a minimal impact on the βarr2 recruitment, which may reflect a weak interaction between its side chain and the cholesterol molecule.

On the contrary, although the residues in the lipid binding site are conserved between βarr1 and βarr2, no lipid densities were observed in any of the cryo-EM maps of chemerin-GPR1-βarr1. In agreement with the structural data, the above mutations have no detrimental effect on the chemerin-induced βarr1 binding of GPR1 (Fig. 2L; fig. S6, D and E; and table S1). These data support the importance and selectivity of cholesterol in mediating the βarr2 recruitment. Further structural alignment displayed a clash between CHS in the βarr2-bound structure and arrestin in conformations 3 and 4 of chemerin-GPR1-βarr1, which indicates that CHS might have a role in excluding the largely tilted binding conformation (Fig. 2K). Thus, cholesterol may serve to stabilize the chemerin-GPR1-βarr2 complex in a conformation that potentially promotes internalization and ERK phosphorylation by exposing the arrestin C-edge and reduces conformational dynamics of the βarr2-bound complex relative to those of the βarr1-bound complex. The different binding modes of βarr1 and βarr2 to GPR1 may provide a basis for the differential signaling patterns and cellular effects mediated by the two arrestins for this receptor.

Constitutive arrestin recruitment of GPR1

Our ligand-free structure of the GPR1-βarr1 complex provides molecular details of the constitutive arrestin recruitment for a GPCR. Lacking the agonist, the receptor adopts an inactive conformation, which is reflected by an inward shift of the intracellular end of helix VI by ~6 Å relative to those in the chemerin-GPR1-βarr1 structures (Fig. 3A). The inward positioning of helix VI blocks the binding of the arrestin finger loop to the same binding site, like what occurs in the chemerin-bound complex (Fig. 3A). Alternatively, the finger loop may shift toward helix VII by ~7 Å (measured at the Cα atom of L71), occupying a shallow cavity shaped by the first intracellular loop (ICL1), helices III and VI, and the joint between helices VII and VIII. To allow the arrestin binding, the intracellular tip of helix VII appears to move outward by ~7 Å (Fig. 3A). The receptor-arrestin binding in this region is mediated by two interaction cores, including one formed by multiple GPR1 residues in ICL1 and the VII-VIII joint and the residues E66, L68 to L71, and L73 in the turn region of the βarr1 finger loop, and another one engaged by $H138^{3.53}$ and $H244^{6.33}$ in helices III and VI of GPR1 and the bulky residues Y63 and F75 at the N- and C-ends of the finger loop (Fig. 3B). Our cysteine cross-linking data showed that the $S308^{7.57}C$ mutant of GPR1 successfully cross-linked with the βarr1 mutant L71C but not L68C (fig. S1C). This is consistent with the ligand-free GPR1-βarr1 structure, in which L71 in the βarr1 finger loop is adjacent to $S308^{7.57}$ in the VII-VIII joint of the receptor, whereas the side chain of L68 approaches the receptor ICL1 (Fig. 3B). Associated with the movement of the finger loop, the arrestin rotates clockwise by ~20° (intracellular view) compared with that in the conformations 1 and 2 of chemerin-GPR1-βarr1, and the C-edge approaches the membrane and adopts an intermediate positioning between those in the conformations 1 and 2 and conformations 3 and 4 of the chemerin-bound complex (Fig. 3C).

We verified the different GPR1-βarr1 binding modes in the agonist-stimulated and agonist-free states by mutagenesis studies. Alanine and tryptophan mutations of the residues $H141^{ICL2}$, $Y226^{5.58}$, $I248^{6.37}$, and $V251^{6.40}$, which mediate interaction with the finger loop of βarr1 in the chemerin-bound complex but not in the ligand-free complex, impaired chemerin-induced binding of βarr1 in BRET assays but had little effect on constitutive arrestin recruitment measured by a transcriptional activation after arrestin translocation (Tango) assay, despite their cell-surface expression in amounts comparable to that of the wild-type receptor (Fig. 3, E and F; fig. S6F; and tables S1 and S4). The diverse interaction patterns were also verified by site-specifically labeling the

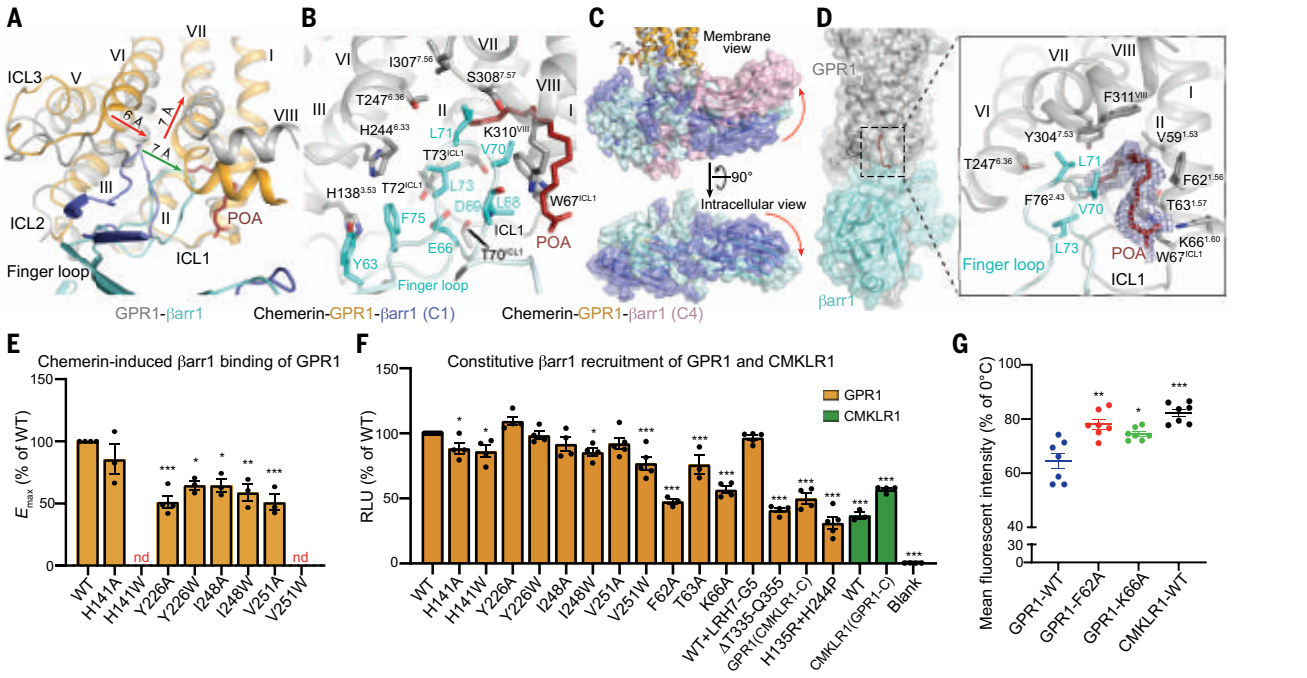

Fig. 3. Constitutive arrestin recruitment of GPR1. (**A**) Comparison of the ligand-free GPR1-βarr1 structure and the conformation 1 (C1) of chemerin-GPR1-βarr1. The movements of helices VI and VII in the ligand-free structure relative to the chemerin-bound structure are indicated by red arrows, and the shift of the βarr1 finger loop is indicated by a green arrow. POA in the ligand-free structure is shown as brown sticks. (**B**) Interactions between GPR1 and the βarr1 finger loop in the ligand-free GPR1-βarr1. (**C**) Comparison of the arrestin binding poses in the ligand-free and chemerin-bound (C1 and C4) structures of GPR1-βarr1. In intracellular view, only the arrestins in the ligand-free and chemerin-bound (C1) structures are shown for clarity. The red arrows indicate the movement of βarr1 in the ligand-free structure relative to the chemerin-bound complex (C1). (**D**) Binding mode of the fatty acid POA in the ligand-free GPR1-βarr1. The electron densities for the fatty acid are colored light blue. (**E** and **F**) Chemerin-induced βarr1 binding measured by BRET assay (E) and constitutive βarr1 recruitment measured by Tango assay (F) for GPR1 and CMKLR1. The E_{max} [in (E)] and relative luciferase units (RLU) [in (F)] are represented by bars. The cells transfected with empty vector (blank) were measured as a negative control (F). Data are shown as means ± SEMs from at least three independent experiments performed in technical duplicate. nd, not determined; $*P < 0.05$; $**P < 0.001$; $***P < 0.0001$ (one-way ANOVA followed by Dunnett's post hoc test, compared with the response of wild-type GPR1). Tables S1 and S4 provide detailed independent experiment numbers (*n*), statistical evaluation, and expression levels. (**G**) The amount of GPR1 and CMKLR1 remaining at the cell surface measured by flow cytometry. The mean fluorescent intensity measured after a 45-min incubation at 37°C are presented as percentage of the mean fluorescent intensity under ice-cold conditions (0°C) and are shown as means ± SEMs from seven independent experiments performed in technical duplicate. $**P < 0.001$; $***P < 0.0001$ (one-way ANOVA followed by Dunnett's post hoc test, compared with the mean fluorescent intensity under ice-cold conditions).

βarr1 finger loop with the environmentally sensitive probe monobromobimane (mBBr) at the residue L71 (L71mBBr). Upon binding to GPR1, an increase in fluorescence of βarr1-L71mBBr was observed, which reflects insertion of the finger loop into a hydrophobic environment. The fluorescent signal was further elevated when the receptor was activated by a peptide comprising the C-terminal nine residues of chemerin (C9), an agonist of GPR1 (*38*) (fig. S6H). These data are consistent with the ligand-free and chemerin-bound structures of GPR1-βarr1, showing that the βarr1 finger loop occupies a hydrophobic binding cavity deep within the receptor helical bundle upon agonist binding (conformations 1 and 2), whereas the binding pocket for the finger loop is shallower and has more solvent accessibility in the ligand-free complex. Taken together, our structural and functional data indicate that the plasticity of the arrestin finger loop is required for recognizing the receptor in different conformational states. However, the current data do not rule out existence of other binding conformations, given the dynamic nature of the receptor-arrestin interaction.

The inactive receptor conformation that allows constitutive arrestin binding by GPR1 is further supported by our functional data, which show that adding the GPR1 antagonist LRH7-G5 (*39*) does not alter basal βarr1 binding by the wild-type receptor (Fig. 3F and table S4). Similarly, receptor activation is not required for the constitutive internalization of some other GPCRs, such as cannabinoid receptor 1, β_2 adrenergic receptor, M3 muscarinic acetylcholine receptor, and chemokine receptor CCR1, as evidenced by the fact that their specific antagonists have no effect on the constitutive endocytosis (*15*, *40*, *41*). This implies that in the basal state, these receptors may also adopt an inactive conformation to bind arrestin.

In human cells, there are a few C-terminally truncated variants of chemerin with distinct physiological activities, including chemS157 (residues E21 to S157) and chemF156 (residues E21 to F156) with agonistic activities and chemA155 (residues E21 to A155) that acts as an antagonist (*4*, *15*, *42*). Our structural and functional data indicate that GPR1 internalizes both kinds of chemerin isoforms by adopting distinct conformations to recruit the arrestins, which allows the receptor to scavenge ligands with broader specificity. This is consistent with evidence that some chemerin-derived peptides that cannot activate GPR1 are still internalized by this receptor (*9*).

Determinants of the constitutive arrestin recruitment and internalization of GPR1

We further investigated the agonist-independent and -dependent internalization of GPR1 with live-cell confocal microscopy. Human embryonic kidney 293T (HEK293T) cells expressing the N-terminally Flag-tagged GPR1 that had been labeled with mouse antibody to Flag and secondary antibody to mouse immunoglobulin G (IgG) conjugated to Alexa Fluor 647 on ice showed surface staining of the receptor

(Fig. 4A). When cells were incubated for 15 to 30 min at 37°C, the βarr1- and βarr2-mediated internalization was observed for GPR1 in both the absence and presence of agonist (Fig. 4A and fig. S8). This is in contrast to results with CMKLR1, which did not recruit βarr1 when its agonist was absent (Fig. 4B). On chemerin stimulation, βarr1 was recruited quickly to the plasma membrane by CMKLR1, but no obvious internalization was observed (Fig. 4B). These findings further highlight the distinct properties of these two chemerin receptors in regulating arrestin.

As a key determinant of arrestin binding, the C-terminal region of GPR1 is not only required for agonist-stimulated arrestin recruitment (fig. S6A) but is also important for constitutive arrestin engagement. This is evidenced by a 50 to 60% reduction in basal βarr1 recruitment when the PxPP motif (^{335}TVSE^{338}) at the GPR1 C terminus was removed (ΔT335 to Q355) or the C-terminal residues L323 to Q355 in GPR1 were substituted with the C terminus of CMKLR1 (residues L338 to L373) [GPR1(CMKLR1-C)] (Fig. 3F and table S4). To further elucidate the contribution of site-specific phosphorylation to arrestin recruitment by GPR1, we compared the extent of phosphorylation of apo and chemerin-bound GPR1 by quantitative mass spectrometry analysis of the respective protein complexes. We identified eight phosphorylation sites in the C-terminal region of apo GPR1 that completely overlap with those identified from the chemerin-bound GPR1 (Fig. 5A, fig. S5, and table S3). Furthermore, quantitative analysis revealed that six of these C-terminal phosphosites have comparable phosphorylation in both ligand-free and chemerin-bound receptors (Fig. 5A; fig. S5, A to G; and table S3), which supports the high constitutive arrestin-binding activity of GPR1. In line with enhanced arrestin binding to GPR1 upon agonist stimulation, the remaining two phosphosites (T326 and T335, located in the PxxP and PxPP motifs, respectively) showed substantially increased phosphorylation in chemerin-bound receptors relative to those in a ligand-free state (Fig. 5A; fig. S5, B and E; and table S3).

Compared with GPR1, CMKLR1 has lower constitutive arrestin recruitment, as evidenced by the data of the Tango assay (34% of GPR1) and confocal microscopy (Fig. 3F, Fig. 4B, and table S4). Consistently, our mass spectrometry analysis of apo CMKLR1 identified only five phosphosites at the C terminus, all showing low phosphorylation intensities, whereas phosphorylation was increased by 3- to 89-fold in chemerin-bound CMKLR1, which had a total of eight C-terminal phosphosites (Fig. 5B, fig. S9, and table S3). These results corroborate the role of basal phosphorylation in regulating the constitutive arrestin recruitment of GPR1, which is largely absent for CMKLR1. However, replacing the C-terminal region in CMKLR1 with the counterpart of GPR1 [CMKLR1(GPR1-C)] only mildly increased basal βarr1 recruitment (57% of that of GPR1) (Fig. 3F and table S4). Thus, other determinants may also be important.

The inactive conformation of GPR1 observed in the ligand-free GPR1-βarr1 structure raises a possibility that the stability of the receptor-inactive conformation may correlate with constitutive internalization of GPR1. In CMKLR1, because of the lack of any acidic residue in the intracellular region of helix VI, the conserved class A GPCR residue $R^{3.50}$ does not form an ionic lock—an ionic interaction between the intracellular regions of helices III and VI that was believed to stabilize

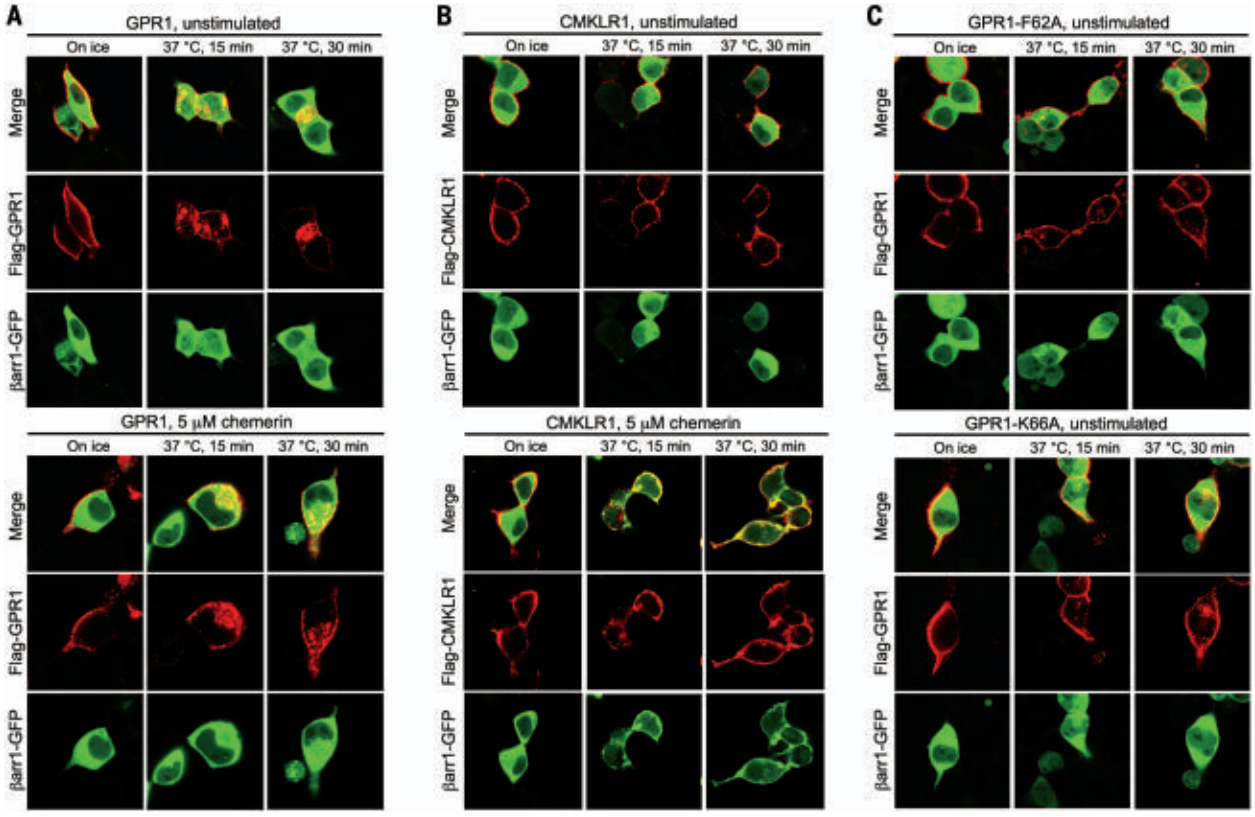

Fig. 4. βarr1 recruitment and internalization of GPR1 and CMKLR1 monitored by live-cell confocal microscopy. (**A**) The wild-type GPR1 in the absence (unstimulated) or presence of agonist (5 μM chemerin). GFP, green fluorescent protein. (**B**) The wild-type CMKLR1 in the absence or presence of agonist. (**C**) The GPR1 mutants F62$^{1.56}$A and K66$^{1.60}$A in the absence of agonist. The images are shown for the cells after labeling on ice, 15-min incubation at 37°C, or 30-min incubation at 37°C. The receptors and βarr1 are colored red and green, respectively. The images are representative of three or four independent experiments (unstimulated GPR1 and CMKLR1, $n = 3$; agonist-stimulated GPR1 and CMKLR1, $n = 3$; unstimulated GPR1 mutants F62$^{1.56}$A and K66$^{1.60}$A, $n = 4$).

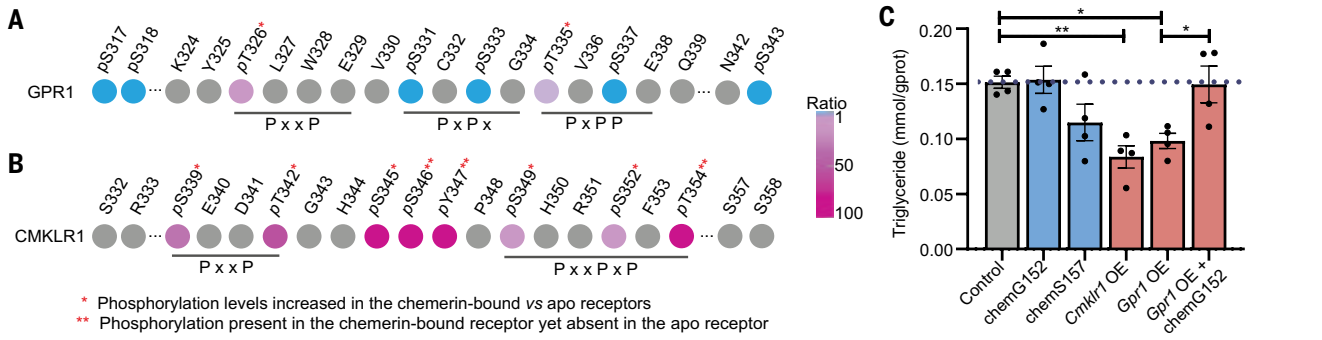

Fig. 5. C-terminal phosphorylation patterns in GPR1 and CMKLR1 and lipid accumulation in WAT SVF. (**A** and **B**) The C-terminal phosphorylation patterns determined for apo GPR1-βarr1 versus chemerin-bound GPR1-βarr1 (A) or apo CMKLR1 versus chemerin-bound CMKLR1-βarr1 (B) by mass spectrometry (MS) analysis. The color-coded phosphorylation sites indicate unchanged phosphorylation levels (blue) or increased phosphorylation levels (pink) at specific sites in the chemerin-bound receptor compared with those in the apo receptor. Potential phosphorylation motifs are annotated underneath the protein sequences. P, phosphorylated S or T or acidic residue; x, any residue. MS-based quantification of site-specific phosphorylation between different complexes is provided in figs. S5 and S9 and table S3. (**C**) Lipid accumulation induced by chemerin supplementation or overexpression of GPR1 or CMKLR1 in WAT SVF. Intracellular triglyceride levels were assayed in mature adipocytes treated with 500 ng ml^{-1} chemG152 or chemS157 or overexpression (OE) of GPR1 or CMKLR1. Data are shown as means ± SEMs from at least three independent experiments. $n = 4$ biologically independent samples. $^{*}P < 0.05$; $^{**}P < 0.01$. Statistical differences were analyzed by one-way ANOVA followed by Dunnett's post hoc test.

the inactive state of the receptor (*43*). By contrast, the residue at position 3.50 in GPR1 is a nonconserved histidine ($H135^{3.50}$) and tends to form a cation-π interaction with the residue $H244^{6.33}$ to stabilize the inward positioning of helix VI, as observed in the ligand-free GPR1-βarr1 structure. Mutating residues $H135^{3.50}$ and $H244^{6.33}$ to their counterparts in CMKLR1 ($H135^{3.50}$R and $H244^{6.33}$P) reduced basal βarr1 recruitment of GPR1 by about 70% (Fig. 3F and table S4). The above data imply a joint control by the receptor transmembrane core and C-terminal region of constitutive arrestin recruitment and internalization of GPR1.

GPR1 constitutive internalization mediated by fatty acids

The ligand-free GPR1-βarr1 structure shows that a lipid-like molecule has a crucial role in stabilizing the interaction between GPR1 and βarr1 by coupling to the receptor-arrestin binding interface (Fig. 1, E and F). To identify putative ligands associated with the complex, we performed mass spectrometry analysis and found preferential binding of two fatty acids, palmitoleic acid (POA) and palmitic acid (PA), to the agonist-free GPR1-βarr1 complex (fig. S10). These fatty acids are both abundant in the cytoplasm of adipocytes as key intermediates in lipid metabolism (*44*) and agree with the cryo-EM map (fig. S3F). They appear to not only stabilize the conformation of the receptor intracellular surface but also strengthen receptor-arrestin binding, with the head group bridging the receptor ICL1 and the finger loop of βarr1 and the fatty-acyl chain inserting into a tunnel formed by helices I, II, VI, VII, and VIII of the receptor and the arrestin finger loop (Fig. 3D).

Thus, endogenous fatty acids may be important in mediating constitutive arrestin recruitment and internalization of GPR1. This is evidenced by our mutagenesis data showing that the alanine replacements of the GPR1 residues $F62^{1.56}$, $T63^{1.57}$, and $K66^{1.60}$, which interact with the fatty acid but not with the arrestin in the ligand-free GPR1-βarr1 structure, decrease basal arrestin recruitment by 25 to 50% (Fig. 3F and table S4). Additionally, mutants $F62^{1.56}$A and $K66^{1.60}$A exhibit attenuated constitutive internalization, as detected by confocal microscopy (Fig. 4C). Constitutive internalization of GPR1 was also monitored by measuring the amount of receptor remaining at the cell surface by flow cytometry. Approximately 35% of wild-type GPR1 molecules were internalized after a 45-min incubation at 37°C, whereas $F62^{1.56}$A and $K66^{1.60}$A mutants showed less constitutive internalization with the percentage of the receptor molecules remaining at the cell surface close to that of the wild-type CMKLR1 (~80%) (Fig. 3G). Additional mass spectrometry analysis of the $F62^{1.56}$A mutant revealed an almost unchanged phosphorylation pattern in the C terminus of the mutant compared with that of wild-type receptors, indicating that these alanine mutations impair the constitutive arrestin recruitment and receptor internalization mainly through their detrimental effect on fatty acid binding rather than basal phosphorylation (fig. S5, A to G). Structural alignment of the ligand-free and chemerin-bound structures of GPR1-βarr1 revealed a clash between the fatty acid ligand and helices VII and VIII in the chemerin-bound structures owing to the inward positioning of these two helices in the active conformation (Fig. 3A), which implies that the fatty acid does not promote agonist-stimulated arrestin recruitment. Indeed, our BRET data showed a wild-type amount of chemerin-induced βarr1 binding for the mutants $F62^{1.56}$A, $T63^{1.57}$A, and $K66^{1.60}$A (fig. S6G and table S1).

As an adipokine, chemerin regulates adipocyte metabolism (*5*, *45*, *46*). Upon chemerin stimulation, CMKLR1 promotes lipolysis and decreases lipid accumulation, which counters lipotoxicity induced by lipid overload in cardiomyocytes (*5*, *45*). GPR1 also functions in adipocyte metabolism and lipid homeostasis in various types of cells; however, some reported results are conflicting (*46*–*48*). To further explore the functionality of GPR1, we measured lipid accumulation in adipocytes derived from the white adipose tissue stromal vascular fraction (WAT SVF) after stimulation of cells with high concentrations of palmitate and oleate, two free fatty acids (FFAs). WAT SVF cells initially differentiated into mature adipocytes and were then treated with FFA along with either the agonist chemS157 or the antagonist chemG152 (residues E21 to G152) (*49*). Addition of chemS157 decreased cellular triglyceride concentrations, whereas adding chemG152 had no effect (Fig. 5C). These data are consistent with CMKLR1 being highly expressed in white adipocytes and having a key role in reducing lipid accumulation (*5*). This is further supported by our detection of decreased triglyceride concentrations in adipocytes overexpressing CMKLR1 and treated with FFA (Fig. 5C).

In adipocytes overexpressing GPR1, FFA treatment also decreased triglyceride accumulation. This effect was reversed by the addition of a high concentration of chemG152 (Fig. 5C). One possible explanation for decreased lipid accumulation is that upon stimulation with FFA, GPR1 may promote scavenging of antagonistic chemerin isoforms produced by adipose tissue (*50*). FFA treatment likely has a beneficial

effect on the complex assembly between the antagonistic chemerin-bound inactive GPR1 and arrestin, given that POA and PA appear to promote arrestin recruitment to the inactive GPR1, as evidenced by our structural and functional data. Removal of antagonistic chemerin may facilitate CMKLR1-mediated lipid metabolism by allowing more CMKLR1 molecules to be activated by the agonist forms of chemerin. When the concentration of chemG152 exceeds the scavenging capability of GPR1, CMKLR1 can no longer effectively reduce lipid accumulation in adipocytes. These data imply a joint control of lipid metabolism by CMKLR1 and GPR1. Nevertheless, this does not rule out possible roles of GPR1 in modulating lipid accumulation through other pathways.

A ligand-scavenging mechanism was also proposed for the ACKRs and some chemokine receptors, such as CCR1 and US28, and may be physiologically important for the regulation of inflammatory and immune responses by maintaining chemokine gradients and receptor responsiveness (*14*, *15*, *51*–*53*). Similar to GPR1, these receptors also undergo β-arrestin–mediated internalization in both agonist-dependent and -independent manners, despite differential abilities of transducing G protein signals (*9*, *14*–*16*). Thus, these receptors and GPR1 may adopt a similar molecular pattern to mediate ligand scavenging. Taken together, our work provides a framework to elucidate the GPR1-arrestin interaction in different functional states and highlight the complexity and diversity of the molecular mechanisms underlying the arrestin-mediated modulation of GPCRs.

Materials and methods

Construct cloning and protein expression

The genes of the human GPR1 and chemerin were codon-optimized and synthesized by BGI Genomics for insect cell expression. For the βarr-bound GPR1 complexes, the gene of GPR1 was cloned into a modified pFastBac1 vector (Invitrogen) with a haemagglutinin (HA) signal peptide followed by a 2× strep tag and a Flag tag at the N terminus, and the C-terminal residues L323 to Q355 of GPR1 were replaced with the C-terminal tail of V_2R (residues A343 to S371). The genes of βarr1 and βarr2 were cloned into a pFastBac1 vector. To facilitate complex formation, the C termini of βarr1 and βarr2 (residues I377 to R418 in βarr1 and residues D377 to C409 in βarr2) were replaced with the antibody scFv30 followed by a 6× His tag, aiming to improve protein stability (*54*), and eight mutations (βarr1, C59A, C125S, C140I, C150V, R169E, C242V, C251V, and C269S; βarr2, C17G, C60V, C126S, C141L, C151V, C243V, C252V, and C270S) were introduced to remove all cysteines in the two arrestins. To facilitate formation of the chemerin-GPR1-βarr2 complex, the C-terminal region (residues H350 to F376) in βarr2 was substituted with its counterpart in βarr1 (residues K357 to L376) to enable interaction with scFv30. To improve homogeneity of the ligand-free GPR1-βarr1 complex, a disulfide bond was further introduced between GPR1 and βarr1 by mutating the GPR1 residue V143 and βarr1 residue Y249 to cysteines. The chemerin was cloned into a pFastBac1 vector with the HA signal peptide at N terminus.

The modified GPR1 was coexpressed with βarr1-scFv30 in presence or absence of chemerin in HighFive insect cells (Thermo Fisher Scientific, B85502) using Bac-to-Bac Baculovirus Expression System (Invitrogen). The cells at a density of 1.5×10^6 cells per ml were infected with high-titer viral stocks at an MOI (multiplicity of infection) ratio of 5:2:2:2 for GPR1, chemerin, βarr1-scFv30, and GRK2. Cells were grown at 27°C for 48 hours and then harvested by centrifugation and stored at −80°C until use. The chemerin-GPR1-βarr2 complex was expressed following the same protocol as that for the βarr1-bound complex.

Expression and purification of Nb32

The gene of nanobody 32 (Nb32) with an 8× His tag at the C terminus was cloned into a pET28a vector (Sangon Biotech) and expressed in the *Escherichia coli* BL21(DE3) cells. The cells were cultured in LB medium containing 50 μg ml^{-1} kanamycin at 37°C for 4 hours and then induced by 1 mM isopropyl-β-D-thiogalactopyranoside (IPTG) at 16°C for 16 hours. The cells were harvested by centrifugation at 4000*g* for 30 min and lysed in 25 mM HEPES, pH 7.5, 150 mM NaCl, and EDTA-free protease-inhibitor cocktail (Roche) by sonication. The supernatant was collected by ultracentrifugation at 100,000*g* for 30 min and loaded to Ni affinity chromatography (Clontech). The eluted protein sample was concentrated using a 3 kDa molecular weight cut-off concentrator (Millipore) and loaded onto a Superdex 75 Increase 10/300 column (GE Healthcare) that was equilibrated with a buffer containing 25 mM HEPES, pH 7.5 and 150 mM NaCl. The peak fractions were pooled and concentrated to 2 mg ml^{-1}. The purified Nb32 was flash-frozen in liquid nitrogen and stored at −80°C until use.

Purification of the βarr-bound GPR1 complexes

The cell pellets from 500 ml of cell culture were resuspended in 25 ml of suspension buffer containing 25 mM HEPES, pH 7.5, 50 mM NaCl, 2 mM sodium orthovanadate, 1 mM adenosine triphosphate (ATP), and EDTA-free protease-inhibitor cocktail tablets, and incubated at 30°C for 1 hour. Then the cells were collected by centrifugation at 100,000*g* for 30 min and solubilized in 50 ml of 25 mM HEPES, pH 7.5, 150 mM NaCl, 0.5% (w/v) lauryl maltose neopentyl glycol (LMNG) (Anatrace), 0.17% (w/v) glyco-diosgenin (GDN) (Anatrace), 0.05% (w/v) CHS (Sigma), and EDTA-free protease-inhibitor cocktails at 4°C for 3 hours. The solubilized proteins were isolated by centrifugation at 100,000*g* for 30 min and then incubated with Nb32 and 1 ml Strep-Tactin Sepharose resin (IBA Lifesciences) at 4°C overnight. The strep resin was then transferred to a gravity column and washed with 20 column volumes of wash buffer containing 25 mM HEPES, pH 7.5, 150 mM NaCl, 0.0075% (w/v) LMNG, 0.0025% (w/v) GDN, and 0.00075% (w/v) CHS. The complexes were eluted with 5 column volumes of elution buffer containing 200 mM Tris-HCl, pH 8.0, 150 mM NaCl, 0.0075% (w/v) LMNG, 0.0025% (w/v) GDN, 0.00075% (w/v) CHS, and 50 mM biotin. The elution was further incubated with TALON Superflow Metal Affinity Resin (Clontech) at 4°C for 4 hours. The resin was collected by centrifugation and washed with 10 column volumes of wash buffer containing 25 mM HEPES, pH 7.5, 150 mM NaCl, 0.0075% (w/v) LMNG, 0.0025% (w/v) GDN, and 0.00075% (w/v) CHS. The complex was eluted with 5 column volumes of 25 mM HEPES, pH 7.5, 150 mM NaCl, 0.0075% (w/v) LMNG, 0.0025% (w/v) GDN, 0.00075% (w/v) CHS, and 300 mM imidazole. The eluted protein was loaded to size-exclusion chromatography using a Superdex 200 Increase 10/300 column (GE Healthcare) pre-equilibrated with 25 mM HEPES, pH 7.5, 150 mM NaCl, 0.0075% (w/v) LMNG, 0.0025% (w/v) GDN, and 0.00075% (w/v) CHS. The complex fractions were collected and concentrated to 1.5 to 4.5 mg ml^{-1} (chemerin-GPR1-βarr1, 1.5 mg ml^{-1}; chemerin-GPR1-βarr2, 1.5 mg ml^{-1}; GPR1-βarr1, 4.5 mg ml^{-1}) using a 100-kDa molecular-weight cutoff concentrator (Millipore) for cryo-EM grid preparation. Protein purity and homogeneity were analyzed by SDS–polyacrylamide gel electrophoresis (SDS-PAGE), native PAGE, and analytical size-exclusion chromatography using a 4.6 × 250 mm Nanofilm SEC-250 column (Sepax Technologies).

Cryo-EM data acquisition and processing

To prepare samples for the cryo-EM experiments, 3 μl of the purified complex proteins were applied onto freshly glow-discharged amorphous NiTi foil R1.2/1.3 300 mesh Au grids. After blotting in Vitrobot Mark IV (Thermo Fisher Scientific) with blot time of 1 s and blot force of 0, the grids were plunged into frozen liquid ethane, and the chamber condition was maintained to 4°C temperature and 100% humidity. After vitrification, the grids were transferred and stored in liquid nitrogen for further analysis. To obtain reliable initial models, five different sessions of sample screening and test data collection were performed using 200 kV Arctica transmission electron microscope (TEM) (FEI).

All images were collected using 300 kV Titan Krios G3 TEM (FEI) equipped with K3 direct electron detector (DED, Gatan Inc.) and a GIF-Quantum energy filter. The nominal magnification was set to

×81,000, resulted in a calibrated physical pixel size of 1.071 Å at specimen level, or 0.5355 Å under super-resolution mode. Each super-resolution movie was collected in a total exposure time of 3 s, fractioned into 40 frames and the total dose was set to 70 electrons per square angstrom. The slit width was set to 20 eV, and nominal defocus was set to between −0.8 and −1.5 μm. All images used in this study were collected using a beam-image-shift facilitated acquisition scheme within SerialEM software (*55*).

For the chemerin-GPR1-βarr1 complex, three datasets were collected with 5742, 4051, and 4049 movies, respectively. Beam-induced motion correction and CTF estimation were suffered using MotionCor2 (*56*) and CTFFIND4 (*57*) in CryoSPARC (*58*). The following data processing was also performed using CryoSPARC. 4,782,898, 3,344,277, and 4,456,894 particles were picked from the three datasets and extracted with a box size of 128 pixels (bin 2, 2.142 Å per pixel) using template picker. After several rounds of two-dimensional (2D) classification, ab initio reconstruction, and heterogeneous refinement, we selected 331,134, 349,742, and 360,637 particles for these three independent sessions. These particles were merged and re-extracted to unbin with a box size of 256 pixels (1.071 Å per pixel). Upon nonuniform refinement and Bayesian polishing, we obtained a map with an overall resolution at 3.4 Å. However, the density map of the receptor region was not well determined. These refined particles were then subjected to another round of heterogeneous refinement with four classes. Two classes were well classified and show different conformations. To further classify the particles, the particles with different conformations were further processed following different procedures.

For the first class with 547,922 particles (54%), another round of heterogeneous refinement was performed, and the best class with 71% particles was subjected to 2D classification, of which 362,751 particles were retained. First, these particles were subjected to 2D classification and 3D classification in CryoSPARC without initial references. In this step, we got three different conformations of the complex in six classes, among which class 4 was classified into conformation 1; classes 1, 2, 3, and 5 were classified into conformation 2; and class 6 was classified into conformation 3. These particles with different conformations were further subjected to nonuniform refinement. Finally, we got a cryo-EM map of conformation 1 with an overall resolution at 3.3 Å, but the densities of the receptor in conformations 2 and 3 were not well resolved. To further improve map quality, we took classes 4 to 6 as initial references for 3D classification with the selected 362,751 particles. The results revealed that 33% particles were classified into conformation 1, 31% particles into conformation 2, and 36% particles into conformation 3. Then we subjected these different classes for nonuniform refinement separately, yielding the cryo-EM maps of conformation 1 (118,567 particles) with an overall resolution at 3.2 Å, conformation 2 (112,084 particles) at 3.2-Å overall resolution, and conformation 3 (132,110 particles) at 3.3-Å overall resolution. Compared with the previously refined maps, we found that the newly refined maps of conformations 2 and 3 had better resolution and density features, but the new map of conformation 1 was worse. Thus, another round of reference-free 3D classification was performed on the class of particles of conformation 1 (33%). A subset comprising 58% of the particles (69,349 particles) was then subjected to nonuniform refinement, resulting in a map at 3.3-Å resolution. This map displayed the most well-defined features and was used for subsequent analysis. Collectively, in the first class we acquired the cryo-EM maps in three different conformations at resolutions of 3.3 Å (conformation 1), 3.2 Å (conformation 2), and 3.3 Å (conformation 3). For the second class with 281,114 particles (28%), 116,237 particles were retained upon 2D classification and heterogeneous refinement. By performing nonuniform refinement, a cryo-EM map of another conformation (conformation 4) at 3.3-Å overall resolution was obtained.

For the chemerin-GPR1-βarr2 complex, two datasets containing 3142 and 5111 movies were collected. With the first dataset, after motion correction and CTF estimation, 1,227,186 particles were picked using template picker. After 2D classification, ab initio reconstruction and heterogeneous refinement, the particles from the best class (45%) were used as a template for Topaz (*59*) training to pick particles from the entire dataset, and 454,639 particles were picked. After several rounds of 2D classification and heterogeneous refinement, the particles from the best class (40%) were merged with the particles used as the template for Topaz training. After removing duplication, the particles were transferred to RELION-3 (*60*) for polishing. Finally, 202,191 particles were used for nonuniform refinement, yielding a map with an overall resolution at 3.5 Å. The dataset 2 was processed as dataset 1, which yielded a cryo-EM map at 3.3-Å resolution using 225,945 particles. To further improve the map quality for chemerin and βarr2, we merged the refined particles from the two datasets and subjected to focused 3D classification with a mask containing the receptor and chemerin. The class (123,307 particles, 29%) showing the best densities of chemerin was refined using nonuniform refinement, generating a map with an overall resolution at 3.4 Å. Finally, by performing local refinements, the cryo-EM maps for the chemerin-GPR1 and βarr2 regions were obtained at resolutions of 3.5 Å and 3.2 Å, respectively. A composite map of the chemerin-GPR1-βarr2 complex was generated with ChimeraX (*61*).

For the GPR1-βarr1 complex, 5421 movies were collected. After motion correction and CTF estimation, 2,101,634 particles were picked and extracted using template picker. After several rounds of 2D classification, ab initio reconstruction along with heterogeneous refinement, the best class containing 329,539 particles (71%) was subjected to nonuniform refinement, yielding a density map with an overall resolution at 3.2 Å. These particles were then used as a template for Topaz training to pick particles from the entire dataset, and 1,057,480 particles were repicked. After 2D classification, ab initio refinement, and heterogeneous refinement, 433,016 particles (57%) were subjected to nonuniform refinement and yielded a map at 3.3-Å resolution. These particles were then merged with the aforementioned 329,539 particles, and the duplicated particles were removed. The merged data were polished using RELION-3 and subjected to focused 3D classification with a mask containing the receptor region only. Finally, 413,367 particles were selected and subjected to nonuniform refinement, yielding a cryo-EM map at 2.9-Å resolution.

All particles were converted from CryoSPARC to RELION using pyem (*62*). Resolutions of all the maps were determined using the Fourier shell correlation (FSC) cut-off criteria at 0.143. FSC validations were performed to assess local resolutions of the receptor and arrestin individually using CryoSPARC. Local resolution maps were colored using ResMap (*63*). 3D variability analysis was performed to track arrestin motion in the chemerin-GPR1-βarr1 complex using CryoSPARC with the polished particles before heterogeneous refinement, and a conformational dynamics movie was generated using ChimeraX with variability analysis outputs.

Model building and refinement

The initial models of the chemerin-GPR1-βarr1 and GPR1-βarr1 complexes were built using the AlphaFold2-predicted models of GPR1 and chemerin, the βarr1 and scFv30 portions from the M2R-βarr1 structure [Protein Data Bank (PDB) ID: 6U1N], and the Nb32 portion from the βarr1-V2T subcomplex (PDB ID: 6NI2) as templates. The initial model of the chemerin-GPR1-βarr2 complex was built using the AlphaFold2-predicted model of chemerin and the GPR1, βarr1, and scFv30 portions from the structure of the chemerin-GPR1-βarr1 complex (conformation 2) as templates, with the residues of βarr1 mutated to their counterparts in βarr2 in COOT (*64*). All the models were docked into the cryo-EM electron density maps using Chimera (*65*), followed by iterative manual adjustments in COOT and real-space refinement using phenix.real_space_refine in Phenix (*66*). Regions with poor or missing densities were not modeled. In regions where main-chain densities

were well-resolved but side-chain densities were absent, models were built with side chains omitted to avoid overinterpretation. Regions with a relatively high proportion of side-chain deletions are highlighted below, whereas other regions might also contain minor side-chain omissions.

In conformation 1 of chemerin-GPR1-βarr1, residues E2–G35, F191–T199, and S318–I322 in GPR1, as well as residues G2–G5, P89–D93, F190–P196, and S330–S341 in βarr1 were not modeled due to poor densities. The regions with backbone modeled but a large portion of side chains deleted include V37–L51, L200–F217, L264–S278, and L173–N183 in GPR1, and E176–Q189, T224–K232, R307–I314, and K355–E364 in βarr1.

In conformation 2 of chemerin-GPR1-βarr1, residues E2–G35 and S317–I322 in GPR1, as well as residues G2–G5, A90–K95, G131–K138, F190–P196, and S330–S340 in βarr1 were not modeled. The regions with backbone modeled but a large portion of side chains deleted include V36–L51, F105–N113, L264–T271, H146–L156, L173–L200, and F231–R236 in GPR1, and I31–D38, N153–R165, M255–K270, R307–I314, and K355–E364 in βarr1.

In conformation 3 of chemerin-GPR1-βarr1, residues E2–G35 and R314–I322 in GPR1, as well as residues G2–G5, R65–T74, A90–K94, F190–S193, and S330–S341 in βarr1 were not modeled. The regions with backbone modeled but a large portion of side chains deleted include W39–I53, L88–L92, L173–L198, and Y226–R243 in GPR1.

In conformation 4 of chemerin-GPR1-βarr1, residues E2–S41, D195–L200, F231–V250, and V305–I322 in GPR1, as well as residues G2–G5, R65–T74, P89–K94, D135–K138, F190–P196, and V329–S341 in βarr1 were not modeled. The regions with backbone modeled but a large portion of side chains deleted include all transmembrane helices in GPR1 and N153–K160, R307–R312, and K357–E359 in βarr1.

In the chemerin-GPR1-βarr2 complex, residues E2–L18, E29–L34, H194–D195, I238–I240, and V319–I322 in GPR1, as well as residues G2–G6, P85–R96, G133–K139, K153–E157, H190–S197, K308–E314, and V330–G334 in βarr2 were not modeled. The regions with backbone modeled but a large portion of side chains deleted include Q192–L200, K232–R236, and I272–Q283 in GPR1, and R66–D70, H160–R162, E186–R189, Q256–Q262, and K348–E357 in βarr2.

In the ligand-free GPR1-βarr1 complex, residues E2–G35 and S318–I322 in GPR1, as well as residues G2–G5, A90–K94, F190–K195, and R331–S341 in βarr1 were not modeled. The regions with backbone modeled but a large portion of side chains deleted include Q192–L200 and K357–E359 in GPR1, and N153–K160 and R307–R312 in βarr1.

The models were validated using MolProbity (*67*). Structural figures were prepared by Chimera, ChimeraX or PyMOL (https://pymol.org/2/). The data collection and structure refinement statistics are provided in table S2.

Purification of chemerin

To prepare the protein sample of chemerin for functional assays, gene of the human chemerin (residues E21 to S157) was cloned into a pET32a vector (Sango Biotech) with a ThioredoxinA (TrxA) fusion partner and a 10× His tag followed by an S tag and a PreScission protease site at the N terminus. The recombinant plasmid was transformed into the BL21/DE3 competent *E. coli* cells and cultured at 37°C until the optical density at 600 nm (OD600) reached 0.6 to 0.8. Then IPTG was added to a final concentration of 1 mM. The cells were cultured at 37°C for 4 hours and then harvested by centrifugation. The cell pellets were resuspended in a solution containing 25 mM Tris, pH 8.0, 300 mM NaCl, and protease inhibitor (ITW Reagents). To isolate inclusion bodies, the resuspended cells were subjected to sonication and then centrifuged at 14,000*g* for 30 min. The inclusion body pellets were subsequently washed with a solution containing 25 mM Tris, pH 8.0, 300 mM NaCl, and 2 M Urea. The washed pellets were then solubilized with 25 mM Tris, pH 8.0, 300 mM NaCl, and 8 M urea. The denaturing protein supernatant was isolated by centrifugation and incubated with Ni-NTA resin for 1 hour at 4°C. The resin was then washed with 25 mM Tris, pH 8.0, 300 mM NaCl, 6 M urea, and 30 mM imidazole, and the protein was eluted with 25 mM Tris, pH 8.0, 300 mM NaCl, 6 M urea, and 300 mM imidazole. The eluted chemerin was refolded in a series of refolding buffers with decreased concentrations of urea. In brief, the eluted protein was dialyzed against buffer A (25 mM Tris, pH 8.0, 300 mM NaCl, 400 mM KCl, 2 mM $MgCl_2$, 2 mM $CaCl_2$, 500 mM L-arginine, 0.055% polyethylene glycol 8000, 5% glycerol, 1 mM reduced L-glutathione, and 0.1 mM oxidized L-glutathione) supplemented with 4 M urea overnight at 4°C, followed by dialysis against buffer A supplemented with 2 M urea for 12 hours at 4°C, and then dialyzed against 25 mM Tris, pH 8.0 and 300 mM NaCl for 8 hours at 4°C. The dialyzed sample was treated with PreScission Protease overnight at 4°C to cleave off the TrxA tag, and further purified by Ni-NTA affinity chromatography. The final protein sample was concentrated to 0.6 to 6 mg ml^{-1}, flash-frozen, and stored at −80°C until use.

BRET assay

To measure the chemerin-induced βarr binding of GPR1, the Rluc8 donor was added to the C termini of the wild-type GPR1 and mutants, and the GFP2 acceptor was fused to the C termini of human βarr1 and βarr2. The Flag-tagged receptor and the arrestins were cloned into the pTT5 vector (Invitrogen). Two milliliters of HEK293F cells (Thermo Fisher Scientific, R79007) were transiently cotransfected with a total of 4 μg plasmids of GPR1-Rluc8 (or mutants) and βarr1-GFP2 (or βarr2-GFP2) at an MOI ratio of 1:1. The cells were harvested after 48 hours posttransfection and the cell-surface expression of the receptor was measured by mixing 10 μl cells with 15 μl of tris-buffered saline (TBS) buffer supplemented with 4% bovine serum albumin (BSA), 20% (v/v) viability-staining solution 7-AAD (Invitrogen, cat. no. 00-6993-50), and 0.1% (v/v) anti-FLAG M2-FITC antibody (Sigma, cat. no. F4049) at 4°C for 20 min. Then the mixture was diluted by adding 175 μl of TBS buffer, and the fluorescent signal was measured using a flow-cytometry reader (Guava easyCyte HT, Millipore).

The cells were plated into the 96-well opaque cell culture plates (Beyotime) at a density of 30,000 cells per well in 60 μl of BRET2 assay buffer containing 1× Hanks' balanced salt solution (HBSS) (Gibco) and 20 mM HEPES, pH 7.4. After incubating for 30 min at 37°C, 10 μl of freshly prepared 50 μM coelenterazine 400a (Nanolight Technologies) was added into each well. After 5 to 10 min, the BRET baselines were read by the Synergy II (Bio-Tek) plate reader with 410 nm (RLuc8-coelenterazine 400a) and 515 nm (GFP2) emission filters for 16 min. Then 30 μl chemerin at different concentrations (1 pM to 10 μM) were added into the wells and the BRET signals were monitored continuously five times. The BRET ratios were calculated as the ratio of the GFP2 emission to RLuc8 emission and the data were analyzed using GraphPad Prism 8.0.

Constitutive β-arrestin recruitment assay

The constitutive βarr1 recruitment of GPR1 and CMKLR1 was measured by the Tango assay system (*68*, *69*). The genes of the wild-type receptors and mutants with a Flag tag at the N termini and an expression cassette containing the tobacco etch virus (TEV) protease cleavage site and a tetracycline transcriptional activator tTA at the C termini were cloned into the pTT5 vector. The gene of the wild-type βarr1 with a C-terminal TEV protease site was cloned into the pcDNA6 vector (Invitrogen). The interaction between the receptor and βarr1 leads to the cleavage of the TEV site, thus releasing tTA to trigger the tTA-dependent luciferase reporter gene expression. Two milliliters of HTL cells (a gift from W. Yin) were cultured in 6-well plates and transfected with a total of 4 μg plasmids of GPR1 (or CMKLR1) and βarr1 at an MOI ratio of 1:1. After 24 hours posttransfection, pancreatic enzymes were used to digest the cells from the plates and then the cell-surface expression was measured as described above. The cells were then plated into the 96-well opaque cell culture plates at a density of 60,000 cells per well in 100 μl of 1× Dulbecco's modified Eagle's medium (DMEM)

(Gibco) and cultured in 5% CO_2 at 37°C for 24 hours. Then firefly luciferase activities were evaluated following the manufacturer's protocols of the Dual-Lite Luciferase assay system (Vazyme).

Disulfide cross-linking

The 2× strep-tagged GPR1 and 8× His-tagged βarr1 containing the respective single cysteine mutation were coexpressed in HighFive insect cells with GRK2 cotransfected. The complex protein was purified as above described and analyzed by 8% nonreducing Nu-PAGE and Western blot to identify the strep-tagged receptor and His-tagged βarr1. The nitrocellulose membrane preincubated with methanol was used to perform the Western blot. The membrane was incubated in 5% milk (w/v) for 1 hour at room temperature followed by incubation with the primary antibody [mouse monoclonal anti-poly histidine antibody (Sigma, H1029; 1:2000 diluted in PBS) or mouse monoclonal anti-strep antibody (Sigma, SAB2702216; 1:2000 diluted in PBS)]. The nonspecifically bound antibody was washed with 10 ml PBST buffer [PBS buffer supplemented with 0.1% Tween (v/v)] three times. The membrane was then incubated with the secondary antibody [goat anti-mouse IgG (Sigma AP124; 1:2000 diluted in PBS)] for 1 hour at room temperature and washed with PBST three times. The cross-linked complex was detected by 5-bromo-4-chloro-3-indolyl-phosph ate (BCIP) (Sigma).

Receptor internalization measured by flow cytometry

The genes of the wild-type GPR1 and CMKLR1 and mutants with a Flag tag at the N termini and the wild-type βarr1 were cloned into the pTT5 vector and expressed in HEK293F cells. Two milliliters of cells were cotransfected with a total of 2 μg plasmids of the receptor and βarr1 at an MOI ratio of 1:1. After 24 hours, the cells were washed with HBSS buffer supplemented with 0.5% BSA and 20 mM HEPES, pH 7.4. The receptors at the cell surface were labeled with anti-FLAG M2-FITC antibody (Sigma, F4049) for 30 min on ice instantly or after incubation in prewarmed FreeStyle 293 expression medium for 45 min at 37°C. After labeling, the cells were plated in 96-well plates (100,000 cells per well) and the mean fluorescent-intensity values used to quantify the amount of receptor remaining at the cell surface were measured by a flow-cytometry reader (Guava easyCyte HT, Millipore). Data were analyzed using GraphPad Prism 8.0.

Live-cell confocal microscopy

The Flag-tagged GPR1 and CMKLR1, βarr1-GFP2, and βarr2-GFP2 were cloned into the pTT5 vector. HEK293T cells (obtained from Cell Bank at the Chinese Academy of Sciences) were seeded in glass bottom cell culture dish (NEST) and transfected with a total of 2 μg plasmids of the receptor and βarr1-GFP2 (or βarr2-GFP2) at an MOI ratio of 1:1. After one day posttransfection, the cells were incubated with primary antibody [anti-Flag mouse monoclonal antibody (Sigma, F3165; 1:1000 diluted in DMEM)] in serum-free DMEM for 1 hour at 37°C. The cells were washed with cold DMEM three times, and then incubated with secondary antibody [Goat anti-Mouse IgG (H+L) Highly Cross-Adsorbed Secondary Antibody, Alexa Fluor 647 (Invitrogen, A-21236; 1:2000 diluted in DMEM)] for 15 min on ice. The cells were then washed with cold DMEM and imaged on a confocal microscope (LSM 900, Zeiss) with a 63× oil immersion objective. After that, the medium was replaced with prewarmed DMEM (37°C). The cells were subsequently incubated at 37°C for 15 to 30 min in the absence or presence of 5 μM chemerin and then the fluorescence imaging was performed.

Bimane fluorescence measurement

The βarr1(L71C)–scFv30 construct was prepared using the same βarr1-scFv30 construct used in the chemerin-GPR1-βarr1 structure determination, with the L71C mutation introduced. The protein was expressed in HighFive insect cells following the same protocol as that used for the βarr1-bound complex. The harvested cell pellets were resuspended in a buffer containing 25 mM HEPES, pH 7.5, 150 mM NaCl, 2 mM dithiothreitol (DTT), and protease-inhibitor cocktail tablets (Roche). The resuspended cells were subjected to sonication and then centrifuged at 100,000*g* for 30 min. The supernatant was incubated with Ni-NTA resin for 1 hour at 4°C. The resin was then washed with a buffer containing 25 mM HEPES, pH 7.5, 150 mM NaCl, 2 mM DTT, and 30 mM imidazole. The protein was eluted with a buffer containing 25 mM HEPES, pH 7.5, 150 mM NaCl, and 300 mM imidazole. The eluted protein was loaded to size-exclusion chromatography (SEC) using a Superdex 200 Increase 10/300 column pre-equilibrated with 25 mM HEPES, pH 7.5 and 150 mM NaCl. The monomeric protein factions were collected and concentrated to 2 mg ml^{-1} for further use.

To prepare the GPR1 sample, the same receptor construct used in the chemerin-GPR1-βarr1 structure determination was expressed in HighFive insect cells following the same protocol used for the βarr1-bound complex. The cells were coinfected with high-titer baculoviruses encoding GPR1 and GRK2 at an MOI ratio of 5:2. After expression, the harvested cell pellets were resuspended with suspension buffer containing 25 mM HEPES, pH 7.5, 50 mM NaCl, 2 mM sodium orthovanadate, 1 mM ATP, and EDTA-free protease-inhibitor cocktail tablets, and incubated at 30°C for 1 hour. Then the cells were collected by centrifugation at 100,000*g* for 30 min and solubilized at 4°C for 3 hours in 50 ml of buffer containing 25 mM HEPES, pH 7.5, 150 mM NaCl, 0.5% (w/v) LMNG, 0.17% (w/v) GDN, 0.05% (w/v) CHS, and EDTA-free protease-inhibitor cocktail tablets. The solubilized proteins were isolated using Strep-Tactin Sepharose resin following the same protocol used for the βarr1-bound complex. The eluted protein was further purified by SEC using a Superdex 200 Increase 10/300 column pre-equilibrated with 25 mM HEPES, pH 7.5, 150 mM NaCl, 0.0075% (w/v) LMNG, 0.0025% (w/v) GDN, and 0.00075% (w/v) CHS. The monomeric GPR1 fractions were collected and concentrated to 2 mg ml^{-1} for further use.

The purified βarr1(L71C)–scFv30 was fluorescently labeled through incubation with a sixfold molar excess of mBBr (Sigma-Aldrich) at room temperature for 1 hour. The unreacted mBBr was subsequently removed using SEC. For the bimane fluorescence experiments, the GPR1 receptor was pre-equilibrated with either 5 μM C9 peptide (the last nine residues at the C terminus of chemerin, ^{150}YFPGQFAFS^{157}) or purification buffer as a control for 20 min at room temperature. The mBBr-labeled βarr1(L71C)–scFv30 was then added to the reaction mixture at a final concentration of 200 nM at a molar ratio of 3:2 relative to GPR1. After a 30-min incubation in dark, the samples were transferred to quartz cuvettes with 120 μl for spectral analysis. Fluorescence emission spectra were acquired using an Agilent Cary 60 spectrophotometer configured in scanning mode, with excitation at 370 nm and emission collected from 400 to 600 nm at 5-nm resolution.

Mass spectrometry analysis of receptor phosphorylation patterns

The proteins of the chemerin-GPR1-βarr1, GPR1-βarr1, and chemerin-CMKLR1-βarr1 complexes and CMKLR1 (prepared in the presence of βarr1, but the complex was not formed due to poor binding ability) were prepared as described above, and then were resolubilized and denatured using 8 M urea in 50 mM Tris-HCl, pH 8.0. Each protein sample (10 μg) was reduced and alkylated on resin using 5 mM Tris(2-carboxyethyl)phosphine-hydrochloride (TCEP) and 20 mM iodoacetamide (IAA), respectively. Subsequently, the protein samples were digested in solution first using chymotrypsin (Promega) at a ratio of 1:80 (enzyme to protein) at 25°C for 3 hours, then using trypsin (Promega) at a ratio of 1:50 (enzyme to protein) at 37°C overnight. The protease digestion was terminated by adding 1% TFA, and then the peptides were desalted using C18 microspin columns (Omicsolution, China).

The peptide samples were redissolved with 0.1% FA and analyzed using a nanoElute LC system coupled to a timsTOF Pro 2 mass spectrometer (Bruker). The samples were separated on an analytical column (75 μm i.d., 300 mm) in-house packed with C18-AQ 1.9-μm C18 resin (Dr. Maisch GmbH) with a gradient of 5 to 22% solvent B (0.1% FA in ACN) in 40 min,

22 to 37% B in 20 min, 37 to 80% B in 25 min, and 80% B for 5 min at a flow rate of 300 nl min^{-1}. DDA mass spectrometry (MS) data were acquired in the DDA PASEF mode with the following settings: capillary voltage, 1500 V; mass range for MS scans, 100 to 1700 m/z; ion mobility scanning from 0.6 to 1.6 Vs cm^{-2}; ramp time, 166 ms; total cycle time, 1.9 s; target intensity (20,000); intensity threshold (1000); charge range (0 to 5); isolation width (2 m/z for m/z < 700 and 3 m/z for m/z > 700); collisional energy (20 to 59).

Peptide sequences and phosphorylation sites were identified by data search using FragPipe (version 22.0) integrating MSFragger (version 4.1) (*70*) against a database containing GPR1, CMKLR1, chemerin, βarr1, and contaminant protein sequences. Decoys are added to the database to restrict the false discovery rate below 1% at both protein and PSM levels. All searches were performed with carbamidomethyl (C) as a fixed modification, and oxidation (M), acetylation (Protein N-term), and phosphorylation (STY) set as variable modifications. For all searches, five modifications at maximum were allowed. In the validation step, PSM validation and protein inference were processed by Percolator and ProteinProphet integrated in Philosopher (version 5.1.1). In the command line options of PTMProphet, MINPROB indicating the PTM site probability threshold was set to 0.75 to report class I phosphosites. In all searches, the match-between-run function was enabled and other settings remained as default. The sum of MS intensities for all peptide precursors bearing the same class I phosphosite was used to represent the site-specific phosphorylation level which was further compared between different protein complexes.

Liquid chromatography–mass spectrometry (LC-MS) identification of the endogenous fatty acids associated with GPR1

The endogenous fatty acids bound to the GPR1-βarr1 complex or GPR1 were identified as previously described (*71*). Briefly, ~20 μg of each protein sample were reduced with 5 mM TCEP and alkylated with 20 mM iodoacetamide at 25°C. The samples were then subjected to trypsin digestion at an enzyme-to-protein ratio of 1:50 (w/w) at 37°C for 12 to 14 hours. The digested protein samples were dried in a SpeedVac machine and then extracted with ice-cold methanol: chloroform (1:2, v/v) by vortex and sonication. The supernatants were collected by centrifugation at 16,000*g* for 20 min at 4°C and lyophilized. The ligand extracts were resuspended in methanol: chloroform (9:1, v/v) to an equivalent concentration of 2 μM. The resulting samples were analyzed on a Q Exactive HF mass spectrometer (Thermo Fisher Scientific) operating in the negative ion mode coupled to a Waters Acquity UPLC system (Waters). The LC separation was performed on a CSH C18 column (10 × 2.1 mm, 1.7 μm) (Waters, Milford, MA) at a flow rate of 0.2 ml min^{-1} at 40°C, with the mobile phase A consisting of water with 0.01% acetic acid, and B consisting of 2-propanol: acetonitrile (50:50, v/v). The LC gradient was set as follows: 50% B in 0 min; 95% B in 0 to 10 min; 95% B in 10 to 12 min; 10% B in 12 to 13 min; 95% B in 13 to 15 min. MS data acquisition was set to the following parameters: mass range 160 to 1500 m/z; spray voltage 3.5 kV; sheath gas (nitrogen) flow rate 35 units; auxiliary gas (nitrogen) flow rate 10 units; capillary temperature 320°C. MS1 scan parameters included resolution 60,000, AGC target 3e6, and maximum injection time 250 ms. Tandem mass spectrometry (MS/MS) spectra were acquired on the top 10 precursors with normalized collision energy set at 40 and 60 eV. All samples were prepared in four independent replicates.

In MS data analysis, the abundance of POA or PA dissociated from the GPR1-βarr1 complex or GPR1 alone is determined by extracting ion chromatograms (EICs) based on accurate mass [<3 parts per million (ppm) deviation] and retention time (<0.3 min deviation) matched with those of the reference compounds using Xcalibur (version 4.0, Thermo Fisher Scientific). Preferential binding of POA or PA to the GPR1-βarr1 complex was reflected by the substantial increase of their EIC responses in the complex samples relative to GPR1 alone.

Lipid accumulation in white adipocytes

The SVF of murine inguinal WAT was isolated as previously described (*72*). After centrifugation, the SVF was resuspended in growth medium containing DMEM/F12 (Gibco, MA, USA), 10% FBS, and 1% penicillin/streptomycin (Gibco, MA, USA).

For generation of *Gpr1* and *Cmklr1* overexpressing lentiviruses, HEK293T cells were transfected with PGMLV-CMV-Puro, PGMLV-CMV-*Gpr1*-Puro, or PGMLV-CMV-*Cmklr1*-Puro. Lentiviruses were harvested at 48 hours posttransfection, centrifugated at 4000 rpm for 30 min, filtrated by use of 0.45 μm filter membrane, and stored at −80°C until use.

The SVF was grown to 100% confluence and then infected with *Gpr1*-expressing or *Cmklr1*-expressing lentiviruses. After 48 hours, the cells were induced to differentiate using 0.5 mM 3-isobutyl-1-methylxanthine, 125 nM indomethacin, 1 μM dexamethasone, 10 nM triiodothyronine, 850 nM insulin, and 1 μM rosiglitazone in growth medium. After 2 days of induction, the cells were maintained in growth medium containing 10 nM triiodothyronine, 850 nM insulin, and 1 μM rosiglitazone for additional 4 days. The medium was replaced every other day. After adipocytes matured, the cells were treated with FFA (PA: oleic acid = 1:2, 0.4 mM) for 48 hours. ChemS157 or chemG152 at a concentration of 500 ng ml^{-1} was added to the differentiation maintenance medium, Intracellular triglyceride contents were determined with each colorimetric assay kit from Nanjing Jiancheng Bioengineering Institute (Jiangsu, China).

REFERENCES AND NOTES

1. F. Bachelerie *et al.*, New nomenclature for atypical chemokine receptors. *Nat. Immunol.* **15**, 207–208 (2014). doi: 10.1038/ni.2812; pmid: 24549061
2. S. Okinaga *et al.*, C5L2, a nonsignaling C5A binding protein. *Biochemistry* **42**, 9406–9415 (2003). doi: 10.1021/bi034489v; pmid: 12899627
3. O. De Henau *et al.*, Signaling Properties of Chemerin Receptors CMKLR1, GPR1 and CCRL2. *PLOS ONE* **11**, e0164179 (2016). doi: 10.1371/journal.pone.0164179; pmid: 27716822
4. V. Wittamer *et al.*, Specific recruitment of antigen-presenting cells by chemerin, a novel processed ligand from human inflammatory fluids. *J. Exp. Med.* **198**, 977–985 (2003). doi: 10.1084/jem.20030382; pmid: 14530373
5. K. B. Goralski *et al.*, Chemerin, a novel adipokine that regulates adipogenesis and adipocyte metabolism. *J. Biol. Chem.* **282**, 28175–28188 (2007). doi: 10.1074/jbc.M700793200; pmid: 17635925
6. J. L. Rourke, H. J. Dranse, C. J. Sinal, Towards an integrative approach to understanding the role of chemerin in human health and disease. *Obes. Rev.* **14**, 245–262 (2013). doi: 10.1111/obr.12009; pmid: 23216632
7. S. S. Chang *et al.*, Chemerin activation in human obesity. *Obesity* **24**, 1522–1529 (2016). doi: 10.1002/oby.21534; pmid: 27222113
8. A. J. Kennedy, A. P. Davenport, International Union of Basic and Clinical Pharmacology CIII: Chemerin Receptors CMKLR1 (Chemerin$_1$) and GPR1 (Chemerin$_2$) Nomenclature, Pharmacology, and Function. *Pharmacol. Rev.* **70**, 174–196 (2018). doi: 10.1124/pr.116.013177; pmid: 29279348
9. T. F. Fischer *et al.*, Ligand-binding and -scavenging of the chemerin receptor GPR1. *Cell. Mol. Life Sci.* **78**, 6265–6281 (2021). doi: 10.1007/s00018-021-03894-8; pmid: 34241650
10. G. N. Degroot, V. Lepage, M. Parmentier, J. Y. Springael, The Atypical Chemerin Receptor GPR1 Displays Different Modes of Interaction with β-Arrestins in Humans and Mice with Important Consequences on Subcellular Localization and Trafficking. *Cells* **11**, 1037 (2022). doi: 10.3390/cells11061037; pmid: 35326488
11. T. A. Kohout, F. S. Lin, S. J. Perry, D. A. Conner, R. J. Lefkowitz, β-Arrestin 1 and 2 differentially regulate heptahelical receptor signaling and trafficking. *Proc. Natl. Acad. Sci. U.S.A.* **98**, 1601–1606 (2001). doi: 10.1073/pnas.98.4.1601; pmid: 11171997
12. V. Markova, L. Hejnova, A. Benda, J. Novotny, B. Melkes, β-Arrestin 1 and 2 similarly influence μ-opioid receptor mobility and distinctly modulate adenylyl cyclase activity. *Cell. Signal.* **87**, 110124 (2021). doi: 10.1016/j.cellsig.2021.110124; pmid: 34450275
13. A. Srivastava, B. Gupta, C. Gupta, A. K. Shukla, Emerging Functional Divergence of β-Arrestin Isoforms in GPCR Function. *Trends Endocrinol. Metab.* **26**, 628–642 (2015). doi: 10.1016/j.tem.2015.09.001; pmid: 26471844
14. E. Galliera *et al.*, β-Arrestin-dependent constitutive internalization of the human chemokine decoy receptor D6. *J. Biol. Chem.* **279**, 25590–25597 (2004). doi: 10.1074/jbc.M400363200; pmid: 15084596
15. C. T. Gilliland, C. L. Salanga, T. Kawamura, J. Trejo, T. M. Handel, The chemokine receptor CCR1 is constitutively active, which leads to G protein-independent, β-arrestin-mediated

internalization. *J. Biol. Chem.* **288**, 32194–32210 (2013). doi: 10.1074/jbc.M113.503797; pmid: 24056371
16. T. Mokros *et al.*, Surface expression and endocytosis of the human cytomegalovirus-encoded chemokine receptor US28 is regulated by agonist-independent phosphorylation. *J. Biol. Chem.* **277**, 45122–45128 (2002). doi: 10.1074/jbc.M208214200; pmid: 12244063
17. X. Lin *et al.*, Structural insights into the distinct ligand recognition and signaling of the chemerin receptors CMKLR1 and GPR1. *Protein Cell* **16**, 381–385 (2025). doi: 10.1093/procel/pwae073; pmid: 39752296
18. V. V. Gurevich, E. V. Gurevich, The structural basis of arrestin-mediated regulation of G-protein-coupled receptors. *Pharmacol. Ther.* **110**, 465–502 (2006). doi: 10.1016/j.pharmthera.2005.09.008; pmid: 16460808
19. P. Scheerer, M. E. Sommer, Structural mechanism of arrestin activation. *Curr. Opin. Struct. Biol.* **45**, 160–169 (2017). doi: 10.1016/j.sbi.2017.05.001; pmid: 28600951
20. Y. Kang *et al.*, Crystal structure of rhodopsin bound to arrestin by femtosecond X-ray laser. *Nature* **523**, 561–567 (2015). doi: 10.1038/nature14656; pmid: 26200343
21. W. Yin *et al.*, A complex structure of arrestin-2 bound to a G protein-coupled receptor. *Cell Res.* **29**, 971–983 (2019). doi: 10.1038/s41422-019-0256-2; pmid: 31776446
22. D. P. Staus *et al.*, Structure of the M2 muscarinic receptor-β-arrestin complex in a lipid nanodisc. *Nature* **579**, 297–302 (2020). doi: 10.1038/s41586-020-1954-0; pmid: 31945772
23. W. Huang *et al.*, Structure of the neurotensin receptor 1 in complex with β-arrestin 1. *Nature* **579**, 303–308 (2020). doi: 10.1038/s41586-020-1953-1; pmid: 31945771
24. Y. Lee *et al.*, Molecular basis of β-arrestin coupling to formoterol-bound β_1-adrenoceptor. *Nature* **583**, 862–866 (2020). doi: 10.1038/s41586-020-2419-1; pmid: 32555462
25. J. Bous *et al.*, Structure of the vasopressin hormone–V2 receptor–β-arrestin1 ternary complex. *Sci. Adv.* **8**, eabo7761 (2022). doi: 10.1126/sciadv.abo7761; pmid: 36054364
26. C. Cao *et al.*, Signaling snapshots of a serotonin receptor activated by the prototypical psychedelic LSD. *Neuron* **110**, 3154–3167.e7 (2022). doi: 10.1016/j.neuron.2022.08.006; pmid: 36087581
27. Y. Wang *et al.*, Cryo-EM structure of cannabinoid receptor CB1-β-arrestin complex. *Protein Cell* **15**, 230–234 (2024). doi: 10.1093/procel/pwad055; pmid: 38102480
28. C. C. Lally, B. Bauer, J. Selent, M. E. Sommer, C-edge loops of arrestin function as a membrane anchor. *Nat. Commun.* **8**, 14258 (2017). doi: 10.1038/ncomms14258; pmid: 28220785
29. D. S. Kang *et al.*, Structure of an arrestin2-clathrin complex reveals a novel clathrin binding domain that modulates receptor trafficking. *J. Biol. Chem.* **284**, 29860–29872 (2009). doi: 10.1074/jbc.M109.023366; pmid: 19710023
30. X. Tian, D. S. Kang, J. L. Benovic, in *Arrestins - Pharmacology and Therapeutic Potential*, V. V. Gurevich, Ed., vol. 219 of *Handbook of Experimental Pharmacology* (Springer, 2014), pp. 173–186.
31. N. R. Latorraca *et al.*, How GPCR Phosphorylation Patterns Orchestrate Arrestin-Mediated Signaling. *Cell* **183**, 1813–1825.e18 (2020). doi: 10.1016/j.cell.2020.11.014; pmid: 33296703
32. A. Sente *et al.*, Molecular mechanism of modulating arrestin conformation by GPCR phosphorylation. *Nat. Struct. Mol. Biol.* **25**, 538–545 (2018). doi: 10.1038/s41594-018-0071-3; pmid: 29872229
33. J. Maharana *et al.*, Structural snapshots uncover a key phosphorylation motif in GPCRs driving β-arrestin activation. *Mol. Cell* **83**, 2091–2107.e7 (2023). doi: 10.1016/j.molcel.2023.04.025; pmid: 37209686
34. Q. T. He *et al.*, Structural studies of phosphorylation-dependent interactions between the V2R receptor and arrestin-2. *Nat. Commun.* **12**, 2396 (2021). doi: 10.1038/s41467-021-22731-x; pmid: 33888704
35. N. A. Perry-Hauser *et al.*, The Two Non-Visual Arrestins Engage ERK2 Differently. *J. Mol. Biol.* **434**, 167465 (2022). doi: 10.1016/j.jmb.2022.167465; pmid: 35077767
36. J. Grimes *et al.*, Plasma membrane preassociation drives β-arrestin coupling to receptors and activation. *Cell* **186**, 2238–2255.e20 (2023). doi: 10.1016/j.cell.2023.04.018; pmid: 37146613
37. J. A. Ballesteros, H. Weinstein, in *Receptor Molecular Biology*, S. C. Sealfon, Ed., vol. 25 of *Methods in Neurosciences* (Elsevier, 1995), pp. 366–428.
38. K. Shimamura *et al.*, Identification of a stable chemerin analog with potent activity toward ChemR23. *Peptides* **30**, 1529–1538 (2009). doi: 10.1016/j.peptides.2009.05.030; pmid: 19540290
39. C. Huang *et al.*, A Screened GPR1 Peptide Exerts Antitumor Effects on Triple-Negative Breast Cancer. *Mol. Ther. Oncolytics* **18**, 602–612 (2020). doi: 10.1016/j.omto.2020.08.013; pmid: 33005727
40. N. A. McDonald, C. M. Henstridge, C. N. Connolly, A. J. Irving, An essential role for constitutive endocytosis, but not activity, in the axonal targeting of the CB1 cannabinoid receptor. *Mol. Pharmacol.* **71**, 976–984 (2007). doi: 10.1124/mol.106.029348; pmid: 17182888
41. M. Scarselli, J. G. Donaldson, Constitutive internalization of G protein-coupled receptors and G proteins via clathrin-independent endocytosis. *J. Biol. Chem.* **284**, 3577–3585 (2009). doi: 10.1074/jbc.M806819200; pmid: 19033440
42. A. Mattern, T. Zellmann, A. G. Beck-Sickinger, Processing, signaling, and physiological function of chemerin. *IUBMB Life* **66**, 19–26 (2014). doi: 10.1002/iub.1242; pmid: 24446308
43. A. J. Venkatakrishnan *et al.*, Molecular signatures of G-protein-coupled receptors. *Nature* **494**, 185–194 (2013). doi: 10.1038/nature11896; pmid: 23407534
44. C. G. Walker *et al.*, Fatty acid profile of plasma NEFA does not reflect adipose tissue fatty acid profile. *Br. J. Nutr.* **114**, 756–762 (2015). doi: 10.1017/S0007114515002251; pmid: 26205910
45. R. Liu *et al.*, Adipocyte-derived chemerin rescues lipid overload-induced cardiac dysfunction. *iScience* **26**, 106495 (2023). doi: 10.1016/j.isci.2023.106495; pmid: 37096038
46. L. Zhu, J. Huang, Y. Wang, Z. Yang, X. Chen, Chemerin causes lipid metabolic imbalance and induces passive lipid accumulation in human hepatoma cell line via the receptor GPR1. *Life Sci.* **278**, 119530 (2021). doi: 10.1016/j.lfs.2021.119530; pmid: 33887347
47. R. Pohl *et al.*, Hepatocyte expressed chemerin-156 does not protect from experimental non-alcoholic steatohepatitis. *Mol. Cell. Biochem.* **477**, 2059–2071 (2022). doi: 10.1007/s11010-022-04430-3; pmid: 35449483
48. B. Huang *et al.*, Impact of GPR1 signaling on maternal high-fat feeding and placenta metabolism in mice. *Am. J. Physiol. Endocrinol. Metab.* **316**, E987–E997 (2019). doi: 10.1152/ajpendo.00437.2018; pmid: 30835511
49. M. Yu *et al.*, Chemerin: A Functional Adipokine in Reproductive Health and Diseases. *Biomedicines* **10**, 1910 (2022). doi: 10.3390/biomedicines10081910; pmid: 36009457
50. L. Zhao, Y. Yamaguchi, W. J. Shen, J. Morser, L. L. K. Leung, Dynamic and tissue-specific proteolytic processing of chemerin in obese mice. *PLOS ONE* **13**, e0202780 (2018). doi: 10.1371/journal.pone.0202780; pmid: 30161155
51. R. J. Nibbs, G. J. Graham, Immune regulation by atypical chemokine receptors. *Nat. Rev. Immunol.* **13**, 815–829 (2013). doi: 10.1038/nri3544; pmid: 24319779
52. R. Bonecchi, G. J. Graham, Atypical Chemokine Receptors and Their Roles in the Resolution of the Inflammatory Response. *Front. Immunol.* **7**, 224 (2016). doi: 10.3389/fimmu.2016.00224; pmid: 27375622
53. J. R. Randolph-Habecker *et al.*, The expression of the cytomegalovirus chemokine receptor homolog US28 sequesters biologically active CC chemokines and alters IL-8 production. *Cytokine* **19**, 37–46 (2002). doi: 10.1006/cyto.2002.0874; pmid: 12200112
54. K. Chen *et al.*, Tail engagement of arrestin at the glucagon receptor. *Nature* **620**, 904–910 (2023). doi: 10.1038/s41586-023-06420-x; pmid: 37558880
55. D. N. Mastronarde, SerialEM: A program for automated tilt series acquisition on Tecnai microscopes using prediction of specimen position. *Microsc. Microanal.* **9**, 1182–1183 (2003). doi: 10.1017/S1431927603445911
56. S. Q. Zheng *et al.*, MotionCor2: Anisotropic correction of beam-induced motion for improved cryo-electron microscopy. *Nat. Methods* **14**, 331–332 (2017). doi: 10.1038/nmeth.4193; pmid: 28250466
57. A. Rohou, N. Grigorieff, CTFFIND4: Fast and accurate defocus estimation from electron micrographs. *J. Struct. Biol.* **192**, 216–221 (2015). doi: 10.1016/j.jsb.2015.08.008; pmid: 26278980
58. A. Punjani, J. L. Rubinstein, D. J. Fleet, M. A. Brubaker, cryoSPARC: Algorithms for rapid unsupervised cryo-EM structure determination. *Nat. Methods* **14**, 290–296 (2017). doi: 10.1038/nmeth.4169; pmid: 28165473
59. T. Bepler, K. Kelley, A. J. Noble, B. Berger, Topaz-Denoise: General deep denoising models for cryoEM and cryoET. *Nat. Commun.* **11**, 5208 (2020). doi: 10.1038/s41467-020-18952-1; pmid: 33060581
60. J. Zivanov *et al.*, New tools for automated high-resolution cryo-EM structure determination in RELION-3. *eLife* **7**, e42166 (2018). doi: 10.7554/eLife.42166
61. E. F. Pettersen *et al.*, UCSF ChimeraX: Structure visualization for researchers, educators, and developers. *Protein Sci.* **30**, 70–82 (2021). doi: 10.1002/pro.3943; pmid: 32881101
62. D. Asarnow, E. Palovcak, Y. Cheng, asarnow/pyem: UCSF pyem v0.5, Zenodo (2019). doi: 10.5281/zenodo.3576630
63. A. Kucukelbir, F. J. Sigworth, H. D. Tagare, Quantifying the local resolution of cryo-EM density maps. *Nat. Methods* **11**, 63–65 (2014). doi: 10.1038/nmeth.2727; pmid: 24213166
64. P. Emsley, K. Cowtan, *Coot*: Model-building tools for molecular graphics. *Acta Crystallogr. D* **60**, 2126–2132 (2004). doi: 10.1107/S0907444904019158; pmid: 15572765
65. E. F. Pettersen *et al.*, UCSF Chimera—A visualization system for exploratory research and analysis. *J. Comput. Chem.* **25**, 1605–1612 (2004). doi: 10.1002/jcc.20084; pmid: 15264254
66. P. D. Adams *et al.*, The Phenix software for automated determination of macromolecular structures. *Methods* **55**, 94–106 (2011). doi: 10.1016/j.ymeth.2011.07.005; pmid: 21821126
67. C. J. Williams *et al.*, MolProbity: More and better reference data for improved all-atom structure validation. *Protein Sci.* **27**, 293–315 (2018). doi: 10.1002/pro.3330; pmid: 29067766
68. G. Barnea *et al.*, The genetic design of signaling cascades to record receptor activation. *Proc. Natl. Acad. Sci. U.S.A.* **105**, 64–69 (2008). doi: 10.1073/pnas.0710487105; pmid: 18165312

69. W. K. Kroeze *et al.*, PRESTO-Tango as an open-source resource for interrogation of the druggable human GPCRome. *Nat. Struct. Mol. Biol.* **22**, 362–369 (2015). doi: 10.1038/nsmb.3014; pmid: 25895059
70. V. Demichev *et al.*, dia-PASEF data analysis using FragPipe and DIA-NN for deep proteomics of low sample amounts. *Nat. Commun.* **13**, 3944 (2022). doi: 10.1038/s41467-022-31492-0; pmid: 35803928
71. X. Qu *et al.*, Structural basis of tethered agonism of the adhesion GPCRs ADGRD1 and ADGRF1. *Nature* **604**, 779–785 (2022). doi: 10.1038/s41586-022-04580-w; pmid: 35418679
72. Y. N. Wang *et al.*, Slit3 secreted from M2-like macrophages increases sympathetic activity and thermogenesis in adipose tissue. *Nat. Metab.* **3**, 1536–1551 (2021). doi: 10.1038/s42255-021-00482-9; pmid: 34782792

ACKNOWLEDGMENTS

The cryo-EM studies were performed at the electron microscopy facility of the Shanghai Institute of Materia Medica (SIMM), Chinese Academy of Sciences. We thank Q. Wang from SIMM for cryo-EM data collection. **Funding:** This study was supported by National Key R&D Program of China 2022YFA1302900 (B.W., W.Sh., and S.H.); National Science Foundation of China grant 82121005 (B.W.); National Science Foundation of China grant 32161133011 (Q.Z.); CAS Strategic Priority Research Program XDB0830000 (B.W. and C.X.) and XDB1060000 (Q.Z.); Shanghai Pilot Program for Basic Research – Chinese Academy of Sciences, Shanghai Branch JCYJ-SHFY-2021-008 (B.W.); Shanghai Academy of Natural Sciences (SANS) Exploration Scholar (B.W.); Shanghai Science and Technology Development Foundation grant 22QA1412000 (Y.Z.); National Science Foundation of China grant 32401012 (M.H.); Zhejiang Provincial Natural Science Foundation of China grant LQ24C050004 (M.H.); research funds from Hangzhou Institute for Advanced Study 2024HIAS-Y011 (M.H.); National Science Foundation of China grant 82521004 (Q.Z. and C.X.); National Science Foundation of China grant 32471496 (W.Sh.); National Science Foundation of China grant 32301250 (B.Z.); and Shanghai Frontiers Science Center for Biomacromolecules and Precision Medicine at ShanghaiTech University (W.Sh.). **Author contributions:** Confocal experiments: X.L., K.C.; Cryo-EM data collection: H.C.; Cryo-EM data processing and analysis, model building, and structure determination: H.C., M.H., S.H.; Functional assays: H.C., X.L., L.Z., X.Cha., Y.T., T.L., W.So.; Lipid accumulation assay: Y.M., J.J.; Mass spectrometry analysis for fatty acid binding and receptor phosphorylation: J.Y., B.Z., M.M.; Protein expression: L.M., X.Chu, C.Y.; Protein preparation of cryo-EM studies and mass spectrometry analysis: H.C., X.L., L.Z., X.Cha., Y.T., T.L.; Supervision: C.X., W.Sh., Q.Z., Y.Z., B.W.; Writing – original draft: Q.Z., Y.Z., B.W.; Writing – review & editing: C.X., W.Sh., Q.Z., Y.Z., B.W. **Competing interests:** The authors declare that they have no competing interests. **Data and materials availability:** Atomic coordinates and cryo-EM density maps for the structures of chemerin-GPR1-βarr1 (conformations 1 to 4), chemerin-GPR1-βarr2, and GPR1-βarr1 complexes have been deposited in the PDB under identification codes 9UYH, 9UYI, 9UYJ, 9UYL, 9UYM, and 9UYN, respectively, and in the Electron Microscopy Data Bank under accession codes EMD-64610, EMD-64611, EMD-64612, EMD-64614, EMD-64618, and EMD-64619, respectively. The LC-MS/MS raw data generated in this study for receptor phosphorylation analysis or fatty acid ligand identification have been deposited to the ProteomeXchange Consortium2 via the iProX partner repository3 with the dataset identifier IPX0009725000 or PXD066650. All other data are available in the main text or the supplementary materials. **License information:** Copyright © 2025 the authors, some rights reserved; exclusive licensee American Association for the Advancement of Science. No claim to original US government works. https://www.science.org/about/science-licenses-journal-article-reuse

SUPPLEMENTARY MATERIALS

science.org/doi/10.1126/science.adt8794
Figs. S1 to S10; Tables S1 to S4; MDAR Reproducibility Checklist; Movie S1

Submitted 15 October 2024; accepted 19 August 2025

10.1126/science.adt8794

RESEARCH ARTICLE SUMMARY

IMMUNOLOGY

Rebalancing viral and immune damage versus repair prevents death from lethal influenza infection

Hiroshi Ichise*, Emily Speranza, Federica La Russa, Tibor Z. Veres, Colin J. Chu, Anita Gola, Beatrice H. Clark, Ronald N. Germain*

Full article and list of author affiliations: https://doi.org/10.1126/science.adr4635

INTRODUCTION: Pulmonary viral infections account for substantial numbers of deaths annually and many more during pandemics such as influenza in 1918 and severe acute respiratory syndrome coronavirus 2 (COVID-19) in 2020. Most studies ascribe loss of pulmonary function to a combination of viral destruction of infected cells and tissue damage from excessive innate inflammatory responses, and thus, inhibition of such innate activity in infected individuals has been the focus of much research.

RATIONALE: Given the strong evidence that innate immunity makes a major contribution to lethality in influenza, we screened a broad array of agents to identify those capable of preventing lethal influenza in a mouse model. The experimental model was designed to cause death within a narrow time window (8 to 10 days) in all infected animals so that survival of even a few animals in a group given any single treatment would constitute a consequential signal. If such signs of activity were found and with the treatments acting on different innate immune elements, a limited number of combinatorial therapies could be examined for additive synergy.

RESULTS: Apart from neutrophil depletion at one day after infection, none of 50 different therapies led to survival of infected animals. This was despite the use of some treatments focused on one inflammatory mediator, such as interleukin-6, and others that blocked signaling pathways affecting multiple downstream innate responses. These data suggested a tipping point model in which early damage from the combination of viral pathogenicity and inflammation led to delayed, but inevitable, death and where inhibition of further innate inflammatory responses could not rescue pulmonary function. Prior data indicated that repair processes begin almost immediately upon infection. This led us to hypothesize that failure of repair processes to counterbalance early and ongoing damage was insufficient to sustain pulmonary function in the absence of extrinsic gas exchange support (e.g., mechanical ventilation). We designed late postinfection treatments that combined partial limitation of viral spread using Tamiflu with either an anti–interferon-α/β receptor (αIFNAR) treatment, to reverse type I interferon (IFN) suppression of alveolar type 1 (AT1) pneumocyte replacement, or depletion of cytotoxic $CD8^+$ effector T cells, to prevent killing of infected pneumocytes late in disease. Despite starting treatment late after infection, both combinations, of Tamiflu and αIFNAR or Tamiflu and anti-CD8 (αCD8), led to a substantial increase in animal survival beyond antiviral therapy alone.

CONCLUSION: This study clarified why anti-inflammatory therapies other than high-dose steroids have had limited impact on the course of advanced pulmonary viral infections. Hosts with severe disease late in the infectious cycle are likely to be past the point at which arresting the damage caused by innate immune cells is enough to prevent loss of essential pulmonary function; rather, it is the failure to repair tissue damage or the additional damaging effect of adaptive, T cell–mediated, immunity that are critical at this time. This view is consistent with the prolonged time on ventilators often required for recovery of patients with severe disease and low blood oxygen saturation. Our results also indicate that antiviral drugs can be beneficial well after symptoms begin if combined with treatments that encourage repair directly or that ameliorate subsequent adaptive immune damage. □

*Corresponding author. Email: rgermain@niaid.nih.gov (R.N.G.); hiroshi.ichise@nih.gov (H.I.) Cite this article as H. Ichise *et al.*, *Science* **390**, eadr4635 (2025). DOI: 10.1126/science.adr4635

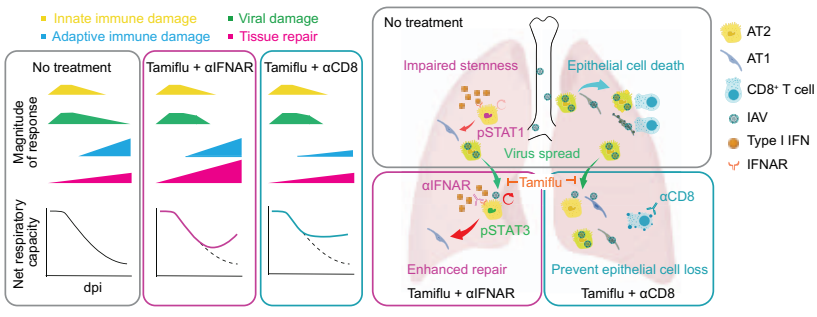

Combining antiviral drug therapy with inhibition of type I IFN signaling or depletion of $CD8^+$ effector T cells improves survival from influenza infection. In severe influenza, early innate immune and viral damage reduces lung function below a tipping point, beyond which limiting further damage alone cannot restore function. $CD8^+$ T cells further exacerbate damage by eliminating infected epithelial cells, despite repair induction. Combining antiviral therapy with type I IFN blockade or $CD8^+$ T cell depletion enhances survival by shifting the balance toward repair over damage, maintaining pulmonary function. dpi, days postinfection; pSTAT, phospho-signal transducer and activator of transcription; IAV, influenza A virus. [Figure created with BioRender.com]

IMMUNOLOGY

Rebalancing viral and immune damage versus repair prevents death from lethal influenza infection

Hiroshi Ichise[1]*, Emily Speranza[2], Federica La Russa[1], Tibor Z. Veres[1], Colin J. Chu[3], Anita Gola[1], Beatrice H. Clark[1], Ronald N. Germain[1,4]*

Maintaining tissue function while eliminating infected cells is fundamental, and inflammatory damage plays a major contribution to lethality after lung infection. We tested 50 immunomodulatory regimes to determine their ability to protect mice from lethal infection. Only neutrophil depletion soon after infection prevented death from influenza. This result suggests that the infected host passed an early tipping point after which limiting innate damage alone could not rescue lung function. We investigated treatments that could have efficacy when administered later in infection. We found that partial limitation of viral spread together with enhancement of epithelial repair, by interferon blockade or limiting $CD8^+$ T cell–mediated killing of epithelial cells, reduced lethality. This finding highlights the importance of rebalancing repair and damage processes in the survival of pulmonary infections.

Despite wide availability of antiviral drugs and vaccines, seasonal influenza can be life-threatening and lead to pneumonia and acute respiratory distress syndrome (ARDS) (*1*). Beyond this typical seasonal threat, influenza has caused multiple worldwide pandemics in the past 100 years (*2*, *3*). Fatal influenza is associated with widespread pneumonia (*4*), and dysregulated innate immunity is a major cause of the tissue damage in such infections (*5*–*8*). Preclinical studies have identified type I interferon (IFN) (*6*), neutrophils (*5*, *9*), and $CCR2^+$ monocyte-derived dendritic cells (*8*) as major contributors to this damage. Excessive innate immune responses are also a hallmark of severe acute respiratory syndrome (SARS), Middle East respiratory syndrome (MERS), and COVID-19 (*10*–*13*). Anti-inflammatory treatments have been extensively studied in attempts to ameliorate severe influenza (*14*), but antiviral treatment remains the only option recommended by the Centers for Disease Control and Prevention (*15*). For COVID-19, high-dose steroids have been found to be moderately effective (*16*), whereas immunosuppressive agents with greater selectivity have modest effects when used late in the course of infection (*17*).

Temporal understanding of pathogenesis is important for developing clinical interventions in diverse disease states. An early fatal gene signature associated with a neutrophil-mediated inflammatory feed forward circuit is seen at very early stages of influenza infection, and acute depletion of neutrophils improves survival (*5*). Other research has shown that while type I IFNs contribute to rapid antiviral responses that limit pathogen spread, the timing of production of this cytokine is critical to preventing a pathogenic innate immune response in severe acute respiratory syndrome coronavirus (SARS-CoV) infection (*18*). This suggests that the limited treatment success of agents that inhibit the innate immune response in viral pneumonias might be due to their late administration. One of the earliest gene expression signatures accompanying the intense innate inflammatory response to severe influenza infection is that of tissue repair (*5*). Tissue repair is essential to compensate for damage caused by viral cytopathic effects and the activity of immune cells. The tissue disruption caused by the innate inflammatory response may have already passed a tipping point that does not allow return to a lung physiological state solely through further limitation of damage from such pathways. In this study, we examined this tipping point model in the context of a balance between tissue damage and repair, seeking to identify potential protective interventions.

Results

An oropharyngeal lethal influenza infection causes severe lung pathology

To develop a lethal influenza infection model that causes severe lung pathology, we used the oropharyngeal route and titrated the dose of influenza A/Puerto Rico/8/34 (PR8) used for infection (fig. S1, A and B). We identified the minimum viral load that produced a uniformly lethal outcome and performed a time-resolved multiplex immunological profiling of the lungs, blood, bone marrow, and lung-draining lymph nodes of the infected animals (Fig. 1A). After infection, mice showed ruffled fur, hunching, and strained breathing starting around 3 days postinfection (dpi). Viral RNA in the lung peaked at 2 dpi, and animals lost weight starting at 4 dpi, succumbing to infection between 8 and 10 dpi (Fig. 1B and fig. S1, C and D). RNA sequencing (RNA-seq) was conducted on the whole lung at 4, 6, and 8 dpi. Reads associated with viral RNA matched with the quantitative polymerase chain reaction (qPCR) results and showed an increase at 4 dpi that was sustained to 6 dpi. By 8 dpi, when animals were in a preterminal condition, the viral RNA began to decline (fig. S1E). Transcriptional analysis showed early and strong signals associated with interferon signaling and inflammation by 4 dpi, followed by T cell responses at 6 dpi and a burst in cell proliferation at 8 dpi, suggesting ongoing repair processes (Fig. 1, C and D). Cell type deconvolution of the transcriptional data showed early loss of alveolar type 2 (AT2) cells by 4 dpi, with infiltration of neutrophils and macrophage-like populations at 6 dpi (fig. S1F). These changes were confirmed by flow cytometric analysis showing sequential recruitment of neutrophil, myeloid, and T cell populations to the lung (Fig. 1E and fig. S2). Additional flow cytometric analysis highlighted the temporal differences between lung and peripheral blood with respect to increases in these immune cell populations (fig. S3).

Multicolor immunofluorescence microscopy confirmed the spread of virus with increasing time after infection (Fig. 1, F to H, and fig. S4A). Virus-containing AT2 cells exhibited diminished prosurfactant protein C (pSPC) expression that matched loss of surfactant protein C (*Sftpc*) gene expression by 6 dpi (fig. S4B). This correlated with the predicted decrease in AT2s by cell deconvolution at 4 dpi, suggesting that tissue damage observed as a loss of pSPC presents from a very early phase in this PR8 infection model (Fig. 1F and fig. S4C). Neutrophils and monocytes accumulated in the lungs and induced bronchiolitis at 4 dpi and persisted to 7 dpi (Fig. 1G). At 7 dpi, pSPC expression was almost completely lost, indicating severe pathology (Fig. 1H). Conventional histologic examination using hematoxylin and eosin staining also confirmed the severe lung pathology with evidence of neutrophil and mononuclear cell infiltration into bronchi(oles) and alveoli (fig. S4, D and E). We concluded that in this fatal PR8 infection model there were distinct phases of virus- and immune cell–associated damage and severe pathology, including data consistent with the emphasis on innate inflammatory processes reported in prior studies (*5*, *6*, *8*, *9*).

[1]Lymphocyte Biology Section, Laboratory of Immune System Biology, National Institute of Allergy and Infectious Diseases, National Institutes of Health, Bethesda, MD, USA. [2]Florida Research and Innovation Center, Cleveland Clinic Lerner Research Institute, Port Saint Lucie, FL, USA. [3]UCL Institute of Ophthalmology, University College London, London, UK. [4]Center for Advanced Tissue Imaging, Laboratory of Immune System Biology, National Institute of Allergy and Infectious Diseases, National Institutes of Health, Bethesda, MD, USA. ***Corresponding author. Email: rgermain@niaid.nih.gov (R.N.G.); hiroshi.ichise@nih.gov (H.I.)**

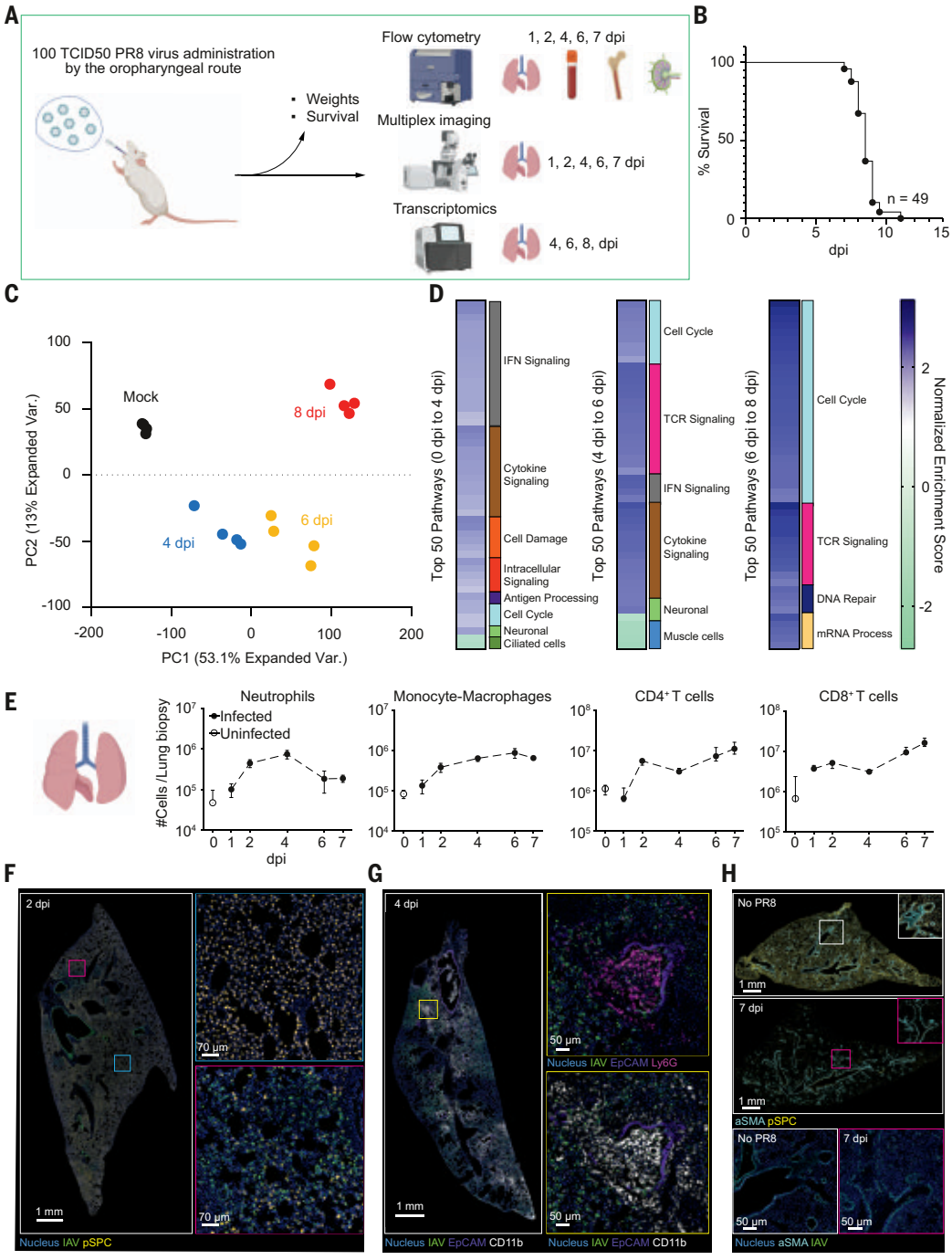

Fig. 1. Characterization of a lethal PR8 infection model. (**A**) Overview of the experimental setup. Mice were infected with 100 $TCID_{50}$ (median tissue culture infectious dose) of PR8 via the oropharyngeal (OPh.) route, and body weight and survival were monitored. Infected animals were euthanized on 1, 2, 4, 6, and 7 dpi, and the lungs, peripheral blood, lung-draining lymph nodes, and bone marrow were collected for flow cytometry and imaging. Lung samples from 4, 6, and 8 dpi were used for RNA-seq. (**B**) Kaplan-Meier plot of survival after PR8 infection. (**C**) Principal components analysis (PCA) of the global transcriptional changes from RNA-seq data at mock (black), 4 dpi (blue), 6 dpi (yellow), and 8 dpi (red) time points. (**D**) Groupings of the top 50 pathways based on adjusted *P* value ranking from differential expression results at each day compared with the previous day. Values presented are the normalized enrichment score (NES) and are clustered into major groups on the basis of the Jaccard index similarity between the genes in each pathway. (**E**) Flow cytometric analysis of the absolute number of different immune cell types in the lung samples. Each dot represents the mean, and error bars represent the standard error of the mean (SEM). (**F** to **H**) Fluorescence microscopy imaging of lungs from control and infected animals at 2, 4, and 7 dpi. Colored squares show the region magnified in the panels to the right. IAV, influenza A virus nucleoprotein; pSPC, prosurfactant protein C; EpCAM, epithelial cell adhesion molecule; aSMA, alpha-smooth muscle actin. Scale bars: 1 mm on the left and 70 µm on the right images (F); 1 mm on the left and 50 µm on the right images (G); 1 mm on the top two images and 50 µm on the bottom two images (H). Data are representative of at least five independent experiments with at least seven animals in a group, except for (C) to (E); data from one experiment, $n = 4$ mice per group.

Early innate immunomodulation is not sufficient to rescue severe PR8 infection

To examine whether interference with inflammatory damage would ameliorate lethality in this model, we tested >50 regimens that inhibited innate immune cell activity, signaling pathways, cytokines, and alarmins, with early or midcourse dosing of the drugs from 1 to 4 dpi (figs. S5 and S6 and table S2). With the exception of treatments targeting neutrophils [zileuton and anti-Ly6G (lymphocyte antigen 6G) depleting antibody], whose effects were very modest, none of these regimens resulted in survival of infected animals (fig. S5, B and C). In contrast, early high-dose treatment with the antiviral neuraminidase inhibitor Tamiflu led to complete survival of the treated cohort (fig. S5D). Thus, we concluded that interference with innate immune function is not sufficient to robustly prevent death from infection even when used relatively early after infection or in combination with drugs having distinct targets.

Lethality-associated viral and immune damage occurs at very early stages

Our results prompted us to investigate when and how damage leading to death became apparently irreversible in our model. In influenza infections, there are two major pathways of tissue damage: immune-mediated tissue damage and direct cytopathic effect of the virus (*19*). To unravel the contributions of these two pathologic processes, we titrated anti-Ly6G antibody and Tamiflu to enable interference with innate immune-mediated tissue damage (*5*) and virus-mediated tissue damage, respectively.

Titration of anti-Ly6G antibody showed a dose-dependent effect on host survival, although at higher concentrations of antibody than previously reported (fig. S7, A and B) (*5*). This form of antibody treatment had an incomplete effect on lung infiltration by neutrophils seen on day 3 dpi (fig. S7C), a time when these cells filled some of the airways (movie S1). Compared with phosphate-buffered saline (PBS) treatment, neutrophil attenuation improved host survival only when administered on 1 dpi (Fig. 2, A and B). In line with the drop of total neutrophils in the lung at 3 dpi (fig. S6C), animals treated with anti-Ly6G at 1 dpi showed less bronchiole clogging (Fig. 2, C and D). A combination of anti-Ly6G and anti-rat immunoglobulin κ light chain (*20*) resulted in a five times greater depletion of neutrophils in lung tissue, and a preinfection depletion of neutrophils with an anti-Ly6G treatment at −1 dpi, did not increase survival (fig. S7, B and C). The failure of predepletion to improve survival was consistent with evidence that neutrophils not only cause tissue damage contributing to lethality but also contribute to constraining viral pathology. Moreover, anti-Ly6G treatment could also have led to depletion of $Ly6G^+$ macrophages that can enhance tissue repair (*21*), which may also have limited the utility of treatments involving anti-Ly6G. We conclude that tissue damage caused by neutrophils becomes irreversible at relatively early stages of infection.

To determine when lethality-associated viral-mediated damage occurred, we conducted a time course study with Tamiflu (Fig. 2E). Starting treatment at 2 dpi, when the viral RNA reached a peak, followed by daily administration of the drug, resulted in uniform survival (Fig. 2F). However, treatment starting on 3 dpi resulted in only partial animal rescue, suggesting that existing viral-mediated damage and associated immune effects could not be overcome by inhibition of further viral spread. Notably, animals treated with Tamiflu starting at 2 dpi had lung damage that was visible at 50 dpi, with scarring, loss of AT2 cells and/or cell function, and myeloid cell infiltration as dominant features (Fig. 2, G and H). Thus, lethality-associated tissue damage mediated by virus and the innate immune system were established early during infection, before animals started losing body weight.

Limiting immune or viral damage enhances tissue repair responses

We addressed what biological processes were promoted when we limited viral- or immune-mediated damage early during infection. Epithelial cell proliferation can be an indication of tissue repair (*22*), and bulk RNA-seq data from the lungs of infected but untreated animals showed evidence of a burst of proliferation at 8 dpi (Fig. 1C). Infected animals treated with PBS only showed a moderate increase in $Ki67^+$bronchial epithelial cells at 6 dpi compared with uninfected controls (Fig. 3A). However, animals treated with Tamiflu on 2 dpi showed an increase in Ki67 in the airway epithelium when compared with PBS-treated animals at 6 dpi (Fig. 3, A and B). When animals were treated with anti-Ly6G antibody to limit neutrophil influx, there was an increase in $Ly6C^+$Arginase-1^+ macrophages, known to be inducers of tissue repair (*23*), in the lung at 6 dpi compared with PBS-treated animals (Fig. 3C and fig. S7, D and E) in addition to reduced bronchiolitis (Fig. 2, C and D). These macrophages were found in proximity to an increased number of $Ki67^+$ airway epithelial cells (Fig. 3, C and D, and fig. S7D). We concluded that ongoing viral propagation and immune responses limited tissue repair. In the context of infection that initiates severe viral and innate immune damage during early stages, unaided tissue repair may not be able to maintain an adequate level of pulmonary function.

Combination treatments to enhance repair and limit both viral and late adaptive immune damage improve host survival

The differentiation and proliferation of AT2 cells are important for repairing the lung epithelial layer, as AT2 cells act as a reservoir of stem cells for replacement of alveolar type 1 (AT1) cells in the presence of insults causing pulmonary epithelial damage (*24*). Patients dying of COVID-19 showed evidence of stressed AT2 cells, consistent with ineffective tissue repair (*25*). Type I IFN signaling pathways suppress proliferation and induce the death of AT2 cells during recovery from influenza infection (*26*). The activity of $CD8^+$ T cells, part of the adaptive immune response, may override ongoing tissue repair by killing infected AT1 and AT2 cells (*24*, *27*–*29*), with loss of AT1 contributing to decreased lung gas exchange capacity.

In our model of lethal influenza, we observed early and sustained expression of many type I IFN–responsive genes (fig. S8A). We also found evidence of T cell–associated signaling and accumulation of $CD8^+$ T cells in the lung beginning at 6 dpi that was correlated with further loss of surfactant proteins and the corresponding gene transcripts (Fig. 1, D and E, and fig. S4, B and C). We hypothesized that to rescue animals that had already passed the early "tipping-point" following lethal infection, tissue repair would have to be enhanced to overcome the existing damage or pathology mediated by adaptive immune responses that arise later during infection would need to be limited, all while restricting viral replication. This led us to consider a combination of late inhibition of viral spread together with blocking of type I IFN signaling or depletion of $CD8^+$ T cells to rebalance tissue damage and repair and salvage animals.

We altered the timing and dose of Tamiflu to determine the conditions when the drug, when administered alone, no longer induced robust host survival. A clinically relevant dose (20 mg/kg) had a moderate effect even when used beginning on 2 dpi, with treatments starting on 4 and 5 dpi showing comparable results, with around 40% survival and a delayed time to death (fig. S8B). On the basis of these data, we proceeded with a treatment starting with 4 dpi at 20 mg/kg, a protocol that mimics a clinically relevant scenario in which patients seek treatment several days to a week after symptoms begin.

We treated infected animals with either anti–interferon-α/β receptor antibody (αIFNAR) or anti-CD8 antibody (αCD8) concurrently with Tamiflu, Tamiflu alone, or PBS (Fig. 4A) and verified the efficacy of the drug (fig. S8, C and D). Both combination treatments improved the survival rate compared with Tamiflu alone (Fig. 4B). The combination of Tamiflu with anti-IFNAR antibody improved body weight beginning at 12 dpi compared with Tamiflu alone, and this difference was maintained to 14 dpi (fig. S8E). Combining anti-IFNAR and anti-CD8

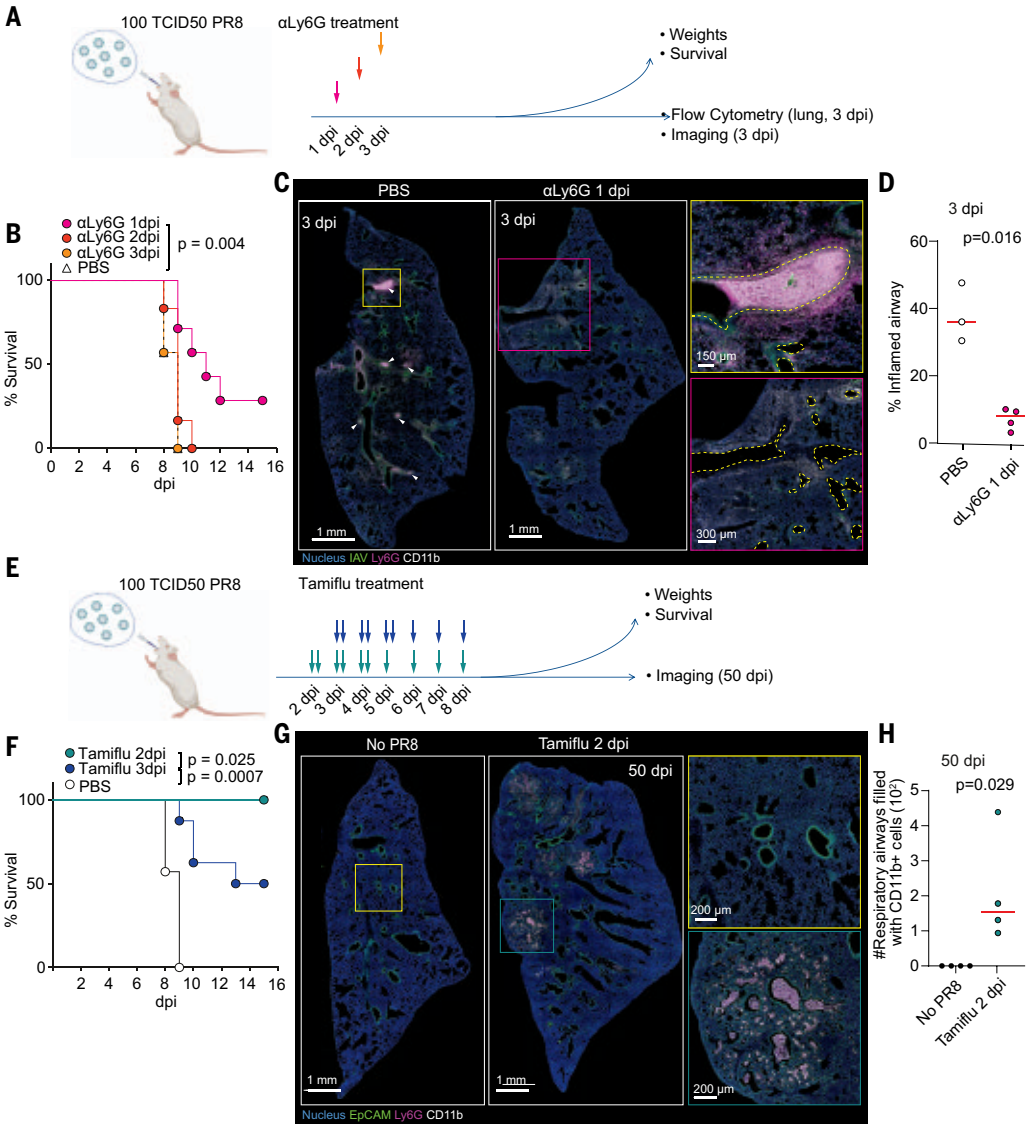

Fig. 2. Irreversible viral and immune damage occur at very early stages of infection. (**A**) Overview of neutrophil depletion experiment. Mice were infected with 100 $TCID_{50}$ of PR8 via the OPh. route, and anti-Ly6G antibody was administered intraperitoneally on either 1, 2, or 3 dpi. Weight and survival were monitored. (**B**) Kaplan-Meier curve of PR8-infected mice treated with anti-Ly6G antibody. $n = 10$ mice per group. Log-rank test was used to calculate the *P* value. (**C**) Representative immunofluorescence images of lungs from PR8-infected mice treated with anti-Ly6G antibody on 1 dpi. The lungs were harvested on 3 dpi. Magnified views of highlighted regions are shown on the right. Dashed lines outline bronchi and bronchiole structures. Scale bars: 1 mm (left and middle), 150 μm (top right), and 300 μm (bottom right). (**D**) Quantification of airways infiltrated with neutrophils as shown in (C). *P* value was calculated from a two-tailed Welch's *t* test. (**E**) Overview of the oseltamivir (Tamiflu) treatment experiment. Mice were infected as shown in (A), and Tamiflu was administered intraperitoneally starting on either 2 or 3 dpi. Two doses per day were administered for the first three consecutive days, with a single dose on the fourth and fifth days of administration. (**F**) Survival curve of PR8-infected mice treated with Tamiflu. Data are from one cohort with $n = 7$ mice per group. Log-rank test was used to calculate a *P* value. (**G**) Representative immunofluorescence images of lungs of PR8-infected mice treated with Tamiflu starting on 2 dpi. Magnified views of highlighted regions are shown on the right. The lungs were harvested on 50 dpi from animals surviving after Tamiflu treatment. Scale bars: 1 mm (left and middle) and 200 μm (top and bottom right). (**H**) Quantification of myeloid infiltration in the alveoli shown in (G). *P* value was calculated from a two-tailed Mann-Whitney *U* test. In (D) and (H), each dot represents an individual animal, and the red bars represent the median. Data are representative of two independent experiments unless otherwise specified.

antibodies with Tamiflu did not show a synergistic effect but rather a worsened outcome (Fig. 4B). This result indicates that either type I IFN signaling or a $CD8^+$ T cell response is necessary for host defense, even in animals treated with Tamiflu. Treatment with anti-IFNAR or anti-CD8 antibodies alone did not have a survival benefit, highlighting the necessity of limiting ongoing viral-mediated damage. To examine the generalizability of the findings beyond male B6 mice, we used mice of different sex and genetic backgrounds. Combining anti-IFNAR or anti-CD8 antibodies with Tamiflu was effective in both B6 and Balb/c female mice but less so in Balb/c male mice (fig. S8, F to H). The latter results fit with the evidence that males are more susceptible to severe COVID-19 and show delayed $CD8^+$ T cell responses (*30*, *31*).

To gain insights into the basis for the prosurvival effects of Tamiflu plus anti-IFNAR or Tamiflu plus anti-CD8, we carried out bulk RNA-seq on whole lung tissues (Fig. 5A). At 6 dpi, lung tissues had similar transcriptional profiles, but by 8 dpi, the Tamiflu plus anti-IFNAR

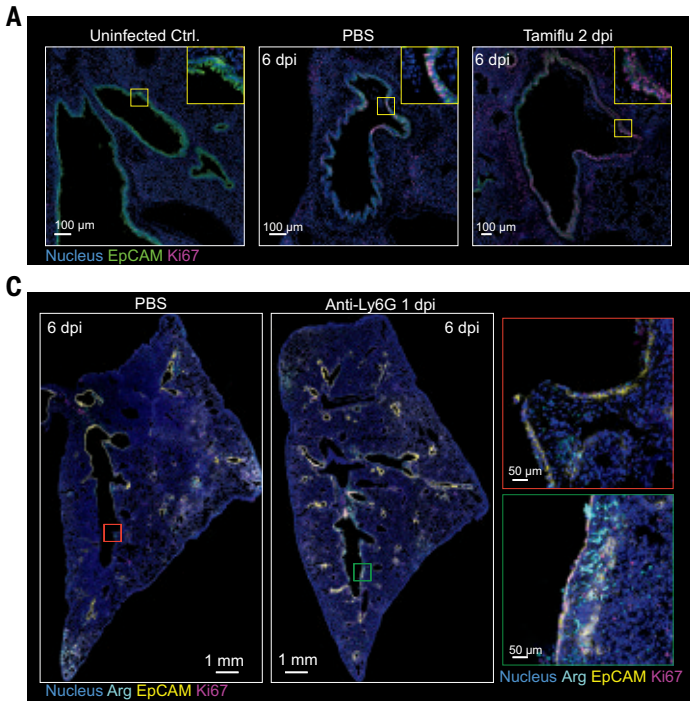

Fig. 3. Limiting immune- or viral-mediated damage changes tissue repair responses. (**A**) Representative immunofluorescence images of lungs of PR8-infected mice treated with Tamiflu starting on 2 dpi. The lungs were harvested on 6 dpi. Scale bar: 100 μm. (**B**) Quantification of Ki67^{+}EpCAM^{high} bronchial epithelial cells as shown in (A). *P* values were calculated from a two-tailed Welch's *t* test with multiple comparison correction. (**C**) Representative immunofluorescence images of lungs of PR8-infected mice treated with anti-Ly6G antibody on 1 dpi. The lungs were harvested on 6 dpi. Magnified views of highlighted regions are shown on the right. Arg, arginase 1. Scale bars: 1 mm (left and middle) and 50 μm (top and bottom right). (**D**) Quantification of Ki67^{+}EpCAM^{high} bronchial epithelial cells after indicated treatments as shown in (C). *P* values were calculated by a two-tailed Welch's *t* test. In (B) and (D), each dot represents an individual animal, and the red bars represent the median. Data are representative of two independent experiments with $n = 4$ to 7 mice per group.

samples were distinctive and differed in gene expression associated with cell proliferation, DNA repair, and cilia formation (Fig. 4, C and D, and fig. S9, A to C).

Blocking type I interferon signaling promotes early progenitor cell accumulation and enhanced epithelial repair

In comparison to infected PBS-treated animals at 8 dpi, lung tissues from mice treated with both Tamiflu and anti-IFNAR had evidence of down-regulated type I IFN signaling, but keratinization was enriched (Fig. 5A). Three keratin (KRT)–related genes (*Krt14*, *Trp63*, and *Krt5*) were only expressed in Tamiflu plus anti-IFNAR samples and not in tissues from mice treated with PBS (Fig. 5B). These genes are markers of differentiating basal epithelial cells whose expression increases in the lung after injury, and KRT14^{+}p63^{+}KRT5^{+} cells can act as progenitors to damaged epithelial layers (*32*). In addition, the data from the Tamiflu plus anti-IFNAR condition predicted enrichment of mesenchymal-like cells at 8 dpi compared with uninfected controls (fig. S10A). These cells play an important role in promoting proliferation of AT2 cells and regenerating the epithelial layers of the lung (*33*, *34*). By 12 dpi, the lung tissue from infected mice treated with Tamiflu alone had up-regulated similar gene programs, suggesting a delayed repair response owing to ongoing interferon responses in the lungs. We concluded that anti-IFNAR treatment in combination with Tamiflu induced an earlier and/or enhanced repair program in the lungs that promoted pulmonary function. Indeed, compared with mice treated with Tamiflu alone, at 8 dpi, animals given anti-IFNAR antibody with Tamiflu maintained bronchial epithelial cells (fig. S10, B and C), consistent with the prorepair basal epithelial cell differentiation gene signature. These data are consistent with pSTAT1 (phospho-signal transducer and activator of transcription 1) staining in immune cells, AT2, AT1, and mesenchymal cells. All populations had higher pSTAT1 compared with uninfected controls, indicating direct IFN responses in these cell types (fig. S10D).

STAT3 signaling in AT2 cells promotes alveolar epithelial regeneration through the brain-derived neurotrophic factor (BDNF)–tropomyosin-related kinase receptor B (TrkB) axis (*33*). The combination of anti-IFNAR antibody with Tamiflu increased the frequency of cells showing phosphorylation of STAT3 as well as the expression of Ki67 in the AT2 population (Fig. 5, C to F). The absolute number of total and proliferating pSTAT3^{+} AT2 cells was higher in the animals treated with the combination of anti-IFNAR antibody and Tamiflu (fig. S10, E and F). These cellular changes were associated at 14 dpi in the Tamiflu plus anti-IFNAR condition with an improvement in pulmonary function as compared with 8 dpi that was not observed in the Tamiflu-alone condition (Fig. 5G). Thus, inhibition of the type I IFN response promoted early stem-like cell accumulation that can induce repair of the epithelial layers and facilitate proliferation of AT2 cells, countering the effects of immune and virus-mediated damage and maintaining or improving gas exchange capacity.

Inhibition of CD8^{+} T cell responses limits severe loss of pneumocytes

Compared with infected PBS-treated animals at 8 dpi, lung tissues from mice given Tamiflu plus anti-CD8 had indications of decreased T cell receptor–associated signaling (fig. S11A). In PBS-treated animals, T cell responses were enriched by 6 dpi (Fig. 1D). This was associated with a loss of surfactant gene expression (fig. S4B) and loss of pSPC staining (Fig. 1H) in the whole lungs, suggesting the contribution of CD8^{+} T cells to a reduction of AT2 cells. When analyzing the expression of surfactant genes from the RNA-seq data across the time course (Fig. 4A), tissues from mice treated with Tamiflu plus anti-CD8 showed a mild decrease in surfactant genes at 6 dpi compared with uninfected controls and no increase in the loss at 8 dpi (fig. S11B). This was accompanied by reduced viral clearance with a high level of viral RNA still present on 12 dpi (fig. S11, C to H). Lungs from animals treated with the combination of anti-CD8 antibody and Tamiflu had more staining for the virus at 8 dpi (fig. S11I), associated with an increased number of pSPC-producing cells that were positive for IAV (Fig. 6, A to D, and fig. S12). Consistent with infected AT2 cells being preserved, the total number of such cells was higher in animals treated with Tamiflu plus anti-CD8 than in animals treated with Tamiflu alone (Fig. 6E). Tamiflu plus anti-CD8–treated animals also had more AT1 cells than animals treated with Tamiflu alone (Fig. 6, F and G) and less apoptosis in this cell population (Fig. 6H). Mice treated with Tamiflu plus anti-CD8 had higher blood oxygen saturation (SpO_2) values compared with those treated with Tamiflu alone (Fig. 6I), indicating better gas exchange capacity in the lung. These data suggested that Tamiflu can diminish viral damage despite not entirely preventing continued epithelial cell infection and that CD8^{+} effector T cells contribute to loss of respiratory function at late times by killing these infected cells.

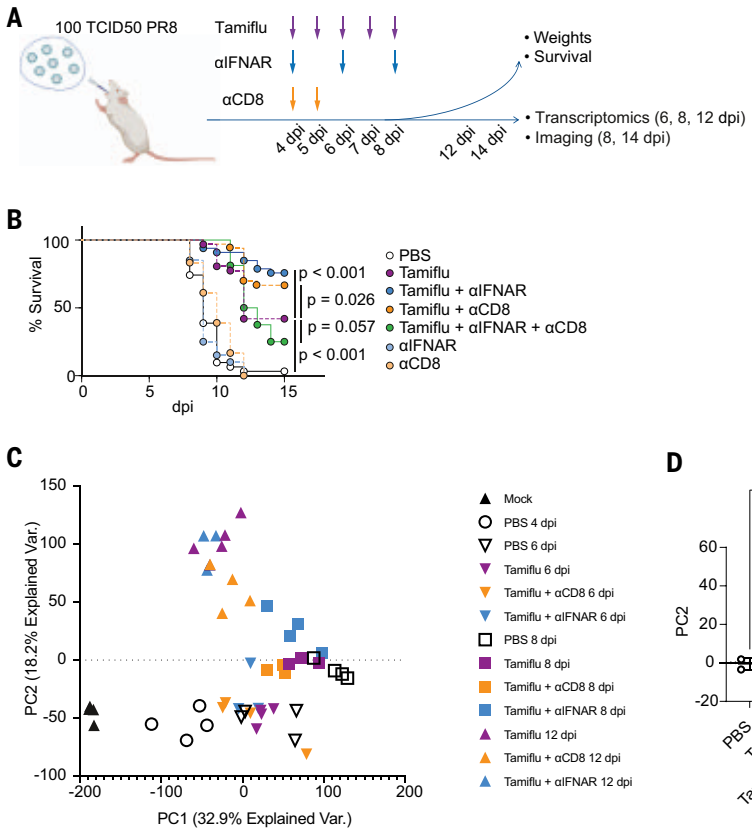

Fig. 4. Combination strategies that target type I IFN signaling or CD8$^+$ T cell response in addition to viral-mediated damage improve host survival. (**A**) Overview of combination treatments to enhance repair and limit both viral and adaptive immune damage. Mice were infected with 100 $TCID_{50}$ of PR8 via the OPh. route, and Tamiflu and/or anti-CD8 antibody and/or anti-IFNAR antibody were administered intraperitoneally at the indicated time points. Weight and survival were monitored. RNA-seq and immunofluorescence imaging were carried out at 4, 6, and 8 dpi and 8 and 14 dpi, respectively. (**B**) Kaplan-Meier plot of infected mice given PBS ($n = 32$), Tamiflu ($n = 31$), Tamiflu plus αIFNAR ($n = 33$), Tamiflu plus αCD8 ($n = 33$), Tamiflu plus αIFNAR plus αCD8 ($n = 16$), αIFNAR ($n = 20$), and αCD8 ($n = 20$). Log-rank test was used to calculate *P* values. Data are aggregated from two to four independent experiments. (**C**) PCA from RNA-seq of all samples and all conditions, showing the first two principal components. (**D**) Location of samples from 8 dpi along principal component (PC) 2. An ordinary one-way analysis of variance (ANOVA) was used to compare samples to Tamiflu plus αIFNAR. In (C) and (D), each symbol represents an individual animal, and the error bars represent mean ± SD (standard deviation). Data are from one experiment. $n = 3$ or 4 mice per group.

Discussion

Finding treatment strategies that prevent death when administered late in the course of severe viral pneumonia has proven difficult. Antiviral drugs are the primary choice for hospitalized patients in addition to supportive care, and early treatment with such agents is highly recommended (*15*). Here, we applied multiple analytical technologies to uncover the factors preventing effective treatment with either anti-inflammatory or antiviral agents when started late in disease. Our findings indicate that the damage arising shortly after disease onset overwhelms the repair capacity of the tissue and passes a tipping point of minimal pulmonary function, with homeostasis being difficult to regain. Thus, we propose that later in viral pneumonias, and possibly also in the case of various forms of ARDS, recovery will be favored if there is a rebalancing of immune- and viral-mediated damage and tissue repair.

Two lines of evidence suggest that type I IFNs might be key to rebalancing damage and repair. First, although type I IFNs are a crucial component of host immunity with antiviral and immune regulatory functions, these cytokines have been recognized to be pathogenic in pulmonary infectious diseases such as influenza, SARS-CoV, and SARS-CoV2 (*13*, *35*, *36*). Previous studies have highlighted that the timing of type I IFN production is critical to the protective versus pathogenic influence of this innate response in SARS-CoV infection and MERS-CoV infection models (*18*, *37*). Early administration (≤5 days after hospitalization) of IFN-α2b was associated with reduced mortality of hospitalized patients with COVID-19, whereas late administration was associated with increased mortality (*38*). Additionally, type I and type III IFNs inhibit AT2 cell proliferation and action as a source of stem cells for repair (*26*). Given the robust effect of anti-IFNAR treatment in our experiments, it appears that the type III IFNs play a secondary role in our infection model, but additional work is needed to determine whether adding inhibition of the latter would enhance the rescue effect we see (*26*).

In addition to AT2 cells, cell types such as KRT5$^+$KRT14$^+$p63$^+$ basal cells also serve as sources of regeneration after lung damage (*39*, *40*). Mesenchymal cells provide fibroblast growth factor ligands that act on epithelial stem cells to promote airway regeneration and on AT2 cells to promote alveolar repair (*41*). Our findings indicate that these cell types accelerate repair upon inhibition of type I IFN signaling. A requirement for effective function of AT2 cells and associated stromal elements supporting epithelial repair is consistent with the observations from patients dying of COVID-19 that revealed stress of the AT2 population as a major signal (*25*).

The strategy to deplete CD8$^+$ T cells emerged from considering that cytotoxic CD8$^+$ lymphocytes might kill cells that, although infected, may have some remaining function. Robust but late-arising CD8$^+$ T cell responses have been associated with a worse outcome in COVID-19 infection (*42*). Our data were consistent with depletion of CD8$^+$ T cells promoting enhanced survival, although this was permissive to continued viral replication, which was attenuated by the simultaneous use of Tamiflu.

Our studies showed that different mechanisms accounted for the benefit of these two late treatment regimes, suggesting that there are multiple ways to balance the rate of cell death and tissue preservation to maintain organ function. Thus, it is possible that the other immunomodulatory agents we evaluated in our study might have efficacy in combination with effective antiviral therapy even though single treatment with such drugs show marginal-moderate effects in human trials in COVID-19 (*16*, *43*–*47*) in combination with high O_2 or mechanical ventilation.

Our approach highlights the value of focusing on the temporal evolution of distinct causes of tissue damage in viral ARDS and of the effects of the evolving immune response on repair processes in designing more-effective therapies when early use of potent antivirals has not occurred. Indeed, we propose that our results suggest that the current recommendation against use of Paxlovid and Tamiflu more than 5 days after symptoms begin for COVID-19, or 3 days in the case of influenza, may not maximize use of these drugs, particularly if employed in combination with additional treatments to limit severe disease. These findings provide a rationale for future clinical studies aimed at ameliorating severe influenza when antiviral treatments are no longer effective on their own.

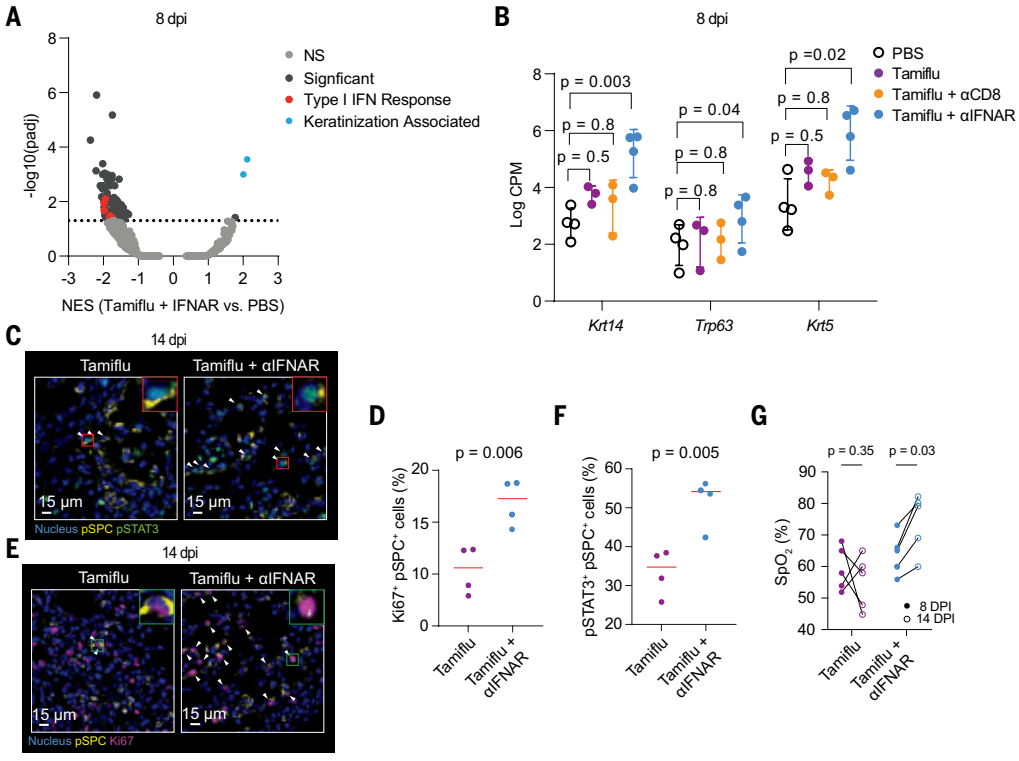

Fig. 5. Combination strategies that target type I IFN signaling in addition to viral-mediated damage enhance early tissue repair. (**A**) Pathway analysis of Tamiflu plus αIFNAR compared with PBS only. The NES score is on the *x* axis, and the $-\log_{10}$(adjusted *P* value) is on the *y* axis. Pathway groupings are colored dots (NS, not significant). (**B**) Differential expression analysis of three genes in each condition compared with PBS. False discovery rate is shown from the edgeR glmLRT (generalized linear model likelihood ratio test). Each dot represents an individual animal, and the error bars represent mean ± SD. (**C** to **F**) Immunofluorescence images and quantification of pSTAT3$^+$ [(C) and (D)] or Ki67$^+$ [(E) and (F)] AT2 cells in lungs from PR8-infected mice treated with Tamiflu or Tamiflu plus anti-IFNAR antibody starting on 4 dpi. The lungs were harvested on 14 dpi. White arrowheads indicate pSTAT3$^+$pSPC$^+$ cells in (C) or Ki67$^+$pSPC$^+$ cells in (E). Scale bars: 15 μm. In (D) and (F), *P* values were calculated from a two-tailed Mann-Whitney *U* test. (**G**) SpO_2 of animals given the indicated treatments after PR8 infection. SpO_2 was measured at 8 and 14 dpi. In (G), two-way ANOVA with Sidak's multiple comparison test was used to calculate *P* values. Each dot represents an individual animal, and in (D) and (F), the red bars represent the median. In (G), the data for individual mice at each time are indicated by the connecting line. Data are representative of two independent experiments, except for (A) and (B), where data are from one experiment. $n = 3$ or 4 mice per group.

Materials and methods

Animals, infections, and tissue collection

Eight- to twelve-week-old male C57BL/6 mice were infected with different doses of H1N1 influenza A viruses via the oropharyngeal route under isoflurane anesthesia. For studies to address generalizability, C57BL/6 female mice, Balb/c male mice, and Balb/c female mice were used. Infectious doses were supplied in a volume of 50 μl sterile 0.9% sodium chloride (Farris Laboratories). Drugs or antibodies were injected intraperitoneally in 200 μl volumes. Peripheral blood, the lung-draining lymph nodes, bone marrow, and lungs were harvested at various time points after infection. For histology, left lobes were fixed with BD CytoFix/CytoPerm (BD Biosciences) diluted in PBS solution (1:4) for 1 day at 4°C. After fixation, tissues were washed briefly three times (5 min per wash) in PBS and incubated in 30% sucrose for 1 day at 4°C before embedding in OCT (optimal cutting temperature) compound (Sakura Finetek, Cat. #4583).

All mice were maintained in specific pathogen–free conditions at an Association for Assessment and Accreditation of Laboratory Animal Care accredited animal facility at the National Institute of Allergy and Infectious Diseases (NIAID). Animals are housed in sterile individually ventilated cages on Allentown NexGen racks. Cages are supplied with sterile LabDiet 5V0T - Verified 75 IF/Auto EXT MOD or LabDiet 5V0G Select Mouse 50 IF/9F Auto rodent diets (Animal Specialties and Provisions), acidified water in sterile bottles, and sterile bedding with fewer than five mice per cage, 22.2° ± 1.6°C, 30 to 70% humidity, and 14 hours light–10 hours dark cycle. Euthanasia was performed with prolonged exposure of CO_2. All procedures were approved by the NIAID Animal Care and Use Committee (NIH) under ASP LISB-4E and follow the Public Health Service Policy and the Guide for the Care and Use of Laboratory Animals.

Virus

All studies used influenza H1N1 A/PR/8/34 (*48*, *49*) seeds (a kind gift from J. R. Bennink, NIAID, NIH) propagated in EX-CELL MDCK Serum-Free Medium for MDCK Cells (Millipore Sigma, Cat. #14581C-1000ML).

Experimental design for drug treatment after PR8 infection

For screening purposes aimed at reducing animal usage and allowing experiments initially conducted during early COVID pandemic research restrictions to proceed, single experiments were performed for each regimen to determine the efficacy according to power calculations in which we assumed 100% fatalities in the untreated group, and with time to death between 6 and 10 dpi, with most occurring at day 7, we would need about three survivors (effect of 0.7) for a significant difference with an alpha of 0.05. This allowed us to run the studies with fewer animals (10 per group) while still expecting some benefit from treatments without expecting very high survival rates. This strategy used dosing regimens derived from prior studies showing that the agents achieved their expected in vivo effects when used in the manner we employed. These expected effects were validated for several of the agents, such as anti–IL-6R and anti–IL-6 (IL, interleukin), whose use led to increased circulating IL-6 and vice versa. In addition, a few of the treatments were repeated without change in dosing, with identical results. Per our animal study protocol guidelines, animals were monitored by facility veterinarians daily and euthanized when their weight decreased by 30%. All drugs and the regimens used in this study are listed in tables S1 and S2.

Oxygen saturation measurement

SpO_2 level was measured with a pulse oximeter (Kent Scientific Corporation, Cat. # MSTAT-JR) according to the manufacturer's guide.

Immunostaining

Frozen lung tissues were cut at 30 μm on a CM3050S cryostat (Leica) and adhered to Superfrost Plus slides (VWR, Cat. # 48311-703) coated with 15 μl of chrome alum-gelatin adhesive (Newcomer Supply, Cat. #1033A). Frozen sections were washed with PBS and then made permeable and blocked in PBS containing 0.3% Triton X-100 (Sigma, Cat. #

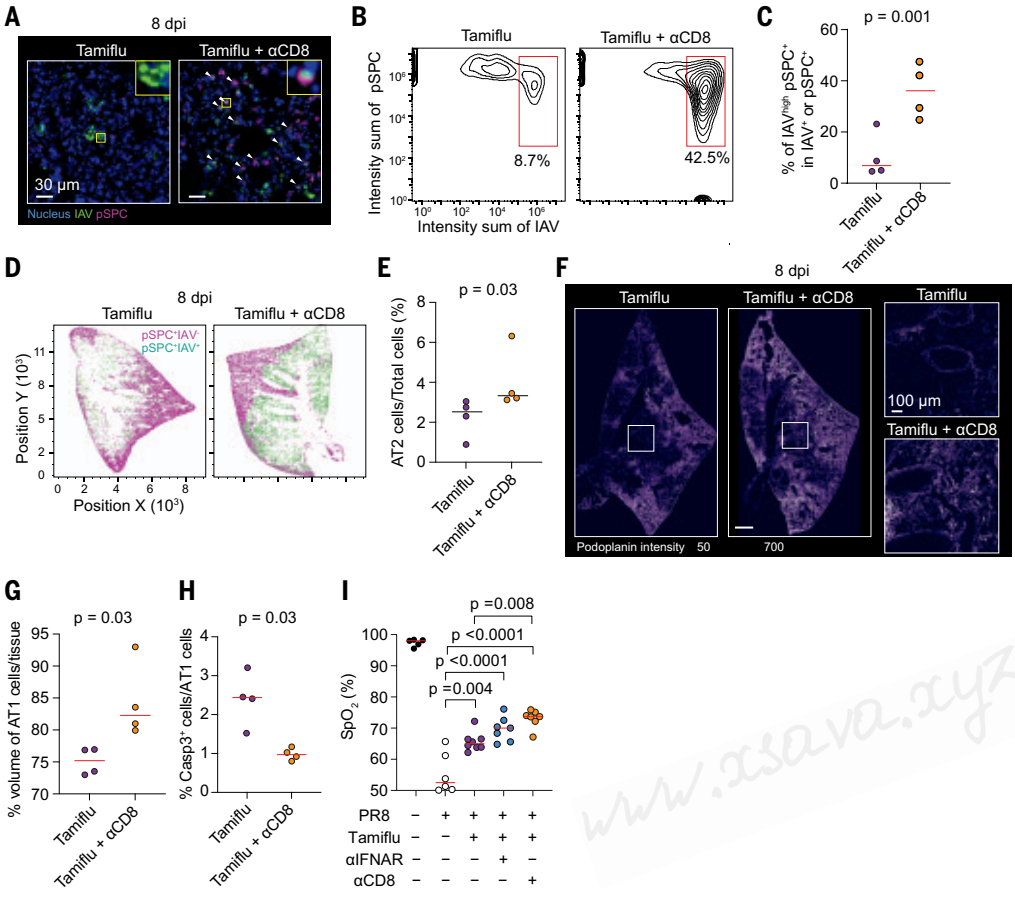

Fig. 6. Combination strategies that target CD8$^+$ T cells in addition to viral-mediated damage prevent loss of pneumocytes. (**A**) Immunofluorescence images of lungs from PR8-infected mice treated with Tamiflu or Tamiflu plus anti-CD8 antibody starting on 4 dpi. The lungs were harvested on 8 dpi. Low magnified views are shown in fig. S11. White arrowheads indicate IAV$^+$pSPC$^+$ cells. Scale bars: 30 μm. (**B** and **C**) Contour plots of AT2 population by histocytometry (B) and the quantification (C). *P* value was calculated from a two-tailed Welch's *t* test. (**D**) Histocytometric visualization of pSPC$^+$ IAV$^-$ and pSPC$^+$IAV$^+$ populations. (**E**) Quantification (percentage) of AT2 cells. *P* value was calculated from a two-tailed Mann-Whitney *U* test. (**F**) Representative podoplanin staining of lungs from PR8-infected mice treated with Tamiflu or Tamiflu plus anti-CD8 antibody starting on 4 dpi. The lungs were harvested on 8 dpi. Magnified views of highlighted regions are shown on the right. (**G**) Quantification of podoplanin$^+$ region from *z*-stack immunofluorescence images. (**H**) Quantification of cleaved caspase-3$^+$ AT1 cells from *z*-stack immunofluorescence images. *P* values were calculated from a two-tailed Mann-Whitney *U* test for (G) and (H). (**I**) SpO_2 of animals with the indicated treatments after PR8 infection. SpO_2 was measured at 8 dpi. *P* values were calculated from a Tukey's multiple comparison test. Each dot represents an individual animal, and the red bars represent the median. Data are representative of at least two independent experiments. $n = 4$ to 7 mice per group.

T8787-100ML) and 1% bovine serum albumin (Sigma-Aldrich, Cat. # 10735086001), and 1% mouse Fc block (BD Bioscience, Cat. #553142) followed by staining with antibodies diluted in blocking buffer. The antibodies used in this study are listed in table S3. After staining, slides were mounted with Fluormount G (Southern Biotech, Cat. #0100-01) and examined on a Leica Thunder Imager or TCS SP8 confocal microscope.

Iterative bleaching extends multiplexity (IBEX)

Iterative staining was performed in the principle of the IBEX protocol (*50*, *51*). Briefly, followed by the procedure of immunostaining above, fluorophore inactivation was performed with 1 mg/ml of lithium borohydride for 15 min to inactivate all fluorophores except for Hoechst after image acquisition. Samples were further stained with the antibodies for the second cycle of imaging. Image acquisition was carried out on the same microscope with the same *x* and *y* positions. *Z* plane was adjusted to match the previous round of image with the focus map function in LAS X Software (Leica Microsystems). Image registration was performed with SimpleITK as previously described (*50*, *51*).

Microscope configuration

Images were acquired using an inverted Leica TCS SP8 X confocal microscope equipped with a 20× objective (NA 0.75), 4 HyD and 1 PMT detectors, a white light laser that produces a continuous spectral output between 470 and 670 nm as well as 405, 685, and 730 nm lasers or Leica THUNDER Imager Tissue equipped with a 20× objective (NA 0.75) (Leica, Cat #11506343), DFC9000 GTC cMOS camera (Leica), LED 8 Fluorescent light source (Leica), CYR71010 filter cube (Leica). Images were captured at 12-bit, with a line average of 3, and 1024-by-1024-pixel format for the confocal imaging or 8-bit depth or 16-bit, 2048-by-2048-pixel format for the Thunder imaging. Tiling images were acquired and merged using the LAS X software.

Image acquisition

Images were acquired using an inverted Leica SP8 confocal microscope equipped with a 20× objective (NA 0.75) (Leica, Cat #11506343) or 40× objective (NA 1.3) (Leica, Cat #11506429), 4 HyD and 1 PMT detectors, a white light laser that produces a continuous spectral output between 470 and 670 nm as well as 405, 685, and 730 nm lasers or Leica THUNDER Imager Tissue equipped with a 20× objective (NA 0.75), DFC9000 GTC cMOS camera (Leica), LED 8 Fluorescent light source (Leica), CYR71010 filter cube (Leica, Cat. #11525416), and DFT51010 filter cube (Leica, Cat. #11525418). Panels consisted of antibodies conjugated to the following fluorophores and dyes: Hoechst, eFluor (eF) 450, Alexa Fluor (AF) 488, AF532, PE, AF594, AF647, AF700, AF750, DyeLight 755. Single *z* plane tiled-images were acquired from whole left lobe sections. To quantify AT1, AT2, and mesenchymal cells and their pSTAT-1 signaling, tiled-*z*-stack (*z*-step size: 0.5 μm, 20 slices) images from whole tissue sections were acquired with a Leica SP8 confocal microscope equipped with a 40× objective.

Image processing and analysis

Images were converted to .ims file with Imaris File Converter (Oxford Instruments) and Gaussian filters were applied to all images with Imaris (10.2.0). For cell segmentation and quantification, .ims files were converted to OME-tiff format. The Tissuenet model in Cellpose 2.0 (*52*, *53*), further trained with our dataset, was used to segment cells. Mean intensity of each marker and *x*, *y* coordinates were extracted by 3D ImageJ Suite for FIJI (*54*). Extracted values were combined into a single csv file and analyzed by histocytometry as previously described

www.xsava.xyz

(*55*). To quantify IAV-NP^{high} pSPC^{+} cells, a composite image of IAV-NP and pSPC was created by adding those channels with Imaris channel arithmetic function after subtracting background. After segmentation of IAV-NP^{+} and/or pSPC^{+} cells with Imaris surface function based on IAV-NP and pSPC intensity, intensity sum of IAV-NP and pSPC were exported and analyzed by Flowjo software as described previously (*55*). For the quantification of AT1 and AT2 cells in *z*-stack images, we used the Imaris Surface function to segment podoplanin, pSPC, and nucleus signal. The nuclear staining of Ki67, pSTAT1, and pSTAT3 were further quantified on the basis of the threshold function from Imaris.

RNA preparation for RNA-seq

Right inferior lobe was immediately transferred into 1 ml Trizol (Thermo, Cat. #15596018), snap-frozen in liquid nitrogen, and kept at −80°C. RNA extraction was performed by QIAGEN Nucleic Acid Isolation Service (QIAGEN, Germany). RNA integrity number (RIN) was determined with Agilent RNA 6000 Nano Kit (Agilent, Cat. # 5067-1511) for quality check and all samples were above 8.5.

Next-generation sequencing

Sequencing libraries were made from 1 μg total RNA using the TruSeq Stranded mRNA kit, according to the manufacturer's guide (Illumina, San Diego, CA). To obtain reads per sample, 2 μl of each purified library was combined into a single pool, quantified using the Kapa Library Quantification kit (Roche Sequencing Solutions, Pleasanton, CA), diluted to 10 pM, and sequenced as 2 × 151 bp reads on the MiSeq instrument using the Nano kit, V2 (Illumina, San Diega, CA). A second library pool was created where the volume of each library was calculated on the basis of the read distribution from the MiSeq run to create a normalized pool for deep sequencing. The normalized pool was quantified using the Kapa Library Quantification kit, diluted to 1.8 pM, and sequenced as 2 ×151 bp paired-end reads on three NextSeq 550 instrument runs using the High Output v2.5, 300 cycle sequencing kit. A total depth of 1.04 billion paired-end reads with an average of 15.3 million paired-end reads per sample was generated.

RNA-seq data processing

After sequencing, samples were aligned to the mouse genome (GRcm39) appended to contain the influenza virus genome (GCF_000865725.1) to account for viral RNA reads. Alignment to the genome was done using STAR v2.7.10 (*56*), and counts were generated using featureCounts in the SubRead package v2.0.4 (*57*). The count tables were read into R v4.2.1. Data normalization and differential expression analysis were performed using edgeR v3.40.2 (*58*). Pathway analysis was performed using the fgsea package v1.24.0 (*59*) and the c2cp gene set from the MSigDB (*60*). Pathways were clustered into groups using a Euclidean distance metric on the Jaccard index of similarity calculation between genes included in the pathway list. Cell type deconvolution from RNA-seq data was performed using the MuSIC package v1.0.0 (*61*) in R and using the naïve lung single cell data form (*62*) as a background. Results were exported to GraphPad/Prism v10.1.1 for display only.

Serum cytokine measurement

Blood obtained by cardiac puncture was placed in Microvette 500 Serum Gel tubes (Sarstedt, 20.1344) and allowed to clot before analysis with the Lunaris Mouse 12-Plex Cytokine Kit (Ayoxxa Biosystems).

Quantitative polymerase chain reaction

Lung samples were collected into tubes containing Trizol (Invitrogen) and manually disassociated in the Trizol followed by processing on direct-zol columns (Zymo Research). RNA concentration was determined on a nanodrop (Thermo Fischer Scientific). cDNA was generated using the SuperScript IV VILO master mix (Invitrogen) and 100 ng/μl of RNA following a program of 25°C for 10 min, 50°C for 10 min, and 85°C for 5 min. cDNA was added to a master mix containing Platinum Quantitative PCR Supermix UDG with ROX (Invitrogen) and the TaqMan (Invitrogen) primer/probe set for influenza A or *Hprt*. Readout was performed in triplicate for each sample using a 15-μl reaction volume in a 384-well plate on the Quant Studio 6 (Thermo Fischer). The viral cycle threshold values were normalized against *Hprt* using the ΔΔ method, and the change compared to the average of the controls was calculated.

Flow cytometry

For the lungs, the right cranial lobes were used for all experiments. Harvested lungs were chopped in 2 ml of a mixture of liberase thermolysin medium (TM; 100 μg/ml) (Sigma, Cat. #5401127001) and DNaseI (100 μg/ml) (Roche, Ct. #04716728001) in RPMI-1640 (Thermo Fisher Scientific, Cat. #11875093) and transferred to gentleMACS C Tubes (Miltenyi Biotech, Cat. #130-093-237). Samples were homogenized by two cycles of mechanical dissociation with a gentleMACS Dissociator (Miltenyi Biotech, Cat. #130-093-235) and incubated at 37°C for 30 min for enzymatic digestion in between. Single-cell suspensions were obtained by adding EDTA at a final concentration of 20 mM to stop the enzymatic reaction and passing through a 70 μm nylon mesh. Cells were washed in PBS with 2% fetal bovine serum, 5 mM EDTA (hereafter FACS buffer) twice. The lung-draining lymph nodes were harvested and digested in 500 μl of RPMI with liberase TM (200 μg/ml) at 37°C for 30 min. Single-cell suspensions were obtained by adding EDTA at a final concentration of 20 mM to stop the enzymatic reaction and passing through a 70 μm nylon mesh. Cells were washed in FACS buffer twice. Bone marrow cells were flushed from the femora and tibiae. Suspensions were passed through a 70 μm nylon mesh. Peripheral blood was collected from the inferior vena cava. BD Pharm Lyse Lysing Buffer (BD Biosciences, Cat. #555899) was used to lyse red blood cells. Cells in FACS buffer were blocked with anti-CD16/CD32 (BioLegend, Cat. #101302) and then were incubated with fluorochrome-conjugated antibodies with LIVE/DEAD fixable dead cell stain dye (Thermo Fisher Scientific, Cat. # 423108). Staining and washing were performed at 4°C. CountBright Absolute Counting Beads (Thermo Fisher Scientific, Cat. # C36950) were added into cell suspension before analysis. Cells were analyzed on an LSR Fortessa flow cytometer (BD Biosciences), and data were analyzed with FlowJo software (BD).

Tissue clearing

Volumetric imaging with optically cleared samples were performed as described previously with slight modification (*63*). Briefly, frozen lung samples were sectioned at 500 μm on a CM3050S cryostat. The samples were hydrated and washed with PBS to remove OCT in a 24-well plate. Samples were incubated for at least 12 hours in BD Perm/Wash Buffer (BD Bioscience) containing 1% mouse Fc block (BD Bioscience, Cat. #553142) and stained with titrated antibodies in BD Perm/Wash Buffer (BD Bioscience, Cat. #554723) containing 1% Fc block for 24 hours at room temperature on a shaker. Stained samples were washed with BD Perm/Wash Buffer three times for at least 20 min at room temperature on a shaker. Samples were transferred on a slide with two silicon isolators (Grace BioLabs, Cat. #664407) and treated with 200 μl of Ce3D medium [1.82 g Histodenz (Millipore Sigma, Cat. #D2158-100G, 0.1% triton, and 0.5% thioglycerol (Millipore Sigma, Cat. #M1753) per 1 ml 40% *N*-methylacetamide (Millipore Sigma, Cat. #M26305–500G) in PBS] inside a chemical fume hood and sealed with a cover slip (Electron Microscopy Sciences, Cat. #63766-01) and incubated at room temperature on a shaker overnight. After removing the old Ce3D, cleared samples were mounted with 40 μl of new Ce3D and sealed with a coverslip with two SecureSeal Imaging Spacers (Grace Bio-Labs, Cat. #654002).

Quantification and statistical analysis

Statistical tests performed for a given analysis are denoted in the figure legends. For this manuscript, $P < 0.05$ was considered as a significance threshold. All statistical tests were performed in R or GraphPad/Prism v10.

REFERENCES AND NOTES

1. World Health Organization, Influenza (seasonal); https://www.who.int/news-room/fact-sheets/detail/influenza-(seasonal).
2. D. M. Morens, J. K. Taubenberger, A. S. Fauci, The persistent legacy of the 1918 influenza virus. *N. Engl. J. Med.* **361**, 225–229 (2009). doi: 10.1056/NEJMp0904819; pmid: 19564629
3. N. P. Johnson, J. Mueller, Updating the accounts: Global mortality of the 1918-1920 "Spanish" influenza pandemic. *Bull. Hist. Med.* **76**, 105–115 (2002). doi: 10.1353/bhm.2002.0022; pmid: 11875246
4. J. K. Taubenberger, D. M. Morens, The pathology of influenza virus infections. *Annu. Rev. Pathol.* **3**, 499–522 (2008). doi: 10.1146/annurev.pathmechdis.3.121806.154316; pmid: 18039138
5. M. Brandes, F. Klauschen, S. Kuchen, R. N. Germain, A systems analysis identifies a feedforward inflammatory circuit leading to lethal influenza infection. *Cell* **154**, 197–212 (2013). doi: 10.1016/j.cell.2013.06.013; pmid: 23827683
6. S. Davidson, S. Crotta, T. M. McCabe, A. Wack, Pathogenic potential of interferon αβ in acute influenza infection. *Nat. Commun.* **5**, 3864 (2014). doi: 10.1038/ncomms4864; pmid: 24844667
7. J. R. Teijaro *et al.*, Endothelial cells are central orchestrators of cytokine amplification during influenza virus infection. *Cell* **146**, 980–991 (2011). doi: 10.1016/j.cell.2011.08.015; pmid: 21925319
8. K. L. Lin, Y. Suzuki, H. Nakano, E. Ramsburg, M. D. Gunn, $CCR2^+$ monocyte-derived dendritic cells and exudate macrophages produce influenza-induced pulmonary immune pathology and mortality. *J. Immunol.* **180**, 2562–2572 (2008). doi: 10.4049/jimmunol.180.4.2562; pmid: 18250467
9. T. Narasaraju *et al.*, Excessive neutrophils and neutrophil extracellular traps contribute to acute lung injury of influenza pneumonitis. *Am. J. Pathol.* **179**, 199–210 (2011). doi: 10.1016/j.ajpath.2011.03.013; pmid: 21703402
10. A. L. Totura, R. S. Baric, SARS coronavirus pathogenesis: Host innate immune responses and viral antagonism of interferon. *Curr. Opin. Virol.* **2**, 264–275 (2012). doi: 10.1016/j.coviro.2012.04.004; pmid: 22572391
11. Y. Liang *et al.*, Highlight of immune pathogenic response and hematopathologic effect in SARS-CoV, MERS-CoV, and SARS-Cov-2 infection. *Front. Immunol.* **11**, 1022 (2020). doi: 10.3389/fimmu.2020.01022; pmid: 32574260
12. S. A. Lowery, A. Sariol, S. Perlman, Innate immune and inflammatory responses to SARS-CoV-2: Implications for COVID-19. *Cell Host Microbe* **29**, 1052–1062 (2021). doi: 10.1016/j.chom.2021.05.004; pmid: 34022154
13. R. Channappanavar, S. Perlman, Pathogenic human coronavirus infections: Causes and consequences of cytokine storm and immunopathology. *Semin. Immunopathol.* **39**, 529–539 (2017). doi: 10.1007/s00281-017-0629-x; pmid: 28466096
14. I. Ramos, A. Fernandez-Sesma, Modulating the innate immune response to influenza A virus: Potential therapeutic use of anti-inflammatory drugs. *Front. Immunol.* **6**, 361 (2015). doi: 10.3389/fimmu.2015.00361; pmid: 26257731
15. Centers for Disease Control and Prevention, Influenza Antiviral Medications: Summary for Clinicians; https://www.cdc.gov/flu/hcp/antivirals/summary-clinicians.html.
16. RECOVERY Collaborative Group, Dexamethasone in hospitalized patients with Covid-19. *N. Engl. J. Med.* **384**, 693–704 (2021). doi: 10.1056/NEJMoa2021436; pmid: 32678530
17. P. Mathur, S. Kottilil, Immunomodulatory therapies for COVID-19. *Front. Med. (Lausanne)* **9**, 921452 (2022). doi: 10.3389/fmed.2022.921452; pmid: 35991665
18. R. Channappanavar *et al.*, Dysregulated type I interferon and inflammatory monocyte-macrophage responses cause lethal pneumonia in SARS-CoV-infected mice. *Cell Host Microbe* **19**, 181–193 (2016). doi: 10.1016/j.chom.2016.01.007; pmid: 26867177
19. S. Herold, C. Becker, K. M. Ridge, G. R. S. Budinger, Influenza virus-induced lung injury: Pathogenesis and implications for treatment. *Eur. Respir. J.* **45**, 1463–1478 (2015). doi: 10.1183/09031936.00186214; pmid: 25792631
20. G. Boivin *et al.*, Durable and controlled depletion of neutrophils in mice. *Nat. Commun.* **11**, 2762 (2020). doi: 10.1038/s41467-020-16596-9; pmid: 32488020
21. C. Ruscitti *et al.*, Recruited atypical $Ly6G^+$ macrophages license alveolar regeneration after lung injury. *Sci. Immunol.* **9**, eado1227 (2024). doi: 10.1126/sciimmunol.ado1227; pmid: 39093958
22. M. F. Beers, E. E. Morrisey, The three R's of lung health and disease: Repair, remodeling, and regeneration. *J. Clin. Invest.* **121**, 2065–2073 (2011). doi: 10.1172/JCI45961; pmid: 21633173
23. L. Campbell, C. R. Saville, P. J. Murray, S. M. Cruickshank, M. J. Hardman, Local arginase 1 activity is required for cutaneous wound healing. *J. Invest. Dermatol.* **133**, 2461–2470 (2013). doi: 10.1038/jid.2013.164; pmid: 23552798
24. C. E. Barkauskas *et al.*, Type 2 alveolar cells are stem cells in adult lung. *J. Clin. Invest.* **123**, 3025–3036 (2013). doi: 10.1172/JCI68782; pmid: 23921127
25. T. M. Delorey *et al.*, COVID-19 tissue atlases reveal SARS-CoV-2 pathology and cellular targets. *Nature* **595**, 107–113 (2021). doi: 10.1038/s41586-021-03570-8; pmid: 33915569
26. J. Major *et al.*, Type I and III interferons disrupt lung epithelial repair during recovery from viral infection. *Science* **369**, 712–717 (2020). doi: 10.1126/science.abc2061; pmid: 32527928
27. I. Y. Adamson, D. H. Bowden, The type 2 cell as progenitor of alveolar epithelial regeneration. A cytodynamic study in mice after exposure to oxygen. *Lab. Invest.* **30**, 35–42 (1974). pmid: 4812806
28. W. J. Zacharias *et al.*, Regeneration of the lung alveolus by an evolutionarily conserved epithelial progenitor. *Nature* **555**, 251–255 (2018). doi: 10.1038/nature25786; pmid: 29489752
29. A. N. Nabhan, D. G. Brownfield, P. B. Harbury, M. A. Krasnow, T. J. Desai, Single-cell Wnt signaling niches maintain stemness of alveolar type 2 cells. *Science* **359**, 1118–1123 (2018). doi: 10.1126/science.aam6603; pmid: 29420258
30. S. A. Kharroubi, M. Diab-El-Harake, Sex-differences in COVID-19 diagnosis, risk factors and disease comorbidities: A large US-based cohort study. *Front. Public Health* **10**, 1029190 (2022). doi: 10.3389/fpubh.2022.1029190; pmid: 36466473
31. T. Takahashi *et al.*, Sex differences in immune responses that underlie COVID-19 disease outcomes. *Nature* **588**, 315–320 (2020). doi: 10.1038/s41586-020-2700-3; pmid: 32846427
32. V. Ievlev *et al.*, Krt14 and Krt15 differentially regulate regenerative properties and differentiation potential of airway basal cells. *JCI Insight* **8**, e162041 (2023). doi: 10.1172/jci.insight.162041; pmid: 36512409
33. A. J. Paris *et al.*, STAT3–BDNF–TrkB signalling promotes alveolar epithelial regeneration after lung injury. *Nat. Cell Biol.* **22**, 1197–1210 (2020). doi: 10.1038/s41556-020-0569-x; pmid: 32989251
34. T. Peng *et al.*, Hedgehog actively maintains adult lung quiescence and regulates repair and regeneration. *Nature* **526**, 578–582 (2015). doi: 10.1038/nature14984; pmid: 26436454
35. F. McNab, K. Mayer-Barber, A. Sher, A. Wack, A. O'Garra, Type I interferons in infectious disease. *Nat. Rev. Immunol.* **15**, 87–103 (2015). doi: 10.1038/nri3787; pmid: 25614319
36. S. Davidson, M. K. Maini, A. Wack, Disease-promoting effects of type I interferons in viral, bacterial, and coinfections. *J. Interferon Cytokine Res.* **35**, 252–264 (2015). doi: 10.1089/jir.2014.0227; pmid: 25714109
37. R. Channappanavar *et al.*, IFN-I response timing relative to virus replication determines MERS coronavirus infection outcomes. *J. Clin. Invest.* **129**, 3625–3639 (2019). doi: 10.1172/JCI126363; pmid: 31355779
38. N. Wang *et al.*, Retrospective multicenter cohort study shows early interferon therapy is associated with favorable clinical responses in COVID-19 Patients. *Cell Host Microbe* **28**, 455–464.e2 (2020). doi: 10.1016/j.chom.2020.07.005; pmid: 32707096
39. A. E. Vaughan *et al.*, Lineage-negative progenitors mobilize to regenerate lung epithelium after major injury. *Nature* **517**, 621–625 (2015). doi: 10.1038/nature14112; pmid: 25533958
40. W. Zuo *et al.*, $p63^+Krt5^+$ distal airway stem cells are essential for lung regeneration. *Nature* **517**, 616–620 (2015). doi: 10.1038/nature13903; pmid: 25383540
41. E. El Agha, V. J. Thannickal, The lung mesenchyme in development, regeneration, and fibrosis. *J. Clin. Invest.* **133**, e170498 (2023). doi: 10.1172/JCI170498; pmid: 37463440
42. L. Bergamaschi *et al.*, Longitudinal analysis reveals that delayed bystander CD8+ T cell activation and early immune pathology distinguish severe COVID-19 from mild disease. *Immunity* **54**, 1257–1275.e8 (2021). doi: 10.1016/j.immuni.2021.05.010; pmid: 34051148
43. I. O. Rosas *et al.*, Tocilizumab in hospitalized patients with severe Covid-19 pneumonia. *N. Engl. J. Med.* **384**, 1503–1516 (2021). doi: 10.1056/NEJMoa2028700; pmid: 33631066
44. P. O. Guimarães *et al.*, Tofacitinib in patients hospitalized with Covid-19 Pneumonia. *N. Engl. J. Med.* **385**, 406–415 (2021). doi: 10.1056/NEJMoa2101643; pmid: 34133856
45. Y. Cao *et al.*, Ruxolitinib in treatment of severe coronavirus disease 2019 (COVID-19): A multicenter, single-blind, randomized controlled trial. *J. Allergy Clin. Immunol.* **146**, 137–146.e3 (2020). doi: 10.1016/j.jaci.2020.05.019; pmid: 32470486
46. REMAP-CAP Investigators, Interleukin-6 receptor antagonists in critically ill patients with Covid-19. *N. Engl. J. Med.* **384**, 1491–1502 (2021). doi: 10.1056/NEJMoa2100433; pmid: 33631065
47. J. H. Stone *et al.*, Efficacy of tocilizumab in patients hospitalized with Covid-19. *N. Engl. J. Med.* **383**, 2333–2344 (2020). doi: 10.1056/NEJMoa2028836; pmid: 33085857
48. T. Francis Jr., Transmission of influenza by a filterable virus. *Science* **80**, 457–459 (1934). doi: 10.1126/science.80.2081.457.b; pmid: 17795179
49. T. Francis Jr., T. P. Magill, Immunological studies with the virus of influenza. *J. Exp. Med.* **62**, 505–516 (1935). doi: 10.1084/jem.62.4.505; pmid: 19870430
50. A. J. Radtke *et al.*, IBEX: A versatile multiplex optical imaging approach for deep phenotyping and spatial analysis of cells in complex tissues. *Proc. Natl. Acad. Sci. U.S.A.* **117**, 33455–33465 (2020). doi: 10.1073/pnas.2018488117; pmid: 33376221
51. A. J. Radtke *et al.*, IBEX: An iterative immunolabeling and chemical bleaching method for high-content imaging of diverse tissues. *Nat. Protoc.* **17**, 378–401 (2022). doi: 10.1038/s41596-021-00644-9; pmid: 35022622
52. C. Stringer, T. Wang, M. Michaelos, M. Pachitariu, Cellpose: A generalist algorithm for cellular segmentation. *Nat. Methods* **18**, 100–106 (2021). doi: 10.1038/s41592-020-01018-x; pmid: 33318659
53. M. Pachitariu, C. Stringer, Cellpose 2.0: How to train your own model. *Nat. Methods* **19**, 1634–1641 (2022). doi: 10.1038/s41592-022-01663-4; pmid: 36344832
54. J. Ollion, J. Cochennec, F. Loll, C. Escudé, T. Boudier, TANGO: A generic tool for high-throughput 3D image analysis for studying nuclear organization. *Bioinformatics* **29**, 1840–1841 (2013). doi: 10.1093/bioinformatics/btt276; pmid: 23681123

55. M. Y. Gerner, W. Kastenmuller, I. Ifrim, J. Kabat, R. N. Germain, Histo-cytometry: A method for highly multiplex quantitative tissue imaging analysis applied to dendritic cell subset microanatomy in lymph nodes. *Immunity* **37**, 364–376 (2012). doi: 10.1016/j.immuni.2012.07.011; pmid: 22863836
56. A. Dobin *et al.*, STAR: Ultrafast universal RNA-seq aligner. *Bioinformatics* **29**, 15–21 (2013). doi: 10.1093/bioinformatics/bts635; pmid: 23104886
57. Y. Liao, G. K. Smyth, W. Shi, featureCounts: An efficient general purpose program for assigning sequence reads to genomic features. *Bioinformatics* **30**, 923–930 (2014). doi: 10.1093/bioinformatics/btt656; pmid: 24227677
58. M. D. Robinson, D. J. McCarthy, G. K. Smyth, edgeR: A Bioconductor package for differential expression analysis of digital gene expression data. *Bioinformatics* **26**, 139–140 (2010). doi: 10.1093/bioinformatics/btp616; pmid: 19910308
59. G. Korotkevich *et al.*, Fast gene set enrichment analysis. bioRxiv 060012 [Preprint] (2021); https://doi.org/10.1101/060012.
60. A. Subramanian *et al.*, Gene set enrichment analysis: A knowledge-based approach for interpreting genome-wide expression profiles. *Proc. Natl. Acad. Sci. U.S.A.* **102**, 15545–15550 (2005). doi: 10.1073/pnas.0506580102; pmid: 16199517
61. X. Wang, J. Park, K. Susztak, N. R. Zhang, M. Li, Bulk tissue cell type deconvolution with multi-subject single-cell expression reference. *Nat. Commun.* **10**, 380 (2019). doi: 10.1038/s41467-018-08023-x; pmid: 30670690
62. L. M. Roberts *et al.*, Pulmonary infection induces persistent, pathogen-specific lipidomic changes influencing trained immunity. *iScience* **24**, 103025 (2021). doi: 10.1016/j.isci.2021.103025; pmid: 34522865
63. W. Li, R. N. Germain, M. Y. Gerner, Multiplex, quantitative cellular analysis in large tissue volumes with clearing-enhanced 3D microscopy (C_e3D). *Proc. Natl. Acad. Sci. U.S.A.* **114**, E7321–E7330 (2017). pmid: 28808033

ACKNOWLEDGMENTS

We thank J. R. Bennink for providing PR8 influenza A virus. RNA-seq was performed by the Genomics Research Section, Research Technologies Branch, NIAID. Figures were created with BioRender.com. We thank Calithera Biosciences for providing CB-280. We thank U. Andersson for providing anti-HMGB1 antibody. **Funding:** This research was supported by the Intramural Research Program of the National Institutes of Health (NIH). The contributions of the NIH author(s) were made as part of their official duties as NIH federal employees, are in compliance with agency policy requirements, and are considered works of the United States government. However, the findings and conclusions presented in this paper are those of the author(s) and do not necessarily reflect the views of the NIH or the US Department of Health and Human Services. **Author contributions:** Conceptualization: R.N.G.; Methodology: H.I., F.L.R., T.Z.V., C.J.C., A.G., E.S., B.H.C.; Validation: H.I., F.L.R., C.J.C., A.G.; Formal analysis: H.I., F.L.R., E.S.; Investigation: H.I., F.L.R.; Data curation: H.I., E.S.; Writing – original draft: H.I., E.S.; Writing – review & editing: R.N.G.; Supervision and data review: R.N.G.; Project administration: H.I., R.N.G.; Funding acquisition: R.N.G. **Data and materials availability:** All data needed to evaluate the conclusions in the paper are present in the paper or the supplementary materials. RNA-seq data are available from the Gene Expression Omnibus with accession number GSE271812. **Competing interests:** The authors declare that they have no competing interests.

License information: Copyright © 2025 the authors, some rights reserved; exclusive licensee American Association for the Advancement of Science. No claim to original US government works. https://www.science.org/about/science-licenses-journal-article-reuse

SUPPLEMENTARY MATERIALS

science.org/doi/10.1126/science.adr4635
Figs. S1 to S12; Tables S1 to S3; Reference (*64*); MDAR Reproducibility Checklist; Movie S1

Submitted 2 July 2024; resubmitted 21 April 2025; accepted 14 August 2025

10.1126/science.adr4635

QUALITY CONTENT FOR THE GLOBAL SCIENTIFIC COMMUNITY

Multiple ways to stay informed on issues related to your research

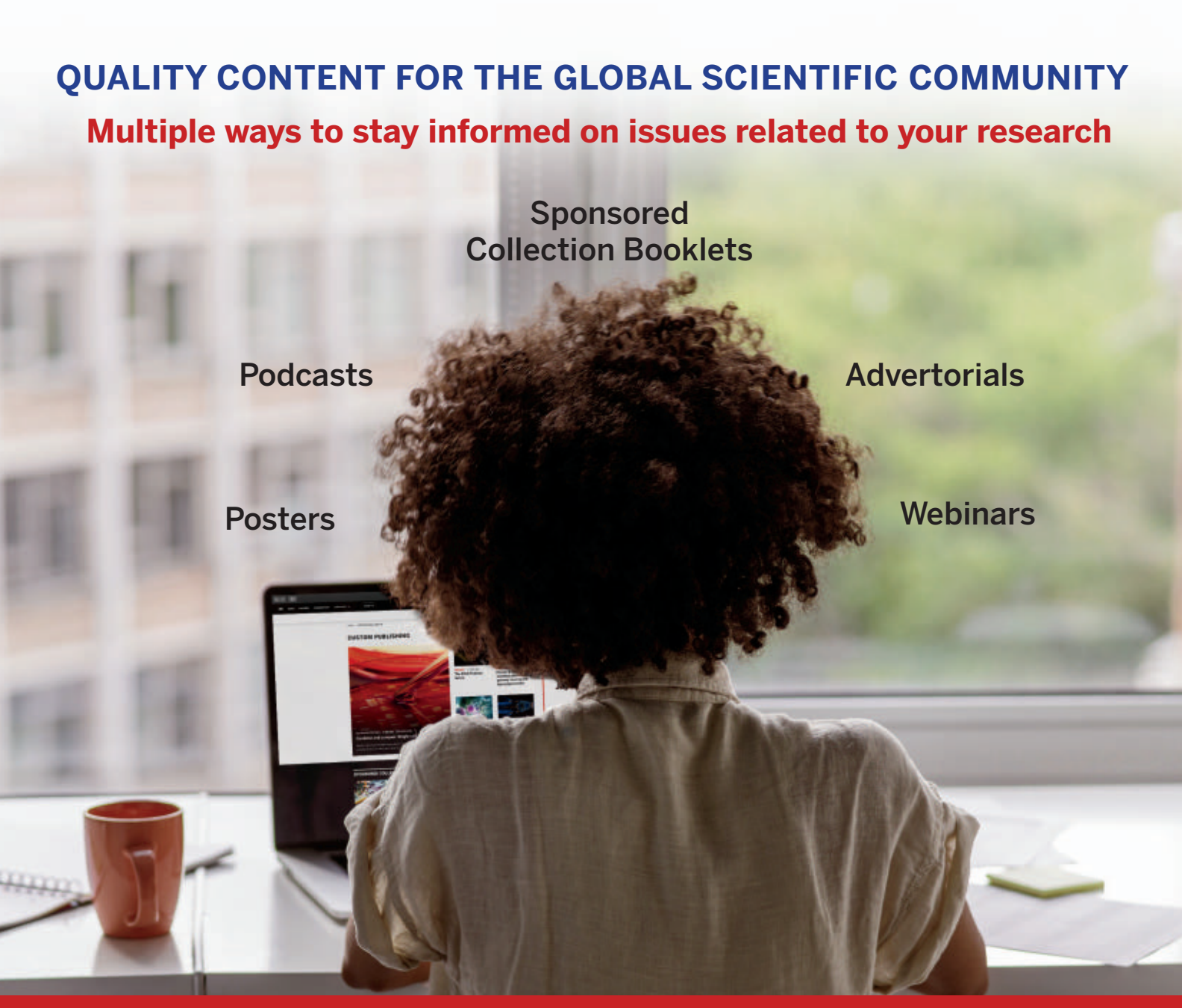

Science
AAAS

Scan the code and start exploring the latest advances in science and technology innovation!

Science.org/custom-publishing

Brought to you by the *Science*/AAAS Custom Publishing Office.

Posters **Podcasts** **Sponsored Collection Booklets** **Advertorials** **Webinars**

RESEARCH ARTICLE SUMMARY

GENETIC CODE

An archaeal genetic code with all TAG codons as pyrrolysine

Veronika Kivenson*, Samantha L. Peters, Guillaume Borrel, Aleksandr Kivenson, Leah T. Roe, Noah X. Hamlish, Khaled Fadhlaoui, Alanna Schepartz, Simonetta Gribaldo, Robert L. Hettich, Jillian F. Banfield*

Full article and list of author affiliations: https://doi.org/10.1126/science.adu2404

INTRODUCTION: Although the genetic code was originally thought to be universal, alternative codon assignments have since been documented in bacteria and eukaryotes. In archaea, no alternative genetic code is known. However, a few archaeal genes use the standard stop codon TAG to encode pyrrolysine (Pyl), the 22nd proteinogenic amino acid. Additionally, the machinery for Pyl insertion has also become widely used for genetic code expansion, enabling precise incorporation of diverse noncanonical amino acids into proteins. Although Pyl was discovered in archaea more than two decades ago, it remains unknown whether the TAG codon has a dual encoding (stop/Pyl) or could be fully reassigned in some archaea.

RATIONALE: Pyl-encoding archaeal genomes are thought to restrict TAG codon use and contain downstream stop codons after TAG to mitigate potential effects of readthrough. However, it remains unknown how TAG codons are interpreted throughout the genome. To systematically assess how TAG is used and search for Pyl-containing proteins, we analyzed codon usage patterns across archaeal genomes, revealing evidence for genome-wide reassignment of TAG from stop to Pyl in a subset of Pyl-encoding archaea. We tested these predictions experimentally through the cultivation of human gut and marine isolates followed by global and targeted proteomics.

RESULTS: Bioinformatically, we predicted the presence of Pyl in >1800 proteins of various function. Proteomic data show that select archaea have genome-wide incorporation of Pyl at TAG codons. These archaea use an alternative genetic code, that we named the Pyl code, where the TAG stop codon is fully repurposed as a sense codon. The Pyl code is the only genetic code with 62 dedicated sense codons encoding 21 amino acids. Pyl is only conserved in the methylamine methyltransferases, suggesting that a functional role for Pyl is limited to these proteins. Additionally, Pyl tRNA synthetase pairs derived from Pyl-code archaea identified in this study enabled the incorporation of Pyl analogs into target proteins of *Escherichia coli*.

CONCLUSION: We uncovered archaeal lineages in which the standard stop codon TAG has been reassigned genome-wide to encode Pyl, and the need to retain Pyl insertion in methylamine methyltransferases likely drives the adoption of this alternative genetic code. The sporadic distribution of the Pyl code and the presence of Pyl in essential proteins suggest that this genetic code may be more easily gained than lost. Finally, Pyl systems occurring in these archaea can be used to add Pyl analogs into proteins in *E. coli*, underscoring their applications for genetic code expansion and biotechnology. □

*Corresponding author. Email: kivenson@berkeley.edu (V.K.); jbanfield@berkeley.edu (J.F.B.) Cite this article as V. Kivenson *et al.*, *Science* **390**, eadu2404 (2025). DOI: 10.1126/science.adu2404

Discovery of a new genetic code in archaea. The interpretation of TAG codons in Pyl-encoding archaeal genomes was unknown. We predicted genome-wide TAG codon reassignment in silico and then tested these predictions in *Methanomethylophilus alvi* and *Methanococcoides burtonii* isolates using targeted and global proteomics. We confirmed that the TAG codon is encoded as Pyl genome-wide. The Pyl code has 62 sense codons and only two stop codons and has a sporadic distribution among archaea.

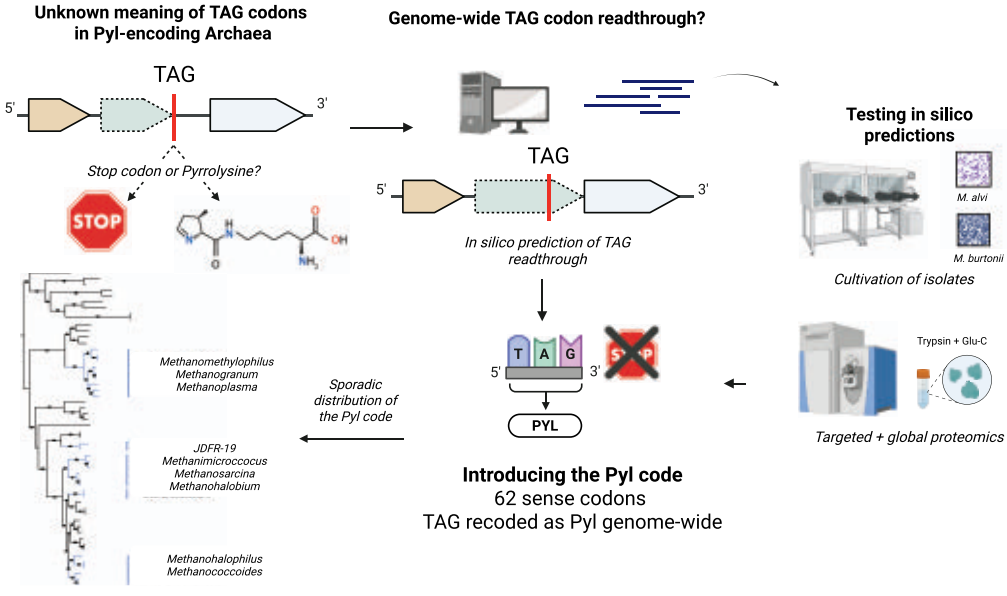

GENETIC CODE

An archaeal genetic code with all TAG codons as pyrrolysine

Veronika Kivenson[1]*, Samantha L. Peters[2], Guillaume Borrel[3], Aleksandr Kivenson†, Leah T. Roe[4], Noah X. Hamlish[5], Khaled Fadhlaoui[6,7], Alanna Schepartz[4,5,8,9], Simonetta Gribaldo[3], Robert L. Hettich[2], Jillian F. Banfield[1,10,11,12,13]*

Multiple genetic codes developed during the evolution of eukaryotes and bacteria, yet no alternative genetic code is known for archaea. We used proteomics to confirm our prediction that certain archaea consistently incorporate pyrrolysine (Pyl) at TAG codons, supporting an alternative archaeal genetic code that we designate the Pyl code. This genetic code has 62 sense codons encoding 21 amino acids. In contrast to monophyletic genetic code distributions in bacteria, the archaeal Pyl code occurs sporadically, indicating that it arose independently in multiple lineages. We discovered that more than 1800 archaeal proteins contain Pyl, increasing the number of such proteins by two orders of magnitude. Additionally, five Pyl transfer RNA (tRNA) pyrrolysyl–tRNA synthetase pairs from Pyl-code archaea were used to introduce Pyl analogs into proteins in *Escherichia coli*.

The genetic code is neither universal nor immutable (*1*); subsequent to its initial discovery, analysis of genetic material from diverse lineages revealed substantial code variation. More recently, alternative genetic codes in which either TGA or TAG stop codons incorporate a standard amino acid were identified in bacteria and bacteriophages (*2*–*7*). Interestingly, these stop codons can also be selectively interpreted as either selenocysteine (Sec; the 21st amino acid, at TGA) or pyrrolysine (Pyl; the 22nd amino acid, at TAG) (*8*, *9*). Pyl is a derivative of lysine that features a pyrroline ring (*9*, *10*). Its biosynthesis requires the Pyl B, C, and D genes, whereas its incorporation into proteins requires a pyrrolysyl–tRNA synthetase (PylRS) and a Pyl tRNA ($tRNA^{Pyl}$) carrying a CUA anticodon (*9*, *11*–*14*). We refer to the Pyl B, C, and D genes and the PylRS/$tRNA^{Pyl}$ pair as the Pyl machinery. The PylRS/$tRNA^{Pyl}$ pairs are widely used tools for genetic code expansion (GCE), in which noncanonical α-amino acids or their analogs are incorporated into ribosomal products to modify protein function (*15*). PylRS/$tRNA^{Pyl}$ pairs act on α-amino acid substrates with diverse side chains and are orthogonal in many bacterial and mammalian systems, showing limited reactivity with canonical α-amino acids, and neither interfere nor integrate with prokaryotic or eukaryotic aminoacyl-tRNA pairs.

In organisms that naturally encode the Pyl machinery, understanding of the mechanism that signals Pyl incorporation is incomplete, and the extent to which Pyl occurs in proteins remains unclear. It has been suggested that a Pyl insertion sequence (PYLIS), a structure analogous to the Sec insertion sequence (SECIS) required to selectively signal selenocysteine incorporation, enables dual encoding of TAG (*16*, *17*). However, in a subset of genes that encode Pyl proteins, the PYLIS structure has not been detected (*18*, *19*). In bacteria, Pyl has been reported in one L-serine dehydratase and a few methylamine methyltransferases (*9*, *11*, *20*, *21*), and otherwise, TAG is read as a stop codon. Pyl has been predicted to occur in proteins of 11 major groups of archaea (*9*, *22*–*32*). All archaea without Pyl machinery use TAG as a stop codon, and those with Pyl machinery are believed to also use TAG as a stop codon, except in the very few enzymes in which Pyl occurs. Additionally, Pyl has been hypothesized to occur within proteins when internal TAG codons were observed during in silico analysis (*22*, *33*, *34*). However, incorporation has been experimentally confirmed in only five proteins (mono-, di-, and trimethylamine methyltransferases; tRNA guanylyltransferase; and PylB) (*10*, *18*, *35*, *36*). The archaeon *Methanosarcina acetivorans* has five additional proteins presumed to contain Pyl because their detected molecular masses are consistent with TAG readthrough (*18*). The latter authors suggest that TAG may not be selectively reassigned in *M. acetivorans* (*18*), but genome-wide incorporation of Pyl at this codon has not been established.

We asked whether some archaea broadly incorporate Pyl into proteins using an alternative genetic code and whether these genomes would yield biotechnologically relevant PylRS/$tRNA^{Pyl}$ pairs. Our analysis revealed that organisms within two archaeal phyla contain multiple genes with internal in-frame TAG codons. Using global and targeted proteomics, we analyzed two such archaea, a human gut and a marine isolate, and confirmed in both cases the genome-wide incorporation of Pyl at TAG codons, including within multiple enzyme classes. On this basis, we propose the existence of a previously unrecognized genetic code, presently confined to archaea, and designate it the Pyl code. We confirmed that five PylRS/$tRNA^{Pyl}$ pairs predicted by our analysis efficiently introduce Pyl analogs into proteins in *Escherichia coli*. This work demonstrates that Pyl-code organisms can add distinct "parts" to the GCE toolbox and facilitate the synthesis of heteropolymers. We found that the distribution of the Pyl code among archaea is not monophyletic, which is consistent with multiple independent code transitions and hints that codon reassignment to Pyl could be facile. We infer features indicative of recoding that occurred recently compared with the distant past and propose a series of steps that may lead to genetic code transition.

Results

Phylogenetic distribution of Pyl

To investigate the phylogenetic distribution of archaea with Pyl machinery (Pyl-encoding archaea, or Pyl archaea), we augmented a collection of genomes from all families known to incorporate Pyl, together with taxa we have identified that carry the Pyl machinery (tables S1 to S4). Most Pyl archaea belong to the Halobacteriota (Methanosarcinia, Archaeoglobi, and Methanonatronarchaeia) and Thermoplasmatota (Methanomassiliicocci) phyla, with a few others within the phyla of Asgardarcheota, Thermoproteota, and Hydrothermarchaeota (Fig. 1 and tables S3 and S5). Notably, organisms that encode the Pyl machinery have a discontinuous phylogenetic distribution (Fig. 1), sometimes even at the genus level. For example, the Pyl pathway is encoded and actively utilized by a single member of the Archaeoglobi (*Ca*. Methanoglobus hypatiae LCB24) but absent from the closely related Archaeoglobi LCB024-003 [98.6% average amino acid identity (AAI)] (*24*). Similarly, Pyl is limited to a single family within the Asgardarcheota and Hydrothermarchaeota phyla, and in the *Ca*. Methanomethylicus genus, only two of five archaea encode Pyl.

Given the intermixing of closely related archaea that do and do not encode the Pyl machinery, we compared the phylogenies of the Pyl machinery (fig. S1) to that of the organisms (Fig. 1). Consistent with prior suggestions (*37*, *38*), discordance between the tree structures provides evidence for lateral transfer of the Pyl genes. For example,

[1]Innovative Genomics Institute, University of California, Berkeley, Berkeley, CA, USA. [2]Biosciences Division, Oak Ridge National Laboratory, Oak Ridge, TN, USA. [3]Institut Pasteur, Unit Evolutionary Biology of the Microbial Cell, Paris, France. [4]Department of Chemistry, University of California, Berkeley, Berkeley, CA, USA. [5]Department of Molecular and Cell Biology, University of California, Berkeley, Berkeley, CA, USA. [6]Université Clermont Auvergne, CNRS, Laboratoire Microorganismes: Génome et Environnement, Clermont-Ferrand, France. [7]Université Clermont Auvergne, UMR 454 MEDIS UCA-INRAE, Clermont-Ferrand, France. [8]Chan Zuckerberg Biohub, San Francisco, CA, USA. [9]Arc Institute, Palo Alto, CA, USA. [10]Earth and Planetary Science, University of California, Berkeley, Berkeley, CA, USA. [11]Department of Environmental Science Policy, and Management, University of California, Berkeley, Berkeley, CA, USA. [12]Earth and Environmental Sciences, Lawrence Berkeley National Laboratory, Berkeley, CA, USA. [13]Biomedicine Discovery Institute, Monash University, Clayton, VIC, Australia. ***Corresponding author. Email: kivenson@berkeley.edu (V.K.); jbanfield@berkeley.edu (J.F.B.)** †Independent researcher, New York, NY, USA.

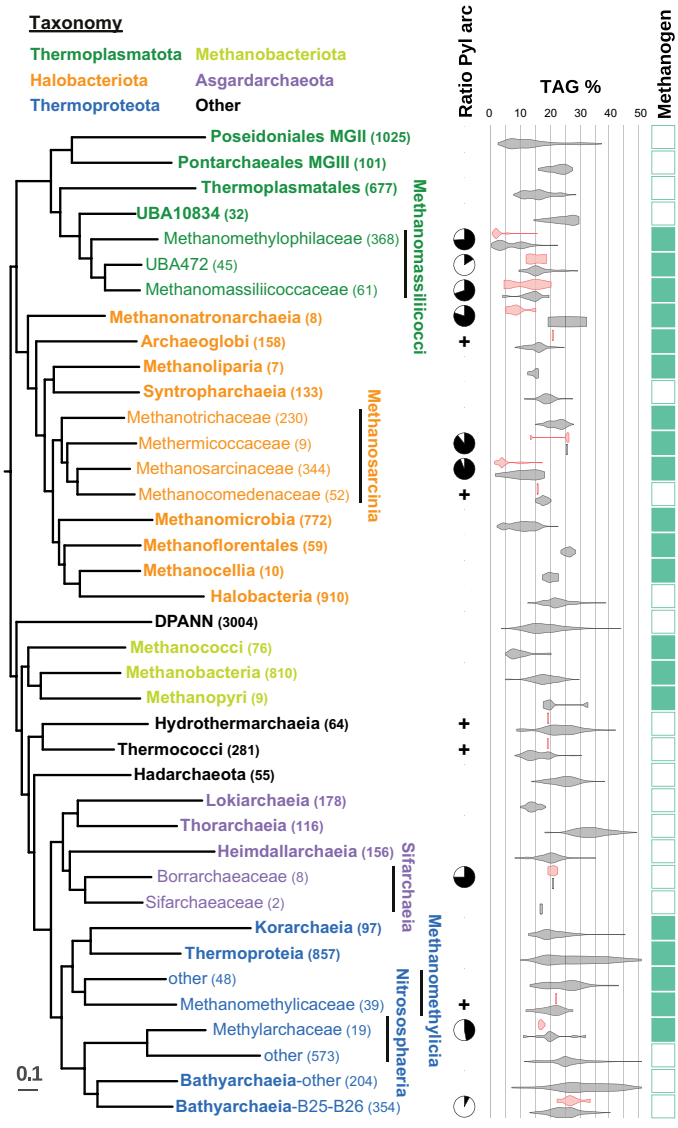

Fig. 1. Distribution of the Pyl machinery in archaea is paraphyletic. The Pyl machinery is variably present among representatives of the same family (pie charts). The range of TAG frequency in Pyl genomes (salmon violins) shows that low TAG frequency is not a hallmark of Pyl archaea, in contrast to previous reports. Gray violins correspond to genomes without Pyl. The highest TAG percentage (TAG %) values for Thermoproteia (up to 66.9%), Bathyarchaeia-other (up to 52.2%), and Nitrososphaeria-other (up to 57.1%) are not shown. The "+" symbols indicate that Pyl genomes represent less than 5% of the genomes in the displayed lineage. The total number of genomes per lineage displayed in the tree is indicated next to the lineage name.

MSBL1 archaea (Hadarchaeota) and *Ca*. Methanoglobus may have gained their Pyl machinery through horizontal gene transfer from a Methanonatronarchaeia and a Thermoproteota, respectively.

TAG frequency varies among Pyl archaea

Given that organisms almost always interpret TAG as a stop codon (*39*), we reasoned that there may be detrimental consequences associated with the acquisition of the Pyl machinery, such as the erroneous incorporation of Pyl and readthrough of the normal gene end. It is also possible that TAG codons possess a dual encoding in organisms that carry Pyl machinery; however, there exist no validated mechanisms for recognizing a dual-message TAG codon. Initial studies suggested that the PYLIS, an RNA stem-loop downstream of the TAG codon, is required to interpret a TAG codon as Pyl (*16*, *17*). However, consistent with subsequent reports that the PYLIS is not required for Pyl incorporation (*18*, *19*), we did not find the PYLIS motif flanking TAG codons of genes encoding Pyl-containing proteins, except for a small subset of the methylamine methyltransferases (table S6). Although there may be an unknown means by which TAG is interpreted independently for each gene, there is no evidence for this process at present. Regulatory sequences may be selected against owing to the cost of maintaining additional contextual requirements.

Loss of the TAG codon would eliminate readthrough. It has long been thought that low TAG frequency (≤5%) is a hallmark of archaea that encode Pyl machinery (*19*, *20*), yet a few outliers have been reported (*22*, *25*, *29*). We calculated the percentage of genes with a TAG codon in the genomes of Pyl archaea and found that the TAG frequencies are always high (>15%) among Pyl archaea that are intermixed phylogenetically with genomes lacking Pyl machinery (Fig. 1 and table S5). The discrepancy from expected TAG content in many Pyl archaea highlights the need to determine the distribution of TAG codons and investigate their function.

TAG is recoded genome-wide as a sense codon

To determine how TAG is used by Pyl archaea, we first predicted the genes in each organism using Genetic Code 11, which is standard for bacteria and archaea. We then repredicted all TAG codons as sense codons and classified the resulting genes into four categories (figs. S2 and S3). Category 1 genes contain one or more TAG codons in which the sequences before and after the TAG codon possess >30% sequence identity to that of a known protein. In addition, readthrough of the TAG codon in category 1 genes extends the protein sequence by >15 amino acids. Based on this analysis, we predict that genes in category 1 read the TAG as an internal sense codon. Category 2 genes were characterized by short extensions of ≤15 amino acids and had no overlap with sense codon(s) of an adjacent gene. This scenario was originally thought to be the main outcome of TAG readthrough (*19*). Genes in category 3 were characterized by an extension of >15 amino acids after TAG readthrough (the sequence extension lacks similarity with known genes) and/or a short (<60 nucleotide) gene overlap and/or an in-frame gene fusion. For categories 2 and 3, it is not possible to predict whether TAG is a stop or sense codon based on sequence analysis alone. For category 4, readthrough led to a large (>60 nucleotide) out-of-frame overlap. In this case, there is no support for TAG reassignment, as large gene overlaps are rare in prokaryotes (*40*). The prevalence of category 1 and absence, or extreme rarity, of category 4 cases in a genome may be an indicator of genome-wide TAG reassignment.

Notably, Pyl archaea from nine genera (*Methanomethylophilus*, *Ca*. Methanogranum, *Ca*. Methanoplasma, *Methanimicrococcus*, *Methanosarcina*, *Methanohalobium*, *Methanohalophilus*, *Methanococcoides*, and *JDFR-19*) have numerous category 1 genes and very few, or no, category 4 genes (Fig. 2 and table S7). This pattern is consistent with reliance only on TGA and TAA as stop codons. We infer that in these genomes, TAG is completely recoded as a sense codon (Pyl).

We predicted 1903 Pyl-containing proteins in genomes inferred to use the Pyl code (tables S8 to S11). The largest number of predicted Pyl proteins of a single organism, 191 in total, occurs in the uncultured archaean, *JDFR-19* (Methermicoccaceae; table S12). This archaeon is a recoding outlier with a 13% TAG frequency. Contrary to its initial discovery in a narrow class of enzymes, Pyl is incorporated into a functionally diverse set of proteins. The position of Pyl is conserved in a Per-Arnt-Sim (PAS) family protein in genomes of three archaeal genera (fig. S4). Pyl also occupies a position close to RNA and/or DNA binding sites in the CRISPR-Cas9–related nuclease IscB and in the binding site of methylcobalamin:CoM methyltransferase (figs. S5 and S6). However, whereas Pyl-containing proteins are functionally enriched in Gene Ontology (GO) terms associated with methylamine

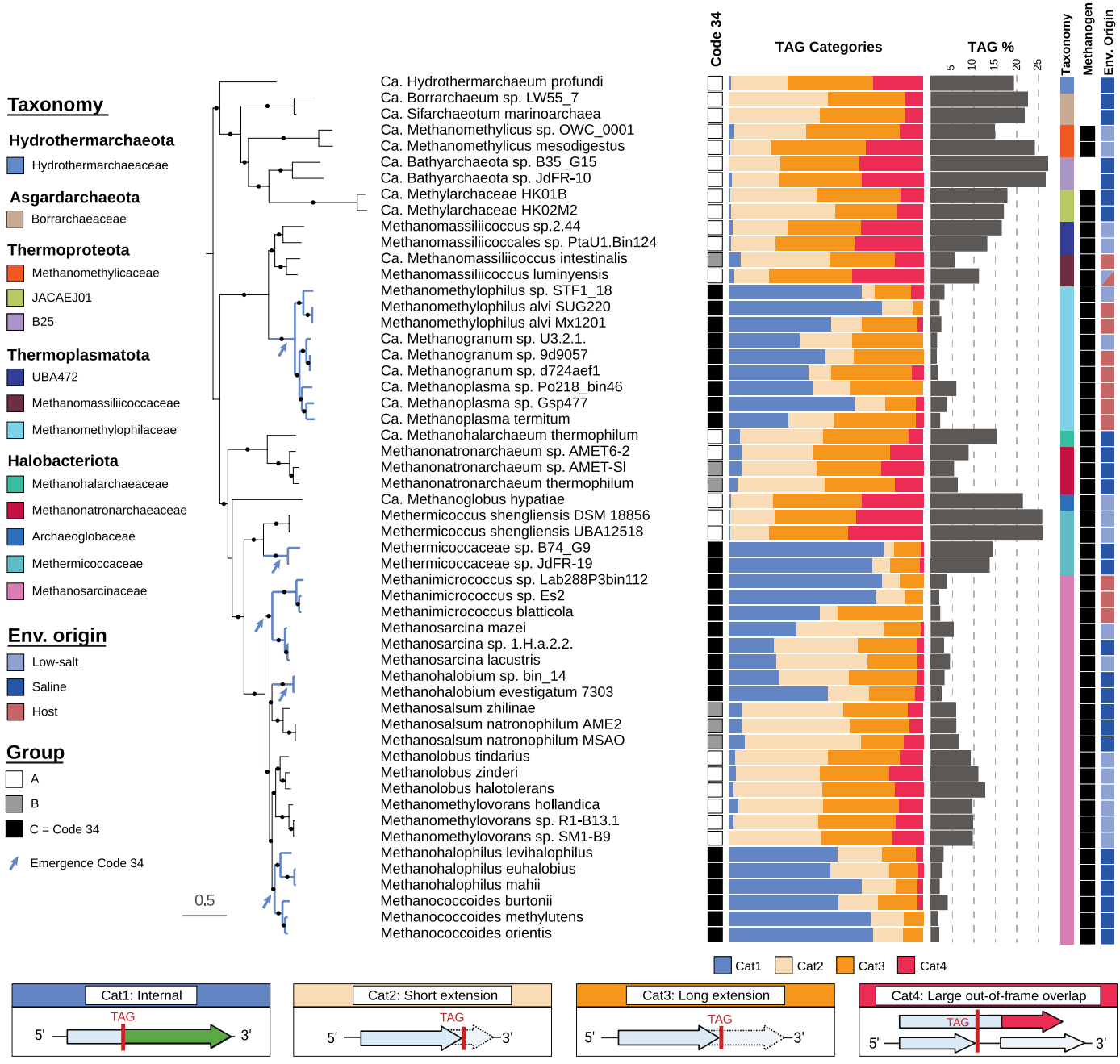

Fig. 2. Phylogenetic tree showing evidence for sporadic distribution of the Pyl code in archaea. Genomes inferred to be fully recoded (black boxes, group C) have a large fraction of internal TAG codons (category 1) and very few cases where TAG readthrough lead to large out-of-frame gene overlaps (category 4). In group A genomes, TAG content is high (>15%), whereas group B genomes typically have 5 to 15% TAG content and internal TAG in genes, in addition to the methylamine methyltransferases. Within group C, the TAG content is variable, probably due in part to the time since code transition. Tree construction used 40 universally conserved proteins, with 9816 positions and ultrafast bootstrap values >90% displayed.

methyltransferases (table S13), the functions of other proteins that incorporate Pyl are not consistent within or between evolutionary clades. All complete genomes with the Pyl code encode one or more of the methylamine methyltransferases, the only Pyl-containing proteins that archaea have in common. Outside of the methylamine methyltransferases, the presence of Pyl in other proteins has a narrow phylogenetic distribution (generally at the species level), suggesting that mutations leading to Pyl incorporation are not maintained. This is consistent with a neutral role for Pyl in nearly all proteins in which it occurs and suggests that the necessity of methylamine metabolism alone drove the evolution of the Pyl code. Next, we sought experimental evidence to confirm that these archaea read the TAG codon as Pyl.

Proteomic validation of the Pyl code

To test for recoding of TAG, we chose two isolates from different lineages and environments with genomes that are predicted to contain a large fraction of category 1 genes and used mass spectrometry to identify proteolytic peptides and their subsequent fragmentation whose exact masses confirmed the presence of a Pyl residue. *Methanococcoides burtonii* is a psychrophilic Halobacteriota from an

Antarctic lake (*41*), and *Methanomethylophilus alvi* (formerly *M. alvus*) is a Thermoplasmatota from the human gut (*27*, *42*). To increase the probability of detection of the specific peptides of interest, we used both trypsin and endoproteinase Glu-C, which cleave between different amino acids and thus increased the number of peptides suitable for analysis. Pyl-containing tryptic or GluC-fragments will be observed only if two criteria are met: The Pyl-containing protein is sufficiently abundant, and the Pyl-containing fragment(s) possesses the appropriate mass and charge to be detected. Although comprehensive detection of all peptides is not possible owing to their variable abundance, searching specifically for peptides of interest based on their predicted masses (targeted peptide detection) greatly improved our ability to identify Pyl-containing peptides (see Materials and methods). Peptides with the mass-to-charge ratio (m/z) expected for a Pyl-containing tryptic or GluC-product were manually validated by analysis of the tandem mass spectrometry (MS/MS) spectra.

For both *M. burtonii* and *M. alvi*, the proteomic data confirmed genome-wide recoding of TAG as a sense codon (tables S14 and S15). The detection of ≥2 unique peptide matches in the global tryptic or Glu-C datasets was used to confirm protein expression (tables S14 and S15). Notably, for all proteins that were expressed and predicted to contain Pyl, and for which a proteolytic peptide (>6 and <50 amino acids) spanning the region predicted to contain Pyl was detected, the presence of Pyl was confirmed. For *M. burtonii*, peptides containing Pyl were detected in 27 of 39 expressed Pyl proteins. Similarly, for *M. alvi*, Pyl was detected in 12 of the 15 expressed Pyl proteins. Expressed proteins in which Pyl was not detected had low sequence coverage and/or had a Pyl-containing proteolytic peptide that was too short or too long for detection. As an additional confirmation of Pyl incorporation at TAG codons, de novo–assisted database searches were conducted to enable identification of any of the standard amino acids at the TAG codon. We did not detect any peptides with another amino acid in the TAG position in the de novo–assisted database searches. Pyl was detected in 24 additional proteins that had low levels of expression (<2 unique peptide matches in the global datasets). In total, Pyl was detected in 54 proteins not previously shown to contain Pyl (table S16).

Examples of proteins found to contain Pyl in *M. burtonii* include 12,18-didecarboxysiroheme deacetylase, thiouridine synthase, DNA helicase, histidine tRNA synthetase, isocitrate dehydrogenase, epimerase, glycosyltransferase, DNA polymerase, and multiple hypothetical proteins (Fig. 3A, fig. S7A, and table S15). Additionally, we observed Pyl in CRISPR-Cas1 in the *M. burtonii* proteomic data, and other archaeal genomes encode both Pyl-containing CRISPR-Cas proteins and RNA-guided nucleases that have been missed or misannotated in previous studies (fig. S8 and table S17). Pyl proteins in *M. alvi* include a transacetylase-like protein, a methyltransferase, a kinase, an acetyltransferase, hypothetical and domain of unknown function (DUF)–containing proteins, and an ATPases associated with various cellular activites (AAA) family protein (Fig. 3B and table S14). Pyl was also identified in trimethylamine methyltransferase (fig. S7B), as previously reported (*10*, *36*). Thus, we conclude that *M. burtonii* and *M. alvi* archaea have adopted a nonstandard genetic code with 62 sense codons encoding 21 amino acids and only two stop codons. It is probable that the other Pyl-encoding archaea for which we detected evidence for numerous internal TAG codons (category 1) also use the Pyl code.

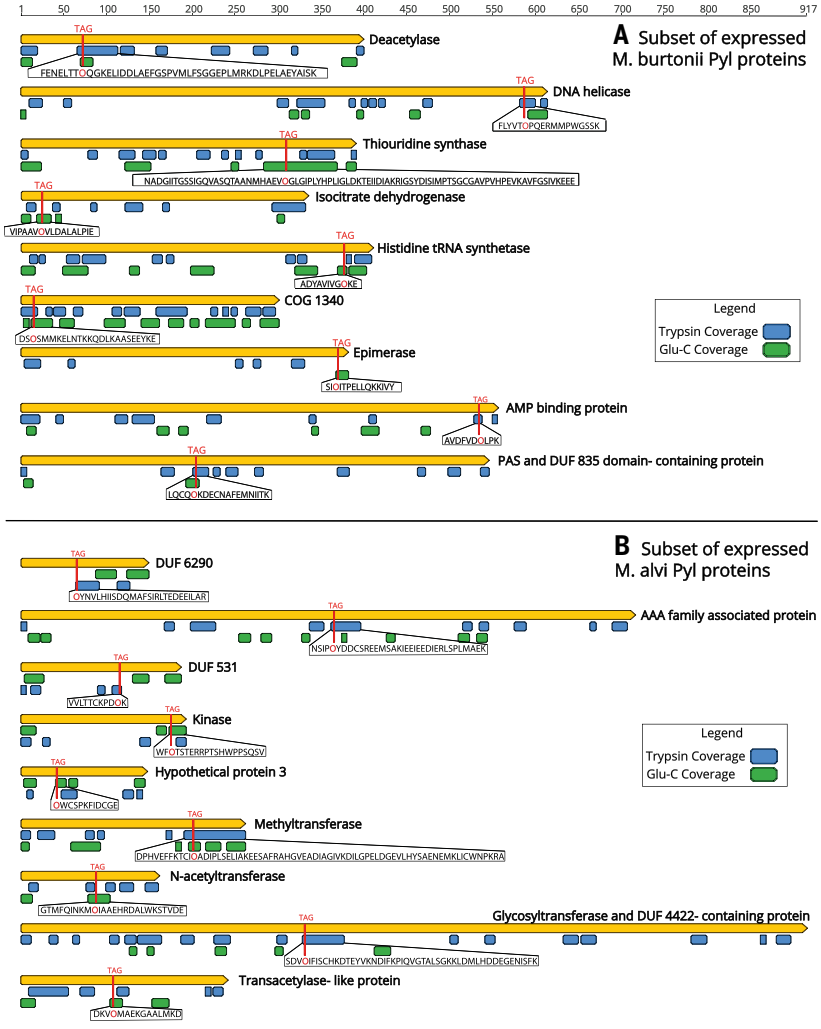

Fig. 3. Proteomic coverage confirms the presence of Pyl residues and extensions past TAG codons in expressed archaeal proteins. Data are shown for proteins from (**A**) *M. burtonii* and (**B**) *M. alvi*. Coverage based on enzymatic cleavage using trypsin is shown in blue, and Glu-C is shown in green. The TAG location is shown with a vertical red line, and Pyl is denoted by the one-letter abbreviation "O." Single-letter abbreviations for the amino acid residues are as follows: A, Ala; C, Cys; D, Asp; E, Glu; F, Phe; G, Gly; H, His; I, Ile; K, Lys; L, Leu; M, Met; N, Asn; P, Pro; Q, Gln; R, Arg; S, Ser; T, Thr; V, Val; W, Trp; and Y, Tyr.

PylRS/tRNA^{Pyl} pairs from Pyl-code organisms support GCE in *E. coli*

PylRS/tRNA^{Pyl} pairs enable GCE, yet their widespread use has been hindered by unpredictable stop codon suppression. Pyl-code organisms appear to have naturally overcome this challenge. The high incidence of TAG codon(s) encoding Pyl within genes of some archaeal genomes suggests a robust system for Pyl incorporation that may be leveraged for the site-specific incorporation of unnatural monomers into ribosomal products. Indeed, the PylRS/tRNA^{pyl} pairs from *Methanosarcina mazei*, *Methanosarcina barkeri*, and *M. alvi* are already widely used for GCE in bacterial, yeast, and mammalian cells (*43*). Here, we tested whether PylRS/tRNA^{Pyl} pairs from Pyl-code archaea support the incorporation of two widely used analogs of Pyl (1), the α-amino acid Boc-Lys (2) and the α-hydroxy acid HO-Boc-Lys (3) [see (1), (2), and (3) in Fig. 4A] into a model protein, superfolder green fluorescent protein (sfGFP) (*44*), containing an in-frame TAG codon located at position 3 (sfGFP-3TAG). At least one representative sequence from each recoded genus was evaluated. Eight PylRS/tRNA^{Pyl} pairs were tested for their ability to support GCE in *E. coli*,

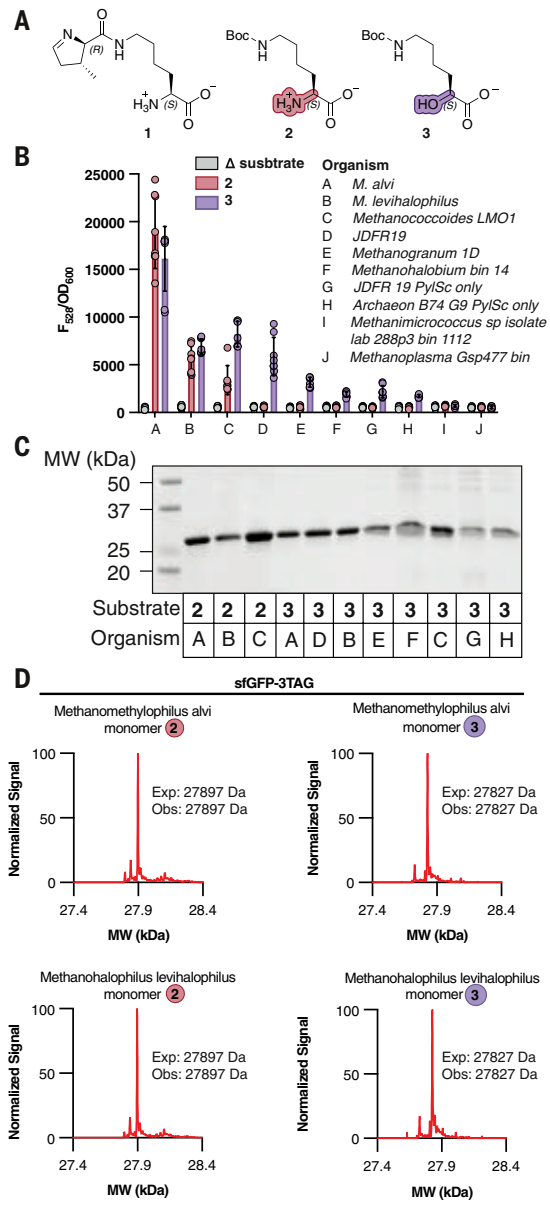

Fig. 4. PylRS variants from organisms that use the Pyl code support the incorporation of noncanonical α-amino and α-hydroxy acids into the model protein sfGFP. (**A**) Chemical structures of three established PylRS substrates: Pyl (substrate 1), the natural substrate for PylRS; Boc-Lysine (BocK; substrate 2), a synthetic α-amino acid substrate; and HO-Boc-Lysine (BocK-HO; substrate 3), an α-hydroxy acid substrate. (**B**) Shown is the F_{528} signal normalized to OD_{600} for bacterial cultures of BL21(DE3) cells doubly transformed with a pMega plasmid harboring the PylRS/tRNA^{Pyl} from candidate organisms A to J and a pET22A reporter plasmid containing sfGFP with an in-frame amber codon at position 3. Cells were grown to an OD_{600} of ~0.6 and supplemented with 1 mM of the indicated PylRS substrate, and sfGFP expression was induced with 1 mM isopropyl-β-D-thiogalactopyranoside (IPTG). The F_{528}/OD_{600} signal was acquired for more than a 20-hour time frame, and the final signal at the 20-hour timepoint is shown here. We note the presence of separately encoded PylSc and PylSn domains of the PylRS protein in the JDFR19 genus. Because prior studies have found PylRS enzymes naturally lacking PylSn to be active, we also evaluated two JDFR19 PylRS homologs with only their PylSc domain. (**C**) SDS-PAGE analysis of purified sfGFP-3TAG constructs in the presence of either 1 mM substrate 2 or 3 and the corresponding PylRS/tRNA^{Pyl} pair. (**D**) Intact MS of sfGFP-3TAG expressed in the presence of a control PylRS/tRNA^{Pyl} pair (from *M. alvi*) or in the presence of the best-performing candidate PylRS/tRNA^{Pyl} pair (*M. levihalophilus*) as determined by expression tests in (B). sfGFP was expressed in the presence of 1 mM substrate 2 or 3. MW, molecular weight.

using the PylRS/tRNA^{Pyl} pair from *M. alvi* as a benchmark for present GCE efficiency levels. Initial screenings evaluated whether organisms supplemented with Boc-Lys (2) or HO-Boc-Lys (3) developed higher levels of sfGFP fluorescence (F_{528}) as a function of cell growth [optical density at 600 nm (OD_{600})] over 20 hours (Fig. 4B and fig. S9). When BL21(DE3) *E. coli* were supplemented with Boc-Lys (2), the PylRS/tRNA^{Pyl} pairs from *M. alvi* and *Methanohalophilus levihalophilus* developed substantial levels of sfGFP compared with nonsupplemented growths, whereas the PylRS/tRNA^{Pyl} pair from *Methanococcococides LMO-1* supported moderate sfGFP expression. SDS–polyacrylamide gel electrophoresis (SDS-PAGE) analysis of sfGFP-3TAG proteins expressed in BL21(DE3) *E. coli* supplemented with either 1 mM of Boc-Lys (2) or HO-Boc-Lys (3) indicates that the major protein product has a molecular mass of ~27 kDa, the expected molecular weight of sfGFP (Fig. 4C and fig. S10). Liquid chromatography–mass spectrometry (LC-MS) analysis of intact sfGFP-3TAG purified from cells expressing the PylRS/tRNA^{Pyl} pair from *M. alvi* and *M. levihalophilus* confirmed the introduction of Boc-Lys (2) or HO-Boc-Lys (3) into sfGFP-3TAG (Fig. 4D). The activity of the PylRS/tRNA^{Pyl} pair from *M. levihalophilus* is sufficient to support robust GCE with α-amino acid and α-hydroxy acid Pyl analogs in *E. coli*.

A surprising result was the greater effectiveness of some PylRS/tRNA^{Pyl} pairs for incorporation of α-hydroxy acid HO-Boc-Lys (3) than the α-amino acid Boc-Lys (2). In particular, the PylRS/tRNA^{Pyl} pairs from Methanomicrobia JDFR-19 and *Methanogranum* 1D supported sfGFP expression only in the presence of HO-Boc-Lys (3). This finding is important because, unlike Boc-Lys (2), HO-Boc-Lys (3) generates an ester linkage within the protein backbone. Site-specific ester linkages can be exploited to posttranslationally edit the protein backbone to introduce backbone elements that cannot otherwise be introduced in cells, such as β^2-, γ-, and δ-amino acid linkages (*45*) and reactive 1,3-diketones (*46*). LC-MS analysis of intact sfGFP-3TAG purified from large-scale *E. coli* growths expressing PylRS/tRNA^{Pyl} pairs from JDFR 19 and *Methanogranum* 1 as well as *Methanohalobium* bin 14 and supplemented with α-hydroxy acid HO-Boc-Lys (3) showed unambiguous evidence for the ester linkage (Fig. 4C and fig. S11). The selectivity for an α-hydroxy acid substrate by the PylRS/tRNA^{Pyl} pairs identified here avoids well documented problems (*47*, *48*) associated with metabolic conversion of α-hydroxy acids into α-amino acids that would circumvent posttranslational backbone editing (*45*, *46*).

Discussion

The patterns of TAG use in archaea that incorporate Pyl suggest steps in the process by which the Pyl code is established (fig. S12). We propose an early stage, represented by group A; an intermediate stage, represented by group B; and a final stage, with genome-wide reassignment of the TAG codon, represented by group C (Fig. 2).

Group A is characterized by internal TAG codons exclusively in the methylamine methyltransferases and high TAG codon frequencies, similar to those in archaea that lack the Pyl system (Fig. 1). Additional features of group A are patchy taxonomic distribution of the Pyl machinery and incongruence between Pyl machinery and organismal phylogenies. These traits are consistent with recent acquisition of the Pyl cassette, potentially by lateral gene transfer. Upon acquisition of the Pyl system, TAG codons that were used exclusively as stop codons may be interpreted as Pyl. Unintended stop codon readthrough can be mitigated or prevented by tandem stop codons that can reduce extension after TAG readthrough. Substrate-dependent transcriptional regulation can minimize TAG readthrough, as some organisms downregulate Pyl machinery when not grown on methylamines (*20*, *49*). Finally, archaeal release factor 1 (which recognizes TGA, TAG, and TAA) is present in all complete and near-complete archaeal genomes examined and may compete with the Pyl tRNA for the TAG codon.

A second, transitory stage in the evolution of the Pyl code, exemplified by group B genomes, involves the progressive reduction of TAG

codons to reduce stop codon readthrough and a higher prevalence of internal (category 1) TAG codons compared with group A (Fig. 2 and fig. S13). The organisms in this group are obligate methylotrophic or methyl-reducing methanogens in environments where methylamine is highly available, such as saline environments, where they are produced from osmoprotectant degradation, and the animal gut, where methylamine precursors are abundant in certain diets (*50*).

At the third and final stage, group C genomes have fully recoded TAG to a sense codon. The defining feature of group C archaea are abundant internal (category 1) TAG codons, usually coupled with low TAG frequencies. Similar to group B, group C archaea are methanogens specialized in methyl-compound utilization and generally live in methylamine-rich environments. The constant requirement for Pyl in methylamine methyltransferases may enable loss of Pyl regulation, leading to insertion of TAG in many genes, including those essential for function. Critically, the insertion of TAG in essential genes would require constitutive expression of the Pyl machinery, even if cells grow on compounds other than methylamines. The presence of TAG in essential genes and constitutive expression of the Pyl machinery would establish the Pyl code.

Once the Pyl code has been established, code reversal would result in loss of methylamine metabolism and premature truncation of essential genes. These barriers to reversal and the sporadic distribution of the Pyl code suggest multiple independent code transitions. Ancestral character reconstruction indicates that the Pyl code may have emerged independently five times (Fig. 2). Thus, we infer that transition to the Pyl code is facile and more easily gained than lost. Interestingly, this parallels inferences of ease of code switching in some phages (*6*) and contrasts with the monophyletic pattern of bacterial recoding (*2*, *7*). A metabolic process driving the adoption of an unusual genetic code may explain why the Pyl code is not observed in bacteria, as they are generally metabolically versatile and cannot perform methanogenesis, an archaea-specific metabolism.

Despite genome-wide TAG recoding in group C archaea, Pyl is an order-of-magnitude less abundant in any proteome than the next rarest amino acid (table S18). This rarity may be because Pyl is bulky and chemically reactive and has a ring nitrogen that may introduce a positive charge into proteins at physiological pH (*38*). Thus, most mutations that introduce Pyl into organisms with Pyl machinery would be selected against. Two Methermicoccaceae (*JDFR-19*) genomes have up to four Pyl within a single protein and represent an exception regarding the low TAG frequency among the group C genomes. Given that it takes time for the proteome to accumulate Pyl in positions where it is either neutral or beneficial, we suspect that JDFR-19 underwent code transition long ago.

We found that archaea, previously not known to use more than a single genetic code, contains clades in which a genome-wide code switch has occurred such that the TAG stop codon is interpreted as Pyl. These clades, composed of group C genomes, require a translation table interpreting all TAG codons as coding for Pyl for correct protein prediction. We propose an evolutionary path to code switch and provide evidence that this code transition is relatively facile, occurring in unrelated lineages. Finally, we demonstrate the biotechnological value of the Pyl incorporation machinery from recoded genomes. Future work is needed to explore the functional role (if any) of Pyl in proteins, the mechanism by which disparate lineages acquire the Pyl machinery, and potential regulatory mechanisms in archaea that apparently do not fully recode TAG as Pyl.

Materials and methods

Identification and annotation of Pyl-encoding archaeal genomes

Genomes encoding Pyl were identified based on the presence of cellular machinery required for production and incorporation of this amino acid. A database of 14,257 archaeal genomes from GenBank with more than 60% completeness and less than 5% contamination (as estimated by CheckM) (*51*) was assembled in April 2024. For these genomes, Prodigal (*52*) v.2.6.3 was used to predict genes using default parameters (single genome mode, translation table 11), and hmmer (*53*, *54*) v.3.3.1 was used via hmmscan against the NCBI-fam database (*55*) v.13. The HMM gene annotation used to identify the Pyl pathway is as follows: TIGR03912 (PylSn), TIGR02367 (PylSc), TIGR03910 (PylB), TIGR03909 (PylC) and TIGR0391 (PylD), and Pyl-containing methyltransferases (MtmB, MtbB and MttB) using manually curated HMM profiles. For *pylT*, a HMM profile was constructed using the few previously identified *pylT* genes. Sequences were recovered together with their 10 bp flanking regions. They were aligned with known *pylT*, checked for the presence of an aligned CTA (CUA) and trimmed to remove 5′ and 3′ extra bases. Secondary structure was checked using RNAFold (*56*) and an additional trimming was performed, if needed. Sequences of *pylT* are provided with and without the CCA modification of the tail (table S4). Information on genomes identified as encoding Pyl contain at least one of the Pyl-specific genes and the detail on the presence/absence of these markers are listed in tables S2 and S3, respectively.

Taxonomic distribution and evolution of the Pyl machinery and Pyl code in archaea

The reference species tree of Archaea was built from a concatenation of the sequences of 36 universally conserved proteins from the phylosift dataset (*57*) together with sequences of L30 and S4 ribosomal proteins and of the RNA polymerase subunit A and B. Proteins were retrieved from the selected proteomes with HMM search (*53*, *54*) [hmmer v3.3.2 (http://hmmer.org/)]. They were aligned with MAFFT (v7.453) with the accuracy-oriented methods, L-INS-i (*58*), trimmed with BMGE (v2) with the Blosum30 parameter (*59*), and concatenated. A maximum likelihood tree was built with IQ-TREE (v2.0.6) (*60*) using the LG+F+R10 model. This tree was used as a guide to run the Posterior Mean-Site Frequency (PMSF) model under the LG + C60 + F + G4 model implemented in IQ-TREE (*61*) using a 1,000-replicate, ultra-fast bootstrap. Genome taxonomy was determined using GTDBTk 2.1.1 (*62*). Taxonomy, TAG categories and TAG% were mapped on the species tree using the ITOL server (*63*).

PylBCDS proteins from archaea and bacteria were separately aligned using MAFFT (*58*) and trimmed with BMGE (*59*) using the above mentioned parameters, and then concatenated. A maximum likelihood tree was built with IQ-TREE (v2.0.6) (*60*) using the LG+R9. Presence/absence of PylSn and its fusion were mapped on the tree, together with taxonomy using ITOL server (*63*). Horizontal gene transfers were predicted by comparing PylBCDS topology with the reference species tree topology.

Ancestral presence and emergence of Pyl code in archaea was determined using GLOOME (*64*). The input tree of archaea comprises 428 taxa covering the phylogenetic diversity of the domain and includes archaea inferred to use Pyl code. This species tree was built as described above.

Quantification of TAG frequency

To quantify the mean TAG frequency of archaeal taxa, Pyl-encoding genomes were dereplicated for each phylum with dRep (*65*) v.3.4.1 with default parameters. Then, Prodigal (*52*) v2.6.3 was used to predict open reading frames (ORFs) using default parameters and the -d option used for nucleotide output. The Python script “find_tag_end.py” was used to retrieve all genes with an in-frame TAG codon. The TAG frequency was calculated as the total number of predicted ORFs containing an in-frame TAG codon, divided by the total number of predicted ORFs.

Identification and quantification of genes by TAG codon category

To quantify TAG codon categories, we first extracted genes with in-frame TAG codons. NCBI genome coding sequence (CDS) files were used for gene identification. Prokka (*66*) V.1.14.5 was used for gene identification for genomes without NCBI CDS files. Each TAG codon

was treated as a sense codon, and sequences containing TAG were extended until the nearest in-frame TAA or TGA stop codon. The resulting genes were then translated and annotated using the UniProt-SwissProt database version 2023_05 and the Uniprot Archaeal and Bacterial Reference Proteome databases (*67*) version 2023_05 (8 November 2023 release). TAG- containing genes were then grouped into one of the four designated categories, based on the location of the TAG codon: (1) Internal (2) Short extension (3) Long extension/short overlap/fusion and (4) Large out-of-frame overlap. Each gene was assigned to only a single category, using the lowest category number for which criteria were satisfied. Genes that were truncated due to being located at the end of a contig were excluded when extension length could not be determined. Category 1 (Internal) genes contain an internal TAG codon, and encode proteins for which the amino acid sequence before and after the TAG codon has ≥30% sequence identity with sequences from the UniProt databases. Additionally, for category 1, the gene must also encode a protein that is >15 amino acids longer than if TAG was a stop. For category 2 (short extension), readthrough of TAG results in a protein sequence extension of ≤15 amino acids. Sequences overlapping an adjacent gene by ≥1 sense codon were excluded from category 2. The category 3 designation was assigned for genes if TAG readthrough resulted in (a) gene overlap of ≤60 nt with an adjacent gene, and/or (b) genes encoding a protein with >15 amino acid extension and/or (c) gene fusion (in-frame overlap) with an adjacent gene. Finally, TAG readthrough in category 4 genes results in overlap of an adjacent gene by >60 nt, including overlap of an entire gene in a different reading frame or oriented in the opposite direction.

Prediction and analysis of Pyl-containing proteins

We initially used the genetic code prediction tool, Codetta (*68*), to identify Pyl proteins. By default, Codetta does not detect the recoding of TAG to Pyl. First, Codetta completes a six-frame translation of a genome nucleotide sequence that is aligned to profile HMMs. The software then recognizes recoding events when a codon has a specific nonstandard interpretation based on profile HMM alignments. For Codetta to complete this task, there must be a primary meaning that can be deduced from the alignments. For example, Codetta detected reassignment of AGG (a canonical arginine codon) to methionine (*69*). When TAG is recoded to Pyl, TAG occurs in place of different codons such that there is no consensus for which codon it replaces. Thus, Codetta does not determine a single amino acid (re)interpretation for TAG. Identification of known Pyl proteins may be enabled with Codetta, but Pyl detection in this case is limited exclusively to methylamine methyltransferases because they are the only proteins with Pyl- containing profile HMMs that are available for Codetta. However, the alignment output produced by Codetta includes gene matches (profile HMMs) for each codon, including TAG. Using this Codetta alignment output, we identified Pyl-containing proteins when TAG is internal in a gene in a Pyl code genome. We implemented the alignment step using the Codetta v.2.0 codetta_align.py command with a compatible profile HMM database prepared with the hmmer (*53*, *54*) v.3.1 hmmbuild command (–enone option) for the PGAP (*55*) v.15 database, which includes TIGRFAM (*70*) v.15.0 entries.

A secondary annotation for ORFs was performed by modifying the protein prediction software, Prodigal, to include TAG as a sense codon in the archaeal genetic code. The modified version of Prodigal is available at https://github.com/VeronikaKivenson/Prodigal and can be invoked using the -g 34 (translation table 34) option. Geneious was used to visualize and overlay the standard genetic code annotation and the TAG readthrough annotation. Sequences with in-frame TAG codon(s) were searched against Blast to identify protein matches. For gene ontology (GO) enrichment analysis, GOATOOLS (*71*) v. 1.2.3 was used after protein functional annotation was performed using InterProScan (*72*) v.5.69. Fisher's Exact Test was used to determine the statistical significance of enrichment for each GO term in the study set relative to the background. The resulting *p*-values were corrected for multiple hypothesis testing using the Bonferroni, Sidak, and Holm methods. Searches for PYLIS structures were performed with Infernal (*73*) v.1.1.4 using covariance model(s) via cmsearch with the RFAM (*74*) v.14.10 database. Regions of 200 nt flanking TAG-containing genes were examined to determine if matches to the RFAM database were present. Prediction and annotation of Pyl- containing proteins was performed using the Bridges-2 computing resource (*75*).

Structural prediction of Pyl-containing proteins

Structures for homologous proteins were obtained from RCSB PDB (*76*). Structure 4AY8 was used for MtaA (*77*) and structure 7UTN was used for IscB (*78*). The Visual Molecular Dynamics software package (*79*) was used for visualization.

Anaerobic cultivation

Methanomethylophilus alvi (formerly *M. alvus*) strain Mx-05^T (JCM 31474^T) was grown as previously described (*80*), with methanol and ruminal fluid. *Methanococcoides burtonii* strain ACE-M^T (DSM 6242^T) was obtained from Deutsche Sammlung für Mikroorganismen und Zellkulturen (DSMZ) and grown on DSMZ Methanococcoides medium 141c (with 5 mM trimethylamine hydrochloride), with the following modifications: instead of Wolin's mineral solution and Wolin's vitamin solution, ATCC trace mineral supplement (MD-TMS) and ATCC Vitamin Supplement (MD-VS) were used. *M. burtonii* was grown at room temperature in 15 ml Hungate tubes with a headspace of 85% N_2, 10% CO_2, 5% H_2 gas in Anaerobe Systems anaerobic chamber (AS-150).

Sample preparation for LC-MS/MS

Twenty-milligram cell pellets were resuspended in 100 mM ammonium bicarbonate, pH 8.0 and subjected to mechanical lysis by bead beating with 0.15 mm zirconium oxide beads for five min (Geno/Grinder 2010; SPEX). Resulting cell lysates were adjusted to 4% sodium dodecyl sulfate (SDS)/10 mM dithiothreitol (DTT), incubated at 90°C for 10 min to denature and reduce proteins, and pre-cleared by centrifugation at 21,000*g*. Samples were adjusted to 30 mM iodoacetamide (Sigma) and incubated in the dark at room temperature for 20 min to alkylate cysteine residues. The alkylated proteins were further cleaned and prepared for proteolytic digestion via the protein aggregation capture (PAC) method (*81*). In brief, 300 µg of hydrophobic magnetic beads (1 micron, SpeedBead Magnetic Carboxylate; GE Healthcare UK) and acetonitrile (ACN) were added to protein samples for a final concentration of 80% ACN to induce protein aggregation on the beads. Samples were incubated for 20 min at room temperature. The aggregated proteins were placed on a magnet and the supernatant was removed. The pelleted beads were subjected to a wash with 1 ml of ACN, followed by 1 ml of 70% ethanol. The final wash buffer was removed from tubes and the beads were resuspended in 200 µl of 100 mM ammonium bicarbonate for in-solution proteolytic digestion. Protein amounts were quantified by corrected absorbance (Scopes) at 205 nm (NanoDrop OneC; Thermo Fisher). After protein quantitation, samples were digested using either MS-grade GluC Endoproteinase or trypsin (Thermo Scientific) with a 1:75 protease:protein (wt:wt) ratio at 37°C, shaking overnight at 600 rpm. An additional round of protease was added for a second 3-hour digestion period at 37°C, shaking at 600 rpm. The resulting tryptic peptides were filtered on 10 kDa MWCO filter plate (AcroPrep Advance, Omega 10 K MWCO) at 1500*g* and adjusted to 1% formic acid before quantification by NanoDrop OneC.

LC-MS/MS

Three micrograms of peptide solution were analyzed by automated 1D LC-MS/MS analysis using a Vanquish ultra-HPLC (uHPLC) system plumbed directly in-line with a QExactive-Plus mass spectrometer (Thermo Scientific) with an in-house-pulled 100 µm inner diameter nanospray emitter [packed to 15 cm with 1.7 µm Kinetex C18 reverse-phase

resin (Phenomenex)]. Peptides were loaded, desalted, and separated by uHPLC under the following conditions: sample injection followed by 100% solvent A (98% H_2O, 2% acetonitrile, 0.1% formic acid) from 0 to 30 min to load and desalt, a linear gradient from 0 to 30% solvent B (70% acetonitrile, 30% water, 0.1% formic acid) from 30 to 220 min for separation, a column wash from 0 to 100% solvent B from 220 to 255 min, and 100% solvent A from 255 to 275 min for column reequilibration. Eluting peptides were analyzed with the following MS settings for global searches: positive mode, data-dependent acquisition, top-20 method; mass range 400–1500 m/z; MS and MS/MS resolution 70 and 17.5 K, respectively; MS/MS loop count 20; isolation window 1.8 m/z; isolation offset 0.3 m/z; charge state exclusion of unassigned, +1, +6–8 charges.

For targeted searches, parallel reaction monitoring inclusions lists were constructed to detect peptides of interest in the predicted pyrrolysine containing proteins. An in-silico digest of the proteins was conducted with UniPept (*82*) using either GluC or trypsin as the protease with a minimum peptide length of six amino acids. Based on the predicted peptides from the in silico digest, peptides were selected for the PRM measurements if they were classified as any of the following peptide types: (1) the first proteolytic peptide in the protein, (2) the proteolytic peptide containing the pyrrolysine residue, (3) the first proteolytic peptide downstream of the pyrrolysine-containing peptide, and (4) the last proteolytic peptide in the sequence. For the peptides of interest, the PRM inclusion list included the monoisotopic precursor m/z of the peptide including a static modification of carbamidomethylation (+57.021) of cysteine and a charge state (z) of +2. No variable modifications of oxidation (+15.995) of methionine, deamidation of (+0.984) of asparagine and glutamine, or methyl loss (−14.016) for pyrrolysine were considered for the inclusion list. A maximum of 50 entries were monitored for each PRM measurement. The same LC-MS/MS method was used as the global measurements.

Proteomics data analysis

Global database searches were conducted with Proteome Discoverer 3.0 (Comet/Percolator) (*83*, *84*) against custom organism specific protein databases constructed from all predicted proteins in the respective, as well as common mass spectrometry contaminants. Protein sequences were included with the predicted pyrrolysine residue represented with "X" as well as the sequence version that terminated in a stop codon. For all database searches, the peptide mass tolerance was set at 20 ppm. Accepted modifications included static modifications of carbamidomethylation (+57.021) of cysteine residues and pyrrolysine (+237.148) of "X" residues. Database searches were performed with variable modifications of oxidation (+15.995) of methionine, deamidation of (+0.984) of asparagine and glutamine residues, and a methyl loss (−14.016) for pyrrolysine (X) residues, and a maximum of three variable modifications allowed per peptide. Semi-proteolytic digestion of peptides was allowed for either trypsin or GluC depending on the sample, and a 1% peptide-level FDR threshold was applied.

Preliminary confirmation of pyrrolysine expression was based on (1) a unique peptide match in the global datasets that passed the 1% peptide-level FDR threshold for the pyrrolysine containing proteins or (2) a detected precursor mass in the PRM measurement that was within 10 ppm of the monoisotopic precursor m/z of the peptides of interest. Peptides were considered unique if the amino acid sequence was not predicted in any other protein for the respective organism. To more confidently confirm pyrrolysine expression, MS/MS spectra from all peptides of pyrrolysine-containing proteins were manually inspected and validated. A MS/MS spectrum of a peptide was considered for evidence of pyrrolysine expression if each of following criteria was met: (1) Precursor ion (MS1) mass error <10 ppm, (2) Fragmentation ion (MS/MS) mass error <0.02 Da and (3) Location of the fragment ion along the peptide sequence, with either direct sequencing of the fragment ending in pyrrolysine or fragment ions that were longer than the pyrrolysine-containing fragment.

In addition to the database searches, we searched the data using a de novo–assisted database search workflow using PEAKS StudioX (*85*) to recognize any of the standard amino acids at the TAG=pyrrolysine/stop position (represented as "X" in the database). This workflow will recognize the 20 standard amino acids if they were detected at the Pyl position in the MS/MS spectrum. The same modifications as previous database searches were included and the parent and fragment ion mass error tolerances were set to ± 10 ppm and ±0.02 Da, respectively. De novo only parameters were left at default settings with average local confidence (ALC) scores of >80% and de novo sequence tags displayed if at least six amino acids were shared with the database sequence.

Construction of plasmids encoding PylRS/tRNA^{Pyl} pairs

Plasmids encoding the PylRS/tRNA^{Pyl} pairs evaluated in Fig. 4 were derivatives of the previously reported pMEGA vector (parent backbone Addgene Plasmid no. 200225). pMEGA plasmids containing each PylRS homolog (table S19) were ordered as circular, dsDNA plasmids from Twist Bioscience. Each one was then modified to eliminate the M. alvi pylT gene and replace it with the one corresponding to each PylRS homolog (table S19). Briefly, each circular pMEGA vector obtained from Twist was linearized using oligonucleotides P1 and P2 (table S19). PCR using the Q5 High-Fidelity 2X Master Mix (NEB M0492S) was performed for 30 cycles according to manufacturer protocols. The PCR reaction was subject to a PCR clean up with the QIAquick PCR Purification Kit (Qiagen, catalog no. 28104). The concentration of purified, linearized products was determined by absorbance at 260 nm using a NanoDrop ND-1000 Spectrophotometer. Next, 33.3 ng of each purified, linearized pMEGA plasmid was combined with 100 ng of a gBlock containing the appropriate pylT sequence (table S19) in a 20 μl Gibson Assembly reaction using HiFi DNA Assembly Master Mix (NEB, catalog no. E2621L). The reaction mixture was incubated at 50°C for 1 hour to generate a family of circular pMEGA vectors containing the coding sequence for the appropriate pylT.

The circularized pMega plasmids from the previous step were then transformed into NEB 5-alpha competent *E. coli* (NEB, catalog no. C2987H) as follows. Frozen stocks of cells were thawed on ice for 10 min. Upon thawing, the entirety of the previous Gibson Assembly reaction was added to cells and incubated on ice for 30 min. Cells incubated with plasmid were then subjected to heat shock at 42°C for 30 s and placed on ice for 2 min. Then, 350 μl of Super Optimal broth with Catabolite repression (S.O.C.) outgrowth medium (NEB, catalog no. B9020S) was added to cells and cells were incubated at 37°C for 1 hour with shaking at 220 rpm. Agar plates containing spectinomycin were inoculated with 50 μl of transformed cells and grown overnight at 37°C. Three single colonies per construct were picked and inoculated into liquid cultures containing 5 ml LB with spectinomycin and grown for 16 hours at 37°C. Pure plasmid was isolated from 5 ml cultures using Qiaprep Spin Miniprep Kit (Qiagen, catalog no. 27106) and sequences were confirmed by whole plasmid sequencing with Primordium Labs. The new pMEGA plasmids were double transformed with a pET22b-3TAG-GFP into BL21(DE3) cells following the transformation protocol detailed below.

Transformation protocol

BL21(DE3) *E. coli* (NEB, catalog nos. C2987H and C2527H, respectively) were transformed in accordance with manufacturer protocols with some modifications as follows. Frozen stocks were thawed on ice. Upon thawing, 100 ng of each relevant plasmid was added. After a 30 min incubation on ice, cells were heat-shocked for 30 s at 42°C and allowed to recover on ice for 2 min. Then, 350 μl of Super Optimal broth with Catabolite repression (S.O.C.) was immediately added and cells were allowed to recover at 37°C with shaking for 1 hour before plating 50 μl

on LB agar plates containing the appropriate antibiotics. Plates were incubated overnight at 37°C.

Expression assays of sfGFP-3TAG containing Boc-Lys or HO-Boc-Lys

Starter *E. coli* cultures were grown overnight in 5 ml of LB Miller (AmericanBio, catalog no. AB01201) in 15 ml culture tubes supplemented with carbenicillin and spectinomycin at 37°C. The next morning, 500 µl of the saturated overnight culture was added to 50 ml LB in a 250 ml baffled flask with carbenicillin and spectinomycin and grown at 37°C to an OD_{600} of 0.6. Prior to cultures reaching OD_{600} 0.6, the appropriate amount of each monomer (stored as 25 mM stocks) were allotted into the wells of a black, clear bottom, 96-well plate (1 mM final concentration). Once cultures reached an OD_{600} of 0.6 (roughly 3 hours), protein expression was induced by addition of 1 mM IPTG. The culture was transferred into the wells of the plate to a total volume of 200 µl in each well. A Breathe-Easy sealing membrane (Sigma Z380059) was placed over the 96-well plate and the plate was loaded into a BioTek Synergy HTX microplate reader with no lid. OD_{600} and F_{528} values (λ_{ex} = 485 nm) were measured every 10 min for 20 hours. The plate was maintained at 37°C and was shaken during this time. Points represented in Fig. 4B represent three biological replicates where three random colonies were picked on a plate from a single transformation.

Expression and purification sfGFP-3TAG containing Boc-Lys or HO-Boc-Lys

Starter cultures of 5 ml of Miller's LB Broth (AmericanBio, catalog no. AB01201) supplemented with carbenicillin and spectinomycin were inoculated with a single colony of BL21(DE3) *E. coli* cells harboring pET22b-sfGFP-3TAG-6xHis alongside pMEGA-JDFR19-PylRS-pylT, pMEGA-JDFR19-PylRSCTD-pylT, pMEGA-B74G9-PylRSCTD-pylT, pMEGA-LMO1-PylRS-pylT, pMEGA-Bin14-PylRS-PylRS-pylT, pMEGA-1D-PylRS-pylT, pMEGA-Levihalophilus-PylRS-pylT, or pMEGA-MaPylRS and grown overnight for 16 hours at 37°C with shaking at 220 rpm until the culture was saturated. The starter culture was used to inoculate a 100 ml expression culture in a 1:100 dilution of Miller's LB Broth supplemented with 1 mM Boc-Lys (Combi-Blocks, CAS no. 2418-95-3) or 1 mM HO-Boc-Lys (Accela, CAS no. 111223-31-5) with carbenicillin and spectinomycin. The expression culture was grown at 37°C with shaking at 220 rpm to an OD_{600} of 0.6 at which point it was induced with 1 mM IPTG and grown for 16 hours under the same conditions. The expression culture was harvested by centrifugation at 4300*g* at 4°C for 30 min. The resulting cell pellet was suspended in 10 ml of Lysis Buffer (50 mM sodium phosphate pH 6.8 and 300 mM NaCl) containing half a tablet of cOmplete, mini EDTA-free ULTRA protease inhibitor cocktail (Sigma-Aldrich, St. Louis, MO). The cell suspension was disrupted by sonication on ice (Branson Sonifier 250, 5 cycles of 30 s pulse at 50% duty cycle and microtip limit of 5 followed by 30 s pause). The cell lysate was cleared by centrifugation at 10,000*g* at 4°C for 20 min. TALON Metal Affinity Resin (1 ml) (Takara Biosciences, catalog no. 635504) was equilibrated with Lysis Buffer, added to the cleared cell lysate, and incubated on a rotisserie at 4°C for 1 hour. The TALON resin-lysate mixture was then passed through a gravity flow Poly-Prep Chromatography Column (Bio-Rad Laboratories, Hercules, CA). Nonspecifically bound proteins were removed by washing the TALON resin with 10 ml of Lysis Buffer. The 6xHis-tagged protein was eluted by washing the TALON resin with 2 ml of Elution Buffer (50 mM sodium phosphate pH 6.8 and 250 mM imidazole). The purified protein was quantified using absorbance at 280 nm, snap frozen as single-use aliquots, and stored at −80°C. Protein yields are reported in table S20.

Intact protein LC-MS for GCE

LC-MS analysis of all protein samples were performed on an Agilent 1290 Infinity II HPLC connected to an Agilent 6530B QTOF AJS-ESI. The mobile phase for LC-MS was water and acetonitrile with 0.1% (v/v) formic acid at a flow rate of 0.4 ml/min. Each protein sample was injected onto a Poroshell 300SB-C8 column (2.1 × 75 mm, 5 µM, room temp, Agilent) and separated using a linear gradient from 5% acetonitrile for 0 to 2 min and ramping to 95% acetonitrile over 7.5 min, and then washing with 95% acetonitrile for 2 min. The following parameters were used during acquisition: Fragmentor voltage 225 V, gas temperature 300°C, drying gas flow 10 liters/min, sheath gas temperature 350°C, sheath gas flow 11 liters/min, nebulizer pressure 35 psi, skimmer voltage 65 V, Vcap 5000 V, 1 spectra/s.

REFERENCES AND NOTES

1. F. H. Crick, The origin of the genetic code. *J. Mol. Biol.* **38**, 367–379 (1968). doi: 10.1016/0022-2836(68)90392-6; pmid: 4887876
2. J. M. Bové, Molecular features of mollicutes. *Clin. Infect. Dis.* **17**, S10–S31 (1993). doi: 10.1093/clinids/17.Supplement_1.S10; pmid: 7691196
3. K. C. Wrighton *et al.*, Fermentation, hydrogen, and sulfur metabolism in multiple uncultivated bacterial phyla. *Science* **337**, 1661–1665 (2012). doi: 10.1126/science.1224041; pmid: 23019650
4. N. N. Ivanova *et al.*, Stop codon reassignments in the wild. *Science* **344**, 909–913 (2014). doi: 10.1126/science.1250691; pmid: 24855270
5. S. L. Peters *et al.*, Experimental validation that human microbiome phages use alternative genetic coding. *Nat. Commun.* **13**, 5710 (2022). doi: 10.1038/s41467-022-32979-6; pmid: 36175428
6. A. L. Borges *et al.*, Widespread stop-codon recoding in bacteriophages may regulate translation of lytic genes. *Nat. Microbiol.* **7**, 918–927 (2022). doi: 10.1038/s41564-022-01128-6; pmid: 35618772
7. J. H. Campbell *et al.*, UGA is an additional glycine codon in uncultured SR1 bacteria from the human microbiota. *Proc. Natl. Acad. Sci. U.S.A.* **110**, 5540–5545 (2013). doi: 10.1073/pnas.1303090110; pmid: 23509275
8. F. Zinoni, A. Birkmann, T. C. Stadtman, A. Böck, Nucleotide sequence and expression of the selenocysteine-containing polypeptide of formate dehydrogenase (formate-hydrogen-lyase-linked) from *Escherichia coli*. *Proc. Natl. Acad. Sci. U.S.A.* **83**, 4650–4654 (1986). doi: 10.1073/pnas.83.13.4650; pmid: 2941757
9. G. Srinivasan, C. M. James, J. A. Krzycki, Pyrrolysine encoded by UAG in Archaea: Charging of a UAG-decoding specialized tRNA. *Science* **296**, 1459–1462 (2002). doi: 10.1126/science.1069588; pmid: 12029131
10. B. Hao *et al.*, A new UAG-encoded residue in the structure of a methanogen methyltransferase. *Science* **296**, 1462–1466 (2002). doi: 10.1126/science.1069556; pmid: 12029132
11. M. A. Gaston, R. Jiang, J. A. Krzycki, Functional context, biosynthesis, and genetic encoding of pyrrolysine. *Curr. Opin. Microbiol.* **14**, 342–349 (2011). doi: 10.1016/j.mib.2011.04.001; pmid: 21550296
12. M. Rother, J. A. Krzycki, Selenocysteine, pyrrolysine, and the unique energy metabolism of methanogenic archaea. *Archaea* **2010**, 1–14 (2010). doi: 10.1155/2010/453642; pmid: 20847933
13. M. A. Gaston, L. Zhang, K. B. Green-Church, J. A. Krzycki, The complete biosynthesis of the genetically encoded amino acid pyrrolysine from lysine. *Nature* **471**, 647–650 (2011). doi: 10.1038/nature09918; pmid: 21455182
14. D. G. Longstaff, S. K. Blight, L. Zhang, K. B. Green-Church, J. A. Krzycki, In vivo contextual requirements for UAG translation as pyrrolysine. *Mol. Microbiol.* **63**, 229–241 (2007). doi: 10.1111/j.1365-2958.2006.05500.x; pmid: 17140411
15. D. D. Young, P. G. Schultz, Playing with the molecules of life. *ACS Chem. Biol.* **13**, 854–870 (2018). doi: 10.1021/acschembio.7b00974; pmid: 29345901
16. O. Namy, J.-P. Rousset, S. Napthine, I. Brierley, Reprogrammed genetic decoding in cellular gene expression. *Mol. Cell* **13**, 157–168 (2004). doi: 10.1016/S1097-2765(04)00031-0; pmid: 14759362
17. A. Théobald-Dietrich, R. Giegé, J. Rudinger-Thirion, Evidence for the existence in mRNAs of a hairpin element responsible for ribosome dependent pyrrolysine insertion into proteins. *Biochimie* **87**, 813–817 (2005). doi: 10.1016/j.biochi.2005.03.006; pmid: 16164991
18. P. O'Donoghue *et al.*, Reducing the genetic code induces massive rearrangement of the proteome. *Proc. Natl. Acad. Sci. U.S.A.* **111**, 17206–17211 (2014). doi: 10.1073/pnas.1420193111; pmid: 25404328
19. Y. Zhang, P. V. Baranov, J. F. Atkins, V. N. Gladyshev, Pyrrolysine and selenocysteine use dissimilar decoding strategies. *J. Biol. Chem.* **280**, 20740–20751 (2005). doi: 10.1074/jbc.M501458200; pmid: 15788401
20. L. Prat *et al.*, Carbon source-dependent expansion of the genetic code in bacteria. *Proc. Natl. Acad. Sci. U.S.A.* **109**, 21070–21075 (2012). doi: 10.1073/pnas.1218613110; pmid: 23185002
21. V. Kivenson, B. G. Paul, D. L. Valentine, An ecological basis for dual genetic code expansion in marine deltaproteobacteria. *Front. Microbiol.* **12**, 680620 (2021). doi: 10.3389/fmicb.2021.680620; pmid: 34335502
22. G. Borrel *et al.*, Comparative genomics highlights the unique biology of Methanomassiliicoccales, a Thermoplasmatales-related seventh order of methanogenic

archaea that encodes pyrrolysine. *BMC Genomics* **15**, 679 (2014). doi: 10.1186/1471-2164-15-679; pmid: 25124552
23. T. Mukai *et al.*, RNA-dependent cysteine biosynthesis in Bacteria and Archaea. *mBio* **8**, e00561-17 (2017). doi: 10.1128/mBio.00561-17; pmid: 28487430
24. M. M. Lynes, Z. J. Jay, A. J. Kohtz, R. Hatzenpichler, Methylotrophic methanogenesis in the *Archaeoglobi* revealed by cultivation of *Ca.* Methanoglobus hypatiae from a Yellowstone hot spring. *ISME J.* **18**, wrae026 (2024). doi: 10.1093/ismejo/wrae026; pmid: 38452205
25. Y. Guan, M. F. Haroon, I. Alam, J. G. Ferry, U. Stingl, Single-cell genomics reveals pyrrolysine-encoding potential in members of uncultivated archaeal candidate division MSBL1. *Environ. Microbiol. Rep.* **9**, 404–410 (2017). doi: 10.1111/1758-2229.12545; pmid: 28493460
26. D. Y. Sorokin *et al.*, Discovery of extremely halophilic, methyl-reducing euryarchaea provides insights into the evolutionary origin of methanogenesis. *Nat. Microbiol.* **2**, 17081 (2017). doi: 10.1038/nmicrobiol.2017.81; pmid: 28555626
27. G. Borrel *et al.*, Genome sequence of "*Candidatus* Methanomethylophilus alvus" Mx1201, a methanogenic archaeon from the human gut belonging to a seventh order of methanogens. *J. Bacteriol.* **194**, 6944–6945 (2012). doi: 10.1128/JB.01867-12; pmid: 23209209
28. K. Lang *et al.*, New mode of energy metabolism in the seventh order of methanogens as revealed by comparative genome analysis of "*Candidatus* methanoplasma termitum." *Appl. Environ. Microbiol.* **81**, 1338–1352 (2015). doi: 10.1128/AEM.03389-14; pmid: 25501486
29. J. Sun *et al.*, Recoding of stop codons expands the metabolic potential of two novel Asgardarchaeota lineages. *ISME Commun.* **1**, 30 (2021). doi: 10.1038/s43705-021-00032-0; pmid: 36739331
30. L.-T. Guo *et al.*, Ancestral archaea expanded the genetic code with pyrrolysine. *J. Biol. Chem.* **298**, 102521 (2022). doi: 10.1016/j.jbc.2022.102521; pmid: 36152750
31. B. A. Berghuis *et al.*, Hydrogenotrophic methanogenesis in archaeal phylum Verstraetearchaeota reveals the shared ancestry of all methanogens. *Proc. Natl. Acad. Sci. U.S.A.* **116**, 5037–5044 (2019). doi: 10.1073/pnas.1815631116; pmid: 30814220
32. S. P. Gilmore *et al.*, Genomic analysis of methanogenic archaea reveals a shift towards energy conservation. *BMC Genomics* **18**, 639 (2017). doi: 10.1186/s12864-017-4036-4; pmid: 28826405
33. B. N. Chaudhuri, T. O. Yeates, A computational method to predict genetically encoded rare amino acids in proteins. *Genome Biol.* **6**, R79 (2005). doi: 10.1186/gb-2005-6-9-r79; pmid: 16168086
34. C. Theil Have, S. Zambach, H. Christiansen, Effects of using coding potential, sequence conservation and mRNA structure conservation for predicting pyrrolysine containing genes. *BMC Bioinformatics* **14**, 118 (2013). doi: 10.1186/1471-2105-14-118; pmid: 23557142
35. I. U. Heinemann *et al.*, The appearance of pyrrolysine in tRNAHis guanylyltransferase by neutral evolution. *Proc. Natl. Acad. Sci. U.S.A.* **106**, 21103–21108 (2009). doi: 10.1073/pnas.0912072106; pmid: 19965368
36. J. Li *et al.*, Insights into pyrrolysine function from structures of a trimethylamine methyltransferase and its corrinoid protein complex. *Commun. Biol.* **6**, 54 (2023). doi: 10.1038/s42003-022-04397-3; pmid: 36646841
37. J.-F. Brugère, J. F. Atkins, P. W. O'Toole, G. Borrel, Pyrrolysine in archaea: A 22nd amino acid encoded through a genetic code expansion. *Emerg. Top. Life Sci.* **2**, 607–618 (2018). doi: 10.1042/ETLS20180094; pmid: 33525836
38. J. A. Krzycki, "Translation of UAG as pyrrolysine" in *Recoding: Expansion of Decoding Rules Enriches Gene Expression*, J. F. Atkins, R. F. Gesteland, Eds. (Springer, 2010), pp. 53–77.
39. E. V. Koonin, A. S. Novozhilov, Origin and evolution of the universal genetic code. *Annu. Rev. Genet.* **51**, 45–62 (2017). doi: 10.1146/annurev-genet-120116-024713; pmid: 28853922
40. B. W. Wright, M. P. Molloy, P. R. Jaschke, Overlapping genes in natural and engineered genomes. *Nat. Rev. Genet.* **23**, 154–168 (2022). doi: 10.1038/s41576-021-00417-w; pmid: 34611352
41. M. A. Allen *et al.*, The genome sequence of the psychrophilic archaeon, *Methanococcoides burtonii*: The role of genome evolution in cold adaptation. *ISME J.* **3**, 1012–1035 (2009). doi: 10.1038/ismej.2009.45; pmid: 19404327
42. G. Borrel *et al.*, *Methanomethylophilus alvi* gen. nov., sp. nov., a novel hydrogenotrophic methyl-reducing methanogenic archaea of the order *methanomassiliicoccales* isolated from the human gut and proposal of the novel family *Methanomethylophilaceae* fam. nov. *Microorganisms* **11**, 2794 (2023). doi: 10.3390/microorganisms11112794; pmid: 38004804
43. N. G. Koch, N. Budisa, Evolution of pyrrolysyl-tRNA synthetase: From methanogenesis to genetic code expansion. *Chem. Rev.* **124**, 9580–9608 (2024). doi: 10.1021/acs.chemrev.4c00031; pmid: 38953775
44. J.-D. Pédelacq, S. Cabantous, T. Tran, T. C. Terwilliger, G. S. Waldo, Engineering and characterization of a superfolder green fluorescent protein. *Nat. Biotechnol.* **24**, 79–88 (2006). doi: 10.1038/nbt1172; pmid: 16369541
45. L. T. Roe *et al.*, Site-selective protein editing by backbone extension acyl rearrangements. *Nat. Chem. Biol.* **21**, 1621–1630 (2025). doi: 10.1038/s41589-025-01999-w; pmid: 40841495
46. C. K. Schissel *et al.*, Peptide backbone editing via post-translational O to C acyl shift. *J. Am. Chem. Soc.* **147**, 6503–6513 (2025). doi: 10.1021/jacs.4c14103; pmid: 39933167
47. J. Guo, J. Wang, J. C. Anderson, P. G. Schultz, Addition of an α-hydroxy acid to the genetic code of bacteria. *Angew. Chem. Int. Ed.* **47**, 722–725 (2008). doi: 10.1002/anie.200704074; pmid: 18069708
48. R. Fricke *et al.*, Expanding the substrate scope of pyrrolysyl-transfer RNA synthetase enzymes to include non-α-amino acids in vitro and in vivo. *Nat. Chem.* **15**, 960–971 (2023). doi: 10.1038/s41557-023-01224-y; pmid: 37264106
49. M. Ferrer *et al.*, Proteomic analysis of Methanonatronarchaeum thermophilum AMET1, a representative of a putative new class of Euryarchaeota, "Methanonatronarchaeia." *Genes* **9**, 28 (2018). doi: 10.3390/genes9020028; pmid: 29360740
50. C. M. Thomas, E. Desmond-Le Quéméner, S. Gribaldo, G. Borrel, Factors shaping the abundance and diversity of the gut archaeome across the animal kingdom. *Nat. Commun.* **13**, 3358 (2022). doi: 10.1038/s41467-022-31038-4; pmid: 35688919
51. D. H. Parks, M. Imelfort, C. T. Skennerton, P. Hugenholtz, G. W. Tyson, CheckM: Assessing the quality of microbial genomes recovered from isolates, single cells, and metagenomes. *Genome Res.* **25**, 1043–1055 (2015). doi: 10.1101/gr.186072.114; pmid: 25977477
52. D. Hyatt *et al.*, Prodigal: Prokaryotic gene recognition and translation initiation site identification. *BMC Bioinformatics* **11**, 119 (2010). doi: 10.1186/1471-2105-11-119; pmid: 20211023
53. R. D. Finn, J. Clements, S. R. Eddy, HMMER web server: Interactive sequence similarity searching. *Nucleic Acids Res.* **39**, W29–W37 (2011). doi: 10.1093/nar/gkr367; pmid: 21593126
54. S. R. Eddy, Accelerated profile HMM searches. *PLOS Comput. Biol.* **7**, e1002195 (2011). doi: 10.1371/journal.pcbi.1002195; pmid: 22039361
55. W. Li *et al.*, RefSeq: Expanding the Prokaryotic Genome Annotation Pipeline reach with protein family model curation. *Nucleic Acids Res.* **49**, D1020–D1028 (2021). doi: 10.1093/nar/gkaa1105; pmid: 33270901
56. A. R. Gruber, R. Lorenz, S. H. Bernhart, R. Neuböck, I. L. Hofacker, The Vienna RNA websuite. *Nucleic Acids Res.* **36**, W70–W74 (2008). doi: 10.1093/nar/gkn188; pmid: 18424795
57. A. E. Darling *et al.*, PhyloSift: Phylogenetic analysis of genomes and metagenomes. *PeerJ* **2**, e243 (2014). doi: 10.7717/peerj.243; pmid: 24482762
58. K. Katoh, D. M. Standley, MAFFT multiple sequence alignment software version 7: Improvements in performance and usability. *Mol. Biol. Evol.* **30**, 772–780 (2013). doi: 10.1093/molbev/mst010; pmid: 23329690
59. A. Criscuolo, S. Gribaldo, BMGE (Block Mapping and Gathering with Entropy): A new software for selection of phylogenetic informative regions from multiple sequence alignments. *BMC Evol. Biol.* **10**, 210 (2010). doi: 10.1186/1471-2148-10-210; pmid: 20626897
60. B. Q. Minh *et al.*, IQ-TREE 2: New models and efficient methods for phylogenetic inference in the genomic era. *Mol. Biol. Evol.* **37**, 1530–1534 (2020). doi: 10.1093/molbev/msaa015; pmid: 32011700
61. H.-C. Wang, B. Q. Minh, E. Susko, A. J. Roger, Modeling site heterogeneity with posterior mean site frequency profiles accelerates accurate phylogenomic estimation. *Syst. Biol.* **67**, 216–235 (2018). doi: 10.1093/sysbio/syx068; pmid: 28950365
62. P.-A. Chaumeil, A. J. Mussig, P. Hugenholtz, D. H. Parks, GTDB-Tk v2: Memory friendly classification with the genome taxonomy database. *Bioinformatics* **38**, 5315–5316 (2022). doi: 10.1093/bioinformatics/btac672; pmid: 36218463
63. I. Letunic, P. Bork, Interactive Tree of Life (iTOL) v6: Recent updates to the phylogenetic tree display and annotation tool. *Nucleic Acids Res.* **52**, W78–W82 (2024). doi: 10.1093/nar/gkae268; pmid: 38613393
64. O. Cohen, H. Ashkenazy, F. Belinky, D. Huchon, T. Pupko, GLOOME: Gain loss mapping engine. *Bioinformatics* **26**, 2914–2915 (2010). doi: 10.1093/bioinformatics/btq549; pmid: 20876605
65. M. R. Olm, C. T. Brown, B. Brooks, J. F. Banfield, dRep: A tool for fast and accurate genomic comparisons that enables improved genome recovery from metagenomes through de-replication. *ISME J.* **11**, 2864–2868 (2017). doi: 10.1038/ismej.2017.126; pmid: 28742071
66. T. Seemann, Prokka: Rapid prokaryotic genome annotation. *Bioinformatics* **30**, 2068–2069 (2014). doi: 10.1093/bioinformatics/btu153; pmid: 24642063
67. A. Bateman *et al.*, UniProt: The universal protein knowledgebase in 2021. *Nucleic Acids Res.* **49**, D480–D489 (2021). doi: 10.1093/nar/gkaa1100; pmid: 33237286
68. Y. Shulgina, S. R. Eddy, Codetta: Predicting the genetic code from nucleotide sequence. *Bioinformatics* **39**, btac802 (2023). doi: 10.1093/bioinformatics/btac802; pmid: 36511586
69. Y. Shulgina, S. R. Eddy, A computational screen for alternative genetic codes in over 250,000 genomes. *eLife* **10**, e71402 (2021). doi: 10.7554/eLife.71402; pmid: 34751130
70. D. H. Haft *et al.*, TIGRFAMs and Genome Properties in 2013. *Nucleic Acids Res.* **41**, D387–D395 (2013). doi: 10.1093/nar/gks1234; pmid: 23197656
71. D. V. Klopfenstein *et al.*, GOATOOLS: A Python library for Gene Ontology analyses. *Sci. Rep.* **8**, 10872 (2018). doi: 10.1038/s41598-018-28948-z; pmid: 30022098
72. P. Jones *et al.*, InterProScan 5: Genome-scale protein function classification. *Bioinformatics* **30**, 1236–1240 (2014). doi: 10.1093/bioinformatics/btu031; pmid: 24451626
73. E. P. Nawrocki, S. R. Eddy, Infernal 1.1: 100-fold faster RNA homology searches. *Bioinformatics* **29**, 2933–2935 (2013). doi: 10.1093/bioinformatics/btt509; pmid: 24008419

74. I. Kalvari *et al.*, Rfam 14: Expanded coverage of metagenomic, viral and microRNA families. *Nucleic Acids Res.* **49**, D192–D200 (2021). doi: 10.1093/nar/gkaa1047; pmid: 33211869
75. S. T. Brown *et al.*, "Bridges-2: A platform for rapidly-evolving and data intensive research" in *Proceedings PEARC '21: Practice and Experience in Advanced Research Computing 2021: Evolution Across All Dimensions* (Association for Computing Machinery, 2021), art. 35.
76. H. M. Berman *et al.*, The Protein Data Bank. *Nucleic Acids Res.* **28**, 235–242 (2000). doi: 10.1093/nar/28.1.235; pmid: 10592235
77. A. Hoeppner *et al.*, Structure of the corrinoid:coenzyme M methyltransferase MtaA from Methanosarcina mazei. *Acta Crystallogr. D Biol. Crystallogr.* **68**, 1549–1557 (2012). doi: 10.1107/S090744491203853X; pmid: 23090404
78. G. Schuler, C. Hu, A. Ke, Structural basis for RNA-guided DNA cleavage by IscB-ωRNA and mechanistic comparison with Cas9. *Science* **376**, 1476–1481 (2022). doi: 10.1126/science.abq7220; pmid: 35617371
79. W. Humphrey, A. Dalke, K. Schulten, VMD: Visual molecular dynamics. *J. Mol. Graph.* **14**, 33–38, 27–28 (1996). doi: 10.1016/0263-7855(96)00018-5; pmid: 8744570
80. A. Hocher *et al.*, Growth temperature and chromatinization in archaea. *Nat. Microbiol.* **7**, 1932–1942 (2022). doi: 10.1038/s41564-022-01245-2; pmid: 36266339
81. T. S. Batth *et al.*, Protein aggregation capture on microparticles enables multipurpose proteomics sample preparation. *Mol. Cell. Proteomics* **18**, 1027–1035 (2019). doi: 10.1074/mcp.TIR118.001270; pmid: 30833379
82. B. Mesuere *et al.*, High-throughput metaproteomics data analysis with Unipept: A tutorial. *J. Proteomics* **171**, 11–22 (2018). doi: 10.1016/j.jprot.2017.05.022; pmid: 28552653
83. J. K. Eng, T. A. Jahan, M. R. Hoopmann, Comet: An open-source MS/MS sequence database search tool. *Proteomics* **13**, 22–24 (2013). doi: 10.1002/pmic.201200439; pmid: 23148064
84. M. The, M. J. MacCoss, W. S. Noble, L. Käll, Fast and accurate protein false discovery rates on large-scale proteomics data sets with Percolator 3.0. *J. Am. Soc. Mass Spectrom.* **27**, 1719–1727 (2016). doi: 10.1007/s13361-016-1460-7; pmid: 27572102
85. N. H. Tran *et al.*, Deep learning enables de novo peptide sequencing from data-independent-acquisition mass spectrometry. *Nat. Methods* **16**, 63–66 (2019). doi: 10.1038/s41592-018-0260-3; pmid: 30573815
86. V. Kivenson, An archaeal genetic code with all TAG codons as pyrrolysine. Zenodo (2025); https://doi.org/10.5281/zenodo.15478078.

ACKNOWLEDGMENTS

We thank J.-F. Brugere, J. Rylee, and P. Penev for helpful discussions. S.G. wishes to thank the Miller Institute at UC Berkeley for a Visiting Professorship. **Funding:** This work was supported by a Tory Burch Foundation Fellowship to V.K. at the Innovative Genomics Institute. This work used Bridges-2 at the Pittsburgh Supercomputing Center through allocation BIO230230 to V.K., from the Advanced Cyberinfrastructure Coordination Ecosystem: Services & Support (ACCESS) program, which is supported by National Science Foundation (NSF) grant nos. 2138259, 2138286, 2138307, 2137603, and 2138296. L.T.R. was supported by the NSF Graduate Research Fellowship Program (DGE-1752814). Experimental validation of PylRS activity for α-amino and α-hydroxy acids was supported by the NSF Center for Genetically Encoded Materials (C-GEM; CHE 2002182). Funding was provided by the Chan-Zuckerberg Initiative Foundation, Technology Enabled Biological Carbon Capture and Sequestration (CZIF2022-007203), and NSF Collaborative Research: TRTech-PGR Track (2334028) to J.F.B. G.B. was supported by Agence Nationale de la Recherche (ANR-19-CE02-0005). Research in S.G.'s laboratory is supported by the Fondation pour la Recherche Médicale (Programme equipes FRM EQU202203014614). Proteome work done at Oak Ridge National Laboratory was supported by a US Department of Energy Genome Sciences Program project (ERKPA50). **Author contributions:** V.K. and J.F.B. conceived and designed the study. V.K. performed codon analysis, identification of Pyl proteins, and anaerobic cultivation of *M. burtonii*. G.B. prepared the genome database and identified Pyl machinery proteins and tRNA. Experimental validation of PylRS activity for α-amino and α-hydroxy acids was performed by N.X.H. and L.T.R. with oversight by A.S. Proteomics experiments and data analysis were conducted by S.L.P. with oversight by R.L.H. Phylogenetic analysis and discussion were conducted by G.B. and S.G. Structural prediction of Pyl-containing proteins and bioinformatics software development were performed by A.K. Anaerobic cultivation of *M. alvus* was performed by K.F. with oversight by G.B. The manuscript was written by V.K. and J.F.B. with input from all authors. All authors read and approved the manuscript. **Competing interests:** V.K., L.T.R., N.X.H., A.S., and J.F.B. are inventors on provisional patent application 63/698,833 submitted by the University of California, Berkeley, that covers uses of this research. **Data and materials availability:** Proteomic data from this study have been deposited into the ProteomeXchange repository with accession nos. ProteomeXchange-PXD053523 and MassIVE-MSV000095193. The modified version of Prodigal with the Pyl code that has TAG reassigned to Pyl and the python script (find_tag_end.py) can be found on Zenodo (*86*).
License information: Copyright © 2025 the authors, some rights reserved; exclusive licensee American Association for the Advancement of Science. No claim to original US government works. https://www.science.org/about/science-licenses-journal-article-reuse. This research was funded in whole or in part by Agence Nationale de la Recherche (ANR-19-CE02-0005), a cOAlition S organization. The author will make the Author Accepted Manuscript (AAM) version available under a CC BY public copyright license.

SUPPLEMENTARY MATERIALS

science.org/doi/10.1126/science.adu2404
Figs. S1 to S13; Tables S1 to S20; MDAR Reproducibility Checklist

Submitted 2 November 2024; resubmitted 27 May 2025; accepted 5 September 2025
10.1126/science.adu2404

AAAS.ORG/COMMUNITY

AAAS' Member Community is a one-stop destination for scientists and STEM enthusiasts alike. It's "Where Science Gets Social": a community where facts matter, ideas are big and there's always a reason to come hang out, share, discuss and explore.

Member COMMUNITY
AAAS

AMERICAN ASSOCIATION FOR THE ADVANCEMENT OF SCIENCE

RESEARCH ARTICLE SUMMARY

NEUROSCIENCE

The synaptic ectokinase VLK triggers the EphB–NMDAR interaction to drive injury-induced pain

Kolluru D. Srikanth†, Hajira Elahi†, Praveen Chander†, Halley R. Washburn† *et al.*

Full article and list of author affiliations: https://doi.org/10.1126/science.adp1007

INTRODUCTION: Protein phosphorylation is a central mechanism of intracellular regulation, but its function outside the cell remains poorly understood. Although the secreted milk protein casein was shown to be phosphorylated more than a century ago in the 1880s, the biological relevance of extracellular phosphorylation has remained largely unexplored. Recent studies have identified two families of secreted kinases and revealed that many synaptic proteins are phosphorylated in their extracellular domains. However, whether such phosphorylation events modulate synaptic signaling or behavior in vivo has remained an open question.

RATIONALE: We sought to define a role for extracellular phosphorylation in regulating receptor interactions at synapses. Specifically, we tested whether a secreted kinase could control the interaction between the receptor tyrosine kinase EphB2 and the *N*-methyl-D-aspartate receptor (NMDAR), a key regulator of glutamate signaling, and pain. Because EphB2 extracellular phosphorylation at the evolutionarily conserved tyrosine Y504 is required for binding to the NMDAR, we asked whether this modification might be controlled by secreted tyrosine kinases, and whether this signaling could modulate pain behaviors in vivo. Our goal was to define a synaptic signaling pathway linking presynaptic activity to extracellular receptor phosphorylation and downstream NMDAR function.

RESULTS: We identified vertebrate lonesome kinase (*VLK*/*Pkdcc*) as the only member of a six-gene ectokinase family that is both secreted and sufficient to induce EphB2–NMDAR interaction. VLK phosphorylated EphB2 at Y504 in an ATP-dependent manner, and this effect was blocked by extracellular phosphatase and absent with VLK-kinase–dead mutants. Recombinant VLK (rVLK) induced EphB2–NMDAR complex formation in cultured neurons and spinal tissue, whereas *Pkdcc* knockout abolished the interaction. VLK localized to synaptic vesicles and was released in a SNARE-dependent manner following ephrin-B stimulation or elevated neuronal activity, consistent with regulated synaptic release.

In vivo, conditional deletion of *Pkdcc* from presynaptic sensory neurons disrupted EphB2 phosphorylation and prevented EphB2–NMDAR interaction in dorsal horn projection neurons after injury, without altering baseline expression of either protein. Mice lacking VLK in sensory neurons failed to develop mechanical hypersensitivity following surgical injury but retained normal motor coordination and responses to heat and chemical stimuli. Intrathecal injection of rVLK induced EphB2–NMDAR interaction and pain-like behaviors, and this effect required NMDAR activity. Postsynaptic deletion of EphB2 in spinothalamic neurons blocked injury-induced pain behaviors, confirming the necessity of this signaling pathway for pain sensitization.

CONCLUSION: Our findings reveal an extracellular phosphorylation pathway that links presynaptic activity to postsynaptic receptor organization and behavior. By releasing a kinase that acts on the outside of the postsynaptic membrane, neurons can modulate NMDAR function in a spatially and behaviorally specific manner—without invoking canonical intracellular pathways—highlighting an underappreciated dimension of synaptic signaling that occurs in the extracellular space. Given the essential role of NMDARs in synaptic plasticity and the embryonic lethality of neuronal VLK knockout, this pathway likely extends beyond pain and may offer new therapeutic opportunities for modulating receptor function. □

Corresponding author: Theodore J. Price (theodore.price@utdallas.edu); Matthew B. Dalva (mdalva@tulane.edu) †These authors contributed equally to this work. **Cite this article as** K.D. Srikanth *et al.*, *Science* **390**, eadp1007 (2025). DOI: 10.1126/science.adp1007

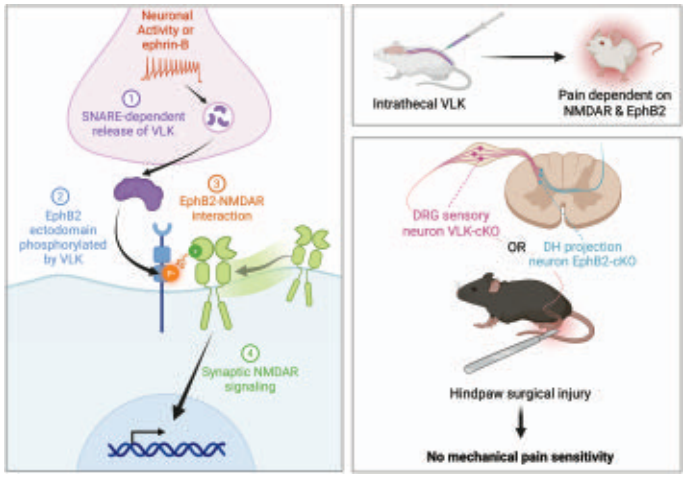

A synaptic ectokinase induces the EphB2–NMDAR interaction and mechanical hypersensitivity. (**A**) Neuronal activity or ephrin-B triggers presynaptic release of vertebrate lonesome kinase (VLK), which phosphorylates EphB2 at Y504, inducing the EphB2–NMDAR interaction and enhancing NMDAR signaling and pain-like behaviors (**B**). (**C**) In the dorsal horn, VLK from sensory neurons and EphB2 in projection neurons are required for injury-induced hypersensitivity but not motor function.

NEUROSCIENCE

The synaptic ectokinase VLK triggers the EphB2–NMDAR interaction to drive injury-induced pain

Kolluru D. Srikanth[1,2]†, Hajira Elahi[3,4,5]†, Praveen Chander[1,2]†, Halley R. Washburn[2,6]†‡, Shayne Hassler[3,7], Juliet M. Mwirigi[3,4], Moeno Kume[3,4], Jessica Loucks[3], Rohita Arjarapu[3], Rachel Hodge[2]§, Lucy He[3,4], Khadijah Mazhar[3,4], Stephanie I. Shiers[3,4], Ishwarya Sankaranarayanan[3,4], Hediye Erdjument-Bromage[8], Thomas A. Neubert[8], Patrick M. Dougherty[5], Zachary T. Campbell[9], Raehum Paik[9,10], Theodore J. Price[3,4]*, Matthew B. Dalva[1,2]*

Phosphorylation of hundreds of protein extracellular domains is mediated by two kinase families but the functional role of these kinases is underexplored. We find that the presynaptic release of the tyrosine-directed ectokinase, vertebrate lonesome kinase (VLK/*Pkdcc*), is necessary and sufficient for the direct extracellular interaction between EphB2 and GluN1 at synapses for phosphorylation of the ectodomain of EphB2 and mediation of injury-induced pain. *Pkdcc* is an essential gene in the nervous system, and VLK is enriched at synapses and released from neurons in an activity- and soluble *N*-ethylmaleimide-sensitive factor activating protein receptor (SNARE)–dependent manner to drive extracellular interactions. Our results show that presynaptic sensory neuron–specific VLK knockout attenuates postsurgical pain in mice without changing sensorimotor performance, suggesting that VLK critically regulates synaptic protein-protein interactions and acute pain in response to injury.

Mass spectrometry analysis of the extracellular domains of proteins reveals hundreds of extracellular phosphorylation events on specific serine, threonine, and tyrosine residues (*1*). Phosphorylation of these residues is thought to be mediated by two families of kinases, but the functional role of extracellular kinases in the nervous system is unknown. Biallelic loss-of-function mutations in the serine/threonine-directed FAM20C kinase results in Raine syndrome (*2*), whereas the tyrosine-directed vertebrate lonesome kinase (VLK) is an essential gene in mice (*3*). These data indicate that further exploration of the function of these proteins might shed light into an underappreciated area of biology: the regulation of synaptic plasticity and behavior through extracellular phosphorylation.

One example of the importance of extracellular phosphorylation is the interaction between Eph receptor tyrosine kinase B2 (EphB2) and *N*-methyl-D-aspartate receptor (NMDAR) that occurs at excitatory synapses throughout the brain and spinal cord (*4*, *5*). The EphB-NMDAR interaction is induced by the phosphorylation of a highly conserved extracellular tyrosine residue Y504 in the fibronectin type III (FNIII) domain of EphB2 (*6*). The direct extracellular interaction, induced by Y504 phosphorylation, between EphBs and the NMDAR, increases NMDA-type glutamate receptor channel open time and is required for the retention and clustering of normal numbers of NMDAR at synaptic sites, whereas disruption of the EphB-NMDAR interaction results in loss of NMDARs from synaptic sites (*7*–*9*). Extracellular phosphorylation of EphB2 at Y504 promotes EphB2's interaction with the N-terminal domain of GluN1 through a charge-mediated mechanism that regulates the mobility of GluN1 at synaptic sites (*5*). Phosphorylation of EphB2 at Y504 also promotes NMDAR-dependent pain in mice and is involved in acute postsurgical pain, suggesting an important physiological role for this extracellular phosphorylation in the dorsal horn of the spinal cord after injury and potentially providing pathways for new tools to reduce reliance on opioids for acute pain (*6*, *10*).

Ectokinase VLK secretion is ephrin-dependent and is sufficient and necessary for EphB2-NMDAR interaction

We hypothesized that an ectokinase might be required to induce the EphB2-NMDAR interaction by specifically phosphorylating extracellular tyrosine residues on EphB2 (*6*). To test this hypothesis, we assessed the ability of the VLK family of tyrosine-directed ectokinases to stimulate the EphB2-NMDAR interaction in cell lines, primary cortical neurons, and at spinal cord synapses from mouse and human tissue. Phosphorylation of Y504 on EphB2 occurs in the extracellular space, and ephrin-B2 stimulation of neurons releases soluble, protein-based activity that phosphorylates the EphB2 ectodomain at Y504 in an ATP-dependent manner (*6*). Therefore, we sought a protein kinase that could induce the EphB2-NMDAR interaction and that could be secreted from neurons in an ephrin-B2–dependent manner. To test whether any of the VLK-related tyrosine kinases (VLK, DIA1, DIA1R, FAM69A, FAM69B, and FAM69C) could induce the EphB2-NMDAR extracellular interaction, each of these six kinases (FLAG-tagged) was coexpressed with GluN1, GluN2B, and EphB2 in HEK293T cells. GluN1 coimmunoprecipitated with EphB2 from protein lysates only when either VLK or Fam69A was cotransfected (Fig. 1, A and B), indicating that of the six kinases, only two (VLK and FAM69A) were able to induce the EphB-NMDAR interaction.

To determine which of the kinases were secreted, each of the six kinases were overexpressed in HEK293T cells. After 24 hours, the culture media was replaced with a physiological salt solution [artificial cerebrospinal fluid (ACSF)] for 45 min. FLAG immunoprecipitation from the conditioned ACSF (cACSF) revealed that only VLK, FAM69C, and DIA1R were constitutively secreted from the HEK293T cells (Fig. 1, C and D). Thus, only VLK is secreted and able to induce the EphB-NMDAR interaction when expressed in HEK293T cells.

To determine whether endogenous VLK is secreted from neurons in an ephrin-B–dependent manner, cultured rat cortical neurons at day in vitro (DIV) 7 and induced pluripotent stem cell (iPSC)–differentiated human sensory neurons (hiSNs) were treated with either control reagents (C) or activated ephrin-B2 (eB2) for 45 min in ACSF. The secreted tyrosine-phosphorylated proteins were immunoprecipitated from the cACSF, and subsequent probing for VLK revealed that endogenous VLK was secreted by both primary rat cortical neurons and hiSNs (Fig. 1, E to H). Similarly, in cultured rat cortical neurons overexpressing VLK tagged with mCherry (VLK-mCherry), VLK was secreted upon treatment with activated ephrin-B2 (fig. S1A). Thus, in contrast to the constitutive secretion of VLK in HEK293T cells, VLK secretion from transduced or uninfected rat cortical neurons and uninfected hiSNs was regulated and elicited upon ephrin-B2 stimulation. In addition, ephrin-B2 stimulation selectively up-regulated VLK mRNA

[1]Tulane Brain Institute, Department of Cell and Molecular Biology, Tulane University, New Orleans, LA, USA. [2]Jefferson Synaptic Biology Center, Department of Neuroscience, Thomas Jefferson University, Philadelphia, PA, USA. [3]Department of Neuroscience, The University of Texas at Dallas, Richardson, TX, USA. [4]Center for Advanced Pain Studies, University of Texas at Dallas, Richardson, TX, USA. [5]Department of Pain Medicine, University of Texas MD Anderson Cancer Center, Houston, TX, USA. [6]Department of Molecular Biology, Princeton University, Princeton, NJ, USA. [7]College of Medicine, University of Houston, Houston, TX, USA. [8]Department of Neuroscience and Physiology and Neuroscience Institute, NYU Grossman School of Medicine, New York, NY, USA. [9]Department of Anesthesiology, University of Wisconsin-Madison, Madison, WI, USA. [10]Department of Genetics, University of Texas Health Science Center at San Antonio, San Antonio, TX, USA. ***Corresponding author. Email: theodore.price@utdallas.edu (T.J.P.); mdalva@tulane.edu (M.B.D.)** †These authors contributed equally to this work. ‡Present address: Temple University, Philadelphia, PA, USA. §Present address: American Association for Cancer Research, Philadelphia, PA, USA.

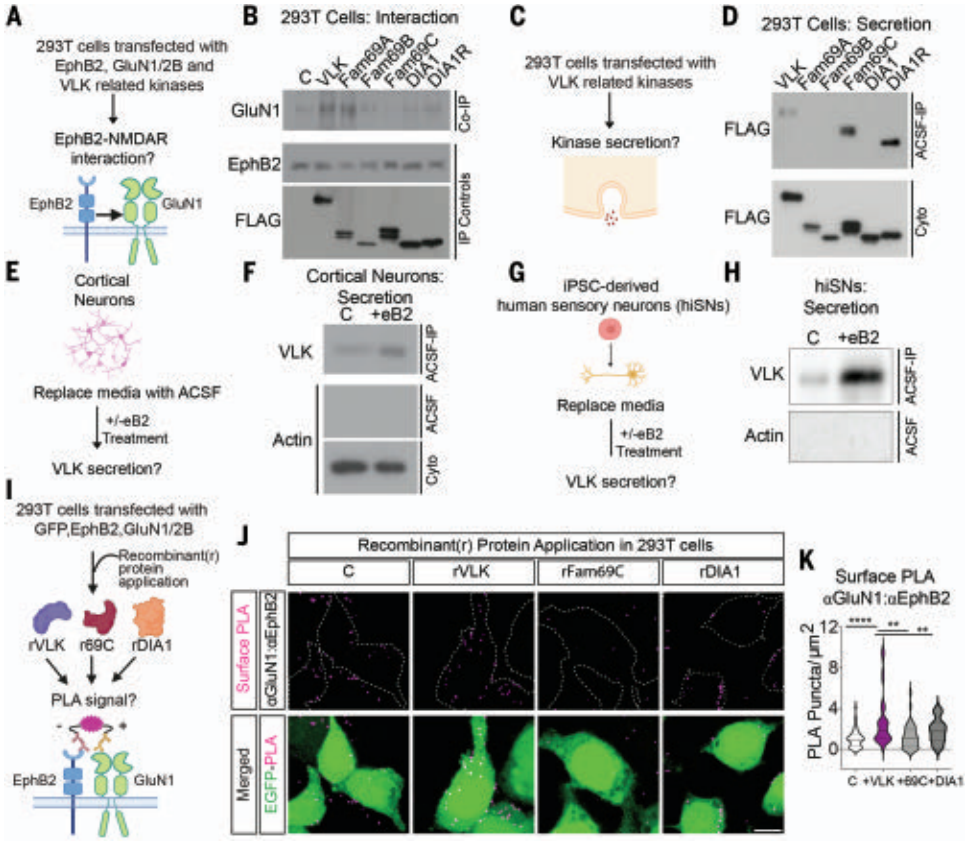

Fig. 1. VLK induces EphB2-NMDAR interaction and is secreted following ephrin-B treatment. (**A**) Schematic depicting the experimental setup to test whether VLK-related kinases can induce the EphB2-NMDAR interaction. Each FLAG-tagged VLK-related kinase was cotransfected in HEK293T cells with EphB2 and GluN1 and GluN2B and tested for EphB2-NMDAR interaction. (**B**) Immunoblotting for coimmunoprecipitated GluN1 with EphB2 in stable VLK knockdown HEK293T cells (CoIP, top). Control (C) cells were transfected with GluN1, GluN2B, and EphB2. Cells in other experimental conditions were transfected with VLK or each indicated VLK-related kinase FAM69A, FAM69B, FAM69C, DIA1, or DIA1R along with EphB2, GluN1, and GluN2B. Amounts of EphB2 immunoprecipitated from cell lysates are shown by immunoblotting for EphB2 (IP Controls, middle). Extracellular kinase expression amounts in cell lysates are shown by immunoblotting for FLAG after FLAG immunoprecipitation (FLAG, IP Controls, bottom). (**C**) Model illustrating the experimental setup to test whether VLK-related kinases can be secreted. Each FLAG-tagged VLK-related kinase was transfected in HEK293T cells and checked for their secretion. (**D**) Immunoblotting to detect the expression of secreted kinases in cell-conditioned ACSF from HEK293T cells transfected with kinases described above (ACSF-IP, top). Cell-conditioned ACSF and cell lysates (Cyto, bottom) were immunoprecipitated with a monoclonal anti-FLAG antibody and immunoblotted with a polyclonal anti-FLAG antibody. (**E**) Model depicting the experimental setup to test whether VLK can be secreted from cortical neurons upon ephrin-B (eB2) stimulation. (**F**) Untransfected cultured rat cortical neurons (DIV 7 to 8) treated with clustered ephrin-B2 (+eB2) or with its respective control (C) reagents in ACSF for 45 min. Phospho-tyrosine–specific antibody pY99 was used to immunoprecipitate conditioned ACSF and immunoblotted with a custom-generated VLK antibody (ACSF-IP, top). Conditioned ACSF (ACSF, middle) and cell lysates (Cyto, bottom) were probed with beta-actin as a control to show that the conditioned media was free of any intracellular protein. (**G**) Model same as in (E), for iPSC-derived hiSNs. (**H**) iPSC-derived hiSNs cultured for 4 weeks and subjected to control or clustered eB2 treatment as above. Immunoprecipitation and immunoblotting were identical to (F) above. (**I**) Schematic depicting the experimental setup to test whether application of soluble recombinant (r) VLK or indicated related kinases can induce PLA between EphB2 and GluN1 in HEK293T. (**J**) Representative images of PLA of EphB2-NMDAR after treatment with soluble recombinant kinases. HEK293T cells were transfected with GluN1, GluN2B, EphB2, and EGFP. Cells were treated with active recombinant VLK, DIA1, or FAM69C proteins (as indicated) for 45 min before fixation. The upper panels show PLA signal alone (magenta). The lower panels are the merged images with EGFP in green. Scale bar is 10 μm. (**K**) Quantification of the PLA puncta number. PLA puncta numbers were quantified by counting the puncta per 100 μm^2 in $EGFP^+$ cells and normalized to the Control. [$^{****}P \leq 0.0001$, $^{*}P = 0.038$, one-way analysis of variance (ANOVA) followed by Tukey's; control $n = 70$ fields from seven repeats; VLK $n = 70$ fields from seven repeats; DIA1 $n = 40$ fields from four repeats; FAM69C $n = 40$ fields from four repeats].

(*PKDCC*) expression in rat cortical neurons and hiSNs (fig. S1, B to D). These data indicate that VLK can be secreted into the media by stimulation of neurons with ephrin-B2, that ephrin-B2 stimulation induces VLK expression, and that these effects are found in both rat and human neurons.

To test whether extracellular VLK is sufficient to induce the EphB2-NMDAR interaction, HEK293T cells were transfected with EphB2, GluN1, GluN2B, and EGFP. As expected, in control experiments, ephrin-B2 treatment robustly induced EphB2-NMDAR interaction (fig. S1, F and F). Next, transfected cells were treated with either control reagents, activated ephrin-B2, or purified recombinant (r) VLK, FAM69C, or DIA1. Proximity ligation assay (PLA) was performed on unpermeabilized transfected cells to determine whether the addition of recombinant kinases induced the EphB2-NMDAR interaction on the cell surface (Fig. 1I) (*4*). Neither rFAM69C nor rDIA1 increased the EphB-NMDAR interaction compared with the control (Fig. 1, I and K). By contrast, the rVLK application induced an EphB2-NMDAR interaction similar to that found with ephrin-B2 treatment alone (Fig. 1, I and K, versus fig. S1, E and F). Moreover, a kinase-dead mutant of VLK [(rVLK-KD; fig. S1, E and F] failed to increase the PLA puncta density, suggesting that VLK-dependent induction of the EphB2-NMDAR interaction requires VLK kinase activity.

To determine whether rVLK might induce the EphB2-NMDAR interaction in neurons, seven to nine DIV untransfected rat cortical neurons were treated with activated ephrin-B2 (eB2), rVLK, or rVLK-KD. rVLK but not rVLK-KD induced the endogenous EphB2-NMDAR interaction (Fig. 2, B and C). Intracellular phosphorylation of EphB2 at pY662 (p*EphB2 Int) is essential for EphB kinase activation, whereas phosphorylation at the extracellular tyrosine residue 504 is necessary and sufficient for the EphB-NMDAR interaction (*6*, *9*). The phosphorylation of these residues on EphB2 can be detected using two different phospho-specific antibodies that recognize the extracellular phosphorylation at Y504 or the intracellular Y662 phosphorylation. The use of these antibodies allowed us to distinguish events that drove activation of the EphB2 kinase (pEphB2 Int) from those that induced the EphB-NMDAR interaction and the extracellular phosphorylation (pY504, Fig. 2A). We would expect that if VLK is acting selectively to induce the EphB-NMDAR interaction by phosphorylating Y504, rVLK but not rVLK-KD should induce phosphorylation of Y504. As expected,

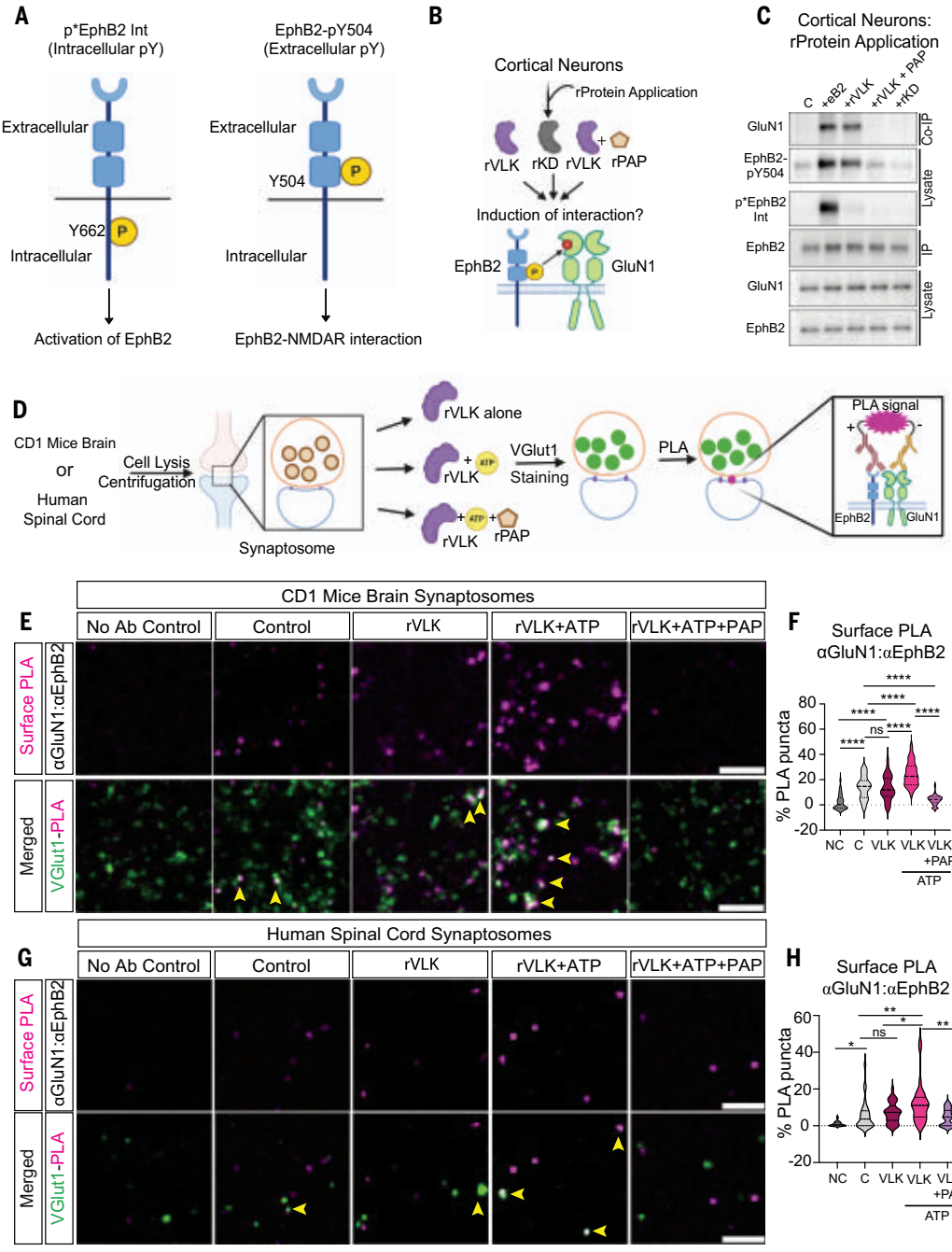

Fig. 2. VLK is sufficient to induce the EphB2-NMDAR interaction. (**A**) Model depicting both the intracellular (p*EphB2 Int) and extracellular phosphorylation (EphB2-pY504) sites of EphB2. Intracellular phosphorylation at Y662 leads to the activation of EphB2 forward signaling. Extracellular phosphorylation of EphB2 at pY504 is responsible for the EphB2-GluN1 interaction. (**B**) Model illustrating the experimental setup to test whether VLK kinase activity is sufficient for inducing EphB2-NMDAR interaction in rat cortical neurons. Recombinant VLK (purple); kinase-dead mutant VLK (gray); and rVLK (purple) along with the prostatic acid phosphatase, PAP (orange). (**C**) Untransfected rat cortical neurons (DIV 7 and 8) were treated with either Fc control (C), clustered EphrinB2-Fc (+eB2), recombinant VLK (+rVLK), recombinant VLK and PAP phosphatase (+rVLK+rPAP), or recombinant kinase dead VLK (+rKD) as indicated for 45 min. EphB2 was immunoprecipitated from the cell lysates, and coimmunoprecipitated GluN1 was immunoblotted (CoIP, top). A fraction of the same sample was immunoblotted for EphB2 (EphB2, IP). Neuronal lysates controls were probed as indicated for EphB2 and GluN1, and both EphB2 extracellular (EphB2-pY504) and intracellular phosphorylation (p*EphB2 Int). (**D**) Model illustrating the isolation of synaptosomes from either CD1 mouse brain or human spinal cord. The isolated synaptosomes were treated with rVLK alone, or with rVLK in combination with ATP or PAP, followed by VGlut1 staining and proximity ligation assay (PLA). (**E**) Representative images of PLA of EphB2-NMDAR in CD1 mouse brain synaptosomes after treatment with recombinant VLK kinase with or without ATP or with ATP along with VLK with PAP phosphatase (as indicated). The upper panels show the PLA signal alone (magenta). The lower panels are merged images of synaptosomes immunostained for presynaptic marker vGlut1 (green). The yellow arrows indicate colocalized puncta of presynaptic marker (vGlut1) and EphB2-NMDAR PLA puncta. The no-antibody control condition was performed without primary antibodies for EphB2 and GluN1. Scale bar is 10 μm. (**F**) Quantification of the percentage of VGlut1$^+$ synaptosomes that colocalize with PLA puncta. ($n = 40$ fields from four different mice, one-way ANOVA followed by Tukey's test ****$P < 0.0001$). (**G**) Representative images of PLA of EphB2-NMDAR in human spinal cord synaptosomes. The yellow arrows indicate colocalized puncta of presynaptic marker (vGlut1) and EphB2-NMDAR PLA puncta. Scale bar is 10 μm. (**H**) Quantification of the percentage of VGlut1$^+$ synaptosomes that colocalize with PLA puncta ($n = 30$, fields from three different human samples, one-way ANOVA followed by Tukey's test, *$P = 0.04, 0.04$, **$P = 0.006, 0.0067$).

ephrin-B2 induction of the EphB-NMDAR interaction results in increases in both pEphB2-Int and pY504 signal. By contrast, although rVLK is as effective as ephrin-B2 treatment in inducing the EphB2-NMDAR interaction, rVLK was able to induce an increase in only the pY504 signal (Fig. 2C). These data support a model in which rVLK drives the phosphorylation of Y504 on EphB2.

There are many phosphatases present in the extracellular space (*11*, *12*), suggesting that the regulation of phosphorylation in this compartment may be biologically important. Consistent with this model, the extracellular phosphatase prostatic acid phosphatase (PAP) is a negative regulator of acute pain in the spinal cord (*13*). PAP is found in both a secreted and transmembrane (TM-PAP) form generated by alternative splicing of the *Acp* gene. In dorsal root ganglion (DRG) neurons, TM-PAP is the predominant isoform and is inserted into the plasma membrane with its active phosphatase domain facing the extracellular space (*13*, *14*). Because of the link to pain, we tested whether cotreatment of neurons with recombinant PAP (rPAP) and rVLK might block the rVLK-dependent induction of the EphB2-NMDAR interaction. The rVLK-dependent increase in the EphB2-NMDAR interaction, as well as in pY504, was prevented by cotreatment of cortical neurons with rPAP (Fig. 2C). These data suggest that rVLK is sufficient to induce EphB2-NMDAR interaction even in the absence of ephrin-B2 or induction of EphB2 kinase activity, likely by VLK-dependent phosphorylation of Y504 on EphB2.

To test whether VLK might induce the EphB2-NMDAR interaction at synapses, we performed PLA for EphB2 and GluN1 in synaptosomes purified from mouse brain (Fig. 2D) and human spinal cord from male and female donors (Fig. 2, G and H). Synaptosomes were treated with control reagents, rVLK, or rVLK with ATP. Addition of rVLK and ATP increased the percentage of synaptosomes with EphB2 and GluN1 PLA puncta (Fig. 2, F and H) (*4*), and PAP blocked VLK-dependent increases in PLA puncta density in synaptosomes (Fig. 2, E to H). Together, these data indicate that VLK is sufficient to induce the EphB2-NMDAR interaction at mouse cortical and human spinal cord synapses, likely by a VLK-dependent extracellular phosphorylation of EphB2 at Y504.

Mechanism of VLK action on EphB2

Extracellular phosphorylation of EphB2 at Y504 imparts a negative charge on the FNIII domain of EphB2, which interacts with a positively charged pocket in the N-terminal hinge region of GluN1 to mediate EphB2-NMDAR interaction (*4*, *6*). To determine whether rVLK phosphorylates the extracellular domain of EphB2, we conducted an in vitro cell-free kinase assay (Fig. 3A). Addition of rVLK and ATP, but not rVLK-KD and ATP, resulted in the robust phosphorylation of the EphB2 ectodomain at Y504 (Fig. 3B). Neither of the ectokinases rFAM69C or rDIA1 induced phosphorylation of the EphB2 ectodomain (Fig. 3C), suggesting that the extracellular domain of EphB2 is selectively phosphorylated by rVLK.

VLK can phosphorylate the ectodomain of EphB2, and a negative charge at Y504 on EphB2 is necessary and sufficient for the EphB2-NMDAR interaction (*6*). To determine whether VLK induces the EphB2-NMDAR interaction by phosphorylating Y504, stable VLK knockdown HEK293T cells (fig. S2, A and B)—which lacked constitutive EphB2-NMDAR interaction (Fig. 3D)—were transfected with GluN1, GluN2B, and either wild-type (WT) EphB2 (Fig. 3D; EphB2-WT), an EphB2 phospho-null mutant (noninteracting mutant, Fig. 3E; Y504F), or an EphB2 phosphomimetic mutant (constitutively interacting mutant, Fig. 3F; Y504E). Consistent with the requirement for VLK kinase activity, the EphB2-NMDAR interaction was rescued by WT VLK expression (Fig. 3D; +VLK) but not by expression of the VLK-KD mutant (Fig. 3D; +VLK-KD). Similarly, the expression of VLK failed to induce the EphB2-NMDAR interaction in cells expressing EphB2-Y504F that cannot undergo phosphorylation at Y504 (Fig. 3E), and the EphB2-NMDAR interaction was constitutive in cells transfected with negatively charged constitutively interacting mutant EphB2-Y504E (Fig. 3F). These data further validate that VLK induces the EphB2-NMDAR interaction by phosphorylating Y504 on EphB2.

VLK is secreted by neurons and can phosphorylate the extracellular domain of EphB2. To test whether VLK is necessary for the EphB2-NMDAR interaction in vitro and in vivo, we engineered an inducible VLK knockout (KO) mouse model by inserting lox-P sites around the first exon of the *Pkdcc* gene (Fig. 3G). We cultured neurons from the $Pkdcc^{flox/flox}$ mice and infected them with either AAV-EGFP (control) or AAV-CRE-EGFP (cKO) virus and assayed for EphB2-Y504 and EphB2-NMDAR interaction. We observed a lack of EphB2 pY504 and a concomitant reduction in the EphB2-NMDAR interaction in the cKO neurons. Both pY504 and the EphB2-NMDAR interaction were rescued following bath application of rVLK but not rVLK-KD (Fig. 3H and fig. S2, C to F), suggesting that VLK is necessary and sufficient for the EphB2-NMDAR interaction.

A neuron-specific VLK KO mouse line was generated by crossing $Pkdcc^{flox/flox}$ mice with a *Nestin*-CRE line. However, no *Pkdcc* KO mice were born from this line (0/106, eight litters), suggesting that VLK is required for nervous system development and viability. Therefore, we generated a forebrain excitatory neuron–specific knockout using the *CaMKII*-CRE line (Fig. 3G). $Pkdcc^{flox/flox}CaMKII^{Cre/+}$ mice were viable and showed a reduction in *Pkdcc* mRNA amount with no change in mRNA amounts of the two other VLK-family secreted kinases, FAM69C (*Dipk1c*) or DIA1R (*Dipk2b*; fig. S2G) in the P35 mouse cortex. Moreover, we also verified ephrin-B2 and several pre (Syt1) and post (GluA2, GluN1, PSD-95) synaptic proteins and observed that the expression of these proteins was unchanged (fig. S2H). Consistent with the necessity of VLK for the EphB2-NMDAR interaction, GluN1 coIP with EphB2 was reduced in the cortex of $Pkdcc^{flox/flox}CaMKII^{Cre/+}$ mice (Fig. 3I and fig. S2, I to L). These results show that VLK is necessary for the EphB2-NMDAR interaction.

Presynaptic VLK regulates postsynaptic EphB2-NMDAR interaction

Ephrin-B–induced activation of EphB2 results in the secretion of VLK from neurons (Fig. 1). To determine the mechanism that mediates the release of VLK, we performed subcellular fractionation from the mouse forebrain to determine VLK subcellular localization. VLK cofractionated with synaptic vesicles (Fig. 4A and fig. S3A) and not with dense-core vesicles (fig. S3A). The presence of VLK proteins in the synaptic vesicle fraction in the mouse forebrain was confirmed using a targeted mass spectrometry analysis (fig. S3, B to E). These data suggest a model in which VLK is positioned to be secreted from the presynaptic terminal to induce the postsynaptic interaction between EphB2 and the NMDAR.

If VLK functions presynaptically to induce the EphB2-NMDAR interaction by being released with synaptic vesicles, we expect that (i) VLK should localize to synaptic sites and co-traffic in axons with markers for synaptic vesicles; (ii) blocking synaptic vesicle fusion should block ephrin-B–dependent secretion of VLK; and (iii) knocking out VLK presynaptically should block the EphB2-NMDAR interaction in postsynaptic neurons. To determine whether VLK localizes to presynaptic terminals, we asked whether VLK is found in axons and traffics with synaptic vesicle markers. Timelapse imaging of live neurons coexpressing VLK-mCherry and Synaptophysin1-EGFP (Syp1-EGFP) revealed that both stable and moving VLK puncta colocalized with Synaptophysin1 (Fig. 4B and D to E). Consistent with fast axonal transport (*15*), the average velocity of VLK was 0.6 ± 0.4 μm/sec (Fig. 4B and movie S1). Post hoc staining for PSD-95, VLK, and Syp1 shows that VLK is preferentially localized to synaptic sites (Fig. 4, C to F). These data suggest that VLK traffics in axons with presynaptic proteins and is found presynaptically at many excitatory synapses.

Ephrin-B activation of EphB2 induces the secretion of VLK (Fig. 1, F and G, and fig. S1A). To test whether ephrin-B–induced VLK release is mediated by a SNARE-dependent mechanism, rat cortical neurons

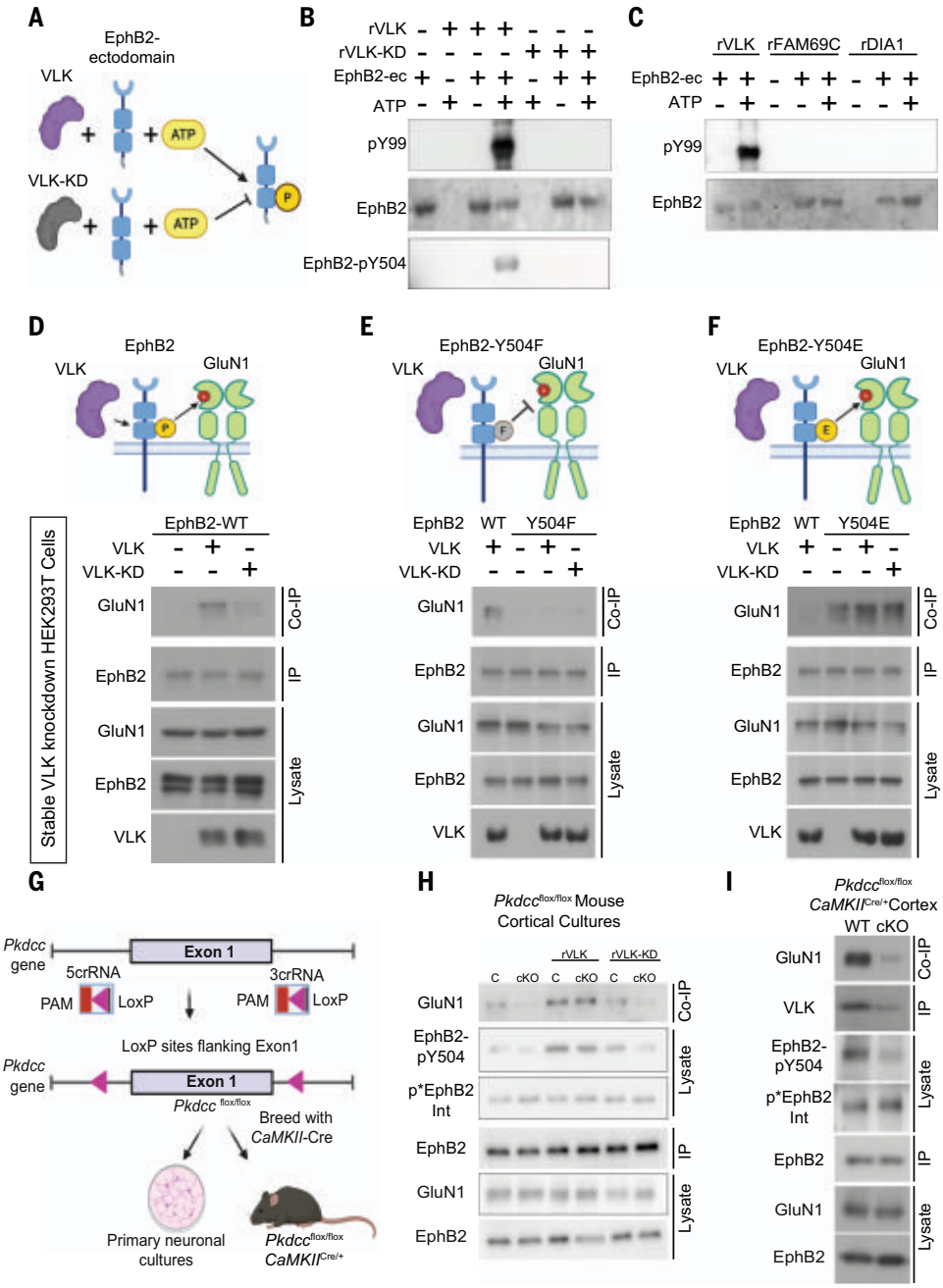

Fig. 3. VLK extracellularly phosphorylates EphB2 and is necessary for the EphB2-NMDAR interaction. (**A**) Schematic of the experimental approach to test the in vitro phosphorylation (yellow circle with capital P) of EphB2 extracellular domain (EphB2-ectodomain) by recombinant VLK (VLK, purple) or kinase-dead VLK (VLK-KD, gray). (**B**) In vitro kinase assay to test the tyrosine phosphorylation of EphB2 extracellular domain (EphB2-ec) by recombinant VLK (rVLK) or kinase-dead recombinant VLK (rVLK-KD). The extracellular domain of EphB2 fused to the Fc fragment of immunoglobulin G was incubated with rVLK or rVLK-KD either with or without ATP as indicated. EphB2-Fc was immunoprecipitated with Protein G agarose beads and immunoblots were probed with a phospho-tyrosine antibody pY99, EphB2, and EphB2 pY504 as indicated. (**C**) In vitro kinase assay to test the tyrosine phosphorylation of EphB2 extracellular domain (EphB2-ec) by recombinant FAM69C (rFAM69C) and DIA1 (rDIA1). The experimental setup is identical to that of (B). rVLK was included as a positive control for comparison. Immunoblots were probed as indicated. (**D** to **F**) Model illustrating VLK (purple)–dependent extracellular phosphorylation (yellow circle with capital P) at WT EphB2 extracellular tyrosine residue Y504 introduces a negative charge at that site on EphB2 that is necessary for its interaction with the positively charged N-terminal domain of the NMDAR (red circle with plus sign) (D). VLK cannot induce the EphB2-NMDAR interaction in the presence of a neutrally charged phospho-null mutant Y504F (gray circle with capital F) in (E), and the interaction is constitutive in the presence of the negatively charged phospho-mimetic mutant Y504E (yellow circle with capital E) in the absence of VLK in (F). HEK 293T cells with stable VLK knockdown were transfected with GluN1, GluN2B, and either VLK or kinase-dead VLK (VLK-KD), and with WT EphB2 in (D), EphB2 Y504F in (E), or EphB2 Y504E in transduced with VLK-mCherry lentivirus were pretreated with either Botulinum toxin A or B (BoNT-A/B) to cleave SNAP-25 or synaptobrevin, respectively, and treated with ephrin-B2 for 45 min (Fig. 4G). Cleavage of the SNARE complex with either BoNT-A or BoNT-B blocked the release of VLK-mCherry and reduced the expression of VLK in the media with and without ephrin-B2 stimulation of EphB kinase signaling but did not block ephrin-B2–dependent activation of EphB2 (Fig. 4H). This shows that VLK is released into the media by a mechanism that requires the SNARE complex. Thus, VLK copurifies and colocalizes with presynaptic vesicle makers, and secretion of VLK is abrogated by blocking synaptic transmission.

Next, we sought to determine whether neuronal activity might result in VLK release, as would be expected if VLK is in the synaptic vesicle fraction and is released in a SNARE-dependent fashion. To test this, we treated cortical neurons cultured with control reagents, or bicuculline for 15 min, or tetrodotoxin (TTX, 30 min) followed by bicuculline and TTX for 15 min (Fig. 4, I and J). Bicuculline treatment resulted in release of VLK into the media, induction of the EphB2-NMDAR interaction, and phosphorylation of EphB2 at Y504. These effects were blocked by TTX, and the bicuculline-dependent release of VLK did not induce the activation of the EphB2 kinase (p*EphB2 Int). Treatment of neurons with ephrin-B2 induced a similar increase in VLK release; the amount of release was not increased by treating the neurons with ephrin-B2 for 30 min or ephrin-B2 and bicuculline for 15 min. TTX blocked the effects of cotreatment of neurons with ephrin-B2 and bicuculine, suggesting that the ephrin-B2–dependent effects may result from changes in neuronal activity. As expected, ephrin-B2 treatment resulted in activation of the EphB2 kinase (pEphB2 Int), which was not blocked by TTX. EphB2 pY504 was found in all conditions where VLK was released, and in only these conditions was the EphB2-NMDAR interaction induced (Fig. 4J). These results indicate that the secretion of VLK and the induction of the EphB2-NMDAR interaction are activity-dependent.

NMDARs are localized both at synaptic and extrasynaptic sites, where their activation engages distinct signaling pathways. Synaptic NMDAR activation promotes cAMP response element–binding protein (CREB) phosphorylation (pCREB) and expression of Mu-Calpain whereas extrasynaptic NMDAR activation leads to increased Calpain-2 expression without pCREB activation (*16*–*18*). Because EphB2 is localized to the core of

(F). The cell lysates were immunoprecipitated for EphB2 and immunoblotted to detect coimmunoprecipitated GluN1. A fraction of the same EphB2 immunoprecipitated sample was immunoblotted for EphB2 (EphB2, IP), and lysate controls were probed as indicated. VLK blot is generated as described in Fig. 1B. (**G**) A schematic illustrating the conditional knockout of the *Pkdcc* gene that encodes for the VLK protein. *Pkdcc* floxed mice harboring loxP sites flanking the Exon 1 of the *Pkdcc* gene were bred with *CaMKII-Cre* mice to generate excitatory cell specific conditional KO $Pkdcc^{flox/flox}CaMKII^{Cre/+}$ mice. (**H**) Immunoblotting for coimmunoprecipitated GluN1 with EphB2 from lysates derived from the cultured cortical neurons of $Pkdcc^{flox/flox}$ that have either been transduced with control EGFP (C) or Cre-EGFP (cKO) AAV. Infected neurons were treated either with recombinant VLK (+rVLK), or recombinant kinase-dead VLK (+rKD) for 45 min as indicated. A fraction of the same EphB2 immunoprecipitated sample was immunoblotted for EphB2 (EphB2, IP). Neuronal lysates controls were probed as indicated for EphB2 and GluN1, and both the EphB2 extracellular (EphB2-pY504) and intracellular phosphorylation (p*EphB2 Int). (**I**) Immunoblotting for coimmunoprecipitated GluN1 with EphB2 from cortical lysates of $Pkdcc^{flox/flox}CaMKII^{Cre/+}$ (cKO, top), compared with WT (top) littermate controls. A fraction of the same EphB2 immunoprecipitated sample was immunoblotted for EphB2 (EphB2, IP). pY99 immunoprecipitation from cortical lysate was immunoblotted for coimmunoprecipitated VLK (VLK, IP). Cortical lysate controls were probed as indicated for EphB2 and GluN1, and both the EphB2 extracellular (EphB2-pY504) and intracellular phosphorylations (p*EphB2 Int).

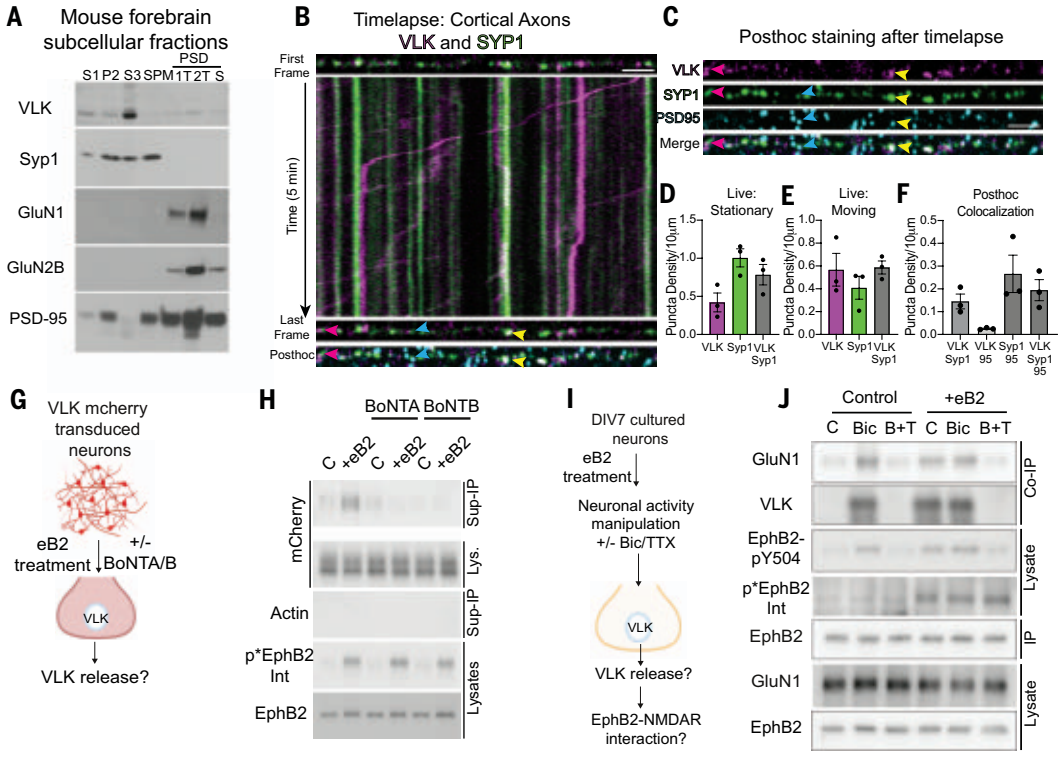

Fig. 4. VLK is enriched in the presynaptic terminal and is secreted in activity dependent manner. (**A**) Western blots of subcellular fractions prepared from WT CD1 mouse forebrain show VLK is enriched in the crude synaptic vesicle fraction (S3). Gels were loaded with nonsynaptic (S1), crude synaptosomal (P2), crude synaptic vesicle (S3), synaptic plasma membrane (SPM), and postsynaptic density (PSD) fractions. PSD fractions (from left to right) are least-insoluble first triton extraction (1T), second triton extraction (2T), and most-insoluble sarcosyl extraction (S). Blots were probed with VLK, Syp1, GluN1, GluN2B, and PSD-95 (as indicated). (**B**) The first and last frame of the same axon segment from cultured rat cortical neurons (DIV 21 to 23) transfected with VLK-mCherry (VLK, magenta), Synaptophysin1-EGFP (Syp1, green). mTurquoise was transfected as a cell fill (omitted for clarity). Kymograph generated from the indicated axon showing time (*y* axis) versus distance (*x* axis). The same axon segment was fixed after live imaging and stained for PSD-95 (Posthoc, cyan). Scale bar is 5 μm. Yellow arrowhead shows an example of colocalized VLK and Syp1 that remain stationary during live imaging and colocalize with PSD95. Pink arrowhead shows an example of colocalized VLK and Syp1 that remain stationary during live imaging but do not colocalize with PSD95. Orange arrowhead shows an example of Syp1 that remains stationary and colocalized with PSD95. (**C**) The individual channels for VLK, Syp1, PSD95, and Merged are shown for the same axon segment as (B) above. Scale bar is 5 μm. (**D** and **E**) Graph depicting the density of stable and moving VLK (magenta), Syp1 (green), and VLK+Syp1 (gray). (**F**) Graph depicting the puncta density of colocalized puncta after posthoc staining with PSD95 (95) VLK and Syp1 that remained stationary during live imaging and were maintained after fixation were quantified. (**G**) Schematic illustrating the experiment to test whether ephrin B2 (eB2) stimulated VLK secretion from neurons can be blocked by botulinum toxins, A or B (BoNT A/B). (**H**) Cultured rat cortical neurons were transduced with lentivirus expressing VLK-mCherry at DIV3 and assayed at DIV 7 and 8. Neurons were pretreated with BoNT A or B for 60 min followed by treatment with clustered ephrinB2-Fc (+eB2) or control Fc (C) reagents with or without toxins in ACSF for 45 to 60 min. Cell-conditioned ACSF were immunoprecipitated with RFP Trap agarose and immunoblotted for mCherry (top blot, ACSF IP). Cell-conditioned ACSF were probed for beta-actin to show no intracellular protein leaked into the ACSF (Actin, Sup). Cell lysates were probed for mCherry, EphB2, and p*EphB2 Int (as indicated). (**I**) Schematic illustrating the experiment to test whether neuronal synaptic activity stimulation with bicuculline (bic) or blockade with tetrodotoxin (TTX) affects VLK secretion from and whether this would affect EphB2-NMDAR interaction. (**J**) Cultured rat cortical neurons at DIV 7 and 8 were treated either with clustered Fc (Control) or ephrinB2-Fc (+eB2) for 45 min alone (C) or with 20 μM bicuculline (bic) or 20 μM bicuculline and 1 μM tetrodotoxin (B+T). Bic was added to the control or +eB2 treatments in all the experiments in the last 15 min. Tetrodotoxin was applied with control and +eB2 treatments for the entire duration. Immunoblotting probing for coimmunoprecipitated GluN1 with EphB2 from lysates derived from the cultured cortical neurons treated as indicated (top blot, CoIP). A fraction of the same sample was immunoblotted for EphB2 (EphB2, IP). Phospho-tyrosine–specific antibody pY99 was used to immunoprecipitate conditioned ACSF and immunoblotted with anti-VLK antibody (CoIP, VLK). Cell lysates were probed as indicated for EphB2 and GluN1, and both the EphB2 extracellular (EphB2-pY504) and intracellular phosphorylations (p*EphB2 Int).

postsynaptic density and recruits NMDARs to synapses (*4*, *6*, *19*), we hypothesized that VLK might preferentially act on synaptic NMDARs. To test this idea, we used established stimulation protocols to selectively activate either synaptic (bic+4-AP) or extrasynaptic (NMDA+glycine following MK-801 pre-blockade) NMDARs (Fig. 5, A and B) (*16*). In control neurons, synaptic stimulation induced pCREB and expression of Mu-Calpain, but not of Calpain-2 (Fig. 5C). Treatment with rVLK alone, but not rKD-VLK, enhanced pCREB and Mu-Calpain expression, consistent with selective activation of synaptic NMDARs. These effects were blocked by NMDAR antagonists (Fig. 5C). Anti-pCREB immunostaining of neurons confirmed that rVLK increased nuclear pCREB following synaptic stimulation (Fig. 5, E and F).

To determine whether VLK might induce the activation of extrasynaptic NMDAR signaling, synaptic NMDAR was blocked using the irreversible NMDAR pore-blocker MK-801. In control extrasynaptic NMDAR activation experiments, NMDA stimulation induced Calpain-2 expression without increasing pCREB or Mu-Calpain (Fig. 5, A and B). Despite these conditions that isolate extrasynaptic NMDAR activation, treatment with rVLK alone in this context activated the synaptic NMDAR signaling pathway with an increases in pCREB and expression of Mu-Calpain, (Fig. 5D). Anti-pCREB immunostaining similarly showed increased nuclear pCREB following extrasynaptic stimulation in the presence of rVLK (Fig. 5, E and F). All effects of rVLK were NMDAR-dependent. These findings demonstrate that VLK selectively promotes "synaptic" NMDAR signaling pathways, even under conditions designed to stimulate extrasynaptic pathways, supporting a model in which VLK acts to regulate synaptic NMDARs, perhaps by promoting EphB2-NMDAR interactions that stabilize or recruit NMDARs to synaptic sites.

If presynaptic axonal terminals release VLK to induce the EphB2-NMDAR interaction at synaptic sites in postsynaptic cells, removal of VLK from axons should block the EphB2-NMDAR interaction, even in the presence of postsynaptic cells expressing VLK. Accordingly, we sought to identify a circuit in which we could isolate presynaptic terminals of projection neurons. One such circuit is formed by the DRG neurons that project into the dorsal lamina of the spinal cord (*20*). The EphB2-NMDAR interaction is pathologically upregulated in the spinal cord by injury to peripheral tissues which drives activation of DRG neurons (*21*), suggesting that DRG

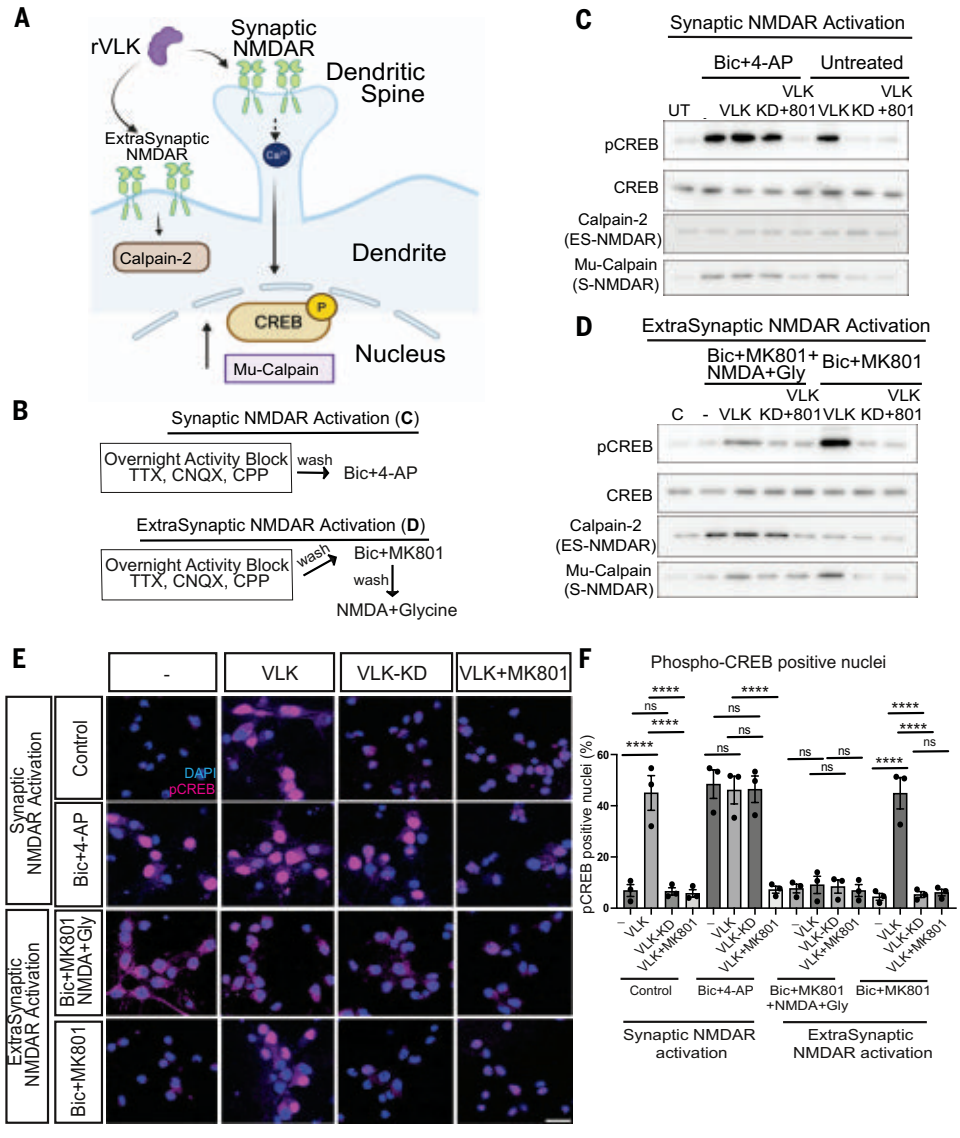

Fig. 5. VLK activates synaptic NMDARs but not extrasynaptic NMDARs. (**A**) Model illustrating the experiment to test whether recombinant VLK (rVLK) treatment of neurons activates synaptic or extrasynaptic NMDARs. Although activation of synaptic NMDARs would lead to increased phosphorylation of CREB (pCREB) and increased expression of Mu-Calpain, activation of extrasynaptic NMDARs would lead to increased expression of Calpain 2. (**B**) Model showing the experimental protocols for synaptic NMDAR and extrasynaptic NMDAR activation. (**C** and **D**) Western blots probing for the amount of pCREB, total CREB (CREB), extrasynaptic NMDAR activation marker Calpain 2 (Calpain-2 ES-NMDAR), and synaptic NMDAR activation marker Mu-Calpain (Mu-Calpain S-NMDAR), as indicated in cell lysates from rat cortical cultures that underwent synaptic or extrasynaptic NMDAR stimulations in the presence or absence of recombinant VLK (VLK), kinase-dead VLK (KD), or VLK+MK801 (VLK+801) as indicated. Stimulations: All neurons except naïve (described below) underwent an overnight block with TTX, 6-cyano-7-nitroquinoxaline-2,3-dione (CNQX), and 3-(2-Carboxypiperazin-4-yl) propyl-1-phosphonic acid (CPP). For synaptic NMDAR stimulations (bic + 4-AP): Neurons were additionally treated with bic and 4-AP alone (−) or followed by treatment with the indicated kinases for 45 min. The untreated group only received the overnight block followed by treatment with the indicated kinases for 45 min and the naïve untreated condition did not receive any treatment (UT). For extrasynaptic NMDAR stimulations (bic+MK801+NMDA+gly): Synaptic NMDARs were first blocked with MK-801 in the presence of bic. This was followed by activation of extrasynaptic NMDAR with NMDA and glycine (gly) alone (−) or followed by treatment with the indicated kinases for 45 min. The untreated group (bic+MK801) received an overnight block followed by treatment with bic and MK801 to block synaptic NMDAR, followed by the indicated kinases for 45 min. (**E**) Representative images of cultured rat cortical neurons stained with pCREB (magenta) and counterstained with nuclear stain DAPI (blue). Neurons were treated to induce activation of synaptic or extrasynaptic NMDARs as described above. The stimulations were paired with recombinant kinase treatments for rVLK, rVLK-KD, or rVLK in the presence of MK-801 (rVLK+MK801) as indicated for 45 min followed by fixation and staining. Scale bar is 20 μm. (**F**) Quantification of the percentage of pCREB^{+} DAPI nuclei. One-way ANOVA with Sidak's multiple comparison. ($n = 3$ independent biological repeats from seven fields of imaging per treatment condition, **** $P < 0.0001$).

neurons might express VLK. Consistent with this model, analysis of publicly available scRNAseq datasets (figs. S4 to S7), revealed that *Pkdcc/PKDCC* expression is found across populations of nociceptors and low-threshold mechanoreceptors in the DRG. *Pkdcc*/*PKDCC*$^+$ cells were isolated from mouse and human DRG datasets, and the coexpression of *Pkdcc*/*PKDCC* and specific genes indicative of cell type identity in this population was determined (*22*). In the mouse DRG, *Scn10a* was expressed in ~85% of *Pkdcc*+ neurons, *Trpv1* in ~45%, *Efnb1* in ~30%, *Efnb2* in ~30%, and *Mrgprd* in ~15%. Similarly, in the human DRG, *TRPV1* was expressed in ~75% of *PKDCC*+ neurons, *SCN10A* in ~70%, *EFNB1* in ~70%, *EFNB2* in ~50%, and *MRGPRD* in ~12% (Fig. 6A). Neurons in mouse and human DRGs also coexpressed *Pkdcc/PKDCC* and *EphB2/EPHB2* or *EphB1/EPHB1* (Fig. 6A). These data show that in both mouse and human DRGs, the *Pkdcc/PKDCC*$^+$ population strongly expresses the nociceptive markers *SCN10A* and *TRPV1*, with a subset also expressing *EFNB1* and *EFNB2*, which could be important for induction of VLK release, and show considerably less expression of the nonpeptidergic nociceptor marker *MRGPRD*. To further characterize *Pkdcc/PKDCC* expression in DRG neurons, we performed RNAscope in situ hybridization on DRG tissues. In mice, ~80% of neurons exhibited detectable *Pkdcc* puncta (Fig. 6, B and C). The number of *Pkdcc* puncta per neuron varied substantially, with some neurons showing only a few puncta (1 to 10) and others exhibiting much higher numbers (>10 puncta) (fig. S8). Among the neurons with high expression, *Pkdcc* was found in 11% of *Scn10a*$^+$ nociceptors and 24% of *Nf200*$^+$ myelinated mechanoreceptors (Fig. 6D), and this pattern was conserved in both female and male mice (fig. S8). In human DRG tissue obtained from male and female organ donors (table S1), *PKDCC* was observed in 21% of DRG neurons, including 17% of *SCN10A*$^+$ neurons and 36% of *SCN10A*$^-$ neurons (Fig. 6, E to G). *PKDCC*$^+$ neurons were small- to medium-sized and showed similar expression patterns between sexes (fig. S6, C and D). To further support the presence of VLK in human DRGs, we examined VLK protein amounts using the Somascan proteomic platform, which confirmed expression of VLK protein in the human DRG (fig. S6E). These data indicate that in both mouse and human DRGs, *PKDCC* is expressed in neurons associated with nociception that send axonal projections to the dorsal lamina of the spinal cord.

Based on the pattern of VLK transcript expression in the DRG, we tested whether VLK is required presynaptically to induce the EphB2-NMDAR interaction. To generate a presynaptic loss of function, VLK was knocked out in all DRG sensory neurons by crossing the *Pirt*-Cre driver line with the *Pkdcc*$^{flox/flox}$ mice (Fig. 6, H and I, and fig. S9, A to C) (*23*). *Pkdcc* transcript expression in the spinal cord was normal in the *Pkdcc*$^{flox/flox}$*Pirt*$^{Cre/+}$ DRG KO mice (fig. S9D). In addition, *Pkdcc*$^{flox/flox}$*Pirt*$^{Cre/+}$ mice had no changes in expression of peptidergic DRG neuron markers, in the patterns of DRG afferent projections into the dorsal horn, or reduction in synapse density in the outer lamina of dorsal horn of the spinal cord, suggesting that DRG axonal projections to the spinal cord are intact following conditional deletion of *Pkdcc* in DRG sensory neurons (fig. S9, E to H, and fig. S10, A to C).

To determine the effect of the presynaptic loss of VLK on the EphB2-NMDAR interaction, the dorsal horn region of the spinal cord was isolated from the *Pkdcc*$^{flox/flox}$*Pirt*$^{Cre/+}$ KO mice (VLK-cKO), in which only the afferent DRG axon terminals lack VLK, and compared with that of WT controls. Coimmunoprecipitation of GluN1 with EphB2 was reduced in the dorsal horn of DRG-restricted VLK-cKO compared with WT controls, whereas overall EphB2 and GluN1 expression was unaffected (Fig. 6, H to J, and fig. S9, I to K). These data indicate that postsynaptic expression of VLK cannot compensate for the presynaptic loss of expression of VLK and demonstrate that in the DRG to DH circuit, VLK is necessary for the EphB2-NMDAR interaction. Collectively, these results support a model in which VLK is released presynaptically by neuronal activity or ephrin-B activation from axon terminals in a SNARE-dependent manner to act extracellularly on the postsynaptic neurons to promote the EphB2-NMDAR interaction by selective phosphorylation of EphB2-Y504.

VLK drives an acute pain-like state in mice dependent on kinase activity and the NMDAR

In acute and chronic pain states, NMDARs are activated by sustained nociceptive stimulation, and NMDAR activation mediates both short and long-term plasticity that enhances pain detection by amplifying ascending nociceptive neurotransmission to the brain (*17*). Up-regulation of NMDAR function by induction of the EphB-NMDAR interaction through overexpression of a phosphomimetic mutant EphB2 receptor (Y504E) induces pain hypersensitivity in mice (*6*). Moreover, in models of surgical wound acute pain, the EphB-NMDAR interaction is increased (*6*). These data suggest that extracellular phosphorylation of EphBs may drive NMDAR-dependent hypersensitivity and pain plasticity. Therefore, we tested whether the ectokinase VLK might mediate pain plasticity in vivo.

To test whether VLK can induce pain-like behaviors, rVLK was injected intrathecally into naïve mice, targeting the lumbar spinal cord and DRGs (Fig. 7A). Mice received rVLK or VLK family kinases (rFAM69C or rDIA1) or heat-denatured recombinant proteins. Effects on mechanical sensitivity were determined with von Frey filaments and spontaneous pain by the mouse grimace scale (*18*). Neither rDIA1 nor rFAM69C produced any changes in grimacing or mechanical sensitivity. By contrast, injection of rVLK resulted in an increase in mechanical sensitivity and grimace (Fig. 7, B and C). These effects were long-lasting (post rVLK injection) and specific to VLK kinase activity, as heat-denatured rVLK (Fig. 7, B and C) or the rVLK-KD mutant did not cause any behavioral changes (Fig. 7, D to F). Cotreatment of the pain-modulating ecto-phosphatase rPAP blocks VLK-dependent phosphorylation of Y504 on EphB2 in neurons and the induction of the EphB2-NMDAR interaction in neurons and synaptosomes (Fig. 2, E to H) (*13*). Therefore, we asked whether coinjection of rPAP might block the induction of mechanical hypersensitivity by VLK (Fig. 7G). Consistent with this model, coinjection of rPAP and rVLK, blocked the effects of rVLK injection (Fig. 7, H and I, and fig. S10, D to F), whereas coinjection of heat-inactivated rPAP had no effect on rVLK induction of hypersensitivity. Furthermore, rPAP coinjection did not affect grimace behaviors (Fig. 7I). Similar effects were seen with preinjection of rPAP (fig. S10, D to F). These findings suggest that the kinase activity of VLK is necessary for rVLK-induced mechanical hypersensitivity. Collectively, the effect of rPAP on rVLK-induced mechanical hypersensitivity suggests a model in which endogenous PAP phosphatase activity may limit the activity of VLK released from DRG neurons (*13*).

rVLK induces the EphB2-NMDAR interaction, and the induction of the EphB2-NMDAR interaction increases the synaptic localization of the NMDAR, open time of the channel, and NMDAR-dependent calcium influx in neurons while also inducing mechanical pain hypersensitivity (*6*, *7*). To determine whether rVLK might act to modulate pain behavior through the NMDAR, we blocked the NMDAR in the presence of rVLK. Intrathecal injection of naïve mice with rVLK and the NMDAR blocker AP5 prevented the rVLK-dependent induction of a pain-like phenotype (Fig. 7, J to L). Stimulation of synaptic activity associated with pain-like behavior induces expression of activity-dependent immediate early genes such as cFos (*24*). To test whether cFos expression can be stimulated by VLK, mice received intrathecal injection of rVLK, rVLK with the NMDAR blocker AP5, or denatured rVLK protein. Ninety minutes following the injections, spinal cords were processed for immunostaining. cFos-positive cells were observed in the superficial and deeper lamina of the dorsal horn, where projection neurons that send ascending nociceptive signaling to the brain are found (Fig. 7M). The expression of cFos was greater with rVLK administration than with the denatured-VLK, and this increase was blocked by NMDAR antagonism (Fig. 7N). Accordingly, rVLK drives the induction of pain-like behaviors and increases NMDAR-dependent neuronal activity, linking VLK-dependent induction of the EphB2-NMDAR interaction directly to acute pain plasticity.

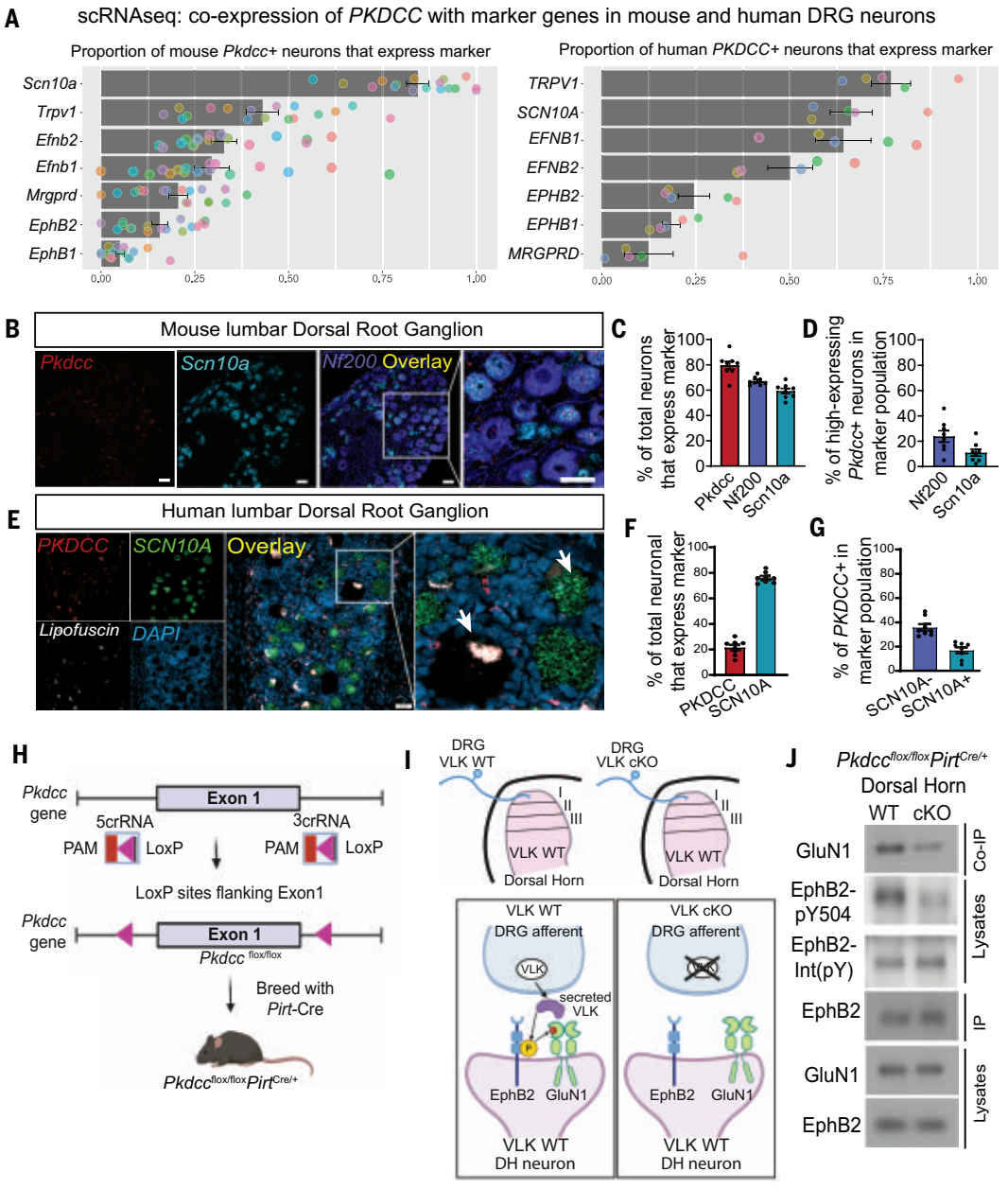

Fig. 6. VLK knockout in the presynaptic DRG neurons down-regulates postsynaptic dorsal horn EphB-NMDAR interaction. (**A**) Proportions of *PKDCC*+ neurons in mouse (top) and human (bottom) DRGs which express target genes (*SCN10A*, *TRPV1*, *EFNB1*, *EFNB2*, *MRGPRD*, *EPHB1*, *and EPHB2*); analysis of single-cell RNAseq datasets from PMID 38905344 and PMID 38905344. (**B**) RNAscope in situ hybridization for *Pkdcc* (magenta) in mouse lumbar DRG, in *Scn10a* nociceptors (cyan), and merged overlay with Nf200 mechanoreceptor cells (blue). Scale bar is 50 μm. (**C**) Quantification of the percent of mouse DRG neurons types expressing *Pkdcc*, *Nf200*, *or Scn10a* mRNA ($n = 8$, *Pkdcc* M =79.64, SEM = 3.154; *Nf200* M = 67.15, SEM = 1.156, *Scn10a* M = 59.31, SEM = 2.048). (**D**) Quantification of high-*Pkdcc*–expressing neurons in the *Nf200*+ and *Scn10a*+ populations ($n = 8$, Nf200 mean = 23.83, SEM ± 4. 490, Scn10a mean = 10.95, SEM ± 2.740). (**E**) RNAscope in situ hybridization for *PKDCC* (magenta) in human lumbar DRG, *SCN10A* (cyan), lipofuscin (white), DAPI (blue). Scale bar is 50 μm. Merged overlay, scale bar is 50 μm. Inset from overlay showing *PKDCC* expression in neurons (white arrows). Scale bar is 50 μm. (**F**) Quantification of human DRG neurons expressing *PKDCC* or *SCN10A* ($n = 8$, *PKDCC* mean = 21. 41, SEM ± 2. 156; *SCN10A* mean = 75.98, SEM ± 1.509). (**G**) Quantified percentage of *PKDCC* expression in nociceptor and non-nociceptor populations. ($n = 8$, non-nociceptor mean = 35.82, SEM ± 2.706; nociceptor mean = 16.95, SEM ± 2. 443). (**H**) A schematic illustrating the conditional knockout of the *Pkdcc* gene that encodes for the VLK protein. *Pkdcc* floxed mice harboring loxP sites flanking Exon 1 of the *Pkdcc* gene were bred with *Pirt-Cre* mice to generate DRG sensory neuron–specific conditional KO $Pkdcc^{flox/flox}Pirt^{Cre/+}$ mice. (**I**) A model of WT and cKO mice (as described above) detailing the experiment to test the effect of VLK conditional knockout (cKO) in the presynaptic DRG sensory neurons on the EphB2-NMDAR interaction in the postsynaptic neurons in the dorsal horn (DH). (**J**) Immunoblot showing amounts of GluN1 coimmunoprecipitated with EphB2 in the DH of cKO mice compared with WT littermate controls. A fraction of the same sample was immunoblotted for EphB2 (EphB2, IP). DH lysates were probed as indicated for EphB2 and GluN1 and both the EphB2 extracellular (EphB2-pY504) and intracellular(p*EphB2-Int) phosphorylation sites.

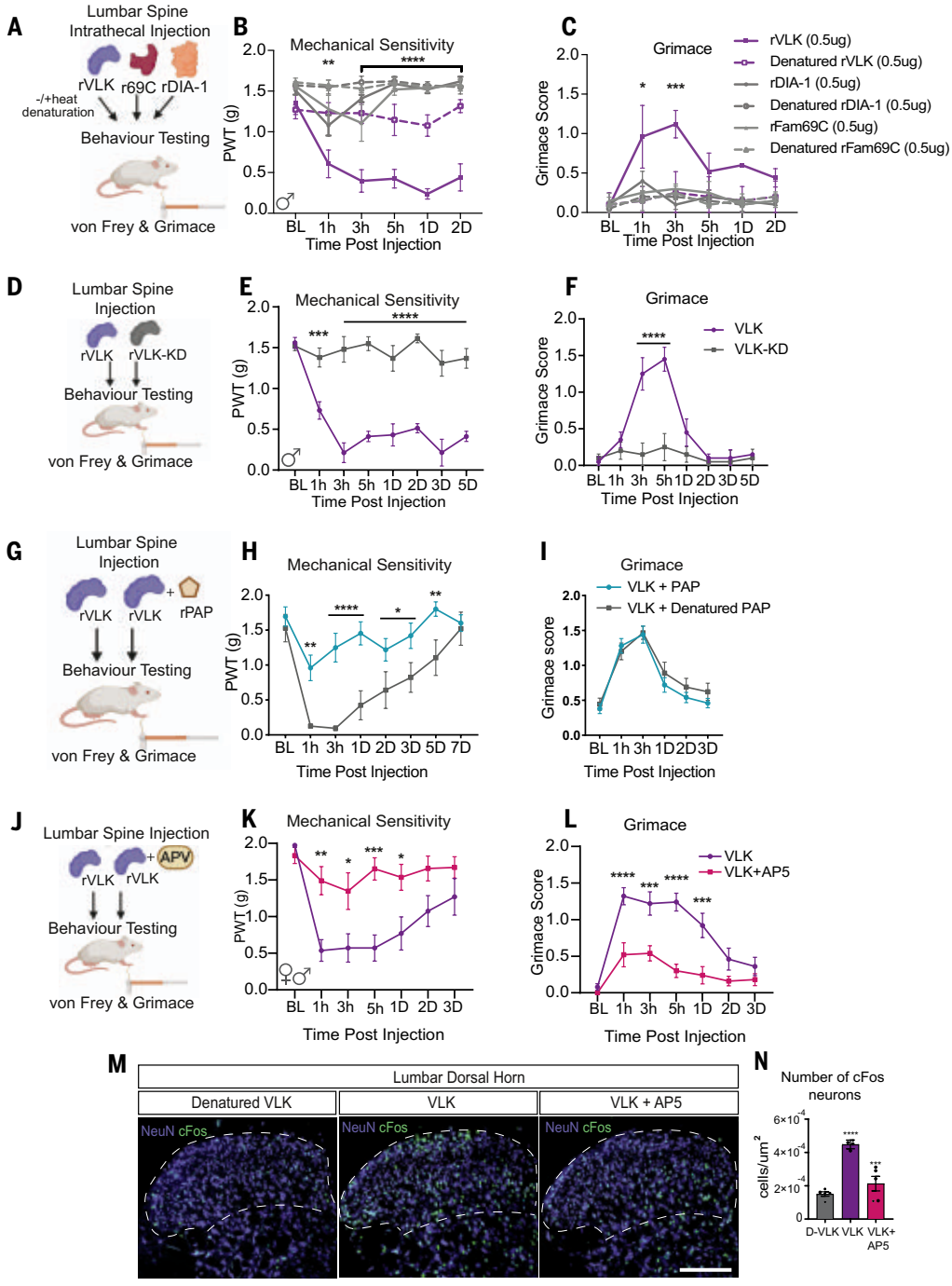

Fig. 7. VLK induces a robust pain state dependent on NMDA receptor activation. (**A**) Schematic illustration of intrathecal administration of VLK–family of kinases and heat-denatured kinases for measurement of pain-like behaviors. von Frey measurement of paw withdrawal thresholds (PWT) is used as a measure of mechanical sensitivity and grimace scores depict magnitude of affective pain. (**B** and **C**) Quantification of mechanical hypersensitivity or grimace following intrathecal injection (IT) of rVLK, rDIA-1, or rFAM69C with and without heat denaturing [$n = 4$, two-way repeated measures ANOVA, von Frey $F\,(5, 162) = 82.33$, $^{**}P = 0.001$, $^{****}P < 0.0001$; grimace $F\,(5, 162) = 9.759$, $^{***}P < 0.0001$. Posthoc Dunnett's test]. (**D**) Model representing lumbar spine injections of rVLK and VLK-KD followed by testing of pain behaviors. (**E** and **F**) Quantification of mechanical hypersensitivity or grimace following IT injection of rVLK or VLK-KD [$n = 5$, repeated measures ANOVA, von Frey $F\,(2, 11) = 26.19$, $^{****}P < 0.0001$; two-way repeated measures ANOVA, grimace $F\,(2, 11) = 11.07$, $^{**}P = 0.0023$. posthoc: Dunnett's test]. (**G**) Schematic illustrating that coadministration of the extracellular phosphatase PAP along with rVLK followed by testing of pain behaviors. (**H** and **I**) Quantification of mechanical hypersensitivity or grimace following IT injection of rVLK and rPAP or rVLK and heat denatured rPAP [$n = 10$ VLK+PAP, $n = 9$ VLK+ denatured-PAP, mixed-effects model REML, $F\,(7, 117) = 3.498$, $^{**}P = 0.0019$ posthoc: Bonferroni; grimace two-way repeated measures ANOVA, $F\,(5, 85) = 0.7750$, $P = 0.5704$]. (**J**) Model showing coadministration of rVLK and rVLK and AP5 (NMDAR antagonist) followed by testing of pain behaviors. (**K** and **L**) Quantification of mechanical hypersensitivity or grimace following IT injection heat-denatured rVLK, rVLK, or rVLK and APV [$n = 8$, two-way repeated measures ANOVA von Frey $F\,(1, 18) = 18.85$, $^{***}P = 0.0004$; grimace $F\,(1, 18) = 19.93$, $^{****}P = 0.0003$. post hoc: Bonferroni]. (**M**) The lumbar spinal cord dorsal horn from mice administered denatured VLK, VLK, or VLK + AP5 was immunohistochemically stained for NeuN and cFos markers. (**N**) Quantification of number of $cFos^{+}$ cells following IT injection of heat-denatured rVLK, rVLK, or rVLK+APV (one-way ANOVA with Bonferroni multiple comparisons $^{****}P < 0.0001$, $^{***}P < 0.001$).

Sensory neuronal VLK expression mediates surgical pain

rVLK is sufficient to induce pain-like behaviors. Extracellular phosphorylation of EphB2 is a key mechanism driving the EphB2-NMDAR interaction in the dorsal horn and mechanical pain hypersensitivity in the postsurgical pain model (*6*). rVLK administration is sufficient to produce pain-like behaviors in naïve mice (Fig. 7) and induce the EphB-NMDAR interaction (Fig. 2), and VLK mRNA is expressed in DRG neurons (figs. S4, S6, and S8). To test the necessity of VLK in the development of mouse postsurgical pain, *Pkdcc*/VLK was deleted in sensory neurons using *Pirt*-Cre mice (Fig. 6, H and I, and fig. S9). The pattern of axonal projections, synapses, and cell types found in the DRG appeared normal in $Pkdcc^{flox/flox}Pirt^{Cre/+}$ mice (fig. S9). Consistent with this model, no defects in responses to hot plate, Hargreaves' tests of thermal nociception, or intraplantar injections of capsaicin were observed, and mice performed normally on the rotarod assay, showing that although rVLK can induce pain-like responses in mice, expression of *Pkdcc* is not required for normal sensory-motor behavior and circuit function (Fig. 8, A to E).

To test whether VLK regulates injury-induced pain-like responses in mice, we measured the response of $Pkdcc^{flox/flox}Pirt^{Cre/+}$ mice to surgical wound pain. We performed hindpaw incision surgery on VLK-cKO and VLK-WT littermates (Fig. 8F). The control group showed an acute increase in mechanical hypersensitivity that took up to a week to return to baseline. The mechanical sensitivity was attenuated in the VLK-cKO group and returned to baseline by day 4 (Fig. 8G). In addition to differences in mechanical sensitivity, the VLK-cKO group also showed less facial grimacing after surgery, indicating a decrease in spontaneous pain (Fig. 8H). To understand the specific contribution of sensory neuron-derived VLK to the acute and chronic pain components of peripheral nerve injury, we conducted the spared nerve injury (SNI) assay in $Pkdcc^{flox/flox}Pirt^{Cre/+}$ mice and examined mechanical hypersensitivity of the injured paw. Shortly after injury, VLK-cKO mice had reduced mechanical sensitivity, delaying the onset of mechanical sensitivity, but there were no differences after 2 days post injury (Fig. 8, J and K). Collectively, these data indicate that VLK drives acute injury-induced mechanical hypersensitivity and spontaneous pain behaviors but is dispensable for normal sensory and sensory-motor activity.

VLK is expressed in DRG neurons and is required there for injury-induced pain signaling. To begin to determine whether this effect was caused by the selective expression of VLK in only DRG neurons, the expression pattern of *Pkdcc*/*PKDCC* was determined in the dorsal horn of the spinal cord of mice and humans. In mice, *Pkdcc* mRNA expression was distributed broadly across dorsal horn neurons (41% of neurons), with substantial overlap (64%) with *Tacr1*+ neurons (fig. S11), a population of neurons that includes projection neurons of the spinothalamic tract involved in ascending pain signaling (*25*, *26*). Similarly, the human organ-donor spinal cord showed expression of *PKDCC* in 60% of dorsal horn neurons, including large neurons in the outer lamina that are likely projection neurons (fig. S12A). Thus, *Pkdcc* is expressed in both the spinal cord and DRG, suggesting that the decreased mechanical sensitivity in the DRG VLK cKO mice may be driven by the loss of presynaptic VLK, which in turn reduces the EphB2-NMDAR interaction and pain plasticity.

To determine whether the decreases in pain-like behavior in VLK sensory neuron–specific cKO mice might be related to loss of the VLK-dependent EphB2-NMDAR interaction in the dorsal horn of the spinal cord, we first validated that DRG-specific knockout of *Pkdcc* had no effect on the expression of *Pkdcc* mRNA in the spinal cord (fig. S9D). Next, the ability of EphB2 and NMDAR to interact was determined by coimmunoprecipitation from $Pkdcc^{flox/flox}Pirt^{Cre/+}$ mice and littermate controls following hindpaw incision surgery. Twenty-four hours after surgery, $Pkdcc^{flox/flox}Pirt^{Cre/+}$ and littermate controls dorsal horns had similar expression of VLK, EphB2 and GluN1, but the EphB2-NMDAR interaction was decreased in the dorsal horn of the spinal cord of DRG-specific *Pkdcc* KO mice (Fig. 8I and fig. S12G). These data indicate that VLK is necessary for injury-induced increases in the EphB2-NMDAR interaction and are consistent with a model in which the EphB2-NMDAR interaction serves as an underlying mechanism modulating NMDAR signaling in injury-induced pain signaling in DRG to spinal cord circuits.

Pain information is carried to the brain through Tacr1+ projection neurons (*25*, *26*), and postsynaptic EphBs are required for the EphB-NMDAR interaction. Analysis of RNA sequencing databases indicates that *EPHB2*, *GRIN1 (GluN1)*, *TACR1*, and *PKDCC* are coexpressed by excitatory dorsal horn neurons in the human and mouse spinal cord (figs. S10 and S11), including in TacR1+ and verified projection neurons in mice (fig. S12C) (*27*–*29*). To test whether VLK-driven pain-like behaviors require EphB2 expression in Tacr1+ spinal cord neurons, we generated an $EphB2^{flox/flox}Tacr1^{Cre/+}$ mouse [Fig. 8, L and M; (*30*), EphB2-cKO]. Conditional deletion of *EphB2* was validated in $EphB2^{flox/flox}Nestin^{Cre/+}$ mice (fig. S12, H and I). Although Tacr1 is expressed only by a subset of the spinothalamic tract neurons and the expression of Cre in the $Tacr1^{Cre/+}$ line is only seen in about 40% of the *Tacr1*+ population of projection neurons (*25*, *26*), rVLK-induced mechanical sensitivity was attenuated in $EphB2^{flox/flox}Tacr1^{Cre/+}$ KO mice following intrathecal injection (Fig. 8N). Consistent with this, the surgical wound model failed to induce increased mechanical sensitivity in the $EphB2^{flox/flox}Tacr1^{Cre/+}$ KO mice (Fig. 8P). Together, these findings indicate that EphB2 expression in the Tacr1+ neurons of the spinal cord likely mediates the effects of VLK in producing mechanical hypersensitivity after injection and injury. In neither of these experiments was grimace affected by genotype (Fig. 8, O and Q). The lack of effect on grimacing may reflect that a different subset of ascending projection neurons carry information on acute pain behaviors, such as grimacing, after injury in mice (*31*) or may be due to the small percentage of projection neurons targeted in the $Tacr1^{Cre/+}$ line (*25*, *26*). Collectively, these results indicate that the synaptically released ectokinase VLK is necessary for the development of postsurgical pain and demonstrate that extracellular kinase activity is essential for the regulation of protein-protein interactions at synapses onto spinal neurons that express EphB2 to regulate pain-related behavioral responses to injury.

Discussion

We describe a previously unappreciated role for the ectokinase VLK in regulation of protein-protein interactions, synaptic receptor localization, and injury-induced pain behaviors. Our data support a model in which VLK is released from synaptic vesicles—the same type of vesicles that co-release glutamate and ATP—and VLK secretion is mediated by neuronal activity in a SNARE-dependent manner. Once released, VLK phosphorylates an evolutionarily conserved tyrosine residue in the extracellular FNIII domain of EphB receptors (*6*). This phosphorylation promotes the formation of the EphB2-NMDAR complex, likely increasing the synaptic localization and function of NMDARs and enhancing nociceptive signaling. Loss of VLK from presynaptic afferents selectively disrupts EphB2 extracellular but not intracellular phosphorylation, reduces the EphB2-NMDAR interaction, and attenuates injury-induced pain behaviors, establishing extracellular phosphorylation as a key modulator of pain plasticity in the spinal cord, presumably driven by activity-dependent release of VLK from sensory neurons. More broadly, these findings suggest that ectokinase signaling may represent a conserved mechanism for regulating synaptic function and animal behavior. Our work creates a set of molecular reagents, genetic tools, and a perspective on synaptic biology that will likely enable new insights into ectokinase and synapse function. Accordingly, extracellular phosphorylation may be important more broadly in synaptic plasticity and behavior as a result of the widespread requirement for NMDARs in central nervous system (CNS) function (*32*, *33*). Given the essential role of VLK in neuronal function and the association of related kinases with human disease

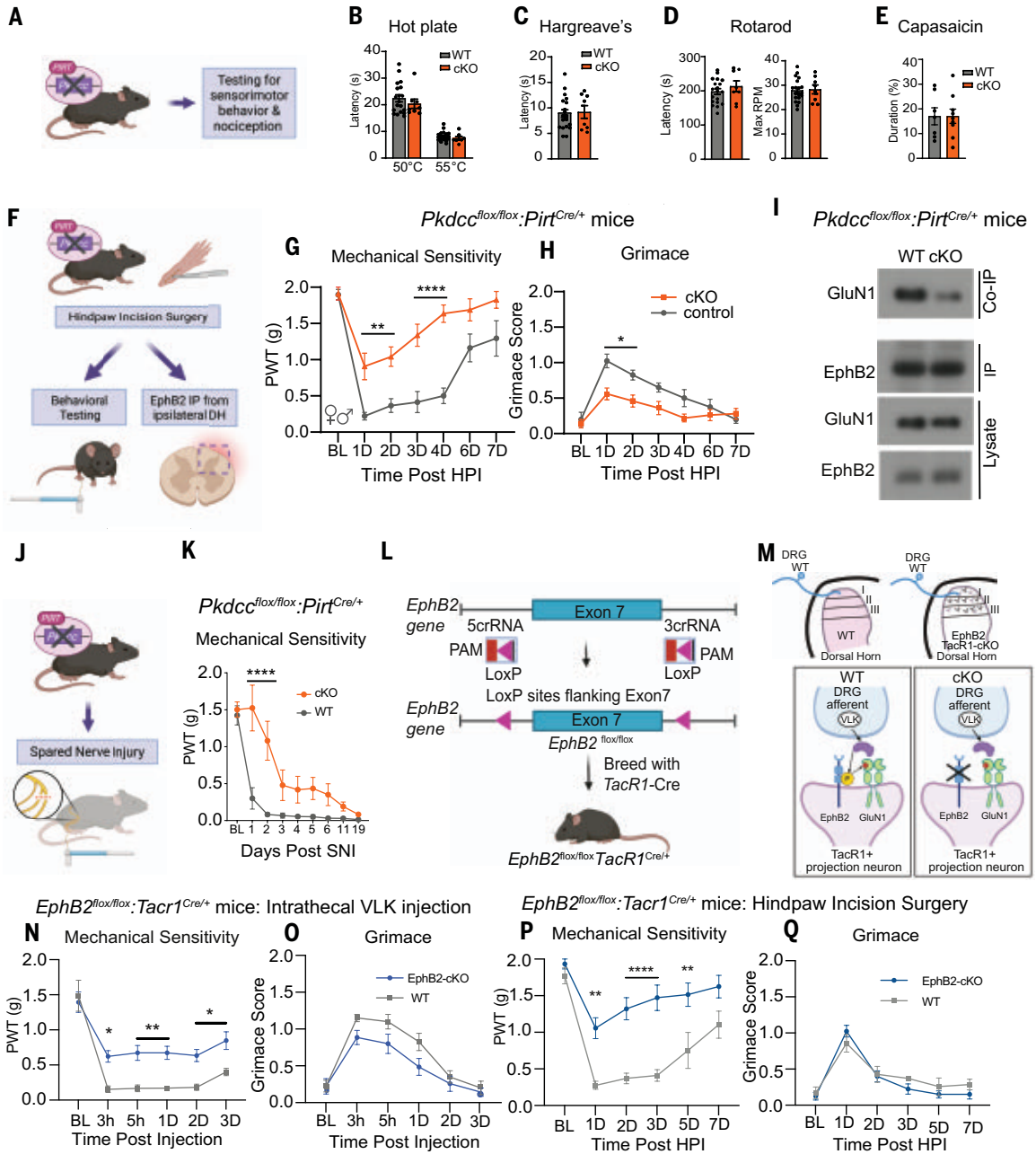

Fig. 8. Endogenous VLK expression in DRG sensory neurons is necessary for postoperative pain. (**A**) A model of the *Pkdcc*$^{flox/flox}$*Pirt*$^{Cre/+}$ mice subjected to sensorimotor behavior and nociception. (**B** to **D**) *Pkdcc*$^{flox/flox}$ *Pirt*$^{Cre/+}$ mice (cKO) and *Pkdcc*$^{flox/flox}$ littermate controls (WT) were subjected to behavioral testing for normal sensorimotor development. Quantification of (B) paw withdrawal latencies from a hot plate, (C) Hargreaves assay, (D) rotarod test mean latency (left) and RPM (right), and (**E**) duration of time spent licking the hindpaw 5 min after a capsaicin injection. (**F**) A model of the *Pkdcc* conditional KO mice (cKO). *Pkdcc*-flox mice were crossed to the *Pirt*-Cre line to generate *Pkdcc* sensory neuron–specific cKO mice. cKO and WT littermates were subjected to hindpaw incision (HPI) surgeries. (**G** and **H**) Behavioral data showing effects of sensory neuron–specific VLK knockout on postsurgical mechanical hypersensitivity and affective pain [$n = 9$ CKO, $n = 8$ littermate; two-way repeated measures ANOVA von Frey $F\,(1, 16) = 21.38$, $^{***}P = 0.0003$; grimace $F\,(1, 16) = 9.902$, $^{**}P = 0.0062$. posthoc: Bonferroni]. (**I**) Immunoblots showing amounts of GluN1 coimmunoprecipitated with EphB2 in the ipsilateral dorsal horn (DH) in cKO mice compared with WT littermate controls. A fraction of the same sample was immunoblotted for EphB2 (EphB2, IP). DH lysates were probed as indicated for EphB2 and GluN1. (**J**) Model showing the spared nerve injury to measure acute pain in the *Pkdcc*$^{flox/flox}$*Pirt*$^{Cre/+}$ mice. (**K**) Mechanical sensitivity data showing effects of sensory neuron–specific VLK knockout on spared nerve injury model (SNI) ($n = 13$ CKO, $n = 12$ littermate; mixed-effects model REML $F\,(8,133) = 6.643$, $^{****}P < 0.0001$. Posthoc: Bonferroni). (**L**) Schematic illustrating the conditional knockout of the *EphB2* gene that encodes for the EphB2 protein. *EphB2* floxed mice harboring loxP sites flanking Exon 7 of the *EphB2* gene were bred with *TacR1-Cre* mice to generate a projection neuron conditional KO EphB2$^{flox/flox}$*TacR1*$^{Cre/+}$ mouse. (**M**) A model of WT and cKO mice (as described above) detailing the experiment to test the effect of *EphB2* deletion in the TacR1-positive projection neurons. (**N** and **O**) Measurement of pain-like behaviors using von Frey (V) [$n = 7$, two-way repeated measures ANOVA, $F\,(5, 65) = 2.641$, $^{**}P = 0.003$, posthoc: Bonferroni] and grimace (W) ($n = 7$, $P =$ not significant, posthoc: Bonferroni). (**P** and **Q**) Behavioral data (von Frey and grimace) of EphB2 cKO following hindpaw incision surgery. Mechanical sensitivity measured using von Frey (X) [$n = 8$ CKO, $n = 7$ littermates; two-way repeated measures ANOVA $F\,(5, 65) = 3.557$, $^{**}P = 0.0066$, $^{****}P < 0.0001$, posthoc: Bonferroni], grimace ($n = 8$ CKO, $n =$ 7 littermates; two-way repeated measures ANOVA, $P =$ not significant, posthoc: Bonferroni).

(*1*, *34*), these findings provide a framework for understanding extracellular kinase signaling in the nervous system and suggest strategies for targeting synaptic mechanisms in pain and other CNS disorders (*1*, *34*).

Eph receptors and their ephrin ligands are well-established regulators of axon guidance and synapse formation, acting predominantly through contact-mediated, activity-independent mechanisms during development (*35*–*37*). EphBs are not developmentally transient but persist at mature synapses, where they regulate NMDAR function—a key regulator of activity-dependent plasticity in the brain (*7*, *33*, *38*–*40*). Might there be a mechanistic link between Eph-ephrin signaling and neuronal activity? VLK is localized to synaptic vesicles and is released in response to neuronal activity in a SNARE-dependent manner whereas activation of Ephs by soluble ephrin-B2 increases VLK expression, suggesting dual modes of control. This positions VLK as a modulator that may enable Eph receptors to integrate molecular guidance cues with activity-dependent signaling at mature synapses. Several models are consistent with the data: (i) Activity alone may be sufficient to trigger VLK release and EphB2 extracellular phosphorylation, recruiting NMDARs to synapses; (ii) ephrin-B2 activation of Ephs may act to increase VLK expression, setting the amount of available VLK kinase; (iii) ephrin-dependent signaling and neuronal activity may act sequentially: ephrin-Eph signaling to drive VLK expression and activity to drive VLK release. These findings reframe EphB function at mature synapses as a hub for integration between activity-independent and activity-dependent signaling and identify VLK as a presynaptic effector that modulates EphB2-NMDAR interactions, providing a mechanism for regulating synaptic function and plasticity, both adaptive and maladaptive.

The ability to respond to injury with amplified nociceptive signaling is critical for the survival of multicellular organisms with complex nervous systems (*41*). Augmented NMDAR activity at the DRG to spinal cord synapse (peripheral nervous system to CNS) is a conserved mechanism in vertebrates (*41*, *42*). However, therapeutic intervention at the NMDAR is limited by the strong CNS effects that arise when inhibiting this receptor (*43*). Our findings identify a distinct approach targeting the VLK-EphB2-NMDAR signaling complex that modulates NMDAR-dependent pain in the dorsal horn without interfering with basal sensory processing. VLK is released presynaptically by sensory neuron activity and acts locally to promote EphB2 phosphorylation and NMDAR recruitment in neurons. VLK appears to selectively drive the enhanced NMDAR activity associated with acute injury–induced pain. Consistent with this, VLK deletion in sensory neurons attenuates mechanical and spontaneous pain after injury while leaving intact baseline sensory thresholds and motor behavior. PAP treatment did not block spontaneous pain behaviors caused by VLK treatment, but this difference may be driven by limited diffusion of PAP to all synaptic sites accessible to VLK, or by kinetics of phosphorylation and dephosphorylation events that differentially contribute to these different types of behaviors. For acute pain treatment we envision developing small-molecule direct inhibitors of VLK kinase activity selectively active in the extracellular space, or small molecules or peptides that would block VLK extracellular interactions with EphBs. Effects in VLK-deficient mice at later time points in the SNI model were not distinguishable from WT mice, suggesting that chronic neuropathic mechanical hypersensitivity involves additional mechanisms, possibly intracellular EphB signaling, including the kinase activity and oligomerization of EphB1 and EphB2 receptors. This notion is supported by extensive previous work demonstrating the importance of EphB1 signaling in the DRG and spinal dorsal horn in several chronic pain models in mice (*44*, *45*). These findings position VLK as a candidate for selective modulation of NMDAR-dependent plasticity in acute pain states, with the potential to improve on the safety profile of existing NMDAR-targeting therapies such as ketamine.

One limitation to the findings is that although elimination of VLK from sensory neurons or blocking NMDARs during rVLK treatment blocked both mechanical hypersensitivity and grimacing in mice, spinal manipulation of EphB2 gene expression in a small subset of projection neurons only affected mechanical hypersensitivity. Overall, these data highlight the importance of future work to understand VLK's modality-specific functions, regulation of synaptic function, targeting of specific projection neuron subtypes, and effect on local interneuron circuits in pain sensation and plasticity. Additional opportunities come from the conservation of VLK expression, release, and effects on the EphB-NMDAR interaction in mice and humans, highlighting the translational potential of this non-opioid–dependent approach.

Materials and methods

Animals

The Institutional Animal Care and Use Committee (IACUC) of Thomas Jefferson University, Tulane University, and UT Dallas approved all animal procedures. All behavior tests were conducted during the light hours of the cycle, between 6:00 a.m. and 6:00 p.m. Animals were group-housed, with each cage having an equal balance of treatment conditions/genotypes. Long Evans rat (Charles River) from E17-18 were used to prepare dissociated cortical cultures. WT CD-1 mice (Charles River) and transgenic mice (generated for and described in this study) were housed (3 to 5 mice per cage) in the Thomas Jefferson University, Tulane University, and UT Dallas laboratory animal facilities.

Human tissue

The Institutional Review Boards of UT Dallas (UTD) reviewed and approved protocols. All experiments conformed to relevant guidelines and regulations. Dorsal root ganglia and spinal cords were collected from the donors after neurological determination of death within 2 to 3 hours of cross-clamp. Donor information is provided in table S1. Tissues designated for immunohistochemical experiments were immediately frozen on powdered dry ice and transferred to a −80°C freezer for long-term storage.

HEK293T cell culture and transfection

HEK293T cells were cultured and maintained in DMEM supplemented with 10% Heat inactivated FBS (gibco), Glutamax and Pen/Strep and transfected using Calcium phosphate as described (*4*). NMDAR-transfected HEK293T media was supplemented with 50 μM AP5 (Tocris Bioscience) and 10 μM MK801 (Tocris Bioscience) to prevent excitotoxicity (*4*). Stable 293T VLK knockdown cell line was generated by transfecting cells with a shRNA targeting *PKDCC* (5′-CCCAACGTGCTGCAGCTCT-3′; Horizon Discovery Ltd.) followed by prolonged Puromycin (2 μg/ml) selection over 10 passages. The stable *PKDCC* knockdown clone was maintained in Puromycin (0.5 μg/ml) containing media.

Primary neuronal culture and transfection

Primary rat neuronal cultures were derived from embryonic days 17-18 (E17-18) rat cortex and maintained as described previously (*4*,*6*). 8×10^6 neurons were plated for 10 cm dishes, and 1×10^6 neurons were plated per well of 6-well dishes for biochemical assays. 2×10^5 neurons were plated on glass-bottom dishes for live cell imaging experiments and on 12mm glass coverslips for immunostaining. As previously described, neuronal cultures were transfected using Lipofectamine 2000 (*4*,*6*). Primary mouse cortical cultures were derived from postnatal day 0-1 pups (P0-1) as described previously (*46*). 1×10^6 cells were plated per well in 6-well dishes for biochemical assays. All neurons were maintained in Neurobasal supplemented with 1× B27, Glutamax, and Pen/Strep. Mouse neurons were fed by replacing half of the volume with fresh media twice a week.

Human iPSC neuronal differentiation and maturation (hiSNs)

Human iPSC-derived immature sensory neurons (RealDRGx) were produced by Anatomic Inc. with the Anatomic SensoX-DM kit (Anatomic #7007). Neurons at day 7 postdifferentiation were plated on glass coverslips coated with Poly-L-Ornithine (Sigma, Castle Hill Australia) and

Matrix 3 (Anatomic Inc., Minneapolis, USA) in 96-well tissue culture plates (Corning) at a density of 40,000 cells/cm^2, and maintained in Chrono Senso-MMx1 maturation medium (Anatomic cat# 7008) for 3 days followed by Chrono Senso-MMx2 for the remaining 28 days (DIV28). Growth media was exchanged three times a week, and stimulations were performed at DIV28.

Expression constructs

Myc-GluN1, GluN2B, FLAG-EphB2, mutant FLAG-EphB2 (Y504E and Y504F), and EGFP have been previously described (*4*, *6*). Syp1-EGFP and mTurquoise2 were previously described (*47*, *48*). Flag-tagged constructs of VLK, VLK-Kinase dead (KD), DIA1, DIA1R, Fam69A, Fam69B, and Fam69C have been described (*1*, *49*). The Flag-tagged VLK rescue construct (shRNA resistant) was created by using site-directed mutagenesis (Stratagene, La Jolla, CA) to convert the *PKDCC* shRNA target site described above to 5′- CCaAAtGTaCTaCAaCTa 3′ with the following primers Fwd 5′-CTGCTGGAGCGGCTGCGGCACCCAAATGTACTACAAC TATATGGCTACTGCTACCAGGAC-3′ and Rev 5′-TCCTGGTAGCAGT AGCCATATAGTTGTAGTACATTTGGGTGCCGCAGCCGCTCCAGCAG-3′ without changing the protein sequence. The VLK-mCherry lentiviral construct was generated by PCR amplifying VLK from above and subcloning it downstream of the human synapsin promoter to replace NSG2 in pFCK-NSG2-mCherry (*46*) using standard restriction cloning.

Viral transduction

Lentivirus was packaged using a second-generation packaging system by transfecting HEK293T cells with VLK-mCherry, psPAX2, and pMD2.G as previously described (*46*). Lentivirus was harvested from transfected cell media by ultracentrifugation of 0.45 μm filter-sterilized supernatant at 110,000xG for 2h. DIV3 neurons were transduced with VLK-mCherry lentivirus (MOI 2-3) and assayed at DIV7-8 for ephrin-B2–dependent VLK secretion. Human synapsin promoter driven EGFP-CRE (105540-AAV1) and control EGFP (50465-AAV1) viruses were purchased from Addgene. 10^{12} vg/mL virus was used to infect 100,000 cells of Mouse cortical neurons on DIV3 for performing experiments on DIV7-8.

Western blotting, immunoprecipitation (ip) and coip

HEK293T cells and cultured neurons were lysed in RIPA buffer to generate protein lysates. Cortices of postnatal day 35 (P35) transgenic mice *Pkdcc*$^{flox/flox}$*CaMKII*$^{Cre/+}$ and its Wildtype (WT) littermate controls were also lysed using RIPA buffer and an equal amount of protein was used to perform IP. Pooled dorsal horns from *Pkdcc*$^{flox/flox}$*Pirt*$^{Cre/+}$ uninjured mice and their WT littermate controls were lysed in RIPA. Following lysis, an additional Percoll gradient spin was carried out to remove myelin and unwanted cellular debris (*50*) and an equal amount of protein was used to perform IP. For conditioned ACSF IP, ACSF was filtered through a 0.22 μm syringe filter (Millipore, cat#SLGV004SL) and incubated with antibody for 2h at 4°C followed by addition of Protein-G Agaraose beads and incubated overnight at 4°C. IP, CoIP, and Western blotting were performed as previously described (4, 6). Red fluorescent protein (RFP) Trap agarose beads (ChromoTek, cat# rta) were used to IP VLK-mCherry as per manufacturer's instructions. For RFP Trap IP conditioned ACSF was filtered as described above and further modified by addition of a final concentration of 10mM Tris pH 7.5, NaCl 150mM, 0.5mM EDTA and 0.5% NP-40. Antibodies used for IP were mouse monoclonal Anti-FLAG M2 (Sigma, cat# F1804, lot# SLCN3722), goat polyclonal anti-EphB2 (R&D Systems, cat# AF467, lot# CVT0315041), mouse monoclonal anti-pTyr (pY99) (Santa Cruz, Cat# SC-7020; lot# L022). Additionally, the lysate and IP controls have no statistical differences.

Cellular stimulations

Ephrin-B2: Control or clustered ephrin-B2 treatments were performed as previously described (*9*). Briefly, control IgG-Fc (Cat#110-HG-100; R&D Systems) and recombinant ephrin-B2-Fc (Cat#7397-EB-050; R&D Systems) were clustered with Donkey anti-Human IgG (Cat#709-005-149; Jackson ImmunoResearch) for 30min at room temperature. Multimerized control and ligand were mixed in 37°C artificial cerebrospinal fluid (ACSF, 140 mM NaCl, 5 mM KCl, 1 mM MgCl2, 2 mM CaCl2, 20 mM glucose, and 10 mM HEPES, pH 7.3) and applied on cells for 45 min. The ACSF was collected from the wells to detect secreted VLK, passed through a 0.22 μm filter, and immediately subjected to IP as indicated or stored at -80°C until used.

Recombinant protein: HEK293T cells were treated with 35 μg/ml recombinant VLK, Fam69C, or DIA1. Synaptosomes were treated with recombinant VLK (rVLK). 1mM ATP (Cat#A9187; Sigma) was applied as indicated. Recombinant PAP treatment was applied at 35 μg/ml. (PAP was a gift from Mark Zylka).

Botulinum toxin: Active Botulinum toxin A or B (BoNTA/B) (Cat#128C and 138B (discontinued; List labs, CA) were applied at 100pM in ACSF. Cells were pretreated for 1h with toxins in ACSF followed by application of ACSF containing toxins with either control or ephrin-B2 for 45min.

Synaptic and extrasynaptic treatments

Synaptic and extrasynaptic treatments were carried out as previously described (*16*) with minor modifications. The NMDAR antagonist CPP (Sigma, Cat#C104) was used instead of AP-5.

For synaptic NMDAR activation, cultured rat cortical neurons (DIV7) were incubated overnight with TTX (1 μm), CNQX (40 μm) and CPP (100 μm). The cells were then washed thrice with ACSF for 10 min each wash to remove the inhibitors. Neurons were treated with Bicuculline (Bic) (20 μm) and 4-Aminopyridine (4-AP) (100 μm) for 30 min. Untreated neurons were used as a negative control for synaptic NMDAR activation.

For extrasynaptic NMDAR activation, rat cortical neurons (DIV7) were pretreated with TTX(1 μm), CNQX (40 μm), and CPP (100 μm). Cells were washed three times with ACSF for 10 min each wash to remove inhibitors. Neurons were treated with Bicuculline (Bic) (10 μm) and MK801 (40 μm) for 2 min to activate and block the synaptic NMDA receptors. The cells were then washed three times with ACSF; following this, the cells were treated with NMDA (100 μm) and Glycine (10 μm) for 1 hour. Extrasynaptic NMDAR activation without NMDA and Glycine treatments was used as a negative control for extrasynaptic NMDAR activation.

Following this, cells were treated with recombinant VLK, VLK-KD, and VLK with MK-801 for 45 min. Treated neurons were lysed either lysed in RIPA for Western Blotting or fixed and processed for Immunostaining for pCREB as described.

Proximity ligation assay (PLA)

PLA experiments on HEK293T cells, mouse brain, and human spinal cord synaptosomes were performed, as previously described (*4*). Synaptosome PLA combined with vGlut1 immunostaining was also previously described (*4*).

In vitro kinase assay

In vitro Kinase assay was performed as previously described (*6*). Briefly, purified recombinant EphB2 extracellular domain (EphB2 (300 ng), active; Millipore) and active VLK (0.35 μg), VLK-KD (0.35 μg), Fam69C (0.35 μg), DIA1(0.35 μg) were used. The kinase reaction was started by adding 10 mM MnCl2, 10 mM MgAc, and 100 μM ATP in ACSF. After 30 min of incubation at 37°C, phosphorylated proteins were separated by SDS-PAGE and analyzed for pY99, EphB2, and EphB2-pY504.

RNA extraction and qPCR

Total RNA from HEK293T cells was extracted using TRI reagent (Cat#TR118; Molecular Research Center Inc.) as per the manufacturer's

instruction. Total RNA from mice cortices was extracted using the Direct-zol RNA microprep kit (Cat#R2062; Zymo Research) following the manufacturer's instructions. RNA was quantified using a Nanodrop and 1ug of total RNA was used to prepare cDNA using qScript cDNA Synthesis kit (Cat# 90547-100; Quantabio) as per manufacturer's instructions for quantitative polymerase chain reaction (qPCR). PCR was set in triplicates using SYBR green (Applied Biosystems) in a 20 μL volume and using 15 ng cDNA template. PCR was run using the StepOne Plus system, and the quantification was performed using the comparative Ct (ΔΔCt) method. The qPCR primers used are described in table S2.

VLK, Fam69C, DIA1, and VLK-KD protein purification

GST-tagged kinase containing plasmids were transformed into competent BL21 cells. A single colony was picked and grown overnight in 5 mL LB-ampicillin starter culture. 1 Liter LB-ampicillin cultures were inoculated and grown at 37°C and 250 rpm until OD600 reached 0.8-1. Cultures were cooled to 16°C. 0.03 mM IPTG (optimized for VLK) was added. The cultures were induced overnight at 16°C. A 2 mL glutathione resin slurry was loaded into a column and washed with 5 mL resuspension buffer by gravity flow. The column was stored in a resuspension buffer at 4°C for next day use. The following day, the bacteria were pelleted at 6000 rpm for 10 min, and the pellet was resuspended in 35 mL resuspension buffer. Lysozyme and PMSF were added and mixed. Lysate was incubated on ice for 10 min. Lysate was sonicated 20 × 3 s ON, 3 s OFF on ice using a probe sonicator. Lysate was centrifuged at 15,000 rpm (~28,000 × g) for 20 min at 4°C. The supernatant was transferred to a clean container immediately. The supernatant was loaded slowly onto the glutathione column. The column was washed 4X with wash buffer, 5 mL each. The column was plugged, and 4mL elution buffer was added. Beads were suspended and incubated for 10 min. The 4 mL elution was collected, and another 2 mL elution buffer was added to the column and collected. Protein elution was then dialyzed overnight.

Brain fractionation

Synaptosomes: Synaptosomes from WT CD-1 mice brains were prepared and plated as previously described (*4*, *6*).

Postsynaptic density (PSD) fractionation: PSD fractions were prepared from Postnatal day 21 (P21) WT CD-1 mice (*51*). Brains were homogenized on ice in 0.32 M sucrose, 4 mM HEPES, pH 7.4, containing a protease inhibitor cocktail (Sigma) and 1 mM PMSF. After removing the nuclear fraction (P1) by centrifugation at 1,000 × g for 15 minutes at 4°C, S1 was further centrifuged at 10,000 × g at 4°C to obtain the crude synaptosomal fraction (P2). This pellet was resuspended in 10 volumes of HEPES-buffered sucrose and then spun again at 10,000 × g for another 15 min. The resulting pellet was lysed by hypo-osmotic shock in water, rapidly adjusted to 4mM HEPES pH 7.4, and mixed constantly for 30 min at 4°C. The lysate was centrifuged at 25,000 × g for 20 min and the pellet (P3) was resuspended in HEPES-buffered sucrose. The crude synaptic vesicle supernatant (S3) was saved for further purification of synaptic vesicles. The resuspended membranes were carefully layered on a discontinuous gradient containing 0.8 to 1.0 to 1.2 M sucrose and centrifuged at 150,000 × g for 2 h. Synaptic plasma membranes were recovered in the layer between 1.0 and 1.2 M sucrose and diluted to 0.32 M sucrose by adding 2.5 volumes of 4 mM HEPES pH 7.4. Membranes were pelleted by centrifugation at 150,000 × g (36,000 rpm in SW50.1) for 30 minutes. Pellet (SPM) was resuspended in 3-5 ml of ice-cold 50 mM HEPES pH7.4, 2mM EDTA, plus protease/phosphatase inhibitors. Triton X-100 was added to 0.5%. Samples were rotated in the cold room for 15 min. Samples were centrifuged at 32,000 × g (16,318 rpm in SW50.1) for 20 min to obtain the PSD-1T pellet. Pellet was resuspended in 3 mL ice-cold 50 mM HEPES pH7.4, 2 mM EDTA plus protease/phosphatase inhibitors. 1 mL was saved as PSD-1T. To half of the remaining resuspended pellet (~1 mL), Triton X-100 was added to 0.5% and rotated in the cold room for 15 min. Sample was centrifuged at 200,000 × g (41,000 rpm in SW50.1) for 20 min to obtain the PSD-2T pellet. In a separate experiment, resuspend the second half of the PSD-1T pellet and incubate for 10 min in ice-cold 3% sarcosyl (N-lauroyl sarcosine) in 50 mM HEPES pH7.4, 2 mM EDTA, plus protease/phosphatase inhibitors. Centrifuge at 200,000 × g (41,000 rpm in SW50.1) for 1 hour to obtain the PSD-S pellet. Pellets were resuspended in 50 mM HEPES pH7.4, 2 mM EDTA plus protease/phosphatase inhibitors.

Dense-core vesicles (DCVs) isolation: DCVs were prepared from Postnatal day 21 (P21) WT CD-1 mice (*52*). Brains were homogenized on ice in a homogenization medium (0.26 M sucrose, 5 mM MOPS, and 0.2 mM EDTA). Homogenate was then spun at 4000 rpm (1000 × g) for 10 min at 4°C in a fixed-angle microcentrifuge to pellet nuclei and larger debris. The post nuclear supernatant (PNS) was collected and spun at 11,000 rpm (8000 × g) for 15 min at 4°C to pellet mitochondria. The postmitochondrial supernatant (PMS) was then collected, adjusted to 5 mM EDTA, and incubated for 10 min on ice. A working solution of 50% OptiPrep (iodixanol) [five volumes of 60% OptiPrep (one volume of 0.26 M sucrose, 30 mM MOPS, and 1 mM EDTA)] and homogenization medium were mixed to prepare solutions for discontinuous gradients in Beckman SW 55 tubes: 0.5 ml of 30% iodixanol on the bottom and 3.8 ml of 14.5% iodixanol, above which 1.2 ml of EDTA-adjusted PMS was layered. Samples were spun at 45,000 rpm (190,000 × g) for 5 hours. 10 fractions were collected and analyzed by Western blot. A clear white band at the interface between the 30% iodixanol and the 14.5% iodixanol was the DCV sample (fraction 9 of Western blot).

Proteomic analysis

Proteins samples from S3 crude synaptic vesicle fraction from three male and three female mice were concentrated by short SDS-PAGE runs into single-protein bands before tryptic digestion and peptide extraction. Peptides were desalted with Empore C18 High Performance Extraction Disks (*53*), and the eluted peptide solutions were partially dried under vacuum and then analyzed by LC-MS/MS with a Thermo Easy nLC 1000 system coupled online to a Q Exactive HF with a NanoFlex source (Thermo Fisher Scientific) as previously described (*54*). All data were analyzed by MaxQuant proteomics software (version 1.5.5.1) with the Andromeda search engine (*55*, *56*) using a mouse protein FASTA (mouse [*Mus musculus*] protein database; Uniprot; Reviewed, 21,989 entries [06182020]). Additionally, targeted mass spectrometry analysis was carried out to identify extracellular tyrosine-protein kinase (VLK) in both female and male preparations. Theoretical monoisotopic masses of 6 tryptic peptides of VLK that are commonly seen and documented in the Global Proteome Machine resource (GPM, (*57*)) were used in an inclusion list. The resulting raw mass spectrometry files were imported into Skyline proteomics software (*58*), and the presence of precursor and transition ions confirmed to identify VLK in both male and female peptide pools unequivocally.

Live cell imaging, immunocytochemistry and image analysis

Live imaging was carried out on rat cortical neurons plated on 35 mm glass bottom dishes (Cell E&G). DIV17 cultured rat cortical neurons were cotransfected with VLK-mCherry, Syp1-EGFP, and mTurquoise2. Live cell imaging was carried out on DIV21-22 neurons by replacing cell media with 37°C ACSF for the duration of live imaging. Timelapse images of live neurons were acquired on the Leica SP8 using a 63x objective lens. Images of neuronal axons (determined by the mTurquoise cell fill) were acquired at 2 frames/sec for 5 min as a single focal plane. Laser power was kept at low levels to avoid photobleaching. After live imaging, cells were immediately fixed with 4%PFA/2% sucrose for 8 min for posthoc immunostaining as previously described (*4*). PSD95 primary antibody was applied overnight at 4°C. PSD95 signal was detected with an AF647 conjugated secondary antibody. Permanent

markers of different colors were used on the glass dish for reference of reimaging. Additionally, the location of each imaged axon was recorded using a computer-controlled stage. These recorded references were used to re-locate the same axons reimaged to visualize PSD95, VLK-mCherry, and Syp1-EGFP (Posthoc). Posthoc fixed cell confocal images were acquired as Z stacks at 0.4 to 0.6 μm intervals.

Images were analyzed using Fiji (ImageJ). A segmented line was drawn along the axon segments to measure axon length and generate kymographs using the reslice tool. On the kymographs, puncta were categorized into two groups: Stationary and Moving. Moving puncta were distinguished as slanted straight lines. Stationary puncta were vertical straight lines that did not deviate from the first to the last frame of live imaging. Stationary, moving, and colocalized puncta were manually scored. The number of puncta in each category was divided by the total length of the axon to derive puncta density. For posthoc analysis, images were background subtracted, Gaussian blurred, and registered with live images using Turboreg (*47*, *48*). The straightened axon segments from posthoc image were added as a new frame to the live image after the last frame of the identical axon segment from live imaging to assess and determine which stationary puncta were maintained after fixation. The stationary VLK-mCherry and Syp1-EGFP puncta maintained after fixation were manually scored. A custom macro (*4*, *48*) was used to determine colocalization of maintained puncta with each other and PSD95. If the stationary puncta present in axon segments during live imaging were lost after fixation they were excluded from the analysis. Moving VLK puncta velocities were determined by manually tracking moving puncta using the MTrackJ plugin.

Single-cell transcriptomic analysis of dorsal root ganglia

Human DRG: A single-nuclei dataset of 5 human DRG samples from 4 donors from both sexes (*22*) was processed with the R tool Seurat (v4.1.3) using its standard sample integration (*59*) and clustering (*60*) workflow with default parameters. A group of 3927 neurons was identified and the Seurat functions FindTransferAnchors and TransferData were utilized to label them using a human DRG neuronal dataset (*61*) as a reference. The expression of *PKDCC* across neuronal subpopulations, the neuron type composition of PKDCC^{+} neurons, and the expression of subpopulation marker genes in *PKDCC*$^{+}$ neurons were evaluated to assess the specificity of *PKDCC*. Figures were generated using Seurat's inbuilt plotting functions along with the R packages ggplot2 (v 3.5.1) and lessR (v4.4.2).

Mouse DRG: Mouse data was obtained from a published transcriptomic atlas of the DRG with 58198 neurons from 17 mouse DRG single-cell RNA-seq datasets (*22*). The same human DRG dataset (*61*) was used as reference to label the mouse neurons, and *Pkdcc* expression was evaluated in a similar manner.

DRG dissection, RNAScope, immunohistochemistry

Immunohistochemistry and RNAScope were carried out on mouse and human DRG as previously described (*62*). Briefly, adult mice were euthanized by isoflurane inhalation. Lumbar DRGs and spinal cords were dissected and immediately embedded in OCT (Fisher #1437365) and frozen on dry ice. Frozen tissues from mouse and human subjects were cryostat sectioned at 20 μM onto SuperFrost Plus charged slides. mRNA transcripts were detected using the RNAscope Fluorescent Multiplex Assay (Advanced Cell Diagnostics) and RNAscope Fluorescent Multiplex Reagent Kit (#320851 & #323100). The RNAscope catalog probes used to detect were (For mouse *Pkdcc* (#516961), *Scn10a* (#426011-C2), *Tacr1* (#428781-C3), and human *PKDCC* (#525121), *SCN10A* (#406291-C2)). Counterstaining for NF200 and NeuN was done with immunohistochemistry on the same tissues. Tissues were blocked in 0.1M Phosphate Buffer with 10% Normal Goat Serum and 0.3% Triton-X. Primary antibody was incubated overnight at 4°C. Secondary antibodies were incubated for 1 hour at room temperature. Coverslips were mounted with Prolong Gold Antifade (Fisher #P36930). IB4 and Cgrp staining was performed identically on mouse DRG and spinal cord sections. Images were taken on an Olympus Fluoview FV1000 confocal microscope at 20X magnification. Histological analyses were carried out using Olympus Cellsens software. Frequency distribution, colocalization data, and diameter measurements were calculated as described before (*63*). The Cellsens Count and Measure tool was used to conduct colocalization and cell area analyses in the DRG and spinal cord. To characterize the expression level-based distribution of *Pkdcc* transcripts in the mouse DRG neurons, expression levels were defined as Low (1 to 10 puncta) and High (>10 puncta).

cFos and NeuN staining were conducted on free-floating mouse lumbar spinal cord sections. Adult mice were euthanized by isoflurane inhalation. Lumbar spinal cords were dissected and drop-fixed in 10% formalin for 2 hours, cryoprotected, embedded in OCT (Fisher #1437365), and frozen on dry ice. Tissues were cryostat sectioned at 40 μm. Tissues were blocked in 0.1M Phosphate buffer with 10% Normal Goat Serum and 0.3% Triton-X and incubated in cFos and NeuN primary antibodies for 48 hours at 4°C. Secondary antibodies were incubated for 2 hours at room temperature. Sections were slide-mounted and coverslipped with Prolong Gold Antifade. Images were taken on an Olympus Fluoview FV1000 confocal microscope at 20X magnification. cFos^{+} cell counts were carried out using Imaris software.

Generation of a VLK-specific antibody

Antibodies against the ATP binding region of VLK were generated in rabbits against a peptide of the sequence Ac-CKALKAVDFSGHDLGS-NH2 (Covance, Denver, PA). Serum was collected and passed through a column containing SulfoLink Coupling Resin (Thermo Scientific, Cat # 20402) conjugated to KLH peptide. The serum was then incubated overnight in a column containing resin conjugated to the above VLK peptide. The antibody was eluted with glycine, pH 2.0, and then extensively dialyzed in PBS.

Somascan assay

Tissue lysates were prepared from fresh-frozen DRG and from the dorsal and ventral horn portions of the lumbar spinal cord. The tissues were placed in T-PER Tissue Protein Extraction Reagent (Thermo Scientific, Cat # 78510) with additional 1X Halt Protease Inhibitor Cocktail (Thermo Scientific, Cat # 87786) and homogenized using Precellys Soft Tissue Homogenizing beads (Bertin Corp, Cat # P000933-LYSK0-A.0). Samples were centrifuged at 14,000 × *g* for 15 min in the cold room. The resulting supernatant was quantified Micro BCA Protein Assay Kit (Thermo Scientific, Cat# 23235) and normalized accordingly. Proteins were profiled using the SOMAScan platform. 7000 analytes were measured on the SOMAScan assay. The quality controls were performed by SomaLogic to correct technical variability within and between runs for each sample.

Generation of *Pkdcc*$^{flox/flox}$ mice and respective cKO mice lines

Pkdcc-floxed mice were generated at the UT Health San Antonio Mouse Genome Engineering Facility via CRISPR/Cas9-mediated HDR in zygote. Briefly, two DSBs flanking the first exon and upstream enhancer sites of the *Pkdcc* gene were produced, and LoxP cassettes were introduced via homologous recombination (shown in Fig. 2). The recombination induced by Cre-recombination of exon 1 would result in *Pkdcc* loss of function. Thus, the resulting mice were bred, and homozygous *Pkdcc*$^{flox/flox}$ was selected by PCR genotyping. For genotyping, DNA was extracted from the ear samples during weaning to determine the genotypes of *Pkdcc* flox mice (KAPA mouse genotyping kit). The primers used for genotyping were mentioned in Table S2. The PCR products were visualized by electrophoresis on a 2-3% agarose gel. The *Pkdcc* floxed mice were bred with *CaMKII-Cre* mice to delete *Pkdcc* in excitatory neurons. The *Pirt*-Cre transgenic mouse line in this study was obtained from Xinzhong Dong at Johns Hopkins University (C13783-*Pirt*-Cre mice) and used to generate sensory neuron–specific knockout of *Pkdcc*. To

determine if VLK is acting on EphB2 receptors expressed, we generated a mouse line expressing LoxP sites flanking the third exon of the *Ephb2* gene. These mice were crossed with the *Tacr1*-Cre driver line to create conditional knockouts of EphB2 in spinal cord projection neurons.

Behavior

Mechanical Withdrawal Thresholds were determined using von Frey Filament testing, following the method of (*64*). Animals were habituated to plexiglass chambers (11.4 × 7.6 × 7.6 cm) suspended on wire mesh racks. Baseline withdrawal thresholds were measured before experimental treatments, and subsequent testing was done at various timepoints indicated in each figure. Mechanical sensitivity was determined by applying von Frey filaments to the plantar aspect of the hindpaws, and a response was indicated by flicking or withdrawal of the paw. For mice subjected to hindpaw incision surgeries, filaments were instead applied to the heel of the hindpaw near the site of injury, but avoiding scar tissue.

Mouse grimace scoring was conducted using the Mouse Grimace Scale (MGS) described by (*65*). After acclimating to the suspended plexiglass chambers for an hour, mice were scored according to the MGS by blinded experimenters at baseline and posttreatment time points, which are indicated in each figure. The grimace scores were averaged by group at each time point and plotted respectively.

Intrathecal injections were performed as previously described under isoflurane anesthesia (*6*). Drugs were administered in a 5 uL volume with a Hamilton syringe. Drugs were diluted in sterile saline. Heat denaturation was done by heating proteins at 70°C for 30 min. VLK, KD-VLK, DIA1, FAM69c, and denatured controls were administered at concentrations of 0.1mg/mL; PAP was administered at 1.5mg/mL (*13*). APV was administered at 0.2mg/mL. Drugs were administered with a Hamilton syringe in a 5 uL volume, except for when PAP was coadministered with VLK, which was done using an 8.5 uL volume. VLK used for injections was either purified in-house or purchased from Sinobiological (Cat# V05-31G).

Radiant heat sensitivity was determined using the Hargreaves method (*66*). Mice were placed on a warmed glass floor (29°C) 20 min before each testing, and, using a Hargreaves apparatus (IITC Model 390), a focused beam of high-intensity light was aimed at the plantar nonglabrous surface of the hindpaws. The intensity of the light was set to 30% of maximum with a cutoff value of 20 s. The latency to withdraw either hindpaw was measured to the nearest 0.01 s. The withdrawal latencies for both paws were averaged for each animal.

Heat tolerance/sensitivity was measured using the Hot Plate assay. A day prior to testing, mice were habituated to the Hot Plate Plexiglass box (IITC) for 10 min. For testing, mice were placed individually on the hot plate, heated to either 50°C or 55°C, and the latency to the first sign of paw licking or jumping was recorded. The experiment was repeated 3 times with at least 48 hours between measurements. Stimulus cutoffs of 45 s and 1 min were used, respectively, for 50°C and 55°C.

Cold sensitivity was measured using the cold plantar assay (*67*). Mice were habituated for 30 min to plexiglass chambers with breathing holes resting atop a 1/8th in thick glass base. The cold probe was made of finely crushed dry ice packed into a modified 3mL BD syringe. Mice were tested by pressing the cold probe against the glass directly underneath the center of the hindpaw, and latency to withdraw the paw from the cold glass was recorded with a maximum cutoff time of 20 s. Mice were tested 4 times with at least 15 min between trials.

Sensorimotor evaluation was done using the rotarod test. Mice were acclimated to the Rotarod apparatus (IITC) a day before testing for 5 min at 4 RPM. For testing, mice were placed on the rotating rod, and the RPM was increased from 4 to 40 at a constant rate over 5 min. Latency to fall, RPM at fall, and total distance traveled were all recorded automatically by the apparatus. Three trials were conducted, with at least 15 min between trials.

Acute nociception was determined by the capsaicin test. WT and cKO mice were placed for a 30-min acclimation period in the plexiglass chambers. After this period, the mice were gently restrained and administered hindpaw intraplantar injections of 125ug/mL capsaicin (Sigma) in 20 uL saline solution. The mice were immediately returned to their respective chambers, and their behavior was recorded for 5 min following the injection. The time spent licking/biting the injected paw was determined by averaging the scores of two experimenters blinded to genotype.

Hindpaw incision surgeries were performed on transgenic animals as previously described (*6*, *68*). Briefly, a ~5 mm incision was made on the plantar skin of the left hindpaw under isoflurane anesthesia. The flexor digitorum brevis muscle was briefly lifted (not cut) with forceps, and the incision site was sutured closed.

Spared nerve injury was performed as previously described (*69*). Briefly, mice were anesthetized under isoflurane anesthesia. The tibial and peroneal branches of the left sciatic nerve trifurcation were ligated and cut, leaving the sural branch intact. Sham surgeries were performed the same way, but without ligating/cutting the nerve. A single injection of the antibiotic gentamicin (3 mg/kg s.q.) was given immediately following surgery.

Antibodies

The following primary antibodies and dilutions were used:

Mouse monoclonal (IgG1) anti-GluN1 (1:500 (WB), 1:200 (PLA), BioLegend, clone R1JHL, cat# 828201, lot# B383911), goat polyclonal anti-EphB2 (1:1200 (PLA), R&D Systems, cat# AF467, lot# CVT0315041), mouse monoclonal (IgG1) anti-EphB2 (1:500 (WB), Thermo Fisher Scientific, clone 1A6C9, cat# 37-1700, lot# RD2115698), mouse monoclonal (IgG2b) anti-pTyr (PY99) (1:2000 (WB), Santa Cruz, Cat# sc-7020; lot# L022), rabbit polyclonal anti-FLAG (1:1000 (WB), Sigma, Cat #F7425, lot# 078M4886V), mouse monoclonal (IgG2a) anti-PSD-95 (1:2500 (WB), 1:250(ICC), Neuromab, clone 28/43, cat# 75-028, lot# 472-2JU/02), mouse monoclonal (IgG1) anti-NeuN (2 μg/mL (IHC), Millipore, clone A60, cat# MAB377), mouse monoclonal (IgG1) anti-Neurofilament 200 (2 μg/mL (IHC), Millipore, clone N52, cat# MAB5266), rabbit polyclonal anti-Cgrp (1:500 (IHC), Immunostar, cat# 24112), guinea pig recombinant monoclonal (IgG2κ) anti-c-Fos (1:10000 (IHC), Synaptic Systems, cat# 226308), mouse monoclonal (IgG1) anti-Synaptophysin-1 (1:5000 (WB), Synaptic Systems, clone 7.2, cat# 101 111, lot# 1-46), mouse monoclonal (IgG1) anti-Synaptotagmin-1 (1:2000 (WB), Synaptic Systems, Cat# 105011, lot# 1-47), rabbit polyclonal anti-Synaptotagmin-5/9 (1:2000 (WB), Synaptic Systems, Cat#160003 rabbit polyclonal Homer 1 Antibody(1:1000(ICC)), Synaptic Systems, Cat# 105053, lot# 1-8), rabbit polyclonal anti-RFP (1:2000(WB), Rockland, Cat# 600-401-379, lot# 46510), mouse monoclonal (IgG1) anti-GAPDH (1:500 (WB), Millipore, Cat# MAB374, lot# 4045089), rabbit polyclonal anti-Tubulin (1:10,000 (WB), Abcam, Cat# ab18251, lot# GR235480-2), rabbit polyclonal anti-Flotilin (1:1000, Novus Bio, Cat# NBP187498, lot# 000020065), mouse monoclonal (IgG2b) anti-actin (1:2000 (ICC), Biolegend, clone 2F-1, Cat# 643801, lot# B266258), anti-Rabbit VLK (1:2000 (WB), Generated by our lab), anti-rabbit EphB2-pY662 (1:2000 (WB), anti-rabbit EphB2-pY504 (1:1000 (WB) previously described and validated (Kenji paper) (*9*)), guinea pig polyclonal anti-vesicular glutamate transporter 1 (vGlut1; 1:5000, (ICC), Millipore, Cat# AB5905, lot# 3987239) guinea pig polyclonal anti-vesicular glutamate transporter 2 (vGlut2; 1:2000, (ICC) Merck Cat#AB2251-1, phosphor-CREB ser 133 (1:1000, WB,ICC) Cell Signaling, #9198, CREB(1:1000) (WB) Cell Signalling, Cat#4820, Calpain-2 Polyclonal Antibody, (1:1000) (WB) Invitrogen Cat # PA5-17494, Mu-Calpain Monoclonal Antibody, Invitrogen Cat # MA3-940 (1:1000) (WB), DAPI, Invitrogen Cat #D1306 (1:5000)(ICC).

The following secondary antibodies were used:

Donkey anti-mouse-HRP (1:10,000 (WB), Jackson ImmunoResearch, cat# 715035151 lot# 151303), Donkey anti-rabbit-HRP (1:10,000 (WB), Jackson ImmunoResearch, cat# 711035152, lot# 163128), Goat anti-guinea pig DyLight-488 (1:5000 (PLA), Abcam, cat# ab102374, lot# 1041504), Donkey anti-mouse AlexaFluor-647 (1:500 (ICC), Jackson ImmunoResearch,

Donkey- Anti- Rabbit AlexaFluor-594 (1:500) (ICC), Cat#711-587-003, Jackson ImmunoResearch, cat# 715605150, lot#160478), Goat anti- Mouse IgG1 AlexaFluor-555 (1:500 (IHC), Thermo Fisher Scientific, cat# 21127), Goat anti-Mouse IgG1 AlexaFluor-647 (1:500 (IHC), Thermo Fisher Scientific, cat# 21240), Goat anti-Guinea pig AlexaFluor-647 (1:500 (IHC), Thermo Fisher Scientific, cat# A21450).

Statistical analysis

GraphPad Prism Software was used to carry out statistical analyses and generate graphs. The respective figure legends indicate the number of subjects used and the statistical analysis, including post hoc comparison tests, used for individual experiments. Mice were randomly allocated to experimental groups when possible. Behavioral testing was carried out by investigators blinded to treatment or genotype, and different experimenters successfully reproduced the results. *P*-values of less than 5% were considered statistically significant, with * representing $P < 0.05$, ** representing $P < 0.01$, *** representing $P < 0.005$, and **** representing $P < 0.001$ unless otherwise indicated. All the illustrative models were made using Biorender.

REFERENCES AND NOTES

1. V. S. Tagliabracci *et al.*, A single kinase generates the majority of the secreted phosphoproteome. *Cell* **161**, 1619–1632 (2015). doi: 10.1016/j.cell.2015.05.028; pmid: 26091039
2. V. S. Tagliabracci *et al.*, Secreted kinase phosphorylates extracellular proteins that regulate biomineralization. *Science* **336**, 1150–1153 (2012). doi: 10.1126/science.1217817; pmid: 22582013
3. Y. Imuta, N. Nishioka, H. Kiyonari, H. Sasaki, Short limbs, cleft palate, and delayed formation of flat proliferative chondrocytes in mice with targeted disruption of a putative protein kinase gene, Pkdcc (AW548124). *Dev. Dyn.* **238**, 210–222 (2009). doi: 10.1002/dvdy.21822; pmid: 19097194
4. H. R. Washburn, N. L. Xia, W. Zhou, Y. T. Mao, M. B. Dalva, Positive surface charge of GluN1 N-terminus mediates the direct interaction with EphB2 and NMDAR mobility. *Nat. Commun.* **11**, 570 (2020). doi: 10.1038/s41467-020-14345-6; pmid: 31996679
5. H. R. Washburn, P. Chander, K. D. Srikanth, M. B. Dalva, Transsynaptic Signaling of Ephs in synaptic Development, Plasticity, and Disease. *Neuroscience* **508**, 137–152 (2023). doi: 10.1016/j.neuroscience.2022.11.030; pmid: 36460219
6. K. Hanamura *et al.*, Extracellular phosphorylation of a receptor tyrosine kinase controls synaptic localization of NMDA receptors and regulates pathological pain. *PLOS Biol.* **15**, e2002457 (2017). doi: 10.1371/journal.pbio.2002457; pmid: 28719605
7. M. J. Nolt *et al.*, EphB controls NMDA receptor function and synaptic targeting in a subunit-specific manner. *J. Neurosci.* **31**, 5353–5364 (2011). doi: 10.1523/JNEUROSCI.0282-11.2011; pmid: 21471370
8. M. S. Kayser, A. C. McClelland, E. G. Hughes, M. B. Dalva, Intracellular and trans-synaptic regulation of glutamatergic synaptogenesis by EphB receptors. *J. Neurosci.* **26**, 12152–12164 (2006). doi: 10.1523/JNEUROSCI.3072-06.2006; pmid: 17122040
9. M. B. Dalva *et al.*, EphB receptors interact with NMDA receptors and regulate excitatory synapse formation. *Cell* **103**, 945–956 (2000). doi: 10.1016/S0092-8674(00)00197-5; pmid: 11136979
10. J. J. Mojica, G. Eddy, E. S. Schwenk, N-Methyl-D-aspartate receptor antagonists for the prevention of chronic postsurgical pain: A narrative review. *Reg. Anesth. Pain Med.* **50**, 160–167 (2025). doi: 10.1136/rapm-2024-105612; pmid: 39909540
11. C. Minkin, Bone acid phosphatase: Tartrate-resistant acid phosphatase as a marker of osteoclast function. *Calcif. Tissue Int.* **34**, 285–290 (1982). doi: 10.1007/BF02411252; pmid: 6809291
12. H. Rico, L. F. Villa, Serum tartrate-resistant acid phosphatase (TRAP) as a biochemical marker of bone remodeling. *Calcif. Tissue Int.* **52**, 149–150 (1993). doi: 10.1007/BF00308325; pmid: 8443692
13. M. J. Zylka *et al.*, Prostatic acid phosphatase is an ectonucleotidase and suppresses pain by generating adenosine. *Neuron* **60**, 111–122 (2008). doi: 10.1016/j.neuron.2008.08.024; pmid: 18940592
14. I. B. Quintero *et al.*, Transmembrane prostatic acid phosphatase (TMPAP) interacts with snapin and deficient mice develop prostate adenocarcinoma. *PLOS ONE* **8**, e73072 (2013). doi: 10.1371/journal.pone.0073072; pmid: 24039861
15. P. Guedes-Dias, E. L. F. Holzbaur, Axonal transport: Driving synaptic function. *Science* **366**, eaaw9997 (2019). doi: 10.1126/science.aaw9997; pmid: 31601744
16. Y. Wang, V. Briz, A. Chishti, X. Bi, M. Baudry, Distinct roles for μ-calpain and m-calpain in synaptic NMDAR-mediated neuroprotection and extrasynaptic NMDAR-mediated neurodegeneration. *J. Neurosci.* **33**, 18880–18892 (2013). doi: 10.1523/JNEUROSCI.3293-13.2013; pmid: 24285894
17. M. A. Takasu, M. B. Dalva, R. E. Zigmond, M. E. Greenberg, Modulation of NMDA receptor-dependent calcium influx and gene expression through EphB receptors. *Science* **295**, 491–495 (2002). doi: 10.1126/science.1065983; pmid: 11799243
18. G. E. Hardingham, Y. Fukunaga, H. Bading, extrasynaptic NMDARs oppose synaptic NMDARs by triggering CREB shut-off and cell death pathways. *Nat. Neurosci.* **5**, 405–414 (2002). doi: 10.1038/nn835; pmid: 11953750
19. T. Biederer, P. S. Kaeser, T. A. Blanpied, Transcellular Nanoalignment of synaptic Function. *Neuron* **96**, 680–696 (2017). doi: 10.1016/j.neuron.2017.10.006; pmid: 29096080
20. N. Ahimsadasan, V. Reddy, M. Z. Khan Suheb, A. Kumar, "Neuroanatomy, Dorsal Root Ganglion" in *StatPearls* (StatPearls Publishing, 2024); https://www.ncbi.nlm.nih.gov/books/NBK532291/.
21. S. I. Sheffler-Collins, M. B. Dalva, EphBs: An integral link between synaptic function and synaptopathies. *Trends Neurosci.* **35**, 293–304 (2012). doi: 10.1016/j.tins.2012.03.003; pmid: 22516618
22. S. A. Bhuiyan *et al.*, IV, Harmonized cross-species cell atlases of trigeminal and dorsal root ganglia. *Sci. Adv.* **10**, eadj9173 (2024). doi: 10.1126/sciadv.adj9173; pmid: 38905344
23. A. Y. Kim *et al.*, Pirt, a phosphoinositide-binding protein, functions as a regulatory subunit of TRPV1. *Cell* **133**, 475–485 (2008). doi: 10.1016/j.cell.2008.02.053; pmid: 18455988
24. E. V. Brown, A. F. Malik, E. R. Moese, A. F. McElroy, A. C. Lepore, Differential activation of pain circuitry neuron populations in a mouse model of spinal cord injury-induced neuropathic pain. *J. Neurosci.* **42**, 3271–3289 (2022). doi: 10.1523/JNEUROSCI.1596-21.2022; pmid: 35256528
25. A. Barik *et al.*, A spinoparabrachial circuit defined by Tacr1 expression drives pain. *eLife* **10**, e61135 (2021). doi: 10.7554/eLife.61135; pmid: 33591273
26. S. Choi *et al.*, Parallel ascending spinal pathways for affective touch and pain. *Nature* **587**, 258–263 (2020). doi: 10.1038/s41586-020-2860-1; pmid: 33116307
27. O. Gautier *et al.*, Challenges of profiling motor neuron transcriptomes from human spinal cord. *Neuron* **111**, 3739–3741 (2023). doi: 10.1016/j.neuron.2023.10.035; pmid: 38061330
28. A. M. Bell *et al.*, Deep sequencing of Phox2a nuclei reveals five classes of anterolateral system neurons. bioRxiv 2023.08.20.553715v1 [Preprint] (2020); doi: 10.1101/2023.08.20.553715
29. J. A. Blum *et al.*, Single-cell transcriptomic analysis of the adult mouse spinal cord reveals molecular diversity of autonomic and skeletal motor neurons. *Nat. Neurosci.* **24**, 572–583 (2021). doi: 10.1038/s41593-020-00795-0; pmid: 33589834
30. T. L. Daigle *et al.*, A Suite of Transgenic Driver and Reporter Mouse Lines with Enhanced Brain-Cell-Type Targeting and Functionality. *Cell* **174**, 465–480.e22 (2018). doi: 10.1016/j.cell.2018.06.035; pmid: 30007418
31. T. Huang *et al.*, Identifying the pathways required for coping behaviours associated with sustained pain. *Nature* **565**, 86–90 (2019). doi: 10.1038/s41586-018-0793-8; pmid: 30532001
32. J. P. Dupuis, O. Nicole, L. Groc, NMDA receptor functions in health and disease: Old actor, new dimensions. *Neuron* **111**, 2312–2328 (2023). doi: 10.1016/j.neuron.2023.05.002; pmid: 37236178
33. R. C. Malenka, R. A. Nicoll, NMDA-receptor-dependent synaptic plasticity: Multiple forms and mechanisms. *Trends Neurosci.* **16**, 521–527 (1993). doi: 10.1016/0166-2236(93)90197-T; pmid: 7509523
34. B. C. Park, M. Reese, V. S. Tagliabracci, Thinking outside of the cell: Secreted protein kinases in bacteria, parasites, and mammals. *IUBMB Life* **71**, 749–759 (2019). doi: 10.1002/iub.2040; pmid: 30941842
35. J. Egea, R. Klein, Bidirectional Eph-ephrin signaling during axon guidance. *Trends Cell Biol.* **17**, 230–238 (2007). doi: 10.1016/j.tcb.2007.03.004; pmid: 17420126
36. J. G. Flanagan, Neural map specification by gradients. *Curr. Opin. Neurobiol.* **16**, 59–66 (2006). doi: 10.1016/j.conb.2006.01.010; pmid: 16417998
37. J. G. Flanagan, P. Vanderhaeghen, The ephrins and Eph receptors in neural development. *Annu. Rev. Neurosci.* **21**, 309–345 (1998). doi: 10.1146/annurev.neuro.21.1.309; pmid: 9530499
38. C. J. Woolf, M. W. Salter, Neuronal plasticity: Increasing the gain in pain. *Science* **288**, 1765–1768 (2000). doi: 10.1126/science.288.5472.1765; pmid: 10846153
39. D. L. Hunt, P. E. Castillo, synaptic plasticity of NMDA receptors: Mechanisms and functional implications. *Curr. Opin. Neurobiol.* **22**, 496–508 (2012). doi: 10.1016/j.conb.2012.01.007; pmid: 22325859
40. N. T. Henderson, M. B. Dalva, EphBs and ephrin-Bs: Trans-synaptic organizers of synapse development and function. *Mol. Cell. Neurosci.* **91**, 108–121 (2018). doi: 10.1016/j.mcn.2018.07.002; pmid: 30031105
41. A. Latremoliere, C. J. Woolf, Central sensitization: A generator of pain hypersensitivity by central neural plasticity. *J. Pain* **10**, 895–926 (2009). doi: 10.1016/j.jpain.2009.06.012; pmid: 19712899
42. R. Ruscheweyh, O. Wilder-Smith, R. Drdla, X. G. Liu, J. Sandkühler, Long-term potentiation in spinal nociceptive pathways as a novel target for pain therapy. *Mol. Pain* **7**, 20 (2011). doi: 10.1186/1744-8069-7-20; pmid: 21443797

43. C. N. Sang, NMDA-receptor antagonists in neuropathic pain: Experimental methods to clinical trials. *J. Pain Symptom Manage.* **19**, S21–S25 (2000). doi: 10.1016/S0885-3924(99)00125-6; pmid: 10687335
44. V. Cibert-Goton *et al.*, Involvement of EphB1 receptors signalling in models of inflammatory and neuropathic pain. *PLOS ONE* **8**, e53673 (2013). doi: 10.1371/journal.pone.0053673; pmid: 23341972
45. H. Kobayashi *et al.*, Involvement of EphB1 receptor/EphrinB2 ligand in neuropathic pain. *Spine* **32**, 1592–1598 (2007). doi: 10.1097/BRS.0b013e318074d46a; pmid: 17621205
46. P. Chander, M. J. Kennedy, B. Winckler, J. P. Weick, Neuron-specific gene 2 (NSG2) encodes an AMPA receptor interacting protein that modulates excitatory neurotransmission. *eneuro* **6**, ENEURO.0292-18.2018 (2019). doi: 10.1038/s41593-018-0138-9; pmid: 29686261
47. M. Hruska, N. Henderson, S. J. Le Marchand, H. Jafri, M. B. Dalva, synaptic nanomodules underlie the organization and plasticity of spine synapses. *Nat. Neurosci.* **21**, 671–682 (2018). doi: 10.1038/s41593-018-0138-9; pmid: 29686261
48. Y. T. Mao *et al.*, Filopodia Conduct Target Selection in Cortical Neurons Using Differences in Signal Kinetics of a Single Kinase. *Neuron* **98**, 767–782.e8 (2018). doi: 10.1016/j.neuron.2018.04.011; pmid: 29731254
49. M. R. Bordoli *et al.*, A secreted tyrosine kinase acts in the extracellular environment. *Cell* **158**, 1033–1044 (2014). doi: 10.1016/j.cell.2014.06.048; pmid: 25171405
50. D. Guez-Barber *et al.*, FACS purification of immunolabeled cell types from adult rat brain. *J. Neurosci. Methods* **203**, 10–18 (2012). doi: 10.1016/j.jneumeth.2011.08.045; pmid: 21911005
51. M. Hruska, N. T. Henderson, N. L. Xia, S. J. Le Marchand, M. B. Dalva, Anchoring and synaptic stability of PSD-95 is driven by ephrin-B3. *Nat. Neurosci.* **18**, 1594–1605 (2015). doi: 10.1038/nn.4140; pmid: 26479588
52. A. J. B. Kreutzberger *et al.*, Reconstitution of calcium-mediated exocytosis of dense-core vesicles. *Sci. Adv.* **3**, e1603208 (2017). doi: 10.1126/sciadv.1603208; pmid: 28776026
53. J. Rappsilber, M. Mann, Y. Ishihama, Protocol for micro-purification, enrichment, pre-fractionation and storage of peptides for proteomics using StageTips. *Nat. Protoc.* **2**, 1896–1906 (2007). doi: 10.1038/nprot.2007.261; pmid: 17703201
54. Y. Xu *et al.*, Cardiolipin remodeling enables protein crowding in the inner mitochondrial membrane. *EMBO J.* **40**, e108428 (2021). doi: 10.15252/embj.2021108428; pmid: 34661298
55. J. Cox *et al.*, Andromeda: A peptide search engine integrated into the MaxQuant environment. *J. Proteome Res.* **10**, 1794–1805 (2011). doi: 10.1021/pr101065j; pmid: 21254760
56. S. Tyanova, T. Temu, J. Cox, The MaxQuant computational platform for mass spectrometry-based shotgun proteomics. *Nat. Protoc.* **11**, 2301–2319 (2016). doi: 10.1038/nprot.2016.136; pmid: 27809316
57. R. Craig, J. P. Cortens, R. C. Beavis, Open source system for analyzing, validating, and storing protein identification data. *J. Proteome Res.* **3**, 1234–1242 (2004). doi: 10.1021/pr049882h; pmid: 15595733
58. S. D. Sherrod *et al.*, Label-free quantitation of protein modifications by pseudo selected reaction monitoring with internal reference peptides. *J. Proteome Res.* **11**, 3467–3479 (2012). doi: 10.1021/pr201240a; pmid: 22559222
59. T. Stu *et al.*, Comprehensive Integration of Single-Cell Data. *Cell* **177**, 1888–1902.e1821 (2019). doi: 10.1021/pr201240a; pmid: 22559222
60. Y. Hao *et al.*, Integrated analysis of multimodal single-cell data. *Cell* **184**, 3573–3587.e29 (2021). doi: 10.1016/j.cell.2021.04.048; pmid: 34062119
61. D. Tavares-Ferreira *et al.*, Spatial transcriptomics of dorsal root ganglia identifies molecular signatures of human nociceptors. *Sci. Transl. Med.* **14**, eabj8186 (2022). doi: 10.1126/scitranslmed.abj8186; pmid: 35171654
62. S. Shiers, R. M. Klein, T. J. Price, Quantitative differences in neuronal subpopulations between mouse and human dorsal root ganglia demonstrated with RNAscope in situ hybridization. *Pain* **161**, 2410–2424 (2020). doi: 10.1097/j.pain.0000000000001973; pmid: 32639368
63. S. I. Shiers *et al.*, Convergence of peptidergic and non-peptidergic protein markers in the human dorsal root ganglion and spinal dorsal horn. *J. Comp. Neurol.* **529**, cne.25122 (2021). doi: 10.1002/cne.25122; pmid: 33550628
64. S. R. Chaplan, F. W. Bach, J. W. Pogrel, J. M. Chung, T. L. Yaksh, Quantitative assessment of tactile allodynia in the rat paw. *J. Neurosci. Methods* **53**, 55–63 (1994). doi: 10.1016/0165-0270(94)90144-9; pmid: 7990513
65. D. J. Langford *et al.*, Coding of facial expressions of pain in the laboratory mouse. *Nat. Methods* **7**, 447–449 (2010). doi: 10.1038/nmeth.1455; pmid: 20453868
66. M. Cheah, J. W. Fawcett, M. R. Andrews, Assessment of Thermal Pain Sensation in Rats and Mice Using the Hargreaves Test. *Bio Protoc.* **7**, e2506 (2017). doi: 10.21769/BioProtoc.2506; pmid: 28920069
67. D. S. Brenner, J. P. Golden, R. W. Gereau IV, A novel behavioral assay for measuring cold sensation in mice. *PLOS ONE* **7**, e39765 (2012). doi: 10.1371/journal.pone.0039765; pmid: 22745825
68. A. M. Cowie, C. L. Stucky, A Mouse Model of Postoperative Pain. *Bio Protoc.* **9**, e3140 (2019). doi: 10.21769/BioProtoc.3140; pmid: 30820443
69. S. Shiers, H. Elahi, S. Hennen, T. J. Price, Evaluation of calcium-sensitive adenylyl cyclase AC1 and AC8 mRNA expression in the anterior cingulate cortex of mice with spared nerve injury neuropathy. *Neurobiol. Pain* **11**, 100081 (2021). doi: 10.1016/j.ynpai.2021.100081; pmid: 35005298

ACKNOWLEDGMENTS

The authors thank E. Vines, P. Horton, G. Funk, A. Cervantes, and others at the Southwest Transplant Alliance for the recovery of tissues from organ donors. The authors thank the organ donors and their families for their gift. We thank M. Zylka at the University of North Carolina, Chapel Hill, for the gift of recombinant PAP. We thank P. Walsh and V. Truong for their assistance with the iSN work. We thank members of the Price and Dalva lab for advice. **Funding:** This work was funded by the following: National Institutes of Health grant R01NS111976 (to T.J.P. and M.B.D.) National Institutes of Health grant R01NS115441 (to T.J.P. and M.B.D.) National Institutes of Health grant U19NS130608 to (T.J.P. and P.M.D.) National Institutes of Health grant RO1DA022727 to (M.B.D.) National Institutes of Health grant S10RR027990 to (T.A.N.) **Author contributions:** Conceptualization: T.J.P. and M.B.D. Methodology: K.D.S., H.E., P.C., H.R.W., R.P., Z.C., T.J.P., and M.B.D. Investigation: K.D.S., H.E., P.C., H.R.W., S.H., M.K., J.M.M., J.L., R.A., L.H., K.M., S.I.S., R.P., and I.S. Visualization: K.D.S., H.E., P.C., and H.R.W. Funding acquisition: P.M.D., T.J.P., and M.B.D. Project administration: T.J.P. and M.B.D. Supervision: P.M.D., T.J.P., and M.B.D. Writing – original draft: K.D.S., H.E., P.C., H.R.W., T.J.P., and M.B.D. Writing – review and editing: K.D.S., H.E., P.C., H.R.W., T.J.P., and M.B.D. **Competing interests:** Disclosures: Paid and unpaid consulting: Grunenthal, Vertex, AbbVie, and Pacira (T.J.P.). Z.T.C. is a consultant for Arrowhead Pharmaceuticals. A patent application has been filed around VLK targeting for pain by UTD and TJU: U.S. Patent Application 19/054,404, based on Provisional Patent Application 63/554,730, entitled "Modulation of Extracellular Kinase Activity and Function for Treatment of Pain and Neurodegenerative/Neuroimmune Disease" by T. J. Price and M. B. Dalva, In the name of: Board of Regents, The University of Texas Systems, and Thomas Jefferson University **Data and materials availability:** All data are available in the main text or the supplementary materials. Raw data files supporting the findings of the manuscript are attached as supplemental files to the manuscript. The EphB2flox/flox (EphB2-cKo) and Pkdccflox/flox (Pkdcc-cKO) mouse lines are available from M.B.D. under a material transfer agreement with the TJU/UTD/University of Texas Health Science Center at San Antonio. **License information:** Copyright © 2025 the authors, some rights reserved; exclusive licensee American Association for the Advancement of Science. No claim to original US government works. https://www.science.org/content/page/science-licenses-journal-article-reuse

SUPPLEMENTARY MATERIALS

science.org/doi/10.1126/science.adp1007
Figs. S1 to S11; Tables S1 and S2; Movie S1; MDAR Reproducibility Checklist; Data S1 to S4

Submitted 15 March 2024; resubmitted 15 April 2025; accepted 27 August 2025
10.1126/science.adp1007

Your Legacy to Science

AN ESTATE GIFT TO THE
AMERICAN ASSOCIATION FOR THE ADVANCEMENT OF SCIENCE

Since 1848, our founding year, the American Association for the Advancement of Science (AAAS) has been deeply committed to advancing science, engineering and innovation around the world for the benefit of all people.

By making AAAS a beneficiary of your will, trust, retirement plan or life insurance policy, you become a member of our 1848 Society, joining Thomas Edison, Alexander Graham Bell and the many distinguished individuals whose vision led to the creation of AAAS and our world-renowned journal, *Science*, so many years ago.

Unlike many of its peers, *Science* is not for-profit. Your estate gift would provide long-term financial stability and durable annual income that will support operations and competitive innovation for years to come. **This support is vital.**

"As a teacher and instructor, I bear responsibility for the younger generations. If you have extra resources, concentrate them on organizations, like AAAS, that are doing work for all."

—Prof. Elisabeth Ervin-Blankenheim, 1848 Society member

If you intend to include AAAS in your estate plans, provide this information to your lawyer or financial adviser:

Legal Name: American Association for the Advancement of Science
Federal Tax ID Number: 53-0196568
Address: 1200 New York Avenue, NW, Washington, DC 20005

If you would like more information on making an estate gift to AAAS, cut out and return the form below or send an email to philanthropy@aaas.org. Additional details are also available online at **www.aaas.org/1848Society**.

1848 SOCIETY AAAS

cut here

Yes, I would like more information about joining the AAAS 1848 Society.

PLEASE CONTACT ME AT:

Name: _____

Address: _____

City: _____ State: _____ Zip code: _____ Country: _____

Email: _____ Phone: _____

RETURN THIS FORM TO:
AAAS Office of Philanthropy and Strategic Partnerships • 1200 New York Avenue, NW • Washington, DC 20005 USA

RESEARCH ARTICLE SUMMARY

IMMUNOLOGY

An *Aeromonas* variant that produces aerolysin promotes susceptibility to ulcerative colitis

Zhihui Jiang†, Ye Wang†, Jianfeng Gong†, Xin Chen† *et al.*

Full article and list of author affiliations: https://doi.org/10.1126/science.adz4712

INTRODUCTION: Ulcerative colitis (UC) is a multifactorial disease involving immune dysregulation, genetic susceptibility, aberrant inflammatory responses to intestinal microbiota, and environmental factors. UC is characterized by an unpredictable clinical course, often alternating between periods of exacerbation and remission. Because the inflammation and ulceration associated with UC are typically confined to the mucosal layer, UC has been often considered a disease of the epithelial barrier. The initiating factors responsible for epithelial barrier impairment remain unclear, and elucidating them could reveal how UC develops and inform new treatment strategies.

RATIONALE: The gut epithelium contains one of the largest populations of tissue-resident macrophages, which serve as the first line of defense against pathogens invading from the intestinal lumen. We hypothesized that gut-resident macrophages are compromised in UC, leading to impaired epithelial integrity, and we therefore examined macrophages in UC colon tissues.

RESULTS: In colon tissues isolated from UC patients, we found that tissue-resident macrophages were depleted in areas that did not show indications of inflammation. We hypothesized that macrophage loss preceded overt inflammation. In mouse models, chemical or genetic ablation of macrophages increased susceptibility to intestinal injury.

To identify potential factors that might impair the function of macrophages, we examined bacteria present in fecal samples from UC patients. We identified a toxin-producing bacterium belonging to the *Aeromonas* genus, designated *Aeromonas* sp. MTB (macrophage-toxic bacteria), which expressed the virulence factor aerolysin. Macrophages exhibited higher sensitivity to aerolysin-induced cell death than epithelial cells, a result that we hypothesized could lead to barrier impairment without direct epithelial damage. MTB persistently colonized mice under pathological conditions, depleting macrophages and enhancing sensitivity to enteric stimuli. MTB promoted colitis in mice exposed to dextran sulfate sodium or lacking interleukin-10 expression, with phenotypes resembling UC, but not in germ-free mice. An aerolysin-deficient MTB mutant failed to cause colitis, supporting the role of this toxin. In mice, pretreatment with polyclonal anti-aerolysin antibodies prevented MTB-induced colitis, and a monoclonal anti-aerolysin ameliorated established disease.

To determine the prevalence of this bacterium in UC patients versus healthy individuals, we developed a real-time polymerase chain reaction assay to detect *Aeromonas* species. *Aeromonas* species were detected more frequently in stools from UC patients compared with healthy controls. We also detected aerolysin in colon tissues isolated from UC patients.

CONCLUSION: We identified a variant of *Aeromonas* in UC patients and demonstrated its ability to promote colon inflammation in mice through aerolysin-mediated impairment of tissue-resident macrophages. Treatment with an anti-aerolysin antibody alleviated disease severity in mice exposed to MTB. Our findings highlight how microbes may contribute to UC pathogenesis and suggest that targeting bacterial virulence factors could be a therapeutic strategy for UC. □

Corresponding author: Minsheng Zhu (zhums@nju.edu.cn); Xuena Zhang (zhangxn@nju.edu.cn); Fangyu Wang (wangfy65@nju.edu.cn) †These authors contributed equally to this work. **Cite this article as Z. Jiang *et al.*, *Science* 390, eadz4712 (2025). DOI: 10.1126/science.adz4712**

An *Aeromonas* variant, MTB, promotes susceptibility to ulcerative colitis (UC) by disrupting colonic macrophages. Under physiological conditions, the macrophage (Mϕ) barrier beneath the colonic epithelium plays a vital role in protecting against gut microbes. However, upon colonization by *Aeromonas* sp. MTB (macrophage-toxic bacteria)—facilitated by conditions such as antibiotic use or intestinal insults—the toxin aerolysin produced by MTB preferentially disrupts tissue-resident macrophages. Loss of this macrophage barrier increases susceptibility to enteric inflammation, leading to the development of UC. Anti-aerolysin antibody treatment may prevent this process.

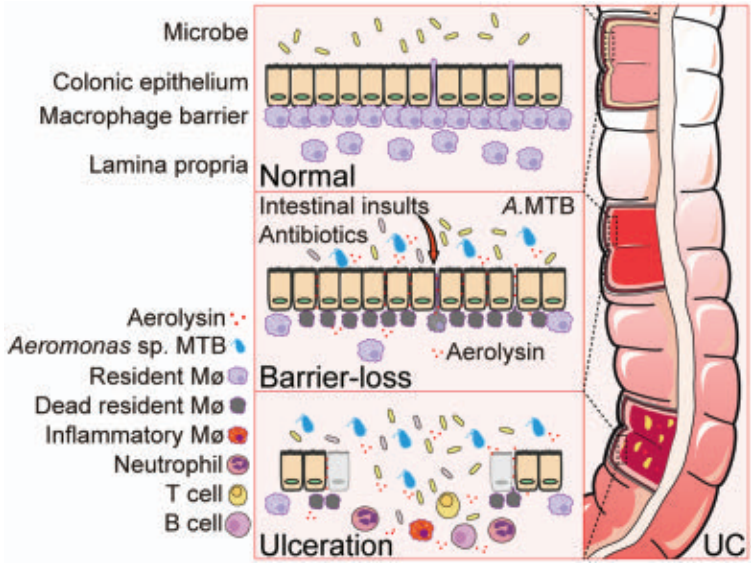

IMMUNOLOGY

An *Aeromonas* variant that produces aerolysin promotes susceptibility to ulcerative colitis

Zhihui Jiang[1]‡‡, Ye Wang[1]†, Jianfeng Gong[2]†, Xin Chen[1]†, Dong Hang[3], Caiping Chen[4], Xin Hong[5], Junhao Zhang[1], Kehui Qiu[1], Yang Liao[1], Pengpeng Li[1], Han Wang[1], Zhuoxin Yang[2], Tiantian Qiu[1], Yuwei Zhou[1], Zexu Chen[1], Hairong Zhou[5], Xinqi Shan[6], Na Zhou[6], Lutao Liu[6], Fan Feng[7], Feng Su[8], Hongfeng Ma[9], Zhifeng Liu[10], Weiqi He[11], Lei Fang[1], Ji Xuan[2], Zhenji Gan[1], Xia Gao[1], Jian Zhang[12]§, Huaqun Chen[6], Fangyu Wang[2]*, Xuena Zhang[1,8,13]*, Minsheng Zhu[1]*

Ulcerative colitis (UC) is a severe inflammatory bowel disease affecting millions of people worldwide, but the factors driving the condition are poorly understood. In tissue samples from individuals with UC, we found that macrophages were depleted from areas of the colon that did not yet exhibit overt epithelial inflammation. We hypothesized that toxins produced by bacteria could impair macrophages and that this could promote wider inflammation. We isolated a variant of *Aeromonas* genus from stool samples from UC patients, which we termed macrophage-toxic bacteria (MTB), because aerolysin secreted by MTB caused macrophage death. MTB colonized mice under pathogenic conditions and triggered colitis. Antibodies against aerolysin alleviated colitis induced by *Aeromonas* in mice. In a cohort, UC patients more frequently tested positive for *Aeromonas* than healthy controls did.

Ulcerative colitis (UC) is a chronic, idiopathic inflammatory bowel disease (IBD) whose global incidence and prevalence have been steadily increasing (*1*–*3*). UC is characterized by an unpredictable clinical course, often alternating between periods of exacerbation and remission (*4*, *5*). Approximately 20 to 25% of patients with recurrent episodes eventually require colectomy owing to the progressive severity of symptoms (*6*). The prevailing view suggests that UC is a multifactorial disease involving immune dysregulation, genetic susceptibility, aberrant inflammatory responses to intestinal microbiota, and environmental factors (*7*–*12*).

The inflammation and ulceration associated with UC are typically confined to the mucosal layer, starting at the rectum and extending to the entire colon (*13*, *14*). The inflamed colon tissue has indications of impaired secretion of mucins, electrolytes, peptides, and other bioactive molecules and physiological defects in the epithelial barrier (*15*, *16*). Genome-wide association studies have identified several UC-specific susceptibility genes involved in epithelial morphogenesis and homeostasis (*17*, *18*). Thus, UC is often considered a disease of the epithelial barrier (*19*, *20*). However, the initiating factors responsible for the epithelial barrier impairment remain unclear.

The intestinal epithelium consists of a single layer of polarized columnar cells that are constantly exposed to both harmless and harmful pathogens. To protect the host against invading pathogens and maintain intestinal homeostasis, the gut harbors one of the largest populations of macrophages, which originate from macrophage precursors seeded during embryogenesis (*21*–*23*). These macrophages are subsequently replenished by circulating hematopoietic monocytes under specific conditions (*22*, *23*). Among these macrophages, subepithelial macrophages, located just beneath the epithelial monolayer, act as the first line of defense against pathogens invading from the lumen (*24*–*26*). Blood vessel–associated macrophages form the gut-vascular barrier, preventing the dissemination of pathogens and recruiting inflammatory cells from the circulation (*27*). Enteric neuron–associated macrophages function as the gut's microglia, regulating secretion and gastrointestinal motility (*28*–*30*). Despite their diverse roles and locations, these tissue-resident macrophages play a fundamental role in maintaining epithelial barrier integrity (*31*, *32*). Indeed, depletion or loss of phagocytic function in intestinal mucosal macrophages is sufficient to trigger epithelial cell death, increase intestinal permeability, and promote the development of colitis (*31*, *33*, *34*).

In this study, we investigated the resident macrophage barrier in human UC colon tissue before epithelial disruption and their interactions with microbiota.

Results

Human UC colons display depleted subepithelial macrophages before epithelial inflammation

We hypothesized that gut-resident macrophages might be compromised in UC, leading to impaired epithelial integrity. We examined the macrophages in colon tissues from UC patients and control individuals. Fresh surgical colon samples were collected from UC patients (n = 17) who were clinically diagnosed based on a combination of symptoms, endoscopic findings, and histological examinations (*35*). All these patients met the criteria for colectomy, presenting with conditions such as uncontrolled hemorrhage, perforation, refractory acute severe UC, or lack of response to medical treatment (*36*). For controls, adjacent normal colon tissues were obtained from patients (n = 17) undergoing surgery for colorectal carcinoma. The tissue from these patients was characterized by immunohistochemistry (IHC) and Western blots and by flow cytometry (tables S1 and S2). IHC revealed a structured organization of tissue-resident macrophages in healthy colon tissue, with macrophages that were detected with an antibody against CD68, a marker of pan-macrophages, forming a defined subepithelial layer and distinct populations dispersed throughout the lamina propria (LP) (Fig. 1A, a to f).

In UC mucosa, we identified three distinct pathological zones: (i) ulcerated areas with complete epithelial destruction and dense immune infiltration (Fig. 1A, g and j); (ii) partially damaged regions exhibiting patchy epithelium and moderate inflammation (Fig. 1A, h and k); and (iii) morphologically intact zones that lacked subepithelial macrophages (Fig. 1A, i and l). There was a 67% reduction in subepithelial $CD68^+$ macrophage density in intact zones versus controls (Fig. 1B), which was confirmed by immunofluorescence (Fig. 1C). This

[1]State Key Laboratory of Pharmaceutical Biotechnology, National Resource Center for Mutant Mice, Department of Gastroenterology of Nanjing Drum Tower Hospital, and Suqian Scientific Research Institute, Medical School of Nanjing University, Nanjing, China. [2]Department of Gastroenterology and Department of General Surgery, Jinling Hospital, Affiliated Hospital of Medical School, Nanjing University, Nanjing, China. [3]Department of Epidemiology, Jiangsu Key Lab of Cancer Biomarkers, Collaborative Innovation Center for Cancer Personalized Medicine, School of Public Health, Nanjing Medical University, Nanjing, China. [4]State Key Laboratory of Natural Medicines, China Pharmaceutical University, Nanjing, China. [5]Department of Non-Communicable Disease Prevention, Nanjing Municipal Center for Disease Control and Prevention, Nanjing, China. [6]Jiangsu Key Laboratory for Molecular and Medical Biotechnology, College of Life Sciences, Nanjing Normal University, Nanjing, China. [7]Department of Digestive Surgery, Xijing Hospital, Fourth Military Medical University, Xi'an, China. [8]Department of Gastroenterology, Affiliated Suqian Hospital of Xuzhou Medical University, Nanjing Drum Tower Hospital Group Suqian Hospital, Suqian, China. [9]Department of Rehabilitation Medicine, Huzhou Rehabilitation Hospital, Huzhou, China. [10]Children's Hospital of Nanjing Medical University, Nanjing, China. [11]Department of Gastroenterology, Children's Hospital of Soochow University, Jiangsu Key Laboratory of Drug Discovery and Translational Research for Brain Diseases, Cambridge-Suda Genomic Resource Center, Soochow Medical College of Soochow University, Suzhou, China. [12]State Key Laboratory for Conservation and Utilization of Bio-Resources, School of Life Sciences, Center for Life Sciences, Yunnan University, Kunming, China. [13]Jinling Pharmaceutical, Nanjing, China. ***Corresponding author. Email: zhums@nju.edu.cn (M.Z.); zhangxn@nju.edu.cn (X.Z.); wangfy65@nju.edu.cn (F.W.)** †These authors contributed equally to this work. ‡Present address: Department of Gastroenterology, Children's Hospital of Soochow University, Cambridge-Suda Genomic Resource Center, Soochow Medical College of Soochow University, Suzhou, China. §Present address: School of Life Sciences, Fudan University, Shanghai, China.

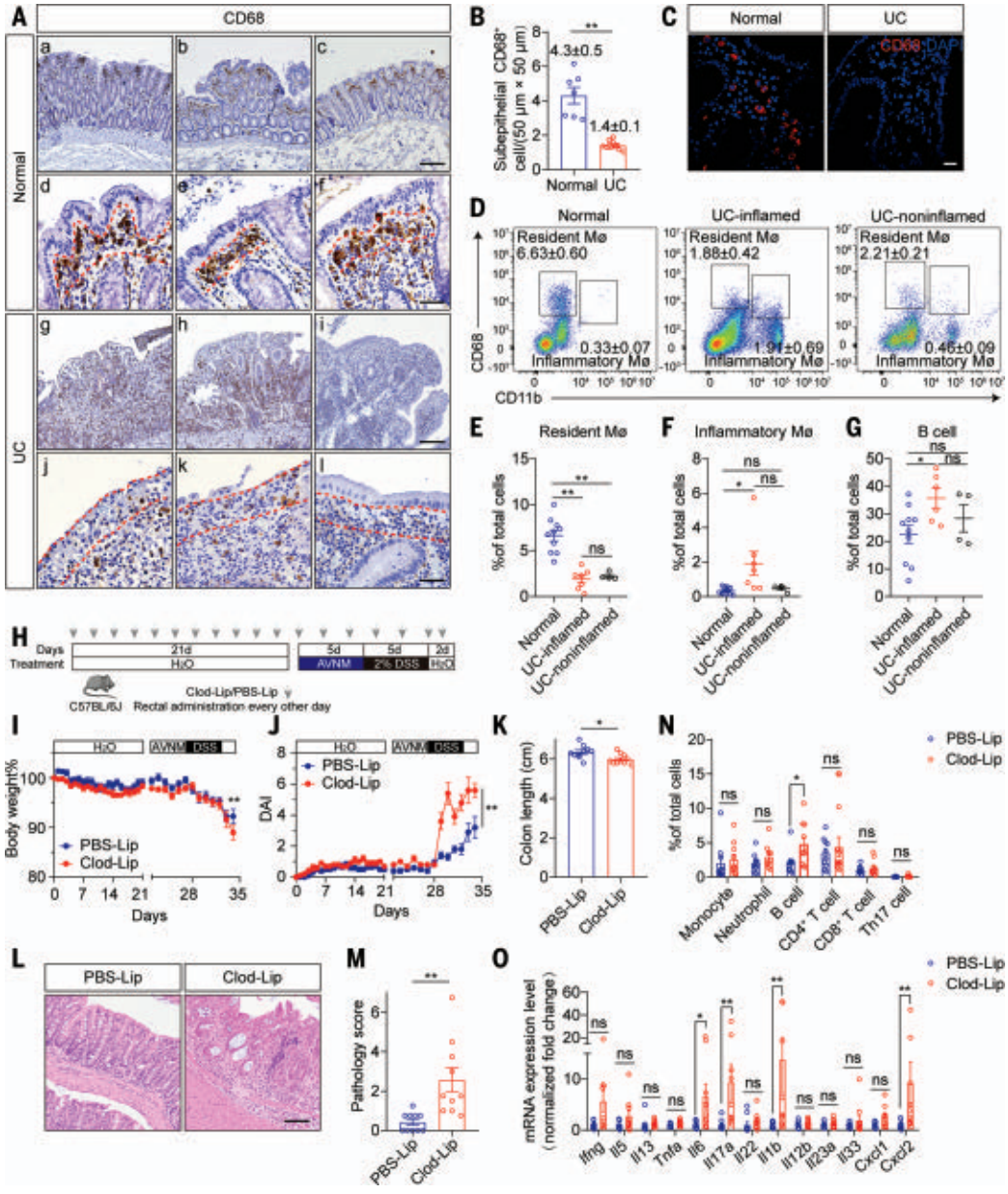

Fig. 1. Colonic epithelial innate macrophages are depleted in ulcerative colitis (UC) patients and cause susceptibility to DSS in animals. Colon tissues were collected from UC patients (UC, $n = 17$) and normal colons of colorectal carcinoma patients (Normal, $n = 17$) for macrophage measurements. (**A**) The mucosal macrophages were visualized by IHC with an anti-CD68 antibody. Dashed red lines indicate the innate macrophage barrier. Scale bars, 200 μm [(a) to (c), (g) to (i)], 50 μm [(d) to (f), (j) to (l)]. (**B**) Quantification of the $CD68^+$ macrophages beneath epithelial barrier within a 50-μm depth. Each dot represents the mean of 10 different observational views from an individual patient. Normal, $n = 7$; UC, $n = 10$. (**C**) Immunofluorescence staining with an anti-CD68 antibody (red) for the macrophages beneath the epithelial barrier. The cell nuclei were stained with 4′,6-diamidino-2-phenylindole (DAPI) (blue). Scale bar, 20 μm. (**D**) Representative flow cytometry plot of human colonic macrophages. (**E** and **F**) Quantification of LP resident and inflammatory macrophages in human UC colons. (**G**) Quantification of LP B cell population in human UC colons. In (E) to (G), dots represent individual patients pooled from four independent experiments. Normal, $n = 10$; UC-inflamed, $n = 6$ or 7; UC-noninflamed, $n = 4$. (**H**) Strategy of DSS colitis induction in mice pretreated with Clod-Lip or PBS-Lip control. Clod-Lip group, $n = 10$; PBS-Lip group, $n = 10$. (**I** and **J**) Changes in body weight and disease activity index (DAI) of Clod-Lip-treated or control mice. (**K**) Colon length. (**L** and **M**) Representative hematoxylin and eosin (H&E) staining and pathology scores of Clod-Lip treated and control colons. (**N**) Quantification of LP immune cell populations in Clod-Lip-treated and control colons (pooled from two independent experiments). (**O**) Relative mRNA expression levels of inflammatory cytokines. In (K) and in (M) to (O), dots represent individual mice. Data are presented as mean ± SEM; ns > 0.05, $*P < 0.05$, $**P < 0.01$. Unpaired Student's *t* test in (B), (K), and (M); one-way analysis of variance (ANOVA) in (E), (F), and (G); and two-way ANOVA in (I), (J), (N), and (O).

selective depletion of mucosal sentinel macrophages preceded overt epithelial damage. Macrophages in human tissues comprise multiple subsets. Those lacking myeloid integrin ($CD11b^-$) are indicative of tissue-resident innate macrophages, whereas $CD11b^+$, $CCR2^+$, and $HLA\text{-}DR^+$ macrophages are associated with inflammatory macrophages (*37*–*39*). Additionally, $CD14^+$ macrophages are also classified as inflammatory macrophages (*38*, *40*, *41*). There was also a deficit in tissue-resident macrophages ($CD68^+CD11b^-$) across both inflamed (with visible ulcerative inflammation) and noninflamed (with no visible inflammation) mucosa isolated from UC patients versus control tissue (Fig. 1, D and

E). Inflammatory macrophages ($CD68^+CD11b^+CCR2^+HLA\text{-}DR^+$ and $CD68^+CD14^+$) and adaptive immune cells (B and T cells) were elevated only in inflamed regions (Fig. 1, F and G, and fig. S1), mirroring prior UC signatures (*42*, *43*). We concluded that our data could be consistent with colon inflammation being preceded by depletion of resident macrophages and that the inflammatory macrophages and adaptive immune cells infiltrated after active inflammation developed. The depletion of macrophages was unlikely to be caused by immunosuppressive agents typically used in UC treatment, as five out of seven patients (table S2, set 2) who underwent cytometry analysis had not received corticosteroids or other immunosuppressive medications.

Colonic macrophage depletion renders animals more susceptible to intestinal insult

Previous studies indicated that resident macrophages are essential for epithelial barrier integrity (*31*, *32*), and their depletion potentially renders the colon more susceptible to pathological insults. We administered clodronate liposomes (Clod-Lip) intrarectally to disrupt colonic macrophages chemically and measured mouse tissue-resident macrophages by detecting their characteristic surface markers: CD45 (immune cell marker), F4/80 (macrophage-specific), CD11b (myeloid lineage), and CX3CR1 (tissue-resident identifier) (*21*, *44*, *45*). Three consecutive treatments reduced mouse colonic LP resident macrophages ($CD45^+F4/80^+CD11b^+CX3CR1^+$) without inhibiting circulatory macrophages (fig. S2). Although three weeks of Clod-Lip treatment did not induce spontaneous colitis (Fig. 1, H to J), subsequent exposure to low-dose dextran sulfate sodium (DSS) triggered much more severe colitis compared with DSS control alone (Fig. 1, H to M). This was accompanied by elevated B cell populations, up-regulation of interleukin-6 (IL-6), IL-17, IL-1b, and Cxcl2 (Fig. 1, N and O).

In addition, we genetically depleted colonic macrophages by crossing *Cx3cr1*-iCre mice with inducible floxed Rosa26-iDTR mice, enabling Cre-mediated excision of the stop cassette and subsequent expression of the human diphtheria toxin receptor (DTR) in $CX3CR1^+$ cells. Upon diphtheria toxin (DT) administration, DTR-expressing tissue-resident $CX3CR1^+$ macrophages were selectively ablated. $Cx3cr1^{Cre/+}$; $Rosa26^{DTR/+}$ mice were intrarectally administered DT (ΔCX3CR1 mice, 100 ng per mouse, every other day) to deplete colonic resident macrophages (fig. S3, A and B). After exposure to DSS, ΔCX3CR1 mice had increased susceptibility to colitis, with more severe disease phenotypes compared with controls [$Cx3cr1^{Cre/+}$; $Rosa26^{DTR/+}$ mice receiving intrarectally administration of phosphate-buffered saline (PBS)] (fig. S3, C to F). This was accompanied by an increase in B cell numbers, which is consistent with the effects observed in Clod-Lip-treated mice (fig. S3F). Because the low-dose DSS alone did not induce overt colitis under our experimental conditions, we concluded that macrophage-depleted animals have heightened susceptibility to intestinal insults.

UC fecal bacteria produce a macrophage-toxic aerolysin

We hypothesized that certain intestinal bacteria might produce a macrophage-toxic factor that could contribute to macrophage depletion in UC patients and that this might be detected in fecal matter. We collected fresh stool samples from 48 UC patients and 47 healthy controls (clinical data in tables S3 and S4). After culturing fecal bacteria aerobically in LB medium for 12 to 16 hours, we tested the cytotoxicity of bacteria-free culture supernatants on mouse bone marrow–derived macrophages (BMDMs) (fig. S4A). Supernatants from 47.9% (23/48) of UC samples induced >15% BMDM cell death, whereas none of those (0/47) derived from healthy controls had this effect (fig. S4B). Moreover, the supernatant taken from mixed fecal stools from 39 UC patients (UC mix) showed more severe cytotoxicity on BMDM, whereas that of mixed healthy fecal bacteria from nine healthy controls (Healthy mix) had no cytotoxicity (Fig. 2, A and B). This cytotoxic effect of the UC mix was abolished by treating it with proteinase K treatment and by heat inactivation (Fig. 2B and fig. S4C), indicating that UC-associated bacteria produced heat-labile proteins toxic to macrophages. As aerobic and anaerobic culture conditions yielded comparable cytotoxicity (fig. S4D), we used the aerobic culture for subsequent experiments.

To identify the macrophage-toxic protein, we fractionated the UC-mix culture supernatant by ion-exchange chromatography and assessed the cytotoxicity of each fraction. We found macrophage-toxic activity in fractions 16 to 19, peaking at fraction 17 (Fig. 2C). SDS–polyacrylamide gel electrophoresis (SDS-PAGE) separation of these fractions (Fig. 2D) yielded four candidate bands for liquid chromatography–tandem mass spectrometry (LC-MS/MS) analysis. Band 2 matched aerolysin (UniProt: Q06304), with 53 peptides covering 38.32% [95% confidence interval (CI)] of the protein sequence (Fig. 2D).

By polymerase chain reaction (PCR) amplification of UC-mix bacterial genomic DNA, we isolated five aerolysin genes. Sequence alignment showed high homology to aerolysin of *Aeromonas veronii* (*A. veronii*) and moderate homology to aerolysin of other *Aeromonas* species (table S5). Recombinant aerolysin expressed in *Escherichia coli* was used to generate polyclonal antibodies (fig. S5, A and B). These antibodies neutralized UC culture cytotoxicity in a dose-dependent manner (Fig. 2E). Thus, we concluded that aerolysin was a macrophage-toxic protein produced by bacteria found in UC patients (hereafter termed UC-aerolysin).

UC-aerolysin depletes mouse macrophages in vivo

We intrarectally administered purified glutathione S-transferase (GST)–fused UC-aerolysin (20 μg in 100 μl) to C57BL/6 mice. At 20 μg per mouse, recombinant aerolysin reduced colonic LP macrophages without affecting epithelium (fig. S5C). Three hours after treatment, the colonic epithelial monolayer remained intact (Fig. 2F), but subepithelial $CX3CR1^+$ macrophages were reduced (Fig. 2, F and G). In addition, in $Cx3cr1^{Cre/+}$; $Rosa26^{mTmG/+}$ mice, in which $CX3CR1^+$ macrophages were genetically labeled with enhanced green fluorescent protein (EGFP), aerolysin treatment induced a marked reduction of $EGFP^+$ macrophages beneath epithelial monolayers (Fig. 2F). On the basis of these data, we concluded that UC-aerolysin disrupted the innate macrophage barrier in vivo without causing direct epithelial damage.

Macrophages are more sensitive to UC-aerolysin than epithelial cells in vitro

We evaluated UC-aerolysin toxicity in vitro by measuring its IC_{50} values (the concentrations causing 50% cell death) in intestinal epithelial cells (human: NCM460, HT-29, Caco-2 Clone 5E6L, Caco-2; mouse: MC-38) and macrophages (human: THP-1; mouse: BMDM, RAW264.7). Macrophages exhibited 20- to 80-fold greater sensitivity, with IC_{50} values of 0.0287 ± 0.0075 nM (BMDM), 0.0376 ± 0.0054 nM (RAW264.7), and 0.0790 ± 0.0100 nM (THP-1), versus 0.7312 ± 0.2228 nM (MC-38) to 6.4003 ± 2.1360 nM (5E6L) for epithelial cells ($P < 0.01$; Fig. 2, H and I, and table S6). UC-aerolysin-induced macrophage death featured necrosis-like morphology, including cell swelling, vacuolization, and membrane rupture (fig. S5D).

As a pore-forming toxin, active aerolysin binds to glycosylphosphatidylinositol (GPI)–anchored proteins on target cells, triggering cell death through multiple cascades (*46*). To identify the anchored proteins mediating macrophage toxicity, we used small interfering RNA (siRNA) to deplete genes encoding GPI-anchored proteins (Cd14, Vnn1, Bst1, Bst2, Ly6e, Pakap, and Smpdl3b) via siRNA (*47*). Knockdown of Cd14, Bst1, or Smpdl3b reduced cytotoxicity (fig. S5, E and F). We concluded that these proteins contributed to aerolysin-induced macrophage death.

A distinct variant of *Aeromonas* genus produced UC-aerolysin

To identify aerolysin-producing strains associated with UC, we cultured fecal bacteria from UC patients and screened individual colonies

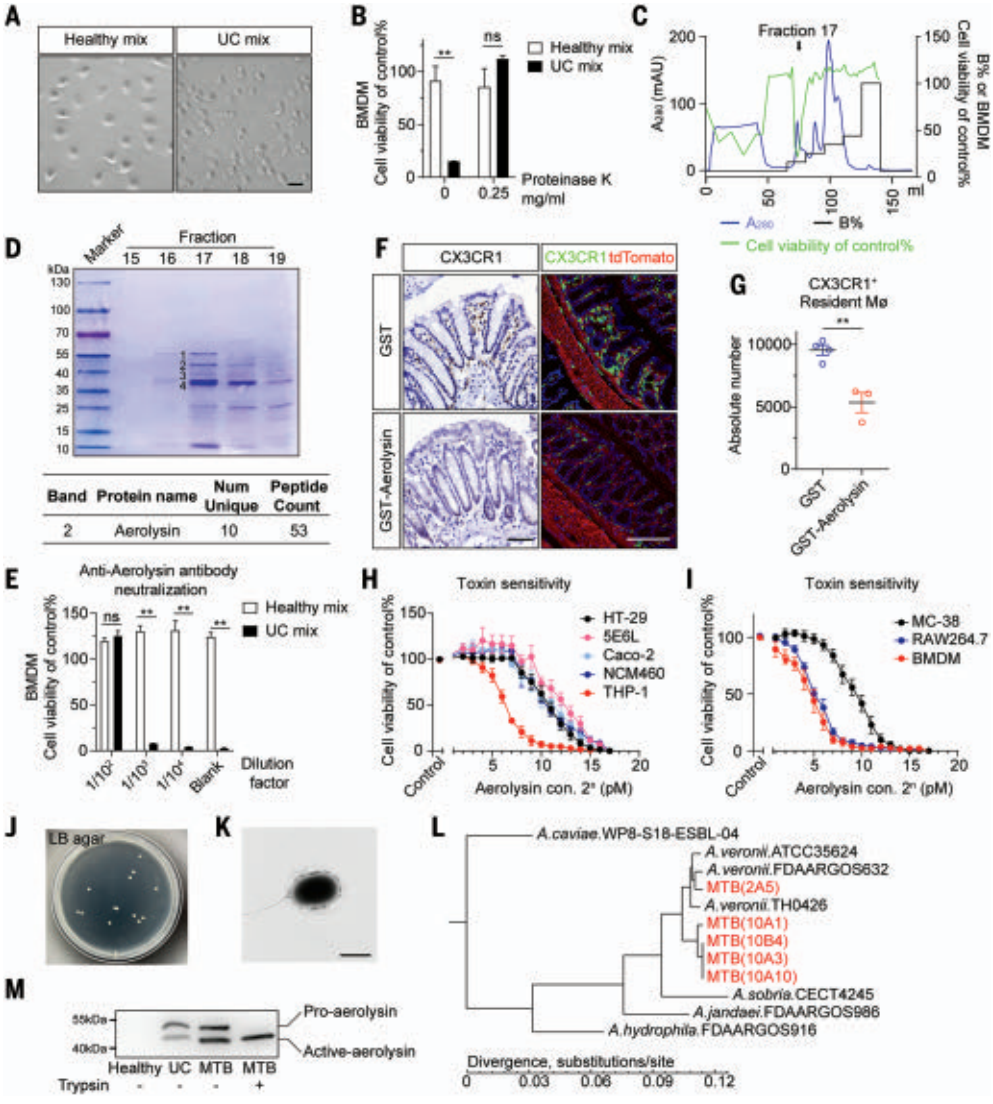

Fig. 2. Macrophages are ultrasensitive to aerolysin secreted by *Aeromonas* sp. MTB. (**A**) Representative cell morphology of BMDM cultured with supernatants from Healthy or UC mix fecal bacteria. Scale bar, 20 μm. (**B**) Cell viability of BMDM cultured with proteinase K–treated bacterial supernatants. (**C**) Representative overlapping of ion-exchange chromatography graphs for UC bacterial supernatant and viability curve of BMDM cells treated with corresponding eluted fractions. Gradient NaCl elution, black line; BMDM cell viability, green line; absorbance at 280 nm ($A_{280\,nm}$) values of eluted fractions, blue line; fraction 17, black arrow. (**D**) Coomassie brilliant blue staining of fractions 15 to 19 separated by SDS-PAGE. Four candidate bands from fraction 17 were subjected to LC-MS/MS analysis. The results from band 2 are shown. (**E**) Anti-aerolysin polyclonal antibodies neutralized the toxin from UC mix bacteria in a dose-dependent manner. (**F**) Representative IHC staining for $CX3CR1^+$ macrophage in colons from C57BL/6J mice (left scale bar, 50 μm), and immunofluorescence of colon tissue from $Cx3cr1^{Cre/+}$; $Rosa26^{mTmG/+}$ mice (right scale bar, 100 μm) received anal administration of 20 μg GST or GST-aerolysin protein for 3 hours. (**G**) Quantification of LP $CD45^+F4/80^+CD11b^+CX3CR1^+$ macrophages in GST-aerolysin–treated ($n = 3$) or control colons ($n = 4$) by flow cytometry (representative of two independent experiments). Dots represent individual mice. (**H**) Cytotoxicity of aerolysin on human-derived cell lines. (**I**) Cytotoxicity of aerolysin on mouse BMDM and cell lines. (H) and (I) are pooled from three independent experiments. (**J**) Representative morphology of MTB colonies on LB agar. (**K**) Representative TEM image of MTB with negative staining. Scale bar, 1 μm. (**L**) Phylogenetic tree based on core-pan gene of MTBs and *Aeromonas* reference strains. (**M**) Western blot analysis detecting aerolysin expression in cultured supernatant from Healthy mix, UC mix, and MTB, with or without trypsin digestion. Data are presented as mean ± SEM; ns > 0.05, $*P < 0.05$, $**P < 0.01$; Two-way ANOVA in (B) and (E), and unpaired Student's *t* test in (G).

through aerolysin gene amplification and macrophage toxicity assays (fig. S6) (*48*). To ensure genetic diversity, we selected five distinct isolates from the positive colonies based on 16*S* ribosomal RNA (rRNA) and whole-genome sequence variations as representative aerolysin-producing strains. On LB agar or Columbia agar plate, these bacterial strains formed white, plump colonies (Fig. 2J). Transmission electron microscopy (TEM) revealed that these Gram-negative bacteria possessed a single polar flagellum and multiple fimbriae (Fig. 2K). Whole-genome sequencing analysis indicated that these isolates belonged to the *Aeromonas* genus, closely related to but distinct from *A. veronii* (Fig. 2L, fig. S7A, and table S7). We designated these strains as *Aeromonas* sp. MTB (macrophage-toxic bacteria). The isolates secreted pro-aerolysin (Fig. 2M), which could be cleaved and activated by enzymes derived from gut microbiota or from the host cells targeted by aerolysin. Because strain 2A5 induced the most severe colitis among these isolates (fig. S7, B to E), we selected it for further study. Furthermore, 1×10^9 colony-forming units (CFU) of MTB (strain 2A5) produced microgram quantities of aerolysin, which is a dose sufficient to reduce colonic LP macrophages (figs. S5C and S7F).

To determine whether MTB represented a distinct *Aeromonas* variant, we performed comparative biochemical analyses with reference *A. veronii* strains (TH0426 and ATCC35624). On Rimler-Shotts agar, both MTB and *A. veronii* formed yellow colonies within 24 hours, but MTB colonies turned to green by 48 hours (fig. S7G), suggesting differential alkaline metabolite production. API-20NE profiling revealed that MTB maintained distinctive L-arginine utilization (arginine dihydrolase positive) compared with *A. veronii* strains (table S8). This metabolic difference likely explains the observed alkaline byproduct accumulation and subsequent color transition. On the basis of the biochemical and genomic analyses, we concluded that MTB was a distinct *Aeromonas* variant.

Under pathological conditions, MTB can persistently colonize mice

To assess the colonization capacity of MTB, we orally administered 1×10^9 CFU of MTB (strain 2A5) to wild-type C57BL/6J mice daily for 3 consecutive days and monitored fecal MTB levels. Fecal MTB CFU in Rimler-Shotts agar declined to undetectable levels by day 4, and MTB aerolysin DNA was also undetectable by PCR (fig. S8, A and B). Because the PCR assay could detect as few as 1 to 10 copies of aerolysin DNA in stool (fig. S8A), we considered that the absence of detectable MTB DNA indicated failed colonization.

Given the established association between antibiotic use and UC prevalence (*49*), we investigated whether antibiotic pretreatment could promote MTB colonization. Mice were treated with an antibiotic

cocktail (ampicillin, vancomycin, neomycin, and metronidazole; hereafter termed AVNM) for 5 days (*50*) and then administrated with 1×10^9 CFU per mouse of MTB bacteria. Although MTB CFU in stool dropped to undetectable levels by day 4 after administration, MTB aerolysin DNA was detectable in 75% (3/4) of mice and persisted for 17 days (fig. S8C), indicating successful MTB colonization in a subgroup.

Pretreatment with 2% (w/v) DSS resulted in colonization in 33% of mice (fig. S8C). Combined AVNM and DSS pretreatment led to sustained colonization in all mice for ≥30 days (fig. S8D). By contrast, other *Aeromonas* species (*A. veronii* strains TH0426 and ATCC35624) failed to colonize the pretreated mice (fig. S8E). Colonized mice became fecal MTB–negative by 70 days after inoculation; however, AVNM reexposure led to MTB DNA detection again (fig. S8D).

Therefore, we concluded that MTB was capable of colonizing mice under pathological conditions (e.g., antibiotic exposure or DSS-induced colitis) and that once MTB infection occurs, it may persistently reside in mice and proliferate again under permissive conditions.

MTB induces colonic macrophage depletion and renders animals more susceptible to enteric stimuli

To determine whether MTB infection could deplete resident macrophages and promote UC-like pathology, we treated C57BL/6 mice with AVNM and DSS, with the initial pretreatment with AVNM and low-dose DSS (2%, w/v) ensuring high MTB colonization efficiency, whereas subsequent DSS together with MTB administrations accelerated colitis induction (Fig. 3A). The low dose of DSS did not induce apparent colitis under our experimental conditions (Fig. 3, B and C). During the initial 2% DSS course (with or without MTB), no intergroup differences were observed in body weight or disease activity index (DAI). However, after the second DSS course, MTB-treated mice developed progressive colitis phenotypes, including weight loss and bloody purulent stool (Fig. 3, B and C). MTB presence was confirmed by dot blot of aerolysin protein in fecal cultures (Fig. 3D). Control mice exhibited abundant, well-organized CX3CR1$^+$ cells beneath the epithelial monolayer, whereas MTB-inflamed colons had a marked reduction in CX3CR1$^+$ macrophages (Fig. 3, E and F), indicating disruption of the epithelial macrophage barrier. Administration of *A. veronii* strains (ATCC 35624 and TH0426) did not deplete CX3CR1$^+$ macrophages (fig. S9, A to C), despite their aerolysin secretion (fig. S7B and fig. S9D), likely because they did not colonize mice.

MTB-infected colons exhibited pronounced inflammatory cell infiltration, crypt distortion, and abscess formation, which are pathological hallmarks resembling human UC, and displayed higher histopathological scores (Fig. 3, G and H) (*14*). The spleens from MTB-induced colitis mice were not enlarged (fig. S10A), mirroring observations in UC patients but contrasting with Crohn's disease (CD), another main form of IBD (*51*, *52*). The mRNA expression of inflammatory cytokine IL-17 was up-regulated (fig. S10B). We concluded that the presence of MTB could disrupt the colonic macrophage barrier and that it contributed to UC-like pathology.

We pretreated C57BL/6 mice with Clod-Lip to deplete colonic macrophages before MTB gavage (Fig. 3I). MTB administration to the mice did not worsen DSS-induced colitis (Fig. 3, J and K, and fig. S10, C to E). Moreover, the expression levels of IL-17 and other cytokines were not elevated (fig. S10E). Thus, we concluded that this data would be consistent with macrophages being involved in the pathology associated with MTB.

Because IL-10 knockout (*Il10*$^{-/-}$) mice exhibit immune dysfunction and serve as a robust model for studying microbiota-dependent colitis, we used young (6- to 8-week-old) *Il10*$^{-/-}$ mice as a model for MTB-mediated colitis. *Il10*$^{-/-}$ mice develop spontaneous colitis around 6 months of age but not at a young age. We treated *Il10*$^{-/-}$ mice aged 6 to 8 weeks with MTB by oral gavage, and within 14 days these mice exhibited progressive colitis phenotypes, whereas controls remained unaffected (Fig. 3, L to P). Resident macrophages were reduced in MTB-exposed colons (Fig. 3, Q and R), with no changes in other immune cell populations except B cells (Fig. 3S). Quantitative PCR (qPCR) analysis revealed that mRNA for IL-17 and Cxcl2 was up-regulated (fig. S10F). Elevation of IL-17 and chemokine expression is also found in human UC (*53*). Because this model did not require administration of DSS, our data are consistent with administration of MTB being sufficient to promote intestinal inflammation in mice with a genetic susceptibility to spontaneous colitis.

In addition, we used germ-free (GF) C57BL/6 mice, which lack gut microbiota–induced intestinal inflammation, to evaluate MTB's role in colitis induction. GF mice were treated with MTB plus 1.5% (m/v) DSS but showed no phenotypic differences compared with those treated with DSS alone (fig. S10, G to K). This result indicated that colon susceptibility to MTB-mediated colitis depended on enteric bacteria.

Aerolysin is indispensable for MTB-induced colitis

In addition to aerolysin, *Aeromonas* produced other virulence factors, including hemolysins, proteases, lecithinases, nucleases, and amylases (*54*). To investigate whether aerolysin was essential for MTB pathogenicity, we generated an aerolysin-deficient MTB strain (Δaer MTB) (Fig. 4A and fig. S11, A and B). In contrast to wild-type MTB, the Δaer mutant showed no cytotoxicity toward cultured macrophages (Fig. 4B). To evaluate its role in vivo, we pretreated mice with an AVNM antibiotic cocktail and exposed them to either Δaer MTB or MTB by oral gavage (Fig. 4C). Aerolysin deletion did not affect CX3CR1$^+$ subepithelial macrophage integrity (Fig. 4, D and E) and colitis severity (Fig. 4, F and G), as evidenced by normal colon length (Fig. 4H) and lower histopathological scores (Fig. 4, I and J). Fecal Δaer MTB CFU counts were comparable to those of wild-type MTB, and the mutant stably colonized the host for at least 30 days (Fig. 4K and fig. S11C), indicating that its reduced pathogenicity was not due to colonization defects. Moreover, reintroducing aerolysin via a complementation vector (Comp) (fig. S12A) restored colitis induction (Fig. 4, L to P); thus we concluded that aerolysin was required for MTB-induced macrophage depletion and colitis development.

MTB bacteria were frequently detected in UC stools, and aerolysin protein was detected in UC colon tissues

To investigate MTB presence frequency in UC patients and healthy people, we designed a real-time PCR method consisting of a PCR primer set and a TaqMan probe targeting the MTB aerolysin gene (fig. S13A), which could not distinguish MTB from other *Aeromonas* species. We analyzed fecal samples from 79 UC patients, 430 healthy participants, and 38 CD patients (for more information, see tables S3 and S4). Of 79 UC patients, 57 (72.15%) had stool samples positive for *Aeromonas* species. Of 430 healthy people, 51 (11.86%) had stool samples that were *Aeromonas* species–positive, and of 38 CD patients, 1 (2.63%) had a positive sample. (Fig. 5A). Thus, the frequency of *Aeromonas* species presence was higher in UC patients compared with healthy people and CD patients ($P < 0.01$).

We also assessed the relative abundance of *Aeromonas* species in cultured UC fecal bacteria using the same PCR method. There was a higher abundance of *Aeromonas* species in UC compared with both CD and healthy controls (Fig. 5A). It should be noted that fecal *Aeromonas* species positivity in healthy people may reflect the presence of species other than MTB that may not produce aerolysin or increase susceptibility to colon inflammation. The UC patients in this study were from 12 provinces across China, suggesting limited geographic difference of MTB positivity (Fig. 5B).

To investigate whether aerolysin protein was present in human UC colons, we collected fresh colonic biopsies from 10 UC patients and adjacent normal colonic tissues from five colon cancer patients (table S1 and table S2). We generated an anti-aerolysin monoclonal

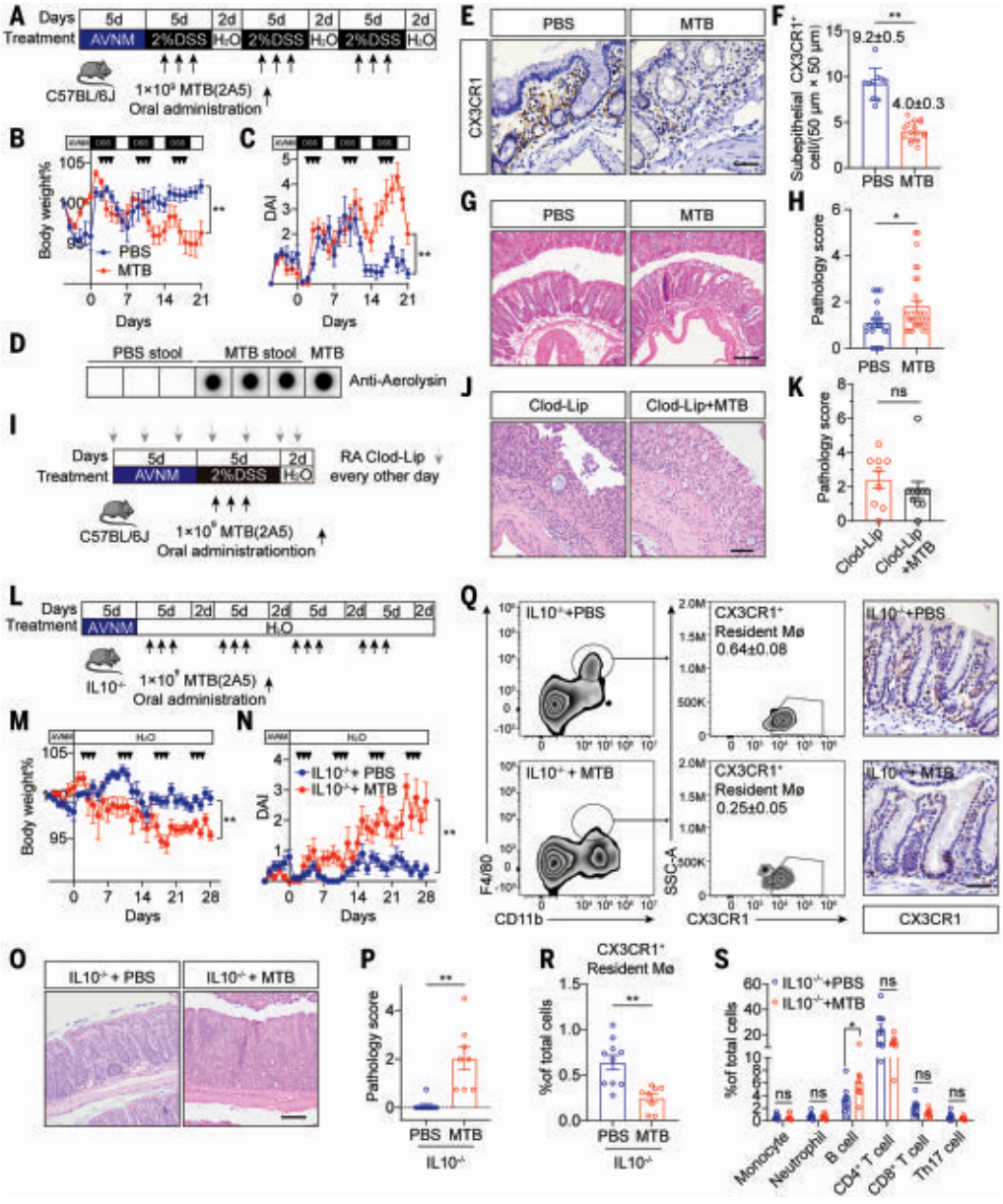

Fig. 3. MTB administration induced UC-like phenotypes and immunological responses. (**A**) Protocol for colitis induction in C57BL/6J mice. Arrows, oral gavage of 1×10^9 MTB (2A5) bacteria or 100 μl PBS. PBS group, $n = 19$; MTB group, $n = 30$ (pooled from three independent experiments). (**B** and **C**) Alterations in body weight and DAI. (**D**) Dot blot assay for aerolysin expression to confirm the presence of MTB bacteria in animal stools. A monoclonal mouse anti-aerolysin antibody (Clone 12) was used as the primary antibody. (**E**) Representative IHC staining for colonic CX3CR1$^+$ macrophages of the animals treated with PBS or MTB (2A5) bacteria. Scale bar, 50 μm. (**F**) Quantification of the CX3CR1$^+$ cells. Dots represent the mean of ≥10 different observational views of an individual animal (PBS group: $n = 10$; MTB group: $n = 16$, pooled from three independent experiments). (**G** and **H**) Representative H&E staining and pathology scores of MTB colitis colons. Scale bar, 100 μm. Dots represent individual mice. (**I**) Strategy for inducing MTB colitis in macrophage-depleted mice. Macrophage depletion was achieved by intrarectal administration (RA) of Clod-Lip. (**J** and **K**) Representative H&E staining and pathology score of colons from Clod-Lip–treated MTB colitis (pooled from two independent experiments). Scale bar, 100 μm. Dots represent individual mice. (**L**) Protocol for *Il10*$^{-/-}$ animals treated with MTB bacteria or PBS. Arrows, oral gavage of 1×10^9 MTB (2A5) bacteria or 100 μl PBS. PBS group: $n = 10$; MTB group: $n = 8$ (pooled from two independent experiments). (**M**) Body weight changes in *Il10*$^{-/-}$ mice. (**N**) DAI of the *Il10*$^{-/-}$ mice. (**O** and **P**) Representative H&E staining and pathology score of *Il10*$^{-/-}$ colons. Dots represent individual mice. (**Q**) Representative flow cytometry plot of LP resident macrophages of *Il10*$^{-/-}$ colons and IHC for colonic CX3CR1$^+$ macrophages. (**R**) Quantification of the LP CD45$^+$F4/80$^+$CD11b$^+$CX3CR1$^+$ macrophage. (**S**) Quantification of LP immune cell populations. Data are presented as mean ± SEM; ns > 0.05, $*P < 0.05$, $**P < 0.01$. Unpaired Student's *t* test in (F), (K), and (R); Mann-Whitney test in (H) and (P); and two-way ANOVA in (B), (C), (M), (N), and (S).

antibody (mAb, Clone 12) to detect the protein (fig. S13, B to D). The normal colon tissue had no detectable aerolysin expression, whereas 4 out of 10 UC colons had obvious aerolysin expression surrounding the CD68$^+$ macrophages within mucosa and muscularis layers (Fig. 5C and fig. S13E). Western blot analyses also detected aerolysin protein in cells isolated from UC colonic mucosa and the muscularis layer, but the protein was barely detected in normal tissue (Fig. 5, D and E).

Anti-aerolysin antibodies prevent and alleviate MTB-induced colitis in mice

We investigated whether anti-aerolysin antibodies could be effective in treating MTB-induced UC in mice. We used a purified polyclonal antibody to treat C57BL/6 mice, with animals receiving an injection intraperitoneally (i.p.) of either 200 μg of the antibody or 200 μl of PBS before MTB administration (Fig. 6A). This regimen was repeated weekly over a 4-week period. Control mice—which did not receive anti-aerolysin—displayed typical colitis phenotypes, including reduced body weight, and increased disease activity (Fig. 6, B and C). However, the mice pretreated with anti-aerolysin antibody did not show evidence of colitis phenotypes during the observation period (28 days) (Fig. 6, B to E). Moreover, at the end of the observation period, antibody-treated mice retained the CX3CR1$^+$ subepithelial macrophage populations (Fig. 6, F and G), their intestinal epithelial monolayer was not disrupted, and they showed lower pathological scores (Fig. 6, H and I). The antibody treatment also decreased the expression of mRNAs for *Il6*, *Il1b*, and *Cxcl2* in colons that were comparable to the levels of mice without MTB treatment (Fig. 6J). Because mice that were treated with purified mouse control immunoglobulin G (IgG) had similar pathology to those treated with PBS (fig. S14), it suggested that the efficacy of anti-aerolysin in providing protection against MTB-mediated colitis was not due to nonspecific IgG activity.

We additionally evaluated the therapeutic potential of an aerolysin mAb (Clone 5) that we generated. After inducing colitis using MTB, we treated mice with 200 μg

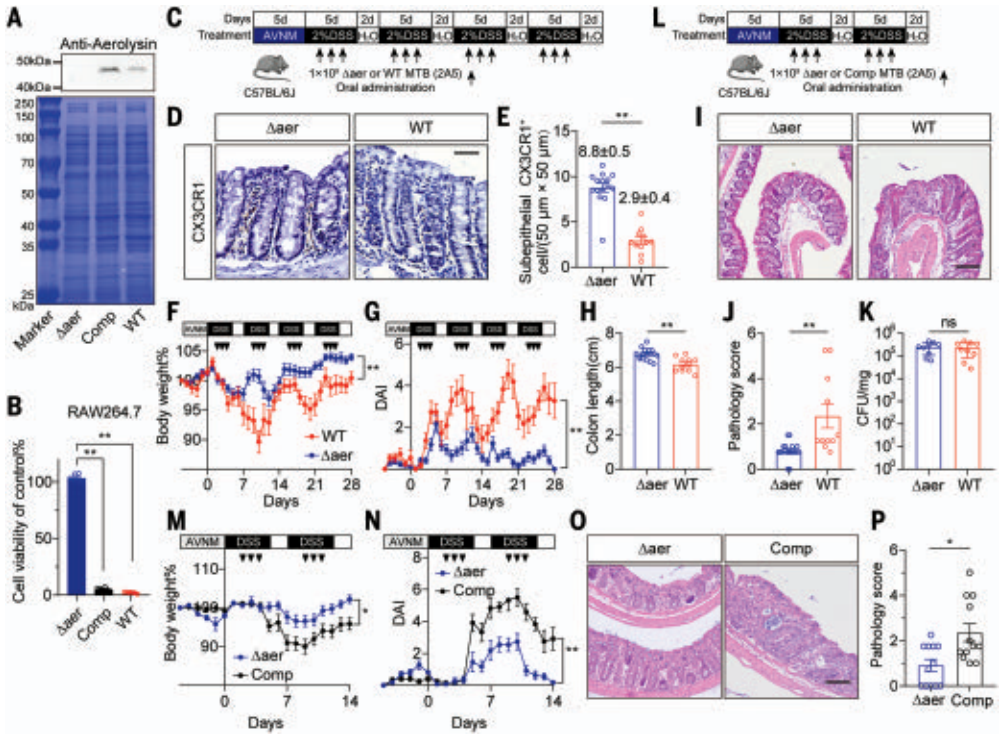

Fig. 4. Aerolysin is indispensable for MTB-induced macrophage disruption and colitis. (**A**) Western blot analysis confirmed knockout (Δaer) and compensation (Comp) of aerolysin protein in the mutant MTB. Coomassie brilliant blue staining of whole bacteria protein separated by SDS-PAGE was used as internal reference. WT, wild type (**B**) Cell viability of RAW264.7 treated with supernatant from Δaer, Comp, and WT MTB. (**C**) Protocol of induction colitis in C57BL/6J mice with Δaer or WT MTB (2A5) bacteria. Δaer group, $n = 17$; WT group, $n = 11$. (**D**) Representative IHC staining was performed to detect CX3CR1$^+$ macrophage in colons from mice treated with Δaer or WT MTB (2A5) (pooled from two independent experiments). Scale bar, 50 μm. (**E**) Quantification of CX3CR1$^+$ cells in the colonic mucosa, with the mean ± SEM values labeled on the diagram. Dots represents the mean of ≥10 different views of an individual animal (pooled from two independent experiments). Δaer group, $n = 15$; WT group, $n = 11$. (**F** and **G**) Changes in body weight and DAI of mice treated with Δaer or WT MTB. (**H**) Colon length of mice. (**I** and **J**) Representative H&E staining and pathology score of mice colon. Scale bar, 100 μm. (**K**) Quantification of fecal Δaer and WT MTB CFU at day 4 after last gavage. In (H), (J) and (K), dots represent individual mice. (**L**) Protocol of colitis induction in C57BL/6J mice with Δaer or Comp MTB (2A5) bacteria. Δaer group, $n = 12$; Comp group, $n = 12$. (**M** and **N**) Changes in body weight and DAI of mice treated with Δaer or Comp MTB. (**O** and **P**) Representative H&E staining and pathology score of Δaer or Comp MTB (2A5) group mice colon (pooled from two independent experiments). Scale bar, 100 μm. Dots represent individual mice. Arrows in (C) and (L) indicate the oral administration of 1×10^9 CFU bacteria. Data are presented as mean ± SEM; ns > 0.05, $*P < 0.05$, $**P < 0.01$. Two-way ANOVA in (F), (G), (M), and (N); unpaired Student's *t* test in (H) and (K); Mann-Whitney test in (E), (J), and (P); and one-way ANOVA in (B).

per mouse of mAb or control mouse IgG (Fig. 6K). MTB colitis was slightly relieved in terms of both body weight and DAI scores (Fig. 6, L and M). These findings suggest that an anti-aerolysin might have efficacy for treating colitis induced by MTB.

Discussion

We found that a species of *Aeromonas* isolated from humans produced aerolysin and colonized the gut of mice under certain conditions, disrupting gut macrophages and increasing the susceptibility of the gut to inflammation.

In UC, epithelial inflammation and damage initially occur in the bacteria-rich distal colon, subsequently extending to proximal segments, while persistent active inflammatory responses are evoked in the gut (*55*, *56*). We propose that in humans, *Aeromonas* spp. including MTB, a group of facultative aquatic microorganisms, may colonize the gut of predisposed individuals after consumption of contaminated drinking water. We hypothesize that after colonization, persistent aerolysin production could disrupt the subepithelial macrophage barrier, increasing the susceptibility of the colon to enteric pathogens, dietary toxins, and microbial metabolites. Although intestinal healing capacity allows for spontaneous or treatment-induced remission, certain pathological stimulations (e.g., antibiotic exposure) could reactivate residual MTB to trigger inflammation. Over time, these recurrent inflammatory episodes may exacerbate mucosal damage, resulting in progressively severe UC manifestations.

Within the *Aeromonas* genus, four species (*A. caviae*, *A. veronii*, *A. dhakensis*, and *A. hydrophila*) account for most human fecal isolates (*57*, *58*). Although these typically cause self-limiting gastroenteritis (*59*, *60*), we found that *A. veronii*, despite aerolysin production and close phylogenetic relationship to MTB, failed to induce chronic colitis in mice under our protocol. Because these bacteria did not colonize the host mice, we concluded that persistent colonization appears to be a prerequisite for macrophage disruption and the development of UC. It is possible that MTB may represent an *Aeromonas* species that has acquired enhanced colonization capacity.

Similar to other *Aeromonas* species, MTB could potentially spread with human-infective potential. Several *Aeromonas* strains have been cultured from UC patient stools in international studies (*61*, *62*), which may have included undiagnosed MTB strains. Thus, future investigations should emphasize laboratory safety when handling UC-associated bacterial cultures. A small proportion of normal stools tested positive for MTB, possibly because of cross-reactivity with other *Aeromonas* species; thus it is important to develop a specific detection method and a broader understanding of other bacteria that could disrupt the gut macrophage layer.

The identification of *Aeromonas* sp. MTB and its aerolysin virulence factor has clinical implications. MTB detection in stool or aerolysin immunostaining in colonic tissue could serve as diagnostic biomarkers. Moreover, our findings point to two potential therapeutic approaches: eradication of MTB through antimicrobial therapy and targeted neutralization of aerolysin activity for both prevention and treatment of UC.

Materials and methods

Mice

C57BL/6J, BALB/c, B6/JGpt-Il10^{em1Cd4885}/Gpt (*Il10*$^{-/-}$) and GF C57BL/6 mice were purchased from GemPharmatech (Jiangsu, China). C57BL/6JCya-Cx3cr1$^{em1(iCre)}$/Cya, and Rosa26-iDTR were purchased from Cyagen (Jiangsu, China). Rosa26-ACTB-tdTomato-EGFP (Rosa26-mTmG, from the Jackson Laboratory, Stock No. 023035) mice were

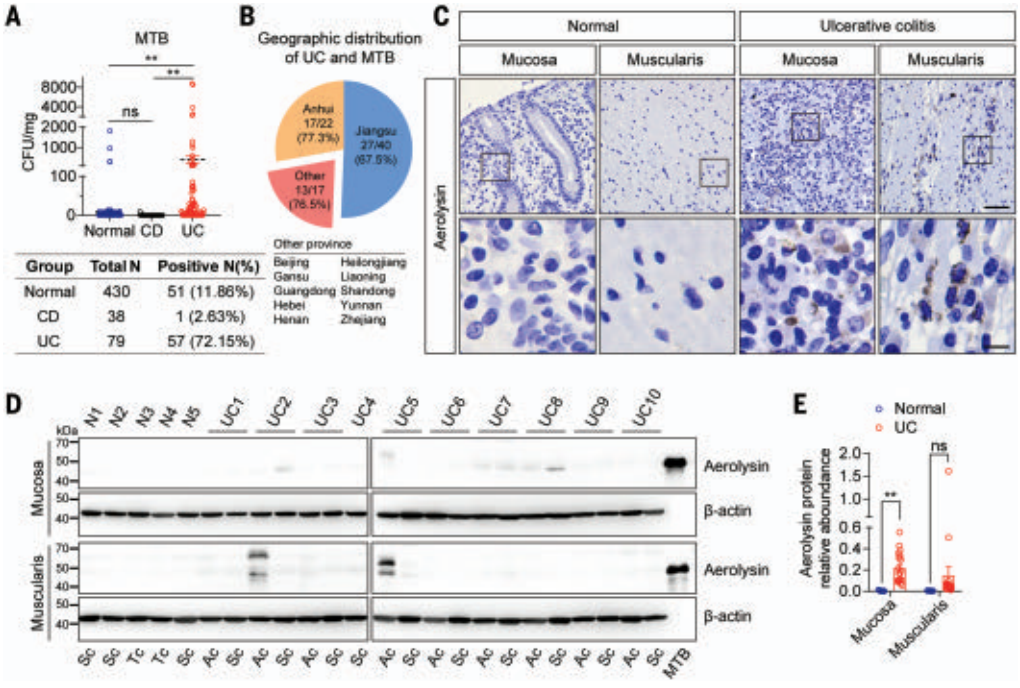

Fig. 5. Presence of MTB in UC stools and aerolysin protein in UC colon tissue. The stools were collected from UC patients, CD patients, and normal populations, and then cultured for qPCR assay. (**A**) Frequency and relative abundance of fecal MTB in human stools. Dots represent individual patients; pooled from four independent experiments. (**B**) Geographic distribution of UC cases involved in the MTB epidemiologic study. Data are shown as the number of MTB-positive cases over the total number of each province (MTB positive%). (**C**) Representative IHC assay for aerolysin protein in UC and normal colon tissues obtained by using an anti-aerolysin mAb. Fresh UC colon biopsies ($n = 10$) and normal regions of colorectal cancer colons ($n = 5$) were collected for IHC. The lower panel (scale bar, 10 μm) shows a magnified view of the area indicated by the box in the upper panel (scale bar, 50 μm). (**D**) Western blot assay for aerolysin protein in UC and normal colon tissues. Mucosa and muscularis layers of fresh UC colon biopsies ($n = 10$) and normal regions of colorectal cancer colons (N1 to N5, $n = 5$) were sampled individually. β-actin was used as an internal reference. Ac, ascending colon; Sc, sigmoid colon; Tc, transverse colon. (**E**) Quantification of Western blot results, normalized by β-actin. Dots represent individual patients. Data are presented as mean ± SEM; ns > 0.05, $^{**}P < 0.01$, $^{**}Q < 0.01$; Kruskal-Wallis test followed by Dunn's post hoc test in (A), and multiple *t* tests with FDR adjustment (two-stage method) in (E).

gifts from the Zhongzhou Yang's lab of Nanjing University. To generate *Cx3cr1*$^{Cre/+}$; Rosa26$^{mTmG/+}$ mice, the homozygous Rosa26-mTmG (Rosa26$^{mTmG/mTmG}$) mice were subsequently crossed to homozygous *Cx3cr1*-iCre (*Cx3cr1*$^{Cre/Cre}$) mice. To generate *Cx3cr1*$^{Cre/+}$; Rosa26$^{DTR/+}$ mice, the homozygous Rosa26-iDTR (Rosa26$^{DTR/DTR}$) mice were subsequently crossed to homozygous *Cx3cr1*-iCre (expression of *Cx3cr1*-iCre excises the floxed stop cassette allowing for DTR expression in CX3CR1^{+} cells) to selectively deplete colonic CX3CR1^{+} macrophages upon intrarectally administration of diphtheria toxin (DT, D0564, Sigma-Aldrich). For genetic depletion of colonic CX3CR1^{+} macrophages, *Cx3cr1*$^{Cre/+}$; Rosa26$^{DTR/+}$ mice were intrarectally administrated with 100 ng DT every other day during experiments (designated throughout the study as ΔCX3CR1 mice), and respective littermate controls *Cx3cr1*$^{Cre/+}$; Rosa26$^{DTR/+}$ mice were intrarectally administrated with 100 μl PBS every other day (designated throughout the study as Litt). For chemical depletion of colonic macrophage, C57BL/6J mice were intrarectally administrated with 100 μl Clodronate Liposomes (Clod-Lip, 40337ES10, Yeasen) every other day and control mice received 100 μl PBS Liposomes (PBS-Lip, 40338ES10, Yeasen). The animals were maintained in SPF animal rooms of the Model Animal Research Center of Nanjing University and the animal facilities of Nanjing Normal University and the Medical School of Nanjing University. Mice were kept under a 12-hour/12-hour LD cycle and supplied with water and food ad libitum.

For colitis induction and in vitro experiments, we used 6- to 8-week-old male mice, including C57BL/6J, *Cx3cr1*$^{Cre/+}$; Rosa26$^{DTR/+}$, *Cx3cr1*$^{Cre/+}$; Rosa26$^{mTmG/+}$, and *Il10*$^{-/-}$ mice. Female BALB/c mice (6 weeks old) were used for antibody production. We determined sample sizes based on prior experience and commonly used standards in the field ($n \geq 6$ mice per group). No data or animals were excluded. All experiments were performed with random allocation of animals, and investigators were blinded to group assignment during both experimentation and outcome assessment.

All animal manipulations in this study were conducted in accordance with the criteria of the Institutional Animal Care and Use Committee (IACUC) of the Model Animal Research Center of Nanjing University [Nanjing, China (AP No.MZ24)] and Nanjing Normal University (Nanjing, China) (AP No. IACUC-20231103), which are members of the Association for Assessment and Accreditation of Laboratory Animal Care (AAALAC).

Human colon tissue collection and analysis

Participants eligible for inclusion in UC were diagnosed according to the criteria as described in (*63*). The UC patients who received colectomy surgery should meet the following criteria: (i) Absolute indications: major hemorrhage, perforation, toxic megacolon, or sepsis. (ii) Relative indications: severe UC unresponsive to medical therapy or associated with significant side effects impacting quality of life. (iii) Elective colectomy options: Persistent symptoms remain despite maximal medical therapy, or in the presence of chronic disease state, dysplasia, or malignancy. The exclusion criteria included the presence of Crohn's disease, and altered colitis. All patients reported disease, medication, and allergy history. Seventeen UC patients who received surgery were hospitalized in the Surgery Department, Jinling Hospital, Medical School of Nanjing University. The 17 patients with colorectal cancer were diagnosed and operated by the Surgery Department of Jinling Hospital (tables S1 and S2). Fresh colon segments were collected from the set 1 patients by colectomy. Colonic tissues were washed with sterile PBS briefly and then fixed 1 cm^3 segments with 4% paraformaldehyde (PFA,16005, Sigma-Aldrich) or nitrogen snap frozen 1 cm^3 segments and further stored at −80°C. The former was used for immunohistochemistry assay and histology examination, immunofluorescence and the latter were used for Western Blot. Fresh colon segments collected from set 2 patients were preserved in 25 ml transport solution at 4°C and subsequently submitted for flow cytometry assay in no more than 2 hours.

The testing of human samples was approved by the Experimentation Ethics Review Committee of Jinling Hospital, Medical School of Nanjing University (no. 2024DZKY-033-01) and Nanjing Medical University (No. NJCDCLL2021009). All participants know the aim of this study and the informed consent was signed by the participant or the participant's legal guardian.

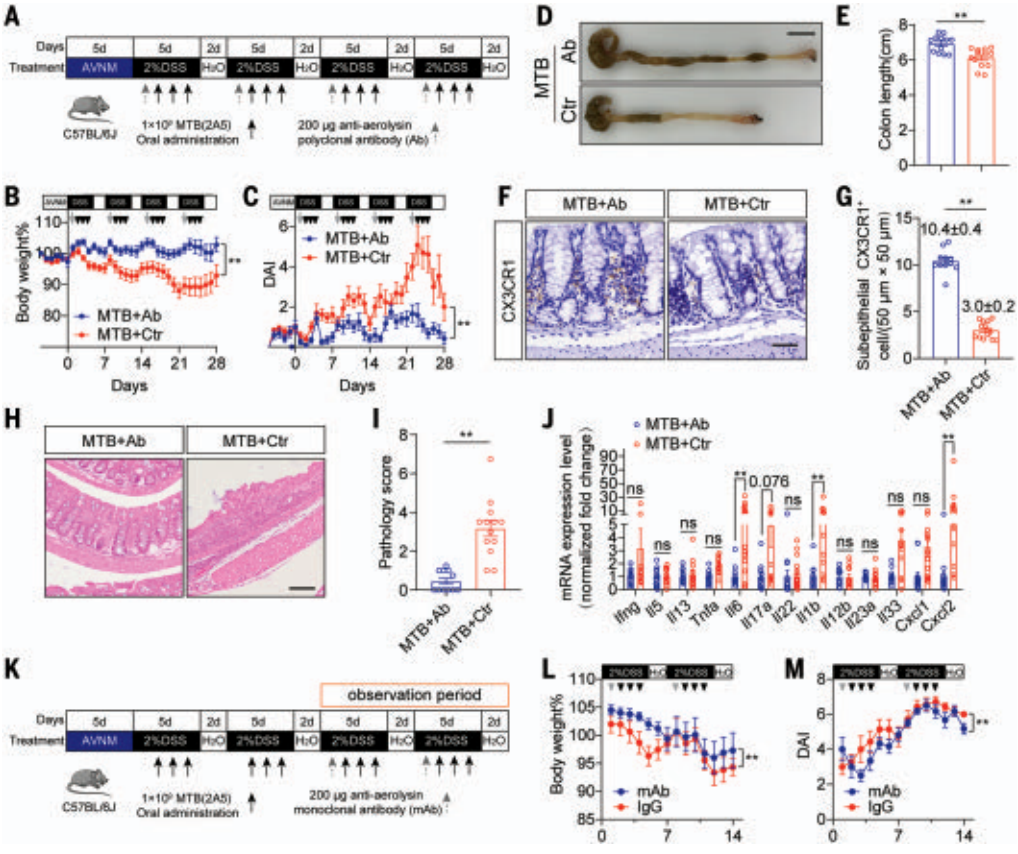

Fig. 6. Anti-aerolysin antibody attenuated MTB-induced colitis. (**A**) Protocol for MTB (2A5) oral administration and treatment with anti-aerolysin polyclonal antibody. Before oral administration of MTB, mice received antibody treatment (MTB+Ab, $n = 12$) or PBS control (MTB+Ctr, $n = 13$). Black arrows indicate the oral administration of MTB bacteria. Gray arrows indicate 200 μg anti-aerolysin polyclonal antibody or 100 μl PBS control injection i.p. (**B**) Changes in body weight. (**C**) DAI. (**D** and **E**) Colon lengths. Scale bar, 1 cm. Dots represent individual mice. (**F**) Representative IHC staining for colonic CX3CR1$^+$ macrophages of MTB-treated mice receiving either antibody or control treatment. Scale bar, 50 μm. (**G**) Quantification of CX3CR1$^+$ cells in the colonic mucosa, with the mean ± SEM values labeled on the diagram. Dots represents the mean of ≥10 different views of an individual animal (pooled from two independent experiments). (**H** and **I**) Representative H&E staining and pathology score of colons. Scale bar, 100 μm. (**J**) Relative mRNA expression levels of inflammatory cytokines in the colons. (**K**) Colitis was induced by two rounds of MTB gavage, followed by treatment with either 200 μg of anti-aerolysin mAb or control IgG. mAb group, $n = 6$; IgG group, $n = 7$ (pooled from two independent experiments). (**L**) Changes in body weight. (**M**) DAI. Data are presented as mean ± SEM; ns > 0.05, *$P < 0.05$, **$P < 0.01$. Mann-Whitney test in (E) and (I); unpaired Student's t test in (G); and two-way ANOVA in (B), (C), (J), (L), and (M).

centrifugation at 500 g for 5 min. The cell pellets were washed once with PBS and used directly for flow cytometry.

Antibody and flow cytometry

Isolated mucosa single-cells were prepared as described above, and then dyed with viability solution (565388, BD) for 15 min at RT, followed by incubation with 2.5 μg/ml Fc blocker (156604 for mouse; 422302 for human, BioLegend) for 10 min at 4°C. Mouse cells were then stained with antibody against CD45 (103138, BioLegend), F4/80 (123137, BioLegend), CX3CR1 (149005, BioLegend), Ly-6c (128023, BioLegend), Ly-6G (127615, BioLegend), CD11b (101217, BioLegend), and CD4 (404-0042-80, Thermo), IL-17A (561020, BD), CD19 (115505, BD), CD3 (100236, BioLegend), CD8a (100734, BioLegend). Human cells were stained with antibody against CD45 (563204, BD), CD68 (25-0689-42, Thermo), CCR2 (357206, BioLegend), HLA-DR (45-9956-42, Thermo), CD11b (101217, BioLegend), CD3 (300412, BioLegend), CD4 (566392, BD), CD8 (562428, BD), IL-17A (560438, BD), CD19 (564456, BD). For IL-17A staining, cells were pre-stimulated with Leukocyte Activation Cocktail (550583, BD) culture medium (RPMI 1640+10% FBS+1%PS) for 4 hours at 37°C under a 5% CO_2 condition. Stained cell samples were fixed with Fixation/Permeablization Kit (554714, BD). For flow cytometry analysis, a four-laser flow cytometer (Cytoflex S, Beckman Coulter) was applied. The flow cytometry data were analyzed with FlowJo software (version 10, BD). All immune cell populations were gated from live CD45$^+$ cells, and all cellular percentages were normalized to and expressed as a percentage of the total live cell population.

Isolation of human and mouse colonic lamina propria cells

Human and mouse colonic lamina propria cells were isolated as reference (*64*, *65*) with some modifications. Briefly, 4 cm^2 human colon tissues were collected after colectomy surgery, mouse colons were collected and washed with PBS to remove fecal contents, and longitudinally cut. Colon tissues were kept in transport solution (RPMI1640+1×GlutaMax+1%PS+50μg/gentamycin) at 4°C and were processed for digestion within 2 hours of collection. Mucosa were carefully separated and shook with pre-digested solution (1mM DTT, $HBSS^{Ca/-Mg}$) at 37°C for 20 min at 200 rpm twice. Tissues were then digested in a digestion solution supplemented with 0.25 mg/ml collagenase VIII (C2139, Sigma-Aldrich) and 5 U/ml DNase I (D4263, Sigma-Aldrich) in a 200-rpm constant temperature shaker at 37°C for 1 hour. Digested tissues were passed through a 70-μm cell strainer (abs7306, absin) to acquire single-cell suspensions and then centrifuged at 500 g for 10 min. Cell pellets were then resuspended in 35% Percoll (P4937, Sigma-Aldrich). After centrifugation at 1000 g for 20 min, cells were resuspended in 10 ml of blood lysis buffer (555899, BD) for 10 min at RT to eliminate red blood cells, and then followed by another

Human fecal bacteria collection and culture

Stool samples from IBD patients, including 79 with UC and 38 with CD who had not undergone surgery, were collected while they were hospitalized in the Department of Gastroenterology at Jinling Hospital. Additionally, healthy stool samples from 430 participants were also collected at the Nanjing Municipal Center for Disease Control and Prevention for a fecal bacteria study (tables S3 and S4). The fresh stools were collected from the participant with a collection kit (ChuTianShu Biotechnology Company, Xi'an, China). For collection of the bacterial culture metabolite, we added 100 μl feces suspension to 0.9 ml LB broth (10 g/liter tryptone, 5 g/liter yeast extract, 10 g/liter NaCl) and cultured for 12 to 16 hours at 37°C. The supernatants were prepared by centrifugation at 12,000 rpm for 10 min at 4°C and then sterilized by passing through a 0.22-μm filter. The resultant supernatants were subjected to cytotoxicity measurement. Fecal bacteria were handled under Biological Safety Level 2 (BSL-2) conditions and biological safety cabinet, with decontamination of waste by autoclaving.

Cultivation of UC bacterial colonies

To grow the fecal bacterial colonies, 100 μl of bacterial culture prepared by overnight culturing stool suspension with LB broth was 10-fold diluted and then inoculated on a Columbia Blood Agar Plate (LA3540, Solarbio) containing 10% Sterile Defidrinated Sheep Blood (MP20026, Shanghai Yuanye) or LB agar, and the colonies usually emerged within 12 to 16 hours. The resultant colonies were then collected and subjected to different experiments such as PCR assay and cytotoxicity assay. For culturing the bacterial colonies of *Aeromonas*, the Rimler-Shotts agar was used.

Bacteria strains and API-20NE test

TH0426 and ATCC35624 strains of *Aeromonas veronii* were purchased from Ningbo Ming Zhou Bio. MTB (2A5), MTB (10A1), MTB (10B4), MTB (10A3), MTB (10A10) colonies were isolated as reported in this paper and stored at our lab. *Klebsiella pneumoniae*, *Proteus mirabilis*, and *Enterobacter hormaechei* subsp. *xiangfangensis* were preserved in our lab. API-20NE identification for those bacterial strains was performed by the China Center of Industrial Culture Collection.

Purification of macrophage toxin from UC fecal bacteria culture

The mixed UC fecal culture was filtered with a 0.22-μm syringe filter and concentrated to 30-fold via Amicon Ultra-15 10K devices. The resultant solution was then dialyzed against 20 mM Tris-HCl (pH6.5) at 4°C for 12 hours and loaded to ÄKTA Pure Protein Purification System (Cytiva Lifesciences) with a column of IexCap DEAE 6FF (SI005C15, Smart-Lifesciences) which was pre-equilibrated with equilibration buffer A (20 mM Bis-tris, pH6.5). The elution buffer B was comprised of 1 M NaCl, 20 mM Bis-tris (pH6.5). The step elution protocol is: 2 column volumes (CV) of 85% buffer A + 15% buffer B; 2CV of 70% buffer A + 30% buffer B; 2CV of 40% buffer A + 60% buffer B, 4CV of 100% B at a flow rate of 1 ml/min. Each eluted fraction was dialyzed against 10 mM PBS (pH7.4) and subsequently used in the BMDM (mouse bone marrow derived macrophage) cytotoxicity assay. The fractions with cytotoxicity were resolved by SDS-PAGE and the candidate bands were subjected to LC-MS/MS analysis.

LC-MS/MS analysis for aerolysin toxin

The candidate bands, separated by SDS-PAGE, were excised and prepared for trypsin digestion and LC-MS/MS analysis. Briefly, the isolated gel was excised and cut into 1 mm^3 cubes and then washed with 50 mM ammonium bicarbonate: acetonitrile (1:1) solution three times. The vacuum-dried gel cubes were then digested overnight with trypsin at 1:50 trypsin-to-protein mass ratio at 37°C. The resultant peptides were extracted using a 10% formic acid: acetonitrile (1:1) solution for 15 min and subsequently dried in a SpeedVac. The protein sample was resuspended in 15 μl of 3% acetonitrile and 2% FA prior to LC-MS/MS analysis by a TripleTOF 5600+ System (AB SCIEX). The original MS/MS file data of the label-free proteomics experiments were submitted to ProteinPilot Software (version 4.5, AB SCIEX) for data analysis. MS/MS data were searched against the UniProt database (Jan. 2021, containing 251,702,059 results, https://www.uniprot.org/proteomes/UP000439123) (*66*). The mass spectrometry proteomics data have been deposited to the ProteomeXchange Consortium with the dataset identifier PXD050471 (https://proteomecentral.proteomexchange.org/cgi/GetDataset).

Genome sequencing and assembly

The genomic DNA of MTB was sequenced using the Oxford nanopore and DNBSEQ platforms at the Beijing Genomics Institute (BGI, Shenzhen, China). The DNBSEQ data was subjected to quality control filtering using SOAPnuke software (version 1.5.6, parameters: -l 20 -q 40% -n 0.1% -d), which further improved the accuracy of the genome sequences. Nanopore data were processed using porechop (version: 0.2.4, parameters: default parameters %Methods) to remove adapter contamination and filter sequences shorter than 2000 bp. Genome sequence accuracy was further enhanced by single-base corrections via GATK (https://software.broadinstitute.org/gatk/). The finalized genomic sequence was submitted to GenBank, under BioProject accession number PRJNA1083721. Predictions and annotations of the genome components were performed as previously described (*67*).

Plasmids construction

To express recombinant aerolysin protein in *E.coli*. Full-length (1 to 1467 nucleotides) of aerolysin gene without N-terminal signal was first amplified from *Aeromonas* sp. MTB genomic DNA by a PCR method with pGEX-Aerolysin F/R primers and constructed PGEX-Aerolysin plasmid. Aerolysin gene were amplified from bacteria genomic DNA extracted from UC mix slurry, and five aerolysin genes (gene ID: PP460999-PP461003) were identified. Aerolysin gene (gene ID: PP460999) was subcloned into the pGEX-5X-1 plasmid through *EcoR* I & *Xho* I restriction sites with a ClonExpress II One Step Cloning Kit (C112, Valzyme). pRE112-Δaer plasmid was used to mutant aerolysin [lacking 636–base pair (bp) partial sequence of aerolysin] expression in MTB, the homologous 500 bp of left-arm and right arm were amplified from MTB genomic DNA (2A5 clone) with pRE112-Δaer-LA F/R and pRE112-Δaer-RA F/R primer sets. The resultant LA and RA arms were subcloned into a *Kpn* I & *Sac* I digested pRE112 plasmid (Nanjing warbio) with a ClonExpress MultiS One Step Cloning Kit (C113, Valzyme) and transformed to λpir *E.coli* competent cell (MingZhoubio). To complement aerolysin expression in Δaer MTB (2A5), aerolysin genes containing 281-bp upstream sequence and 110-bp downstream sequence were amplified from MTB (2A5) with pBBR1MCS2-aer comp F/R primer set and subcloned into pBBR1MCS2 with Chloramphenicol resistance. The primers for plasmid construction were listed in table S9.

Expression and purification of GST-fused aerolysin proteins

pGEX-aerolysin plasmid was transformed into DH5α *E.coli* component cells and the transformed bacteria were induced by 50 nM isopropyl-beta-D-thiogalactopyranoside (IPTG) for 4 hours. The induced bacteria were harvested by centrifugation and subsequently sonicated. The resulting supernatants were filtered and subsequently purified using Glutathione Sepharose 4B resin (#17-0756-01, GE Healthcare), following the manufacturer's instructions.

In vivo cytotoxicity of aerolysin protein

Male C57BL/6J and *Cx3cr1*$^{Cre/+}$; Rosa26$^{mTmG/+}$ (6 to 8 weeks) mice were anesthetized with 250 to 300 mg/kg avertin (T48402, Sigma-Aldrich) via injection (i.p.), then received 20 μg GST-aerolysin in 100 μl PBS containing 1% methyl cellulose (M0512, Sigma-Aldrich) or 100 μl GST protein in solvent via rectal administration. Three hours later, mice were sacrificed to collect colon for immunostaining and flow cytometry analysis. Aerolysin group (C57BL/6J), $n = 3$; GST group (C57BL/6J), $n = 4$. Aerolysin group (*Cx3cr1*$^{Cre/+}$; Rosa26$^{mTmG/+}$), $n = 3$; GST group (*Cx3cr1*$^{Cre/+}$; Rosa26$^{mTmG/+}$), $n = 4$.

Cell line and primary isolated macrophages

SP2/0, MC-38 and HT-29 cell lines were preserved in Zhu lab of Nanjing University; RAW246.7, and THP-1 were the gifts from Jianghuai Liu's lab of Nanjing University; Caco-2 (Clone 5E6L) cell line was a gift from Weiqi He's lab of Soochow University. Caco-2 and NCM460 cell lines were purchased from Haixing Company (China). BMDM, RAW264.7, MC-38, HT-29, Caco-2 cell lines were cultured in Dulbecco's Modified Eagle's Medium (DMEM, #12100046, Life Technologies), with 10% fetal bovine serum (FBS, Gibco), 100 U/ml penicillin and 100 μg/ml streptomycin (1%PS). SP2/0, NCM460 was cultured with RPMI 1640 (#31800-022, Life Technologies) containing 10% FBS and 1%PS. THP-1 was cultured in RPMI 1640 (10% FBS, 1%PS, 50 μM β-mercaptoethanol), and pre-induced into human macrophage by 200 ng/ml PMA (HY-18739, MedChemExpress) for 24 hours. Isolation of mouse bone marrow derived

macrophage (BMDM) was performed as the methods described (*68*). Briefly, the hind legs were cut and peeled from sacrificed male C57BL/6J (6 to 8 weeks) mice, flushed the bone cavity and washed once with PBS (pH7.4). Centrifuged cells at 500 g for 10 min at room temperature. Pellet cells from a mouse were resuspended and followed by seeding to Nunclon Sphera 90-mm dish (174945, Thermo) containing 10 ml macrophage complete medium (DMEM, 30% L929 medium, 10%FBS, 1%PS), and the medium was refreshed once. BMDM was harvested at the seventh day by digesting with 0.25% EDTA (PBS). The resultant primary macrophages were then divided into 96-well plate and cultured with DMEM containing 10% FBS and 1% PS. All the cells were cultured at 37°C under a 5% CO_2 condition.

Toxin treatment, antibody neutralization and measurement of cell viability

For healthy and UC patients fecal bacteria culture supernatant cytotoxicity detection, 20 μl de-bacteria supernatant was added into 100 μl DMEM (10%FBS, 1%PS) and incubated with 2×10^4 BMDM for 6 hours in 96-well plate. Twenty microliters LB broth was added to BMDM as control for normalization. For antibody neutralization analysis, 20 μl bacterial cultures from Healthy mix, UC mix, MTBs or LB broth (control) were mixed with 10 μl of mouse anti-aerolysin polyclonal antibody respectively. The mixtures were then added into a 96-well plate with 100 μl of DMEM or RPMI 1640 (10%FBS, 1%PS) containing 2×10^4 BMDMs or other cells (e.g., MC-38, RAW264.7, 5E6L, Caco-2, NCM460, HT-29 and THP-1) and cultured for approximately 20 hours. Gradient diluted GST-aerolysin were then mixed in the culture medium and incubated for extra 3 hours, PBS without toxin treatment was used as control. The cell viability was measured with a CCK-8 kit (#20118, SUDGEN) according to the manufacturer's instructions. The $OD_{450\ nm}$ and $OD_{600\ nm}$ (used as blank control) were read by a microplate reader (Molecular Devices M3, Molecular Devices). The percentage of cell viability = [($OD_{450\ nm}$ of experiment − $OD_{600\ nm}$ of experiment)/($OD_{450\ nm}$ of control − $OD_{600\ nm}$ of control)] × 100%.

Preparation of mouse polyclonal antibodies against aerolysin

Purified recombinant GST-aerolysin proteins (100 μg in 100 μl PBS) mixed with 100 μl complete Freund's adjuvant (F5881, Sigma-Aldrich) were injected into female BALB/c mice (6 weeks) for the first immunization. Two booster immunizations were conducted by injecting with 50 μg GST-aerolysin proteins plus 50 μl incomplete Freund's adjuvant (F5506, Sigma-Aldrich) with 2 weeks interval. Three days after the last injection, the animals received 2×10^6 SP2/0 myeloma cells i.p. to induce ascites. Polyclonal antibodies from ascites were purified by rProtein G Beads (Smart-Lifesciences, SA016005) according to the manufacturer's instructions. Final antibody titer >1:100000.

Mouse anti-aerolysin mAb preparation

For mAb preparation, female BALB/c mice (6 weeks) were immunized three times with aerolysin proteins mixed with Freund's adjuvant above-mentioned. Three days after the last immunization, the spleen cells were prepared and fused with SP2/0 cells using polyethylene glycol. The fused cells were selected in a RPMI1640-HAT medium (H0262, Sigma-Aldrich) containing 10% FBS, 1% PS, gentamycin for 2 weeks. Two weeks after selection, the culture media were subjected to ELISA for detecting the antibody targeting aerolysin. The antibody-positive colonies were further verified by Western blot with MTB supernatant. The positive colonies were further sub-cloned and amplified once in RPMI1640-HT (H0137, Sigma-Aldrich) medium, 10% FBS, 1% PS. For antibody production in vivo, 0.25 ml incomplete Freund's adjuvant were injected i.p. into female BALB/c mice (8 weeks), and 7 days later, followed with 1×10^6 hybridoma cells injected i.p. (producing mAb Clone 5 and Clone 12). The titration of the resultant ascites usually was higher than 1:100000. The mAb ascites was purified using rProtein G Beads according to the protocol provided by the vendor.

Aerolysin knockout and rescue in MTB

To knock out aerolysin (Δaer) in MTB, we designed a homologous recombination strategy by using a pRE112-Δaer conjugative plasmid in which a 20-to-655-bp region of aerolysin gene had been deleted. Briefly, pRE112-Δaer plasmid amplified in λpir *E.coli* was extracted and transformed into WM3064 *E.coli* (Ningbo Ming Zhou Bio), an auxotroph strain requiring supplemental 25 μg/ml DAP (D836611, Macklin) in culture medium. The resultant transformed colonies as well as MTB (Clone 2A5) colonies were individually inoculated in LB and cultured at 37°C until OD_{600} reached 0.5. One milliliter of MTB bacterial cultures was centrifuged (5000 rpm × 8 min) and suspended with 300 μl LB. We added 100 μl MTB suspension to the pRE112-Δaer WM3064 bacteria pellet at 1:3 ratio, and spread this mixture to LB agar containing 25 μg/ml DAP. Twenty-four hours after culturing at 37°C, all bacterial colonies were collected by washing with 2 ml LB broth and then inoculated on LB agar containing 100 μg/ml Ampicillin and 25 μg/ml Chloramphenicol (Chl, B541015, BBI). After culturing overnight at 37°C, the positive colonies were subjected to the first crossover screening with PCR method. To screen the second crossover, we seeded the positive first crossover variant to liquid LB containing 10% sucrose followed by culturing at 37°C and passaging four times at a 12-hour interval. The variants were then spread on LB agar (100 μg/ml Ampicillin, 10% Sucrose) and grown overnight at 37°C. The edited MTB variants capable of growing on Amp^+, 10% Sucrose LB agar but not Chl^+ LB agar were picked individually for sequencing and other validation experiments. To rescue aerolysin in Δaer MTB (Comp MTB), PBBR1MCS2-aer comp plasmid was introduced into Δaer MTB by conjugation mediated transformation via WM3064 *E.coli*.

siRNA transfection

The procedure of siRNA-mate plus transfect kit (G04002, Genepharma) for introducing siRNA into RAW264.7 was performed according to the manufacturer's instructions. Briefly, 12 hours before siRNA transfection, 2×10^4 RAW264.7 cells were seeded into a 96-well plate in 100 μl of DMEM (10%FBS, 1%PS). Three picomoles each of *Cd14* siRNA, *Bst1* siRNA, *Bst2* siRNA, *Ly6e* siRNA, *Smpd13b* siRNA, *Vnn1* siRNA, *Pakap* siRNA, and control siRNA molecules were added to each well. The stock (20 pmol/μl) was diluted to 1.5 pmol/μl with dilution buffer. Then, 2 μl of diluted siRNA was mixed with 0.55 μl of siRNA-mate plus transfect reagent, and gently pipetted multiple times. Then, 2.55 μl siRNA/plus mix was allocated to each well and the plate was gently shaken to ensure uniform distribution. Cells were also seeded into a 24-well plate for further quantification of mRNA expression, with five-fold the cell number and siRNA amount as in the 96-well plate. The RAW264.7 cells, after interference, were harvested at 36 hours for mRNA analysis. Seventy-two hours after transfection, siRNA interfered RAW264.7 were changed with fresh culture medium containing 39 ng/ml GST-Aerolysin and cultured for 5 hours. The viability of these cells was measured with a CCK8 kit. For siRNA sequences, see table S10.

Western blot and dot blot assay

Fresh or frozen biopsies were homogenized and lysed in RIPA buffer (50 mM Tris-HCl, pH7.5, 150 mM NaCl, 1 mM EDTA, 1% NP-40, 0.25% Sodium deoxycholate) containing 1× protease inhibitor cocktail (HY-K0011, MedChemExpress) on ice for 30 min. The samples were then denatured in 1× Laemmli buffer at 95°C for 5 min, and then separated by SDS-PAGE and transferred to PVDF membranes (Bio-Rad). Alternatively, the lysed samples were dropped on PVDF membranes for dot blot assay. The primary antibodies used were mAbs against aerolysin (1:5000, Clone 12, generated in this study) and β-actin (1:5000, Clone AC-15, A5441, Sigma-Aldrich). HRP-linked goat anti-mouse IgG (H+L) was used as the secondary antibody (1:5000, #31430, Thermo Fisher). After incubation with the secondary antibodies blot for 2 hours at room temperature, the membranes were visualized with High-sig ECL Western Blotting Substrate (180-5001, Tanon) and a Western

blotting detection system (Tanon 4160). For uncut blot data, refer to figs. S15 to S22.

Histology and immunochemistry staining

Four percent PFA-fixed mouse and human tissue sections were embedded in paraffin (39601095, Leica). Hematoxylin-eosin (H&E) staining was performed according to standard protocols. IHC was performed per manufacturer's instructions (KIT-9706, mouse sections; KIT-5920, human section, MXB Biotechnologies). Briefly, antigen retrieval was performed on 5-μm paraffin sections using citrate buffer (E673001, BBI). After peroxidase and serum blocking, primary antibodies including aerolysin (Clone 12, 1:1000, in this study), CD68 (#76437, 1:4000, Cell Signaling Technology), CX3CR1 (ab308613, 1:1000, Abcam) were incubated with sections at 4°C overnight, and then incubated with horseradish peroxidase-conjugated secondary antibody. Development was carried out using a DAB Peroxidase (HRP) Substrate Kit (DAB-0031, MXB Biotechnologies), followed by counterstaining with hematoxylin.

Microscopy imaging

To acquire TEM images, MTB bacteria were absorbed onto Formvar-coated copper grid (WFHM-150, Servicebio) and immersed in 0.5% glutaric dialdehyde (P1126, Solarbio), and then negatively stained with 2% phosphotungstic acid (G1870, Solarbio). Bacteria TEM imaging was obtained by a Transmission Electron Microscopy (H-7650, HITACHI). For cell TEM imaging, 1×10^6 RAW264.7 were seeded into a 10-cm dish for 20 hours, and then incubated with 0.016 pM GST-aerolysin for 3 hours. Cell TEM imaging was completed by Shandong Weiya Company. Briefly, cells were collected and fixed with 3% glutaraldehyde. The fixed cell pellets were fixed with 1% osmium tetroxide followed by washing, dehydration, permeation, Epon812 embedding and making ultrathin sections (LKB-V). Sections were stained with lead citrate and uranyl acetate, and then observed under a JEOL-1200Ex microscope, TEM images were acquired with a Morada-G2 TEM camera. Images of cell morphology under bright field were captured using an inverted microscope with Motic Image Plus 3.0 software. H&E and IHC imaging were performed using a microscope (DP74, OLYMPUS) equipped with a CCD camera.

Immunofluorescent assay

Human and mouse colon tissues were collected and immediately fixed with 4% PFA for 24 hours at 4°C. Tissues were dehydrated through a sucrose gradient (10%, 20% for 1 hour each, followed by 30% overnight) at 4°C. The colon tissues were embedded in OCT compound, snap-frozen in liquid nitrogen, and sectioned at 8-μm thickness using a Leica CM1950 cryostat. For cell preparation, 1×10^5 RAW264.7 and HT-29 cells were seeded onto glass coverslips pre-treated with 1% gelatin. After 13 pM GST-aerolysin treatment for 1 hour, cell coverslips were fixed with 4% PFA (PBS) for 10 min. For immunofluorescence staining, colon sections or cell coverslips were washed with PBS three times for 5 min each, permeabilized with 0.1% Triton X-100 in PBS for 10 min, followed by blocking with 1% bovine serum albumin (BSA)-PBS for 1 hour at room temperature, and then incubated with primary antibodies overnight at 4°C. The primary antibodies used in the present study were: Rabbit anti-CD68 (1:500, #76437, Cell Signaling Technology), Mouse anti-Aerolysin (Clone 12, 1:500, in this study). Sections were washed with PBS three times for 5 min and then incubated with secondary antibodies and DAPI (1:5000, BioSharp) for 1 hour at room temperature. Samples were washed and mounted with 50% glycerol in PBS (pH 7.4). The secondary antibodies used in the present study were: Alexa Fluor 555 conjugated Goat anti-rabbit IgG (1:500, #21428, Life Technologies) and Alexa Fluor 488 conjugated Donkey anti-Mouse IgG (1:500, #A21202, Life Technologies). Colon sections from *Cx3cr1*$^{Cre/+}$; Rosa26$^{mTmG/+}$ mice were embedded and counterstained with DAPI. Images were acquired at 1024 by 1024 pixels using a FV3000 confocal microscope (Olympus, Japan).

Assessment for MTB colonization capacity and fecal abundance quantification

To test colonization capacity of MTB and *A. veronii* (ATCC35624, TH0426) in animals, male C57BL/6J mice (6 to 8 weeks) were pretreated with a water control, antibiotics cocktail and/or 2% (m/v) DSS (36,000 to 50,000 Dextran Sulfate Sodium, 160110, MP Biomedicals) for 5 days, and then were orally inoculated 1×10^9 CFU bacteria for 3 consecutive days. The antibiotics cocktail (AVNM) was composed of 0.2 g/liter ampicillin, 0.1 g/liter vancomycin, 0.2 g/liter neomycin and 0.2 g/liter metronidazole. Stools samples were collected on indicated days following the final inoculation of the bacterial strains. To mitigate DSS-induced PCR inhibition and improve MTB detection sensitivity, stool samples were subjected to two rounds of LB broth culture before PCR amplification. Briefly, stool samples were cultured in 1 ml of LB broth at 37°C overnight, subsequently, 10 μl of the fecal bacteria culture was transferred to a new 1 ml LB broth for a second round of culture. The suspension from this secondary culture was directly used for PCR assays with the primer set ASA. Amplification of 16*S* rRNA of *E. coli* with primer RSS was used as internal reference for amplification efficiency. PCR reaction includes 10 μl Taq Master Mix (P112, Vazyme), 0.5 μl /0.5 μl F/R primer, 1 μl bacteria suspension, 8 μl ddH_2O. The amplification program was set as: (i) pre-incubation at 95°C for 3 min; (ii) 33 cycles of denaturation at 95°C for 30 s and annealing at 62°C(ASA)/58°C(RRS) for 30 s, elongation at 72°C for 30 s; (iii) final elongation at 72°C for 5 min. For PCR primers see table S11. To quantify the fecal MTB abundance, stool sample were collected and homogenized with 20 μl PBS/mg. One-hundred microliters fecal suspension was washed twice with 1 ml PBS and then heated with 80 μl lysis buffer A (25 mM NaOH, 0.2 mM EDTA, pH 12) at 95°C for 30 min, and 80 μl lysis buffer B (40 mM Tris-HCl) was added to stop reaction. Lysis was used directly for TaqMan probe qPCR targeting aerolysin.

TaqMan probe qPCR targeting aerolysin

100 μl stool suspension plus 0.9 ml LB broth was cultured for 12 to 16 hours at 37°C and the bacterial genome DNA was extracted with a Bacterium (G-) Genomic DNA extracting Kit (K2303, Karroten) according to the manufacturer's instructions. Primers and TaqMan probes targeting aerolysin (pASA) and bacteria 16*S* rRNA (p16S) were designed in our lab for real-time quantitative PCR. qPCR reaction includes 10 μl Taq Pro HS Universal U+ Probe Master Mix (QN114, Vazyme), 1 μl of bacterial genome DNA, 0.4 μl/0.4 μl pASA F/R, 0.2 μl/0.2 μl p16S F/R, 0.2 μl pASA probe, 0.1 μl p16S probe and 7.5 μl ddH_2O. The amplification program was set as: (i) pre-incubation at 37°C for 2 min; (ii) 40 cycles of denaturation at 95°C for 30 s and annealing at 60°C for 30 s on an ABI QuantStudio 5 Real-Time PCR System. For primer sequence, see table S12.

Colitis induction and phenotypic evaluation

Male C57BL/6J, ΔCX3CR1, littermate control and Clod-Lip treated mice (6 to 8 weeks) were pretreated with AVNM in drinking water for 5 days and followed with one to four DSS course as described in figure legends. Five days of 2% DSS drinking water and 2 days regular drinking water consist of one DSS course. Those C57BL/6J mice received a gavage of 1×10^9 CFU MTB or 1×10^9 CFU Δaer MTB or 1×10^9 CFU Comp MTB or 100 μl PBS (control) for 3 consecutive days during the period of DSS treatment. For antibody treatment, mice were administered a single dose of 200 μg of anti-aerolysin polyclonal antibody or 200 μg IgG or 200 μg anti-aerolysin mAb (Clone 5) or 200 μl of PBS via injection i.p. 1 day before MTB administration, with one additional dose per DSS cycle (see figure legend for timeline). Male *Il10*$^{-/-}$ mice (6 to 8 weeks) were pretreated with AVNM in drinking water for 5 days, and received gavage of 1×10^9 CFU MTB or 100 μl PBS for consecutive three days on day 2 to day 4 of each week. Male GF C57BL/6J mice (6 to 8 weeks) were orally gavaged with 1×10^9 CFU of MTB (2A5) or PBS (100 μl) for 3 consecutive days at day 1 to day 3.

Six days after the last gavage, colitis was induced in those GF mice by administering 1.5% (w/v) DSS in the drinking water for 5 days, followed by 2 days of regular water. The body weight and DAI of the animals were recorded every day. DAI scores include the following: body weight loss (none = 0, <5% = 1, 5 to 10% = 2, 10 to 20% =3, >20% = 4), stool consistency (normal = 0, loose = 2, diarrhea = 4), bleeding (none = 0, occult blood = 2, gross bleeding = 4) (*69*). The pathological scores were calculated by the method include (*70*): inflammation severity score (0 = none, 1 = mild, 2 = moderate, 3 = severe); inflamed mucosa layer score (0 = none, 1 = mucosa, 2 = mucosa and submucosa, 3 = transmural); extent of epithelial/crypt damage (0 = none, 1 = basal 1/3, 2 = basal 2/3, 3 = crypt loss, 4 = crypt and surface epithelial destruction). Each variable score was multiplied by a factor reflecting the percentage of the colon involved (0.25 = 0 to 25%, 0.5 = 26 to 50%, 0.75 = 51 to 75%, 1.0 = 76 to 100%). The sum of those scores constituted the pathology score.

mRNA quantification by real-time PCR

For analyzing gene expression in colons, total RNAs of the colons were extracted with FastPure Complex Cell/Tissue Total RNA Isolation Kit (RC113-C1, Vazyme) and transcribed with HiScript III RT SuperMix (R323, Vazyme). The cDNA samples were subjected to a real-time qPCR assay including 5 μl Taq Pro Universal SYBR qPCR Master Mix (Q712-02, Vazyme) plus 4.6 μl of each oligonucleotide with 0.2 μl/0.2 μl forward and reverse primers sets (Genscript) (for primer, see table S12). The amplification program was set as: (i) pre-incubation at 95°C for 30 s; (ii) 40 cycles of denaturation at 95°C for 10 s and annealing at 60°C for 20 s on an ABI ViiA 7 Real-Time PCR System. Raw data were analyzed using the ΔCt method, with *gapdh* serving as the normalization control. Relative expression levels were calculated using the 2^-ΔCt formula and then normalized by the control. The result was represented as fold change.

Statistics

Data are presented as mean ± SEM. Significance between two groups was determined using the Shapiro-Wilk test to assess normality. For data satisfying the normality assumption, an unpaired Student's *t* test was applied. Otherwise, the Mann-Whitney U test was used. Significance of inflammatory cytokines, multiple immune cell population and two groups with different treatment were determined by two-way ANOVA. For comparisons among three or more groups, one-way ANOVA was used. Longitudinal data (body weight changes and disease activity index) were analyzed by ordinary two-way ANOVA. Fecal MTB abundance in human stool samples was compared using the Kruskal-Wallis test with Dunn's post hoc correction. For the statistical analysis of human colon sample protein abundance, multiple *t* tests with false discovery rate (FDR) correction using the two-stage step-up method of Benjamini, Krieger, and Yekutieli were performed. All analyses were performed in GraphPad Prism 8 (GraphPad Software). Significance thresholds are denoted in figure legends as follows: ns ($P > 0.05$), * ($P < 0.05$), ** ($P < 0.01$).

REFERENCES AND NOTES

1. S. C. Ng *et al.*, Worldwide incidence and prevalence of inflammatory bowel disease in the 21st century: A systematic review of population-based studies. *Lancet* **390**, 2769–2778 (2017). doi: 10.1016/S0140-6736(17)32448-0; pmid: 29050646
2. C. Le Berre, S. Honap, L. Peyrin-Biroulet, Ulcerative colitis. *Lancet* **402**, 571–584 (2023). doi: 10.1016/S0140-6736(23)00966-2; pmid: 37573077
3. K. T. Thia, E. V. Loftus Jr., W. J. Sandborn, S. K. Yang, An update on the epidemiology of inflammatory bowel disease in Asia. *Am. J. Gastroenterol.* **103**, 3167–3182 (2008). doi: 10.1111/j.1572-0241.2008.02158.x; pmid: 19086963
4. I. L. Monstad *et al.*, Outcome of Ulcerative Colitis 20 Years after Diagnosis in a Prospective Population-based Inception Cohort from South-Eastern Norway, the IBSEN Study. *J. Crohns Colitis* **15**, 969–979 (2021). doi: 10.1093/ecco-jcc/jjaa232; pmid: 33367569
5. T. Ochsenkühn, G. D'Haens, Current misunderstandings in the management of ulcerative colitis. *Gut* **60**, 1294–1299 (2011). doi: 10.1136/gut.2010.218180; pmid: 21504997
6. T. Kobayashi *et al.*, Ulcerative colitis. *Nat. Rev. Dis. Primers* **6**, 74 (2020). doi: 10.1038/s41572-020-0205-x; pmid: 32913180
7. K. M. Das, L. Biancone, Is IBD an autoimmune disorder? *Inflamm. Bowel Dis.* **14** (Suppl 2), S97–S101 (2008). doi: 10.1097/00054725-200810001-00049; pmid: 18816728
8. D. B. Graham, R. J. Xavier, Pathway paradigms revealed from the genetics of inflammatory bowel disease. *Nature* **578**, 527–539 (2020). doi: 10.1038/s41586-020-2025-2; pmid: 32103191
9. L. Jostins *et al.*, Host-microbe interactions have shaped the genetic architecture of inflammatory bowel disease. *Nature* **491**, 119–124 (2012). doi: 10.1038/nature11582; pmid: 23128233
10. J. Lloyd-Price *et al.*, Multi-omics of the gut microbial ecosystem in inflammatory bowel diseases. *Nature* **569**, 655–662 (2019). doi: 10.1038/s41586-019-1237-9; pmid: 31142855
11. R. Caruso, B. C. Lo, G. Núñez, Host-microbiota interactions in inflammatory bowel disease. *Nat. Rev. Immunol.* **20**, 411–426 (2020). doi: 10.1038/s41577-019-0268-7; pmid: 32005980
12. H. Sokol *et al.*, Fungal microbiota dysbiosis in IBD. *Gut* **66**, 1039–1048 (2017). doi: 10.1136/gutjnl-2015-310746; pmid: 26843508
13. D. C. Baumgart, W. J. Sandborn, Inflammatory bowel disease: Clinical aspects and established and evolving therapies. *Lancet* **369**, 1641–1657 (2007). doi: 10.1016/S0140-6736(07)60751-X; pmid: 17499606
14. R. J. Xavier, D. K. Podolsky, Unravelling the pathogenesis of inflammatory bowel disease. *Nature* **448**, 427–434 (2007). doi: 10.1038/nature06005; pmid: 17653185
15. J. R. Turner, Intestinal mucosal barrier function in health and disease. *Nat. Rev. Immunol.* **9**, 799–809 (2009). doi: 10.1038/nri2653; pmid: 19855405
16. I. Ordás, L. Eckmann, M. Talamini, D. C. Baumgart, W. J. Sandborn, Ulcerative colitis. *Lancet* **380**, 1606–1619 (2012). doi: 10.1016/S0140-6736(12)60150-0; pmid: 22914296
17. R. J. Porter, R. Kalla, G. T. Ho, Ulcerative colitis: Recent advances in the understanding of disease pathogenesis. *F1000 Res.* **9**, 294 (2020). doi: 10.12688/f1000research.20805.1; pmid: 32399194
18. J. C. Barrett *et al.*, Genome-wide association study of ulcerative colitis identifies three new susceptibility loci, including the HNF4A region. *Nat. Genet.* **41**, 1330–1334 (2009). doi: 10.1038/ng.483; pmid: 19915572
19. A. H. Gitter, F. Wullstein, M. Fromm, J. D. Schulzke, Epithelial barrier defects in ulcerative colitis: Characterization and quantification by electrophysiological imaging. *Gastroenterology* **121**, 1320–1328 (2001). doi: 10.1053/gast.2001.29694; pmid: 11729111
20. M. E. V. Johansson *et al.*, Bacteria penetrate the normally impenetrable inner colon mucus layer in both murine colitis models and patients with ulcerative colitis. *Gut* **63**, 281–291 (2014). doi: 10.1136/gutjnl-2012-303207; pmid: 23426893
21. J. Sheng, C. Ruedl, K. Karjalainen, Most Tissue-Resident Macrophages Except Microglia Are Derived from Fetal Hematopoietic Stem Cells. *Immunity* **43**, 382–393 (2015). doi: 10.1016/j.immuni.2015.07.016; pmid: 26287683
22. S. De Schepper *et al.*, Self-Maintaining Gut Macrophages Are Essential for Intestinal Homeostasis. *Cell* **175**, 400–415.e13 (2018). doi: 10.1016/j.cell.2018.07.048; pmid: 30173915
23. C. C. Bain *et al.*, Constant replenishment from circulating monocytes maintains the macrophage pool in the intestine of adult mice. *Nat. Immunol.* **15**, 929–937 (2014). doi: 10.1038/ni.2967; pmid: 25151491
24. J. H. Niess *et al.*, CX3CR1-mediated dendritic cell access to the intestinal lumen and bacterial clearance. *Science* **307**, 254–258 (2005). doi: 10.1126/science.1102901; pmid: 15653504
25. C. Varol, E. Zigmond, S. Jung, Securing the immune tightrope: Mononuclear phagocytes in the intestinal lamina propria. *Nat. Rev. Immunol.* **10**, 415–426 (2010). doi: 10.1038/nri2778; pmid: 20498668
26. O. Medina-Contreras *et al.*, CX3CR1 regulates intestinal macrophage homeostasis, bacterial translocation, and colitogenic Th17 responses in mice. *J. Clin. Invest.* **121**, 4787–4795 (2011). doi: 10.1172/JCI59150; pmid: 22045567
27. M. Honda *et al.*, Perivascular localization of macrophages in the intestinal mucosa is regulated by Nr4a1 and the microbiome. *Nat. Commun.* **11**, 1329 (2020). doi: 10.1038/s41467-020-15068-4; pmid: 32165624
28. P. A. Muller *et al.*, Crosstalk between muscularis macrophages and enteric neurons regulates gastrointestinal motility. *Cell* **158**, 300–313 (2014). doi: 10.1016/j.cell.2014.04.050; pmid: 25036630
29. I. Gabanyi *et al.*, Neuro-immune Interactions Drive Tissue Programming in Intestinal Macrophages. *Cell* **164**, 378–391 (2016). doi: 10.1016/j.cell.2015.12.023; pmid: 26777404
30. F. Matheis *et al.*, Adrenergic Signaling in Muscularis Macrophages Limits Infection-Induced Neuronal Loss. *Cell* **180**, 64–78.e16 (2020). doi: 10.1016/j.cell.2019.12.002; pmid: 31923400
31. A. S. Chikina *et al.*, Macrophages Maintain Epithelium Integrity by Limiting Fungal Product Absorption. *Cell* **183**, 411–428.e16 (2020). doi: 10.1016/j.cell.2020.08.048; pmid: 32970988
32. S. D. Fritsch *et al.*, Metabolic support by macrophages sustains colonic epithelial homeostasis. *Cell Metab.* **35**, 1931–1943.e8 (2023). doi: 10.1016/j.cmet.2023.09.010; pmid: 37804836

33. I. Leonardi *et al.*, CX3CR1^{+} mononuclear phagocytes control immunity to intestinal fungi. *Science* **359**, 232–236 (2018). doi: 10.1126/science.aao1503; pmid: 29326275
34. A. Lacy-Hulbert *et al.*, Ulcerative colitis and autoimmunity induced by loss of myeloid alphav integrins. *Proc. Natl. Acad. Sci. U.S.A.* **104**, 15823–15828 (2007). doi: 10.1073/pnas.0707421104; pmid: 17895374
35. A. Dignass *et al.*, Second European evidence-based consensus on the diagnosis and management of ulcerative colitis part 1: Definitions and diagnosis. *J. Crohns Colitis* **6**, 965–990 (2012). doi: 10.1016/j.crohns.2012.09.003; pmid: 23040452
36. A. Kornbluth, D. B. Sachar, Practice Parameters Committee of the American College of Gastroenterology, Ulcerative colitis practice guidelines in adults: American College Of Gastroenterology, Practice Parameters Committee. *Am. J. Gastroenterol.* **105**, 501–523 (2010). doi: 10.1038/ajg.2009.727; pmid: 20068560
37. J. Sheng *et al.*, Topological analysis of hepatocellular carcinoma tumour microenvironment based on imaging mass cytometry reveals cellular neighbourhood regulated reversely by macrophages with different ontogeny. *Gut* **71**, 1176–1191 (2022). doi: 10.1136/gutjnl-2021-324339; pmid: 34253573
38. D. Bernardo *et al.*, Human intestinal pro-inflammatory CD11c^{high}CCR2^{+}CX3CR1^{+} macrophages, but not their tolerogenic CD11c^{-}CCR2^{-}CX3CR1^{-} counterparts, are expanded in inflammatory bowel disease. *Mucosal Immunol.* **11**, 1114–1126 (2018). doi: 10.1038/s41385-018-0030-7; pmid: 29743615
39. D. Domanska *et al.*, Single-cell transcriptomic analysis of human colonic macrophages reveals niche-specific subsets. *J. Exp. Med.* **219**, e20211846 (2022). doi: 10.1084/jem.20211846; pmid: 35139155
40. L. Chapuy *et al.*, Two distinct colonic CD14^{+} subsets characterized by single-cell RNA profiling in Crohn's disease. *Mucosal Immunol.* **12**, 703–719 (2019). doi: 10.1038/s41385-018-0126-0; pmid: 30670762
41. F. Ginhoux, S. Jung, Monocytes and macrophages: Developmental pathways and tissue homeostasis. *Nat. Rev. Immunol.* **14**, 392–404 (2014). doi: 10.1038/nri3671; pmid: 24854589
42. C. S. Smillie *et al.*, Intra- and Inter-cellular Rewiring of the Human Colon during Ulcerative Colitis. *Cell* **178**, 714–730.e22 (2019). doi: 10.1016/j.cell.2019.06.029; pmid: 31348891
43. V. Mitsialis *et al.*, , Single-Cell Analyses of Colon and Blood Reveal Distinct Immune Cell Signatures of Ulcerative Colitis and Crohn's Disease. *Gastroenterology* **159**, 591–608.e10 (2020). doi: 10.1053/j.gastro.2020.04.074; pmid: 32428507
44. C. C. Bain *et al.*, Resident and pro-inflammatory macrophages in the colon represent alternative context-dependent fates of the same Ly6Chi monocyte precursors. *Mucosal Immunol.* **6**, 498–510 (2013). doi: 10.1038/mi.2012.89; pmid: 22990622
45. E. Zigmond *et al.*, Ly6C hi monocytes in the inflamed colon give rise to proinflammatory effector cells and migratory antigen-presenting cells. *Immunity* **37**, 1076–1090 (2012). doi: 10.1016/j.immuni.2012.08.026; pmid: 23219392
46. M. T. Degiacomi *et al.*, Molecular assembly of the aerolysin pore reveals a swirling membrane-insertion mechanism. *Nat. Chem. Biol.* **9**, 623–629 (2013). doi: 10.1038/nchembio.1312; pmid: 23912165
47. J. Qie *et al.*, Integrated proteomic and transcriptomic landscape of macrophages in mouse tissues. *Nat. Commun.* **13**, 7389 (2022). doi: 10.1038/s41467-022-35095-7; pmid: 36450731
48. G. Wang *et al.*, Detection and characterization of the hemolysin genes in Aeromonas hydrophila and Aeromonas sobria by multiplex PCR. *J. Clin. Microbiol.* **41**, 1048–1054 (2003). doi: 10.1128/JCM.41.3.1048-1054.2003; pmid: 12624028
49. A. S. Faye *et al.*, Antibiotic use as a risk factor for inflammatory bowel disease across the ages: A population-based cohort study. *Gut* **72**, 663–670 (2023). doi: 10.1136/gutjnl-2022-327845; pmid: 36623926
50. J. Zhang *et al.*, Elucidation of Proteus mirabilis as a Key Bacterium in Crohn's Disease Inflammation. *Gastroenterology* **160**, 317–330.e11 (2021). doi: 10.1053/j.gastro.2020.09.036; pmid: 33011176
51. K. Kawashima *et al.*, Evaluation of the relationship between the spleen volume and the disease activity in ulcerative colitis and Crohn disease. *Medicine* **101**, e28515 (2022). doi: 10.1097/MD.0000000000028515; pmid: 35029912
52. A. Khashper, D. Shwartz, B. H. Taragin, T. Shalmon, Splenic size as a marker for active inflammation in Crohn's disease. *Clin. Imaging* **84**, 164–167 (2022). doi: 10.1016/j.clinimag.2022.02.012; pmid: 35228021
53. M. F. Neurath, Cytokines in inflammatory bowel disease. *Nat. Rev. Immunol.* **14**, 329–342 (2014). doi: 10.1038/nri3661; pmid: 24751956
54. D. Liu, "Aeromonas" in *Molecular Medical Microbiology, Volume 1, Second Edition*, Y.-W. Tang, M. Sussman, D. Liu, I. Poxton, J. Schwartzman, Eds. (Academic Press, Boston, 2015), pp. 1099–1110.
55. W. S. Garrett *et al.*, Enterobacteriaceae act in concert with the gut microbiota to induce spontaneous and maternally transmitted colitis. *Cell Host Microbe* **8**, 292–300 (2010). doi: 10.1016/j.chom.2010.08.004; pmid: 20833380
56. A. Gilliland, J. J. Chan, T. J. De Wolfe, H. Yang, B. A. Vallance, Pathobionts in Inflammatory Bowel Disease: Origins, Underlying Mechanisms, and Implications for Clinical Care. *Gastroenterology* **166**, 44–58 (2024). doi: 10.1053/j.gastro.2023.09.019; pmid: 37734419
57. A. von Graevenitz, The role of Aeromonas in diarrhea: A review. *Infection* **35**, 59–64 (2007). doi: 10.1007/s15010-007-6243-4; pmid: 17401708
58. A. Fernández-Bravo, M. J. Figueras, An Update on the Genus *Aeromonas*: Taxonomy, Epidemiology, and Pathogenicity. *Microorganisms* **8**, 129 (2020). doi: 10.3390/microorganisms8010129; pmid: 31963469
59. T. Lobatón *et al.*, *Aeromonas* species: An opportunistic enteropathogen in patients with inflammatory bowel diseases? A single center cohort study. *Inflamm. Bowel Dis.* **21**, 71–78 (2015). doi: 10.1097/MIB.0000000000000247; pmid: 25517595
60. J. L. Parker, J. G. Shaw, Aeromonas spp. clinical microbiology and disease. *J. Infect.* **62**, 109–118 (2011). doi: 10.1016/j.jinf.2010.12.003; pmid: 21163298
61. J. M. Willoughby, A. F. Rahman, M. M. Gregory, Chronic colitis after Aeromonas infection. *Gut* **30**, 686–690 (1989). doi: 10.1136/gut.30.5.686; pmid: 2731763
62. C. Baliellas Comellas, X. Xiol Quingles, J. Castellote Alonso, J. Torras Torra, [Severe occurrence of idiopathic ulcerative colitis caused by Aeromonas sobria]. *Rev. Esp. Enferm. Dig.* **79**, 442–443 (1991). doi: 10.1111/1751-2980.12994; pmid: 1910924
63. Inflammatory Bowel Disease Group, Chinese Society of Gastroenterology, Chinese Medical Association, Chinese consensus on diagnosis and treatment in inflammatory bowel disease (2018, Beijing). *J. Dig. Dis.* **22**, 298–317 (2021). pmid: 33905603
64. J. Du *et al.*, Selective oxidative protection leads to tissue topological changes orchestrated by macrophage during ulcerative colitis. *Nat. Commun.* **14**, 3675 (2023). doi: 10.1038/s41467-023-39173-2; pmid: 37344477
65. K. Benmeziane *et al.*, Isolation and phenotypic characterization of human and nonhuman primate intestinal lamina propria mononuclear cells. *STAR Protoc.* **3**, 101815 (2022). doi: 10.1016/j.xpro.2022.101815; pmid: 36595919
66. A. Bateman *et al.*, UniProt: The universal protein knowledgebase in 2021. *Nucleic Acids Res.* **49**, D480–D489 (2021). doi: 10.1093/nar/gkaa1100; pmid: 33237286
67. X. Chen *et al.*, A Shigella species variant is causally linked to intractable functional constipation. *J. Clin. Invest.* **132**, e150097 (2022). doi: 10.1172/JCI150097; pmid: 35617029
68. X. Zhang, R. Goncalves, D. M. Mosser, The isolation and characterization of murine macrophages. *Curr. Protoc. Immunol.* **83**, 14.1.1–14.1.14 (2008). doi: 10.1002/0471142735.im1401s83; pmid: 19016445
69. S. Wirtz *et al.*, Chemically induced mouse models of acute and chronic intestinal inflammation. *Nat. Protoc.* **12**, 1295–1309 (2017). doi: 10.1038/nprot.2017.044; pmid: 28569761
70. S. U. Seo *et al.*, Distinct Commensals Induce Interleukin-1β via NLRP3 Inflammasome in Inflammatory Monocytes to Promote Intestinal Inflammation in Response to Injury. *Immunity* **42**, 744–755 (2015). doi: 10.1016/j.immuni.2015.03.004; pmid: 25862092

ACKNOWLEDGMENTS

We thank all staff members of the State Key Laboratory of Pharmaceutical Biotechnology and Medical School of Nanjing University for invaluable discussions and comments. We thank all staff members of Jinling Hospital and Children's Hospital for their assistance in collection of biopsies and stools samples. **Funding:** This work was supported by the National Natural Science Foundation of China (NSFC) [Grant nos. 82250003 (M.Z.), 32071121 (M.Z.), and 82192862 (X.G., M.Z.)] and Fundamental Research Funds for the Central Universities 2021300242 (M.Z.). **Author contributions:** Conceptualization: M.Z., Z.J., Y.W., J.G., F.W.; Methodology: M.Z., Z.J., Y.W., J.G., X.Z., W.H., Z.G., H.C.; Investigation: Z.J., Y.W., J.G., K.Q., Y.L., P.L., C.C., X.C.; Visualization: Z.J., Y.W., Ju.Z., Y.L.; Validation: Ju.Z., Y.L., P.L., K.Q., H.W., Z.Y., T.Q., Y.Z., Z.C., X.S., N.Z., L.L.; Resources: M.Z., J.G., X.C., F.W., D.H., X.H., H.Z., J.X., F.F., F.S., H.M., Z.L.; Funding acquisition: M.Z., X.G.; Project administration: M.Z., Z.J., Y.W., J.G., F.W., L.F., X.G., X.Z.; Supervision: M.Z., J.G., F.W., X.Z., Ji.Z., H.C.; Writing – original draft: M.Z., Z.J., Y.W.; Writing – review & editing: M.Z., Z.J., Ji.Z., Y.W., F.W., X.Z. **Competing interests:** M.Z., Z.J., and X.Z. are inventors on the patent application (CN 202411359211.4, PCT/CN2025/116530) submitted by Nanjing NysBio Biotechnology that covers MTB and its virulence factor aerolysin as a diagnostic and therapeutic target for UC. The other authors declare that they have no competing interests. **Data and materials availability:** All data needed to evaluate the conclusions in the paper are available in the main text or the supplementary materials. The mass spectrometry proteomics data have been deposited to the ProteomeXchange Consortium with the dataset identifier PXD050471. The 16S rRNA sequence and the genomic sequence of MTB strain reported in this paper have been submitted to GenBank, under BioProject accession no. PRJNA1083721. The nucleotide sequence of UC aerolysin reported in this paper has been deposited to GenBank, under accession nos. BankIt 2804612 (PP460999 to PP461003). **License information:** Copyright © 2025 the authors, some rights reserved; exclusive licensee American Association for the Advancement of Science. No claim to original US government works. https://www.science.org/about/science-licenses-journal-article-reuse

SUPPLEMENTARY MATERIALS

science.org/doi/10.1126/science.adz4712
Figs. S1 to S22; Tables S1 to S12; MDAR Reproducibility Checklist

Submitted 3 June 2025; accepted 12 September 2025

10.1126/science.adz4712

RESEARCH ARTICLE SUMMARY

VOLCANOLOGY

The 2025 Santorini unrest unveiled: Rebounding magmatic dike intrusion with triggered seismicity

Anthony Lomax*, Vasilis Anagnostou, Vasileios Karakostas, Stephen P. Hicks, Eleftheria Papadimitriou

Full article and list of author affiliations: https://doi.org/10.1126/science.adz8538

INTRODUCTION: In early 2025, between the islands of Santorini and Amorgos in the Aegean Sea, intense swarm seismicity alarmed the local population, resulting in school closures and disruptions to tourism. Santorini poses a substantial hazard because it is an active stratovolcano and hosted one of the largest known historical eruptions, the massive and devastating Minoan eruption of ~1620 BCE. The swarm seismicity also occurred just southwest of the destructive moment magnitude (M_w) 7.7 Amorgos earthquake rupture of 1956. Whether the 2025 unrest was caused by a magmatic dike intrusion or tectonic fault slip remains controversial. Imaging and explaining this unrest are therefore essential for basic scientific understanding, public information, hazard assessment, and eruption forecasting.

RATIONALE: Magmatic intrusion in Earth can lead to hazardous volcanic eruptions, but the kinematic and dynamic processes involved remain largely hidden from direct observation. Space-time imaging and modeling of the geometry, emplacement, and internal magma flow of dikes, which are essential to understanding volcanic systems and forecasting eruptions and associated earthquakes, rely on seismological and geodetic measures at Earth's surface, resulting in loss of resolution and constraint of dike activity at depth. To overcome these difficulties, we investigated the cause of the 2025 Santorini-Amorgos unrest using precise, machine learning–derived seismicity (~25,000 earthquakes) as virtual, at-depth measures of Coulomb stress change surrounding possible intrusive and fault slip sources.

RESULTS: Our relocated seismicity reveals intense and complex activity extending up to 50 km northeast of Santorini and more than 15 km in depth. Before mid-January 2025, seismicity was sparse and mainly confined to Santorini's caldera, simultaneous with surface uplift and inferred magmatic inflation under the caldera since mid-2024. From 26 January, dense, swarm-like seismicity developed ~20 km northeast of Santorini, followed by rapid expansion of activity to the northeast between 3 and 6 February. Intense, migrating swarm seismicity between 6 and 19 February extended more than 30 km further to the northeast, widening in a fan-shaped cloud. Using this seismicity as a virtual measure for Coulomb stress change imaging, we demonstrated that the source of the unrest was horizontal magmatic dike propagation and not tectonic fault slip. We imaged, in detail, the space-time evolution of the dike along a ~30-km swath as multiscale rebounding waves of dike opening, magma pressure, and breaking of barriers, together with triggered seismicity.

CONCLUSION: Our relocated seismicity and stress imaging resolve a more complex, rebounding feedback mechanism for dike emplacement than previously recognized, advancing understanding of dike physics and volcanic-tectonic-seismogenic feedback mechanisms. The exemplary time and space resolution of Coulomb-seismicity-stress imaging offers a foundation for advancing the physics-based modeling of dikes and for driving machine learning–based, data-driven procedures for tracking intrusions and forecasting eruptions in near real time. □

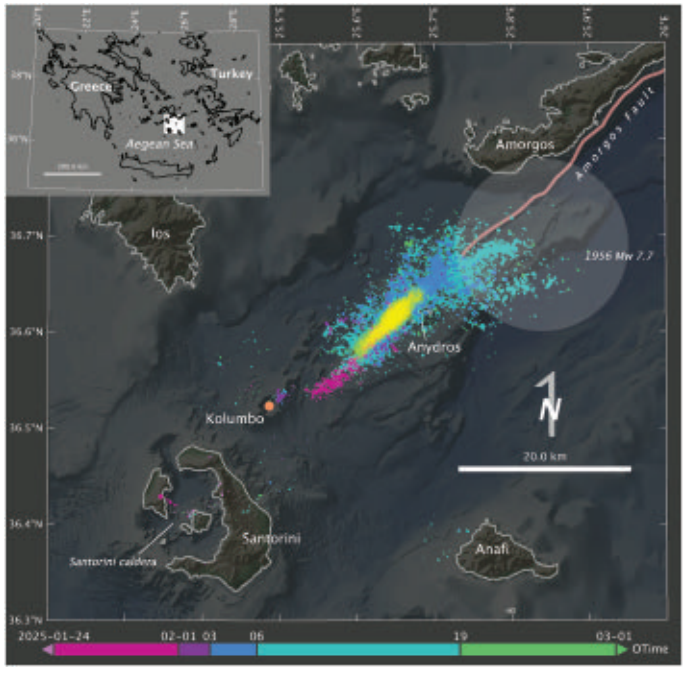

Seismicity and imaged dike. Machine learning–relocated seismicity for 1 January to 28 February 2025, with symbol size proportional to magnitude and color-coded according to occurrence time (OTime). The yellow patch shows the magmatic dike imaged using the seismicity as virtual measures of stress change due to dike opening. The large gray disk shows the epicentral area of the M_w 7.7 Amorgos earthquake of 1956. The inset shows the location of the study area (white filled rectangle) in the Aegean Sea.

*Corresponding author. Email: anthony@alomax.net Cite this article as A. Lomax *et al.*, *Science* **390**, eadz8538 (2025). DOI: 10.1126/science.adz8538

CREDIT: TOPOGRAPHIC AND BATHYMETRIC BASEMAPS WERE MADE WITH GEOMAPAPP (WWW.GEOMAPAPP.ORG) CC BY FROM W. B. F. RYAN *ET AL. GEOCHEM. GEOPHYS. GEOSYST.* **10**, 2008GC002332 (2009)

VOLCANOLOGY

The 2025 Santorini unrest unveiled: Rebounding magmatic dike intrusion with triggered seismicity

Anthony Lomax[1]*, Vasilis Anagnostou[2], Vasileios Karakostas[2], Stephen P. Hicks[3], Eleftheria Papadimitriou[2]

Magmatic intrusion in Earth's crust can lead to hazardous volcanic eruptions, but the physical processes involved remain largely hidden from direct observation. We used machine learning–derived seismicity as virtual stress meters at depth to study the disruptive 2025 seismogeodetic unrest in Greece between the Santorini volcano and the epicenter of the devastating moment magnitude 7.7 Amorgos earthquake that occurred in 1956. We show that the cause of unrest was magmatic dike propagation, which we imaged with ~25,000 relocated earthquakes occurring over 2 months. The dike propagated horizontally ~30 kilometers as multiscale rebounding waves of dike opening, magma pressure, and breaking of barriers while triggering intense surrounding seismicity. Our results establish magmatic intrusion as a more complex feedback process than previously recognized and can facilitate physics-based and data-driven modeling and eruption forecasting.

In early 2025, between the islands of Santorini and Amorgos in the Aegean Sea, intense swarm seismicity, including numerous moment magnitude (M_w) ~5 earthquakes (*1*) (Fig. 1), alarmed the local population, resulting in school closures and the departure of tourists (*2*). Santorini poses a substantial hazard because it is an active stratovolcano and hosted one of the largest known historical eruptions, the massive and devastating Minoan eruption of ~1620 BCE (*3*). The underlying causative source of the 2025 unrest remains controversial but is generally attributed to magmatic dike intrusion or fluid-driven tectonic fault slip (*4*–*7*). Imaging and explaining this source are essential for basic scientific understanding, public information, hazard assessment, and eruption forecasting.

Dikes are subvertical, magma-filled fractures in Earth and are the principal means for crustal extension and the transport and eruption of magma in volcanic settings (*8*, *9*). Dikes form within brittle and ductile rock volumes, typically at a few to tens of kilometers in depth, in a complex process of opening due to interplay between magma overpressure (excess of magma pressure over host-rock normal stress), magma flow and buoyancy, host-rock deformation, preexisting fractures, breaking of barriers, and numerous other phenomena (*10*–*13*).

Space-time imaging and modeling of the geometry, emplacement, and internal magma flow of dikes, which are essential to understanding volcanic systems and forecasting eruptions and associated earthquakes, rely on seismological and geodetic measures at Earth's surface, resulting in loss of resolution and constraint of dike activity at depth (*14*–*16*). Geodetic measures can constrain the shallowest dike activity well, but deeper or complex activity may be masked or subject to large trade-offs [(*12*, *17*–*19*) and figure S16 in (*15*)]. Dike geometry and kinematics are often inferred from relocated seismicity, which can maintain high precision at depth (*20*). However, the spatiotemporal relationships of seismicity to dike geometry and opening remain unclear. Brittle fracture is unlikely within magma, and seismicity may occur far from a dike where the host rock supports fracture and there is congruence between existing fracture orientations, preexisting stress, and dike-induced stress change (*8*, *21*). To overcome these difficulties, we investigated the cause of the 2025 Santorini-Amorgos unrest using precisely located seismicity as virtual measures at depth of the stress change surrounding causative intrusive (tensile opening) and fault (shear) sources (*22*).

Santorini is an active stratovolcano in the Christiana-Santorini-Kolumbo segment of the Hellenic volcanic arc, which developed as a result of the ongoing subduction of the eastern Mediterranean oceanic lithosphere beneath the Aegean microplate (*23*). Santorini (Fig. 1) features a main caldera, which collapsed in the ~1620 BCE eruption (*3*), and several smaller craters, which last erupted in 1950 (*24*). A satellite, submarine polygenic volcano, Kolumbo, lies ~8 km northeast (NE) of Santorini island and was the source of a deadly tsunamigenic eruption in 1650 (*25*). Substantial hazard is also posed by major tectonic earthquakes in the region. The Santorini-Amorgos area hosted the largest earthquake in Greece during the 20th century, the moment magnitude (M_w) 7.7 Amorgos earthquake in 1956, which caused scores of fatalities, a large tsunami, and extensive destruction across the southern Aegean Sea (*26*). The earthquake had a normal faulting mechanism, rupturing the northeast-striking Amorgos fault, which lies parallel to the southern coastline of Amorgos (*27*, *28*) and just NE of the 2025 swarm (Fig. 1).

Recent relocated seismicity in the Santorini-Amorgos area shows low-rate crustal activity in the decades before 2011, except for a prominent cluster at Kolumbo and a smaller cluster near Anydros in 2003, both aligned southwest (SW)–NE, along with almost no seismicity observed inside the Santorini caldera (*29*). In February 2011, intense strike-slip microseismicity inside the caldera and uplift of the volcanic edifice started and lasted ~1 year (*30*, *31*). Normal faulting seismicity expanded in January 2012 to the NE offshore area, near Anydros islet, within the area of the 2025 swarm. Between 2012 and 2024, seismicity inside Santorini's caldera was quiescent, whereas Kolumbo hosted almost continuous, shallow seismicity (*31*, *32*). The 2025 swarm was preceded, from mid-2024, by increasing seismicity along with slow surface uplift and displacement attributed to magma-related inflation under the Santorini caldera (*6*, *7*, *33*). The seismicity intensified after mid-January 2025, expanding, within days, more than 50 km offshore to the NE of Santorini, with notable variations in rate, density, and complexity.

We investigated the nature, detailed geometry, and evolution of the source of the 2025 Santorini-Amorgos unrest primarily using high-precision, machine learning (ML)–derived seismicity because geodetic observations are sparse in this mainly submarine area. We performed ML earthquake detection and seismic phase picking (*34*) and associated the phase picks (*35*) into earthquake events (see materials and methods). From the ML event picks, we obtained multiscale high-precision earthquake relocations with the NLL-SSST-coherence (NLL-SC) methodology, which uses iterative, probabilistic optimization, and similarity of seismogram waveforms to correct for unknown, three-dimensional (3D) Earth structure and improve relative event positions (*36*, *37*) (see materials and methods).

We then applied the high-precision, NLL-SC relocated seismicity within a new, Coulomb-based seismicity-stress (CoulSeS) procedure for imaging elastic dislocation sources in three dimensions (*22*), in which the seismicity acts as virtual observations of stress change at depth (*38*). Under the Coulomb failure criterion (*39*, *40*), fault slip is triggered when shear stress on a fault plane exceeds the sum of cohesion and frictional resistance, assumed to be proportional to normal stress. The triggering of seismicity on specified receiver faults is favored within the positive lobes of the 3D spatial distribution of change in Coulomb failure stress (ΔCFS) and inhibited in the negative ΔCFS lobes (*41*–*46*). CoulSeS reverses this triggering rule to image extended fault slip or dike tensile opening from the distribution of triggered seismicity (*22*). For specified

[1]ALomax Scientific, Mouans-Sartoux, France. [2]Geophysics Department, Aristotle University of Thessaloniki, Thessaloniki, Greece. [3]Department of Earth Sciences, University College London, London, UK. *Corresponding author. Email: anthony@alomax.net

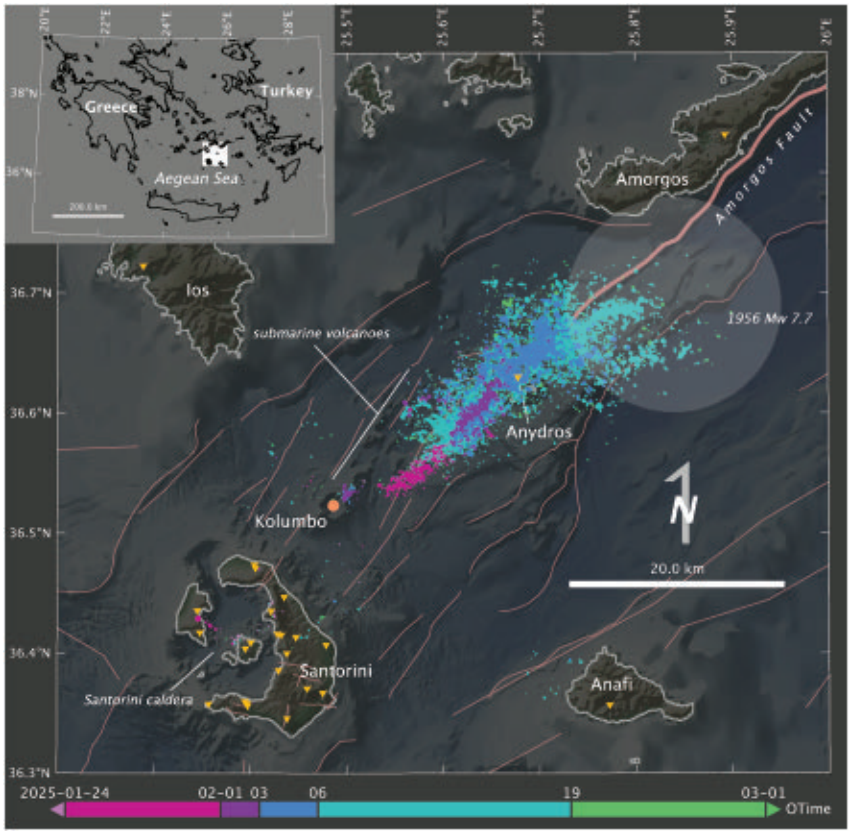

Fig. 1. Santorini-Amorgos study area and ML-derived, NLL-SC relocated 2025 swarm seismicity. Dots show relocated seismicity from 1 January through 28 February for ~25,000 events with hypocenter uncertainty ellipsoid semimajor axis length ≤4 km, with symbol size proportional to moment magnitude (M_w 0.2 to 5.3) and color-coded according to occurrence time (OTime). Yellow triangles show seismic stations used for ML picking and NLL-SC (*36*) relocation. The orange disk marks the submarine Kolumbo volcano. Light red lines show mapped surface faults (*49*), with the thicker line indicating the segment of the Amorgos fault that likely ruptured in the M_w 7.7 earthquake of 1956 (*27*); the large gray disk bounds epicenter estimates (*27*,*51*) for the 1956 mainshock. The inset shows the location of the study area (white filled rectangle) in the Aegean Sea. Topographic and bathymetric basemaps were made with GeoMapApp (www.geomapapp.org) CC BY (65).

target sources and receivers, correlation of a point-source ΔCFS kernel field across the spatial distribution of observed seismicity provides an extended, 3D source image that explains, under the physics of the Coulomb failure stress criterion, the distribution of seismicity. This method has been tested and verified against finite-fault models for large earthquakes (*22*).

With the high-precision seismicity and CoulSeS imaging, we determined that the source of the 2025 unrest was a dike intrusion. Through detailed imaging and analysis of the 3D geometry and temporal evolution of dike emplacement, we found a complex, rebounding feedback mechanism for dike intrusion that has implications for physics-based and data-driven modeling and eruption forecasting.

High-precision, ML-derived seismicity

Our high-precision, ML-derived, NLL-SC relocated seismicity for the 2025 swarm recovered ~34,000 seismic events from 1 January through 28 February 2025, with a magnitude of completeness of M_w ~2.0 (see materials and methods). Moment tensors for 138 M_w >4 earthquakes show mostly pure normal faulting on SW-NE striking, moderately dipping planes, with a few oblique-slip and pure strike-slip events (figs. S1 and S2).

The relocated seismicity indicates intense and complex activity up to 50 km NE of Santorini from near the surface to a depth of almost 20 km (Figs. 1 to 3 and movies S1 and S2). Before mid-January 2025, there was sparse, shallow seismic activity, mainly within the Santorini caldera, simultaneous with the slow surface uplift and inflation that had occurred beneath the caldera since mid-2024 (*6*). From 26 January, a dense patch of swarm-like seismicity developed about 20 km NE of Santorini and 10 km NE of Kolumbo at a depth of around 10 km. On 1 February, more dispersed seismicity occurred around this patch and near Kolumbo, followed by rapid expansion of activity to the NE between 3 and 6 February. The most intense swarm seismicity occurred between 6 and 19 February, extending over 30 km to the NE beyond the Anydros islet, to form a >15-km-wide fan-shaped cloud.

The 2025 swarm seismicity was highly productive, with 48 earthquakes of M_w ≥4.5 but no distinct mainshocks, and exhibited marked complexity, variation in rate, and migration of clusters over multiple space-time scales (Fig. 2). At certain times, waveforms from nearby stations show high-rate, tremor-like bursts of overlapping seismicity lasting several hours (fig. S3). We detected and located these bursts using windowed network covariance matrices, correlation analysis, and back-projection (see materials and methods). More than 10 occurrences of these tremor-like bursts are evidenced in Fig. 2C as periods of low spectral width in the network covariance matrix.

Coulomb seismicity-stress imaging of the swarm

We performed CoulSeS imaging of the 2025 seismicity to determine and map the underlying cause of the activity. As receiver faults, we used both conjugate planes for pure normal faulting with strike N45°E and dip 45°, representing the predominant mechanism from our and other (*4*, *7*, *47*) moment tensor datasets and compatible with the northwest (NW)–southeast (SE) extensional regional stress controlling nearby faults (*48*).

We first tested whether the swarm seismicity could be due to ΔCFS stress change from extended, normal-faulting sources compatible with regional tectonics and large earthquakes in the area (*48*–*50*) using a representative mechanism (*51*) for the M_w 7.7 Amorgos earthquake of 1956 (strike N36°E, dip 65°SE, rake −102°). CoulSeS imaging over the entire swarm using this point-source ΔCFS kernel (fig. S5) shows broad lobes separated from and extending far to the NW and SE of swarm seismicity and highly oblique to the SE dip of the target normal-faulting source. In general, CoulSeS imaging best confirms a given source when the maximum source potential is (i) within the seismicity distribution in areas of low seismicity and (ii) flattened and extended parallel to the tested source orientation. Thus, our CoulSeS results reject normal faulting compatible with regional tectonics as the cause of swarm seismicity.

We next tested whether the swarm seismicity could be due to ΔCFS from extended sources corresponding to tensile opening across horizontal planes (sills) or vertical planes (dikes). The 3D CoulSeS imaging over the swarm seismicity using a horizontal tensile point-source ΔCFS kernel (fig. S6) also shows broad lobes detached from and extending far to the NW and SE, above and below the seismicity. This seismicity-disconnected response rejects tensile opening across horizontal planes as a cause of the swarm.

To test tensile opening across a vertical plane, we used a strike of N45°E, matching the trend of swarm seismicity and the strike of mapped faults and seismic sources in the area (*48*, *49*). The 3D CoulSeS imaging over the seismicity using this point-source ΔCFS kernel (Fig. 3) shows an elongated volume of highest source potential (yellow) that is mainly below and partly surrounded by the seismicity, abuts the highest-density seismicity, is aligned parallel to the trend of the swarm, and is focused on a vertical plane. All of these characteristics are compatible with and support vertical dike intrusion as the stress source that triggered the swarm seismicity.

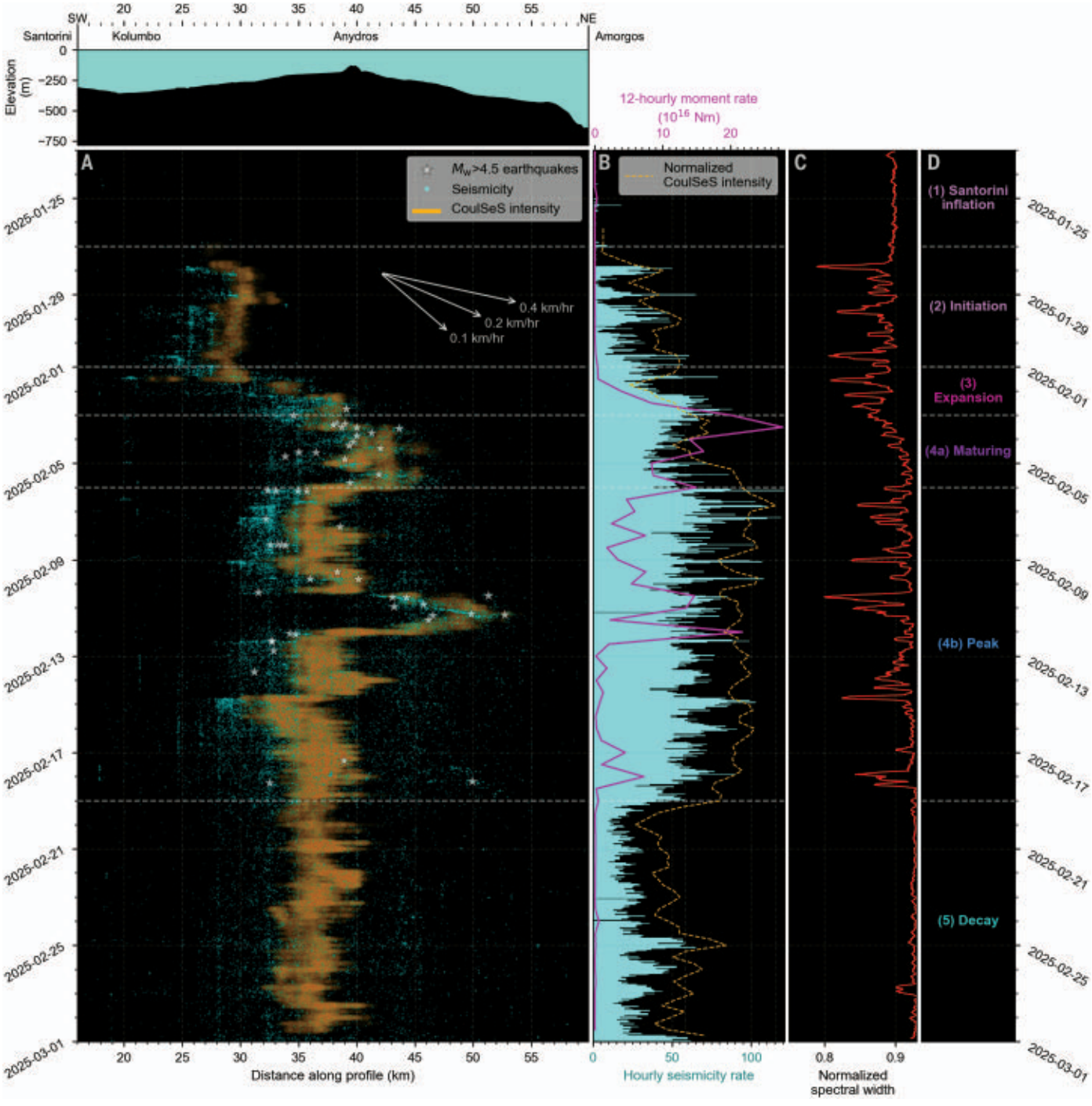

Fig. 2. Temporal and spatial evolution of the Santorini seismic swarm and the resulting CoulSeS imaging. Distances are along the SW-NE profile shown in Fig. 3, with the top-left panel indicating bathymetry and topography along the profile. (**A**) Time-space evolution of seismicity (cyan dots, all ~34,000 relocated events; white stars indicate events of $M_w \geq 4.5$) and high-potential areas of the 3D CoulSeS imaging of relative dike opening in 12-hour windows (dark yellow; normalized correlation ≥0.8). More detailed timelines of seismicity and CoulSeS imaging are shown in fig. S4. (**B**) Seismicity rate, 12-hour seismic moment release rate, and CoulSeS imaging intensity. (**C**) Spectral width of the network covariance matrix. (**D**) Interpretation of the main stages of dike intrusion, as described in the text.

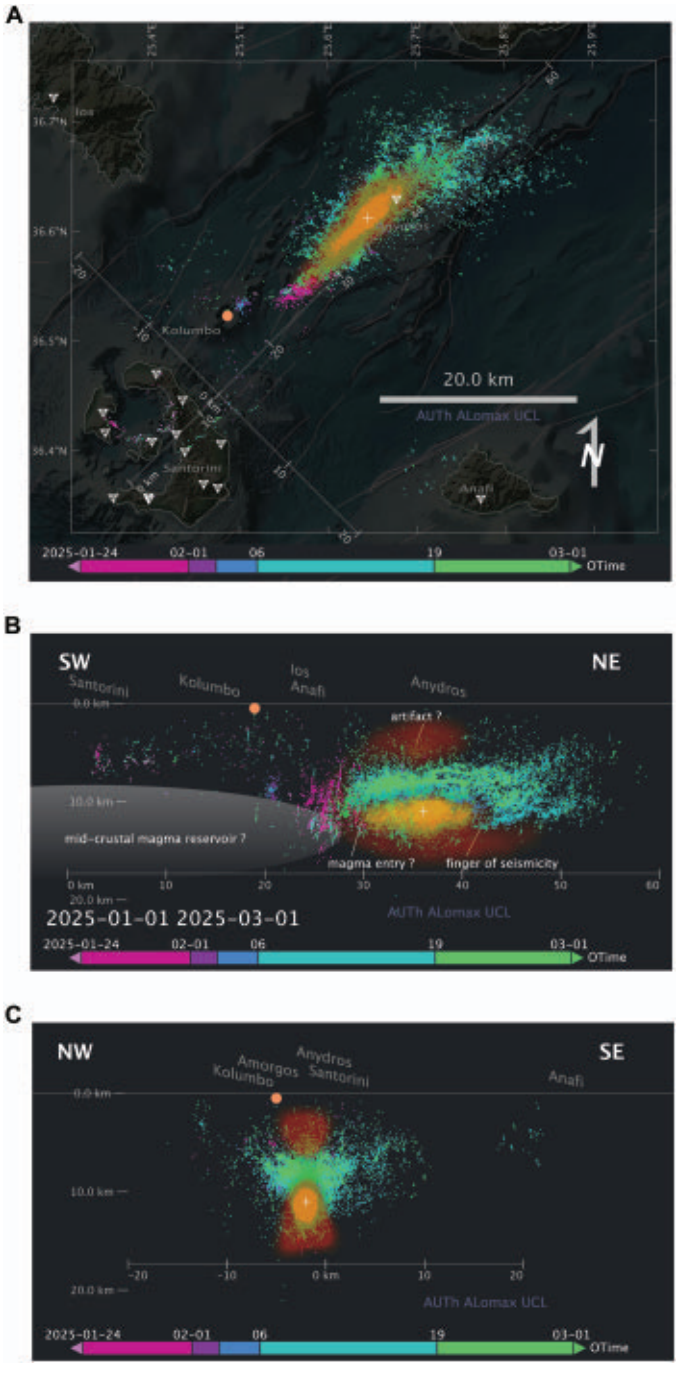

Fig. 3. CoulSeS imaging of the 2025 Santorini-Amorgos swarm seismicity for vertical tensile-opening sources striking N45°E. Projections of the high-potential volumes of the 3D CoulSeS finite-source fields for relative dike opening (yellow-orange and red show normalized correlations ≥0.8 and ≥0.7, respectively; white plus sign shows peak CoulSeS intensity) are shown in (**A**) map view with SW-NE and NW-SE distance scales, (**B**) profile view from the SE with SW-NE distance scale, and (**C**) profile view from the SW with NW-SE distance scale. The CoulSeS-imaged main dike opening falls within the yellow-orange volume. Dots show the projected NLL-SC relocated swarm seismicity from 1 January through 28 February used for imaging (~25,000 events with hypocenter uncertainty ellipsoid semimajor axis length ≤4 km), color-coded according to occurrence time (OTime). White triangles show seismic stations used for ML picking and NLL-SC relocation. Light red lines in (A) show mapped surface faults (*49*). The gray ellipse in (B) shows the inferred mid-crustal magma reservoir under Santorini and Kolumbo. Topographic and bathymetric basemaps were made with GeoMapApp (www.geomapapp.org) CC BY (*65*).

Dike geometry and evolution

Having established a dike intrusion as the causative source for the 2025 Santorini-Amorgos activity, we examined in detail the 3D geometry and evolution of the dike using CoulSeS imaging for the vertical tensile source over the full study period (Figs. 2 and 3 and movie S2) and for sets of sliding time windows (Fig. 4, fig. S7, and movie S1). This CoulSeS imaging defines a 3D envelope or brightness function of potential, relative dike opening and magma overpressure over space and time; any planar, vertical surfaces within this envelope can represent the dike geometry.

The 2025 seismicity was likely triggered by the lateral propagation of magmatic fluids, as indicated by our CoulSeS imaging results, the swarm-like seismicity with a lack of distinct mainshocks, the volcanic nature of the area, and previous studies (*5*, *7*). A shallowing propagation of the seismicity to the NE of Kolumbo from 26 January to 1 February (Fig. 4, A and B) suggests the ascent of fluids from the NE limit of a feeding, mid-crustal magma reservoir under Santorini and Kolumbo (Fig. 1). Subsequent migration of seismicity at a depth of ~5 to 15 km and an imaged dike opening at a depth of ~9 to 15 km toward the NE indicate lateral propagation of the fluids through a dike over a distance of ~20 km (Fig. 4, C to H). Because this stage of propagation was primarily horizontal, the fluids were likely close to neutral buoyancy relative to the surrounding rock (*8*, *11*), which suggests that the fluid was magma, with minimal proportions of lighter components such as gas or water, that would promote shallower opening. As indicated by the NE-aligned submarine volcanoes in the Anydros Basin (Fig. 1) (*52*), lateral dike propagation of magma to the NE of Kolumbo has occurred previously. The 2025 dike propagation forms a separate structure located to the east of this alignment and has not produced observed indications of eruption.

Timeline of dike emplacement

From ground-based geodetic analyses (*6*, *7*, *33*), seismicity, and CoulSeS imaging (see Figs. 2 and 4, fig. S7, and movie S1), we discerned and detailed five stages of activity responsible for the dike intrusion and swarm seismicity (see supplementary text for full details). We excluded an ephemeral and generally isolated CoulSeS-imaged opening located above the main seismicity as an artifact of the vertical symmetry in the seismicity distribution and the apparent lack of shallower seismicity that might break this symmetry. This interpretation is supported by imaging over the full study period (Fig. 3), which shows the largest cumulative opening entirely below the main seismicity. Reported times are Coordinated Universal Time (UTC) and were derived from seismicity and CoulSeS imaging in movie S1; distance values, d, are measured along the SW-NE distance scale shown in the figures and movies.

Stage 1. Santorini inflation: From mid-2024 to 25 January 2025, geodetic observations show inflation below the Santorini-Kolumbo area (*6*, *7*, *33*), which we associate with growth and pressurization of a mid-crustal magma reservoir system within a broad, 20- to 40-km-diameter, dome-shaped void in the seismicity (Fig. 3B).

Stage 2. Santorini deflation and dike initiation: Starting around 26 January, geodesy shows deflation below the Santorini-Kolumbo area (*6*, *7*). From 26 to 29 January, seismicity and the imaged opening (Fig. 4, A and B) suggest that buoyant magma exited the deflating magma reservoir at its NE limit (d = 25 to 30 km) and rose from a depth of ~16 to ~10 km. From 29 January to 1 February, the CoulSeS-imaged magmatic opening mainly remained around d = 27 km at a depth of ~10 km, perhaps near neutral buoyancy.

Stage 3. Dike expansion: On 1 February, seismicity expanded bilaterally SW and NE into a 15-km-long volume (Fig. 4C), including a cluster at a depth of ~8 km under Kolumbo (d = 20 km) and more diffuse events to about 10 km NE of the stage 2 activity at $d \approx 35$ km. Alignments in seismicity and CoulSeS imaging suggest a magma pathway at a depth

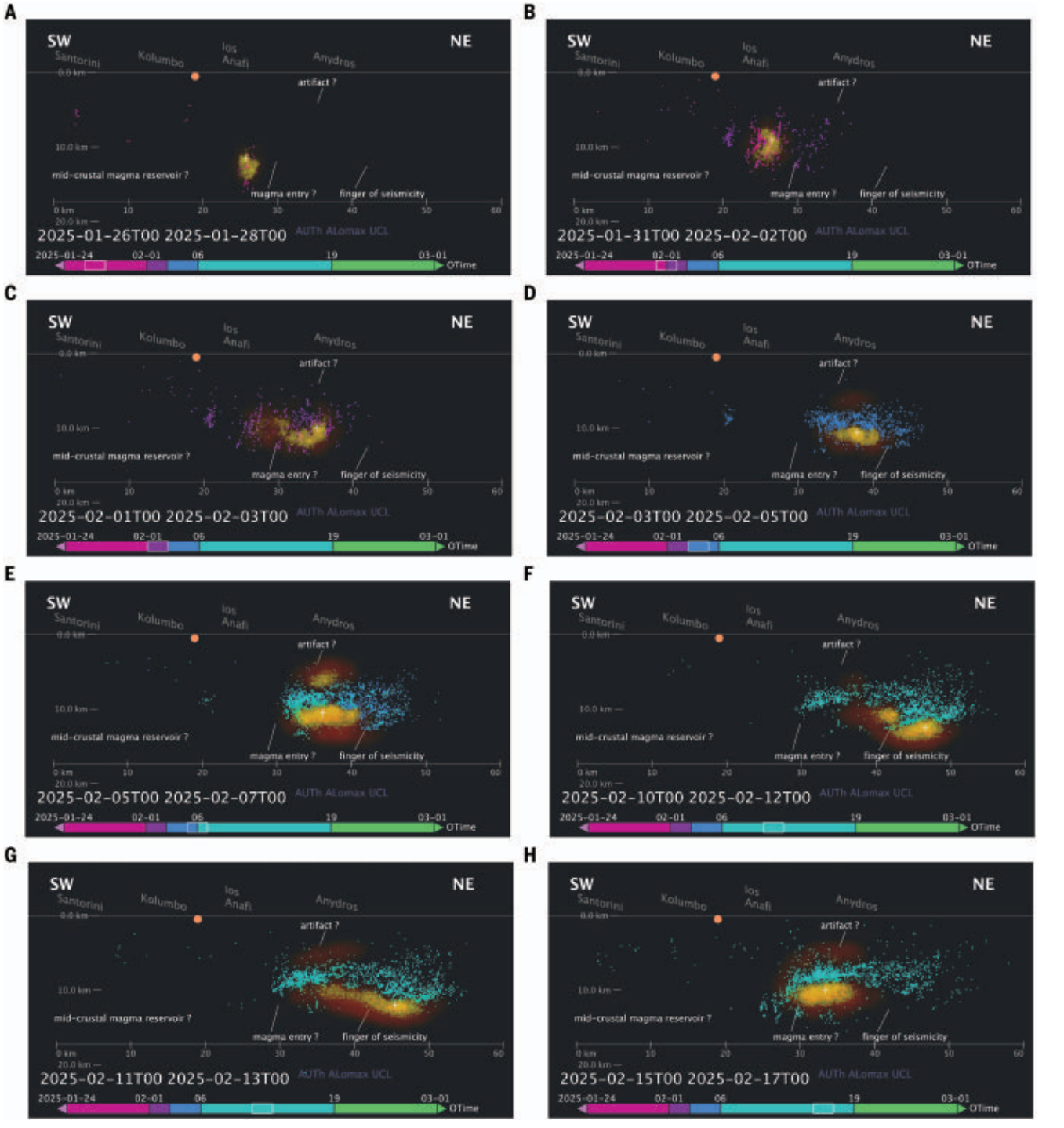

Fig. 4. CoulSeS imaging with vertical tensile sources applied to 2-day windows of the swarm seismicity. (**A** to **H**) Projections of the high-potential volumes of the 3D CoulSeS finite-source fields for relative dike opening are shown for each time step (yellow-orange and red show normalized correlations ≥0.8 and ≥0.7, respectively; the white plus sign shows peak CoulSeS intensity). The color scale indicates the occurrence time of seismicity, with the time windows displayed in each panel (white box). Selected windows are shown; all 2-day time windows are shown in fig. S7, and all 12-hour windows are shown in movie S1. Other figure elements are the same as in Fig. 3. Topographic and bathymetric basemaps were made with GeoMapApp (www.geomapapp.org) CC BY (*65*).

of ~10 km back to the SW under Kolumbo (movies S1 and S2). By late 2 February, most seismicity formed a broad cluster to the NE (d = 30 to 40 km) at a depth of ~10 km, surrounding localized imaged opening.

Stage 4a. Dike maturing: From 3 to 6 February, intense swarm seismicity and a CoulSeS-imaged dike opening of increasing intensity show establishment and maturing of ~10 km of the main dike opening toward the NE over an ~3- to 5-km depth range (Fig. 4D). By 12:00 on 3 February and again by 08:00 on 4 February, incursions of seismicity and opening migrated to the NE as far as d = 45 km before returning to the SW around d = 35 km at 18:00 on 4 February. By 06:00 on 5 February, there was another incursion of seismicity to the

NE as far as $d = 50$ km, along with a notably reduced rate of seismicity back to the SW around $d = 35$ km. Simultaneously, the imaged dike opening reached as far as $d = 43$ km at a depth of ~12 km (Fig. 4E) and was bounded below by a distinct finger of seismicity, an apparent barrier that hosted seismicity during the 3 and 4 February incursions (Fig. 4D). By 06:00 on 6 February, seismicity and opening again migrated and jumped back to the SW end of the main dike opening, concentrating around $d = 34$ km.

Stage 4b. Peak of activity: The most intense swarm activity and highest CoulSeS imaging intensity occurred from 6 to 19 February, with multiscale back-and-forth migration of seismicity and dike opening along with the breaking of barriers (Fig. 2). From 6 February, around $d = 35$ at the SW end of the main dike opening, there were minor incursions and clearly imaged opening bounded to the SW by intense seismicity and identified tremor sources, indicating dike extension.

On 10 February, there was a strong increase in seismicity rate and a marked, rapid jump in seismicity to the NE, starting with a near instantaneous shift to $d = 41$ km, followed by segmented migration at >0.4 km/hour, eventually reaching past $d = 50$ km (Fig. 2). Simultaneously, the imaged dike opening extended to $d = 43$ km at a depth of ~12 km, where it was bounded below by a dense finger of seismicity commensurate with that which was active from 3 to 5 February. This time, however, the dike opening broke through this barrier patch over ~12 hours (~10:00 to ~20:00 on 10 February), with the imaging suggesting that the opening, and thus magma, surrounded the barrier patch (Fig. 4F) before it was fully breached (Fig. 4G). Continued dike opening formed a deeper protuberance as far as $d = 55$ km by 06:00 on 11 February, coinciding with intense seismicity just above. By this time, the seismicity rate was low and there was negligible CoulSeS opening back at the SW end of the previously opened segment ($d = 30$ to 40 km), as occurred during the 5 February incursion. This response indicates a decrease in Coulomb stress and clamping of fractures (*41*) due to dike contraction, highlighting a wave of reduced magma overpressure back toward the reservoir. But by 12 February, after about 78 hours of incursion, the active seismicity and dike opening were back to the SW, concentrating around $d = 34$ km, where the CoulSeS imaging indicates renewed opening and high magma overpressure over ~24 hours (Fig. 2).

From 12 to 19 February, dike opening extended and oscillated SW-NE within the previously established main dike opening at $d = 30$ to 40. In this period, there were episodes of clustered seismicity further to the NE associated with minor or no imaged nearby dike opening (Fig. 2).

Stage 5. Reduced activity: On 19 February, there was a rapid decrease in seismicity rate and CoulSeS imaging intensity, along with no further dense clusters or identified tremor sources, though there are pulses of increased seismicity from 24 February (Fig. 2). The distribution of seismicity and opening suggests that most of the seismicity was triggered by stress transfer from continued opening along the main dike segment.

Seismicity, Coulomb stress change, and imaged main dike opening

An elliptical gap in the seismicity below a depth of 10 km and at $d = 28$ to 42 km surrounds the CoulSeS-imaged main dike opening (Fig. 3B). We interpret this 14-km-long patch, along with the deeper protuberance of opening reaching $d = 55$ km on 10 and 11 February, as defining most dike opening during the 2025 activity. When patches of the imaged opening above the seismicity are ignored as artifacts, most opening occurred in a horizontally extended zone below a depth of ~8 km, which excludes magma ascent to a shallower depth and a possible precursor to eruption (Figs. 3 and 4, fig. S7, and movie S1).

We confirmed the validity of the CoulSeS imaging by forward calculation of ΔCFS for the main dike opening, where areas of positive ΔCFS correspond very well to the distribution of seismicity after 1 February (figs. S13 to S24). Notably, perpendicular to the main dike opening (figs. S21 and S22), the seismicity forms a heart-shaped pattern, as predicted by ΔCFS, above the upper edge of an opening dike (*46*, *53*, *54*). A lack of symmetric, heart-shaped seismicity below the dike may be due to a less brittle lower-crustal rheology, fewer preexisting fractures, or other depth-dependent effects on seismicity. ΔCFS predicted and observed seismicity show very few events adjacent to the opening dike walls, as expected in this area of dike-induced compression (*54*), and confirm that triggered seismicity occurred on fault planes favorably oriented in the regional stress field.

The ΔCFS response for SE-dipping normal receiver faults, representative of the faulting source for the M_w 7.7 Amorgos earthquake of 1956 is shown in fig. S13. This repsonse shows that the imaged dike opening would have likely loaded the Amorgos fault in the area of the 1956 rupture (Fig. 1) and brought it closer to failure.

Fit to geodetic observations

Using the framework of our dike model, we were also able to fit available horizontal and vertical Global Navigation Satellite System (GNSS) displacements (*6*) and vertical displacements derived from ocean-bottom pressure gauges (*7*) from late January to late February 2025. Our model uses three displacement sources: (i) following (*7*), a point (Mogi) deflation source under Kolumbo; (ii) a rectangular tensile Okada source (*55*) approximating our main dike opening; and (iii) normal faulting above the imaged dike, which is indicated by our NLL-SC relocated seismicity and moment tensors and is a well-established phenomenon in the volume above an actively intruding dike (*21*, *54*). With these elements, it is straightforward to fit the observed geodetic displacements with the algorithms of (*56*) (figs. S26 and S27). The results give 9 m of mean dike opening, which corresponds to 486×10^6 m^3 of magma intrusion for the 12-km–by–4.5-km rectangular approximation of our main dike opening. See materials and methods for more details.

Rebounding, wavelike dike activity and magma pumping

The most intriguing feature of the 2025 Santorini-Amorgos activity is the frequent and often abrupt back-and-forth migration of both seismicity and the CoulSeS-imaged opening on multiple space-time scales, highlighting a complex mechanism of dike emplacement. Observations of past dike intrusions show episodic and segmented propagation (*19*, *57*) with back-propagating seismicity (*20*, *58*–*60*). Although numerical modeling predicts complex triggering interactions between magma and seismicity due to reductions or increases in dike pressure during magma advance or stalling, respectively (*61*), such a complex dike emplacement process has not been previously imaged.

Our detailed relocation of seismicity and CoulSeS imaging provide new insights into dike emplacement processes. Zones of diffuse seismicity that are active during the entire unrest period and apparent clusters of repeating earthquakes (e.g., at $d = 35$ km, starting late 4 February) were overprinted by back-and-forth migration phases over distances up to 20 km, lasting hours to days. These rapid migrations were characterized by intense localized high-magnitude seismicity and tremor sources as the dike propagated beyond its previous extent (Fig. 2).

A clear example of this pattern occurred on 10 to 12 February, when the locus of peak opening made an abrupt jump or rapid migration to the NE, with seismicity clearly delineating a new barrier being broken (Fig. 4, F and G). Once the barrier fully broke and a new dike patch was activated, there was a substantial reduction in seismicity and an imaged opening around the previously opening patch of the dike to the SW. This decline signifies an inversion in Coulomb stress and clamping of fractures in the surrounding rock (*41*) due to reduced magma overpressure and partial dike closing and indicates that the magma flow rate from the proposed, sub–Santorini-Kolumbo reservoir to the SW was lower than that into the newly created dike patch.

We thus propose a rebounding, wavelike feedback mechanism for the 2025 Santorini dike emplacement, where the flow of magma into newly opening patches of dike caused a reduction of magma pressure elsewhere, encouraging closure in nearby, established dike patches. However, when a front of reduced pressure reached the mid-crustal reservoir edge to the SW, further high-pressure magma recharge into the dike was enabled while the newly opening patches, through elastic stress transfer, reduced wall-rock normal stress in established patches, which were then subject to an increase in magma overpressure and renewed opening. The ensemble formed a pumping-like process driven by intermittent creation or renewed opening of dike patches, waves of reduced magma pressure, elastic stress transfer between dike patches, and a valve-like control of magma supply rate from the mid-crustal reservoir.

Our relocated seismicity and CoulSeS imaging resolve a more complex, rebounding feedback mechanism for dike emplacement than previously recognized, advancing general understanding of dike physics, eruption forecasting, and volcanic-tectonic-seismogenic feedback mechanisms. The number and variety of physical processes involved, the complexity of the interactions between them, and a lack of direct observation at depth complicate deterministic, physics-based modeling of actual dike emplacement, propagation, and eventual eruption. However, the exemplary time and space resolution of CoulSeS imaging offers a foundation for advancing future physics-based modeling of dikes, as well as ML-based, data-driven procedures (*62*–*64*), for tracking intrusions and forecasting eruptions in near real time.

Materials and methods are available in the supplementary materials.

REFERENCES AND NOTES

1. V. Karakostas *et al.*, 2025 Santorini–Amorgos NLL-SSST-coherence high-precision relocated earthquake catalog, Version 1.0. Zenodo (2025); https://doi.org/10.5281/zenodo.15111649.
2. N. Kitsantonis, "Nonstop quakes leave a tourist island empty and its residents on edge," *New York Times*, 20 February 2025.
3. W. L. Friedrich *et al.*, Santorini eruption radiocarbon dated to 1627-1600 B.C. *Science* **312**, 548–548 (2006). doi: 10.1126/science.1125087; pmid: 16645088
4. I. Fountoulakis, C. P. Evangelidis, The 2024–2025 seismic sequence in the Santorini-Amorgos region: Insights into volcano-tectonic activity through high-resolution seismic monitoring. *Seismica* **4**, 1663 (2025). doi: 10.26443/seismica.v4i1.1663
5. E. Lippiello, G. Petrillo, C. Godano, E. Papadimitriou, V. Karakostas, V. Anagnostou, 2025 Santorini-Amorgos crisis triggered by a transition from volcanic to regular tectonic activity. arXiv:2504.21371 [physics.geo-ph] (2025).
6. P. Briole *et al.*, Volcano-tectonic interaction at Santorini. The crisis of February 2025. Constraints from geodesy. *Geophys. J. Int.* **242**, ggaf262 (2025). doi: 10.1093/gji/ggaf262
7. M. P. Isken *et al.*, Volcanic crisis reveals coupled magma system at Santorini and Kolumbo. *Nature* **645**, 939–945 (2025). doi: 10.1038/s41586-025-09525-7; pmid: 40993256
8. V. Acocella, *Volcano-Tectonic Processes*, *Advances in Volcanology Series*, K. Nemeth, Ed. (Springer, 2021).
9. A. Gudmundsson, L. B. Marinoni, J. Marti, Injection and arrest of dykes: Implications for volcanic hazards. *J. Volcanol. Geotherm. Res.* **88**, 1–13 (1999). doi: 10.1016/S0377-0273(98)00107-3
10. J. R. Lister, R. C. Kerr, Fluid-mechanical models of crack propagation and their application to magma transport in dykes. *J. Geophys. Res.* **96**, 10049–10077 (1991). doi: 10.1029/91JB00600
11. A. M. Rubin, Propagation of magma-filled cracks. *Annu. Rev. Earth Planet. Sci.* **23**, 287–336 (1995). doi: 10.1146/annurev.ea.23.050195.001443
12. F. Sigmundsson *et al.*, Fracturing and tectonic stress drive ultrarapid magma flow into dikes. *Science* **383**, 1228–1235 (2024). doi: 10.1126/science.adn2838; pmid: 38330140
13. P. Traversa, V. Pinel, J. R. Grasso, A constant influx model for dike propagation: Implications for magma reservoir dynamics. *J. Geophys. Res. Solid Earth* **115**, B01201 (2010). doi: 10.1029/2009JB006559
14. D. Dzurisin, "Challenges and opportunities for the 21st century" in *Volcano Deformation: Geodetic Monitoring Techniques*, D. Dzurisin, Ed. (Springer, 2007), pp. 343–362. doi: 10.1007/978-3-540-49302-0_11
15. J. Li *et al.*, Minute-scale dynamics of recurrent dike intrusions in Iceland with fiber-optic geodesy. *Science* **388**, 1189–1193 (2025). doi: 10.1126/science.adu0225; pmid: 40273283
16. P. Segall, A. L. Llenos, S.-H. Yun, A. M. Bradley, E. M. Syracuse, Time-dependent dike propagation from joint inversion of seismicity and deformation data. *J. Geophys. Res. Solid Earth* **118**, 5785–5804 (2013). doi: 10.1002/2013JB010251
17. T. W. Benson *et al.*, Earthquake analysis suggests dyke intrusion in 2019 near Tarawera Volcano, New Zealand. *Front. Earth Sci.* **8**, 606992 (2021). doi: 10.3389/feart.2020.606992
18. S. P. Hicks *et al.*, Faults modulate magma propagation and triggered seismicity: the 2022 São Jorge (Azores) volcanic unrest. EarthArXiv X5HT4V [Preprint] (2025); https://doi.org/10.31223/X5HT4V.
19. F. Sigmundsson *et al.*, Segmented lateral dyke growth in a rifting event at Bárðarbunga volcanic system, Iceland. *Nature* **517**, 191–195 (2015). doi: 10.1038/nature14111; pmid: 25517098
20. J. Woods, T. Winder, R. S. White, B. Brandsdóttir, Evolution of a lateral dike intrusion revealed by relatively-relocated dike-induced earthquakes: The 2014–15 Bárðarbunga–Holuhraun rifting event, Iceland. *Earth Planet. Sci. Lett.* **506**, 53–63 (2019). doi: 10.1016/j.epsl.2018.10.032
21. A. M. Rubin, D. Gillard, Dike-induced earthquakes: Theoretical considerations. *J. Geophys. Res.* **103**, 10017–10030 (1998). doi: 10.1029/97JB03514
22. A. Lomax, Mapping finite-fault earthquake slip using spatial correlation between seismicity and point-source Coulomb failure stress change. *Seismica* **4**, 1412 (2025). doi: 10.26443/seismica.v4i1.1412
23. X. Le Pichon, J. Angelier, The hellenic arc and trench system: A key to the neotectonic evolution of the eastern mediterranean area. *Tectonophysics* **60**, 1–42 (1979). doi: 10.1016/0040-1951(79)90131-8
24. G. C. Georgalas, *Catalogue of the Active Volcanoes of the World Including Solfatara Fields. Part XII Greece* (International Volcanological Association, 1962).
25. D. T. M. Dominey-Howes, G. A. Papadopoulos, A. G. Dawson, Geological and Historical Investigation of the 1650 Mt. Columbo (Thera Island) Eruption and Tsunami, Aegean Sea, Greece. *Nat. Hazards* **21**, 83–96 (2000). doi: 10.1023/A:1008178100633
26. E. A. Okal, C. E. Synolakis, B. Uslu, N. Kalligeris, E. Voukouvalas, The 1956 earthquake and tsunami in Amorgos, Greece. *Geophys. J. Int.* **178**, 1533–1554 (2009). doi: 10.1111/j.1365-246X.2009.04237.x
27. F. Leclerc *et al.*, Large seafloor rupture caused by the 1956 Amorgos tsunamigenic earthquake, Greece. *Commun. Earth Environ.* **5**, 663 (2024). doi: 10.1038/s43247-024-01839-0
28. E. Papadimitriou, G. Sourlas, V. Karakostas, Seismicity variations in the Southern Aegean, Greece, before and after the large (M7.7) 1956 Amorgos earthquake due to evolving stress. *Pure Appl. Geophys.* **162**, 783–804 (2005). doi: 10.1007/s00024-004-2641-z
29. I. Dimitriadis *et al.*, Seismicity and active tectonics at Coloumbo Reef (Aegean Sea, Greece): Monitoring an active volcano at Santorini Volcanic Center using a temporary seismic network. *Tectonophysics* **465**, 136–149 (2009). doi: 10.1016/j.tecto.2008.11.005
30. M. Foumelis, E. Trasatti, E. Papageorgiou, S. Stramondo, I. Parcharidis, Monitoring Santorini volcano (Greece) breathing from space. *Geophys. J. Int.* **193**, 161–170 (2013). doi: 10.1093/gji/ggs135
31. P. Papadimitriou *et al.*, The Santorini Volcanic Complex: A detailed multi-parameter seismological approach with emphasis on the 2011–2012 unrest period. *J. Geodyn.* **85**, 32–57 (2015). doi: 10.1016/j.jog.2014.12.004
32. F. Schmid *et al.*, Heralds of future volcanism: Swarms of microseismicity beneath the submarine Ko-lumbo Volcano indicate opening of near-vertical fractures exploited by ascending melts. *Geochem. Geophys. Geosyst.* **23**, e2022GC010420 (2022). doi: 10.1029/2022GC010420
33. A. Karavias *et al.*, Santorini inflates again: Geodetic monitoring and modeling of the 2024-2025 volcanic unrest. ESS Open Archive 174585004.40126508/v1 [Preprint] (2025); https://doi.org/10.22541/essoar.174585004.40126508/v1.
34. W. Zhu, G. C. Beroza, PhaseNet: A deep-neural-network-based seismic arrival-time picking method. *Geophys. J. Int.* **216**, 261–273 (2019).
35. M. Zhang, W. L. Ellsworth, G. C. Beroza, Rapid earthquake association and location. *Seismol. Res. Lett.* **90**, 2276–2284 (2019). doi: 10.1785/0220190052
36. A. Lomax, A. Savvaidis, High-precision earthquake location using source-specific station terms and inter-event waveform similarity. *J. Geophys. Res. Solid Earth* **127**, e2021JB023190 (2022). doi: 10.1029/2021JB023190
37. A. Lomax, P. Henry, Major California faults are smooth across multiple scales at seismogenic depth. *Seismica* **2**, 324 (2023). doi: 10.26443/seismica.v2i1.324
38. L. Seeber, J. G. Armbruster, Earthquakes as beacons of stress change. *Nature* **407**, 69–72 (2000). doi: 10.1038/35024055; pmid: 10993073
39. C. A. Coulomb, Essai sur une application des regles de maximis et minimis a quelques problemes de statique relatifs a 1'architecture. *Mem. Div. Sav. Acad.* (1773).
40. J. Weiss, V. Pellissier, D. Marsan, L. Arnaud, F. Renard, Cohesion versus friction in controlling the long-term strength of a self-healing experimental fault. *J. Geophys. Res. Solid Earth* **121**, 8523–8547 (2016). doi: 10.1002/2016JB013110
41. R. G. Green, T. Greenfield, R. S. White, Triggered earthquakes suppressed by an evolving stress shadow from a propagating dyke. *Nat. Geosci.* **8**, 629–632 (2015). doi: 10.1038/ngeo2491
42. G. C. P. King, R. S. Stein, J. Lin, Static stress changes and the triggering of earthquakes. *Bull. Seismol. Soc. Am.* **84**, 935–953 (1994).
43. D. H. Oppenheimer, P. A. Reasenberg, R. W. Simpson, Fault plane solutions for the 1984 Morgan Hill, California, Earthquake Sequence: Evidence for the state of stress on the

Calaveras Fault. *J. Geophys. Res.* **93**, 9007–9026 (1988). doi: 10.1029/JB093iB08p09007
44. R. S. Stein, The role of stress transfer in earthquake occurrence. *Nature* **402**, 605–609 (1999). doi: 10.1038/45144
45. R. S. Stein, M. Lisowski, The 1979 Homestead Valley Earthquake Sequence, California: Control of aftershocks and postseismic deformation. *J. Geophys. Res.* **88**, 6477–6490 (1983). doi: 10.1029/JB088iB08p06477
46. S. Toda, R. S. Stein, T. Sagiya, Evidence from the AD 2000 Izu islands earthquake swarm that stressing rate governs seismicity. *Nature* **419**, 58–61 (2002). doi: 10.1038/nature00997; pmid: 12214230
47. J. Zahradnik, E. Sokos, Z. Roumelioti, F. Turhan, Positive isotropic components of the 2025 Santorini-Amorgos earthquakes. EarthArXiv X5RD9S [Preprint] (2025); https://doi.org/10.31223/X5RD9S.
48. N. Feuillet, The 2011–2012 unrest at Santorini rift: Stress interaction between active faulting and volcanism. *Geophys. Res. Lett.* **40**, 3532–3537 (2013). doi: 10.1002/grl.50516
49. A. Ganas, NOAFAULTS KMZ layer Version 6.0. Zenodo (2024); https://doi.org/10.5281/zenodo.13168947.
50. A. Ganas, I. A. Oikonomou, C. Tsimi, NOAfaults: A digital database for active faults in Greece. *Delt. Ell. Geol. Etair.* **47**, 518–530 (2013). doi: 10.12681/bgsg.11079
51. A. Brüstle, W. Friederich, T. Meier, C. Gross, Focal mechanism and depth of the 1956 Amorgos twin earthquakes from waveform matching of analogue seismograms. *Solid Earth* **5**, 1027–1044 (2014). doi: 10.5194/se-5-1027-2014
52. P. Nomikou *et al.*, Submarine volcanoes of the Kolumbo volcanic zone NE of Santorini Caldera, Greece. *Global Planet. Change* **90–91**, 135–151 (2012). doi: 10.1016/j.gloplacha.2012.01.001
53. D. C. Roman, Numerical models of volcanotectonic earthquake triggering on non-ideally oriented faults. *Geophys. Res. Lett.* **32**, 2004GL021549 (2005). doi: 10.1029/2004GL021549
54. A. M. Rubin, D. D. Pollard, Dike-induced faulting in rift zones of Iceland and Afar. *Geology* **16**, 413–417 (1988). doi: 10.1130/0091-7613(1988)016<0413:DIFIRZ>2.3.CO;2
55. Y. Okada, Internal deformation due to shear and tensile faults in a half-space. *Bull. Seismol. Soc. Am.* **82**, 1018–1040 (1992). doi: 10.1785/BSSA0820021018
56. K. Materna, J. Wong, Elastic_stresses_py: v1.0.0. Zenodo (2023); https://doi.org/10.5281/zenodo.7951979.
57. M. Belachew *et al.*, Comparison of dike intrusions in an incipient seafloor-spreading segment in Afar, Ethiopia: Seismicity perspectives. *J. Geophys. Res. Solid Earth* **116**, B06405 (2011). doi: 10.1029/2010JB007908
58. T. Ágústsdóttir *et al.*, Strike-slip faulting during the 2014 Bárðarbunga-Holuhraun dike intrusion, central Iceland. *Geophys. Res. Lett.* **43**, 1495–1503 (2016). doi: 10.1002/2015GL067423
59. C. Cattania, E. Rivalta, S. Hainzl, L. Passarelli, Y. Aoki, A nonplanar slow rupture episode during the 2000 Miyakejima dike intrusion. *J. Geophys. Res. Solid Earth* **122**, 2054–2068 (2017). doi: 10.1002/2016JB013722
60. T. Fischer *et al.*, Swarm seismicity illuminates stress transfer prior to the 2021 Fagradalsfjall eruption in Iceland. *Earth Planet. Sci. Lett.* **594**, 117685 (2022). doi: 10.1016/j.epsl.2022.117685
61. E. R. Heimisson, P. Segall, Physically consistent modeling of dike-induced deformation and seismicity: Application to the 2014 Bárðarbunga Dike, Iceland. *J. Geophys. Res. Solid Earth* **125**, e2019JB018141 (2020). doi: 10.1029/2019JB018141
62. K. J. Bergen, P. A. Johnson, M. V. de Hoop, G. C. Beroza, Machine learning for data-driven discovery in solid Earth geoscience. *Science* **363**, eaau0323 (2019). doi: 10.1126/science.aau0323; pmid: 30898903
63. M. Reichstein *et al.*, Deep learning and process understanding for data-driven Earth system science. *Nature* **566**, 195–204 (2019). doi: 10.1038/s41586-019-0912-1; pmid: 30760912
64. W. Song *et al.*, Towards data-driven discovery of governing equations in geosciences. *Commun. Earth Environ.* **5**, 589 (2024). doi: 10.1038/s43247-024-01760-6
65. W. B. F. Ryan *et al.*, Global Multi-Resolution Topography synthesis. *Geochem. Geophys. Geosyst.* **10**, 2008GC002332 (2009). doi: 10.1029/2008GC002332
66. A. Lomax, Archive of https://github.com/alomax/seismicity_stress_Santorini. Zenodo (2025); https://doi.org/10.5281/zenodo.16992463.

ACKNOWLEDGMENTS

We thank V. Acocella, P. Henry, and two anonymous reviewers for valuable discussions and comments on this study. **Funding:** S.P.H. acknowledges funding from a Natural Environment Research Council (NERC) Independent Research Fellowship (grant nos. UKRI184 and NE/B000184/1). A.L. received no funding support for this study. **Author contributions:** Conceptualization: A.L., V.A., V.K., S.P.H., E.P.; Methodology: A.L., V.A., V.K., S.P.H.; Investigation: A.L., V.A., V.K., S.P.H.; Visualization: A.L., V.K., S.P.H.; Funding acquisition: S.P.H., E.P.; Writing – original draft: A.L., V.A., V.K., S.P.H., E.P.; Writing – review & editing: A.L., V.A., V.K., S.P.H., E.P. **Competing interests:** The authors declare that they have no competing interests. **Data and materials availability:** Continuous waveform data were downloaded from the National Observatory of Athens (NOA) European Integrated Data Archive (EIDA) services (https://eida.gein.noa.gr). Code, data, and scripts for running the CoulSeS imaging and geodetic modeling performed in this study are available at https://github.com/alomax/seismicity_stress_Santorini and Zenodo (*66*). **License information:** Copyright © 2025 the authors, some rights reserved; exclusive licensee American Association for the Advancement of Science. No claim to original US government works. https://www.science.org/about/science-licenses-journal-article-reuse

SUPPLEMENTARY MATERIALS

science.org/doi/10.1126/science.adz8538
Materials and Methods; Supplementary Text; Figs. S1 to S27; References (*67–105*); Movies S1 and S2; Data S1 and S2

Submitted 24 June 2025; accepted 22 September 2025

10.1126/science.adz8538

RESEARCH ARTICLE SUMMARY

NEURODEVELOPMENT

Retinal calcium waves coordinate uniform tissue patterning of the *Drosophila* eye

Ben Jiwon Choi*, Yen-Chung Chen, Claude Desplan*

Full article and list of author affiliations:
https://doi.org/10.1126/science.ady5541

INTRODUCTION: Precise neural function requires accurate tissue organization of multiple cell types. This is often achieved by synchronized waves of calcium activity that enable transient communication and coordination between cells during nervous system development. This evolutionarily conserved activity is observed in both vertebrate and invertebrate systems and occurs in neuronal as well as non-neuronal cells. Neuronal retinal waves in the mammalian eye are among the best-characterized examples, documented across species including the human fetal retina. These neurotransmission-mediated retinal waves play critical roles in refining synaptic connectivity and aligning sensory circuits between processing layers of the brain.

RATIONALE: Non-neuronal support cells such as glial and epithelial cells also exhibit robust calcium waves observed in multiple systems, including the retina. These waves, mediated by gap junction networks, coordinate cellular behaviors over large fields and have been implicated in cell proliferation and specification, although they can also occur at later stages of development. Whether non-neuronal calcium waves also contribute to tissue maturation remains unclear. Clarifying this role could reveal how these calcium waves coordinate neuronal wiring to shape mature tissue architecture of neural tissues.

RESULTS: We describe calcium waves arising exclusively in non-neuronal retinal support cells during the development of the *Drosophila* compound eye. To achieve this, we optimized a dry-lens–based imaging platform that enables robust, versatile in vivo calcium imaging. We found that the waves are sparsely initiated in single ommatidia (unit eyes) by activation of the receptor tyrosine kinase Cad96Ca in one of the four lens-forming "cone cells." This activates phospholipase C–γ (PLC-γ), leading to calcium release from the endoplasmic reticulum via inositol 1,4,5-trisphosphate (IP_3) receptors (IP_3Rs). The calcium signal first propagates vertically to all retinal cells within a single ommatidium (see the figure, panel A), with the exception of photoreceptors, and then laterally to neighboring ommatidia, forming waves that spread across large regions of the retina (see the figure, panels A and B). This propagation occurs through gap junction channels composed of combinations of innexin subunits that differ between different cell types. This cell type–specific "innexin code" determines the order of signal propagation and shapes regional calcium signaling levels.

These wave-induced calcium signals drive myosin II–mediated apical contractions at interommatidial boundaries. The intensity of the calcium signal scales with ommatidial size, with waves occurring more frequently in the antero-ventral region where ommatidia are larger. This size-matched activity thus drives stronger apical contractions in regions with larger boundaries. Through this process, calcium waves progressively remodel the retinal epithelium, correcting early boundary disparities and aligning ommatidia into a uniform array (see the figure, panel C). This developmental remodeling ensures a smooth optical surface and precise lens alignment, potentially accommodating the distinct visual demands of small dorsal ommatidia facing the bright sky and large ground-facing ventral ommatidia optimized for sensitivity.

CONCLUSION: Our findings show that synchronized calcium activity within non-neuronal cells directs the coordinated assembly of sensory tissue architecture. The conserved presence of gap junction–mediated calcium waves in vertebrate glia and epithelia suggests that similar mechanisms integrate cellular patterning with physiological function in many systems. □

*Corresponding author. Email: b.jiwon.choi@gmail.com (B.J.C.); cd38@nyu.edu (C.D.)
Cite this article as B. J. Choi *et al.*, *Science* **390**, eady5541 (2025). DOI: 10.1126/science.ady5541

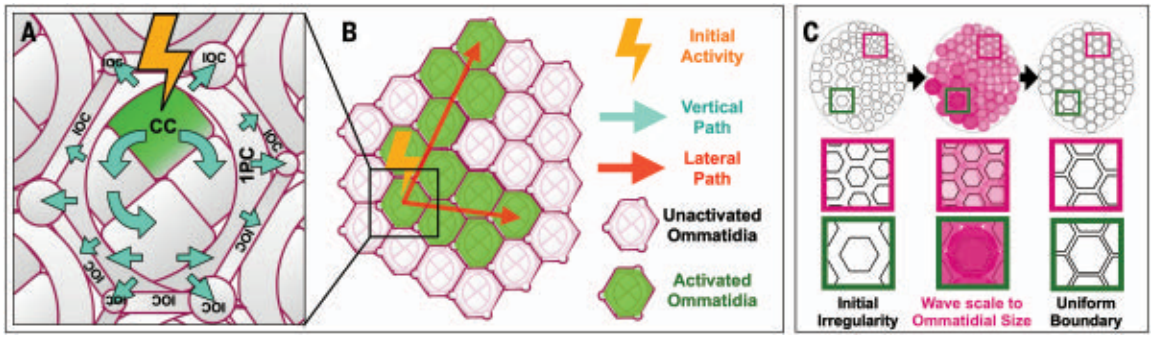

Retinal calcium waves shape regional calcium signals, coordinating ommatidial remodeling. (**A** and **B**) Waves initiate in a cone cell (CC) and follow a stereotypic pathway, propagating vertically from the CC to the primary pigment cell (1PC), then to interommatidial cells (IOCs) within the same ommatidium, and laterally across neighboring ommatidia. (**C**) Wave intensity scales with ommatidial size, correcting initial boundary irregularities to produce uniformly packed ommatidia across the retina.

NEURODEVELOPMENT

Retinal calcium waves coordinate uniform tissue patterning of the *Drosophila* eye

Ben Jiwon Choi*, Yen-Chung Chen, Claude Desplan*

Optimal neural processing relies on precise tissue patterning across diverse cell types. Here, we show that spontaneous calcium waves arise among non-neuronal support cells in the developing *Drosophila* eye to drive retinal morphogenesis. These waves are initiated by Cad96Ca receptor tyrosine kinase signaling, triggering phospholipase C–γ–mediated calcium release from the endoplasmic reticulum. A cell type–specific "innexin code" coordinates wave propagation through a defined gap junction network among non-neuronal retinal cells, excluding photoreceptors. Wave intensity scales with ommatidial size, triggering stronger myosin II–driven apical contraction at interommatidial boundaries in larger ommatidia. This size-dependent mechanism compensates for early boundary irregularities, ensuring uniform ommatidial packing that is critical for precise optical architecture. Our findings reveal how synchronized calcium signaling among non-neuronal cells orchestrates tissue patterning in the developing nervous system.

Precise tissue patterning is crucial for optimal biological function (*1*–*3*). Sensory systems exemplify this principle with their arrangement of functional modules that is essential for processing sensory input (*4*, *5*). To organize sensory modules, non-neuronal cells like glia and epithelia must be precisely patterned and coordinated with sensory neurons (*6*–*8*). Synchronized calcium activity in neuronal cells during development is crucial for the patterning of neuronal circuits (*9*–*12*). In the mammalian visual system, retinal waves guide wiring of visual pathways within the retina and in higher brain areas (*13*–*15*). Though also affecting non-neuronal cells like Müller glia and pigment epithelium, their role in organizing nervous system architecture remains unclear (*16*–*18*). Beyond the nervous system, synchronized calcium activity is critical for morphogenesis in other tissues (*19*–*22*)—for instance, coordinating myoblast fusion into muscles (*23*). This suggests that it may also guide structural patterning of non-neuronal cells in the nervous system.

In contrast to synchronized calcium activity mediated by synaptic transmission between neurons, this activity in non-neuronal cells is primarily mediated by gap junction channels (*19*–*21*) that form multicellular networks (*24*, *25*). Beyond their role in nervous system development, gap junction networks are crucial for various biological processes, including tissue regeneration, cancer metastasis, and aging (*26*–*28*). However, technical difficulties have hindered a comprehensive understanding of their roles. Challenges include complex live imaging and difficulty manipulating gap junctions owing to subunit diversity and essential roles in cellular physiology (*24*, *29*).

The *Drosophila* retina offers an excellent system for investigating the role of intercellular calcium activity among non-neuronal cells (*30*–*32*). Its simplicity, stereotyped organization, and genetic accessibility enable precise live imaging and manipulation. It has recently been used to identify the role of calcium waves during late retinal development (*33*). The fly compound eye has ~800 unit-eyes (ommatidia), each of which houses eight photoreceptor neurons (PRs) (*34*, *35*). These units are surrounded by specialized non-neuronal retinal support cells that exhibit features of glial and epithelial cells (Fig. 2, A to H) (*36*, *37*). They include four cone cells (CCs), two primary pigment cells (1PCs), and a cluster of 12 interommatidial cells (IOCs) that are shared among six adjacent ommatidia (*35*, *37*): six secondary pigment cells (2PCs), three tertiary pigment cells (3PCs), and three bristle cells (BCs).

Both neuronal and non-neuronal cells show regional patterning: The dorsal rim detects polarized light (*34*), and dorsal R7 photoreceptors coexpress two ultraviolet opsins (*38*). The ventral retina features structurally larger ommatidia compared to the dorsal side (*39*, *40*). This regional patterning is evolutionarily conserved across fly species and is linked to optimized visual detection of low-intensity ground features (*39*). The optic lobe circuitry also exhibits regional polarity, with distinct synaptic densities and neuronal subtypes between the dorsal and ventral sides (*41*, *42*). These findings indicate robust regional patterning of neuronal and non-neuronal populations that are critical for visual processing (*43*).

In this study, we monitored live retinal calcium dynamics throughout the pupal stages. We identified robust early retinal waves of synchronized calcium activity in retinal support cells, just prior to synaptogenesis of PRs to their optic lobe targets. We investigated the molecular mechanisms and the developmental role of these waves. Calcium release from the endoplasmic reticulum via inositol 1,4,5-trisphosphate (IP_3) receptor (IP_3R) is initiated by the receptor tyrosine kinase (RTK) Cad96Ca and phospholipase C–γ. It propagates to adjacent cells through gap junctions, with specific innexin subunit combinations involved in distinct cell types. Retinal waves drive calcium-dependent apical contraction of interommatidial boundaries through cell morphogenesis via the myosin II pathway. Wave activity is more frequent in the ventral region of the eye, where larger ommatidia generate stronger calcium signals that promote more robust contractions. This mechanism compensates for initial boundary irregularities, ensuring uniform interommatidial boundaries across the retina, which is critical for establishing consistent lens architecture. Therefore, we reveal the molecular and cellular mechanisms by which synchronized calcium activity in retinal support cells coordinate the overall architecture of the eye.

RESULTS

Early retinal calcium waves in the developing retina

We used a dry-lens imaging platform to monitor calcium dynamics in the developing retina of intact animals (Fig. 1A). Compared to the immersion-lens protocol (*44*, *45*), this approach eliminates the need for coverslips, enabling simpler and contact-free imaging of intact animals (Fig. 1, A and B). We monitored calcium dynamics in the developing retina from ~10 hours after pupal formation (10 hAPF) until eclosion (~100 hAPF) (Fig. 1C; fig. S1, A to K; and Movie 1). We expressed the genetically encoded calcium indicator GCaMP6s in all retinal cells (*46*, *47*). During our observations, two specific developmental windows displayed robust synchronized calcium activity across the whole retina (Fig. 1C and fig. S1, I and K). Early retinal waves, hereafter referred to as "retinal waves," emerged at around 37 hAPF and lasted roughly 3 hours (Fig. 1, C, I and J, and Movie 1H). Previously described and analyzed later-stage calcium waves were observed starting from around 73 hAPF and continued until eclosion (Fig. 1C, fig. S1K, and Movie 1I) (*33*).

We focused on the early retinal waves with fine temporal resolution to determine their overall properties and function (Fig. 1, D to J, and Movie 2). During early pupal development before the onset of retinal waves (37 hAPF), isolated calcium transients were only rarely observed in PRs (fig. S1H, arrow). Retinal waves began as calcium signals in a single retinal cone cell, appearing at 37.1 ± 0.91 hAPF (SD, $n = 19$ retinas), initiating what we define as early stage 1 (Figs. 1D (arrow),

Department of Biology, New York University, New York, NY, USA. *Corresponding author. Email: b.jiwon.choi@gmail.com (B.J.C.); cd38@nyu.edu (C.D.)

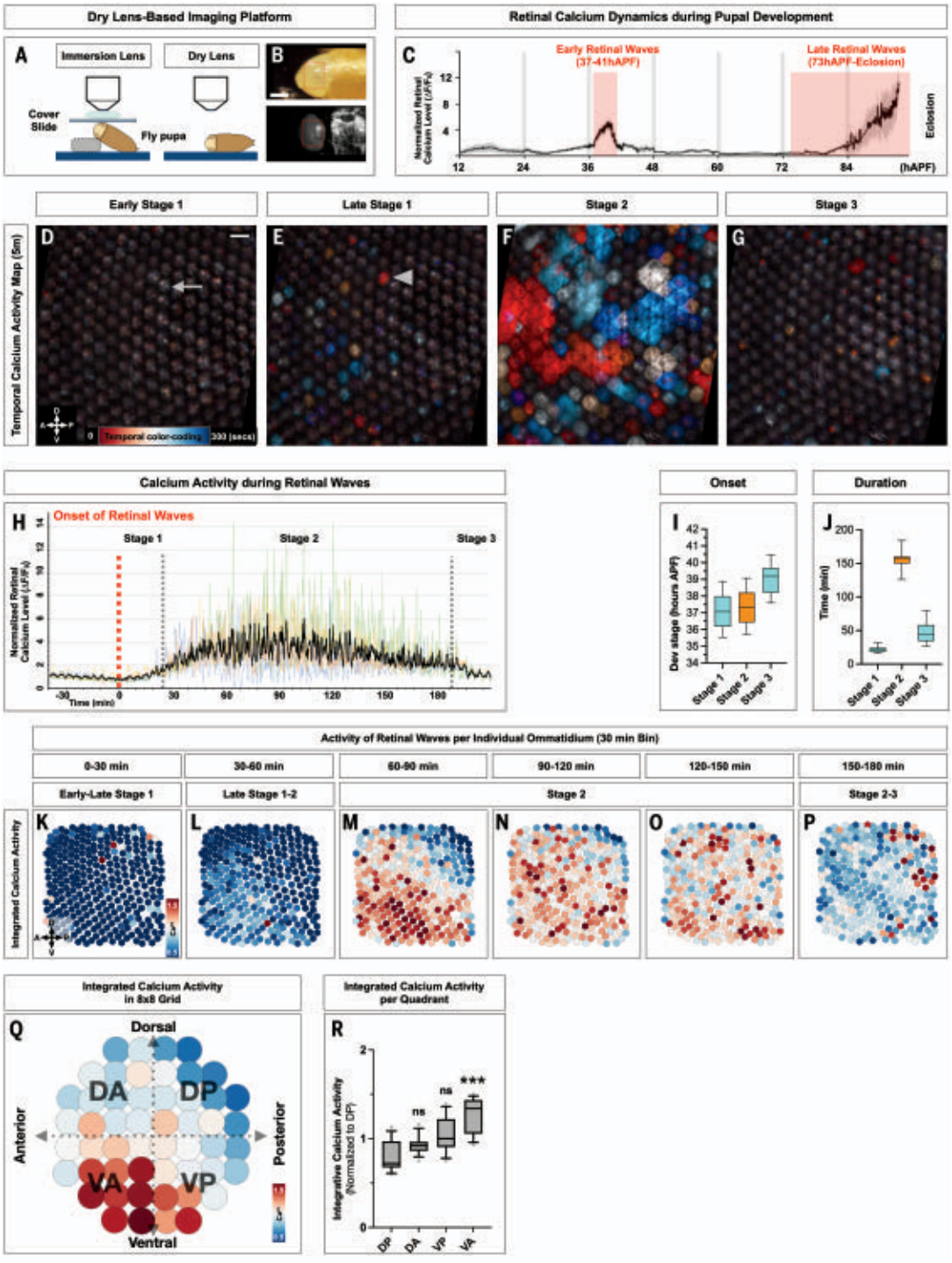

Fig. 1. Retinal calcium wave dynamics during pupal eye development. (**A**) Schematic of imaging platform using a dry-lens setup for intact pupa, shown in comparison with a conventional immersion-lens setup. (**B**) Representative images of sample preparation (top) and retinal calcium imaging (bottom). The red box marks the retinal area analyzed in (D) to (G). Scale bar, 500 μm. (**C**) Average calcium dynamics across pupal retinal development. Imaging was performed every 2 min, and $n \geq 5$ retinas were analyzed for each time window. Details are provided in fig. S1, A to K. See also Movie 1. (**D** to **G**). Retinal calcium wave activity shown as color-coded 5-min temporal activity maps (T-stacks) for early stage 1 (D), late stage 1 (E), stage 2 (F), and stage 3 (G). The arrow in (D) indicates a single cone cell firing, and the arrowhead in (E) indicates full activation of an ommatidium. Images are from the same retina, imaged at 3-s intervals. (A, anterior; P, posterior; D, dorsal; V, ventral). Scale bar, 20 μm (D to G). See also Movie 2. (**H**) Individual calcium traces corresponding to (D) to (G). Four retinas are shown in different colors, and the black trace represents the averaged activity. (**I**) Quantification of retinal wave onset timing ($n = 19$ retinas). Error bars, SD. (**J**) Quantification of retinal wave duration ($n = 19$ retinas). Error bars, SD. (**K** to **P**) Ommatidial-scale integrative calcium activity between 37 and 41 hAPF. Each bin corresponds to a 30-min period, and each hexagon represents a single ommatidium. Signal intensity for each ommatidium is color-coded. Data are from the same retina shown in (D) to (G). (**Q**) Grid-based map of integrative calcium activity. Each circle represents a group of ommatidia arranged in an 8 × 8 grid along dorsoventral (DV) and anteroposterior (AP) axes. Average intensity of integrative calcium activity per grid point is color-coded. $n = 6$ retinas. (**R**) Quantification of quadrant-specific integrative activity shown in (Q). $n \geq 432$ ommatidia from 6 retinas [not significant (ns), $P \geq 0.05$; ***$P < 0.001$]. Error bars, SD.

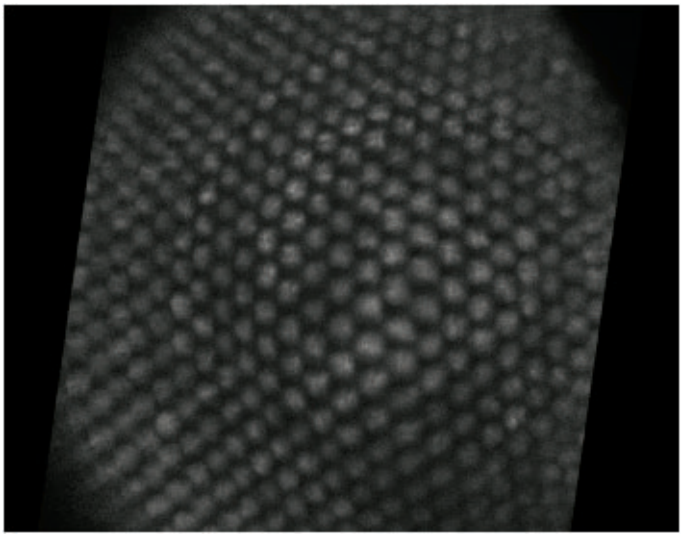

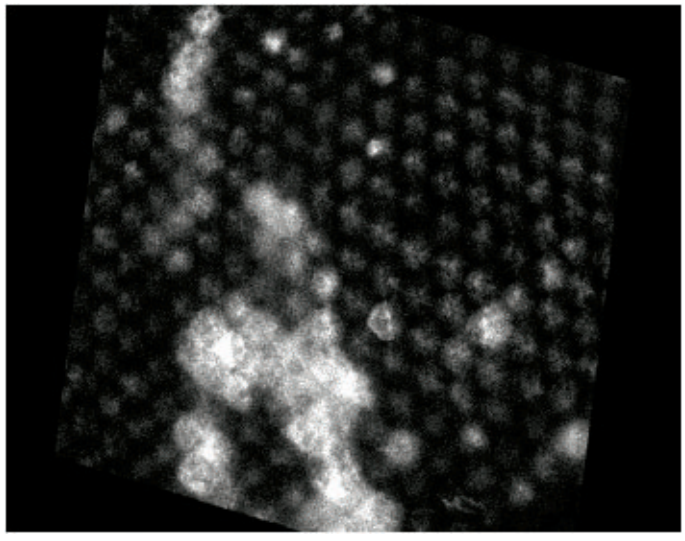

Movie 1. Calcium dynamics of developing pupal retina. (**A** to **I**) From 12 hAPF to eclosion, related to fig. S1, A to K. Representative calcium imaging of intact pupal retinas from 12 to 24 hAPF (A), 24 to 36 hAPF (B), 36 to 48 hAPF (C), 48 to 59 hAPF (D), 60 to 72 hAPF (E), 72 to 84 hAPF (F), 84 hAPF to eclosion (G), early retinal waves (H), and late retinal waves (I) using *UAS-GCaMP6s* driven by *GMR-GAL4* (A) or *longGMR-GAL4* (B to I). Imaging performed with confocal microscopy (488-nm excitation), focusing on retina (A to G) or entire pupa (H and I). Original GMR-GAL4 is expressed in all retinal cells postmorphogenetic furrow, whereas longGMR-GAL4 is photoreceptor-specific during the L3 larval eye disc but becomes pan-retinal by 24 hAPF. Time-lapse imaging was acquired as Z-stacks at 2-min intervals. Imaging duration was limited to a maximum of 12 hours per pupa to minimize phototoxicity for any analysis.

Movie 2. Retinal calcium waves of a single retina. (**A** to **D**) Related to Fig. 1, D to G. Representative retinal calcium wave recordings from a single retina of an intact pupa during early stage 1 (A), late stage 1 (B), stage 2 (C), and stage 3 (D) using *UAS-GCaMP6s* driven by *longGMR-GAL4*. Stages are defined in Fig. 1H. Imaging performed with confocal microscopy (488-nm excitation). Time-lapse imaging was acquired as Z-stacks at 3-s intervals.

H to J, and 2 and Movie 2A). The signals then spread to adjacent cells within the same ommatidium during late stage 1 (Fig. 1E and Movie 2B). These stage 1 waves lasted for 22 ± 4.4 min (Fig. 1J). Then, the waves started spreading to adjacent ommatidia, which marked the onset of stage 2 (Fig. 1, F and H, and Movie 2C). This phase was characterized by intense retinal calcium activity that persisted for 156 ± 14 min (Fig. 1, H and J). Subsequently, at 39.1 ± 0.86 hAPF, the waves became again restricted to a single ommatidium for 46 ± 15 min (stage 3) (Fig. 1, G and H to J, and Movie 2D). Later, most calcium activity faded, leaving sporadic calcium transients, mainly in PRs, which continued until the onset of the late retinal waves at 73.4 ± 1.26 hAPF (SD, $n = 7$ retinas) (fig. S1, J and K) (*33*). The onset and duration of retinal waves were consistent between animals (Fig. 1, H to J), occurring irrespective of the genetic drivers, calcium sensors, and excitation laser used (fig. S1, M to O). When we simultaneously imaged both eyes, the difference in the onset of the waves between eyes was only 2.4 ± 1.7 min (SD, $n = 5$ animals), suggesting that the initiation of retinal waves is a bilaterally synchronized phenomenon (fig. S1L and movie S1).

We examined regional patterns of retinal waves by quantifying the amount of synchronized calcium activity occurring across multiple cells within each ommatidium. During late stage 1, calcium activity first emerged in isolated ommatidia, predominantly in the ventral region (Fig. 1, L and M, and fig. S1, P and Q). As the waves progressed to stage 2, they spread across neighboring ommatidia to encompass other retinal regions (Fig. 1, M to O). To analyze wave activity across the population, we integrated data from multiple retinas by pooling them into an 8 × 8 grid template (Fig. 1Q). This spatial analysis over the entire wave period revealed a distinct regional pattern, with increased wave activity in the ventral-anterior (VA) region, further explored in Fig. 5. (Fig. 1, Q and R).

Single-cell resolution of retinal waves reveals stereotypical patterns of initiation and propagation

To examine retinal wave initiation and propagation at the single-cell level, we used multicolor Flp-out labeling at 40 hAPF to map individual cell configurations (Fig. 2, A to H) (*48*). Within a single ommatidium, all retinal cell types are in direct contact with each other (Fig. 2C), consistent with electron microscopy studies (*35*), providing a structural basis for single-cell tracing of retinal waves.

We performed high-resolution calcium imaging to detect single-cell calcium activity (Fig. 2, I to L, and Movie 3). Initial calcium activity began from single cone cell (CC) (Fig. 2I, arrow, and 2M), with all four cone cells capable of initiating with a slight bias toward dorsal-facing cone cells (fig. S2B). It then propagated stereotypically to neighboring cells (Fig. 2, M to P). During stage 1, the waves began in one cone cell, spread to adjacent cone cells (Fig. 2N), then moved to primary pigment cells (1PCs) (Fig. 2O) before reaching interommatidial cells (IOCs) (Fig. 2P), thus propagating within a single ommatidium (CC>CC>1PC>IOCs) (Fig. 2, M to Q; fig. S2, A and C to E; and Movie 4). Calcium thus spread to all non-neuronal cell types in an ommatidium without involving PRs. These stereotypic propagation patterns progressed from the apical to the basal layer (Fig. 2, M to P), defining CC>CC>1PC>IOCs as a "vertical pathway" (Fig. 2W). Although all retinal cells within a single ommatidium are in physical contact (Fig. 2C), no alternate wave routes were observed, such as 1PC>CC or CC>IOC bypassing 1PC.

Stage 2 calcium activity spread laterally to neighboring ommatidia, mediated by interommatidial cells as a "lateral pathway" (Fig. 2, K and R to W). Two adjacent ommatidia O1 and O2 share interommatidial cells, allowing interommatidial cell in one ommatidium (O1) to directly contact interommatidial cells and cone cells in O2 (Fig. 2, U and V). During wave propagation from O1 to O2 (Fig. 2, R and S), the calcium signal spread from this initial interommatidial cell (2PC labeled "1") to cone cells ("2") and interommatidial cells ("3" and "4") through basal layer connections (Fig. 2, U and V). The lateral propagation moved across successive ommatidia, with interommatidial cell–to–cell signaling forming the leading edge of the wave (Fig. 2W, fig. S2F, and Movie 5). Meanwhile, interommatidial cells also activated cone cells along the

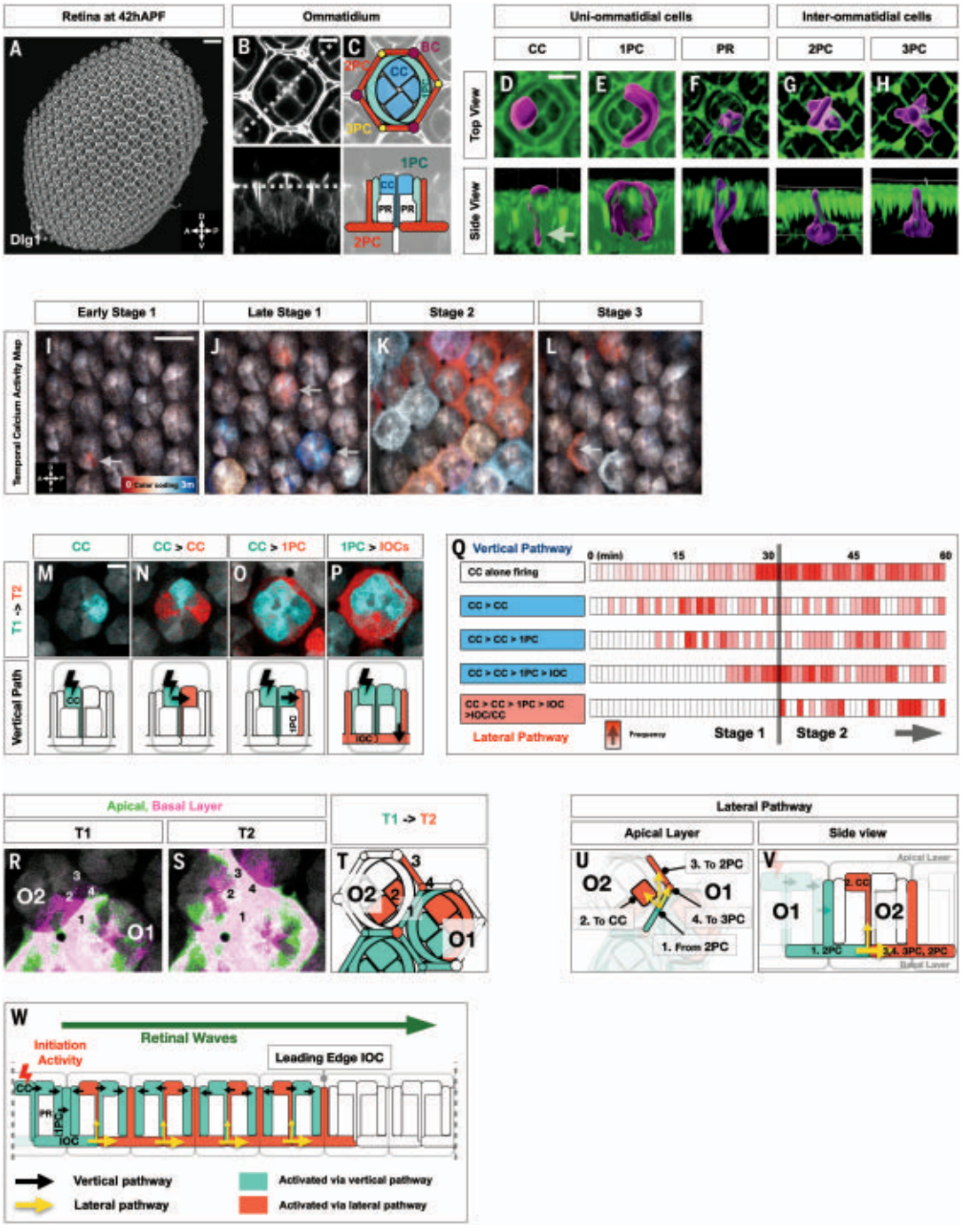

Fig. 2. Single-cell resolution of retinal waves reveals stereotyped initiation and propagation patterns. (**A** to **C**) Retina overview (A), apical side [(B), top], and cross section [(B), bottom] of a single ommatidium immunostained with Dlg1. The dotted line in (B), top, indicates the cutting plane for (B), bottom, and vice versa. (C) Diagram of retinal cell types: cone cell (CC), primary pigment cell (1PC), secondary pigment cell (2PC), tertiary pigment cell (3PC), bristle cell (BC), photoreceptor (PR). Scale bars, 20 μm (A), 5 μm (B and C). (**D** to **H**) Three-dimensional reconstructions of retinal cell morphology in *longGMR-GAL4>UAS-MCFO* retina at 40 hAPF. Top [(D) to (H), top panels] and side views [(D) to (H), bottom panels] show single-cell morphology. Magenta marks single-cell labeling, green marks Dlg1. Arrow in (D), bottom, highlights the leg-like structure of CC-contacting IOCs. Scale bar, 10 μm (D to H). (**I** to **L**) Retinal calcium wave activity at single-cell resolution displayed as color-coded 3-min temporal activity maps for early stage 1 (I), late stage 1 (J), stage 2 (K), and stage 3 (L). The arrow in (I) indicates a single cone cell firing, arrows in (J) indicate vertical waves, and the arrow in (L) indicates a primary pigment cell firing. All images came from the same retina. Scale bar, 10 μm (I to L). See also Movie 3. (**M** to **P**) Vertical pathway patterns including single CC firing (M), CC–CC propagation (N), CC–1PC propagation (O), and CC–IOC propagation (P). Time points are shown at T1 (cyan) and T2 (red, 4 s later). Bottom panels show schematics. Scale bar, 5 μm (M to P). See also fig. S2, A and C to E, and Movie 4. (**Q**) Event log of retinal waves from stage 1 through early stage 2 in a single retina. Each bin represents a 1-min interval, and event frequency is color-coded. Blue box marks the vertical pathway, and red box marks the lateral pathway. (**R** to **T**) Lateral pathway wave patterns. (R) and (S) show T-series with apical (green) and basal (magenta) layers, where T1 and T2 are separated by 4 s. Cells: initial 2PC (1), propagated CC (2), 2PC (3), 3PC (4). (T) shows schematic representation of calcium signaling at T1 (cyan) and T2 (red). Scale bar, 5 μm (R and S). See also fig. S2F and Movie 5. (**U** and **V**) Diagrams of lateral pathway wave patterns as in (R) to (T). (**W**) Diagram of retinal wave propagation along vertical and lateral pathways across multiple ommatidia.

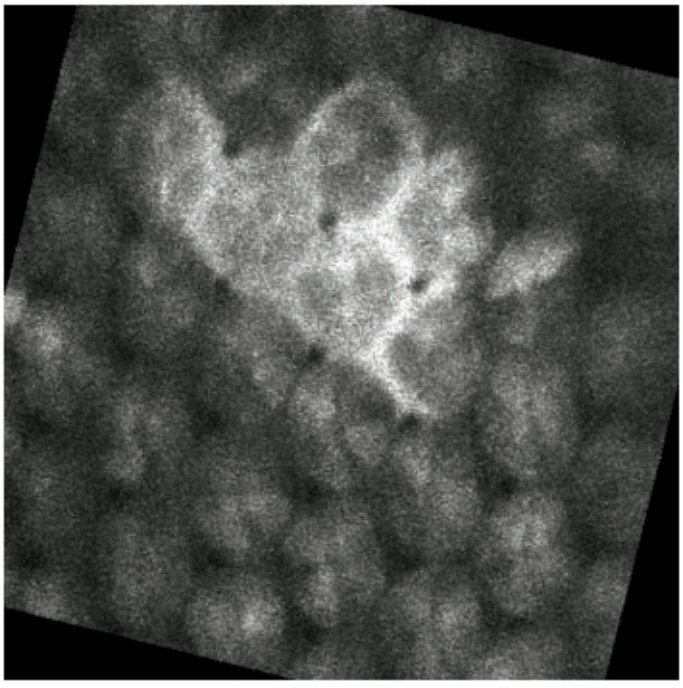

Movie 3. Retinal calcium waves at single-cell resolution. (**A** to **D**) Related to Fig. 2, I to L. Representative recordings of retinal calcium waves from a single retina during early stage 1 (A), late stage 1 (B), stage 2 (C), and stage 3 (D) using *UAS-GCaMP6s* driven by *longGMR-GAL4.* Imaging performed with two-photon microscopy (920-nm excitation). Time-lapse imaging was acquired as Z-stacks at 5-s intervals.

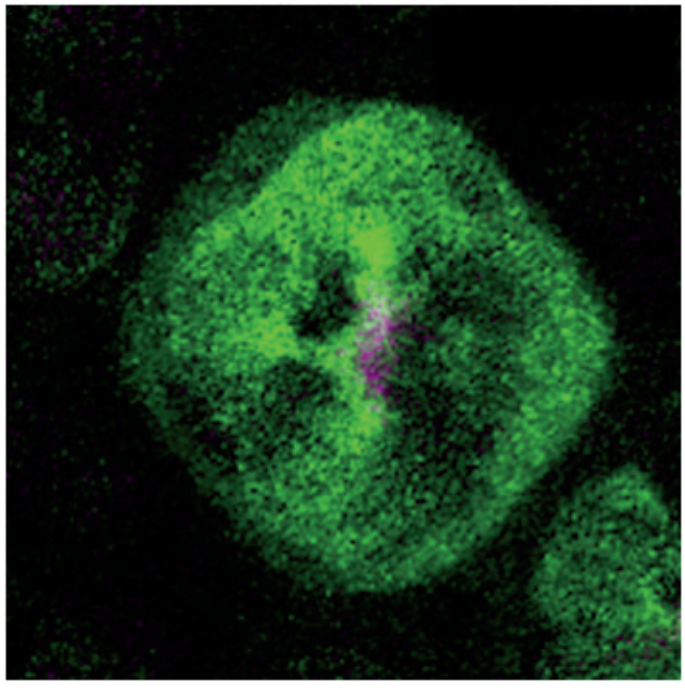

Movie 4. Vertical pathways of retinal calcium waves. (**A** to **D**) Related to Fig. 2, M to P, and fig. S2, A and C to E. Representative recordings of retinal calcium waves during stage 1 showing initial cone cell firing (A), cone cell to cone cell propagation (B), cone cell to cone cell to primary pigment cell propagation (C), and cone cell to cone cell to primary pigment cell to interommatidial cells propagation (D). Imaging performed with two-photon microscopy (920-nm excitation). Z-stacks were acquired every 4 s. Apical and basal layers are color-coded as green (apical) and magenta (basal).

wave's path, activating all other cells and initiating a vertical pathway within each ommatidium. This coordination activated all support cells along the wave path, establishing robust, region-specific calcium signaling (Fig. 2W). (Fig. 2V, "1" and "2").

Vertical and lateral waves then stopped, leaving sporadic calcium activity in cone cells and primary pigment cells that defined stage 3 (Fig. 2L and Movie 3D). We did not observed calcium activity or propagation to PRs: GCaMP6s driven by a PR-specific GAL4 driver (Chaoptin-GAL4) did not show any calcium activity in PRs during the waves (fig. S3, A to C, and movie S2): Retinal waves are entirely driven by non-neuronal retinal cells, similarly to late retinal waves (*33*).

In summary, retinal waves do not diffuse randomly despite full cell interconnections; they initiate in cone cells and follow organized vertical and lateral pathways (Fig. 2W), suggesting an underlying dedicated cellular communication network.

Cad96Ca-PLCγ-IP$_3$R signaling triggers calcium release from the ER

In mammals, the endoplasmic reticulum (ER) is the primary source of calcium for the waves in glia and epithelia (*21*, *49*), suggesting a similar role in *Drosophila*. To simultaneously measure calcium activity in both the ER and the cytoplasm, we used two calcium indicators with different colors: ER-targeted GCaMP (green), and cytosolic jRGECO1a (red) (Fig. 3, A to D, and Movie 6) (*50*–*52*). During the waves, cytoplasmic calcium rose as ER calcium signal fell across all retinal supporting cells (Fig. 3, A to D), indicating active ER calcium release.

We analyzed the role of the inositol 1,4,5-trisphosphate receptor (IP$_3$R), a crucial component of calcium wave dynamics (*49*). We generated retinal Flippase/Flippase Recognition Target (FLP/FRT) mosaic clones, marking wild-type clones with red fluorescent protein (RFP) and leaving IP$_3$R mutant clones unmarked (Fig. 3E) (*33*, *53*). Retinal waves failed to initiate or propagate in *IP$_3$R* mutant clones, even at the borders of the clones (Fig. 3, F and G, and Movie 7), indicating that IP$_3$R-mediated

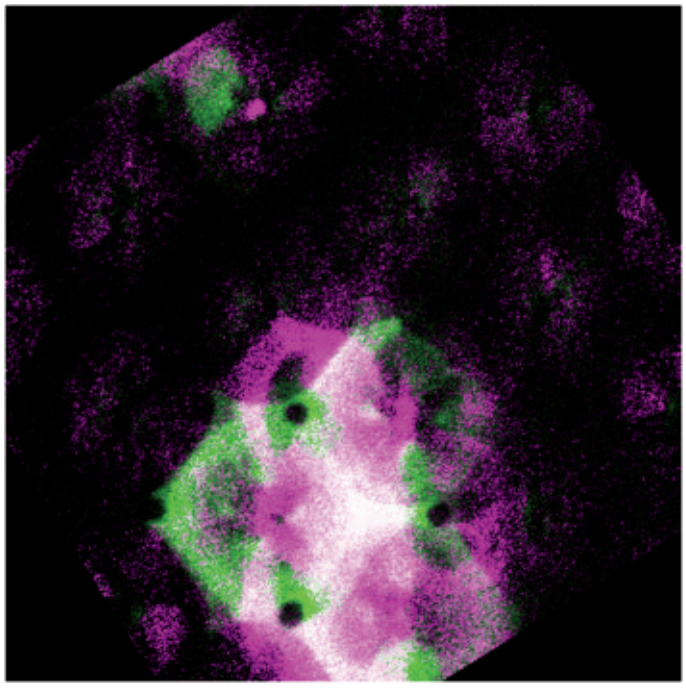

Movie 5. Lateral pathways of retinal calcium waves. Related to Fig. 2, R and S, and fig. S2F. Representative recordings of retinal calcium wave propagation across multiple ommatidia during stage 2 using *UAS-GCaMP6s* driven by *longGMR-GAL4.* Imaging performed with two-photon microscopy (920-nm excitation). Z-stacks were acquired every 4 s. Apical and basal layers are color-coded as green (apical) and magenta (basal).

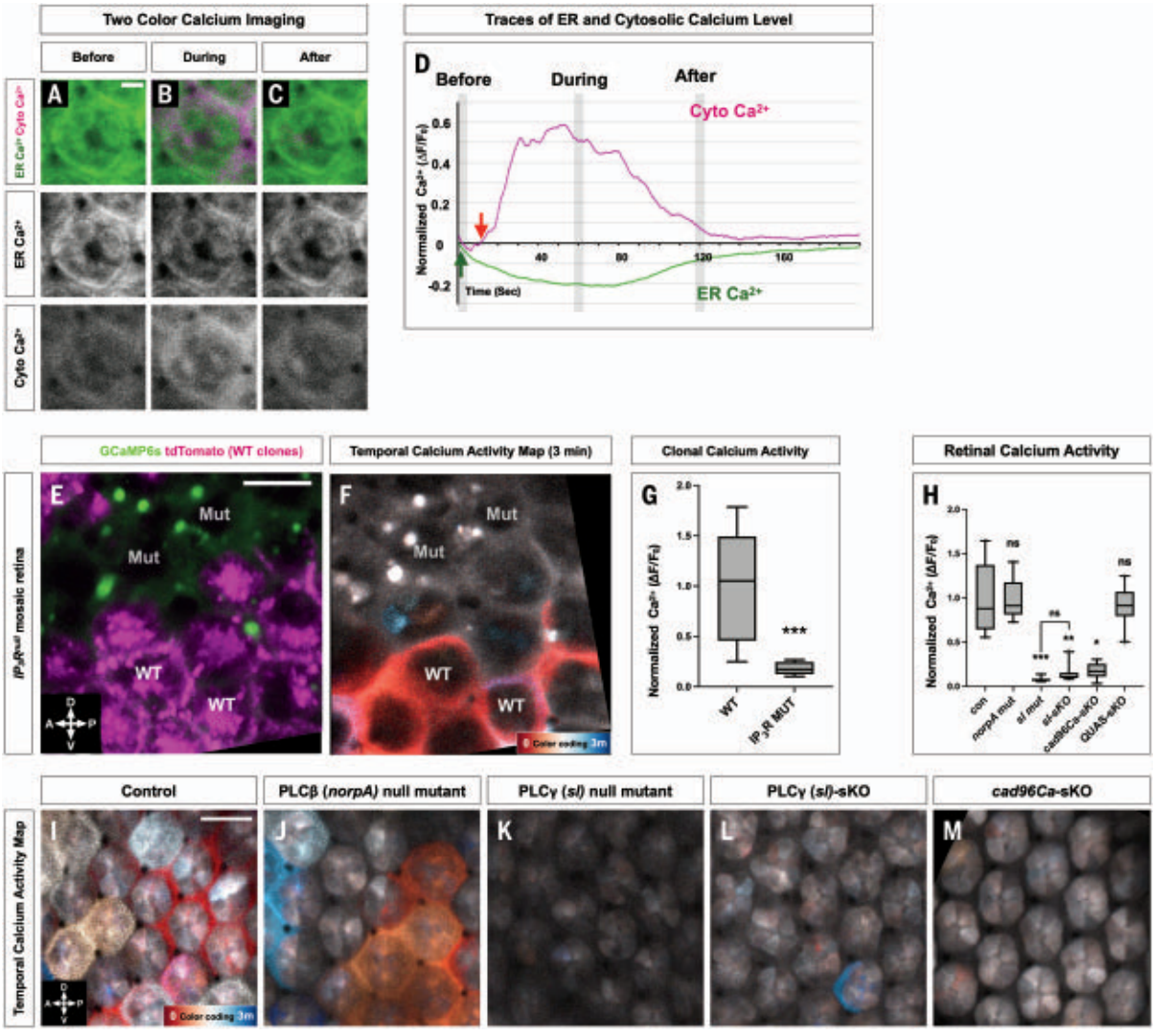

Fig. 3. Cad96Ca-PLCγ-IP$_3$R signaling triggers ER calcium release, initiating retinal waves. (**A** to **C**) Dual-color calcium imaging before, during, and after retinal waves, selected at 60-s intervals. Red, cytosolic jRGECO1a; green, ER-targeted GCaMP6. Imaging was performed at 1-s intervals at the retinal center during stage 2. Scale bar, 5 μm. See also Movie 6. (**D**) Calcium traces during retinal waves. Shaded regions correspond to snapshots in (A) to (C). Arrows indicate wave initiation in each channel. (**E** and **F**) IP$_3$R mutant mosaics. (E) Wild-type (WT) (magenta) versus mutant (Mut) (nonlabeled) clones. (F) Three-minute temporal activity maps using *longGMR-GAL4>UAS-GCaMP8s* in mosaic retina. Scale bar, 10 μm (E and F). See also Movie 7. (**G**) Quantification of calcium activity in wild-type versus mutant ommatidia from IP$_3$R mosaics. $n \geq 8$ ommatidia from 3 retinas. ***$P < 0.001$. Error bars, SD. (**H**) Quantification of retinal wave activity from (I) to (M). $n \geq 10$ retinas. ns, $P \geq 0.05$; *$P < 0.05$; **$P < 0.01$; ***$P < 0.001$. Error bars, SD. (**I** to **M**). Retinal calcium waves displayed as color-coded 3-min temporal activity maps in control (I), *norpA* (J), *sl* (K), *sl-sKO* (L), and *cad96Ca-sKO* (M). sKO, CRISPR-mediated somatic knockout. Scale bar, 10 μm (I to M). See also Movie 8.

ER calcium release is cell-autonomously required for both the triggering and propagation of retinal calcium waves, likely through the sustained release of calcium from the ER in response to stimulation of IP$_3$R.

We then investigated phospholipase C (PLC) that generates IP$_3$ from phosphatidylinositol 4,5-bisphosphate (PIP$_2$) (*54*). Among the five *Drosophila* PLCs, only PLC-β (*norpA*) and PLC-γ (*sl*) are expressed in the retina (*55*, *56*). *norpA* null mutants exhibited normal wave activity, but no waves were observed in *sl* null mutants (Fig. 3, H, J, and K, and Movie 8). Although *sl* null mutants are viable, they exhibit impaired retinal growth (fig. S3, E and H) (*56*). We therefore used longGMR-Cas9 to generate *sl* CRISPR-mediated somatic knockout (sKO) in mid-pupal retinas (*57*), bypassing early retinal development. *sl* somatic knockout retinas exhibited slightly reduced growth (fig. S3, F and H) but showed a 90% decrease in waves (Fig. 3, H and L, and Movie 8D), confirming the specific role of PLC-γ in wave activity.

RTKs are upstream regulators of PLC-γ signaling (*58*). We screened 15 RTKs expressed in the developing retina (*59*) via somatic knockout, RNA interference (RNAi), or dominant negative transgenes (table S1). Only *cad96Ca* (*stit*) was necessary for retinal wave initiation without altering gross retinal morphology (Fig. 3, H and M; fig. S3, G and H; and table S1). *cad96Ca* is a cadherin-like RTK involved in wound healing (*60*, *61*) with no known role in retinal development. *cad96Ca*-GAL4-driven green fluorescent protein (GFP) revealed expression in all support cells, but not PRs (fig. S3, I to L). These results suggest that Cad96Ca activates the PLC-γ–IP$_3$R pathway, inducing ER-release calcium activity during retinal waves.

Retinal waves propagate through gap junctions mediated by cell–specific combinations of innexins.

Gap junctions mediate intercellular calcium wave propagation (*21*, *62*, *63*). In *Drosophila*, eight *innexins* (*inx*) encode subunits that assemble into

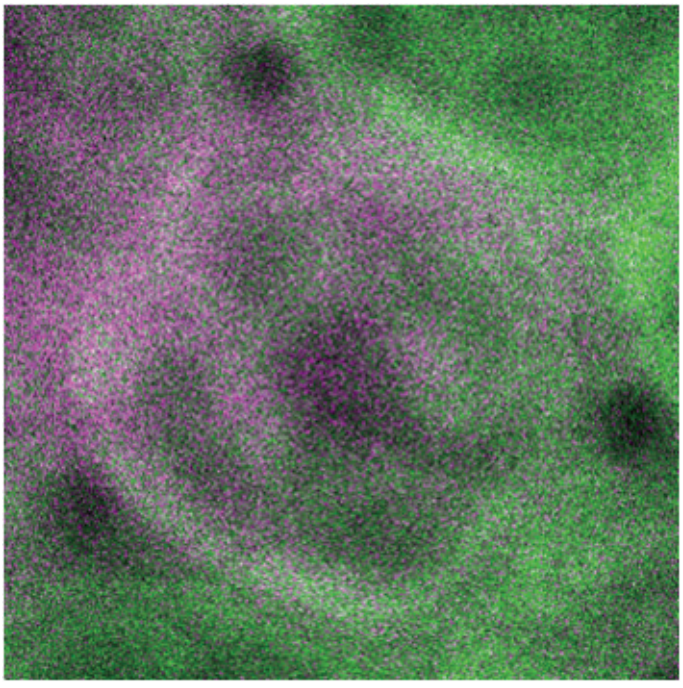

Movie 6. Dual-color calcium imaging of ER-released calcium activity during retinal waves. (**A** to **C**) Related to Fig. 3, A to C. Representative recording of retinal calcium waves during stage 2 using *UAS-ER-GCaMP6* and *UAS-jRGECO1a* driven by *longGMR-GAL4*. Imaging performed with confocal microscopy (488-nm and 561-nm excitation). Time-lapse imaging was acquired as Z-stacks at 1-s intervals. Dual-color imaging with ER-targeted GCaMP (green) and cytosolic jRGECO1a (red) (A), ER-targeted GCaMP alone (B), and cytosolic jRGECO1a alone (C).

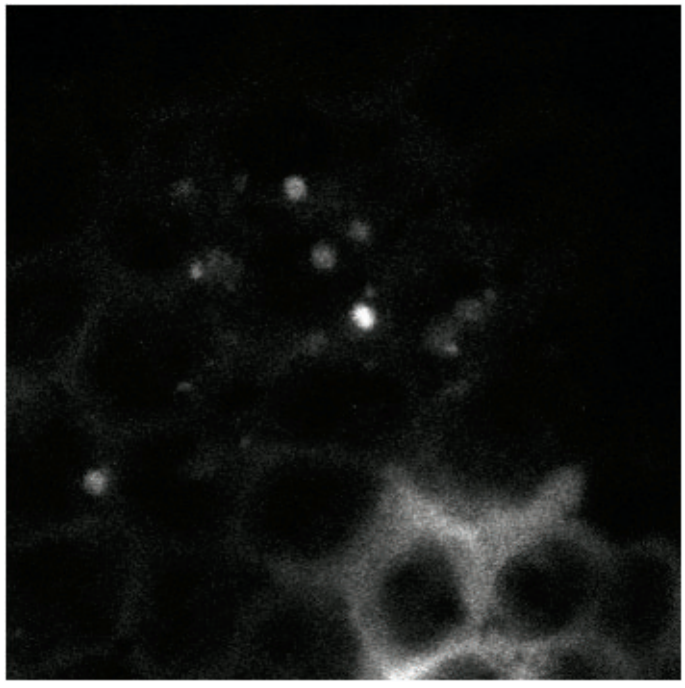

Movie 7. Calcium imaging of IP_3R clonal retinas during retinal waves. Related to Fig. 3F. Representative recording of retinal calcium waves using *UAS-GCaMP8s* driven by *longGMR-GAL4* in *IP_3R* clonal retinas during stage 2. Imaging performed with two-photon microscopy (920-nm excitation). Time-lapse imaging was acquired as Z-stacks at 5-s intervals.

octameric hemichannels forming gap junction channels at cell junctions (*64*–*66*), with some expressed in the developing retina (*66*, *67*). Among them, our immunostaining showed Inx1 (*ogre*), Inx2, and Inx3 at non-neuronal retinal cell junctions at 40 hAPF (Fig. 4, A to I, and fig. S4, A to F) (*66*–*68*). They were localized in puncta that represent gap junction plaques, specialized clusters of gap junction channels, adjacent to the junctional marker Disc large1 (Dlg1) (Fig. 4, A to E) (*69*, *70*). Super-resolution stimulated emission depletion (STED) microscopy imaging confirmed that Inx2 and Inx3 were strictly confined to gap junction plaques (Fig. 4, A to D), whereas Inx1, though mainly at gap junction plaques, was also seen elsewhere in the cell (Fig. 4E, Inx1 row). By contrast, we did not detect Inx4, 5, 6, 7, or 8 at retinal cell junctions (fig. S4, G to K). Inx8 (*shakB*) was only detected at 48 hAPF, after the waves, and only in synapses within the optic lobe (fig. S4, L to N) (*66*, *67*). Retinal waves remained unchanged in *inx8* mutants (fig. S4, O to Q, and movie S3). Given that Inx2 and Inx3 were absent from gap junction plaques in PR somas (fig. S4, D and E, PR layer rows), this suggests that neither Inx8 nor PRs are involved in retinal waves.

To selectively inhibit *innexin* expression at mid-pupal stages, we generated somatic knockouts using longGMR-Cas9. Immunostaining confirmed the near-complete loss of the targeted *innexins* after somatic knockout (Fig. 4, F to H, Inx1–3 rows, and fig. S4, W to Y) in 40 hAPF retinas. Somatic knockout of *inx1*, *inx2*, *or inx3* did not alter cone cell activation (Fig. 4Q and fig. S4Z), but each disrupted stereotyped steps of wave propagation (Fig. 4, J to P and R; fig. S4Z; and Movie 9):

1) Somatic knockout of *inx2* drastically disrupted the propagation of all waves (Fig. 4, L and O to R, and fig. S4Z).

2) Somatic knockout of *inx*1 only exhibited a slight decrease of the vertical and lateral wave pathways (Fig. 4, K and O to R, and fig. S4Z).

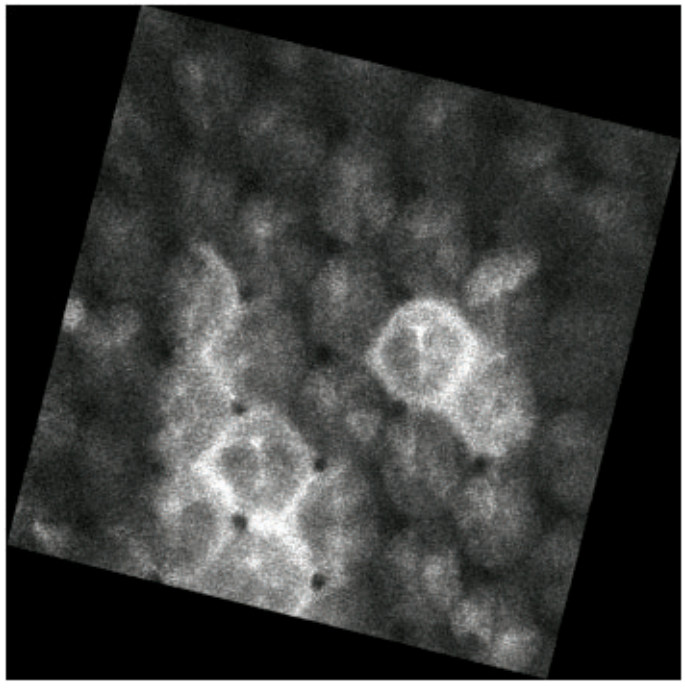

Movie 8. Calcium imaging of mutants affecting wave initiation. (**A** to **E**) Related to Fig. 3, I to M. Representative recordings of retinal calcium waves using *UAS-GCaMP6s* driven by *longGMR-GAL4* in control (A), *norpA* mutants (B), *sl* mutants (C), *sl*-sKO (D), and *cad96Ca*-sKO (E) during a 5-min peak intensity window at stage 2. Imaging performed with two-photon microscopy (920-nm excitation). Time-lapse imaging was acquired as Z-stacks at 5-s intervals.

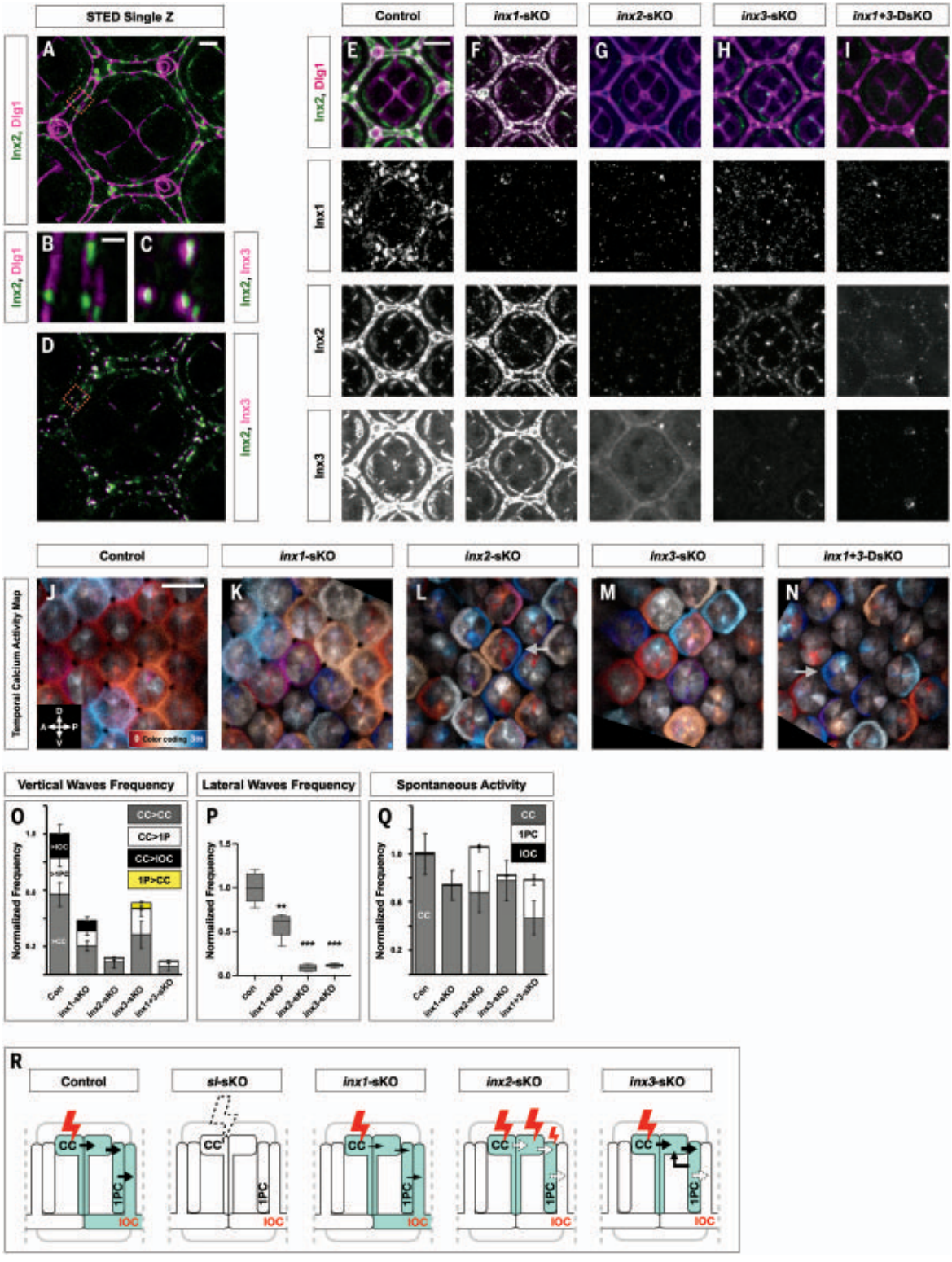

Fig. 4. Retinal waves propagate through gap junctions using cell type–specific combinations of Innexins. (**A** to **D**) STED imaging of a single ommatidium at 40 hAPF stained for Dlg1 and Inx2 (A and B) or Inx2 and Inx3 (C and D). Insets from (A) and (D) show the red-box regions in (B) and (C), respectively. Scale bars, 2 μm (A and D), 0.5 μm (B and C). (**E** to **I**) Immunostaining for Inx1, Inx2, and Inx3 at 40 hAPF in control (E), *inx1-sKO* (F), *inx2-sKO* (G), *inx3-sKO* (H), and *inx1+3-double sKO* (I). Green marks innexins, and magenta marks Dlg1. Images are Z-stacks of the apical retinal layer. Scale bar, 5 μm (E to I). (**J** to **N**) Retinal calcium wave activity as 3-min temporal activity maps in control (J), *inx1-sKO* (K), *inx2-sKO* (L), *inx3-sKO* (M), and *inx1+3-DsKO* (N) during stage 2. Arrows in (L) and (N) indicate unsynchronized cone and pigment cell firing. Scale bar, 10 μm (J to N). See also Movie 9. (**O**) Quantification of vertical pathway frequency in *inx* mutants during stage 2. $n \geq 5$ retinas. Error bars, SD. Detailed statistics are in fig. S4Z. (**P**) Quantification of lateral pathway frequency in *inx* mutants during stage 2. $n \geq 5$ retinas. ns, $P \geq 0.05$; $^{**}P < 0.01$; $^{***}P < 0.001$. Error bars, SD. (**Q**) Quantification of spontaneous cell-autonomous activity by cell type in *inx* mutants during stage 1. $n \geq 5$ retinas. Error bars, SD. Detailed statistics are in fig. S4Z. (**R**) Diagram illustrating vertical propagation pathway in *inx* mutants.

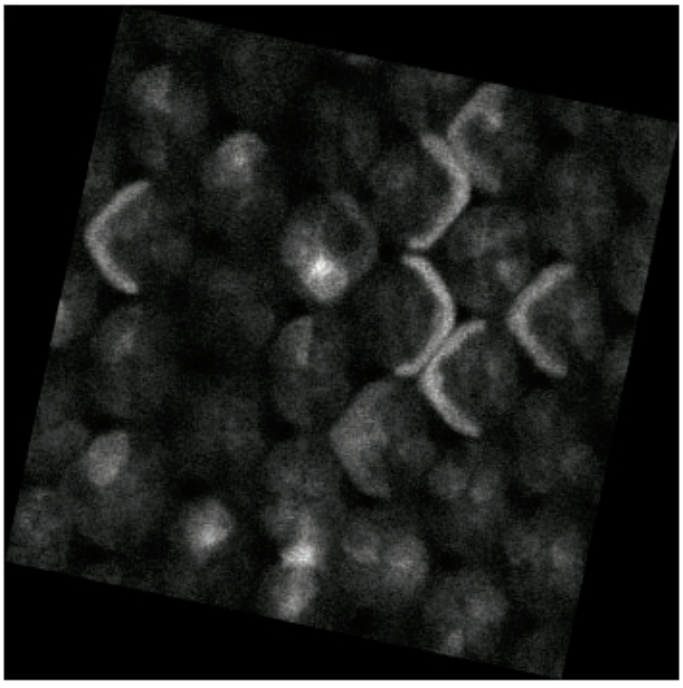

Movie 9. Calcium imaging of *inx* mutants during retinal waves. (**A** to **E**) Related to Fig. 4, J to N. Representative recordings of retinal calcium waves using *UAS-GCaMP6s* driven by *longGMR-GAL4* in control (A), *inx1*-sKO (B), *inx2*-sKO (C), *inx3*-sKO (D), and *inx1+3*-DsKO (E) during a 5-min peak intensity window at stage 2. Imaging performed with two-photon microscopy (920-nm excitation). Time-lapse imaging was acquired as Z-stacks at 5-s intervals.

3) Somatic knockout of *inx3* retinas retained the initial vertical propagation from cone cells to primary pigment cells, but the propagation from primary pigment cells to interommatidial cells was severely disrupted (Fig. 4, M, O, and R, and fig. S4Z), resulting in a substantial reduction of the lateral pathway (Fig. 4P). Somatic knockout of *inx3* also exhibited reverse propagation from primary pigment cell to cone cell (Fig. 4O), which was not observed in wild type.

4) Because somatic knockout of *inx1* and *inx3* each caused partial wave disruptions (Fig. 4, K, M, and O), we examined their double somatic knockout (*inx1+3*-DsKO) (Fig. 4I), which led to complete disruption of wave propagation similar to somatic knockout of *inx2* (Fig. 4, N to Q, and fig. S4Z).

5) Somatic knockout of *inx2*, *inx3*, and the double somatic knockout of *inx1* and *inx3* caused little or no decrease in spontaneous firing in cone cells between 37 and 40 hAPF (Fig. 4Q and fig. S4Z). However, infrequent ectopic firing was also observed in primary pigment cells and interommatidial cells (Fig. 4Q), suggesting that the waves normally suppress ectopic activity in non-cone cells.

To elucidate the distinct roles of each innexin, we focused on the formation of gap junction plaques (Fig. 4, A to D) that are critical for organizing gap junction channels (*69*, *71*). Gap junction plaques disappeared in *inx2* somatic knockout retinas, leading to dispersed staining of Inx1 and Inx3 outside of cell junctions (Fig. 4G and fig. S4, W to Y), showing that Inx2 is important for their junctional localization (*68*). However, gap junction plaques persisted in *inx1* somatic knockout retinas but were slightly reduced in size on the basis of Inx2 and Inx3 staining (Fig. 4F and fig. S4, W to Y). In *inx3* somatic knockout retinas, gap junction plaques were specifically lost in interommatidial cells, consistent with impaired lateral wave propagation, whereas smaller gap junction plaques remained in other cell types (Fig. 4H and fig. S4, W to Y). In the double somatic knockout retina of *inx1* and *inx3*, gap junction plaques were absent at all cell junctions, similar to *inx2* somatic knockout (Fig. 4I and fig. S4, W to Y). As expected, whenever gap junction plaques disappeared upon somatic knockout of a given *innexin*, the nontargeted innexins were still detectable but were dispersed outside of cell junctions (Fig. 4G, Inx1 and Inx3 rows, and 4I, Inx2 row). These data indicate that each cell type has a specific set of innexins contributing to gap junction plaques.

In summary, our data highlight the distinctive roles of innexins in regulating retinal wave activity through the formation of gap junction plaques. All retinal support cells require Inx2 for the formation of gap junction plaques that contain Inx1–3, whereas Inx3 is only required in interommatidial cells. Inx1 has a minor impact on its own but compensates for the absence of Inx3 in cone cells and primary pigment cells. When gap junction plaques were disrupted, the corresponding wave propagation pathway was also disrupted (Fig. 4R), illustrating the importance of precise innexin combinations in plaques for directing waves across distinct retinal cell types.

Retinal waves regulate myosin II–driven apical remodeling that scales with ommatidial size

The ventro-anterior bias in retinal waves corresponds to a region with larger ommatidia (Fig. 5, A and E), established by 24 hAPF and persisting through the wave period (fig. S5, A to C). These larger ommatidia showed stronger and prolonged calcium activity (fig. S5, D and E). To understand how this differential wave activity might influence the development of ommatidia in this region, we compared ommatidia before and after the waves (Fig. 5, F, G, and M to P). Prior to the waves, larger ommatidia displayed wider interommatidial gaps formed by the apical domains of interommatidial cells (Fig. 5F, top and bottom, and M to P). The 20% largest ventro-anterior ommatidia had wider boundaries of interommatidial cells than the 20% smallest dorso-posterior (DP) ommatidia (Fig. 5, O and P). After the waves, interommatidial gaps contracted throughout the retina (Fig. 5, O and P), whereas ommatidial size slightly increased (fig. S5F). Larger ommatidia with initially wider gaps exhibited stronger boundary contraction (Fig. 5, O and P). As a result, interommatidial boundaries became uniformly narrow across the retina (Fig. 5, G and P), despite the regional variability in ommatidial size (fig. S5C). Multicolor Flp-out–based single-cell labeling confirmed that this contraction arose from apical morphogenesis of interommatidial cells (fig. S5, G, K, O, and P).

To assess whether retinal waves were required for this size-dependent contraction of ommatidial boundaries, we analyzed mutants with disrupted wave activity, either across all retinal cells (*sl* somatic knockout retinas) or specifically in interommatidial cells (*inx3* somatic knockout retinas) (Fig. 5, B, C, and E). Before retinal waves, ommatidial size distribution and boundary morphology were similar to control in both retinas (Fig. 5, B and C, bottom panels, and fig. S5, H and J, top panels). However, after retinal waves, boundary contraction failed in both mutants, resulting in ommatidial boundaries that remained immature and wider, independent of ommatidial size (Fig. 5, H, I, and Q, and fig. S5, H and J, bottom panels, detailed in fig. S6A), suggesting that retinal waves are essential for ommatidial boundary contraction.

To further test how retinal waves coordinate boundary contraction in relation to ommatidial size, we analyzed *inx1* somatic knockout retinas, which exhibit uniformly low calcium activity across all ommatidia, uncoupling calcium signaling from ommatidial size (Fig. 5, D and E). As a result, boundary contraction failed selectively in the larger ventral-anterior ommatidia, whereas smaller ommatidia still showed proper contraction (Fig. 5, J and Q, and fig. S6A). This suggests that wider initial boundaries require proportionally stronger wave activity to achieve uniform boundary maturation.

To directly test whether retinal waves drive apical boundary contraction proportionally to their activity, we manipulated calcium activity using the heat-activated calcium channel TrpA1 (*72*, *73*). In *sl* somatic knockout retinas, weak heat induction of TrpA1 (15 min) during the

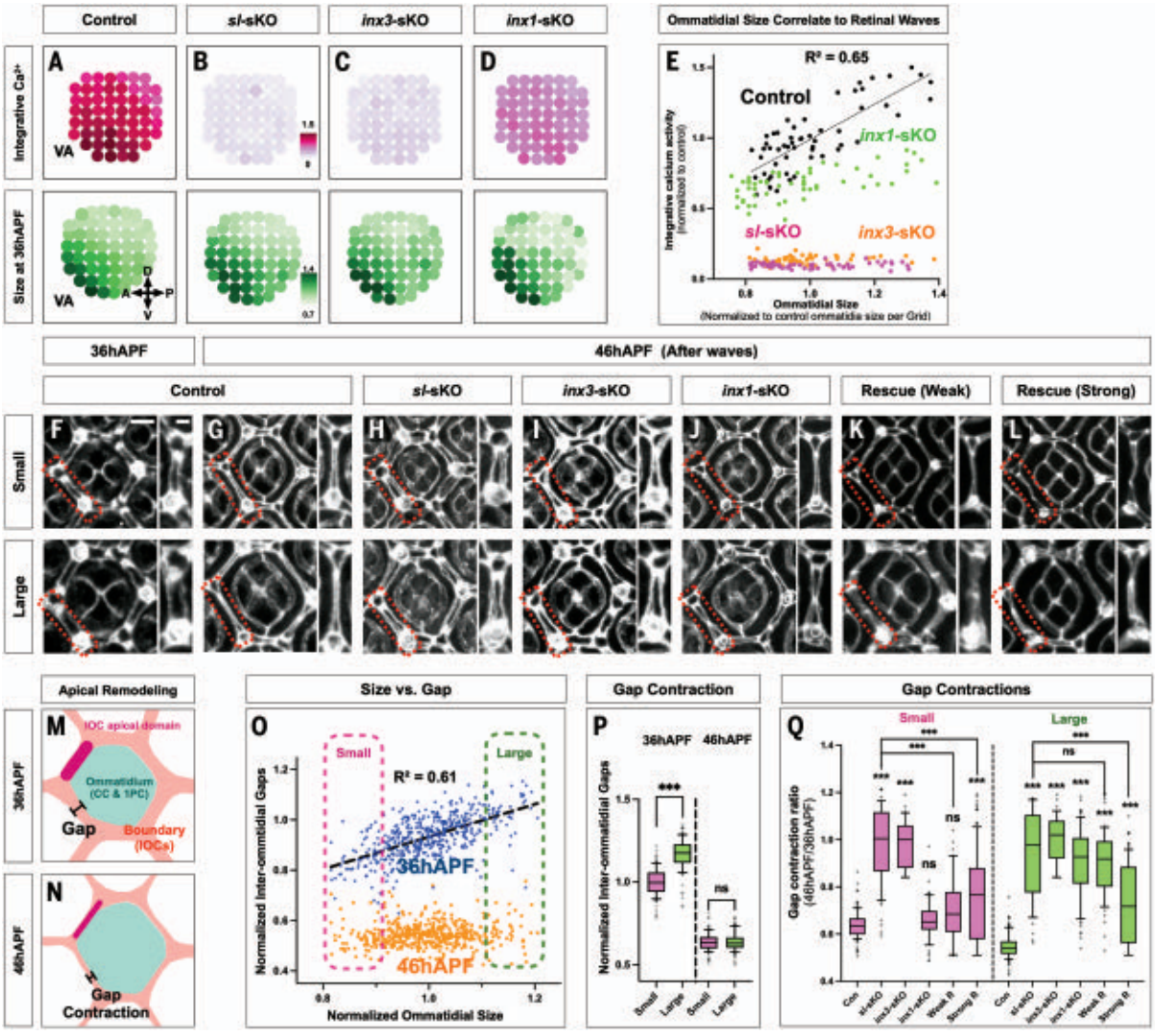

Fig. 5. Retinal wave activity coordinates size-dependent ommatidial remodeling. (**A** to **D**) Ommatidial 8 × 8 grids showing integrated calcium activity from retinal waves (top) and ommatidial size distributions (bottom) in control and mutants. Average intensity of integrative calcium activity and mean ommatidial size per grid point are color-coded in magenta and green, respectively. $n \geq 11$ retinas. (**E**) Scatter plot of normalized ommatidial size (*x* axis) versus calcium signals (*y* axis). Each dot represents a single grid point from (A) to (D). Genotypes are color-coded. The black line shows regression in control. (**F** to **L**) Dlg1 immunostaining of single ommatidia at 36 and 46 hAPF. Top panels show small ommatidia (0 to 20%, dorsal-posterior region) and bottom panels show large ommatidia (80 to 100%, ventral-anterior region). Red insets highlight interommatidial boundary gaps, enlarged at right. Scale bars, 5 μm (F to L), 2 μm (insets). (**M** and **N**) Diagrams of ommatidial apical remodeling at 36 hAPF (M) and 46 hAPF (N). Measurement bars indicate interommatidial gap size at boundaries. (**O**) Scatter plot of ommatidial size (*x* axis) versus gap size (*y* axis) at 36 hAPF (blue) and 46 hAPF (orange) from control (F and G). Each dot represents a single ommatidium. Values are normalized to the average of 36 hAPF. The regression line is shown for 36 hAPF. $n \geq 492$ ommatidia from ≥ 16 retinas per stage. Dashed boxes indicate size groups for (P). (**P**) Quantification of interommatidial gaps in small and large size groups from (O). $n \geq 101$ ommatidia from ≥ 16 retinas per stage. ns, $P \geq 0.05$; ***$P < 0.001$. Error bars, SD. (**Q**) Quantification of gap contraction ratio between 36 and 46 hAPF in small (magenta) and large (green) ommatidia from (F to L). The *y* axis shows the ratio of gap size at 46 hAPF to the average at 36 hAPF for each size group and genotype. $n \geq 36$ ommatidia from ≥ 16 retinas. ns, $P \geq 0.05$; ***$P < 0.001$. Error bars, SD. Detailed statistics are in fig. S6A.

endogenous wave period (37 hAPF) only rescued boundary contraction in smaller ommatidia, whereas larger ommatidia failed to fully contract (Fig. 5, K and Q, and fig. S6A). By contrast, stronger calcium induction (40 min) rescued boundary contraction in larger ommatidia (Fig. 5L, bottom, and Q, and fig. S6A) but caused abnormal contraction in smaller ommatidia, resulting in narrow and wrinkled boundaries (Fig. 5L, top). These results suggest that the higher intensity of calcium signaling due to more frequent retinal waves drives stronger apical contraction and ensures uniform ommatidial organization.

IP_3R-mediated calcium release activates myosin light-chain kinase, which phosphorylates nonmuscle myosin II to form an actomyosin network, promoting contractility (*74*, *75*). To examine myosin II activation in response to calcium, we performed time-lapse imaging of retinas expressing GFP-tagged Sqh (myosin II regulatory light chain). The Sqh-GFP signal was observed primarily as puncta of varying sizes on the apical side of the retina (Fig. 6A and fig. S6, B and C), indicating discrete actomyosin foci representing localized contractile activity (*76*). We quantified these dynamics by calculating the coefficient of variation of Sqh-GFP intensity along interommatidial boundaries (*77*). During retinal waves, this coefficient progressively increased, indicating the formation of larger and more organized actomyosin clusters within the interommatidial boundaries (Fig. 6, A to E and J), consistent

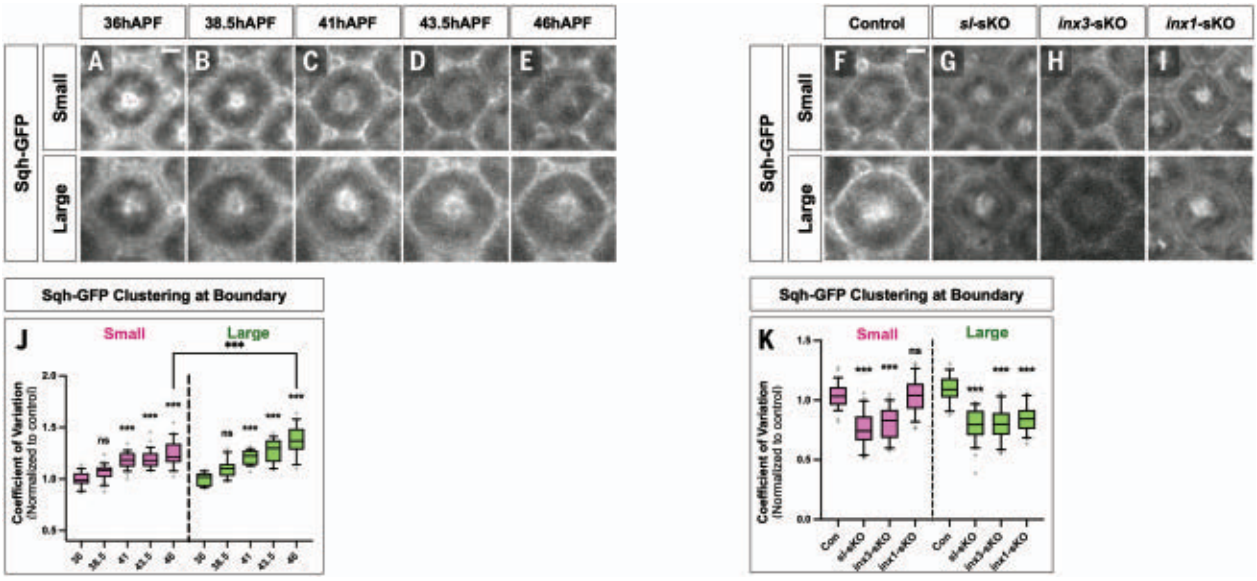

Fig. 6. Retinal wave activity correlates with size-dependent Myosin II clustering. (**A** to **E**) Time-lapse images of single ommatidia from 36 to 46 hAPF at 2.5-hour intervals showing Sqh-GFP puncta. Top panels show small ommatidia, and bottom panels show large ommatidia. Scale bar, 5 μm (A to E). (**F** to **I**) Sqh-GFP puncta in single ommatidia at 46 hAPF. Top panels show small ommatidia, and bottom panels show large ommatidia. Genotypes indicated. Scale bar, 5 μm (F to I). (**J**) Quantification of the coefficient of variation of Sqh-GFP within interommatidial boundaries from (A) to (E). $n \geq 25$ ommatidia from ≥5 retinas per size groups. ns, $P \geq 0.05$; $^{**}P < 0.01$; $^{***}P < 0.001$. Error bars, SD. (**K**) Quantification of the coefficient of variation of Sqh-GFP within interommatidial boundaries at 46 hAPF from (F) to (I). $n \geq 22$ ommatidia from ≥4 retinas per genotype. ns, $P \geq 0.05$; $^{***}P < 0.001$. Error bars, SD.

with wave-driven apical contraction of interommatidial cells. Notably, Sqh-GFP aggregation was stronger in interommatidial cells from larger ommatidia (Fig. 6, A to E, bottom panels, and J), supporting our model that higher local calcium signals drive greater contractile forces, leading to robust apical contraction of interommatidial cells. Actomyosin network formation was markedly impaired in both *sl* and *inx3* somatic knockout retinas (Fig. 6, G, H, and K), whereas *inx1* somatic knockout retinas exhibited reduced Sqh-GFP clustering selectively in large ommatidia (Fig. 6I, bottom, and K).

To examine the temporal relationship between calcium activity and structural remodeling, we overlaid retinal wave timing, Sqh-GFP clustering, and interommatidial cell boundary contraction (fig. S6D). Whereas minor morphological changes occurred during retinal waves, major structural remodeling was only complete by 46 hAPF, suggesting a temporal lag of ~1 to 5 hours between the initial Ca^{2+} rise and detectable morphological changes.

Altogether, these results reveal that retinal waves coordinate apical contraction by scaling actomyosin network assembly proportionally to ommatidial size and boundary width, ensuring effective boundary contraction for uniform retinal morphogenesis.

Retinal wave activity ensures eye uniformity in adults

To determine the functional role of retinal waves, we investigated how disrupted retinal waves during the mid-pupal stage affect adult retinal architecture. By 72 hAPF, the apical domains of interommatidial cells establish distinct ommatidial boundaries (Fig. 7, A and C, red arrow), acting as the basal footings of the corneal lens (Fig. 7B). In the adult eye, these footings are also critical for forming pseudocones, transparent extracellular structures positioned between the lens and photoreceptor neurons (Fig. 7, H and I) (*78*), thereby ensuring precise light transmission to PRs.

We quantified spatial organization of these structures in a single plane at the pseudocone layer (Fig. 7, H to L). In wild type, pseudocone size correlated with ommatidial size: The ventro-anterior (VA) region contained consistently larger pseudocones than the dorso-posterior (DP) region (Fig. 7T, top and bottom, and M). By contrast, *sl* somatic knockout retinas showed severely disrupted pseudocone organization, although the outer lens surface appeared mostly normal (fig. S3F). Lens footings at 72 hAPF were defective as anticipated from earlier interommatidial cell defects (Fig. 7D), resulting in irregular pseudocone arrangements in adult retinas (Fig. 7, P and U). Pseudocone sizes remained comparable (Fig. 7M), but their variability increased in the DP and VA regions (Fig. 7, U and N). These results show that retinal waves are essential for uniformly structured pseudocones by properly maturing interommatidial cells during mid-pupal development.

Mutants with varying retinal wave activity further supported this conclusion. In *inx1* somatic knockout retinas, lens footings and pseudocones remained normal in the DP region, whereas variability greatly increased in the VA region (Fig. 7, Q, V, and N). TrpA rescue experiments in *sl* somatic knockout retinas revealed regional differences: Weak rescue (15-min heat induction) selectively improved lens footing structure and pseudocone uniformity in the DP region but not in the VA region (Fig. 7, R, W, and N). Strong rescue (40-min heat induction) improved pseudocone uniformity in both DP and VA regions (Fig. 7, X, S, and N), although lens footings in the DP region remained defective (Fig. 7, S and X), matching interommatidial cell defects seen in smaller ommatidia at 46 hAPF (Fig. 5L, top).

Overall, these results demonstrate that retinal waves coordinate calcium-driven apical morphogenesis in proportion to ommatidial size, ensuring uniform retinal architecture essential for precise visual function. This highlights how synchronized calcium signaling directs tissue patterning (fig. S6E).

DISCUSSION

We described here the intricate dynamics of calcium activity due to retinal waves during early *Drosophila* retinal development and showed how it shapes retinal architecture by controlling the maturation of interommatidial cells. This provides insight into how directed synchronized calcium activity orchestrates structural patterning in tissues.

Regional variations in ommatidial size are evolutionarily conserved across fly species: Larger ventral ommatidia have larger lenses that

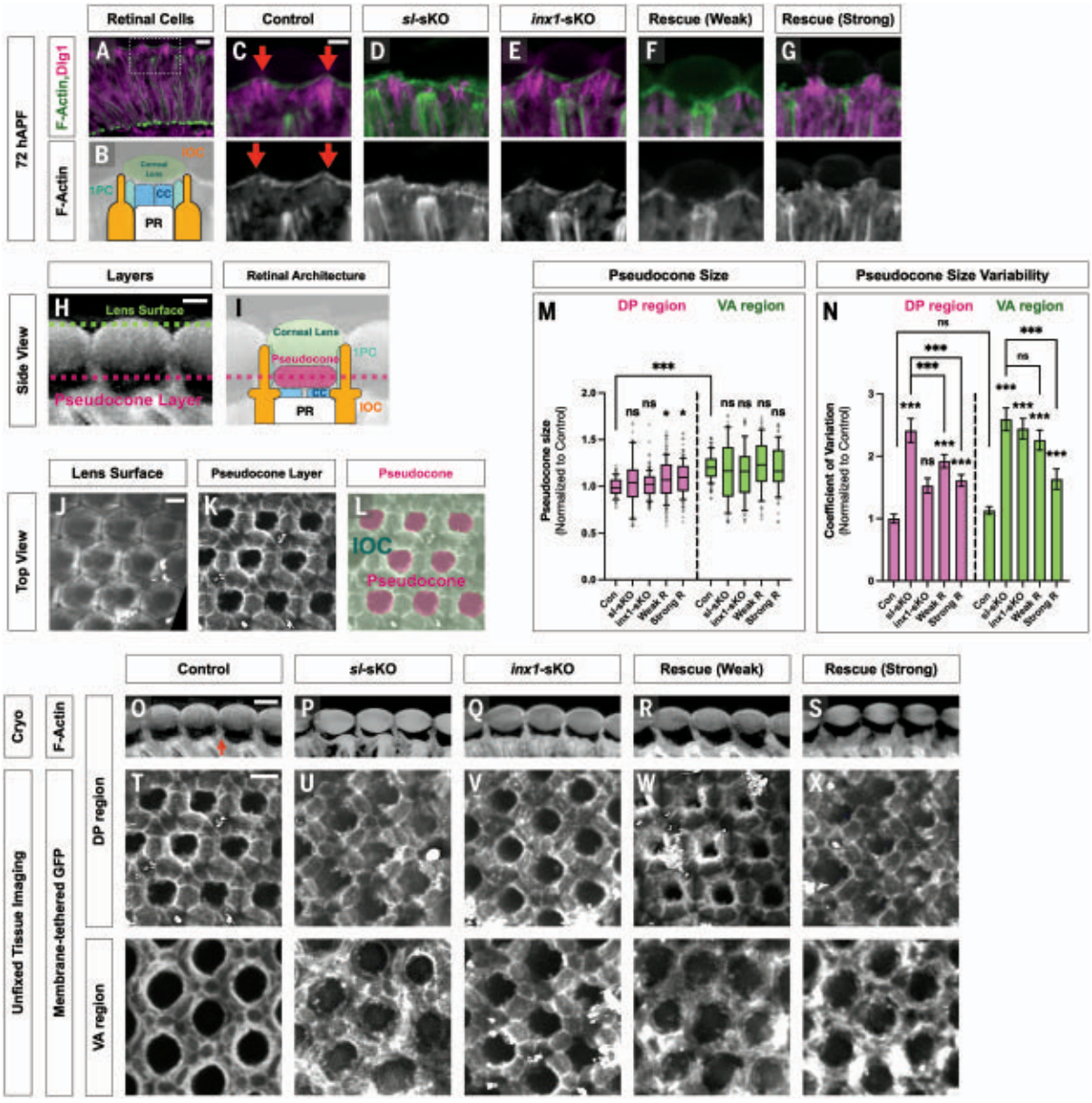

Fig. 7. Retinal wave activity ensures adult eye uniformity. (**A** to **G**) Seventy-two-hour APF retinal surfaces from side view. (A) shows the whole retina section, with an inset of the apical surface in (C). (B) shows a diagram of the retinal cellular configuration, with cell types labeled and color-coded consistently with Fig. 7I. (C) to (G) show the apical surface of an ommatidium, with red arrows in (C) indicating primitive lens footings formed by IOC tips. Images were obtained by confocal imaging of cryosections labeled with phalloidin (green in top panels, gray in bottom panels) and Dlg1 (magenta) to mark actin filaments and cell junctions, respectively. Cryosections were taken from the dorsal-posterior region for optimal sectioning. Z-stack thickness, 5 μm. Scale bar, 10 μm (A), 5 μm (B to G). (**H** and **I**) Diagrams of adult retinal surface from side view, corresponding to (O) to (S). Scale bar: 5 μm (H and I). (**J** to **L**) Adult retinal surface from top view. (J and K) Images and (L) diagram with pseudocones (magenta) and IOCs (green). Scale bar, 10 μm (J to L). (**M**) Quantification of pseudocone size from (T) to (X) normalized to control. $n \geq 70$ pseudocones from ≥15 retinas. ns, $P \geq 0.05$; *$P < 0.05$; ***$P < 0.001$. Error bars, SD. (**N**) Variability of pseudocone size from (T) to (X) measured by coefficient of variation. $n \geq 70$ pseudocones from ≥15 retinas. Permutation test used. Error bars, SD of bootstrap resampling. ns, $P \geq 0.05$; ***$P < 0.001$. (**O** to **S**) Adult retinal surface from side view. Cryosections were labeled with phalloidin. Red arrows in (O) show lens footings. Dorsal-posterior region selected. Z-stack, 5 μm. Scale bar, 10 μm (O to S). (**T** to **X**) Adult retinal surface from top view. Top panels show dorsal-posterior region, and bottom panels show ventral-anterior region. Two-photon images of unfixed adult retinas were labeled with membrane-tethered GFP at the pseudocone layer (L). Z-stack thickness, 10 μm. Scale bar, 10 μm (T to X).

enhance light capture from images of the ground and improve visual sensitivity, whereas smaller dorsal ommatidia increase resolution (*39*, *40*). Despite this regional heterogeneity in ommatidial size, interommatidial boundaries remain uniformly spaced across the *Drosophila* retina and maintain a smooth and regular optical surface, ensuring proper lens alignment in the adult eye. Retinal waves mediate compensatory interommatidial cell maturation, ultimately normalizing interommatidial spacing across the retina.

In the *Drosophila* visual system, three phases of synchronized calcium activity shape development: Two non-neuronal retinal waves are linked to tissue morphogenesis and neuronal synchronized activity is critical for synaptic wiring (*33*, *62*, *79*, *80*). Notably, early non-neuronal activity (early waves) precedes neuronal activity, highlighting a developmental sequence across different cell types. A comparable sequence is observed in vertebrates, where gap junction–mediated calcium waves in the retinal pigment epithelium of the chick eye and radial

glia of the rodent neocortex precede synchronized neuronal activity of corresponding tissue during synaptogenesis (*13*, *14*, *21*). This progression from non-neuronal to neuronal calcium signaling positions *Drosophila* as a valuable model for studying fundamental principles of nervous system development.

The early retinal waves that we observed occur at a precise stage, requiring coordination with other developmental events. This activity is initiated via the Cad96Ca RTK, which suggests that an extrinsic signal activating it determines the timing of retinal waves. The Cad96Ca ligand is unknown, but recent studies suggest that juvenile hormone can directly activate Cad96Ca in cotton bollworm and *Drosophila* S2 cells (*81*). Although the canonical juvenile hormone pathway involves the nuclear receptors Met and Gce that regulate juvenile hormone-responsive genes, Cad96Ca might be a membrane receptor for juvenile hormone, initiating rapid signaling independent of nuclear transcription. Systemic juvenile hormone amounts exhibit multiple peaks, including one at mid-pupal stages coinciding with the retinal wave period (*82*), raising the possibility that juvenile hormone directly activates Cad96Ca to trigger initial calcium activity of retinal waves.

Despite inherent differences in ommatidial size, proper visual function relies on a uniformly shaped pseudocone and lens in each facet. Optically, any mismatch between facet geometry and focal length broadens the point-spread function, reducing local contrast and spatial resolution (*83*, *84*). Although we have not yet assessed visual performance directly, our structural observations imply that such mismatches could produce a mosaic of slightly blurred and sharper retinal areas. Future studies could therefore combine quantitative, high-resolution analyses of adult eye architecture with region-specific behavioral assays such as optomotor or luminance tests (*39*, *85*–*87*). Such approaches may clarify the functional impact of irregular ommatidial packing and uncover how retinal calcium waves more broadly shape adult eye architecture and visual function.

Overall, our findings reveal three previously unappreciated features of calcium-based signaling during tissue morphogenesis. First, we identify Cad96Ca, an RTK, as a trigger of calcium activity. Second, we show that wave propagation is directed by a combinatorial "innexin-code" rather than simple anatomical connectivity. Third, we demonstrate that calcium signaling scales with epithelial unit size to ensure proportional morphogenetic remodeling. These insights suggest a general framework by which calcium-based intercellular communication orchestrates precise tissue patterning across diverse systems.

Materials and methods

A complete list of genotypes and reagents is provided in supplementary materials and tables.

***Drosophila* melanogaster strains and husbandry:** All *Drosophila melanogaster* stocks used are listed in the Materials section of the supplementary materials. Flies were reared on standard cornmeal medium under 12-hour light/dark cycles at 25°C, unless specified otherwise. Only male flies were analyzed to take advantage of enhanced efficacy of somatic knockout of major target genes (*sl*, *inx1*, *inx2*) located on the X chromosome. Pupal staging was performed by marking white pupae adhered to the dry wall of the vial, defined as 0 hAPF (hours after puparium formation). Pupae exhibiting significantly smaller body size were excluded from all experiments. Detailed genotypes corresponding to each figure are provided in Table S2.

Generation of transgenic animals: Transgenic constructs including longGMR-Cas9, customized guide RNAs, and GMR-GCaMP6s were generated by GenScript (Piscataway, NJ, USA). Insertions were synthesized into appropriate plasmid backbones (see table S3 for plasmid details). All transgenes were injected into corresponding attP sites by BestGene (Chino Hills, CA, USA) (see Materials section of the supplementary materials for transgene information). For guide RNAs, we used the pCFD5_w vector (*57*) with the U6:3 promoter to ubiquitously express six tandem guide RNAs, consisting of two duplicated sets targeting three selected sites within the first and second common exons (see table S3 for guide RNA details). This configuration produced a strong somatic knock-out effect across all tested targets, exemplified in fig. S4U.

Live imaging of intact pupal retina: Pupae within the selected developmental window were gently attached to double-sided tape (Scotch) on a slide in the desired position. The pupal case surrounding the head was minimally removed using fine-tip forceps without touching or pulling the pupal body. Samples were imaged using dry-objective lenses with a semi-open chamber surrounded by wet Kimwipes, utilizing either a Leica SP8 confocal microscope or an Olympus FV1000MPE2 two-photon microscope. Imaging was performed using 488 nm (confocal, Leica SP8) or 920 nm (two-photon, Olympus FV1000MPE2; Mai Tai Ti:Sapphire Lasers) excitation lasers.

All images were acquired with a 10x Leica dry-objective (confocal) or a 20x Olympus dry-objective (two-photon). For confocal imaging, the entire retina was scanned using a 10x objective with 3~4x zoom. For two-photon imaging, the flattest local area of each mounted retina, between the central and dorsal retinal regions, was scanned using a 20x objective with 8x zoom. Images were collected using LAS-X (Leica) at 1024-pixel × 800-pixel resolution or Fluoview (Olympus) at 512-pixel × 512-pixel resolution. Laser power was adjusted to the minimum necessary to avoid potential phototoxicity and photobleaching.

Images displaying ectopic local or global increases in basal calcium signals during scanning (indicating potential phototoxicity) or significant reductions in basal calcium signals (indicating abnormal photobleaching) were excluded from further analysis.

Each scanning session lasted up to 12 hours for any analysis to avoid potential phototoxicity. After successful imaging, animals were returned to standard fly food with wet Kimwipes. Successfully scanned animals that were returned to food developed normally into adults without gross morphological defects.

Pan-retinal expression of genetically encoded calcium indicator and Cas9: Calcium imaging was performed using longGMR-GAL4 to drive UAS-GCaMP6s unless otherwise noted. While longGMR-GAL4 is primarily photoreceptor-specific at larval stages, it broadly expresses in all retinal cells, including non-neuronal support cells, by 24 hAPF. Therefore, GMR-GAL4 was used for early developmental stages (12 to 24 hAPF; Fig. 1C and fig. S1A), and longGMR-GAL4 was used as a pan-retinal driver for later stages throughout this study.

Similarly, longGMR-Cas9 does not express in non-neuronal support cells at larval stages, allowing bypass of early developmental requirements for target genes such as *inx1*, *inx2*, *inx3*, and *sl*.

Unfixed tissue imaging of adult retina: Adult animals younger than 5 days old were sacrificed and mounted at the center of a petri dish (10 mm by 35 mm, Thermo Scientific) using nail-polish (Amazon) with cold distilled water. Samples were positioned such that the targeted eye region (dorsal-posterior or ventral-anterior regions) was placed on the flat surface. Imaging was performed using an Olympus two-photon microscope with 920-nm excitation and an Olympus 25x water-immersion objective. Images compromised by air-bubble entrapment, preventing clear visualization, were excluded from analysis.

Confocal imaging of fixed tissue: Fixed samples were imaged using a Leica SP8 confocal microscope or a Leica Stellaris confocal microscope with STED module (Fig. 4, A to D) with a 63x or 100x (STED) glycerol-immersion objective lens. Samples were positioned such that the targeted eye region (dorsal-posterior or ventral-anterior regions) was placed on the flat surface. Images were analyzed using FIJI (ImageJ) and Imaris for further analysis.

Cryosection: Adult or pupal heads were fixed, processed through a sucrose gradient, embedded in OCT, cryosectioned at 12 μm, and post-fixed. We focused exclusively on the dorsal-posterior region, as its proximity to the flat center of the adult eye allows more robust sectioning (Fig. 7, A to G and O to S). Detailed protocols are provided in supplementary references (*88*).

Immunohistochemistry: Fly pupal retina and optic lobes were dissected, fixed, blocked, and stained using standard immunohistochemistry protocols. Full details are provided in supplementary references (*89*).

The following primary antibodies were used for immunofluorescence: mouse anti-Dlg1 (1:200, 4F3, DSHB), rabbit anti-HA (1:200, Cell Signaling Technologies), rat anti-FLAG (1:200, Novus), mouse Anti-V5-tag:DyLight550 (1:200, BioRad), guinea pig anti-inx1 (1:1k, GenScript), rabbit anti-inx2 (1:2k, M. Hoch), guinea pig anti-inx3 (1:1k, GenScript), rabbit anti-inx4 (1:1k, A. Borst), rabbit anti-inx5 (1:1k, A. Borst), rabbit anti-inx6 (1:1k, A. Borst), rabbit anti-inx7 (1:1k, A. Borst), rabbit anti-inx8 (1:1k, A. Borst), chicken anti-GFP (1:1k, EMD), rat anti-Ecad (1:10, DSHB, DCAD2), AlexaFluor660 conjugated Phalloidin (Invitrogen, 1:200), and AlexaFluor405 conjugated Goat Anti-HRP (Jackson ImmunoResearch, 1:100). Secondary antibodies were from Invitrogen and used at 1:200.

TrpA heat activation: Pupae at 37 hAPF were selected, attached to double-sided tape on glass slides, and the pupal case around the retinas was removed. Animals were then incubated in a dark 29°C incubator for the designated time, followed by transfer to a 25°C incubator with wet Kimwipes to maintain humidity. Samples were dissected at 46 hAPF (Fig. 5), 72 hAPF (Fig. 7, F and G), and the adult stage (Fig. 7, R, S, W, and X) for further analysis. Animals showing obvious signs of cellular toxicity from heat induction, such as darker pigmentation or scarring, were excluded from experiments.

Quantification and statistical analysis

Quantification of retinal wave–induced calcium activity: Calcium imaging data from SP8 confocal microscopy of whole retinas was quantified using a hybrid model integrating event detection and intensity measurement for improved sensitivity and accuracy. Time-lapse images were pre-processed in Fiji to obtain corrected F/F0 values. Photobleaching was corrected by exponential decay fitting in Fiji under consistent exposure settings. Regions of interest (ROIs) for individual ommatidia were defined in a semi-automatic manner for further analysis in R. A two-component Gaussian mixture model (GMM) was applied to classify each ROI in each frame as "On" or "Off", with thresholds semi-manually optimized to enhance detection accuracy. Total calcium activity was calculated by summing $\Delta F/F0$ values exclusively during "On" states, reducing background noise and ensuring meaningful activity quantification. This approach improves sensitivity and accuracy by combining event frequency and intensity.

Calcium imaging data from two-photon microscopy with limited ROIs at single-cell resolution was quantified by integrating all ΔF/F0 intensity values to capture total calcium signal magnitude. Time-lapse images were pre-processed in Fiji to obtain corrected F/F_0 values. All $\Delta F/F_0$ values across corresponding frames were summed to quantify total calcium activity. ROIs for individual cell types were defined semi-automatically. Retinal pathways were manually defined, considering sequential activation of calcium activity from adjacent cells.

Imaris-based morphological visualization and analysis

For morphological analysis (Figs. 5 to 7), confocal Z-stacks were imported into Imaris (Bitplane) and visualized in 3D view. Planes and viewing angles were selected based on the region of interest. Single-plane images with optical thickness of 5 μm (Fig. 5) or 10 μm (Fig. 7) were captured from 3D-rendered volumes for representative figures and morphological analysis. Morphological quantification was performed on captured planes, as the structures are much larger than pixel scale and only minimally influenced by standard Imaris 3D rendering steps. Selection of optical sections was based on morphological criteria described in each quantification protocol below. For intensity quantification (Fig. 6), Imaris 3D view was used for ROI selection, but actual quantification was performed using raw voxel data. All images (Figs. 5 to 7) used for figure panels were resized post-capture to match the same physical scale across conditions. Scale bars were adjusted accordingly to reflect accurate physical dimensions.

Quantification of ommatidial morphology (Figs. 5 and 7)

For whole-retina ommatidial size analysis, retinas expressing longGMR-GAL4-driven membrane-tethered GFP were imaged in intact animals using a two-photon microscope at 0.3 μm voxel resolution. Full Z-stacks were used to reconstruct a 3D retinal surface, and individual ommatidial hexagonal areas were calculated using Imaris software, which semi-automatically detected the apical side of each hexagonal corner point.

For high-resolution analysis of ommatidial boundaries, dissected retinas immunostained with Dlg1 were flat-mounted to position the region of interest. Confocal Z-stacks were acquired using an SP8 microscope and imported into Imaris for 3D visualization. To quantify each ommatidium from the correct position, morphologically defined optical sections (5 μm thickness) were selected to capture the most apical tip of Dlg1 staining and were extracted from 3D-rendered views for analysis and figure panels (Fig. 5, F to Q). In each ommatidium, the gap distance was measured between apical Dlg1 staining along a line connecting ommatidial centers. Interommatidial gaps along the dorsal-ventral axis adjacent to 1PC/1PC junctions were excluded due to their consistently reduced apical domains compared to other orientations, and the average of the remaining four gaps was assigned per ommatidium.

Innexin intensity (fig. S4, W to Y): Fixed pupal retinas were stained with innexin antibodies and Dlg1. Images were acquired using an SP8 confocal microscope, and innexin intensity within interommatidial junctional Dlg1 was quantified.

Coefficient of variation of Sqh-GFP (Fig. 6): Retinas expressing Sqh-GFP were imaged in intact animals using a two-photon microscope with a 0.4-μm voxel size to reconstruct the 3D retinal surface. Time-lapse series (Fig. 6J) were corrected for photobleaching using the exponential decay method in Fiji under consistent exposure settings. Images were analyzed using Imaris, with manual refinement to define ROIs corresponding to the apical interommatidial boundary areas. To quantify local clustering of Sqh-GFP signal, the coefficient of variation (CV) was calculated within these defined ROIs. All pixel intensity values within each ROI, based on raw voxel data, were extracted, and the CV was calculated as the ratio of the standard deviation to the mean intensity. Higher CV values indicate greater intensity heterogeneity, reflecting localized clustering or accumulation of fluorescence signal.

Pseudocone quantification (Fig. 7, M and N): Adult eye pseudocones were imaged using a two-photon microscope at pseudocone layers within targeted eye regions (dorsal-posterior or ventral-anterior). Using Imaris, an optical section was selected to capture a consistent pseudocone layer (Fig. 7K). Pseudocone areas were semi-automatically defined as empty spaces enclosed by interommatidial boundaries. For morphological quantification of pseudocones, image display settings were adjusted individually to improve boundary visibility. Measurements were based on shape and size, not signal intensity. Any pseudocones obscured by bubbles or debris were excluded from the quantification.

Statistical analysis: Male pupae at the same developmental stage within a 1-hour time window were randomly selected from fly vials for all experiments. Blinded analysis across different genotypes was not performed, as genotypes were distinguishable by the experimenter. All experiments were conducted with at least three biological replicates (retinas from three different animals) per genotype. Statistical comparisons between genotypes were performed using the Mann–Whitney U test for two-group comparisons and the Kruskal–Wallis test followed by Dunn's multiple comparisons test for comparisons involving more than two groups. Linear regression analyses were performed using GraphPad Prism. Data are presented as mean ± standard deviation (SD) or standard error of the mean (SEM), as indicated in figure legends. To test statistical significance of CV differences between groups (Fig. 7N),

we used a permutation test, which does not assume normality and is well suited for comparing variability metrics such as CV.

REFERENCES AND NOTES

1. Y. C. Chen, N. Konstantinides, Integration of Spatial and Temporal Patterning in the Invertebrate and Vertebrate Nervous System. *Front. Neurosci.* **16**, 854422 (2022). doi: 10.3389/fnins.2022.854422; pmid: 35392413
2. E. Heller, E. Fuchs, Tissue patterning and cellular mechanics. *J. Cell Biol.* **211**, 219–231 (2015). doi: 10.1083/jcb.201506106; pmid: 26504164
3. T. Lecuit, P. F. Lenne, Cell surface mechanics and the control of cell shape, tissue patterns and morphogenesis. *Nat. Rev. Mol. Cell Biol.* **8**, 633–644 (2007). doi: 10.1038/nrm2222; pmid: 17643125
4. T. A. Seabrook, T. J. Burbridge, M. C. Crair, A. D. Huberman, Architecture, Function, and Assembly of the Mouse Visual System. *Annu. Rev. Neurosci.* **40**, 499–538 (2017). doi: 10.1146/annurev-neuro-071714-033842; pmid: 28772103
5. N. Uchida, C. Poo, R. Haddad, Coding and transformations in the olfactory system. *Annu. Rev. Neurosci.* **37**, 363–385 (2014). doi: 10.1146/annurev-neuro-071013-013941; pmid: 24905594
6. M. Takeichi, Dynamic contacts: Rearranging adherens junctions to drive epithelial remodelling. *Nat. Rev. Mol. Cell Biol.* **15**, 397–410 (2014). doi: 10.1038/nrm3802; pmid: 24824068
7. L. E. Clarke, B. A. Barres, Emerging roles of astrocytes in neural circuit development. *Nat. Rev. Neurosci.* **14**, 311–321 (2013). doi: 10.1038/nrn3484; pmid: 23595014
8. U. Tepass, The apical polarity protein network in Drosophila epithelial cells: Regulation of polarity, junctions, morphogenesis, cell growth, and survival. *Annu. Rev. Cell Dev. Biol.* **28**, 655–685 (2012). doi: 10.1146/annurev-cellbio-092910-154033; pmid: 22881460
9. Y. Tezuka, K. M. Hagihara, K. Ohki, T. Hirano, Y. Tagawa, Developmental stage-specific spontaneous activity contributes to callosal axon projections. *eLife* **11**, e72435 (2022). doi: 10.7554/eLife.72435; pmid: 36001081
10. F. J. Martini, T. Guillamón-Vivancos, V. Moreno-Juan, M. Valdeolmillos, G. López-Bendito, Spontaneous activity in developing thalamic and cortical sensory networks. *Neuron* **109**, 2519–2534 (2021). doi: 10.1016/j.neuron.2021.06.026; pmid: 34293296
11. R. A. Baines, M. Landgraf, Neural development: The role of spontaneous activity. *Curr. Biol.* **31**, R1513–R1515 (2021). doi: 10.1016/j.cub.2021.10.026; pmid: 34875237
12. O. Akin, B. T. Bajar, M. F. Keles, M. A. Frye, S. L. Zipursky, Cell-type-Specific Patterned Stimulus-Independent Neuronal Activity in the Drosophila Visual System during Synapse Formation. *Neuron* **101**, 894–904.e5 (2019). doi: 10.1016/j.neuron.2019.01.008; pmid: 30711355
13. J. B. Ackman, M. C. Crair, Role of emergent neural activity in visual map development. *Curr. Opin. Neurobiol.* **24**, 166–175 (2014). doi: 10.1016/j.conb.2013.11.011; pmid: 24492092
14. L. A. Kirkby, G. S. Sack, A. Firl, M. B. Feller, A role for correlated spontaneous activity in the assembly of neural circuits. *Neuron* **80**, 1129–1144 (2013). doi: 10.1016/j.neuron.2013.10.030; pmid: 24314725
15. S. N. Graven, Early neurosensory visual development of the fetus and newborn. *Clin. Perinatol.* **31**, 199-216 (2004).
16. J. M. Tworig, M. B. Feller, Müller Glia in Retinal Development: From Specification to Circuit Integration. *Front. Neural Circuits* **15**, 815923 (2022). doi: 10.3389/fncir.2021.815923; pmid: 35185477
17. A. Lakkaraju *et al.*, The cell biology of the retinal pigment epithelium. *Prog. Retin. Eye Res.* **78**, 100846 (2020). doi: 10.1016/j.preteyeres.2020.100846; pmid: 32105772
18. M. Hoon, H. Okawa, L. Della Santina, R. O. Wong, Functional architecture of the retina: Development and disease. *Prog. Retin. Eye Res.* **42**, 44–84 (2014). doi: 10.1016/j.preteyeres.2014.06.003; pmid: 24984227
19. S. Paudel, R. Sindelar, M. Saha, Calcium Signaling in Vertebrate Development and Its Role in Disease. *Int. J. Mol. Sci.* **19**, 3390 (2018). doi: 10.3390/ijms19113390; pmid: 30380695
20. J. C. Hervé, M. Derangeon, Gap-junction-mediated cell-to-cell communication. *Cell Tissue Res.* **352**, 21–31 (2013). doi: 10.1007/s00441-012-1485-6; pmid: 22940728
21. L. Leybaert, M. J. Sanderson, *Physiol. Rev*, vol. 92 (American Physiological Society, 2012), pp. 1359–1392.
22. G. Dupont, L. Combettes, L. Leybaert, Calcium dynamics: Spatio-temporal organization from the subcellular to the organ level. *Int. Rev. Cytol.* **261**, 193–245 (2007). doi: 10.1016/S0074-7696(07)61005-5; pmid: 17560283
23. J. Chal, O. Pourquié, Making muscle: Skeletal myogenesis *in vivo* and *in vitro*. *Development* **144**, 2104–2122 (2017). doi: 10.1242/dev.151035; pmid: 28634270
24. M. J. Vaughn, J. S. Haas, On the Diverse Functions of Electrical Synapses. *Front. Cell. Neurosci.* **16**, 910015 (2022). doi: 10.3389/fncel.2022.910015; pmid: 35755782
25. A. Arjun McKinney, R. Petrova, G. Panagiotakos, Calcium and activity-dependent signaling in the developing cerebral cortex. *Development* **149**, dev198853 (2022). doi: 10.1242/dev.198853; pmid: 36102617
26. M. J. Zeitz, J. W. Smyth, Gap Junctions and Ageing. *Subcell. Biochem.* **102**, 113–137 (2023). doi: 10.1007/978-3-031-21410-3_6; pmid: 36600132
27. T. Aasen, M. Mesnil, C. C. Naus, P. D. Lampe, D. W. Laird, Gap junctions and cancer: Communicating for 50 years. *Nat. Rev. Cancer* **17**, 74 (2017). doi: 10.1038/nrc.2016.142; pmid: 28704356
28. P. Wong *et al.*, The Role of Connexins in Wound Healing and Repair: Novel Therapeutic Approaches. *Front. Physiol.* **7**, 596 (2016). doi: 10.3389/fphys.2016.00596; pmid: 27999549
29. J. Stephan, S. Eitelmann, M. Zhou, Approaches to Study Gap Junctional Coupling, Approaches to Study Gap Junctional Coupling. *Front. Cell. Neurosci.* **15**, 640406 (2021). doi: 10.3389/fncel.2021.640406; pmid: 33776652
30. J. Malin, C. Desplan, Neural specification, targeting, and circuit formation during visual system assembly. *Proc. Natl. Acad. Sci. U.S.A.* **118**, e2101823118 (2021). doi: 10.1073/pnas.2101823118; pmid: 34183440
31. J. R. Sanes, S. L. Zipursky, Design principles of insect and vertebrate visual systems. *Neuron* **66**, 15–36 (2010). doi: 10.1016/j.neuron.2010.01.018; pmid: 20399726
32. H. J. Bellen, C. Tong, H. Tsuda, 100 years of Drosophila research and its impact on vertebrate neuroscience: A history lesson for the future. *Nat. Rev. Neurosci.* **11**, 514–522 (2010). doi: 10.1038/nrn2839; pmid: 20383202
33. D. F. Ready, H. C. Chang, Calcium waves facilitate and coordinate the contraction of endfeet actin stress fibers in Drosophila interommatidial cells. *Development* **148**, dev199700 (2021). doi: 10.1242/dev.199700; pmid: 34698814
34. M. F. Wernet, M. W. Perry, C. Desplan, The evolutionary diversity of insect retinal mosaics: Common design principles and emerging molecular logic. *Trends Genet.* **31**, 316–328 (2015). doi: 10.1016/j.tig.2015.04.006; pmid: 26025917
35. R. L. Cagan, D. F. Ready, The emergence of order in the Drosophila pupal retina. *Dev. Biol.* **136**, 346–362 (1989). doi: 10.1016/0012-1606(89)90261-3; pmid: 2511048
36. M. A. Charlton-Perkins, M. Friedrich, T. A. Cook, Semper's cells in the insect compound eye: Insights into ocular form and function. *Dev. Biol.* **479**, 126–138 (2021). doi: 10.1016/j.ydbio.2021.07.015; pmid: 34343526
37. J. E. Treisman, Retinal differentiation in Drosophila. *Wiley Interdiscip. Rev. Dev. Biol.* **2**, 545–557 (2013). doi: 10.1002/wdev.100; pmid: 24014422
38. E. O. Mazzoni *et al.*, Iroquois complex genes induce co-expression of rhodopsins in Drosophila. *PLOS Biol.* **6**, e97 (2008). doi: 10.1371/journal.pbio.0060097; pmid: 18433293
39. A. D. Buffry *et al.*, Evolution of compound eye morphology underlies differences in vision between closely related Drosophila species. *BMC Biol.* **22**, 67 (2024). doi: 10.1186/s12915-024-01864-7; pmid: 38504308
40. N. Posnien *et al.*, Evolution of eye morphology and rhodopsin expression in the Drosophila melanogaster species subgroup. *PLOS ONE* **7**, e37346 (2012). doi: 10.1371/journal.pone.0037346; pmid: 22662147
41. A. Nern *et al.*, Connectome-driven neural inventory of a complete visual system. *Nature* **641**, 1225–1237 (2025). doi: 10.1038/s41586-025-08746-0; pmid: 40140576
42. M. N. Özel *et al.*, Neuronal diversity and convergence in a visual system developmental atlas. *Nature* **589**, 88–95 (2021). doi: 10.1038/s41586-020-2879-3; pmid: 33149298
43. F. Pichaud, F. Casares, Shaping an optical dome: The size and shape of the insect compound eye. *Semin. Cell Dev. Biol.* **130**, 37–44 (2022). doi: 10.1016/j.semcdb.2021.11.002; pmid: 34810110
44. O. Akin, S. L. Zipursky, Frazzled promotes growth cone attachment at the source of a Netrin gradient in the *Drosophila* visual system. *eLife* **5**, e20762 (2016). doi: 10.7554/eLife.20762; pmid: 27743477
45. M. Langen *et al.*, The Developmental Rules of Neural Superposition in Drosophila. *Cell* **162**, 120–133 (2015). doi: 10.1016/j.cell.2015.05.055; pmid: 26119341
46. S. E. Escobedo, A. Shah, A. N. Easton, H. Hall, V. M. Weake, Characterizing a gene expression toolkit for eye- and photoreceptor-specific expression in Drosophila. *Fly* **15**, 73–88 (2021). doi: 10.1080/19336934.2021.1915683; pmid: 33899690
47. T. W. Chen *et al.*, Ultrasensitive fluorescent proteins for imaging neuronal activity. *Nature* **499**, 295–300 (2013). doi: 10.1038/nature12354; pmid: 23868258
48. A. Nern, B. D. Pfeiffer, G. M. Rubin, Optimized tools for multicolor stochastic labeling reveal diverse stereotyped cell arrangements in the fly visual system. *Proc. Natl. Acad. Sci. U.S.A.* **112**, E2967–E2976 (2015). doi: 10.1073/pnas.1506763112; pmid: 25964354
49. P. Chakraborty, G. Hasan, ER-Ca^{2+} stores and the regulation of store-operated Ca^{2+} entry in neurons. *J. Physiol.* **602**, 1463–1474 (2024). doi: 10.1113/JP283827; pmid: 36691983
50. C. H. Liu *et al.*, Rapid Release of Ca^{2+} from Endoplasmic Reticulum Mediated by Na^{+}/Ca^{2+} Exchange. *J. Neurosci.* **40**, 3152–3164 (2020). doi: 10.1523/JNEUROSCI.2675-19.2020; pmid: 32156830
51. J. de Juan-Sanz *et al.*, Axonal Endoplasmic Reticulum Ca^{2+} Content Controls Release Probability in CNS Nerve Terminals. *Neuron* **93**, 867–881.e6 (2017). doi: 10.1016/j.neuron.2017.01.010; pmid: 28162809
52. H. Dana *et al.*, Sensitive red protein calcium indicators for imaging neural activity. *eLife* **5**, e12727 (2016). doi: 10.7554/eLife.12727; pmid: 27011354
53. K. Venkatesh, G. Hasan, Disruption of the IP3 receptor gene of Drosophila affects larval metamorphosis and ecdysone release. *Curr. Biol.* **7**, 500–509 (1997). doi: 10.1016/S0960-9822(06)00221-1; pmid: 9273145

54. J. W. Putney, T. Tomita, Phospholipase C signaling and calcium influx. *Adv. Biol. Regul.* **52**, 152–164 (2012). doi: 10.1016/j.advenzreg.2011.09.005; pmid: 21933679
55. S. S. Balakrishnan, U. Basu, P. Raghu, Phosphoinositide signalling in Drosophila. *Biochim. Biophys. Acta* **1851**, 770–784 (2015). doi: 10.1016/j.bbalip.2014.10.010; pmid: 25449646
56. A. Schlesinger, A. Kiger, N. Perrimon, B. Z. Shilo, Small wing PLCgamma is required for ER retention of cleaved Spitz during eye development in Drosophila. *Dev. Cell* **7**, 535–545 (2004). doi: 10.1016/j.devcel.2004.09.001; pmid: 15469842
57. F. Port, H. M. Chen, T. Lee, S. L. Bullock, Optimized CRISPR/Cas tools for efficient germline and somatic genome engineering in Drosophila. *Proc. Natl. Acad. Sci. U.S.A.* **111**, E2967–E2976 (2014). doi: 10.1073/pnas.1405500111; pmid: 25002478
58. K. Kanemaru, Y. Nakamura, Activation Mechanisms and Diverse Functions of Mammalian Phospholipase C. *Biomolecules* **13**, 915 (2023). doi: 10.3390/biom13060915; pmid: 37371495
59. M. A. Charlton-Perkins, E. D. Sendler, E. K. Buschbeck, T. A. Cook, Multifunctional glial support by Semper cells in the Drosophila retina. *PLOS Genet.* **13**, e1006782 (2017). doi: 10.1371/journal.pgen.1006782; pmid: 28562601
60. S. Mele, T. K. Johnson, Receptor Tyrosine Kinases in Development: Insights from *Drosophila*. *Int. J. Mol. Sci.* **21**, 188 (2019). doi: 10.3390/ijms21010188; pmid: 31888080
61. S. Wang *et al.*, The tyrosine kinase Stitcher activates Grainy head and epidermal wound healing in Drosophila. *Nat. Cell Biol.* **11**, 890–895 (2009). doi: 10.1038/ncb1898; pmid: 19525935
62. B. J. Choi, Y. D. Chen, C. Desplan, Building a circuit through correlated spontaneous neuronal activity in the developing vertebrate and invertebrate visual systems. *Genes Dev.* **35**, 677–691 (2021). doi: 10.1101/gad.348241.121; pmid: 33888564
63. R. A. Pearson *et al.*, Ca(2+) signalling and gap junction coupling within and between pigment epithelium and neural retina in the developing chick. *Eur. J. Neurosci.* **19**, 2435–2445 (2004). doi: 10.1111/j.0953-816X.2004.03338.x; pmid: 15128397
64. J. Güiza, I. Barría, J. C. Sáez, J. L. Vega, Innexins: Expression, Regulation, and Functions. *Front. Physiol.* **9**, 1414 (2018). doi: 10.3389/fphys.2018.01414; pmid: 30364195
65. I. M. Skerrett, J. B. Williams, A structural and functional comparison of gap junction channels composed of connexins and innexins. *Dev. Neurobiol.* **77**, 522–547 (2017). doi: 10.1002/dneu.22447; pmid: 27582044
66. L. A. Stebbings *et al.*, Gap junctions in Drosophila: Developmental expression of the entire innexin gene family. *Mech. Dev.* **113**, 197–205 (2002). doi: 10.1016/S0925-4773(02)00025-4; pmid: 11960713
67. G. Ammer, R. M. Vieira, S. Fendl, A. Borst, Anatomical distribution and functional roles of electrical synapses in Drosophila. *Curr. Biol.* **32**, 2022–2036.e4 (2022). doi: 10.1016/j.cub.2022.03.040; pmid: 35385694
68. M. Richard, R. Bauer, G. Tavosanis, M. Hoch, The gap junction protein Innexin3 is required for eye disc growth in Drosophila. *Dev. Biol.* **425**, 191–207 (2017). doi: 10.1016/j.ydbio.2017.04.001; pmid: 28390801
69. S. McCutcheon, R. F. Stout Jr., D. C. Spray, The dynamic Nexus: Gap junctions control protein localization and mobility in distinct and surprising ways. *Sci. Rep.* **10**, 17011 (2020). doi: 10.1038/s41598-020-73892-6; pmid: 33046777
70. S. Roberts, C. Delury, E. Marsh, The PDZ protein discs-large (DLG): The 'Jekyll and Hyde' of the epithelial polarity proteins. *FEBS J.* **279**, 3549–3558 (2012). doi: 10.1111/j.1742-4658.2012.08729.x; pmid: 22846345
71. D. Segretain, M. M. Falk, Regulation of connexin biosynthesis, assembly, gap junction formation, and removal. *Biochim. Biophys. Acta* **1662**, 3–21 (2004). doi: 10.1016/j.bbamem.2004.01.007; pmid: 15033576
72. T. Honda, Optogenetic and thermogenetic manipulation of defined neural circuits and behaviors in *Drosophila*. *Learn. Mem.* **29**, 100–109 (2022). doi: 10.1101/lm.053556.121; pmid: 35332066
73. S. R. Pulver, S. L. Pashkovski, N. J. Hornstein, P. A. Garrity, L. C. Griffith, Temporal dynamics of neuronal activation by Channelrhodopsin-2 and TRPA1 determine behavioral output in Drosophila larvae. *J. Neurophysiol.* **101**, 3075–3088 (2009). doi: 10.1152/jn.00071.2009; pmid: 19339465
74. J. Wang, M. Michel, L. Bialas, G. Pierini, C. Dahmann, Preferential recruitment and stabilization of Myosin II at compartment boundaries in Drosophila. *J. Cell Sci.* **136**, jcs260447 (2023). doi: 10.1242/jcs.260447; pmid: 36718636
75. M. A. Quintanilla, J. A. Hammer, J. R. Beach, Non-muscle myosin 2 at a glance. *J. Cell Sci.* **136**, jcs260890 (2023). doi: 10.1242/jcs.260890; pmid: 36917212
76. M. R. Stachowiak *et al.*, Self-organization of myosin II in reconstituted actomyosin bundles. *Biophys. J.* **103**, 1265–1274 (2012). doi: 10.1016/j.bpj.2012.08.028; pmid: 22995499
77. P. Zhao *et al.*, Aurora-A Breaks Symmetry in Contractile Actomyosin Networks Independently of Its Role in Centrosome Maturation. *Dev. Cell* **49**, 651–653 (2019). doi: 10.1016/j.devcel.2019.05.010; pmid: 31112701
78. M. Charlton-Perkins, N. L. Brown, T. A. Cook, The lens in focus: A comparison of lens development in Drosophila and vertebrates. *Mol. Genet. Genomics* **286**, 189–213 (2011). doi: 10.1007/s00438-011-0643-y; pmid: 21877135
79. B. T. Bajar *et al.*, A discrete neuronal population coordinates brain-wide developmental activity. *Nature* **602**, 639–646 (2022). doi: 10.1038/s41586-022-04406-9; pmid: 35140397
80. O. Akin, S. L. Zipursky, Activity regulates brain development in the fly. *Curr. Opin. Genet. Dev.* **65**, 8–13 (2020). doi: 10.1016/j.gde.2020.04.005; pmid: 32593792
81. Y. X. Li *et al.*, Receptor tyrosine kinases CAD96CA and FGFR1 function as the cell membrane receptors of insect juvenile hormone. *eLife* **13**, RP97189 (2025). doi: 10.7554/eLife.97189.4; pmid: 40085503
82. J. L. Scanlan, C. Robin, C. K. Mirth, Rethinking the ecdysteroid source during Drosophila pupal-adult development. *Insect Biochem. Mol. Biol.* **152**, 103891 (2023). doi: 10.1016/j.ibmb.2022.103891; pmid: 36481381
83. Y. L. Gagnon, D. Wilby, S. E. Temple, Losing focus: How lens position and viewing angle affect the function of multifocal lenses in fishes. *J. Opt. Soc. Am. A Opt. Image Sci. Vis.* **33**, 1901–1909 (2016). doi: 10.1364/JOSAA.33.001901; pmid: 27607515
84. M. F. N. Land, *Dan-Eric, Animal Eyes* (Oxford Univ. Press, 2012).
85. M. D. Ketkar *et al.*, First-order visual interneurons distribute distinct contrast and luminance information across ON and OFF pathways to achieve stable behavior. *eLife* **11**, e74937 (2022). doi: 10.7554/eLife.74937; pmid: 35263247
86. T. A. Schoborg, S. L. Smith, L. N. Smith, H. D. Morris, N. M. Rusan, Micro-computed tomography as a platform for exploring *Drosophila* development. *Development* **146**, dev176685 (2019). doi: 10.1242/dev.176685; pmid: 31722883
87. A. Borst, J. Haag, D. F. Reiff, Fly motion vision. *Annu. Rev. Neurosci.* **33**, 49–70 (2010). doi: 10.1146/annurev-neuro-060909-153155; pmid: 20225934
88. N. Ghosh, J. E. Treisman, Apical cell expansion maintained by Dusky-like establishes a scaffold for corneal lens morphogenesis. *Sci. Adv.* **10**, eado4167 (2024). doi: 10.1126/sciadv.ado4167; pmid: 39167639
89. J. A. Malin, Y. C. Chen, F. Simon, E. Keefer, C. Desplan, Spatial patterning controls neuron numbers in the Drosophila visual system. *Dev. Cell* **59**, 1132–1145.e6 (2024). doi: 10.1016/j.devcel.2024.03.004; pmid: 38531357
90. B. J. Choi, Y. C. Chen, C. Desplan, Data from: Retinal calcium waves coordinate uniform tissue patterning of the Drosophila eye. Dryad Digital Repository, Dataset (2025); https://doi.org/10.5061/dryad.1g1jwsv9d.
91. Y. C. Chen, B. J. Choi, C. Desplan, Scripts associated with the analyses of Choi *et al.* 2025. Zenodo, Dataset (2025); https://doi.org/10.5281/zenodo.16416573.

ACKNOWLEDGMENTS

We thank the members of the Desplan lab for helpful discussions and manuscript feedback; J. Malin, S. Cordoba, and D. Chen for advice on manuscript preparation; N. Ghosh and J. Treisman for technical assistance with cryosectioning; M. Hoch and A. Borst for antibodies; P. Phelan for *shakB*^{2} fly stocks; and M. Courgeon for plasmids. We used stocks obtained from the Bloomington Drosophila Stock Center (NIH P40OD018537). This work also benefited from antibodies and *Drosophila* lines generated with support from the Center for Genomics and Systems Biology at NYU Abu Dhabi. **Funding:** This work was supported by NIH grants EY13010 and EY017916 (C.D.), NIH fellowship F32EY027682 (B.J.C.), the MacCracken Fellowship at New York University (Y.-C.C.), a NYSTEM institutional training grant (C322560GG) (Y.-C.C.), and a scholarship to study abroad from the Ministry of Education, Taiwan (Y.-C.C.). **Author contributions:** B.J.C. and C.D. conceived the project, analyzed the data, and wrote the manuscript. Y.-C.C. performed quantitative analysis of calcium imaging data. B.J.C. performed all experiments. **Competing interests:** The authors declare no competing interests. **Data and materials availability:** All datasets generated during this study are deposited in the Dryad repository (*90*). Antibodies and fly lines will be distributed upon request. All analysis code is available at Zenodo (*91*). **Use of AI technologies:** During manuscript preparation, the authors used ChatGPT Plus (OpenAI, GPT-4 and GPT-5, 2024–2025 versions) for language editing only. All authors reviewed and edited the text after use and take full responsibility for the content of the publication. **License information:** Copyright © 2025 the authors, some rights reserved; exclusive licensee American Association for the Advancement of Science. No claim to original US government works. https://www.sciencemag.org/about/science-licenses-journal-article-reuse

SUPPLEMENTARY MATERIALS

science.org/doi/10.1126/science.ady5541
Figs. S1 to S6; Tables S1 to S3; MDAR Reproducibility Checklist; Movies S1 to S3

Submitted 29 April 2025; accepted 19 September 2025

10.1126/science.ady5541

GAS ADSORPTION

Multigas adsorption with single-site cooperativity in a metal–organic framework

Kurtis M. Carsch[1,2], Henry Z. H. Jiang[1,2,3], Ryan A. Klein[4,5], Andrew S. Rosen[3,6,7,8], Peyton S. Summerhill[9], Jesse L. Peltier[2,3], Adrian J. Huang[1,2,3], Ryan A. Murphy[2,3], Matthew N. Dods[1,10], Hope A. Silva[1,2], Zikri Hasanbasri[11], Hyunchul Kwon[1,2], Sarah L. Karstens[1,2,3], Yuto Yabuuchi[1,2,3], Jonas Börgel[2,3], Jordan W. Taylor[2], Katie R. Meihaus[1,2], Karen C. Bustillo[12], Andrew M. Minor[7,12], Kristin A. Persson[3,7], Craig M. Brown[4,13], R. David Britt[6,11], Nicholas P. Stadie[9], Jeffrey R. Long[1,2,3,7,10]*

Cooperative gas adsorption in metal–organic frameworks (MOFs) is a rare phenomenon that generally involves long-range communication between multiple binding sites. We demonstrate a MOF containing cobalt(II)–methyl sites that selectively and reversibly capture two carbon monoxide (CO) molecules per site, leading to record-high adsorption capacities at ambient temperatures and pressures. Gas adsorption and structural, spectroscopic, and computational analyses support a mechanism in which binding of one CO molecule triggers a spin transition, followed by binding of a second CO molecule and migratory insertion of the first CO molecule into the cobalt–methyl bond to form an acetyl. The greater binding affinity associated with the second CO results in sigmoidal adsorption isotherms, a hallmark of cooperativity and phase-change materials, despite the absence of long-range interactions within the framework.

Cooperativity, broadly defined as a set of molecular interactions in which the occurrence of a single event changes the free energies of other events (*1*), has been observed for gas binding in a small number of metal–organic frameworks (MOFs) (*2*–*6*). This phenomenon can lead to exceptional selectivities and high separation capacities, as observed for cooperative CO_2 uptake in polyamine-appended frameworks amine–Mg_2(dobpdc) (dobpdc^{4-} = 4,4′-dioxidobiphenyl-3,3′-dicarboxylate). At a threshold pressure in these materials, CO_2 inserts into the metal–amine bonds, triggering additional CO_2 binding events and the formation of ammonium carbamate chains running along one-dimensional (1D) channels within the framework (*5*–*9*). This mechanism is specific to CO_2, and as a result, these materials exhibit high capacities for CO_2 even in the presence of other gases such as N_2, O_2, and water. The discovery of new mechanisms of gas binding in MOFs is an important driver of progress in the field of chemical separations with potentially far-reaching impacts, providing high working capacities with minimal pressure and temperature changes (*10*–*12*). However, materials exhibiting cooperative gas binding remain rare, and the only examples of cooperative adsorption discovered to date involve communication between adjacent binding sites and long-range reorganization in at least one dimension.

Another phenomenon that is rare in MOFs is the binding of more than one gas molecule to a single metal site. Indeed, the metal sites in MOFs can generally only accommodate, at most, a single guest molecule, which inherently limits adsorption capacities. Among the thousands of MOF structures studied for gas adsorption to date, there are only three exceptions without long-range structural reorganization: Mn_2(dsbdc) (dsbdc^{4-} = 2,5-disulfido-1,4-benzenedicarboxylate), UTSA-74, an isomer of Zn_2(dobdc) (dobdc^{4-} = 2,5-dioxido-1,4-benzenedicarboxylate), and PCN-224-Co^{II} (*13*–*15*). In the case of PCN-224-Co^{II}, the noncooperative binding of two equivalents of CO per cobalt(II) site occurs only at very low temperatures, and noncooperative binding of two guest molecules in Mn_2(dsbdc) and UTSA-74 is limited to a fraction of the available metal sites with suitable open coordination environments (*13*, *14*).

Notably, an established mode of reactivity involving binding of two gas molecules at a single metal site has been reported for an organometallic complex. The reaction of two molecules of CO with pseudotetrahedral high-spin cobalt(II)–alkyl species yields a low-spin cobalt(II) monocarbonyl, monoacyl species (Fig. 1A) (*16*–*18*). The primary coordination sphere of the cobalt(II) ion in these molecules resembles that of the peripheral cobalt(II)–methyl sites in the framework material $Co_{3.5}Zn_{1.5}(CH_3)_{3.1}Cl_{0.9}$(btdd)$_3$ [CoMe-MFU-4*l*; H_2btdd = bis(*1*H-1,2,*3*-triazolo[4,5-*b*],[4′,5′-*i*])dibenzo[1,4]dioxin] (*19*), prepared through post-synthetic modification of MFU-4*l* [Zn_5Cl_4(btdd)$_3$] (Fig. 1, B and C) (*20*).

We show that at ambient temperatures, CoMe-MFU-4*l* can reversibly and selectively capture two CO molecules per cobalt(II) site (Fig. 1D). In situ structural and spectroscopic analyses, in combination with density functional theory calculations, establish a mechanism of CO binding involving a high- to low-spin cobalt(II) spin state transition and tandem migratory insertion. Notably, the steep CO adsorption profile of this material could be well-modeled with either a sequential binding model, revealing a −6 kJ/mol cooperative binding energy, or a Hill-Langmuir model (*21*) with a Hill coefficient of $n \approx 1.8$, despite the adsorption occurring at individual cobalt(II) sites. This result highlights that long-range reorganization and communication between adjacent binding sites is not a prerequisite for adsorption to be steeper than that demonstrated for a Langmuir-type adsorbent. Both single-component adsorption data and breakthrough analysis revealed that this cooperative mechanism was highly selective for CO over other gases, including π-acids such as C_2H_4, even at very dilute CO concentrations.

Synthesis and gas adsorption analysis

The framework CoMe-MFU-4*l* was previously synthesized from MFU-4*l* by exchange of the peripheral zinc(II) ions for cobalt(II) to yield Co_4ZnCl_4(btdd)$_3$, or CoCl-MFU-4*l* (*22*), followed by anion metathesis with dimethylzinc [$Zn(CH_3)_2$] at ambient temperature to afford CoMe-MFU-4*l* [characterized as $Co_{3.5}Zn_{1.5}(CH_3)_{3.1}Cl_{0.9}$(btdd)$_3$] as a blue, air-sensitive powder (*19*). We found that starting with CoCl-MFU-4*l*, three sequential exchanges with excess $Zn(CH_3)_2$ in tetrahydrofuran at 50°C resulted in a slightly greater extent of methylation, yielding a violet-blue powder with the chemical formula $Co_{3.8}Zn_{1.2}(CH_3)_{3.8}Cl_{0.2}$(btdd)$_3$, based on combustion analysis, inductively coupled plasma optical emission spectroscopy (ICP-OES), and energy-dispersive x-ray spectroscopy (EDX) [see supplementary materials (SM) section 6 for synthesis details and table S7]. Analysis of N_2 adsorption data obtained at 77 K for CoCl-MFU-4*l* and CoMe-MFU-4*l* revealed that both frameworks

[1]Baker Hughes Institute for Decarbonization Materials, University of California, Berkeley, Berkeley, CA, USA. [2]Department of Chemistry, University of California, Berkeley, Berkeley, CA, USA. [3]Materials Sciences Division, Lawrence Berkeley National Laboratory, Berkeley, CA, USA. [4]Center for Neutron Research, National Institute of Standards and Technology, Gaithersburg, MD, USA. [5]Material, Chemical, and Computational Sciences Directorate, National Renewable Energy Laboratory, Golden, CO, USA. [6]Miller Institute for Basic Research in Science, University of California, Berkeley, Berkeley, CA, USA. [7]Department of Materials Science and Engineering, University of California, Berkeley, Berkeley, CA, USA. [8]Department of Chemical and Biological Engineering, Princeton University, Princeton, NJ, USA. [9]Department of Chemistry and Biochemistry, Montana State University, Bozeman, MT, USA. [10]Department of Chemical and Biomolecular Engineering, University of California, Berkeley, Berkeley, CA, USA. [11]Department of Chemistry, University of California, Davis, Davis, CA, USA. [12]National Center for Electron Microscopy, Molecular Foundry, Lawrence Berkeley National Laboratory, Berkeley, CA, USA. [13]Chemical and Biomolecular Engineering, University of Delaware, Newark, DE, USA. ***Corresponding author. Email: jrlong@berkeley.edu**

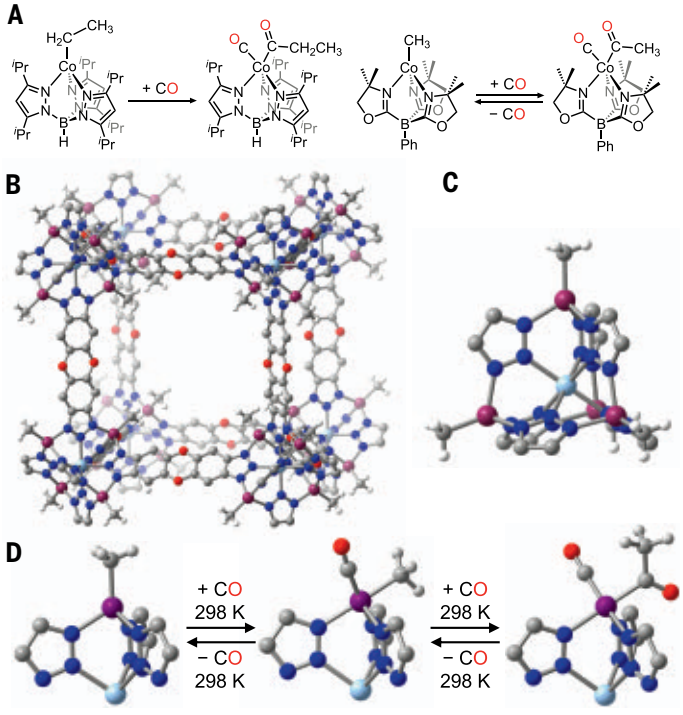

Fig. 1. Design of a metal–organic framework for multiple binding of adsorbates at a single site. (**A**) Literature precedent for carbonyl ligation and migratory insertion into pseudo-tetrahedral cobalt(II)–alkyl complexes (*16*–*18*). (**B**) A portion of the solid-state structure of CoMe-MFU-4*l*, as determined from single-crystal x-ray diffraction analysis (see SM section 8). (**C**) Depiction of the truncated pentanuclear node. (**D**) Coordination environments for a single cobalt(II) site in the structure of CoMe-MFU-4*l* under various CO dosing conditions. The structures were determined from Rietveld refinements against synchrotron powder x-ray diffraction data for the starting and ending states (see SM section 7) with the intermediate geometry calculated using density functional theory (see SM section 10). Upon exposure to CO at ambient temperatures, CoMe-MFU-4*l* reversibly binds two equivalents of CO at its cobalt(II) sites to form a monocarbonyl, monoacetyl adduct. Light blue, purple, gray, blue, red, and white spheres represent Zn, Co, C, N, O, and H atoms, respectively. Hydrogen atoms on the linker are omitted for clarity.

were highly porous, with Brunauer–Emmett–Teller surface areas of 3800(40) and 3710(40) m^2/g, respectively (fig. S1). Single-crystal x-ray diffraction analysis of CoMe-MFU-4*l* (see SM section 8) showed the methyl ligand resided along a threefold symmetry axis with a Co–C_{Me} bond length of 1.981(4) Å (fig. S39), consistent with Co–C_{Me} distances reported for monoalkylated pseudo-tetrahedral high-spin cobalt(II) complexes (*17*, *23*). Single-component CO adsorption and desorption isotherms were collected for CoCl-MFU-4*l* and CoMe-MFU-4*l* at 298 K and pressures up to 1 bar (see fig. S10 and Fig. 2A, respectively). Although CoCl-MFU-4*l* adsorbed very little CO under these conditions (~0.26 mmol/g at 1 bar), CoMe-MFU-4*l* exhibited a high affinity for CO at low partial pressures, adsorbing 5.18 mmol/g at just 10 mbar. This amount is much higher than expected if a single CO were to coordinate to each cobalt(II) site (3.1 to 3.3 mmol/g, see SM section 11 for details). At 1 bar, the CO capacity plateaued at a value of 6.07 mmol/g, near the expected value for binding of two CO molecules per cobalt(II) site.

Notably, the CO capacity achieved at 10 mbar and 298 K is the highest reported to date under these conditions for any MOF (*24*), and the 1 bar capacity is among the top few reported to date (table S12). Most other frameworks reported to date that exhibit high capacities for CO at ambient temperature feature open metal sites capable of binding just a single molecule of CO, for example Ni_2(*m*-dobdc) (*m*-dobdc^{4-} = 4,6-dioxido-1,3-benzenedicarboxylate; capacities of 3.8 and 5.7 mmol/g at 10 mbar and 1 bar, respectively) (*25*), although such sites have not been shown to be highly selective for CO over more polarizable gases such as C_2H_4 (see fig. S18).

The high gravimetric CO capacity measured for CoMe-MFU-4*l* suggests a distinctive CO binding mechanism (discussed further below). Of note, single-component N_2, H_2, CH_4, C_2H_6, and C_2H_4 adsorption data collected for CoMe-MFU-4*l* and CoCl-MFU-4*l* at 298 K and pressures up to 1 bar were nearly identical, in contrast to the results for CO. For both frameworks, uptake of N_2, H_2, and CH_4 was <1 mmol/g at 1 bar, whereas uptake of C_2H_6 and C_2H_4 was slightly higher (~2.2 and ~2 mmol/g, respectively) (Fig. 2A and fig. S6). These data indicate that CoMe-MFU-4*l* and CoCl-MFU-4*l* exhibit similar mechanisms of gas adsorption for all these gases except for CO. As is common for metal–alkyl motifs, CoMe-MFU-4*l* is sensitive to O_2 in the presence or absence of CO. Although the products of dosing CoMe-MFU-4*l* with O_2 have not yet been identified, in situ diffuse reflectance infrared Fourier transform spectroscopy (DRIFTS) measurements on co-dosing CoMe-MFU-4*l* with O_2 and CO are consistent with formation of acetate within the framework, based on the new diagnostic vibrations at 1566 and 1435 cm^{-1} (fig. S58). Finally, CO uptake in CoMe-MFU-4*l* was rapid (see figs. S14 to S16) and fully reversible as the adsorbed CO could be

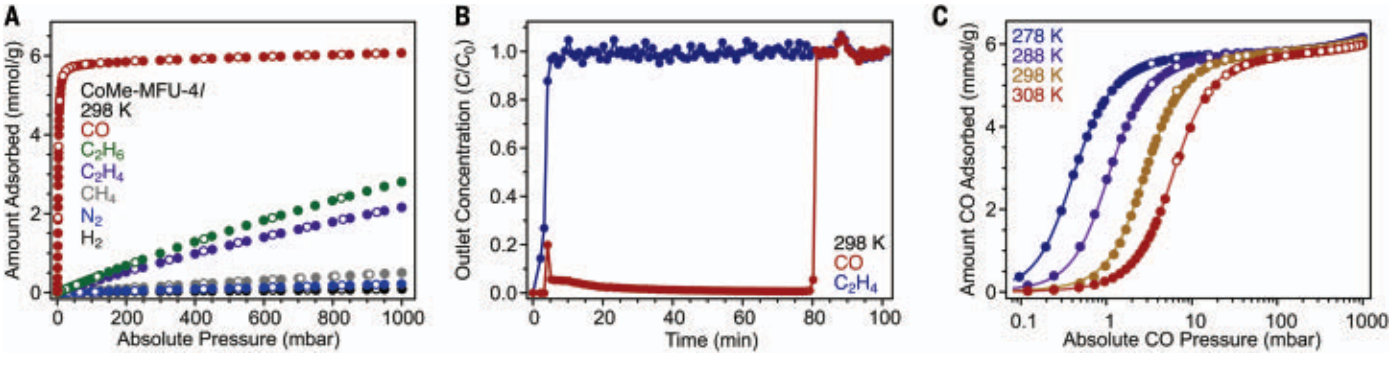

Fig. 2. Gas adsorption studies of CoMe-MFU-4*l*. (**A**) Single-component CO, C_2H_4, C_2H_6, CH_4, N_2, and H_2 adsorption and desorption isotherms obtained for CoMe-MFU-4*l* at 298 K. (**B**) Breakthrough data collected for a pelletized sample of CoMe-MFU-4*l* exposed to a flowing (10-sccm) gas stream consisting of 10% CO in C_2H_4 at 298 K. See SM section 5 for details. (**C**) CO adsorption and desorption isotherms for CoMe-MFU-4*l* obtained at 278, 288, 298, and 308 K. Solid lines represent fits using the Hill equation with an additional Langmuir term (see SM section 3 and table S3 for details). From the fits, a Hill coefficient of $n \approx 1.8$ was obtained.

desorbed under reduced pressure without hysteresis, and the framework retained more than 98% of its initial adsorption capacity after 50 isothermal adsorption (50 mbar CO in N_2)/desorption (5 mbar CO in N_2) cycles (fig. S12).

Analysis of the single-component gas adsorption data suggested that CoMe-MFU-4*l* should be highly selective for CO at dilute concentrations, even over other π-acids and more polarizable gases such as C_2H_4. To investigate this possibility, we conducted breakthrough analysis on a pelletized sample of CoMe-MFU-4*l* exposed to a flowing [10 standard cubic centimeters per minute (sccm)] stream containing 10% CO in C_2H_4 at 298 K. After only 5 min, C_2H_4 was detected at the outlet, corresponding to a capacity of 2.1 mmol/g (Fig. 2B), consistent with the C_2H_4 capacity determined from single-component adsorption data at 900 mbar (2.0 mmol/g). Breakthrough of CO was detected after ~80 min, corresponding to a CO capacity of 5.9 mmol/g, again consistent with the capacity determined from single-component CO adsorption data at 100 mbar (5.8 mmol/g). These data indicate that the framework captured nearly two molecules of CO per cobalt(II) site even in the presence of C_2H_4. The similar capacities obtained from breakthrough analysis and single-component adsorption isotherms suggest that these two adsorbates do not compete for the same primary binding site, in contrast to the adsorption observed with frameworks such as Ni_2(*m*-dobdc) (table S6).

Modeling gas uptake in CoMe-MFU-4*l*

We could fit N_2, H_2, CH_4, C_2H_6, and C_2H_4 adsorption data collected for CoMe-MFU-4*l* over a range of temperatures using a single-site (N_2, CH_4, C_2H_6, and C_2H_4) or dual-site (H_2) Langmuir–Freundlich model. The resulting fit parameters were used with the Clausius–Clapeyron relation to estimate isosteric enthalpies of adsorption (ΔH_{ads}) ranging from −7 to −20 kJ/mol, within the range of values expected for physisorption of these gases (fig. S10 and table S4) (*26*). By contrast, application of a single-site Langmuir model to the low-pressure CO adsorption data for CoMe-MFU-4*l* provided an unsatisfactory fit (fig. S40).

Considering the sharp CO uptake in CoMe-MFU-4*l* and the evidence of multiple guests binding to a single cobalt(II) site, we considered instead that CO binding at the cobalt(II) sites may be occurring in a fashion where binding of one equivalent of CO facilitated a second binding event at the same site. Although mechanistically distinct, cooperative gas uptake in diamine-appended Mg_2(dobpdc) and related diamine–Mg_2(olz) materials [olz^{4-} = (*E*)-5,5′-(diazene-1,2-diyl)bis(2-oxidobenzoate)] (*27*) has been qualitatively modeled using a version of the Hill equation (*21*) adapted for fitting adsorption data. From these fits, the Hill coefficient *n* could be extracted, in which $n > 1$ is indicative of positive cooperativity (*28*–*30*). For diamine–Mg_2(dobpdc) and diamine–Mg_2(olz), values of *n* are typically ≥3 and have been used for comparison of the degree of cooperativity in CO_2 uptake in these materials, with *n* qualitatively interpreted to indicate the average number of CO_2 molecules required for adsorption to occur (*5*, *27*).

In the case of CoMe-MFU-4*l*, the CO adsorption data obtained for CoMe-MFU-4*l* at 278, 288, 298, and 308 K (Fig. 2C and table S5; see SM section 1.4) could be well fit with a sequential binding model (see SM section 3 for statistical mechanics derivation), revealing a cooperative binding energy of −6 kJ/mol, reflecting a stronger binding of the second CO to the cobalt site relative to that of the first CO. Notably, single- or double-site Langmuir models appropriate for describing strong and distinct metal–adsorbate interactions failed to adequately model the adsorption profile. These data could be modeled by including a Hill parameter to describe the strong binding site (see SM section 3 for details). This yields a Hill coefficient of $n = 1.8$ and a saturation capacity of 5.70 mmol/g, consistent with cooperative uptake of two molecules of CO at each cobalt(II) site (fig. S9 and table S3) (*30*). Although the data could be accurately fit with either sequential or Hill models, we favor the sequential binding model as it reflects the underlying reaction progression as ascertained from spectroscopic data (see below). The fit parameters obtained from fitting the full 298 K isotherm for CoMe-MFU-4*l* were then used with the Clausius–Clapeyron relation to calculate ΔH_{ads} as a function of CO loading, revealing a relatively constant ΔH_{ads} of approximately −64 kJ/mol per CO (table S4). The magnitude of the CO binding enthalpy in this case is much greater than reported for most other MOFs (*25*, *31*) and comparable to the enthalpy of CO adsorption reported for Fe_2Cl_2(bbta) ($\Delta H_{ads} = -65$ kJ/mol), which captures one molecule of CO per iron(II) site through a cooperative spin transition mechanism (*3*, *24*). Although the air sensitivity of CoMe-MFU-4*l* may still need to be addressed for some CO separations, it could be of immediate service for a number of potential applications, including purity augmentation for prepurified streams, CO scavenging from H_2 streams for ammonia production and fuel cell technologies, and last-step purification of gas streams in catalysis applications (*32*).

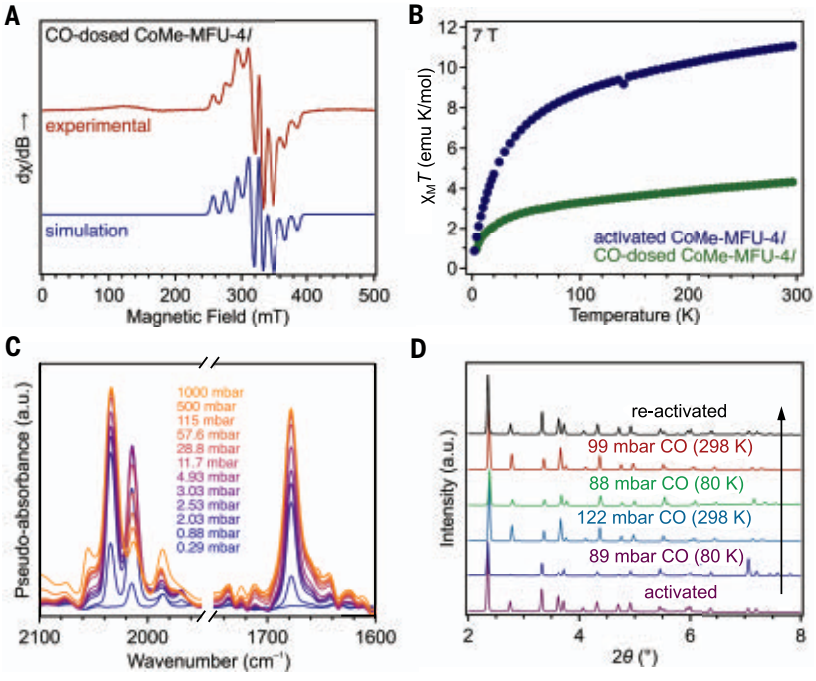

Fig. 3. Spectroscopic and structural characterization of reversible CO uptake in CoMe-MFU-4*l*. (**A**) X-band electron paramagnetic resonance spectrum (red trace, collected at 15 K) for a sample of cobalt-dilute CoMe-MFU-4*l* dosed with 50 mbar of CO at 298 K. A simulated spectrum using the software EasySpin (see SM section 1.13 for details). Fitting parameters are $g_x = 2.076$, $g_y = 2.041$, $g_z = 2.081$, $A_x = 120$ MHz, $A_y = 120$ MHz, and $A_z = 535$ MHz. (**B**) Temperature dependence of the molar magnetic susceptibility–temperature product ($\chi_M T$) for activated CoMe-MFU-4*l* and a sample of CoMe-MFU-4*l* dosed with 500 mbar CO. The lower magnitude of $\chi_M T$ across the entire temperature range upon CO dosing is consistent with a transition from high- to low-spin cobalt(II) upon CO binding. (**C**) Difference spectra generated by subtracting evolving spectra collected for CO-dosed CoMe-MFU-4*l* from the spectrum of CoMe-MFU-4*l* at 298 K. The data revealed the growth of several new vibrations, including a prominent acetyl vibrational band at 1678 cm^{-1} that appears concomitant with a peak for a red-shifted CO. (**D**) Representative synchrotron powder x-ray diffraction patterns collected over the course of the in situ gas dosing experiment (see SM section 7 for details and figs. S31 to S33 for the full set of data). At 80 K, CO only physisorbed within the material whereas upon dosing with ~100 mbar at 298 K, migratory insertion and coordination of CO to the cobalt(II) ions was observed. Select patterns are shown to highlight changes with heating under the different gas atmospheres. a.u., arbitrary units

Mechanism of CO adsorption

Upon exposure to 1 bar of CO, CoMe-MFU-4*l* rapidly changed from violet to light brown, whereas subsequent exposure to vacuum reversed this color change, suggesting a reversible electronic structure change at the cobalt center that occurred upon CO binding (fig. S39). Analysis on a cobalt-dilute sample of CoMe-MFU-4*l* with solid-state electron paramagnetic resonance (EPR) spectroscopy at 15 K revealed an eight-line hyperfine splitting pattern consistent with a high-spin cobalt(II) center (nuclear spin $I_{Co} = 7/2$, fig. S23). By contrast, the EPR spectrum obtained for a sample of CoMe-MFU-4*l* dosed ex situ with 50 mbar of CO featured a prominent eight-line pattern between 240 and 400 mT ($g \approx 2.0$ and 2.1), consistent with a low-spin cobalt(II) center, along with a very low-intensity $S = 3/2$ signal (Fig. 3A).

Direct current magnetic susceptibility data collected for CoMe-MFU-4*l* and a sample of CoMe-MFU-4*l* dosed with 500 mbar of CO also support a cobalt(II) spin state change upon CO adsorption (Fig. 3B). At 300 K and 7 T, the product of the experimental molar magnetic susceptibility and temperature ($\chi_M T$) determined for CoMe-MFU-4*l* was 11.1 electromagnetic units (emu) K mol^{-1}. In contrast, at 300 K and 7 T, the magnitude of $\chi_M T$ for the CO-dosed sample of CoMe-MFU-4*l* was much lower at 4.3 emu K mol^{-1}. The magnitude of $\chi_M T$ for both samples was higher than the predicted magnitude for four isotropic $S = 3/2$ or 1/2 cobalt(II) centers, respectively (7.5 and 1.50 emu K mol^{-1} per formal unit), which can be attributed to the presence of magnetic anisotropy, whereas the much smaller $\chi_M T$ magnitude for the CO-dosed sample was consistent with a change from high-spin to low-spin cobalt(II) upon CO binding (see SM section 5.3 for further discussion).

To monitor chemical changes occurring upon CO binding, in situ variable-pressure and variable-temperature DRIFTS data were obtained upon dosing samples of CoMe-MFU-4*l* with various pressures of CO and ^{13}CO (up to 1 bar, see fig. S28 for the isotopically labeled spectrum). To eliminate any effects arising from electronic communication between cobalt(II) sites in the same cluster node, we synthesized a variant of CoMe-MFU-4*l* with an average ratio of 1.0:4.0 Co:Zn based on ICP-OES, consistent with presence of just one cobalt per cluster node on average (*33*). We collected difference spectra upon dosing with increasing pressures of CO at 300 K, with the activated framework as the baseline. Corresponding spectra for undiluted CoMe-MFU-4*l* appeared similar, with broader features (see fig. S24). This procedure resulted in complex spectra with multiple peaks and overlapping vibrational bands.

Four main CO-based vibrations at 2034, 2015, 1986, and 1678 cm^{-1} (Fig. 3C) were observed. At low pressures, the vibrational band at 1986 cm^{-1} saturated quickly at mbar pressure and persisted even after exposing the sample to dynamic vacuum. While we cannot discount ν(C≡O) vibrations due to CO ligation at defect sites, this ν(C≡O) value resembles that of monocarbonyl cobalt(I) complexes (*34*), potentially located at surface sites and generated from reduction induced by the methyl anion (*3*) (see fig. S25 and table S8). The 2015 cm^{-1} peak initially increased with increasing CO pressures up to ~5 mbar and then decreased in intensity at higher pressures up to 1 bar, thus we assigned this band as ν(C≡O) for a single CO bound at the cobalt site, yielding a monocarbonyl, monomethyl cobalt(II) complex.

Above ~0.3 mbar, two other bands appeared at 1678 and 2034 cm^{-1} and increased in intensity throughout the experiment up to 1 bar. We assigned these features to a cobalt–acetyl (*18*) and a monocarbonyl, monoacetyl cobalt (II) complex, respectively. The ν(C≡O) of the CO on the cobalt–acetyl complex is hypsochromically shifted when compared to the ν(C≡O) of the CO on the cobalt–methyl complex, consistent with observations for molecular analogs in solution (*18*). Furthermore, variable-temperature studies indicated that neither the monocarbonyl, monoalkyl complex, nor the monocarbonyl, monoacetyl cobalt(II) complex form when the material was directly dosed with CO at 100 K. However, if the material was dosed at 300 K and then cooled, these products persist, indicating activation barriers for their formation (figs. S26 and S27).

In situ powder x-ray diffraction data were collected for a sample of CoMe-MFU-4*l* dosed with CO to examine structural changes occurring as a function of temperature (see Fig. 3D and section 7.2 of the SM). Starting from a sample of activated CoMe-MFU-4*l* at 80 K, dosing with increasing pressures of CO ranging from 12 to 89 mbar resulted in clear changes in the diffraction patterns, for example, a decrease in the intensity of peaks at $2\theta = 2.75°$, 3.88°, and 4.07° and an increase in the intensity of the peak at 7.15° (fig. S29A).

A Rietveld refinement of the diffraction pattern obtained after dosing with 12 mbar of CO revealed physisorbed CO within the framework (fig. S35, consistent with DRIFTS data collected at 100 K; see fig. S25). Heating the sample from 80 to 298 K after dosing with 89 mbar of CO resulted in a large unit-cell contraction that was complete at around 150 K, which was consistent with a transition from high- to low-spin cobalt(II) (fig. S32) and consistent with the EPR spectroscopy and magnetic susceptibility data.

After subsequent cooling from 298 K under 89 mbar CO and then heating to 313 K under a vacuum to regenerate the sample, powder x-ray diffraction data were collected at 298 K under increasing pressures of CO from 11 to 99 mbar. Changes in the diffraction data were again consistent with a unit-cell contraction and a conversion from high- to low-spin cobalt(II), and Rietveld refinement of the diffraction pattern collected at 99 mbar supported the presence of a monocarbonyl, monoacetyl adduct of cobalt(II), consistent with the features observed in the vibrational spectra (figs. S36 and S37). Finally, heating at 313 K under a dynamic vacuum regenerated the diffraction pattern for CoMe-MFU-4*l*, illustrating the reversibility of CO coordination and migratory insertion (fig. S37).

To further investigate the mechanism of CO adsorption in CoMe-MFU-4*l*, density functional theory (DFT) calculations were performed with $Co_4Zn(CH_3)_4(bta)_6$ (bta^- = benzotriazolate) as a representative cluster model (Fig. 4; see SM section 10 for details). Key vibrations from DRIFTS measurements could be recapitulated in models with sorption confined to a single cobalt(II) site (table S9). A summary of the most important mechanistic steps is shown in Fig. 4, with additional details provided in figs. S47 to S55 and tables S14 to S30. The

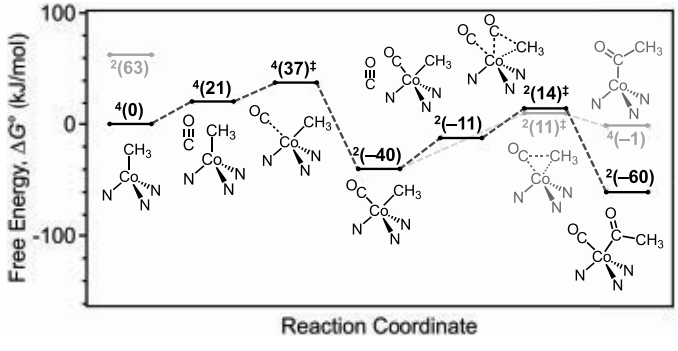

Fig. 4. Calculated free energy landscape for reversible CO coordination and migratory insertion into the Co–Me bond. Standard-state free energy landscape (kJ/mol) at 298.15 K and 1 atm using the M06-L/def2-TZVP level of theory for the reaction of CO with the model cluster $Co_4Zn(CH_3)_4(bta)_6$ at a single cobalt(II) site with initial ligation and spin-transition to yield $Co_4Zn(CH_3)_4(CO)(bta)_6$, followed by coordination and migratory insertion of the second equivalent of CO to yield $Co_4Zn(CH_3)_3(CO)(COMe)(bta)_6$. The superscript preceding the energy values denotes the spin multiplicity ($2S+1$) for the Co site to which CO binding is analyzed. Alternative mechanistic pathways, including direct migratory insertion from $Co_4Zn(CH_3)_4(CO)(bta)_6$ and the coordination of two CO equivalents to the same cobalt site, as depicted in gray, are both thermodynamically and kinetically less favorable. See SM section 10 for computational details.

most energetically favorable series of elementary steps begins with the adsorption of CO to a high-spin cobalt site, resulting in a spin transition from $S = 3/2$ to $S = 1/2$ at the cobalt ion and a corresponding change in coordination geometry from tetrahedral to distorted trigonal bipyramidal. Notably, the DFT calculations suggest that CO binding at one cobalt(II) site does not greatly alter the energetic landscape for CO adsorption elsewhere in the cluster (tables S16 and S18).

After the CO-induced spin transition, a second CO molecule is predicted to adsorb at the same cobalt(II) center, in which chemisorption of the second CO molecule occurs with a concomitant migratory insertion of the first CO adsorbate into the terminal methyl ligand, yielding a monocarbonyl, monoacetyl group (figs. S53 and S55). The concerted adsorption–reaction step, which takes place along the low-spin surface, is predicted to be critical to the adsorption capability of CoMe-MFU-4*l* for multiple equivalents of CO. Alternative reaction pathways, including formation of a dicarbonyl intermediate or direct migratory insertion of the first CO to yield a monoacetyl intermediate were calculated as higher energy pathways (Fig. 4).

Outlook

The foregoing results demonstrate that the highly porous metal–organic framework CoMe-MFU-4*l* selectively and reversibly captures two equivalents of CO per cobalt(II)–methyl site through a tandem spin transition and reversible migratory insertion mechanism. This process resulted in highly selective, high-capacity CO capture with a dependence on substrate that rendered the adsorption profile akin to that of other cooperative adsorbents without the need for long-range structural reorganization. More broadly, this work raises the prospect of judiciously designing porous adsorbents with adsorption sites that can bind multiple guest molecules.

REFERENCES AND NOTES

1. A. Whitty, *Nat. Chem. Biol.* **4**, 435–439 (2008).
2. C. M. McGuirk *et al.*, *Nat. Commun.* **9**, 5133 (2018).
3. D. A. Reed *et al.*, *Nature* **550**, 96–100 (2017).
4. J. Oktawiec *et al.*, *Nat. Commun.* **11**, 3087 (2020).
5. T. M. McDonald *et al.*, *Nature* **519**, 303–308 (2015).
6. E. J. Kim *et al.*, *Science* **369**, 392–396 (2020).
7. R. L. Siegelman *et al.*, *J. Am. Chem. Soc.* **139**, 10526–10538 (2017).
8. J. R. Edison *et al.*, *J. Chem. Phys.* **154**, 214704 (2021).
9. J. Kundu *et al.*, *Phys. Rev. Lett.* **121**, 015701 (2018).
10. B. E. R. Snyder *et al.*, *Nature* **613**, 287–291 (2023).
11. R. C. Rohde *et al.*, *Science* **386**, 814–819 (2024).
12. A. M. Wright, M. T. Kapelewski, S. Marx, O. K. Farha, W. Morris, *Nat. Mater.* **24**, 178–187 (2025).
13. F. Luo *et al.*, *J. Am. Chem. Soc.* **138**, 5678–5684 (2016).
14. T. Runčevski *et al.*, *Chem. Commun.* **52**, 8251–8254 (2016).
15. A. T. Gallagher, C. D. Malliakas, T. D. Harris, *Inorg. Chem.* **56**, 4654–4662 (2017).
16. N. Shirasawa, M. Akita, S. Hikichi, Y. Moro-oka, *Chem. Commun.* **5**, 417–418 (1999).
17. R. R. Reinig, E. L. Fought, A. Ellern, T. L. Windus, A. D. Sadow, *Chem. Commun.* **53**, 11020–11023 (2017).
18. R. R. Reinig, E. L. Fought, A. Ellern, T. L. Windus, A. D. Sadow, *Dalton Trans.* **47**, 12147–12161 (2018).
19. R. Röß-Ohlenroth, B. Bredenkötter, D. Volkmer, *Organometallics* **38**, 3444–3452 (2019).
20. D. Denysenko *et al.*, *Chemistry* **17**, 1837–1848 (2011).
21. R. Gesztelyi *et al.*, *Arch. Hist. Exact Sci.* **66**, 427–438 (2012).
22. D. Denysenko *et al.*, *Chem. Commun.* **48**, 1236–1238 (2012).
23. J. D. Jewson, L. M. Liable-Sands, G. P. A. Yap, A. L. Rheingold, K. H. Theopold, *Organometallics* **18**, 300–305 (1999).
24. X. Ma *et al.*, *Chem. Soc. Rev.* **52**, 3741–3777 (2023).
25. J. E. Bachman *et al.*, *Energy Environ. Sci.* **11**, 2423–2431 (2018).
26. D. Farrusseng *et al.*, *Langmuir* **25**, 7383–7388 (2009).
27. Z. Zhu *et al.*, *J. Am. Chem. Soc.* **145**, 17151–17163 (2023).
28. J. N. Weiss, *FASEB J.* **11**, 835–841 (1997).
29. A. V. Hill, *Biochem. J.* **7**, 471–480 (1913).
30. H. Swenson, N. P. Stadie, *Langmuir* **35**, 5409–5426 (2019).
31. E. D. Bloch *et al.*, *J. Am. Chem. Soc.* **136**, 10752–10761 (2014).
32. J. J. Baschuk, X. Li, *Int. J. Energy Res.* **25**, 695–713 (2001).
33. A. M. Wright, A. J. Rieth, S. Yang, E. N. Wang, M. Dincă, *Chem. Sci.* **9**, 3856–3859 (2018).
34. D. Denysenko, J. Jelic, K. Reuter, D. Volkmer, *Chemistry* **21**, 8188–8199 (2015).

ACKNOWLEDGMENTS

We thank H. Celik, R. Giovine, and the Pines Magnetic Resonance Center's Core NMR Facility (PMRC Core) for assistance with spectroscopic measurements and analyses. The instrument used in this work was supported by the National Science Foundation under grant 2018784. Powder x-ray diffraction data were collected at Beamline 17-BM-B at the Advanced Photon Source, a US Department of Energy (DOE) Office of Science User Facility, operated by Argonne National Laboratory under contract DE-AC02-06CH11357. We thank A. Yakovenko (Argonne National Laboratory) for technical assistance with powder x-ray diffraction data refinement, L. M. Mirica (University of Illinois Urbana-Champaign) for helpful discussions on cooperativity, T. D. Harris (University of California, Berkeley) for editorial assistance, and D. X. Ngo, R. C. Rohde, and B. E. R. Snyder (University of California, Berkeley) for general discussions. **Funding:** Gas adsorption analyses, crystal structure determinations, spectroscopic measurements, and electronic structure calculations were supported by the DOE, Office of Basic Energy Sciences (BES), Separation Science in the Chemical Sciences, Geosciences, and Biosciences Division, under award number DE-SC0019992. The synthesis of materials was supported by the Hydrogen Materials–Advanced Research Consortium (HyMARC), established as part of the Energy Materials Network under the DOE, Office of Energy Efficiency and Renewable Energy, Hydrogen and Fuel Cell Technologies Office, under contract DE-AC02- 05CH11231. K.M.C. was supported by an Arnold O. Beckman Postdoctoral Fellowship, J.L.P. acknowledges support from both the University of California President's and the Ford Foundation Postdoctoral Fellowship Programs, A.S.R. acknowledges support via a Miller Research Fellowship from the Miller Institute for Basic Research in Science at the University of California, Berkeley, and J.B. acknowledges the Deutsche Forschungsgemeinschaft (DFG) for a postdoctoral research fellowship. Magnetic measurements were supported by National Science Foundation (NSF) grant DMR-2206534. R.A.M. was supported in part through the Quantum Information Science and Engineering Network (NSF grant DMR-1747426). This research used the Savio computational cluster resource provided by the Berkeley Research Computing program at the University of California, Berkeley (supported by the UC Berkeley Chancellor, Vice Chancellor for Research, and Chief Information Officer). R.D.B. acknowledges National Institutes of Health (NIH) Grant R35-GM126961 for EPR instrumentation and measurements. R.A.K. acknowledges the DOE Office of Energy Efficiency and Renewable Energy (EERE), Hydrogen and Fuel Cell Technologies Office (HFTO) contract no. DE-AC36-8GO28308 to the National Renewable Energy Laboratory (NREL). Electron microscopy was supported by the DOE, Office of Science, BES, Materials Sciences and Engineering Division under contract DE- AC02-05-CH11231 within the Electron Microscopy of Soft Matter Program (KC11BN) and carried out at the Molecular Foundry, which is supported by the Office of Science, Office of Basic Energy Sciences, of the DOE under contract DE-AC02-05CH11231. P.S.S. and N.P.S. acknowledge funding from NSF grant CHE-2349748. Work at the Molecular Foundry was supported by the Office of Science, Office of BES, of the DOE under contract DE-AC02-05CH11231. Certain commercial equipment, instruments, or materials are identified in this document. Such identification does not imply recommendation or endorsement by the National Institute of Standards and Technology (NIST), nor does it imply that the products identified are necessarily the best available for the purpose. C.M.B. was fully supported and R.A.K was partially supported by NIST during this project. The views expressed in the article do not necessarily represent the views of the DOE or the US Government. The US Government retains and the publisher, by accepting the article for publication, acknowledges that the US Government retains a nonexclusive, paid-up, irrevocable, worldwide license to publish or reproduce the published form of this work, or allow others to do so, for US Government purposes. **Author contributions:** K.M.C., J.B., and J.R.L. conceptualized the research. K.M.C. synthesized and characterized materials, directed the research with J.R.L., and analyzed data. J.L.P. and A.J.H. conducted and interpreted breakthrough analyses. H.Z.H.J., S.H.K., K.M.C., J.L.P., H.A.S., Y.Y., Z.K., R.D.B., and J.B. conducted spectroscopic characterization. R.A.M. conducted and interpreted magnetometry. K.M.C., M.D., and Y.Y. conducted gas adsorption isotherm measurements. K.M.C., J.L.P., H.K., and J.W.T. performed single-crystal x-ray diffraction analyses. R.A.K. and C.M.B. collected and analyzed powder x-ray diffraction data. P.S.S. and N.P.S. developed the sequential binding model for the CO adsorption data. A.S.R. and K.A.P. performed computational analyses. K.M.C. and K.R.M. drafted the manuscript. All authors contributed to revision of the manuscript. **Competing interests:** The authors declare the following competing interests: The University of California, Berkeley, has applied for a patent on some of the technology discussed herein regarding gas separations with coordinatively unsaturated metal carbanions, on which K.M.C., J.L.P., J.B., and J.R.L. are listed as coinventors. **Data and materials availability:** The supplementary materials contain complete experimental and spectral details for all new compounds reported herein. Crystallographic data for solid-state structures obtained from single-crystal x-ray diffraction have been made available free of charge from the Cambridge Crystallographic Data Centre (CCDC) under deposition number 2352633 for CoMe-MFU-4*l*. **License information:** Copyright © 2025 the authors, some rights reserved; exclusive licensee American Association for the Advancement of Science. No claim to original US government works. https://www.science.org/content/page/science-licenses-journal-article-reuse

SUPPLEMENTARY MATERIALS

science.org/doi/10.1126/science.ady2607
Materials and Methods; Figs. S1 to S59; Tables S1 to S30; Technical discussions on magnetometry, powder x-ray diffraction, anion stoichiometry, small molecule reactivity, and sequential binding model; Supplemental adsorption information format (AIF) files; References (*35–84*)

Submitted 15 April 2025; accepted 23 September 2025

10.1126/science.ady2607

DEVICE TECHNOLOGY

Atomic layer bonding contacts in two-dimensional semiconductors

Li Gao[1,2]†, Zhangyi Chen[1,3]†, Zhenghui Fang[1,3], Shucao Lu[1,3], Xiaofu Wei[1,3], He Jiang[1,3], Kuanglei Chen[1,3], Xiaoyu He[1,3], Chao Chen[1,3], Wei Shangguan[1,3], Jinsen Shang[1,3], Huihui Yu[1,3], Mengyu Hong[1,3], Yang He[1,3], Xiankun Zhang[1,3]*, Zheng Zhang[1,3]*, Yue Zhang[1,3]*

Van der Waals contact between two-dimensional semiconductors and metals has always been inferior to covalent bond contacts used in semiconductor industry because of weak band coupling and low bond strength. Here, we report an atomic layer bonding (ALB) contact with strong band coupling and high interfacial cohesion by establishing a metallic coherent bonding interface between the transition-metal atomic layer of transition-metal dichalcogenides and metals. This contact exhibits ultralow contact resistance and superb thermomechanical stability, comparable to those of covalent bond contacts and surpassing all reported contact configurations. ALB contact formed in monolayer molybdenum disulfide and gold demonstrates a contact resistance of 70 ohm-micrometers and thermomechanical stability up to 400°C and delivers a maximum on-current of 1.1 milliamperes per micrometer after high-temperature annealing, all of which meet industrial integration.

Metal-semiconductor contacts are crucial for the development of high-performance electronic devices and their industrial integration, especially as device sizes continue to shrink. Industrial metal-semiconductor contacts necessitate ultralow contact resistance (R_C), superior thermomechanical stability up to 400°C for compatibility with back-end-of-line (BEOL) processes, enhanced thermal and electrical conductivity for heat dissipation, and seamless integration with standard semiconductor techniques. Covalently bonded metal-semiconductor contacts, exemplified by silicon-silicide (Si-M_xSi_y) (*1*), titanium nitride–gallium nitride (TiN-GaN) (*2*), and titanium silicon carbide–silicon carbide (Ti_3SiC_2-SiC) (*3*), represent leading strategies in the semiconductor industry. These contacts exhibit strong interfacial band coupling and high bonding strength, resulting in ultralow R_C and exceptional thermomechanical stability, both of which are most critical for industrial integration (*2*, *4*). However, achieving strong bonding contact in two-dimensional (2D) van der Waals (vdW) semiconductors such as transition-metal dichalcogenides (TMDs) is highly challenging because of the vdW gap and dangling-bond-free surface. The vdW gap blocks charge transfer between the metal and semiconductor, and the dangling-bond-free surface drastically reduces the likelihood of chemical bonding. As a result, the current contact between 2D TMDs and metals is dominated by vdW contacts. The inherent weak band coupling and low bonding strength of the vdW contacts inevitably lead to two limitations: large tunnel barrier [i.e., high R_C (*5*–*9*)] and low contact stability.

[1]Academy for Advanced Interdisciplinary Science and Technology, Key Laboratory of Advanced Materials and Devices for Post-Moore Chips Ministry of Education, State Key Laboratory for Advanced Metals and Materials, University of Science and Technology Beijing, Beijing, China. [2]School of Materials Science and Engineering, Peking University, Beijing, China. [3]School of Materials Science and Engineering, Beijing Key Laboratory for Advanced Energy Materials and Technologies, University of Science and Technology Beijing, Beijing, China. ***Corresponding author. Email: zhangxiankun@ustb.edu.cn (X.Z.); zhangzheng@ustb.edu.cn (Z.Z.); yuezhang@ustb.edu.cn (Y.Z.)** †These authors contributed equally to this work.

Attempts to overcome the limitations of vdW contact include edge contacts (*10*, *11*), low–work function metals (*12*–*14*), ultrahigh vacuum evaporation (*15*, *16*), ultrashallow Y-doping contact (*17*), and the recently much-anticipated semimetal contacts (*18*–*23*). These efforts have reduced the R_C to tens of ohm-micrometers. However, almost all existing contact schemes have failed to break the weak bonding of vdW interfaces. R_C and thermomechanical stability, especially up to 400°C required for BEOL integration, have not yet fully synchronized and are far inferior to strong covalent bonding interfaces, hindering the development of "lab to fab." A prime example is that the vdW contacts between semimetal bismuth or antimony (Bi/Sb) and 2D TMDs either cannot meet the thermal budget for BEOL integration (fig. S1A) or the R_C has increased substantially after heating at <400°C (*14*, *18*, *19*, *24*). In addition, thermal deformation of electrodes at weakly bonded interface threatens contact stability (*25*, *26*).

Here, we report an atomic layer bonding (ALB) contact (Fig. 1A) for 2D TMD semiconductors and metals. We established a metallic coherent bonding interface between the transition-metal atomic layer and the metal electrode by precisely removing the upper sulfur-group atoms, matching electronic structures and lattice structure. ALB contact exhibits strong band coupling and high interfacial cohesion (Fig. 1, C and E), comprehensively overcoming the limitations of vdW contact (Fig. 1, D and E). As a result, we achieved a breakthrough in both ultralow R_C and excellent thermomechanical stability, comparable to those of covalent bonding contacts in the semiconductor industry.

Comparison of ALB contact and vdW contact

Realizing the ALB contact between transition-metal atomic layer in TMDs and metal is theoretically an ideal way to enhance bonding and achieve overall breakthrough in contact performance. This is mainly attributed to the multidirectional and far-extending properties of the d orbitals in transition-metal atoms, which have high bonding probability and strong bonding ability with metal electrodes. That is, the electron on the d orbital of transition-metal atoms can form strong metallic bonds with the electron of the metal at the interface. This provides a favorable electronic structure foundation. Through density functional theory (DFT) calculations, we found that after removing the upper S atomic layer, the Mo atomic layer in monolayer MoS_2 can coherently bond with the Au (111) atoms through lattice relaxation, and the charge transfer and accumulation at the bonding interface are markedly higher than those at the vdW interface (Fig. 1, A and B). This indicates strong bonding ability. The presence of free electron gas demonstrates the metallic bonding properties of Au and Mo atomic layers (fig. S2A). Furthermore, the electrostatic potential profile reveals that the carrier tunneling probability of the ALB interface is 100% ($\phi_t = 0$), whereas the barrier height at the vdW interface is 3.37 eV and the barrier width is 1.11 Å ($\phi_t > 0$) (right graph in Fig. 1, A and B). In addition, the local density of states indicates that the ALB region below the Au electrode is metallic, and the band bending in the ALB contact and MoS_2 channel heterojunction region is very steep in actual space (~0.5 nm), which allows for a high-probability tunneling of charge carriers in the space charge region in the on state (fig. S2B)—i.e., exhibiting good ohmic contact. This is similar to the situation in Si. We also observed multiple hybrid bands composed of Mo d orbitals and Au d orbitals intersecting with the Fermi level (E_F) (Fig. 1C) in ALB contact. By contrast, for the vdW contact, the bands intersecting with E_F are primarily composed of Au d orbitals, with the lowest point of the MoS_2 conduction band located above E_F (Fig. 1D), indicating that ALB contact greatly enhances band coupling. All of these indicate that ALB contact can achieve extremely low R_C. Moreover, the bonding energy of the ALB interface obtained through calculation reaches 0.281 eV/Å^2, which is a highly cohesive bonding interface and is 5.4 times as strong as that of the vdW interface (0.052 eV/Å^2) (Fig. 1E). This highly cohesive coherent bonding interface will guarantee the thermomechanical stability of contact interface and the entire contact structure (Fig. 1F). However,

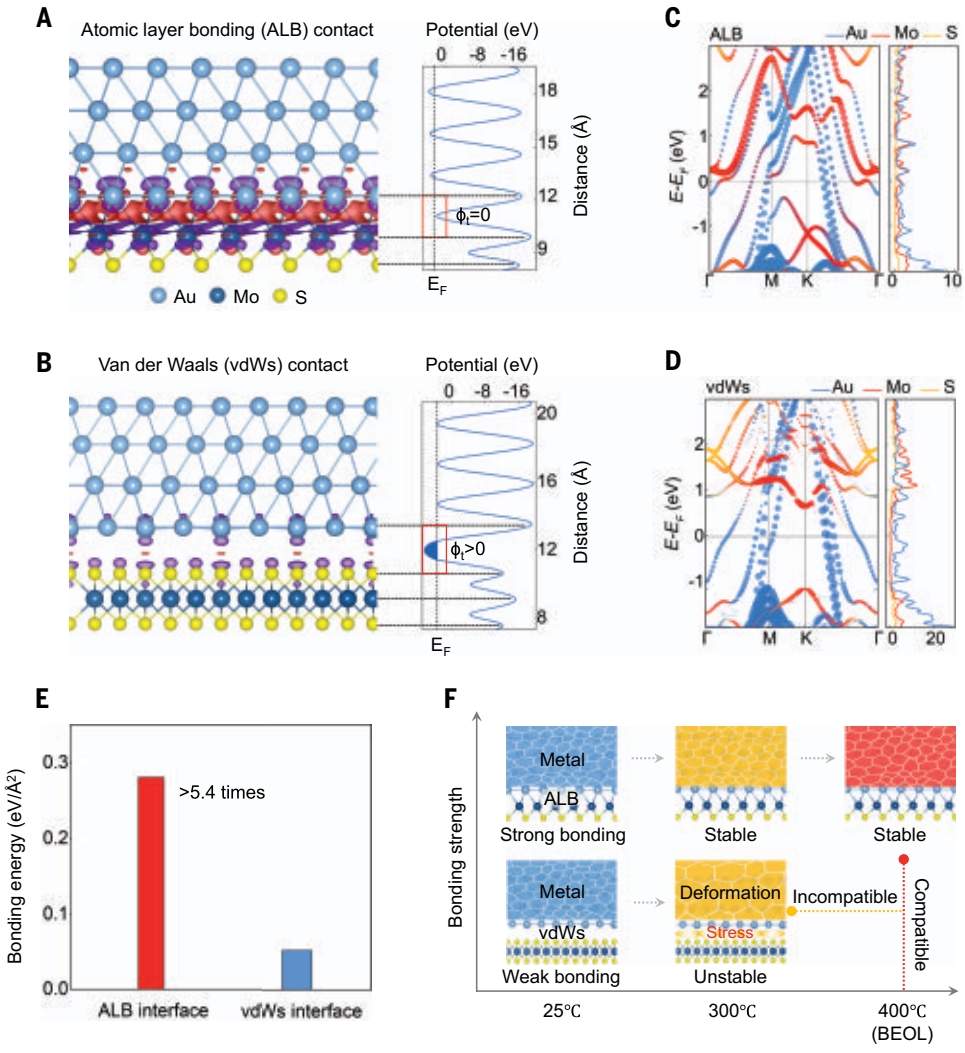

Fig. 1. Comparison of ALB contact and vdW contact. (**A** and **B**) Differential charge density of ALB contact (A) and vdW contact (B) of Au and MoS_2 system (red, positive; purple, negative). The isosurface level is 2.5×10^{-3} e bohr^{-3}. The graph on the right is the corresponding electrostatic potential profile along the vertical direction. (**C** and **D**) Electronic band structure and density of states of ALB contact (C) and vdW contact (D). (**E**) Bonding energy of ALB and vdW interface obtained from calculation. (**F**) Comparison of thermomechanical stability of ALB and vdW contacts before and after heating.

vdW contacts with weak bonding are susceptible to thermal deformation such as recrystallization of the interface electrode, leading to instability and stress concentration. We further demonstrated that the ALB contact system is structurally stable at temperatures up to 400°C by molecular dynamics calculations (fig. S2, C and D), meeting the thermal budget for back-end integration.

Realization of ALB contacts

In reality, ALB contact requires precise removal of the upper S atomic layer. The formation energy of S vacancies is smaller than that of Mo vacancies by a factor of 3 to 4, which provides a larger operating window for precise removal of S without damaging Mo (*27*–*29*). Notably, the transition-metal atomic layer lattice and the metal electrode lattice need to be highly matched; otherwise, large interface stress will be introduced. For the Au and MoS_2 system, Mo atoms can theoretically form a coherent bond with Au on the (111) plane by lattice relaxation, as shown in Fig. 1A. However, in reality, the lattice constant of Mo-Mo (a = 3.151 Å) is larger than that of Au-Au (b = 2.914 Å) on the (111) plane (Fig. 2, A and B), and the lattice mismatch is as high as 8%, making a stress-free and stable coherent bonding interface difficult to form. Ideal Au-Mo coherent bonding means Mo-Mo contraction or Au-Au moderate expansion.

Through DFT calculations, we found that when four layers of Au on the (111) plane are coherently bonded with -MoS, the Mo-Mo lattice shrinks by up to 6.22% (from 3.151 to 2.955 Å), whereas the expansion of Au-Au is only 1.39% (from 2.914 to 2.955 Å) (Fig. 2, C and D). This is because the contraction of Mo-Mo requires lower energy. From these results, the contraction of the Mo-Mo lattice to adapt to the metal lattice is the key to realizing coherent ALB contact in reality. In monolayer MoS_2, we observed that when the upper S atomic layer was completely removed, the Mo-Mo lattice shrank from the initial 3.151 to 2.968 Å because of the loss of upper support, with a shrinkage rate of 5.81% (Fig. 2E and fig. S3). This is very close to the 6.22% required for coherent bonding with Au, and the remaining mismatch can be completely adapted by lattice relaxation and elastic strain. This indicates that removal of the upper S atom provides both matching electronic and lattice structures. We also verified that the addition of more layers of Au does not have a substantial impact on the lattice matching of the bonding interface (fig. S4). The accumulation of Mo-Mo lattice shrinkage within a certain range will inevitably lead to the generation of local cracks (Fig. 2E). These cracks are partially filled with initially slowly deposited Au (red area in Fig. 2F). Moreover, these cracks can provide expansion space for lattice relaxation at the ALB interface when heated, depleting the internal stress of lattice relaxation while further increasing interface continuity, ensuring that the interface has both uniform electrical conductivity and high thermomechanical stability.

In practice, when we used ultrasoft argon (Ar) plasma to precisely etch away the upper S atomic layer of monolayer MoS_2, we obtained an etching interface that conforms to theoretical calculations (Fig. 2G). The finely controlled process is shown in fig. S5 and in the materials and methods. The boundary between the etched and unetched areas is very sharp, with no crack penetration, ensuring the construction of short-channel transistors (fig. S6A). The decrease in Mo3d binding energy of ~0.5 to ~0.6 eV obtained from x-ray photoelectron spectroscopy (XPS) at the etching interface further confirms the effective removal of top S (fig. S6B). Subsequently, we examined the ALB contact formed in multilayer MoS_2 and Au through high-angle annular dark-field scanning transmission electron microscope (HAADF-STEM). Multilayer MoS_2 is more conducive to clearly observing the atomic arrangement and comparing the lattice contraction. We observed that the Mo atoms form a nearly perfect coherent bond with Au (111) atoms (Fig. 2H). The Mo-Mo lattice (2.592 Å) at the bonding interface is almost identical to the Au-Au lattice (2.601 Å) and is smaller than that in bottom nonbonded MoS_2 (2.802 Å), confirming Mo-Mo lattice contraction at the bonding interface, consistent with the calculated results. The Mo-Mo lattice at the bonding interface shrinks by 7.49%

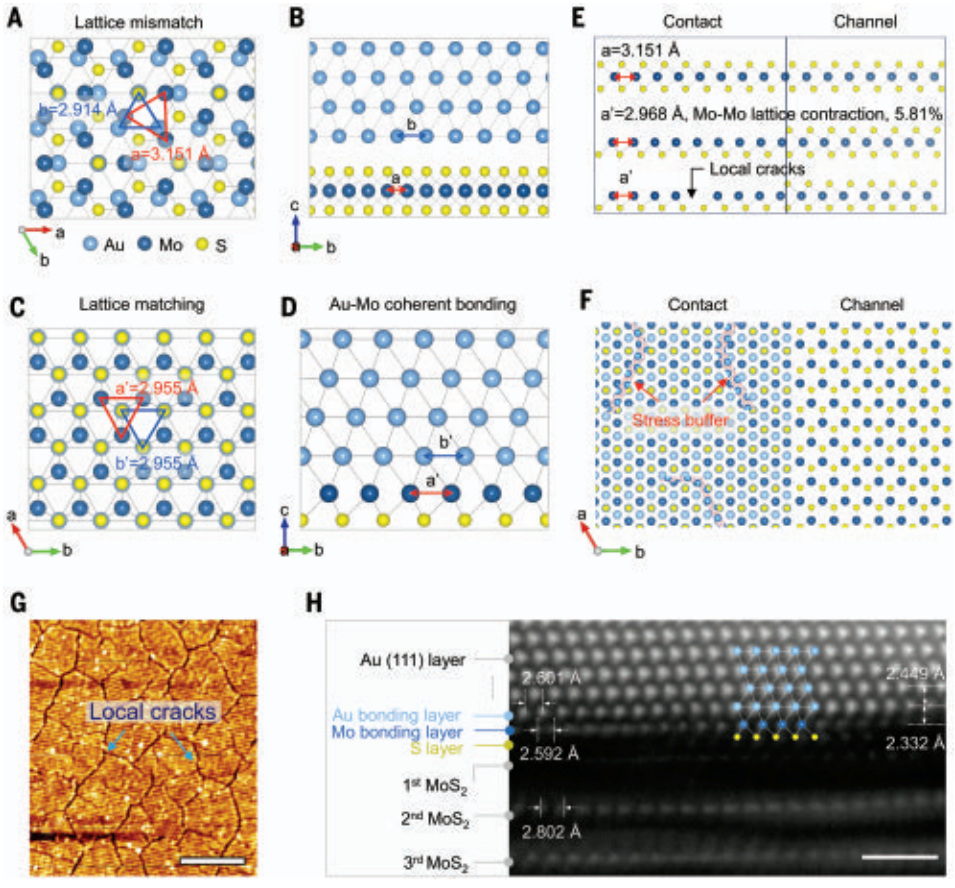

Fig. 2. Realization of ALB contacts between MoS_2 and Au electrode. (**A** and **B**) Bottom (A) and side views (B) of the optimized structure when Au (111) atoms contact MoS_2 monolayer. The Mo-Mo lattice constant (3.151 Å, red triangle side length) is larger than the Au-Au lattice constant (2.914 Å, blue triangle side length). (**C** and **D**) Bottom (C) and side (D) views of the coherent ALB contact formed by the contraction of the Mo-Mo lattice and the appropriate expansion of the Au-Au lattice. (**E**) Mo-Mo lattice contraction and local crack generation after removing the upper S atomic layer of MoS_2 calculated by DFT. (**F**) Overall bottom view of the ALB contact and channel. (**G**) AFM morphology of monolayer MoS_2 after the upper S atoms are etched away. Scale bar, 500 nm. The local cracks caused by the contraction of Mo-Mo lattice are clearly visible. (**H**) HAADF-STEM image of the ALB interface. Scale bar, 1 nm.

compared with the nonbonded part, which is greater than the 6.22% calculated by DFT. This is related to the lattice relaxation of the actual sample after heating. The interplanar spacing between Au and Mo atomic layers (2.332 Å) at the bonding interface is much smaller than that at the Au-MoS_2 vdW interface (4.225 Å) (fig. S7, A and B) and also smaller than the conventional vdW distance (*30*), indicating the formation of non-vdW bonding. The strong Au-Mo bonding even "sucks up" the adjacent MoS_2 layer (marked "1st MoS_2" in Fig. 2H), causing the vdW spacing to change. In addition, XPS results indicate that the binding energy of Mo at the ALB interface is ~0.3 to ~0.4 eV lower than when removing the upper S, confirming the effective Au-Mo bonding (fig. S7C). Overall, the ALB contact interface has a metallic chemical state, highly ordered coherent lattice, and very high bonding energy, ensuring extremely low R_C and excellent thermomechanical stability. By contrast, some reported cases of introducing certain vacancies in the contact area often exhibit localized electronic structures, severe lattice distortions, and low bonding energies, resulting in high R_C and poor stability (*31*, *32*).

Electronic properties of ALB contacts

Then, we evaluated the electronic properties of ALB contacts in monolayer MoS_2 field-effect transistors (FETs) (see materials and methods for fabrication and measurement details). Figure 3A is a schematic diagram of a MoS_2 transistor. Figure 3, B and C, shows the transfer characteristics of variable-channel MoS_2 transistors at V_{bias} of 0.1 V and R_C extracted by transfer-length method (TLM). In pristine conditions, the drain-source current (I_{ds}) increases uniformly as the channel length (L_{CH}) decreases. After annealing at 300°C, the I_{ds} exhibits a marked increase, attributed to the enhanced quality of the ALB. After annealing at 400°C, I_{ds} decreases slightly, which is mainly due to thermal damage of the unpackaged channel rather than degradation of the ALB interface (fig. S8). Accordingly, we obtained a R_C of 170 Ω·μm for the pristine FETs, which decreased to 70 and 110 Ω·μm after progressive annealing at 300° and 400°C. To our knowledge, this is the only type of contact in 2D semiconductors that maintains extremely low resistance after long-term high-temperature annealing. Figure S9 presents the transfer characteristics and R_C of several other groups of FETs. The pristine R_C is ~100 to ~200 Ω·μm, and after 300°C annealing, it is often <100 Ω·μm, with a minimum value of 61 Ω·μm. We determined the Schottky barrier height (SBH) of the pristine ALB contact to be 28 meV, because the pristine bonding interface was not perfect. After annealing at 300° and 400°C, SBH decreased to an extremely low or negligible value (fig. S10), consistent with theoretical calculations. We then examined the limiting performance of the short-channel FET. Figure 3D shows the transmission electron microscope (TEM) image of 30-nm short-channel MoS_2 FET, and Fig. 3, E and F, shows the corresponding transport and output performance of the same device after 300°C annealing. This FET exhibits a switching ratio of 10^7, a drain-induced barrier lowering (DIBL) of 30 mV/V, and a minimum subthreshold swing (SS) of 100 mV/dec. When the source-drain bias (V_{ds}) is only 0.7 V, I_{ds} reaches saturation, and the maximum I_{ds} reaches 1.1 mA/μm, representing the optimal current for the monolayer MoS_2 FET. Figure S11 presents the transport and output characteristics of three transistors with L_{CH} of ≤100 nm. All devices exhibited excellent electrical performance and outstanding thermal stability.

We further examined the transport properties of MoS_2 transistors with ALB contact formed with different S:Mo ratios. Consistent with the above conclusions, transistors with ALB contacts with S:Mo ratio close to 1:1 (almost all upper S is removed) have the highest on-off ratio, the largest on-current, and the best thermomechanical stability (fig. S12C). Insufficient or excessive etching at the bonding interface either fails to ensure the stability of the transistor or causes a decrease in the switching ratio and the on-current (fig. S12, A, B, and D). The durable thermomechanical stability of the ALB contact was further demonstrated after FET annealing at 300°C for 5 hours and 400°C for 3 hours (fig. S12, E and F). Our transistor exhibits the best heat resistance, surpassing all reported 2D transistors (fig. S12G). Conventional hard plasma etching and low-vacuum metal deposition also are

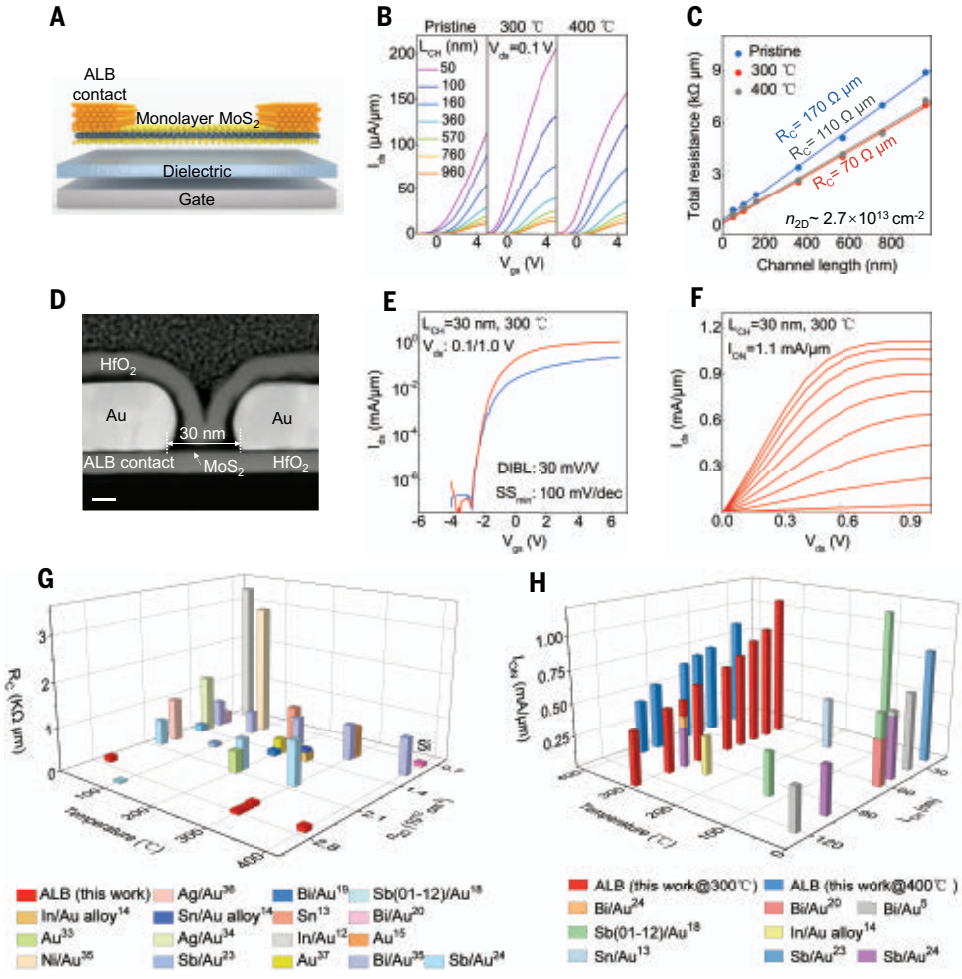

Fig. 3. Electronic properties of ALB contacts. (**A**) Diagram of MoS_2 transistor with ALB contact. (**B**) Transfer curves of a typical TLM structure with L_{CH} ranging from 50 to 960 nm at V_{bias} of 0.1 V. (**C**) R_C extracted by TLM method in (B). (**D**) Cross-sectional TEM image of a 30-nm short-channel MoS_2 FET. Scale bar, 10 nm. The top HfO_2 is deposited only when testing TEM and was not used to gate electrical transport. (**E**) Transfer curves of the same device after 300°C annealing in (D). (**F**) Output curves of the same device in (D). Gate-source voltage (V_{gs}) is from −3.5 to 6.5 V. (**G**) Comparison of R_C and thermomechanical stability of ALB contacts with other contacts. (**H**) Comparison of I_{ON} (V_{ds} = 0.7 V) and high-temperature resistance of the advanced short-channel monolayer MoS_2 transistor reported in the literature.

not conducive to achieving stable bonding contacts, and device performance is poor (fig. S12, H and I). In addition, by statistically comparing the performance of transistors with different channel widths, we have verified that the reliability of the final ALB contact interface is very high and will not be affected by potential cracks at the initial etched interface (fig. S13).

We next benchmarked our device performance with existing contact schemes. We first summarized the relationship between R_C, carrier concentration (n_{2D}), and reported withstood temperature for the state-of-the-art contact types for MoS_2 transistors in Fig. 3G. Our ALB contacts maintain the lowest R_C after high-temperature annealing at 300° and 400°C, surpassing all reported contact types (*13*–*15*, *18*–*22*, *24*, *33*–*37*). We then compared the I_{ON} (on state current density at V_{ds} = 0.7 V) and high-temperature resistance of short-channel monolayer MoS_2 transistors (Fig. 3H). Our devices can achieve high I_{ON} after annealing at 300° and 400°C, whereas most transistors with other types of contacts can only achieve room temperature performance (*13*, *14*, *18*–*21*, *23*, *24*). At V_{ds} of 0.7 V, the I_{ON} of our 30-nm short-channel MoS_2 transistor exceeds the high-performance target of the International Roadmap for Devices and Systems (IRDS) 2028 (*38*).

Table S1 shows the detailed performance of monolayer MoS_2 transistors with different contacts.

Enhanced thermomechanical stability of the ALB contact

ALB interface brings outstanding thermomechanical stability. This advantage is also reflected in the effective resistance to recrystallization plastic deformation of metal electrodes at high temperatures, thereby improving the stability of the entire contact structure (Fig. 4A). By contrast, the bonding strength of the Au direct contact interface is insufficient, and the electrode is prone to recrystallization deformation when heated (Fig. 4B). At this time, the stress is easily transferred to contact and channel regions. The grain orientation spread map obtained by electron backscatter diffraction demonstrates that the degree of recrystallization of the Au on the ALB interface is substantially lower than that of Au on a MoS_2 interface under the same heating conditions (Fig. 4, C and D). As a result, the short-channel MoS_2 transistor with ALB contact has very stable contact structure before and after heating (Fig. 4E), whereas the recrystallization deformation of the direct Au contact causes the channel to stretch by 85% (from 110 to 204 nm) (Fig. 4F). We confirmed that the MoS_2 transistor with ALB contact is not affected by stress before and after heating (Fig. 4G), whereas the channel with Au direct contact suffers severe tensile stress (Fig. 4H) (*25*, *26*, *39*, *40*).

Subsequently, we compared the thermomechanical stability of different types of Au contact, including ALB contact, top contact, edge contact, and vdW contact (Fig. 4I). After annealing at 300°C, except for the devices with ALB contacts, the switching performance of transistors with other contacts dropped or was lost to varying degrees. This is due to the serious channel stress concentration or contact detachment (edge contact) caused by the recrystallization deformation of electrode. Furthermore, we have demonstrated in long-channel MoS_2 transistors (L_{CH} = 1 μm) that the thermal instability caused by direct contact between different types of metal electrodes is common, and ALB strategies can improve their thermal stability (fig. S14). However, high-performance and high-reliability short-channel transistors often require careful consideration of the lattice matching at the ALB interface and the oxidation resistance of the metal electrode; otherwise, thermal stability cannot be guaranteed (fig. S15).

We conducted statistical analysis using XPS on 20 points within a 2-inch (5.08 cm) wafer (*41*, *42*) range (with a test area of ~400 μm per point), verifying the excellent scalability and repeatability of the ultrasoft Ar plasma in removing S and forming ALB contact (fig. S16). Then, we tested the performance of the array transistor on a 2-inch wafer (fig. S17A). All devices exhibited excellent switching characteristics after annealing at 300° and 400°C, demonstrating the scalability of the ALB contact (fig. S17, B and C). We compared the normalized I_{ON} of MoS_2 transistors with ALB, Bi/Au, and Sb/Au contacts (fig. S17D).

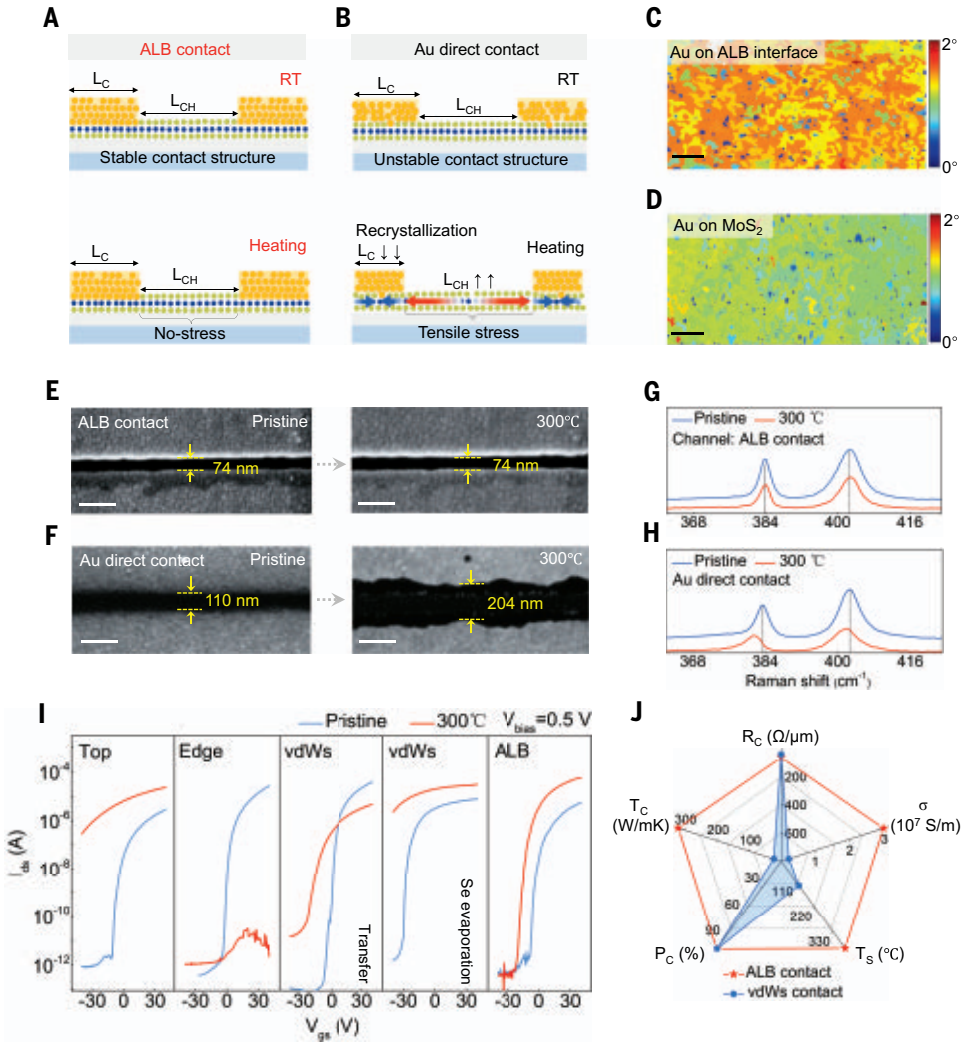

Fig. 4. Enhanced thermomechanical stability of the ALB contact. (**A**) Diagram of stable ALB contact before and after heating. L_C, contact length; RT, room temperature. (**B**) Diagram of stress concentration caused by recrystallization deformation of unstable Au direct contact after heating. (**C** and **D**) Grains orientation spread map of deposited Au electrodes on ALB interface (C) and on MoS_2 interface (D). Scale bar, 1 μm. The 0° to 2° scale represents the recrystallization grain orientation. The larger the orientation, the lower the degree of recrystallization deformation. (**E** and **F**) Scanning electron microscopy images of short-channel MoS_2 transistors with ALB contact (E) and Au direct contact (F) before and after heating. Scale bar, 200 nm. (**G** and **H**) Raman spectrum of channel area of MoS_2 transistor with ALB contact (G) and Au direct contact (H) before and after heating. (**I**) Transport properties of MoS_2 transistor with ALB contact and different types of Au contacts before and after annealing. (**J**) Radar plot of our ALB contact versus Sb vdW contact, benchmarked against industrial-grade contact performance. P_C, process compatibility; R_C, contact resistance (Ω·μm); σ, electrical conductivity (S/m); T_C, thermal conductivity (W/mK); T_S, thermomechanical stability (°C).

After annealing at 300°C, the I_{ON} of ALB devices increase by 400% compared with the pristine current. Even after annealing at 400°C, it remains 235% higher than the pristine current. By contrast, the performance of the Bi/Au and Sb/Au contacted device decayed substantially after annealing at 300°C, and Bi/Au failed completely at 400°C (*24*). These fully validate that ALB contacts play an irreplaceable role in improving stability. In addition, we have confirmed through calculations and experiments that the ALB contact achieved by compensating etching on the basis of bond energy differences (*43*) can be widely extended to other TMD semiconductors, such as tungsten disulfide and molybdenum diselenide (fig. S18 and materials and methods).

ALB contacts not only have ultralow R_C and excellent thermomechanical stability but also have much better heat-dissipation performance than mainstream vdW contacts. Taking the ALB contact formed by Au and MoS_2 as an example, both Au and Mo exhibit excellent thermal conductivity (κ_{Au}: 317 W/mK; κ_{Mo}: 138 W/mK) and electrical conductivity (σ_{Au}: 4.10×10^7 S/m; σ_{Mo}: 1.87×10^7 S/m) that far exceed semimetals such as Sb (κ_{Sb}: 24 W/mK; σ_{Sb}: 2.76×10^6 S/m) (fig. S1, B and C). Therefore, the heat-dissipation characteristics of ALB contact interface are bound to far exceed those of semimetal vdW contact. In this way, we can confirm that ALB contact comprehensively surpasses vdW contact, is comparable to covalent bond contact, and can meet industrial requirements (Fig. 4J).

Conclusions

We proposed and demonstrated ALB contact between 2D TMD semiconductor and metal by establishing metallic coherent bonding interface. ALB contact exhibits ultrastrong band coupling and high cohesive bonding strength and achieves notable synergistic breakthrough in ultralow R_C and thermomechanical stability, surpassing all reported contact configurations and comparable to covalent bonding contacts in semiconductor industry. Thanks to the ALB contact, the R_C of monolayer MoS_2 transistor is as low as 70 Ω·μm, the contact thermomechanical stability is as high as 400°C, and the on-state current after high-temperature annealing is 1.1 mA/μm. All of these surpass equivalent silicon technologies and meet the high-performance target of the 2028 IRDS Roadmap. We demonstrated the scalability of ALB contacts and their generalizability to different 2D TMDs and metals. The ALB contact overcomes the inherent problem of vdW semiconductors, greatly increases the industrial compatibility of vdW electronic devices, and is expected to lead the transformation of 2D electronics from "lab to fab."

REFERENCES AND NOTES

1. G. W. Rubloff, *Ultramicroscopy* **14**, 107–119 (1984).
2. L. L. Smith, R. F. Davis, R. J. Liu, M. J. Kim, R. W. Carpenter, *J. Mater. Res.* **14**, 1032–1038 (2011).
3. Z. Wang, M. Saito, S. Tsukimoto, Y. Ikuhara, *J. Ceram. Soc. Jpn.* **119**, 783–793 (2011).

4. P. S. Ho, G. W. Rubloff, *Thin Solid Films* **89**, 433–446 (1982).
5. Y. Liu *et al.*, *Nature* **557**, 696–700 (2018).
6. G. Kwon *et al.*, *Nat. Electron.* **5**, 241–247 (2022).
7. X. Zhang *et al.*, *Nat. Commun.* **15**, 4619 (2024).
8. G. Liu *et al.*, *Nat. Electron.* **5**, 275–280 (2022).
9. M. Hong *et al.*, *InfoMat* **6**, e12491 (2023).
10. C.-H. Chu *et al.*, *ACS Nano* **13**, 8146–8154 (2019).
11. J. Xiao *et al.*, *Nano Res.* **15**, 475–481 (2021).
12. Y. Wang *et al.*, *Nature* **568**, 70–74 (2019).
13. A.-S. Chou *et al.*, *IEEE Electron Device Lett.* **42**, 272–275 (2021).
14. A. Kumar, K. Schauble, K. M. Neilson, A. Tang, P. Ramesh, H.-S. P. Wong, E. Pop, K. Saraswat, in *2021 IEEE International Electron Devices Meeting (IEDM)* (IEEE, 2021), pp. 7.3.1–7.3.4.
15. C. D. English, G. Shine, V. E. Dorgan, K. C. Saraswat, E. Pop, *Nano Lett.* **16**, 3824–3830 (2016).
16. Y. Wang *et al.*, *Nature* **610**, 61–66 (2022).
17. J. Jiang *et al.*, *Nat. Electron.* **7**, 545–556 (2024).
18. W. Li *et al.*, *Nature* **613**, 274–279 (2023).
19. P.-C. Shen *et al.*, *Nature* **593**, 211–217 (2021).
20. W. Li *et al.*, in *2021 IEEE International Electron Devices Meeting (IEDM)* (IEEE, 2021), pp. 37.33.31–37.33.34.
21. W.-C. Wu *et al.*, in *2024 IEEE Symposium on VLSI Technology and Circuits (VLSI Technology and Circuits)* (IEEE, 2024), pp. 1–2.
22. W.-C. Wu *et al.*, in *2023 IEEE Symposium on VLSI Technology and Circuits (VLSI Technology and Circuits)* (IEEE, 2023), pp. 1–2.
23. W. Li *et al.*, in *2024 IEEE International Electron Devices Meeting (IEDM)* (IEEE, 2024), pp. 1–4.
24. A.-S. Chou *et al.*, in *2021 IEEE International Electron Devices Meeting (IEDM)* (IEEE, 2021), pp. 7.2.1–7.2.4.
25. M. Jaikissoon, E. Pop, K. C. Saraswat, *IEEE Electron Device Lett.* **45**, 1528–1531 (2024).
26. L. Hoang *et al.*, *Nano Lett.* **24**, 12768–12774 (2024).
27. J. Hong *et al.*, *Nat. Commun.* **6**, 6293 (2015).
28. L. Gao *et al.*, *Adv. Mater.* **32**, e1906646 (2020).
29. X. Zhang *et al.*, *Adv. Mater.* **33**, e2007051 (2021).
30. Y. Liu, Y. Huang, X. Duan, *Nature* **567**, 323–333 (2019).
31. J. Xiao *et al.*, *Small Methods* **7**, e2300611 (2023).
32. P. Bolshakov *et al.*, *ACS Appl. Electron. Mater.* **1**, 210–219 (2019).
33. C. J. McClellan, E. Yalon, K. K. H. Smithe, S. V. Suryavanshi, E. Pop, *ACS Nano* **15**, 1587–1596 (2021).
34. K. K. H. Smithe, C. D. English, S. V. Suryavanshi, E. Pop, *Nano Lett.* **18**, 4516–4522 (2018).
35. Z. Sun *et al.*, *ACS Nano* **18**, 22444–22453 (2024).
36. K. K. H. Smithe, S. V. Suryavanshi, M. Muñoz Rojo, A. D. Tedjarati, E. Pop, *ACS Nano* **11**, 8456–8463 (2017).
37. A. Kumar, A. Tang, H. S. P. Wong, K. Saraswat, in *2021 IEEE International Interconnect Technology Conference (IITC)* (IEEE, 2021), pp. 1–3.
38. IRDS 2021: More Moore, IEEE (2021); https://irds.ieee.org/editions/2021/more-moore.
39. Z. Li *et al.*, *Nat. Commun.* **11**, 1151 (2020).
40. H. Shioya, M. F. Craciun, S. Russo, M. Yamamoto, S. Tarucha, *Nano Lett.* **14**, 1158–1163 (2014).
41. H. Jiang *et al.*, *Nat. Mater.* **24**, 188–196 (2025).
42. X. Wei *et al.*, *Nat. Electron.* **7**, 138–146 (2024).
43. X. Liu *et al.*, *Nat. Commun.* **4**, 1776 (2013).

ACKNOWLEDGMENTS

Funding: National Natural Science Foundation of China (grant no. 52225206, 92163205, 52188101, 52303362, 62322402, 52350301, 92463308, 52250398, 62204012, 62304019, 52302162, and 52402169); National Key Research and Development Program of China (grant no. 2022YFA1203803 and 2023YFF1500401); Beijing Nova Program (grant no. 20220484145 and 20230484478); Young Elite Scientists sponsorship program by CAST (grant no. 2022QNRC001); special support from the Postdoctoral Science Foundation (2023TQ0007); Postdoctoral Science Foundation (2023M740031); Fundamental Research Funds for the Central Universities (grant no. FRF-TP-22-004C2, FRF-06500207, and FRF-IDRY-23-038); State Key Lab for Advanced Metals and Materials (no. 2023-Z05); and Postdoctoral Fellowship Program of CPSF (GZC20230233). **Author contributions:** Conceptualization: Y.Z., Z.Z., and L.G. Material preparation: L.G., Z.C., and H.J. Device construction: Z.C., L.G., X.W., K.C., X.H., C.C., J.S., H.Y., and M.H. Investigation: L.G., Z.C., and X.Z. Theoretical calculations: S.L., Z.F., W. SG. Visualization: L.G., Z.C., and Y.H. Funding acquisition: Y.Z., Z.Z., X.Z., and L.G. Project administration: L.G., X.Z., Z.Z., and Y.Z. Supervision: Y.Z., Z.Z., X.Z., and L.G. Writing – original draft: L.G., X.Z., Z.C., S.L., Z.F., and X.W. Writing – review & editing: L.G., X.Z., Z.Z., and Y.Z. **Competing interests:** The authors declare no competing interests. **Data and materials availability:** All data are available in the manuscript or the supplementary materials. All data needed to evaluate the conclusions in this paper are present in the main text or the supplementary materials. **License information:** Copyright © 2025 the authors, some rights reserved; exclusive licensee American Association for the Advancement of Science. No claim to original US government works. https://www.science.org/about/science-licenses-journal-article-reuse

SUPPLEMENTARY MATERIALS

science.org/doi/10.1126/science.adz2405
Materials and Methods; Figs. S1 to S18; Table S1; References
Submitted 23 May 2025; accepted 30 September 2025
10.1126/science.adz2405

COSMOCHEMISTRY

The Moon-forming impactor Theia originated from the inner Solar System

Timo Hopp[1,2]*, Nicolas Dauphas[1,3], Maud Boyet[4], Seth A. Jacobson[5], Thorsten Kleine[2]

The Moon formed from a giant impact of a planetary body, called Theia, with proto-Earth. It is unknown whether Theia formed in the inner or outer Solar System. We measured iron isotopes in lunar samples, terrestrial rocks, and meteorites representing the isotopic reservoirs from which Theia and proto-Earth might have formed. Earth and the Moon have indistinguishable mass-independent iron isotopic compositions; both define one end of the range measured in meteorites. Combining our results with those for other elements, we performed mass balance calculations for Theia and proto-Earth. We found that all of Theia and most of Earth's other constituent materials originated from the inner Solar System. Our calculations suggest that Theia might have formed closer to the Sun than Earth did.

The Moon is thought to have formed following a giant impact between a Mars-sized body, called Theia, and proto-Earth (*1*, *2*). Most models of this process predict that the Moon is predominantly composed of material derived from Theia. If Theia was isotopically distinct from proto-Earth, then this would produce an isotopic difference between the Moon and Earth's mantle. Such isotopic differences between planetary objects can arise through radioactive decay, isotopic fractionation processes, and the uneven distribution of presolar materials in the Solar System's protoplanetary disk. The latter can indicate a planet's provenance by comparison with noncarbonaceous (NC) and carbonaceous chondrite (CC) meteorites, which are thought to represent the inner and outer Solar System, respectively (*3*–*6*). Determining the nucleosynthetic isotopic composition of Theia could therefore indicate whether it formed in the inner (*7*–*9*) or outer Solar System (*10*–*12*).

Measurements of lunar samples have shown that Earth and the Moon have similar mass-independent isotopic compositions for all measured elements, including oxygen (O), calcium (Ca), titanium (Ti), chromium (Cr), zirconium (Zr), and tungsten (W) (*8*, *13*–*19*). Several explanations have been proposed for this isotopic similarity: (i) Theia and proto-Earth might have formed in the same region of the protoplanetary disk (*20*); (ii) the Moon could be derived predominantly from the mantle of proto-Earth (*13*, *21*); (iii) the Moon and Earth's mantle incorporated equal proportions of material from Theia and proto-Earth (*22*); or (iv) the Moon and Earth's mantle compositions were homogenized owing to extensive mixing and isotopic exchange following the giant impact (*23*, *24*). The lack of measurable isotopic differences and uncertainty over which process caused this have prevented a determination of Theia's formation region.

[1]Department of the Geophysical Sciences, The University of Chicago, Chicago, IL, USA. [2]Max-Planck-Institut für Sonnensystemforschung, Göttingen, Germany. [3]Department of Earth and Planetary Sciences, The University of Hong Kong, Hong Kong, China. [4]Laboratoire Magmas et Volcans, Université Clermont Auvergne, Centre National de la Recherche Scientifique, Institut de Recherche pour le Développement, Observatoire de Physique du Globe de Clermont-Ferrand, Clermont-Ferrand, France. [5]Department of Earth and Environmental Sciences, Michigan State University, East Lansing, MI, USA. ***Corresponding author. Email: hopp@mps.mpg.de**

Iron isotopic measurements

We measured the iron (Fe) isotopic compositions of 15 terrestrial rocks, 6 lunar samples retrieved by the Apollo missions, and 20 undifferentiated NC meteorites [enstatite chondrites (ECs), ordinary chondrites (OCs), and Rumuruti-type chondrites]. After purification of Fe by ion exchange chromatography, the isotopic measurements were conducted using multicollector inductively coupled plasma mass spectrometry (*25*). The data are reported as μ^{54}Fe and μ^{58}Fe values (table S1), which express the ^{54}Fe/^{56}Fe and ^{58}Fe/^{56}Fe ratios in the sample, normalized to a fixed ^{57}Fe/^{56}Fe, as deviations in parts per million relative to a synthetic standard solution: $\mu^{i}\text{Fe} = [(^{i}\text{Fe}/^{56}\text{Fe})_{\text{sample}}/(^{i}\text{Fe}/^{56}\text{Fe})_{\text{standard}} - 1] \times 10^{6}$, where i represents the atomic mass of each measured isotope.

The Fe isotopic compositions of all the terrestrial samples are indistinguishable (Fig. 1A), with average values of $\mu^{54}\text{Fe} = 0 \pm 1$ and $\mu^{58}\text{Fe} = +1 \pm 3$; all uncertainties are 95% confidence intervals. We take this composition to be representative of Earth's mantle, referred to as the bulk silicate Earth (BSE). The Fe isotopic compositions of 14 ECs are indistinguishable from each other (Fig. 1B), with average $\mu^{54}\text{Fe} = +6 \pm 1$ and $\mu^{58}\text{Fe} = 0 \pm 2$. This μ^{54}Fe difference between ECs and the BSE indicates that ECs cannot be the sole isotopic reservoir from which Earth is derived.

For the six lunar samples, we found that μ^{54}Fe and μ^{58}Fe are anticorrelated (Fig. 1C). This is consistent with exposure of some of the samples to galactic cosmic rays (GCRs), which causes secondary neutron capture that is predicted to produce a negative correlation (*25*–*27*). Previous measurements of meteorites with low GCR exposure displayed no variations in μ^{58}Fe values (*6*, *27*, *28*). We therefore expect the μ^{58}Fe value of the Moon's mantle [the bulk silicate Moon (BSM)], prior to GCR exposure, to be zero and attribute all the μ^{58}Fe variations among the lunar samples to GCR effects. Three samples have similar μ^{54}Fe and near-zero μ^{58}Fe values, indicating that these are unaffected by GCR; their weighted average is $\mu^{54}\text{Fe} = +2 \pm 3$ (*25*). Thus, the μ^{54}Fe values of the BSM ($+2 \pm 3$) and BSE (0 ± 1) are indistinguishable.

Unsampled constituents of Earth and the Moon

The NC meteorites exhibit correlations between the isotopic anomalies of multiple elements with different geochemical behavior. For Fe and Zr, the BSE lies beyond the range of measured compositions of meteorites but on the same correlation line (Fig. 2) (*29*–*31*); therefore, the BSE cannot be explained by mixtures of NC and CC meteorites. There are several potential explanations for the composition of BSE lying at one end of the range observed in meteorites, including that (i) proto-Earth and Theia had the same isotopic composition and both incorporated material that is not recorded in meteorites; (ii) proto-Earth's mantle (PEM) had a composition not recorded in meteorites, whereas Theia's isotopic composition was within the range of meteorites; or (iii) Theia had an isotopic composition not recorded in meteorites and the PEM's isotopic composition was within the meteoritic range.

The isotopic composition of BSE for elements with different geochemical behavior reflects the materials that accreted during different stages of Earth's growth (*32*). For lithophile (rock-loving, predominantly in the mantle and crust) elements, such as Zr, the isotopic composition of BSE is determined by Earth's full accretion history (fig. S1). For moderately siderophile (metal-loving, predominantly in the core) elements, such as Fe and molybdenum (Mo), the isotopic composition of BSE reflects the final ~40 and ~10%, respectively, of material accreted by Earth, because any of those elements that were contained in material that was accreted earlier will have partitioned into the core (figs. S1 and S2) (*32*). For highly siderophile elements, such as ruthenium (Ru), their abundances in the BSE were predominantly set after core formation ceased, during the final ~0.5% of Earth's accretion (known as late accretion or the late veneer) (*33*, *34*). Lithophile and

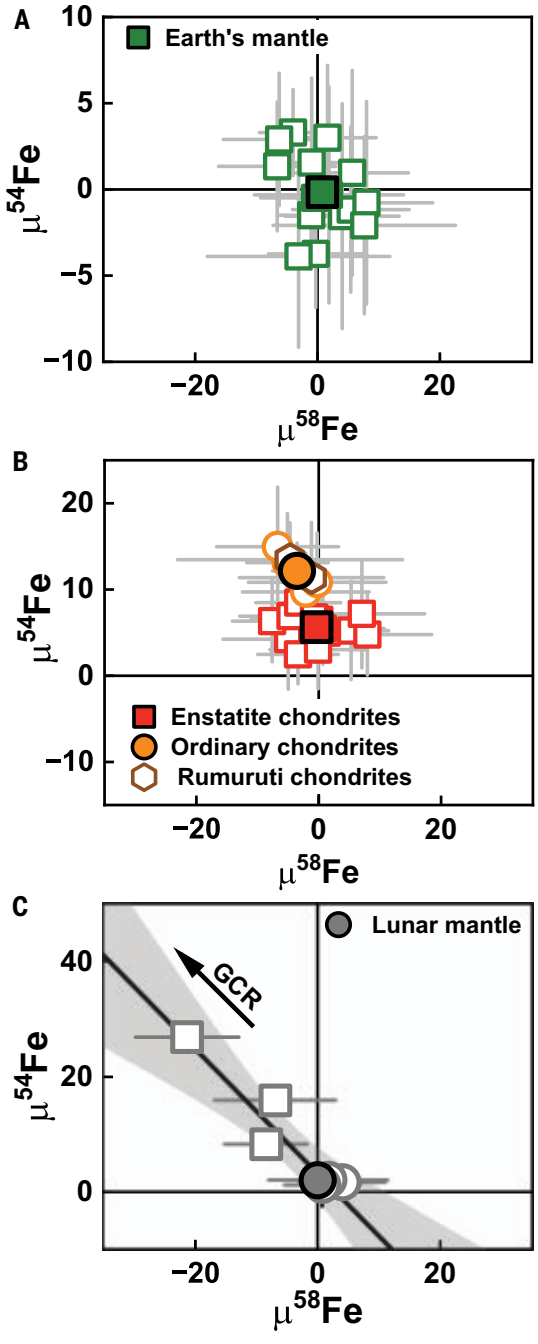

Fig. 1. Fe isotopic compositions of terrestrial rocks, lunar rocks, and meteorites. $\mu^{54}Fe$ and $\mu^{58}Fe$ data are from our laboratory measurements (table S1). Error bars indicate 95% confidence intervals. Horizontal and vertical black lines represent the composition of the reference standard solution (zero by definition). Open symbols represent individual samples and solid symbols the calculated average compositions. (**A**) Samples of terrestrial rocks have indistinguishable Fe isotopic compositions, with average $\mu^{54}Fe = 0 \pm 1$ and $\mu^{58}Fe = +1 \pm 3$. (**B**) Samples of undifferentiated NC meteorites (ECs, OCs, and Rumuruti-type chondrites) have nonzero isotopic anomalies in $\mu^{54}Fe$. (**C**) Lunar samples have anticorrelated values of $\mu^{54}Fe$ and $\mu^{58}Fe$. The black regression line (shaded region represents the 95% confidence intervals) is consistent with exposure of the samples to GCRs, which is expected to move the isotopic composition in the direction indicated by the black arrow. Open squares represent samples that were affected by GCRs and so were discarded from our analysis. Three lunar samples (open circles) have $\mu^{58}Fe$ consistent with zero and similar $\mu^{54}Fe$ values; their weighted average, $\mu^{54}Fe = +2 \pm 3$ (solid circle), was taken to reflect the BSM.

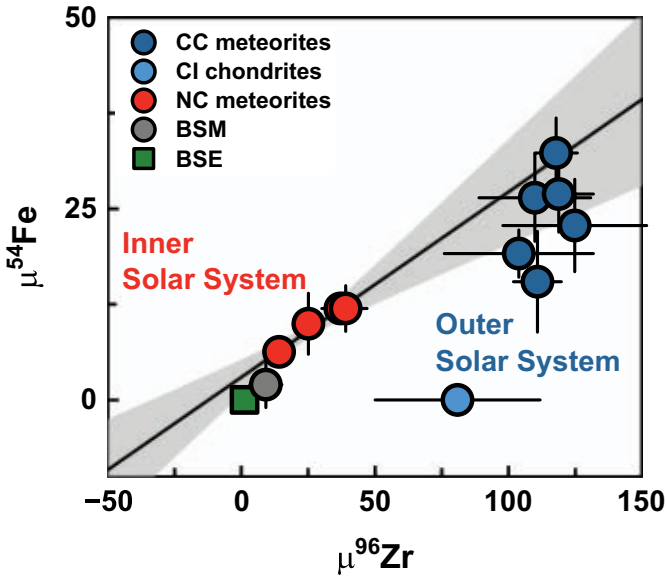

Fig. 2. Fe and Zr isotopic compositions of Earth's mantle, the Moon, and meteorites. $\mu^{54}Fe$ and $\mu^{96}Zr$ are shown for different sample types (see legend); data are from this study and previous work (table S2) (*29*, *30*, *49*). Error bars represent 95% confidence intervals. The black line shows a linear regression fitted to the NC data (red circles), with the gray shaded region indicating the 95% confidence intervals. Earth's mantle (BSE, green square) and the Moon's mantle (BSM, gray circle) are outside the range of NC meteorites and furthest away from CC meteorites.

highly siderophile elements predominantly record earlier and later stages of Earth's accretion, respectively. Because the formation of the Moon occurred near the end of Earth's accretion process (*1*, *2*), Theia likely supplied a considerable amount of siderophile elements to the BSE. If proto-Earth and Theia were isotopically distinct, then we would expect the isotopic composition of a siderophile element in BSE to be closer to that of Theia than for a lithophile element. Comparing the isotopic anomalies of siderophile and lithophile elements in the BSE and BSM can therefore constrain the isotopic composition of Theia.

Mass-balance calculations

Most giant impact models predict that there is no isotopic homogenization and that the Moon predominantly consists of material from Theia (*1*, *2*). In this case, which we refer to as the canonical model, the isotopic similarity between the BSE and BSM requires that Theia and proto-Earth had similar isotopic compositions, implying that both formed in the same region of the protoplanetary disk (*8*, *16*, *20*) (figs. S3 and S4). However, dynamical models of planet formation predict that Earth accreted material that originated from multiple regions of the disk (*35*). Given the measured isotopic variations among meteorites and planets, this makes it unlikely that Theia and proto-Earth had identical compositions (*3*, *15*, *23*).

In the canonical model, the BSE and the BSM are also expected to have different ^{182}W signatures, caused by radioactive decay of hafnium-182 (^{182}Hf). Variations in ^{182}W reflect the timescales and conditions of core formation, which were likely different for Theia and proto-Earth because of their different accretion history (*36*). However, only a small difference in ^{182}W between Earth and Moon rocks has been measured, which can be explained by either radioactive decay in the Moon (*37*) or disproportional late accretion to Earth and the Moon (*18*, *19*). It has therefore been argued that the BSE and BSM had indistinguishable ^{182}W signatures immediately after the giant impact. This is a possible

but unlikely outcome of canonical giant impact models (*38*, *39*). Because ^{182}W variations are produced by radioactive decay, this argument holds regardless of whether proto-Earth and Theia originated in the same region of the disk.

Alternative (noncanonical) giant impact scenarios have been proposed to account for the isotopic similarity between Earth and the Moon. These models either produce the Moon predominantly from PEM material (*13*, *21*) or enable isotopic homogenization of the BSE and BSM (*23*, *24*). These scenarios do not require PEM and Theia to have had similar isotopic compositions but do imply that measurements of lunar samples provide no direct information on Theia's original isotopic composition.

For different assumed isotopic compositions ^{i}E (where E represents an arbitrary element) of the PEM, we determined possible isotopic compositions of Theia through mass-balance calculations. We used the measured composition of Earth's mantle, $\mu^{i}E_{\mathrm{BSE}}$, as a proxy for both the present-day BSE and the Moon (*25*). Then mass balance requires

$$\mu^{i}E_{\mathrm{Theia}} = \frac{\mu^{i}E_{\mathrm{BSE}} - \mu^{i}E_{\mathrm{PEM}}(1-x_E)}{x_E} \qquad \text{(Eq. 1)}$$

where $\mu^{i}E_{\mathrm{Theia}}$ and $\mu^{i}E_{\mathrm{PEM}}$ are the model isotopic compositions of Theia and PEM, and x_E is the mass fraction of element E in the BSE that was delivered by Theia. We rearranged Eq. 1 to calculate $\mu^{i}E_{\mathrm{PEM}}$ for different assumed values of $\mu^{i}E_{\mathrm{Theia}}$:

$$\mu^{i}E_{\mathrm{PEM}} = \frac{\mu^{i}E_{\mathrm{BSE}} - \mu^{i}E_{\mathrm{Theia}}x_E}{1-x_E}. \qquad \text{(Eq. 2)}$$

The value of x_E depends on the mass of the impactor. For siderophile elements, x_E also depends on the assumed redox states of proto-Earth and Theia, which affects the partitioning of siderophile elements between the silicate mantle and metallic core, and the degree to which Theia's core equilibrated with PEM (figs. S1 and S2) (*25*, *32*). To cover the range of potential x_E values, we calculated $\mu^{i}E_{\mathrm{Theia}}$ and $\mu^{i}E_{\mathrm{PEM}}$ separately for several impactor masses: a small Theia, 5% of Earth's mass (*21*); a canonical model, with Theia having 10% of Earth's mass (*1*, *2*); and a large Theia, 50% of Earth's mass (*22*) (table S3). For the small and canonical impactors, x_E was estimated from a previous model (*32*), assuming that Theia was the last giant impact on Earth (figs. S1 and S2). For the large (half-Earth) impactor (fig. S5), we assumed that 50% of all elements in BSE came from Theia (*22*).

Our mass balance calculations only require measurements of the BSE composition (Eqs. 1 and 2). We therefore included Mo in our model, even though its isotopic signature has not been measured in lunar samples. Because Mo is more siderophile than Fe, it records the final ~10% of Earth's accretion, so a substantial fraction of Mo in the BSE could come from Theia (*12*). Some of the Mo in BSE was delivered by late accretion after the giant impact, likely by NC material (*34*, *40*, *41*). To account for this, we corrected the BSE Mo isotopic composition using the fraction of Mo delivered by late accretion, which we calculated to be $x_{\mathrm{Mo\text{-}LV}} = 0.16$ (*25*), and assuming an enstatite chondrite-like isotopic composition for the late veneer (*25*). This correction is small, shifting μ^{94}Mo of the BSE from $+4 \pm 6$ to -2 ± 7; we adopted the corrected value in the mass balance calculations. If we instead assume an Ivuna-type carbonaceous chondrite (CI) isotopic composition of the late accreted material, the results change only slightly (table S4).

Determining Theia's isotopic origin

Our mass balance calculations provide the composition of PEM for different assumed compositions and masses of Theia. In most cases, we found that PEM is required to have had negative anomalies for Fe, Zr, and Mo (Fig. 3 and fig. S5). Such negative anomalies have not been measured in meteorites. The calculated PEM composition is closer to meteoritic compositions when the impactor is small and has CI- or EC-like compositions. For a small Theia with CI-like composition, we calculated that PEM had $\mu^{54}\mathrm{Fe} = 0 \pm 1$ and $\mu^{96}\mathrm{Zr} = -3 \pm 3$, whereas for a small EC-like Theia, we obtained $\mu^{54}\mathrm{Fe} = -1 \pm 1$ and $\mu^{96}\mathrm{Zr} = 0 \pm 2$. These values are indistinguishable from the current BSE composition. For Mo, we calculated that PEM had $\mu^{94}\mathrm{Mo} = -98 \pm 49$ and -50 ± 18 for a small CI-like and EC-like Theia, which are both distinct from BSE (Fig. 3E).

We also calculated the composition of Theia for different assumed PEM compositions (Fig. 4 and fig. S5). If proto-Earth's composition was within the meteoritic range, then Theia must have had a composition outside the meteoritic range, with negative μ^{54}Fe, μ^{96}Zr, and μ^{94}Mo values. For CI- or CC-like isotopic compositions of PEM, the calculated Fe and Zr isotopic compositions of Theia would be highly anomalous, far outside the range measured for meteorites. For example, CI chondrites have a similar Fe isotopic composition to Earth's mantle (*42*) but large positive μ^{96}Zr anomalies (*43*, *44*). Therefore, if

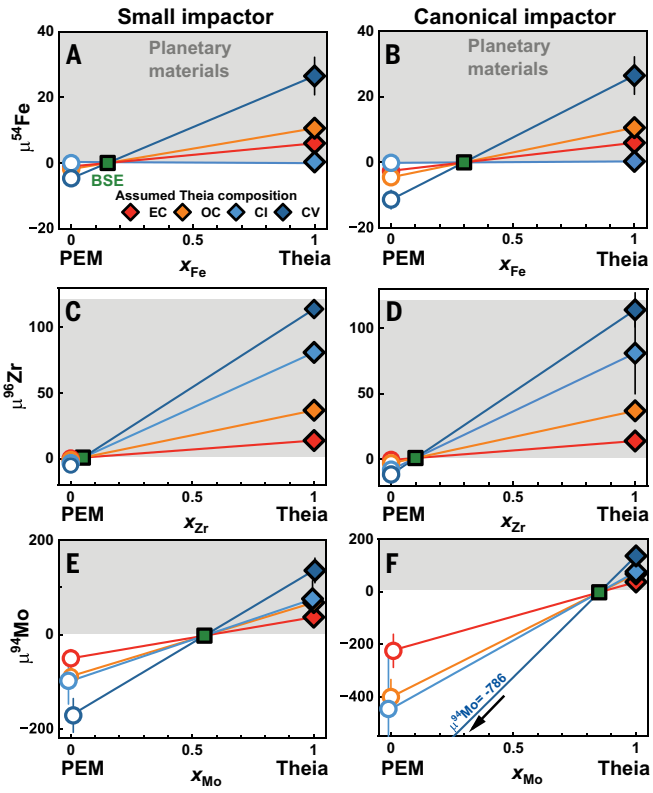

Fig. 3. Mass-balance calculations for different compositions of Theia. Results are shown for (**A** and **B**) Fe, (**C** and **D**) Zr, and (**E** and **F**) Mo. Each panel shows the isotopic composition $\mu^{i}E$ as a function of the mass fraction of element E in the BSE that was delivered by Theia (x_E) under two scenarios: [(A), (C), and (E)] a small 0.05–Earth masses impactor and [(B), (D), and (F)] a canonical 0.1–Earth masses impactor. Error bars indicate 95% confidence intervals. The colored lines follow the mass balance between the assumed isotopic composition of Theia (filled diamonds), the measured isotopic composition of Earth's mantle (BSE, filled green squares), and the calculated isotopic composition of PEM (open circles). The shaded areas indicate the range of isotopic compositions measured in planetary materials (table S2). For Theia, isotopic compositions similar to NC meteorite groups (EC and OC) and CC meteorite groups [CI and Vigarano-type carbonaceous chondrites (CV)] are assumed (see legend). Results for a 0.5–Earth mass impactor are shown in fig. S5. The calculated compositions for each scenario are summarized in table S3.

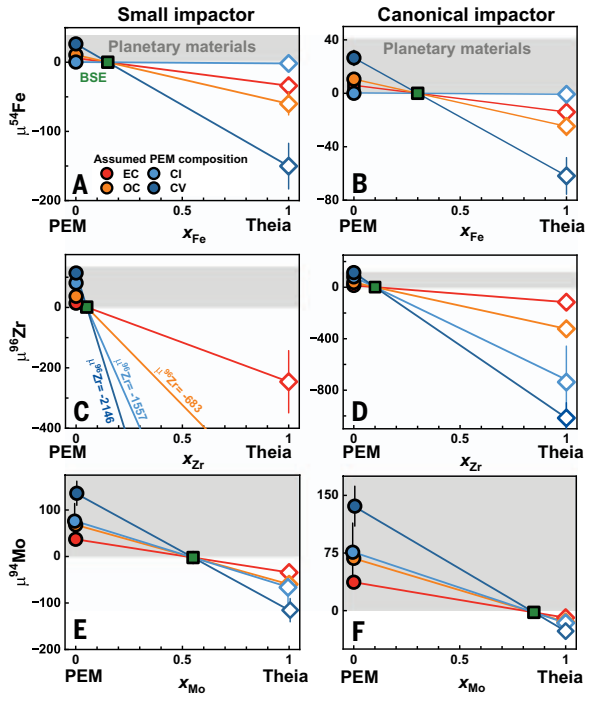

Fig. 4. Mass-balance calculations for different PEM compositions. (**A** to **F**) Same as Fig. 3, except the isotopic composition of Theia was calculated by using the measured isotopic composition of BSE (solid green square) and assuming that PEM (filled circles) had similar isotopic composition to that of different meteorite groups (see legend). The calculated compositions of the different scenarios are summarized in table S3.

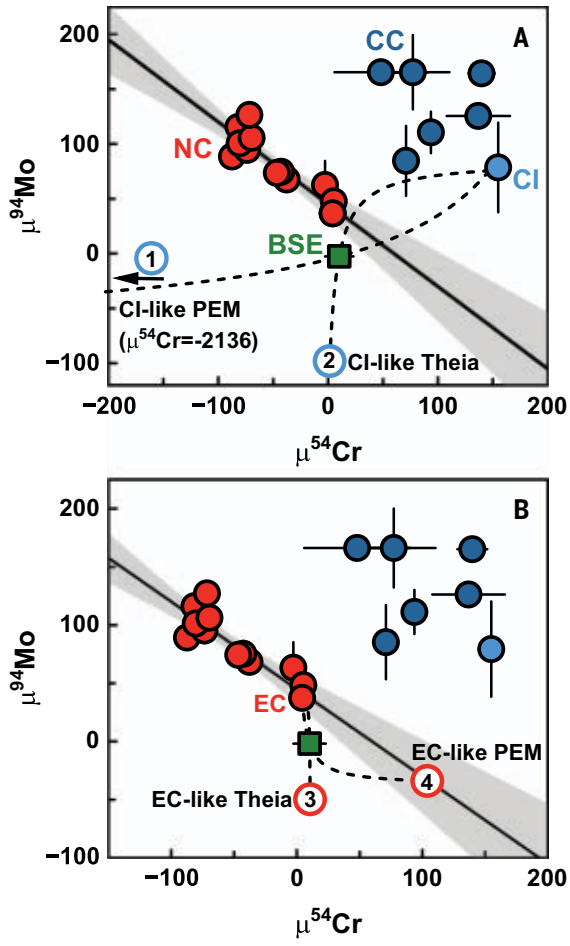

Fig. 5. Mo and Cr isotopic compositions of Earth's mantle and meteorites. Data points in both panels show previous measurements of μ^{94}Mo and μ^{54}Cr for different sample types (table S2) (*29*, *30*, *49*). Nonmagmatic Fe meteorites have been excluded, because Mo and Cr might have different origins in those meteorites (see supplementary text). The black line shows a linear regression fitted to the NC data (red circles). Error bars and the gray shaded region represent 95% confidence intervals. The BSE (green square) is below the correlation defined by NC meteorites. (**A**) Results of the mass-balance calculations for a small impactor scenario, which used the measured composition of the BSE and assumed either a CI-like PEM or Theia (open blue circles labeled 1 and 2). The black arrow indicates that scenario 1 is located beyond the plotted region, at μ^{54}Cr = −2136. The dashed lines represent mixing curves between CI composition (light blue solid circle) and the calculated compositions of Theia and PEM in each scenario. (**B**) Results of the mass-balance calculations for a small impactor scenario assuming an EC-like composition of Theia or PEM (red circles labeled 3 and 4). The calculated compositions for each of the scenarios are summarized in table S3.

PEM had a CI-like isotopic composition, then it would require Theia to be extremely anomalous, with μ^{96}Zr between −81 (for a half-Earth impactor) and −1557 (for a small impactor). By contrast, an NC-like PEM generally implies much less anomalous Theia compositions for Fe, Zr, and Mo (Fig. 4 and table S3). In all our calculations, some exotic material (material with an isotopic composition outside the range measured in meteorites) is always required, but it is less exotic if proto-Earth was similar to NC meteorites and close in composition to the BSE.

We obtained more stringent constraints by examining multiple elements simultaneously. Isotopic anomalies are correlated among NC materials, indicating that they arose through two-component mixing (*30*, *45*). One of these components is not present in measured meteorites, but must form an endmember of the NC correlation, characterized by negative μ^{54}Fe, μ^{96}Zr, and μ^{94}Mo but positive μ^{54}Cr values (*29*, *30*). In plots of μ^{94}Mo versus μ^{54}Cr (Fig. 5) and μ^{54}Fe versus μ^{54}Cr (fig. S6), the BSE is located below the NC correlation and away from CC and CI meteorites (*29*). We interpreted these offsets as due to the different siderophile behaviors of Cr, Fe, and Mo, leading to different fractional contributions from Theia (x_E values).

Figure 5 shows the compositions of different hypothetical components that would be required to explain the BSE composition in the small impactor scenario, which provides the fewest constraints on Theia when examining individual elements separately (Figs. 3 and 4). If either Theia or the PEM had CC- or CI-like compositions, then the hypothetical component would need to be far on the other side of the NC correlation, in a region that has not been measured in meteorites (Fig. 5A). If PEM had an EC-like composition, then the calculated Theia composition falls on an extrapolation of the NC correlation. The μ^{94}Mo versus μ^{54}Cr mixing curve for an EC-like PEM with this hypothetical Theia passes through the composition of BSE (Fig. 5B). In this case, the offset of the BSE away from the NC correlation is due to Theia's differing contributions to the BSE's Cr and Mo inventories (*29*).

Mo isotopic variations among meteorites primarily arise from varying amounts of material produced by the slow neutron capture process (*s*-process) (*46*, *47*), with additional variations from the rapid neutron capture process (*r*-process), which contributed more to the CC reservoir than to the NC reservoir (*5*). Mo in the BSE also has a small *r*-process enrichment compared to NC meteorites, indicating a small contribution from CC material (*11*, *12*). This CC contribution can be reconciled with an NC origin of Theia if the impactor was small or if there was little mixing between Theia's core and PEM; in this case,

the CC material would have been delivered shortly before the Moon-forming impact (*11*, *25*).

The most plausible scenario is that both proto-Earth and Theia were predominantly formed from NC material and that Theia was likely more enriched in *s*-process material than were NC meteorites and the BSE. It has been proposed that the measured *s*-process variation among NC bodies reflects a heliocentric gradient in the inner Solar System (*29*, *30*). If that is correct, then our preferred scenario implies that Theia formed closer to the Sun than did most of the material that accreted to form Earth. Ru isotopic compositions of some ancient Earth rocks display an enrichment in *s*-process nuclides, which has been interpreted as reflecting the Ru isotopic composition of Earth's mantle prior to late accretion (*48*). Some of this Ru could derive from the Moon-forming impactor, consistent with our finding of an *s*-process–enriched composition of Theia.

REFERENCES AND NOTES

1. R. M. Canup, E. Asphaug, *Nature* **412**, 708–712 (2001).
2. R. M. Canup, *Icarus* **168**, 433–456 (2004).
3. P. H. Warren, *Earth Planet. Sci. Lett.* **311**, 93–100 (2011).
4. T. S. Kruijer, C. Burkhardt, G. Budde, T. Kleine, *Proc. Natl. Acad. Sci. U.S.A.* **114**, 6712–6716 (2017).
5. G. Budde *et al.*, *Earth Planet. Sci. Lett.* **454**, 293–303 (2016).
6. T. Hopp *et al.*, *Sci. Adv.* **8**, eadd8141 (2022).
7. S. J. Desch, K. L. Robinson, *Chem. Erde* **79**, 125546 (2019).
8. W. Akram, M. Schönbächler, *Earth Planet. Sci. Lett.* **449**, 302–310 (2016).
9. M. M. M. Meier, A. Reufer, R. Wieler, *Icarus* **242**, 316–328 (2014).
10. M. Schönbächler, R. W. Carlson, M. F. Horan, T. D. Mock, E. H. Hauri, *Science* **328**, 884–887 (2010).
11. G. Budde, C. Burkhardt, T. Kleine, *Nat. Astron.* **3**, 736–741 (2019).
12. T. Hopp, G. Budde, T. Kleine, *Earth Planet. Sci. Lett.* **534**, 116065 (2020).
13. J. Zhang, N. Dauphas, A. M. Davis, I. Leya, A. Fedkin, *Nat. Geosci.* **5**, 251–255 (2012).
14. U. Wiechert *et al.*, *Science* **294**, 345–348 (2001).
15. E. D. Young *et al.*, *Science* **351**, 493–496 (2016).
16. B. Mougel, F. Moynier, C. Göpel, *Earth Planet. Sci. Lett.* **481**, 1–8 (2018).
17. M. Schiller, M. Bizzarro, V. A. Fernandes, *Nature* **555**, 507–510 (2018).
18. T. S. Kruijer, T. Kleine, M. Fischer-Gödde, P. Sprung, *Nature* **520**, 534–537 (2015).
19. M. Touboul, I. S. Puchtel, R. J. Walker, *Nature* **520**, 530–533 (2015).
20. N. Dauphas, C. Burkhardt, P. H. Warren, T. Fang-Zhen, *Philos. Trans. A Math. Phys. Eng. Sci.* **372**, 20130244 (2014).
21. M. Ćuk, S. T. Stewart, *Science* **338**, 1047–1052 (2012).
22. R. M. Canup, *Science* **338**, 1052–1055 (2012).
23. K. Pahlevan, D. J. Stevenson, *Earth Planet. Sci. Lett.* **262**, 438–449 (2007).
24. S. J. Lock *et al.*, *J. Geophys. Res. Planets* **123**, 910–951 (2018).
25. Materials and methods are available as supplementary materials.
26. D. L. Cook, I. Leya, M. Schönbächler, *Meteorit. Planet. Sci.* **55**, 2758–2771 (2020).
27. N. Hopp, N. Dauphas, F. Spitzer, C. Burkhardt, T. Kleine, *Earth Planet. Sci. Lett.* **577**, 117245 (2022).
28. D. L. Cook, B. S. Meyer, M. Schönbächler, *Astrophys. J.* **917**, 59 (2021).
29. C. Burkhardt *et al.*, *Sci. Adv.* **7**, eabj7601 (2021).
30. F. Spitzer *et al.*, *Astrophys. J. Lett.* **898**, L2 (2020).
31. N. Dauphas, A. M. Davis, B. Marty, L. Reisberg, *Earth Planet. Sci. Lett.* **226**, 465–475 (2004).
32. N. Dauphas, *Nature* **541**, 521–524 (2017).
33. D. C. Rubie *et al.*, *Science* **353**, 1141–1144 (2016).
34. M. Fischer-Gödde, T. Kleine, *Nature* **541**, 525–527 (2017).
35. J. E. Chambers, *Icarus* **152**, 205–224 (2001).
36. R. A. Fischer, F. Nimmo, *Earth Planet. Sci. Lett.* **499**, 257–265 (2018).
37. M. M. Thiemens, P. Sprung, R. O. C. Fonseca, F. P. Leitzke, C. Münker, *Nat. Geosci.* **12**, 696–700 (2019).
38. R. A. Fischer, N. G. Zube, F. Nimmo, *Nat. Commun.* **12**, 35 (2021).
39. T. S. Kruijer, T. Kleine, *Earth Planet. Sci. Lett.* **475**, 15–24 (2017).
40. E. A. Worsham, T. Kleine, *Sci. Adv.* **7**, eabh2837 (2021).
41. K. R. Bermingham, R. J. Walker, *Earth Planet. Sci. Lett.* **474**, 466–473 (2017).
42. M. Schiller, M. Bizzarro, J. Siebert, *Sci. Adv.* **6**, eaay7604 (2020).
43. J. Render, G. A. Brennecka, C. Burkhardt, T. Kleine, *Earth Planet. Sci. Lett.* **595**, 117748 (2022).
44. W. Akram, M. Schönbächler, S. Bisterzo, R. Gallino, *Geochim. Cosmochim. Acta* **165**, 484–500 (2015).
45. C. Burkhardt, N. Dauphas, U. Hans, B. Bourdon, T. Kleine, *Geochim. Cosmochim. Acta* **261**, 145–170 (2019).
46. N. Dauphas, B. Marty, A. L. Reisberg, *Astrophys. J.* **565**, 640–644 (2002).
47. C. Burkhardt *et al.*, *Earth Planet. Sci. Lett.* **312**, 390–400 (2011).
48. M. Fischer-Gödde *et al.*, *Nature* **579**, 240–244 (2020).
49. N. Dauphas, T. Hopp, D. Nesvorný, *Icarus* **408**, 115805 (2024).

ACKNOWLEDGMENTS

We thank CAPTEM and R. A. Ziegler for providing the Apollo lunar samples; H. Becker (FU Berlin), N. T. Arndt (CNRS, Grenoble), and B. Marty (CNRS, Nancy) for providing the terrestrial samples; and the Robert A. Pritzker Center for Meteoritics at the Field Museum of Natural History (Chicago), the Smithsonian National Museum for Natural History (Washington, DC), the Institut für Planetologie Münster, and the National Aeronautics and Space Administration (NASA) for providing the meteorite samples. US Antarctic meteorite samples were recovered by the Antarctic Search for Meteorites (ANSMET) program, which has been funded by the National Science Foundation (NSF) and NASA, and characterized and curated by the Department of Mineral Sciences of the Smithsonian Institution and the Astromaterials Curation Office at the NASA Johnson Space Center. **Funding:** N.D. was supported by NASA grants 80NSSC20K1409, 80NSSC23K1022, 80NSSC21K0380, 80NSSC20K0821, and 80NSSC23K1163; NSF grant EAR-2001098; and Department of Energy grant DE-SC0022451. T.K. was supported by the Deutsche Forschungsgemeinschaft (DFG) project ID 263649064 and the European Research Council advanced grant no. 101019380. **Author contributions:** T.H. and N.D. conceived the study. T.H., N.D., and T.K. interpreted the data. T.H. measured the Fe isotopic compositions of the samples. T.K. and M.B. provided samples and discussed the interpretation. T.H. and N.D. wrote the manuscript, with feedback from T.K., M.B., and S.A.J. **Competing interests:** The authors declare that they have no competing interests. **Data and materials availability:** The Fe isotopic data are provided in table S1 and data S1. The isotopic data compiled from the literature are listed (with references) in table S2 and data S2. The results of our mass balance calculations are listed in tables S3 and S4. All lunar, meteorite, terrestrial, and standard samples are archived and available for further study; full details of the sample origins and how readers may request access to them are provided in the supplementary materials.

License information: Copyright © 2025 the authors, some rights reserved; exclusive licensee American Association for the Advancement of Science. No claim to original US government works. https://www.science.org/about/science-licenses-journal-article-reuse. This research was funded in whole or in part by the European Research Council (advanced grant no. 101019380); as required, the author will make the Author Accepted Manuscript (AAM) version available under a CC BY public copyright license.

SUPPLEMENTARY MATERIALS

science.org/doi/10.1126/science.ado0623
Materials and Methods; Supplementary Text; Figs. S1 to S8; Tables S1 to S6; References (*50*–*111*); Data S1 and S2

Submitted 15 January 2024; accepted 19 September 2025

10.1126/science.ado0623

ORGANIC ELECTRONICS

Increasing the dimensionality of transistors with hydrogels

Dingyao Liu[1]†, Jing Bai[1]†, Xinyu Tian[1]†, Yan Wang[1]†, Binbin Cui[1], Shilei Dai[1], Wensheng Lin[1], Zhuowen Shen[2], Chun Kit Lai[2], George G. Malliaras[3]*, Shiming Zhang[1,2]*

Transistors, fundamental to modern electronics, are traditionally rigid, planar, and two-dimensional (2D), limiting their integration with the soft, irregular, and three-dimensional (3D) nature of biological systems. Here, we report 3D semiconductors, integrating organic electronics, soft matter, and electrochemistry. These 3D semiconductors, in the form of hydrogels, realize millimeter-scale modulation thickness while achieving tissue-like softness and biocompatibility. This breakthrough in modulation thickness is enabled by a templated double-network hydrogel system, where a secondary porous hydrogel guides the 3D assembly of a primary redox-active conducting hydrogel. We demonstrate that these 3D semiconductors enable the exclusive fabrication of 3D spatially interpenetrated transistors that mimic real neuronal connections. This work bridges the gap between 2D electronics and 3D living systems, paving the way for advanced bioelectronics systems such as biohybrid sensing and neuromorphic computing.

Transistors are the fundamental building blocks of modern electronic devices (*1*), driving advancements in computing performance by becoming smaller, faster, and more integrated. However, as transistor miniaturization approaches physical and technological limits, as predicted by Moore's law, traditional designs are increasingly constrained (*2*–*4*).

At the same time, emerging fields such as bioelectronics are exploring new paradigms that integrate electronics with living biological systems to enable transformative applications (*5*–*7*), including biohybrid sensing and neuromorphic computing (*8*–*10*). These systems promise low-power operation, high efficiency, and new functionality, but achieving seamless integration between electronics and biology remains a challenge. The core issue lies in the fundamental mismatches between conventional transistors and biological systems. Traditional transistors are rigid, planar, and inherently two-dimensional (2D) (*11*), whereas biological systems are soft, irregular, and three-dimensional (3D) (*12*). These differences make it difficult for traditional electronic components to interact effectively with biological tissues, such as neurons, which require 3D spatial integration (*13*). To address this mismatch, new materials and device architectures capable of operating in three dimensions are needed.

Hydrogels have recently emerged as promising materials for bioelectronics owing to their tissue-like properties (*14*–*16*), including biocompatibility, softness, and 3D nature. Recent advances in redox-active hydrogels have further equipped these materials with semiconducting capabilities (*17*), enabling them to serve as active electronic components in transistors (*18*–*20*). Despite these advancements, hydrogel semiconductors remain limited in their ability to modulate conductivity at larger scales. Current technologies are constrained to nano- to micrometer-thick hydrogels (*18*, *19*), where ion transport and ion-electron coupling are effective. However, as thickness increases beyond the micrometer scale, these mechanisms weaken considerably, leading to a loss of semiconducting functionality. Overcoming the thickness limitation is critical to unlocking the full 3D potential of hydrogel semiconductors to enable their spatial integration with living biological systems.

We overcome the thickness limit of hydrogel semiconductors by designing a double-network hydrogel system synthesized entirely in an aqueous environment. First, a secondary stretchable, porous hydrogel acts as a 3D template to guide the assembly of a primary redox-active conducting hydrogel, enhancing electron transport. Second, the network composition and porosity are controlled to facilitate ion transport. Finally, achieving a balance between ion and electron transport maximizes ion-to-electron conversion efficiency, leading to 3D hydrogel semiconductors with millimeter-scale modulation thickness while maintaining tissue-like properties.

Strategy to enable 3D modulation in 3D hydrogel transistors

The assembled 3D hydrogel transistor is a mixed ion-electron transistor, functioning analogously to organic electrochemical transistors (OECTs) (*21*, *22*). The key difference lies in replacing the thin-film semiconducting channel [poly(3,4-ethylendioxythiophene):poly(styrenesulfonate), PEDOT:PSS] (*23*, *24*) with 3D bulk hydrogels to obtain broad tissue-like properties to facilitate bioelectronic integration (*25*). During operation, ions shuttle through the channel, altering its conductivity. For example, when a positive gate voltage is applied, cations from the electrolyte penetrate into the redox-active hydrogel semiconductor, leading to the reaction: $PEDOT^+:PSS^- + M^+ + e^- \leftrightarrow PEDOT^0 + PSSM$ (*26*, *27*). A typical feature of this reaction is 3D bulk modulation—wherein ions penetrate the entire channel, tuning its conductivity (Fig. 1A). The 3D bulk modulation was experimentally validated through volumetric capacitance measurements, which showed that channel capacitance increases linearly with channel thickness (*28*–*30*).

When attempting to assemble 3D hydrogel transistors by increasing hydrogel thickness, such as through layer-by-layer stacking, the linear relationship between channel capacitance and channel thickness failed to remain consistent at greater thicknesses. This failure resulted in partial 3D modulation and a poor on/off ratio. The underlying issue stems from the limited ability of ions to diffuse into thicker channels (Fig. 1B and figs. S1 and S2) (*31*). Consequently, additional material strategies are required to develop 3D hydrogel semiconductors without compromising their semiconducting properties.

Development of 3D hydrogel semiconductors

To achieve complete 3D modulation in 3D hydrogel semiconductors, the following strategies are used: (i) phase engineering to create a continuous electron transport pathway on the semiconducting backbone (Fig. 2); (ii) structural engineering to optimize hydrogel porosity, facilitating ion transport in the 3D bulk (Fig. 3); and (iii) efficient ion-electron coupling, achieved by the synergy of the above two processes. The process flow in fabricating the hydrogel semiconductor is detailed in the materials and methods in the supplementary materials.

Phase engineering of 3D hydrogel semiconductors

Three phases can exist in a hydrogel semiconductor: water, gel, and a water-gel mixture. For hydrogel semiconductors, achieving a pure gel phase is essential to ensure optimal performance and stability (Fig. 2, A to C). Various methods can be used to evaluate the phase composition (*32*). In the case of PEDOT:PSS hydrogels, the term "reduced viscosity" can be used to characterize the gel-forming process (*33*). An increase in reduced viscosity with higher PEDOT:PSS content is a strong indicator favoring gel formation. To ensure a pure gel phase, the storage modulus should also be substantially larger than the loss modulus. Additionally, under controlled conditions, no water separation or loss should be observed.

[1]Department of Electrical and Electronic Engineering, The University of Hong Kong, Pokfulam, Hong Kong SAR, China. [2]School of Biomedical Engineering, The University of Hong Kong, Pokfulam, Hong Kong SAR, China. [3]Electrical Engineering Division, Department of Engineering, The University of Cambridge, Cambridge, UK. ***Corresponding author. Email: beszhang@hku.hk (S.Z.); gm603@cam.ac.uk (G.G.M.)** †These authors contributed equally to this work.

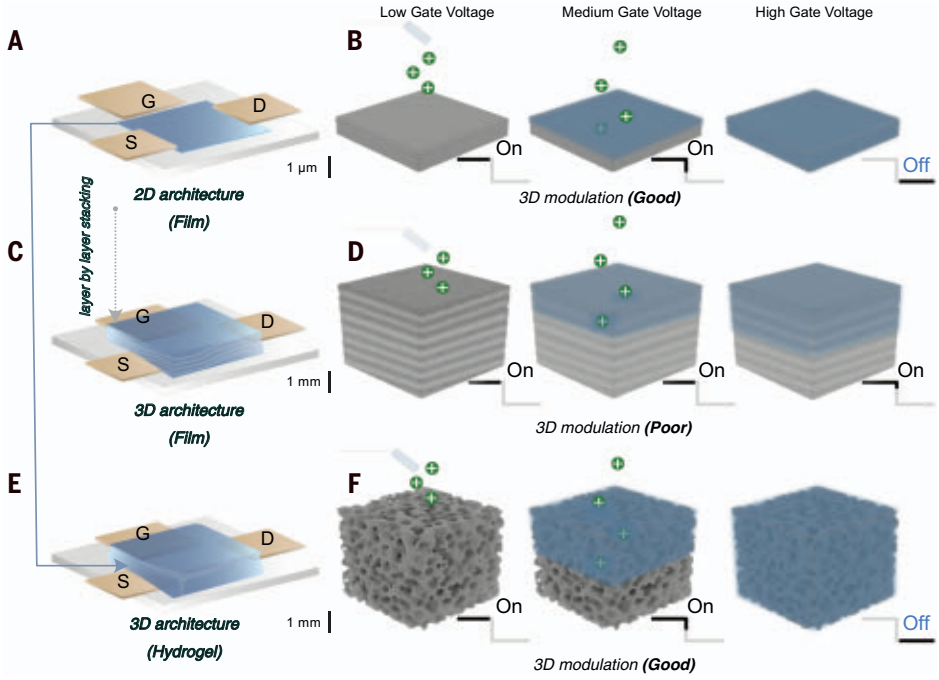

Fig. 1. Strategy to enable 3D modulation in 3D hydrogel transistors. (**A** and **B**) Thin-film OECTs can achieve 3D modulation but are limited to a 2D architecture (with channel thickness ranging between nanometers and micrometers). S, source; G, gate; D, drain. (**C** and **D**) A 3D architecture can be created by directly increasing the channel thickness, but this results in insufficient 3D modulation owing to compromised ion diffusion. (**E** and **F**) Hydrogel semiconductors, through precise phase and structural control, enable efficient 3D modulation in a 3D transistor, achieved by balancing ion and electron transport within the hydrogel.

It is also essential to form a continuous $PEDOT^+$ phase within the hydrogel semiconductor to facilitate electron transport (*34*). For a pure PEDOT:PSS hydrogel semiconductor, the semiconducting polymer network is often discontinuous because of the blockage caused by nonconducting networks, resulting in limited semiconducting properties (Fig. 2D and fig. S3).

We found that phase continuity, and consequently the long-range π-π ordering essential for semiconducting properties, can be controlled by the secondary hydrogel network. (Fig. 2, D to G). For example, combining PEDOT:PSS hydrogels with polyethylene glycol diacrylate (PEGDA), polyvinyl alcohol (PVA), polyacrylamide (PAAm), or polyacrylic acid (PAA) led to increased conductivity from 0.9 S/cm to 1.4, 18, and 100 S/cm, respectively (Fig. 2E), indicating enhanced continuity of the conductive $PEDOT^+$ phase (figs. S4 to S6). These results align with previous reports on the development of conducting hydrogels (*34*–*37*), which have revealed that secondary networks, especially PAA, can serve as efficient templates to guide the formation of continuous $PEDOT^+$ monolayers (*34*, *38*). The increased conductivity is also associated with improved volume capacitance (Fig. 2F and fig. S7), a strong indicator of the formation of a 3D electron-conducting network. The improved phase continuity also does not compromise the mechanical properties of the hydrogel semiconductor (Fig. 2G and figs. S8 to S11).

Structure engineering of 3D hydrogel semiconductors

To achieve 3D modulation at greater thicknesses, such as up to the millimeter scale, requires additional structural design to control porosity that enhances ion transport (*32*). The structure engineering is crucial for enabling efficient ion-electron conversion within 3D hydrogel semiconductors. To tune the porosity of the hydrogel semiconductor, we used the following strategies: (i) controlling the individual concentrations of components in the mixture that assembles the multinetwork hydrogel, including the primary semiconducting network and the secondary stretchable network; (ii) adjusting the cross-linking density by varying the concentration of the cross-linker; and (iii) using solvent exchange to deliberately construct micropores after hydrogel formation (detailed in the materials and methods). The combination of these approaches delivers a hydrogel semiconductor with porosity controllable over a wide range, from 5% to 90% (Fig. 3).

We observed that the porosity of the hydrogel semiconductor is positively correlated with its swelling ratio. For example, the swelling ratio increased from 50% to 100%, and eventually to 500%, as the porosity increased from 5% to 10% and then to 90%. These swelling properties were found to be reversible, demonstrating the mechanical robustness of the microporous structure (Fig. 3, A to C).

To investigate the dependence of charge carrier transport on porosity, we measured both the electronic conductivity and ionic conductivity of the hydrogel semiconductors with varying porosities. We found that increasing the porosity decreases the electronic conductivity but enhances the ionic conductivity. Specifically, increasing the porosity from 5% to 90% resulted in a decrease in electronic conductivity by more than an order of magnitude (Fig. 3D), whereas ionic conductivity increased by more than an order of magnitude (Fig. 3E). This behavior is reasonable and can be explained as follows: Increasing porosity makes the electron-conducting network sparser, thereby reducing electronic conductivity, while simultaneously providing more space for ionic transport, which enhances ionic conductivity.

We observed that an optimal porosity range exists for the 3D hydrogel semiconductor that corresponds to the highest on/off ratio of 10^4, comparable to state-of-the-art OECTs (Fig. 3F) (*39*, *40*). This observation indicates that optimal ion-electron coupling is achieved at this porosity. The results are in line with our steady-state simulation results based on the Bernards-Malliaras model (figs. S12 to S14) (*27*). This phenomenon can be explained as follows: (i) At low porosity, the semiconducting polymer network is dense, which favors electron transport but restricts ion penetration. (ii) At high porosity, the semiconducting polymer network becomes loose, leading to poor electronic transport and limiting ion-electron redox coupling despite enhanced ionic transport.

Validation of 3D modulation in 3D hydrogel semiconductors

To evaluate the degree of 3D modulation in hydrogel semiconductors, we fabricated hydrogel transistors (Fig. 4A and fig. S15). The typical transfer and output curves (Fig. 4, B and C) demonstrate that devices made with a 3D hydrogel semiconductor exhibit superior performance than the reference films of the same channel thicknesses (between 50 and 1000 μm). For instance, at the same thickness of 1 mm—sufficient to sustain a 3D freestanding architecture—the on/off ratio of the hydrogel transistors reaches ~10^4 (Fig. 4), which is three orders of magnitude higher than the reference 1-mm-thick OECTs. This result proves the high doping/dedoping efficiency of the 3D hydrogel semiconductor.

The efficient 3D modulation is further validated by the volumetric capacitance of the hydrogel semiconductor, a standard parameter used to evaluate bulk modulation in OECTs (Fig. 4D). For OECTs fabricated

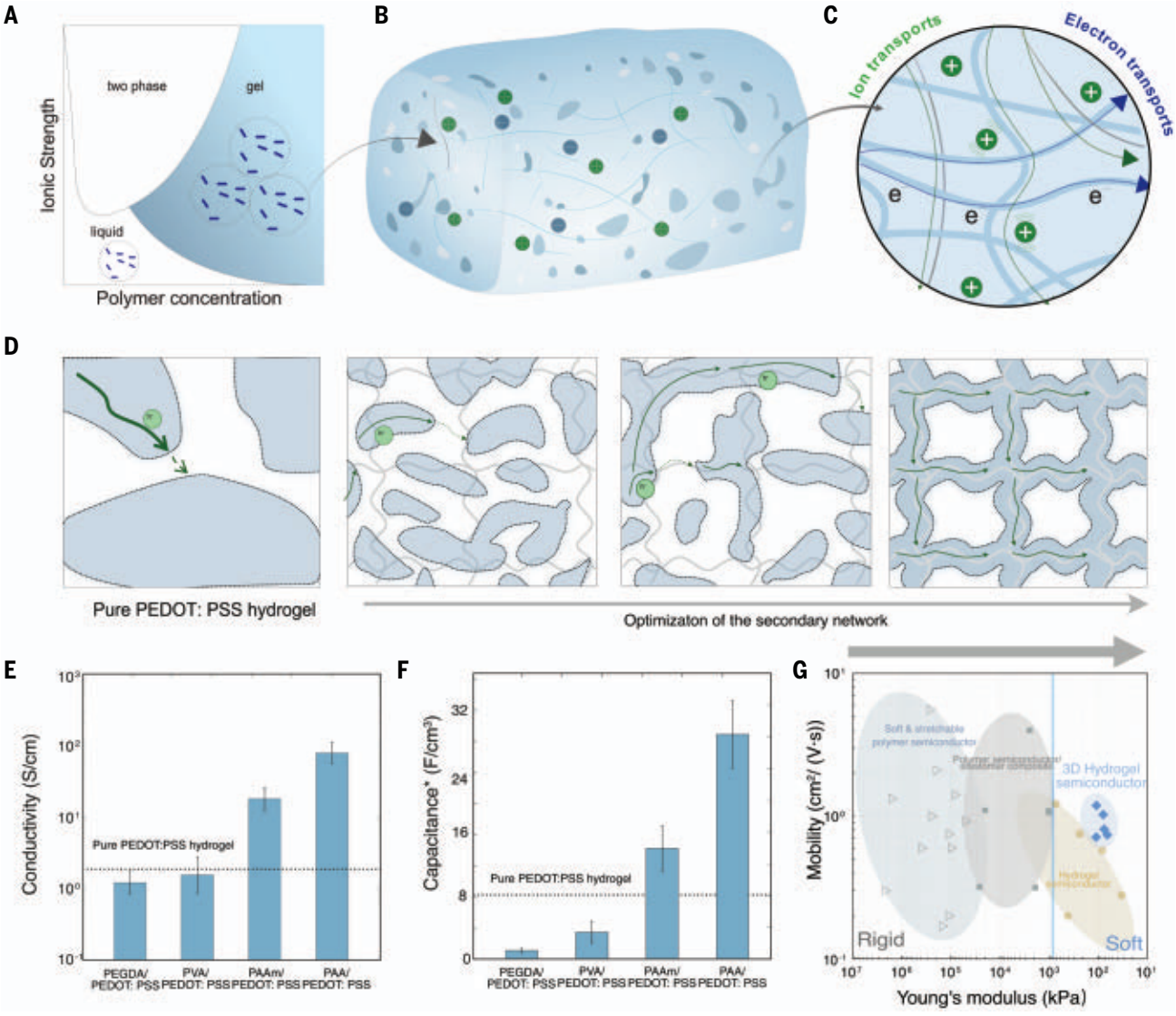

Fig. 2. Phase engineering of 3D hydrogel semiconductors to promote electron transport. (**A** to **C**) A hydrogel may contain three phases: a liquid phase, a gel phase, and a mixture of the two. In a hydrogel semiconductor, mixed conduction pathways exist, including ions and electrons. (**D**) Illustration of phase variations in hydrogel semiconductors (using PEDOT:PSS as the primary semiconducting backbone) by optimizing the secondary hydrogel networks. (**E** and **F**) A comparison of these hydrogel semiconductors shows that a continuous phase favors both high electrical conductivity and high volumetric capacitance. The hydrogel semiconductors include pure PEDOT:PSS hydrogel and double network hydrogel employing polyvinyl alcohol (PVA), polyacrylamide (PAAm), and polyacrylic acid (PAA) as the secondary network. Data are presented as mean ± SD, $N = 3$ independent hydrogel samples per condition. (**G**) The resultant hydrogel semiconductor (PEDOT:PSS/PAA) overcomes the modulus limitations of existing soft semiconductors while maintaining a mobility of ~1 $cm^2/(V{\cdot}s)$ (table S1).

with conventional thin films, the capacitance fails to increase linearly when the channel thickness exceeds ~10 μm (Fig. 4D), which is in line with previous studies (*31*). In contrast, the linear thickness-capacitance dependency of hydrogel semiconductor remains consistent regardless of thickness (up to millimeters), indicating that complete 3D modulation is achieved in the hydrogel semiconductor.

The parameter combination μC^* (where μ is electronic mobility and C^* is the volumetric charge storage capacity) is regarded as a material figure of merit for OECTs (*41*). To provide a fair comparison with conventional films, we further evaluated the thickness-dependent parameter $d\mu C^*$, where channel thickness (d) must satisfy the thickness-capacitance linearity (*28*, *41*). This parameter is essential, as it directly correlates with the transconductance (G_m) of the hydrogel semiconductor transistors. As shown in Fig. 4E, the $d\mu C^*$ of hydrogel semiconductor reaches 0.1 $F{\cdot}V^{-1}{\cdot}s^{-1}$, which is significantly higher than that of conventional OECTs with 2D architecture. This improvement is attributed to the greater channel thickness (up to millimeters), while still retaining linear thickness-capacitance behavior. Consequently, the G_m of the resulting 3D hydrogel transistors surpasses reported 2D counterparts (Fig. 4F).

Scalable production of 3D hydrogel semiconductors

To fully leverage the potential of 3D hydrogel semiconductors for demonstrating 3D transistors, it is essential to enable scalable production using accessible and low-cost methods such as printing and textile manufacturing methods. We developed a one-step water-processable fabrication protocol, detailed in the materials and methods. In this approach, the required materials for assembling the composite

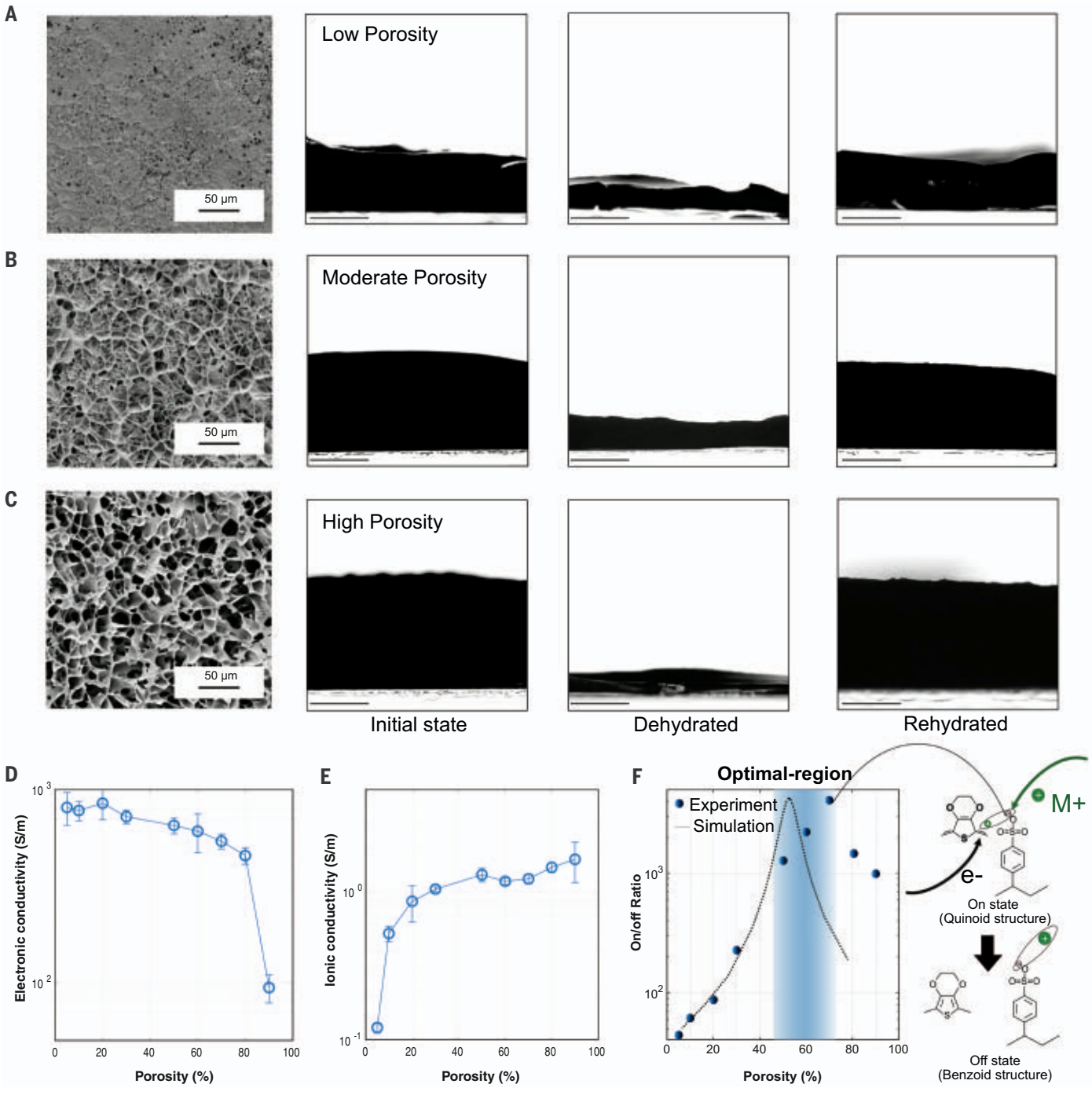

Fig. 3. Structural engineering of 3D hydrogel semiconductors to promote ion transport. (**A** to **C**) Porosity in hydrogel semiconductors (PEDOT:PSS/PAA) can be controlled through solvent exchange and annealing. Cyro–scanning electron microsopy images of hydrogel semiconductors show (A) low porosity (5%), (B) moderate porosity (50%), and (C) high porosity (90%). All hydrogels fully recover their initial volume after dehydration, demonstrating the robustness of the 3D cross-linked network. Scale bars: 500 μm. (**D** and **E**) The increase in porosity decreases electrical conductivity (σ_e) but enhances ionic conductivity (σ_i). Data are presented as mean ± SD, $N = 3$ independent hydrogel samples per condition. (**F**) An optimal porosity range exists (optimal region), corresponding to the highest on/off ratio when characterized with OECT (width of 1 cm, length of 0.5 cm, thickness of 100 μm). These experimental results align with steady-state simulation predictions based on the Bernards-Malliaras model.

hydrogel semiconductor are premixed in a single step. The 3D hydrogel semiconductor can then be formed through a simple cross-linking process. Additional steps can be applied on demand to fine-tune specific parameters. For instance, solvent exchange can be used to adjust porosity.

We mass-produced 3D hydrogel semiconductors with thicknesses ranging from micrometers to millimeters and arbitrary macroscopic shapes (figs. S16 and S17). All these 3D hydrogel semiconductors were examined and found to retain excellent semiconducting properties and mechanical stretchability (Fig. 5A and fig. S18).

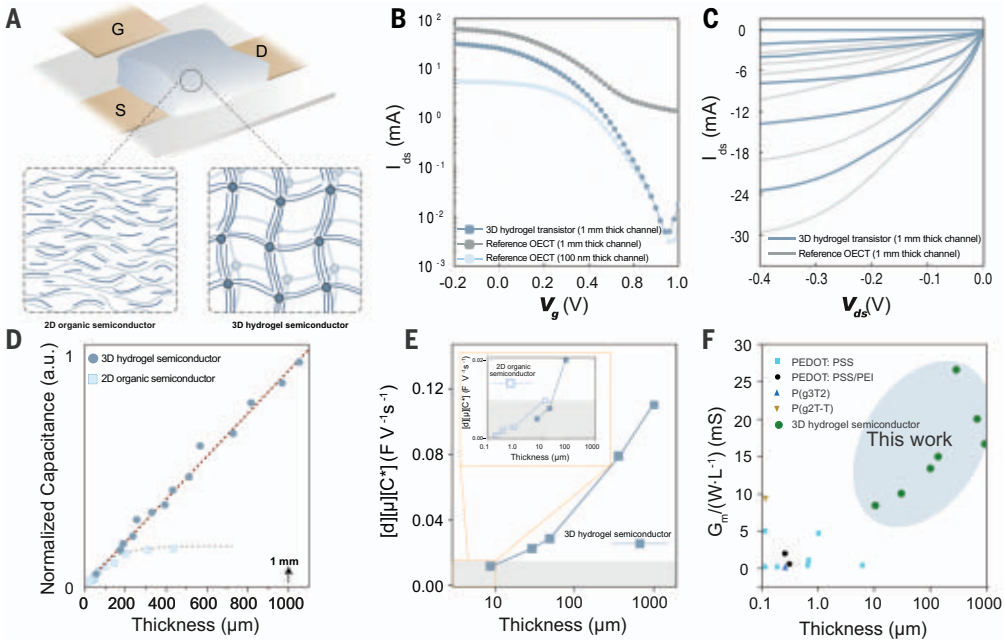

Fig. 4. Electrical performance of 3D hydrogel transistors. (**A**) Comparison of transistors with 2D organic semiconductors (pure PEDOT:PSS film) and 3D hydrogel semiconductors (PEDOT:PSS/PAA) as the channel (with the same thickness of 1 mm). Hydrogel semiconductors, because of their intentionally constructed resilient, three-dimensionally cross-linked micropores, ensure efficient 3D modulation even at greater thicknesses (>50 μm). (**B** and **C**) Comparison of the transfer (V_{ds} = −0.2 V) and output curves (V_g from 0 V to 1 V with 0.2 V increments) of 3D hydrogel transistors (with 1-mm-thick PEDOT:PSS/PAA hydrogel semiconductor as the channel) and reference OECT (with 1 mm and 100 nm PEDOT:PSS film as the channel). The width and length of the device is 1 cm and 0.5 cm, respectively. (**D**) Thickness-capacitance relationship. The 2D organic semiconductor (pure PEDOT:PSS film) fails to maintain linearity at greater thicknesses (~10 μm), whereas the hydrogel semiconductor (PEDOT:PSS/PAA) maintains linearity up to 1000 μm—two orders of magnitude higher. a.u., arbitrary units. (**E**) We fabricated 3D hydrogel transistors with thicknesses ranging from 10 to 1000 μm and reference 2D OECTs with thicknesses ranging from 100 nm to 10 μm. Thicknesses >10 μm for 2D OECTs are not shown, as they failed to achieve complete bulk modulation, meaning they did not maintain a linear thickness-capacitance relationship. In contrast, the volumetric capacitance of the hydrogel semiconductor remains valid at greater thicknesses (up to 1 mm), leading to a significant increase in G_m, which is proportional to $d \times \mu \times C^*$. (**F**) The normalized G_m surpasses previously reported values (table S2).

Building 3D transistors and circuits based on 3D hydrogel semiconductors

The successful development of 3D hydrogel semiconductors, along with the scalable production procedures described above, enables their immediate application in constructing 3D transistors. As a demonstration, we further shaped those 3D semiconductors into self-standing hydrogel fibers, facilitating the construction of brain-inspired 3D neuromorphic circuits, which were assembled into 3D, interpenetrated hydrogel transistor arrays for data computing and analysis (Fig. 5, B and C). To facilitate data acquisition, we integrated the 3D transistors with our recently developed coin-sized readout unit, the Personalized Electronic Reader for Electrochemical Transistors (PERfECT; fig. S19) (*42*–*44*).

To demonstrate the potential of our 3D hydrogel transistor circuits for constructing brain-inspired 3D intelligence, we adopted the reservoir computing (RC) framework—a promising machine learning algorithm known for its minimal computational requirements and ability to operate with small training datasets (*45*, *46*). RC uses neuron-like nonlinear hardware units, a role in which our hydrogel transistors excel (fig. S20). Structurally, hydrogel transistors resemble three-terminal transistors, where the gate electrode functions analogously to the presynapse of a neuron, receiving input ionic signals (*47*). The channel between the source and drain electrodes mimics the postsynapse, responding to the gate signals. Operationally, signals at the gate electrode propagate through nonlinear ionic transport via the electrolyte, modulating the channel conductance through a nonlinear electrochemical doping/dedoping process (*48*).

The detailed implementation of our 3D hydrogel transistor circuits in a RC network is illustrated in Fig. 5D. For demonstration purposes, handwritten digit recognition from the Modified National Institute of Standards and Technology (MNIST) dataset was selected as the application (fig. S21) (*49*). The steps include: (i) Input: Preprocessed image signals serve as input to the gate terminal of the 3D hydrogel transistors. All 16 hydrogel fiber semiconductors share a common gate electrode located at the bottom. (ii) Encoding: The 3D hydrogel transistor circuits encode the digital input signals into distinguishable analog signals, thanks to their nonlinear dynamic response behaviors (Fig. 5E). (iii) Analysis: The entire integrated system processes the input image signal sequence by implementing RC and generating predicted results through a hardware-software coprocessing approach. In this setup, the hardware component (hydrogel transistor array) performs the RC, while the software component handles linear readout and classification. During programming, the modulation of a specific volatile transistor originates from both the common gate and the influence of the weighted equivalent gate voltage from all other channels (Fig. 5B). This intentional design mimics the spatial connectivity of real neural networks, forming the foundation of the hydrogel reservoir layer for RC. Figure 5F presents the confusion matrices showing that the system can achieve a prediction accuracy of up to 91.93%, which is comparable to conventional artificial neural networks (*50*). Each matrix is dominated by its diagonal elements, indicating high class-wise accuracy across all digits. Notably, the prediction accuracy can be maintained under up to 30% strain applied in any direction (Fig. 5G).

Our reported 3D hydrogel semiconductors and transistors achieve millimeter-scale 3D modulation with performance comparable to their thin-film counterparts. These advances are enabled by a standardized water-processable synthesis process that precisely controls phase, porosity, and charge transport properties in three dimensions. Our macroscopic fabrication approach allows the mass production of 3D hydrogel semiconductors and transistors in various 3D shapes, overcoming the dimension limitations of 2D planar electronics, as demonstrated in neuromorphic computing circuits.

Leveraging inherent tissue-like properties such as biocompatibility, stretchability, and permeability, these 3D hydrogel semiconductors and transistors bridge the multidimensional gaps between electronics and living systems, enabling robust and durable 3D interfacing. As an example, we further demonstrate that these 3D semiconductors and transistors enable two-way biology-transistor interactions, including

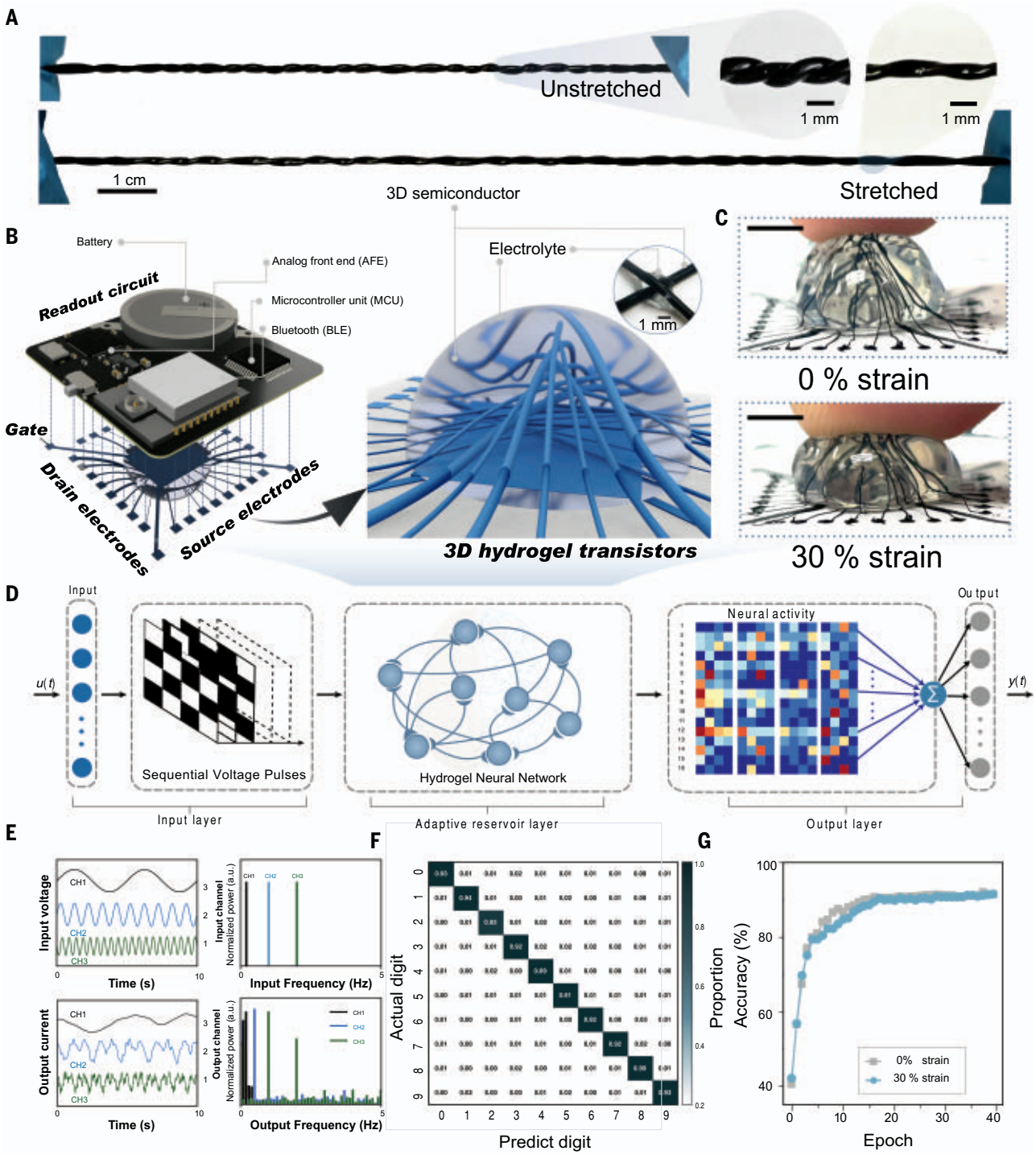

Fig. 5. Increasing the dimensionality of transistors with 3D hydrogel semiconductors. (**A**) The hydrogel semiconductor (PEDOT:PSS/PAA), when fabricated into fiber forms, enables the direct fabrication of 3D, freestanding transistors. (**B**) Illustration of a 3D integrated neuromorphic circuit with the 3D hydrogel transistors. (**C**) Real images of 3D, interpenetrated hydrogel transistors, showing their exclusive ability to resemble the spatial 3D structure of neural circuits in the brain, subjected to strain values of 0% and 30%. Scale bars: 0.5 cm. (**D**) Schematic representation of a 3D RC framework constructed using a 3D hydrogel transistor array. (**E**) Harmonic analysis showing the good nonlinearity of the hydrogel transistors, ensuring high computational efficiency within the reservoir network. (**F**) A confusion matrix showing that handwritten digits are correctly recognized with the hydrogel transistors RC hardware with an accuracy of 91.93%. (**G**) Evolution of prediction accuracy over training epochs when the RC hardware is subjected to strains of 0% and 30%.

cell culture, organoid formation, and programmable cell behavior (fig. S22).

REFERENCES AND NOTES

1. W. Cao *et al.*, *Nature* **620**, 501–515 (2023).
2. C. E. Leiserson *et al.*, *Science* **368**, eaam9744 (2020).
3. J. Shalf, *Philos. Trans. R. Soc. London Ser. A* **378**, 20190061 (2020).
4. I. L. Markov, *Nature* **512**, 147–154 (2014).
5. P. Gkoupidenis *et al.*, *Nat. Rev. Mater.* **9**, 134–149 (2024).
6. A. Carnicer-Lombarte, G. G. Malliaras, D. G. Barone, *Adv. Mater.* **37**, e2408308 (2025).
7. D. Boufidis, R. Garg, E. Angelopoulos, D. K. Cullen, F. Vitale, *Nat. Commun.* **16**, 1861 (2025).
8. Y. Wu *et al.*, *Nat. Commun.* **15**, 4047 (2024).
9. H. Cai *et al.*, *Nat. Electron.* **6**, 1032–1039 (2023).
10. C. Pitsalidis *et al.*, *Sci. Adv.* **4**, eaat4253 (2018).
11. S. D. Brotherton, *Introduction to Thin Film Transistors: Physics and Technology of TFTs* (Springer, 2013).
12. X. Liu, S. Wang, *Chem. Soc. Rev.* **43**, 2385–2401 (2014).
13. T. Schrödel, R. Prevedel, K. Aumayr, M. Zimmer, A. Vaziri, *Nat. Methods* **10**, 1013–1020 (2013).
14. H. Yuk, J. Wu, X. Zhao, *Nat. Rev. Mater.* **7**, 935–952 (2022).
15. Y. Liu *et al.*, *Nat. Biomed. Eng.* **3**, 58–68 (2019).
16. Y. S. Zhang, A. Khademhosseini, *Science* **356**, eaaf3627 (2017).
17. S. Zhang *et al.*, *Adv. Mater.* **32**, e1904752 (2020).
18. P. Li *et al.*, *Science* **384**, 557–563 (2024).
19. Y. Dai *et al.*, *Science* **386**, 431–439 (2024).
20. A. C. Tseng, T. Sakata, *ACS Appl. Mater. Interfaces* **14**, 24729–24740 (2022).
21. J. Rivnay *et al.*, *Nat. Rev. Mater.* **3**, 17086 (2018).
22. Y. Wang *et al.*, *Nat. Rev. Mater.* **9**, 249–265 (2024).
23. D. Khodagholy *et al.*, *Nat. Commun.* **4**, 2133 (2013).
24. T. Someya, Z. Bao, G. G. Malliaras, *Nature* **540**, 379–385 (2016).
25. C. Yang, Z. Suo, *Nat. Rev. Mater.* **3**, 125–142 (2018).
26. D. Nilsson *et al.*, *Adv. Mater.* **14**, 51–54 (2002).
27. D. A. Bernards, G. G. Malliaras, *Adv. Funct. Mater.* **17**, 3538–3544 (2007).
28. J. Rivnay *et al.*, *Sci. Adv.* **1**, e1400251 (2015).
29. D. Ohayon, V. Druet, S. Inal, *Chem. Soc. Rev.* **52**, 1001–1023 (2023).
30. S. Inal, J. Rivnay, A.-O. Suiu, G. G. Malliaras, I. McCulloch, *Acc. Chem. Res.* **51**, 1368–1376 (2018).
31. M. Bianchi *et al.*, *J. Mater. Chem. C* **8**, 11252–11262 (2020).
32. R. Foudazi, R. Zowada, I. Manas-Zloczower, D. L. Feke, *Langmuir* **39**, 2092–2111 (2023).
33. M. M. Michael A Leaf, *Macromolecules* **49**, 4286–4294 (2016).
34. J. Chong *et al.*, *Nat. Commun.* **14**, 2206 (2023).
35. Y. Zhu *et al.*, *ACS Appl. Mater. Interfaces* **16**, 32466–32480 (2024).
36. G. Li *et al.*, *Adv. Mater.* **34**, e2200261 (2022).
37. N. Lopez-Larrea *et al.*, *ACS Appl. Polym. Mater.* **4**, 6749–6759 (2022).
38. V. V. Tsukruk *et al.*, *Macromolecules* **30**, 6615–6625 (1997).
39. D. Liu *et al.*, *Adv. Sci. (Weinh.)* **9**, e2203418 (2022).
40. J. Rivnay *et al.*, *Adv. Mater.* **25**, 7010–7014 (2013).
41. S. Inal, G. G. Malliaras, J. Rivnay, *Nat. Commun.* **8**, 1767 (2017).
42. J. Bai *et al.*, *Sci. Adv.* **10**, eadl1856 (2024).
43. X. Tian *et al.*, *Anal. Chem.* **94**, 6156–6162 (2022).
44. D. Liu *et al.*, *Nat. Electron.* **7**, 1176–1185 (2024).
45. L. Appeltant *et al.*, *Nat. Commun.* **2**, 468 (2011).
46. M. Cucchi *et al.*, *Sci. Adv.* **7**, eabh0693 (2021).
47. X. Ji *et al.*, *Nat. Commun.* **12**, 2480 (2021).
48. X. Liang, Y. Luo, Y. Pei, M. Wang, C. Liu, *Nat. Electron.* **5**, 859–869 (2022).
49. Y. LeCun, C. Cortes, C. J. C. Burges, The MNIST database of handwritten digits (1998); https://web.archive.org/web/20200424075210/http://yann.lecun.com/exdb/mnist/index.html.
50. X. Wu *et al.*, *Nat. Commun.* **14**, 468 (2023).

ACKNOWLEDGMENTS

We thank C. Wong, J. Chan, P. S. Yip, and P. K. L. Chan from the University of Hong Kong (HKU) Central Fabrication Lab (CFL) for their support with clean-room facilities and microfabrication and the HKU Electron Microscope Unit (EMU) for assistance with morphology characterization. We also thank N. Tien and C. K. Chui for their support with printing facilities and wet lab resources at the HKU Tam Wing Fan Innovation Wing. We acknowledge N. Wong (HKU), Z. Wang (Southern University of Science and Technology), C. Li (HKU), I. McCulloch (Princeton University), H. Wang (HKU), and W. Gao (OmniVision Integrated Circuits Group, Inc.) for discussions on neuromorphic computing, molecular electronics, and the semiconductor industry. **Funding:** The Collaborative Research Fund (C7005-23Y), the Early Career Scheme (ECS) (27214224), the General Research Fund (GRF) (17208623, 17200425), and the Theme-based Research Scheme (T45-701/22-R) from the Research Grants Council of the Hong Kong SAR Government, China; the Innovation and Technology Fund (Mainland-Hong Kong Joint Funding Scheme, MHP/053/21) from the Innovation and Technology Commission (ITC) of the Hong Kong SAR Government, China; Shenzhen-Hong-Kong-Macau Technology Research Programme (SGDX20210823103537034) from the Science, Technology and Innovation Commission of Shenzhen Municipality, China; and Seed Funding for Strategic Interdisciplinary Research Scheme from HKU. **Author contributions:** Conceptualization: S.Z.; Funding acquisition: S.Z.; Supervision: S.Z.; Data curation: D.L., J.B., X.T., Y.W.; Methodology (experiment design and characterization): D.L., Y.W.; Methodology (algorithm design and simulation): D.L., X.T., J.B.; Software (miniaturized readout system): X.T., J.B.; Investigation (fabrication of hydrogel transistors): D.L., Y.W., B.C., S.D.; Investigation (sample preparation, electrochemical testing): D.L., Y.W., Z.S., C.K.L.; Investigation (cell culture and data analysis): W.L.; Formal analysis (discussion and result analysis): S.Z., G.G.M.; Writing – original draft: S.Z., D.L.; Writing – review & editing: All authors. **Competing interests:** The authors have filed a US patent on this work titled "3D semiconductor and methods of fabrication" (US application no. 63/816,028). **Data and materials availability:** All data are available in the manuscript or the supplementary materials. **License information:** Copyright © 2025 the authors, some rights reserved; exclusive licensee American Association for the Advancement of Science. No claim to original US government works. https://www.science.org/about/science-licenses-journal-article-reuse

SUPPLEMENTARY MATERIALS

science.org/doi/10.1126/science.adx4514
Materials and Methods; Figs. S1 to S23; Tables S1 and S2; References (*51*–*88*)

Submitted 14 March 2025; accepted 4 September 2025

10.1126/science.adx4514

ORGANIC CHEMISTRY

An anion-binding approach to enantioselective photoredox catalysis

Petra Vojáčková and Eric N. Jacobsen*

Photoredox catalysis has emerged as a transformative strategy in synthetic chemistry, enabling a wide variety of valuable chemical reactions through generation of highly reactive radical ion intermediates. Pairing chiral counteranions with cation radical intermediates provides a potentially generalizable tool for controlling absolute stereochemistry in various reactivity contexts. However, ion-pairing effects on the efficiency of photoinduced processes and the reactivity of radical ion pairs impose severe limits on the chiral anions that can be engaged effectively. In this study, we report that association of neutral chiral small-molecule hydrogen-bond donors with the counteranions of cation radical intermediates can achieve enantioselectivity through ion-pairing and other noncovalent interactions. Applications to four different classes of cycloaddition reactions of electron-rich alkene substrates provide cyclic products with up to four new stereocenters in up to 99% enantiomeric excess.

Photoredox catalysis provides access to rich reactivity manifolds by enabling efficient generation of high-energy intermediates through photoinduced electron-transfer processes (*1*–*5*). Radical ion-pair intermediates are the primary species formed by single-electron oxidation or reduction of neutral substrates. Although proton transfer or fragmentation represent the most common modes of reactivity of radical ion pairs, cation or anion radicals can engage in various carbon-carbon- or carbon-heteroatom-bond–forming transformations to yield products with greatly enhanced molecular complexity (*6*–*8*). However, taking full advantage of the powerful reactions of radical ion pairs in synthesis depends in part on the ability to control the stereochemical course of these processes. Despite the substantial efforts and recent progress in developing methods for asymmetric photoredox catalysis, controlling enantioselectivity of reactions of radical ion pairs remains a considerable challenge.

The existing approaches to avoid undesired racemic background reactivity of these highly reactive intermediates often rely on association of substrates with chiral catalysts before the photoexcitation event. This strategy typically necessitates engineering of substrates to contain functional groups capable of binding to the chiral catalyst (Fig. 1A) (*9*–*11*). Generation of reactive intermediates within enzymes or supramolecular coordination cages has been demonstrated as a promising method to impart enantioselectivity in their reactions (*12*, *13*). The use of chiral counterions has emerged as an alternative and potentially more general approach to enantiocontrol, given the ionic character of many intermediates in photoredox transformations. This method relies on the fact that reductive quenching of the excited state of an ionic photoredox catalyst by substrate to a neutral photoredox catalyst radical leads to formation of a substrate cation radical paired with the anion originally associated with the photoredox catalyst. Initial attempts to apply this strategy for asymmetric catalysis focused on the use of chiral phosphate and phosphoramide anions paired with organic ionic photoredox catalysts to achieve intramolecular hydroetherifications (*14*), (2+4) cycloaddition reactions (*15*), or a single example of a (3+2) cycloaddition to yield a 1,2,4-triazoline product in up to 50% enantiomeric excess (ee) (*16*). In very recent studies, chiral phosphate anions have been identified to promote deracemization processes by facilitating deprotonation of cation radical intermediates (*17*, *18*). The design of substrates bearing directing groups with anion-binding properties has been applied successfully to achieve high enantioselectivity in several other reported examples (*19*–*22*). As a specific example, Ooi and co-workers utilized urea as a redox-active directing group to engage with a chiral borate counteranion associated with an iridium photoredox catalyst to promote (3+2) cycloaddition reactions with excellent enantioselectivity (*19*). In 2023, List and co-workers disclosed highly enantioselective (2+2) cycloaddition reactions between *trans*-anethole and β-unsubstituted styrene derivatives (*23*). The success of the method was attributed to the low basicity of the imidodiphosphorimidate anion associated with a pyrylium photoredox catalyst to prevent undesired deprotonation of the highly acidic cation radical intermediates, along with the confined nature of the active site of the large anion. More recently, List's group reported an expansion of the method to highly enantioselective (2+1) cycloaddition reactions using a broad scope of alkenes and diazoalkanes (*24*).

The effects of the identity of counteranions associated with ionic photoredox catalysts and cation radical intermediates were investigated thoroughly by Yoon and co-workers (*25*). Their studies revealed that highly coordinating and basic anions were detrimental to the efficiency of cation radical processes by affecting multiple aspects of the reaction mechanism. They found that they could rescue the photoredox-catalyzed reactions with coordinating anions by applying a thiophosphotriamide hydrogen-bond donor (HBD) additive that was proposed to associate with the anions and attenuate the deleterious ion-pairing interactions. A similar approach was recently demonstrated by García Mancheño and co-workers to improve the properties of acridinium halide salts by combining them with thiourea HBDs in a variety of cation radical reactions (*26*). In addition, Chiba and co-workers described the beneficial effects of simple HBDs such as hexafluoroisopropanol in hole catalysis under photoredox and electrochemical conditions (*27*).

On the basis of these precedents, we hypothesized that the anion-binding properties of appropriately designed chiral HBDs could be used to induce enantioselectivity in reactions of cation radical intermediates while possibly broadening the scope of counteranions applied in photoredox catalysis (Fig. 1B) (*28*). Chiral small-molecule dual HBDs have been demonstrated to associate with a variety of anions to promote highly enantioselective reactions of cationic intermediates (*29*, *30*). Despite the broad application of this strategy in reactions of cationic species, anion binding with chiral HBDs has not been applied successfully to induce enantioselectivity in reactions of open-shell cation radical intermediates.

The aryl-pyrrolidino–*tert*-leucine-derived class of chiral HBDs has proven broadly effective in promoting highly enantioselective reactions of ion-pair intermediates through networks of different types of stabilizing noncovalent interactions (*31*, *32*). Potential challenges associated with extending the application of this catalyst family to reactions of photogenerated cation radical intermediates included compatibility between the structurally rich HBDs and open-shell intermediates (*33*) and insolubility of many photoredox catalysts in nonpolar solvents that are usually required for achieving high enantioselectivity through ion-pairing catalysis (*34*). Here, we demonstrate anion binding with chiral HBDs to induce high enantioselectivity in photoredox reactions of cation radical intermediates generated from electron-rich alkene substrates. The developed approach was applied to different classes of cycloaddition reactions to provide enantioenriched 3-to-6-membered carbocyclic scaffolds with up to four new stereocenters (Fig. 1C).

Department of Chemistry and Chemical Biology, Harvard University, Cambridge, MA, USA.
*Corresponding author. Email: jacobsen@chemistry.harvard.edu

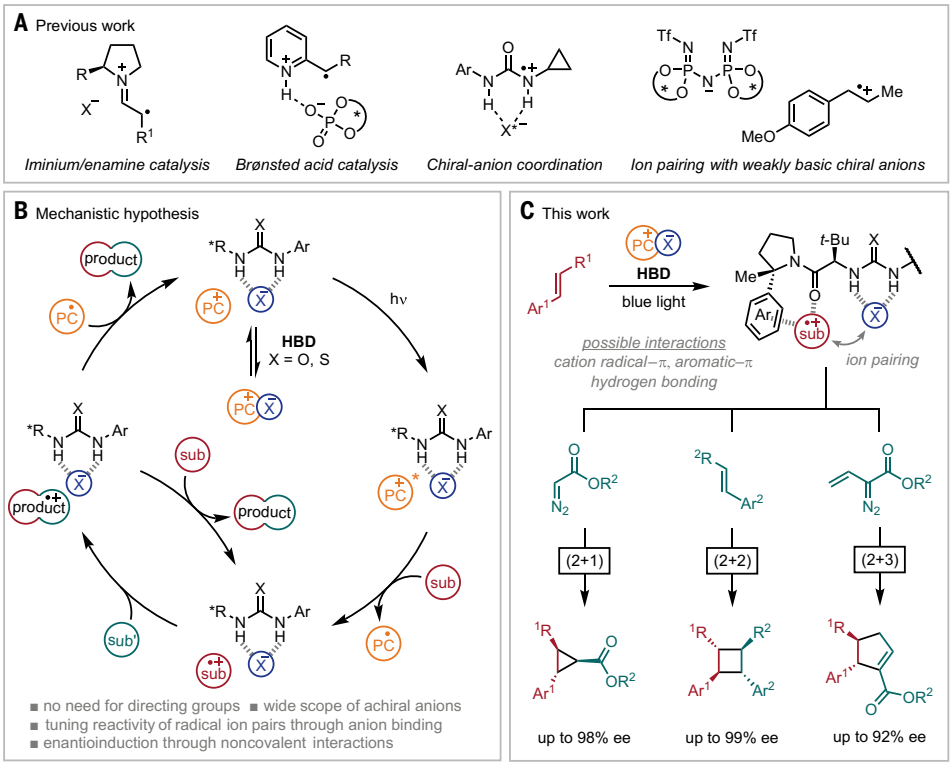

Fig. 1. Enantioselective anion-binding photoredox catalysis. (**A**) Strategies in enantioselective photoredox catalysis. *, chiral; X, anion. (**B**) Proposed catalytic cycle for the application of chiral hydrogen-bond donors in enantioselective reactions of cation radical intermediates generated through photoredox catalysis or a radical-chain mechanism. HBD, hydrogen-bond donor; R*, chiral substituent; Ar, aryl; PC, photoredox catalyst; *, excited state; X, anion; sub, sub', substrate. (**C**) General representation of the developed strategy.

Development of enantioselective (2+2) cycloaddition reactions

We focused our initial efforts on *trans*-anethole derivatives as substrates because of the relatively low oxidation potential of *trans*-anethole [+1.24 V versus saturated calomel electrode (SCE)] and the myriad reported examples of synthetically valuable racemic reactions proceeding through cation radicals derived from *trans*-anethole (*35*–*42*). We decided to explore the application of the asymmetric anion-binding hypothesis in photoredox processes in the context of (2+2) cycloaddition reactions that provide a direct route to analogs of bioactive cyclobutane lignan natural products (*40*). Beyond the lack of known methods for their enantioselective synthesis, we were drawn to the problem because some cyclobutane lignans exist as scalemic mixtures in nature (*43*, *44*). Pyrylium salts were selected as suitable photoredox initiators owing to their monocationic nature, their previous successful use in activation of electron-rich alkene substrates, and their synthetic accessibility (*3*). Prior work in anion-binding cooperative catalysis using the aryl-pyrrolidino–*tert*-leucine HBDs suggested that sulfonates may be suitable counteranions for this approach (*45*, *46*). Therefore, we started our screening efforts using pyrylium tosylate **1a** as the photoredox catalyst.

We found that the combination of **1a** and monomeric thiourea HBD **2a** under blue-light irradiation promoted the homodimerization of *trans*-anethole (**3a**) at −55°C and provided **4a** with complete regio- and diastereoselectivity in 96% ee, but with low conversion of the starting material (Fig. 2A, right). Bis-thiourea HBD **2d** was found to be more efficient in catalyzing the cycloaddition and yielded **4a** in 51% yield and 98% ee. The aryl-pyrrolidine components of the HBD catalysts have been previously shown to engage in various noncovalent interactions with substrates that were identified as crucial for achieving selectivity in their reactions (*46*–*49*). Evaluation of bis-thiourea HBDs bearing different aryl-pyrrolidine groups revealed that the identity of the aryl groups had little effect on the enantioselectivity of the (2+2) cycloaddition reaction of **3a**, but more electron-rich and polarizable aryl groups were found to have a detrimental effect on reaction efficiency. We selected HBD **2c** for further optimizations (see fig. S5 for details) and found that lowering the reaction temperature to −77°C led to formation of the (2+2) adduct as a single diastereomer in improved 68% yield and 99% ee (Fig. 2A, left).

Control experiments demonstrated that light, the pyrylium salt, and the HBD were all essential to the observed reactivity (Fig. 2A, left). To rule out the possibility that the reaction proceeded via a cationic pathway promoted by a trace acid catalyst, we performed the reaction in the presence of bulky base 2,6-di-*tert*-butylpyridine, commonly used to distinguish between ionic and radical mechanisms (*50*). Product **4a** was formed under these conditions in a comparable yield and the same enantioselectivity, which is consistent with the cation radical–promoted pathway being operative. The presence of oxygen was found to be deleterious to the reaction outcome, causing degradation of the bis-thiourea HBD under photochemical conditions. By contrast, the HBD could be recovered in quantitative yield from reactions conducted under rigorously degassed conditions.

Variation of the counteranion of pyrylium **1** revealed that high enantioselectivity was achievable with HBD **2c** in combination with anions of different shapes and coordinating abilities and basicities spanning more than 10 pK_a units (where K_a is the acid dissociation constant) (Fig. 2B) (*23*, *51*). However, nearly racemic product was formed as a 1:3 mixture of *anti*- and *syn*-diastereomers in the reaction promoted in the presence of **2c** and the pyrylium salt **1b** associated with the noncoordinating tetrakis[3,5-bis(trifluoromethyl)phenyl]borate (BAr^F_4) anion. This observation is consistent with the hypothesis that the HBD is inducing stereoselectivity in the (2+2) cycloaddition reaction through an anion-binding mechanism (*46*). In addition, with the exception of the BAr^F_4 salt **1b**, the HBD had a considerable solubilizing effect on the pyrylium salts. In particular, pyrylium tosylate and mesylate salts displayed substantially higher solubility in the presence of the HBD cocatalyst in methyl *tert*-butyl ether (MTBE) than those containing BF_4, PF_6, or TfO counteranions (*52*). Proton nuclear magnetic resonance (^{1}H NMR) analysis of the association between HBD **2d** and pyrylium salt **1a** by the method of continuous variation revealed formation of a 1:1 complex (Fig. 2C) (*53*).

The high levels of both enantio- and diastereoselectivity in the formation of **4a** result from control imparted by the chiral HBD catalyst. In reactions carried out in dichloromethane to ensure complete solubility of all reaction components, nearly perfect absolute and relative stereocontrol was achieved in the formation of *anti*-**4a** in the presence of tosylate salt **1a** and HBD **2c** (Fig. 2D, entry 2). By contrast, racemic product was generated with low diastereoselectivity regardless of the identity of the counteranion if the HBD catalyst was omitted (Fig. 2D, entries 3 and 5).

A variety of *trans*-anethole analogs was evaluated under the developed reaction conditions (Fig. 3A). Substrates bearing ortho substitution

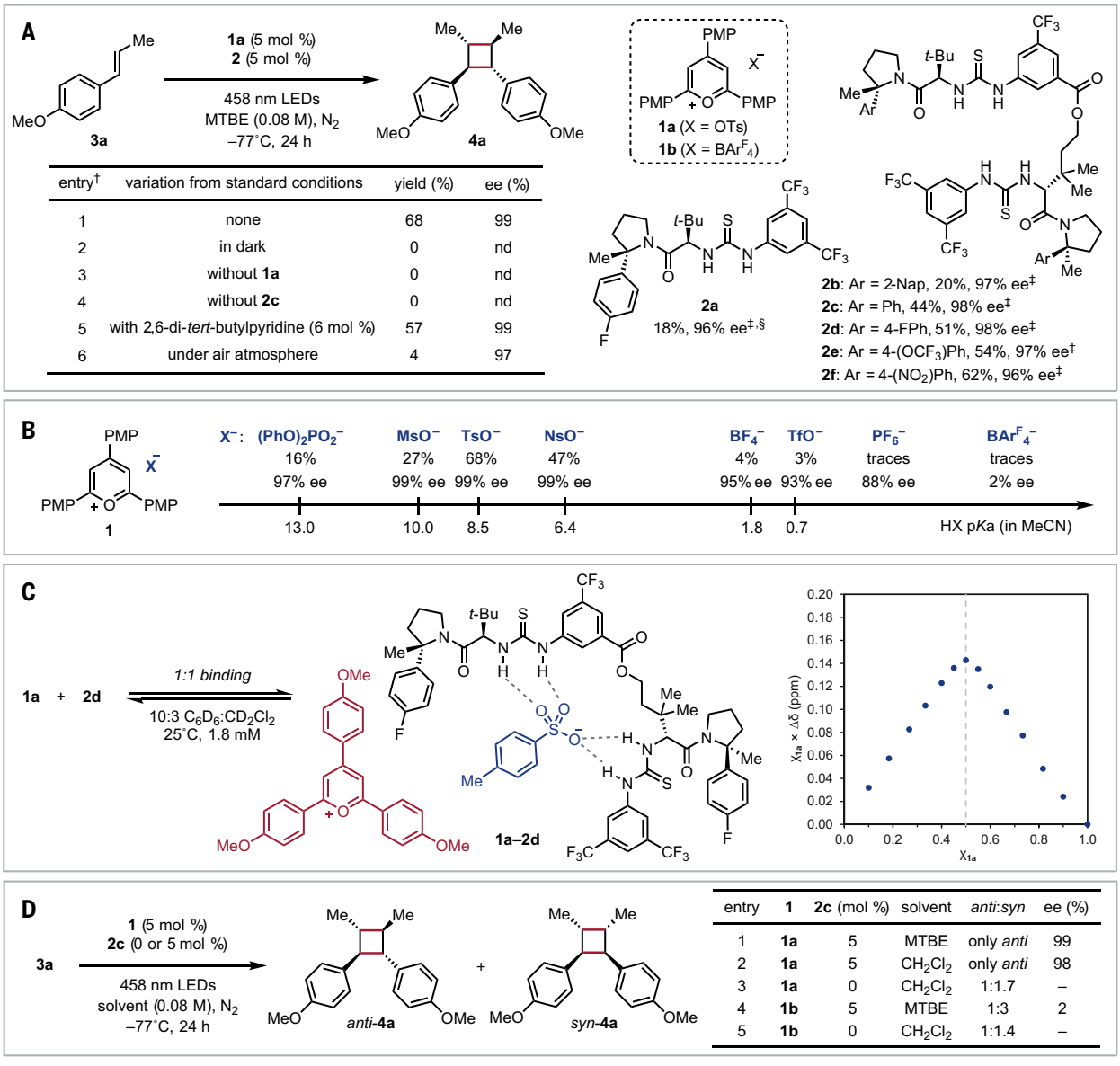

entry†	variation from standard conditions	yield (%)	ee (%)
1	none	68	99
2	in dark	0	nd
3	without **1a**	0	nd
4	without **2c**	0	nd
5	with 2,6-di-*tert*-butylpyridine (6 mol %)	57	99
6	under air atmosphere	4	97

entry	1	2c (mol %)	solvent	*anti*:*syn*	ee (%)
1	**1a**	5	MTBE	only *anti*	99
2	**1a**	5	CH_2Cl_2	only *anti*	98
3	**1a**	0	CH_2Cl_2	1:1.7	–
4	**1b**	5	MTBE	1:3	2
5	**1b**	0	CH_2Cl_2	1:1.4	–

Fig. 2. Catalyst optimization in the (2+2) cycloaddition reaction. (**A**) Effects of HBD structure and of reaction conditions. Reactions were carried out on a 0.05-mmol scale. Yields were determined by proton nuclear magnetic resonance (^{1}H NMR) analysis of crude reaction mixtures relative to an internal standard. †5 mol % of **2c** was used. ‡The reaction was run at –55°C for 20 hours. §10 mol % of **2a** was used. LED, light-emitting diode; PMP, *para*-methoxyphenyl; nd, not determined. (**B**) Evaluation of pyrylium salts containing different anions. Results correspond to reactions conducted as described in Fig. 2A with bis-thiourea **2c** and the specified pyrylium salts. (**C**) Job plot analysis of binding between **1a** and **2d**. The ^{1}H NMR signal corresponding to the methyl group of the tosylate anion was monitored. (**D**) Effects of reaction conditions on diastereoselectivity.

on the aryl ring proved less reactive than the parent substrate, but useful levels of substrate conversion could be achieved replacing HBD **2c** with the more reactive analog **2d**. The corresponding cyclobutane products **4a** to **4e** were obtained with excellent levels of enantioselectivity. *N*-(*trans*-1-Propenyl)carbazole underwent the homodimerization to afford **4f** enantioselectively, although for that substrate the use of $MgSO_4$ additive was needed to suppress the formation of side products likely originating from hydrolysis of carbazole iminium intermediates. High cross-alkene chemoselectivity could be achieved in heterodimerization reactions of *N*-(*trans*-1-propenyl)carbazole and anethole derivatives (**4g** to **4i**). Even the cross-dimerization of **3a** and 4-methylstyrene was promoted with moderately high chemo- and enantioselectivity under the optimized reaction conditions (**4j**) (*39*, *54*). In a simple demonstration of the synthetic applicability of the prepared products, cyclobutane **4a** was converted to the enantiomer of natural product and potent glucocorticoid-receptor binder (+)-endiandrin A in 65% yield and 99% ee according to a modified literature three-step sequence (Fig. 3B) (*40*, *55*).

Extension of the developed reaction conditions to the (2+4) cycloaddition reaction of anethole and cyclopentadiene resulted in formation of adduct **5a** in nearly quantitative yield and diastereoselectivity and in 69% ee (Fig. 3C) (*15*).

Development of enantioselective (2+3) and (2+1) cycloaddition reactions

We chose to explore the generality of the asymmetric anion-binding strategy in the context of (2+3) cycloaddition reactions using vinyldiazoacetate reagents as the three-carbon nucleophilic partners to produce cyclopentene adducts (*38*, *56*). Enantioselective methods for (2+3) cycloadditions of vinyldiazoacetates based on asymmetric rhodium or

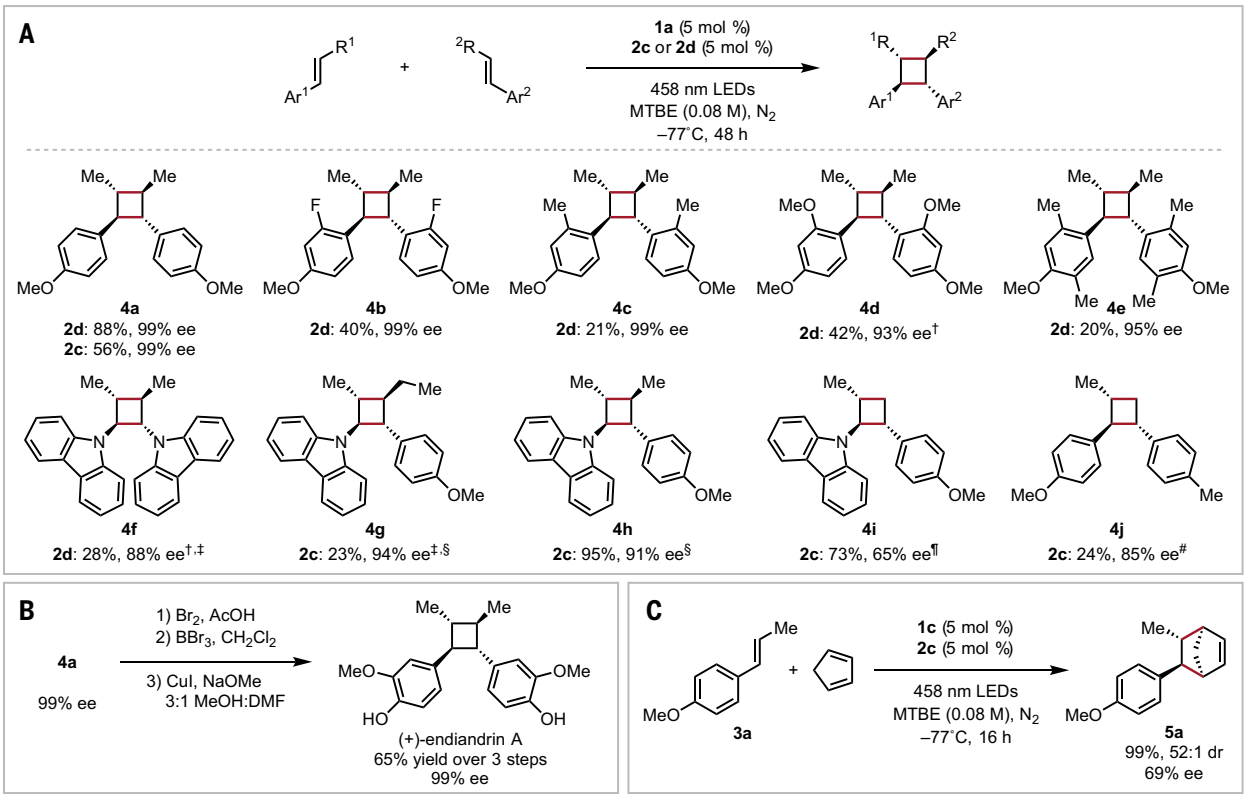

Fig. 3. Substrate scope of the (2+2) and (2+4) cycloaddition reactions. (**A**) Substrate scope of the enantioselective (2+2) cycloaddition reaction. Reactions were carried out on a 0.15-mmol scale. Reported yields represent yields of isolated pure products. The absolute configuration of **4j** was assigned by comparison of its optical rotation value with reported values (*23*). Absolute configuration of all other products was assigned by analogy. See SM for additional examples. †The reaction was carried out at −55°C. ‡The reaction was run with 2 wt equiv $MgSO_4$. §Alkene substrates were used in a 1:1 ratio. ¶The reaction was run with 3 equiv of 4-methoxystyrene. #The reaction was run with 5 equiv of 4-methylstyrene. (**B**) Enantiospecific elaboration of **4a** to (+)-endiandrin A. (**C**) Evaluation of a (2+4) cycloaddition under the developed conditions. The reaction was carried out on a 0.15-mmol scale, using 1.2 equiv of cyclopentadiene. See SM for additional examples.

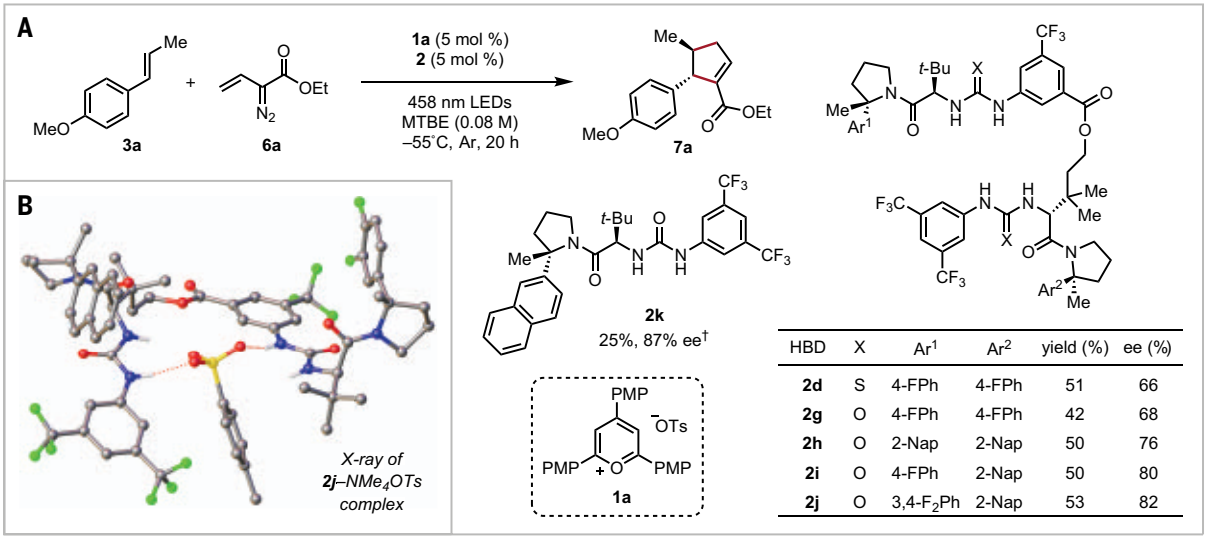

HBD	X	Ar^1	Ar^2	yield (%)	ee (%)
2d	S	4-FPh	4-FPh	51	66
2g	O	4-FPh	4-FPh	42	68
2h	O	2-Nap	2-Nap	50	76
2i	O	4-FPh	2-Nap	50	80
2j	O	3,4-F_2Ph	2-Nap	53	82

Fig. 4. Photocatalytic HBD-cocatalyzed (2+3) cycloaddition reaction. (**A**) Reactions were carried out using **3a** (0.05 mmol) and **6a** (2.0 equiv). Reported yields were determined by ^{1}H NMR analysis of crude reaction mixtures relative to an internal standard. †10 mol % of **2k** was used. (**B**) Shows x-ray crystal structure of a 1:1 complex of **2j** and NMe_4OTs. Selected hydrogen atoms and the ammonium cation were omitted for clarity.

gold catalysis are known, but owing to the electrophilic nature of the corresponding metal carbenoid intermediates, these methods usually necessitate the use of highly nucleophilic two-carbon coupling partners such as indoles or vinyl ethers (*57*–*59*).

We found that the combination of pyrylium tosylate **1a** and bis-thiourea **2d** catalyzed the (2+3) cycloaddition between **3a** and ethyl 2-diazo-3-butenoate (**6a**) to form cyclopentene **7a** in moderate yield and enantioselectivity (Fig. 4A). We noted that **2d** underwent decomposition under the conditions of the photochemical (2+3) cycloaddition reaction but that the urea analog of HBD **2g** was stable and could be recovered after the reaction. Optimization of the aryl components on the pyrrolidine rings of the bis-urea led to the identification of HBD **2j**, which afforded **7a** in 53% yield and the highest levels of enantioselectivity (82% ee). Through x-ray crystallographic analysis of a 1:1 complex of **2j** and tetramethylammonium tosylate, it was revealed that both urea groups associate with the tosylate anion in a manner similar to that proposed previously for bis-thiourea HBD analogs in a solution state (Fig. 4B) (*46*, *60*, *61*).

The monomeric 2-naphthyl urea **2k** was found to be more enantioselective than the bis-urea catalysts but promoted the (2+3) cycloaddition reaction with lower efficiency, potentially because of its lower anion-binding strength and off-cycle self-aggregation (Fig. 4A) (*60*). The enantioselectivity induced by **2k** could be improved further to 91% ee by decreasing the concentration of **6a**, lowering the reaction temperature to –77°C, and using pyrylium mesylate **1c** instead of **1a** [see supplementary materials (SM) for details]. Portion-wise addition of **6a**, addition of extra amounts of the catalysts (5 mol % of **2k** and **1c**), and performing the reaction for an extended time under air atmosphere allowed the isolation of **7a** in 55% yield and 90% ee (Fig. 5A). As was the case in the (2+2) cycloadditions, the pyrylium salt, the HBD, and light were essential components in the enantioselective reaction (see table S8 for details). In contrast to the (2+2) cycloaddition reactions cocatalyzed by bis-thioureas, the (2+3) cycloaddition reaction promoted by the monomeric urea catalyst was found to be less selective in combination with pyrylium salts containing weakly coordinating counteranions (see fig. S6 for details).

The substrate scope of the developed (2+3) cycloaddition reaction was evaluated (Fig. 5A). Vinyldiazoacetate reagents containing different ester groups were well tolerated by the method (**7a** to **7c**). *Trans*-anethole derivatives bearing larger groups at the β-position underwent the (2+3) cycloaddition reaction with high enantioselectivity (**7d** and **7e**), but adduct **7f**, containing a branched substituent, was generated in substantially lower yield and selectivity. The cyclic *cis*-alkene 6-methoxy-1,2-dihydronaphthalene proved to be reactive under the optimal conditions but led to the formation of **7g** in only moderate enantioselectivity.

We extended the conditions developed for the cycloaddition between alkenes and vinyldiazoacetate reagents to (2+1) cycloaddition reactions with diazoester reagents to provide enantioenriched cyclopropane adducts (*37*). In this system, 2-naphthyl bis-urea **2h** was identified as the more effective HBD cocatalyst than the monomeric analog (see fig. S9 for details). Under the optimal conditions, cyclopropane adducts bearing various ester groups were isolated in good yields and excellent enantioselectivities (**8a** to **8d**) (Fig. 5B). In all cases, the 1,2-*anti*-diastereomers were generated in higher enantioselectivity than the corresponding 1,2-*syn*-isomers. Consistent with the substrate effects observed in the (2+3) cycloadditions, larger groups at the β-position of *trans*-anethole or *ortho*-substituents had detrimental effects on the reactivity and selectivity of the (2+1) cycloaddition reaction (**8e** and **8f**). By contrast, 6-methoxy-1,2-dihydronaphthalene proved to be an excellent substrate for the catalytic cyclopropanation reaction, with **8g** generated in good yield and high diastereo- and enantioselectivity.

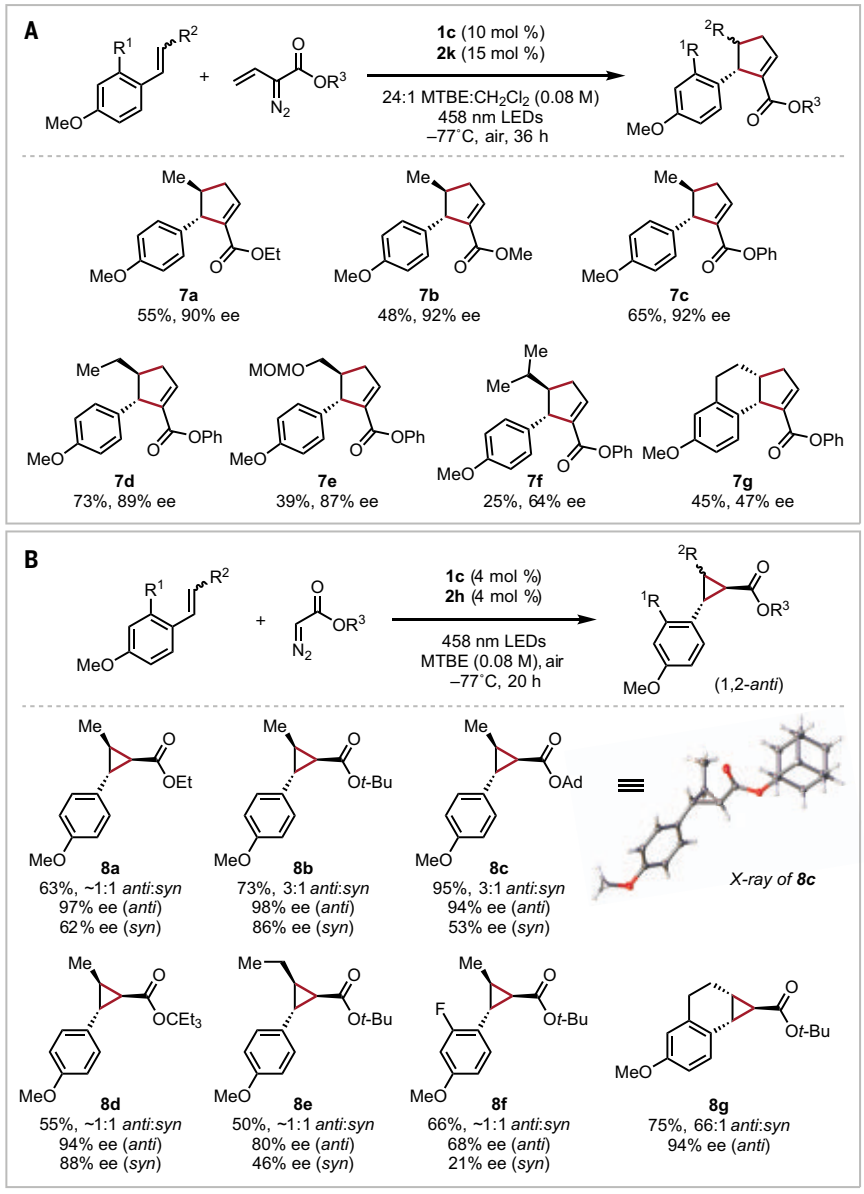

Fig. 5. Enantioselective (2+3) and (2+1) cycloaddition reactions. (**A**) Substrate scope of the (2+3) cycloaddition reaction. Reactions were carried out on a 0.15-mmol scale. Reported yields represent yields of isolated pure products. The absolute configuration of products was assigned tentatively by analogy to the known absolute configuration of **8c**. See SM for additional examples. (**B**) Substrate scope of the (2+1) cycloaddition reaction. Reactions were carried out on a 0.15-mmol scale. Reported yields represent combined yields of isolated pure product diastereomers. The absolute configuration of **8c** was determined by an x-ray crystallographic analysis. Absolute configuration of all other products was assigned by analogy. See SM for additional examples.

Outlook

Association of neutral small-molecule chiral HBD catalysts with counterions of radical ion pairs has now been demonstrated to be an effective strategy to induce enantioselectivity in photoredox hole catalysis. This approach relies on the intrinsic ionic property of the intermediates and avoids the need for specific engineering of substrates to achieve catalyst precoordination. We anticipate that the use of chiral HBDs to modulate the reactivity and selectivity of open-shell cation radical intermediates through anion binding together with other noncovalent interactions may find broad application in asymmetric photoredox catalysis and will be relevant to other catalytic approaches that include open-shell, high-energy intermediates.

REFERENCES AND NOTES

1. J. M. R. Narayanam, C. R. J. Stephenson, *Chem. Soc. Rev.* **40**, 102–113 (2011).
2. C. K. Prier, D. A. Rankic, D. W. C. MacMillan, *Chem. Rev.* **113**, 5322–5363 (2013).
3. N. A. Romero, D. A. Nicewicz, *Chem. Rev.* **116**, 10075–10166 (2016).
4. M. H. Shaw, J. Twilton, D. W. C. MacMillan, *J. Org. Chem.* **81**, 6898–6926 (2016).
5. K. L. Skubi, T. R. Blum, T. P. Yoon, *Chem. Rev.* **116**, 10035–10074 (2016).
6. N. L. Holy, J. D. Marcum, *Angew. Chem. Int. Ed.* **10**, 115–124 (1971).
7. M. Schmittel, A. Burghart, *Angew. Chem. Int. Ed.* **36**, 2550–2589 (1997).
8. N. R. Akkawi, D. A. Nicewicz, *J. Am. Chem. Soc.* **147**, 15482–15489 (2025).
9. E. Meggers, *Chem. Commun.* **51**, 3290–3301 (2015).
10. M. J. Genzink, J. B. Kidd, W. B. Swords, T. P. Yoon, *Chem. Rev.* **122**, 1654–1716 (2022).
11. W. Yao, E. A. B. Bergamino, M.-Y. Ngai, *ChemCatChem* **14**, e202101292 (2022).
12. F. F. Özgen, M. E. Runda, S. Schmidt, *ChemBioChem* **22**, 790–806 (2021).
13. R. Ham, C. J. Nielsen, S. Pullen, J. N. H. Reek, *Chem. Rev.* **123**, 5225–5261 (2023).
14. Z. Yang, H. Li, S. Li, M.-T. Zhang, S. Luo, *Org. Chem. Front.* **4**, 1037–1041 (2017).
15. P. D. Morse, T. M. Nguyen, C. L. Cruz, D. A. Nicewicz, *Tetrahedron* **74**, 3266–3272 (2018).
16. H. Wang *et al.*, *Chem. Commun.* **53**, 9644–9647 (2017).
17. J. Y. Wang, E. Villalona, R. R. Knowles, *J. Am. Chem. Soc.* **147**, 15307–15317 (2025).
18. C. Wen *et al.*, *J. Am. Chem. Soc.* **147**, 14625–14634 (2025).
19. D. Uraguchi, Y. Kimura, F. Ueoka, T. Ooi, *J. Am. Chem. Soc.* **142**, 19462–19467 (2020).
20. E. C. Gentry, L. J. Rono, M. E. Hale, R. Matsuura, R. R. Knowles, *J. Am. Chem. Soc.* **140**, 3394–3402 (2018).
21. Z. Xu *et al.*, *Angew. Chem. Int. Ed.* **64**, e202413601 (2025).
22. S. Ohmura *et al.*, *J. Am. Chem. Soc.* **145**, 15054–15060 (2023).
23. S. Das *et al.*, *Science* **379**, 494–499 (2023).
24. C. Zhu, S. Das, A. Guin, C. K. De, B. List, *Nat. Catal.* **8**, 487–494 (2025).
25. E. P. Farney *et al.*, *J. Am. Chem. Soc.* **141**, 6385–6391 (2019).
26. M. C. Pérez-Aguilar *et al.*, *Chemistry* **30**, e202400541 (2024).
27. N. Shida, Y. Imada, S. Nagahara, Y. Okada, K. Chiba, *Commun. Chem.* **2**, 24 (2019).
28. T. E. Schirmer, B. König, *J. Am. Chem. Soc.* **144**, 19207–19218 (2022).
29. O. García Mancheño, *Anion-Binding Catalysis* (John Wiley & Sons, 2022).
30. A. G. Doyle, E. N. Jacobsen, *Chem. Rev.* **107**, 5713–5743 (2007).
31. D. A. Strassfeld, E. N. Jacobsen, in *Supramolecular Catalysis*, P. W. N. M. van Leeuwen, M. Raynal, Eds. (John Wiley & Sons, Ltd, 2022), pp. 361–385.
32. M. H. Samha *et al.*, *ACS Catal.* **12**, 14836–14845 (2022).
33. C. Estarellas, A. Frontera, D. Quiñonero, P. M. Deyà, *Phys. Chem. Chem. Phys.* **13**, 16698–16705 (2011).
34. G. Bergonzini, C. S. Schindler, C.-J. Wallentin, E. N. Jacobsen, C. R. J. Stephenson, *Chem. Sci.* **5**, 112–116 (2014).
35. H. G. Roth, N. A. Romero, D. A. Nicewicz, *Synlett* **27**, 714–723 (2016).
36. M.-J. Luo, Q. Xiao, J.-H. Li, *Chem. Soc. Rev.* **51**, 7206–7237 (2022).
37. F. J. Sarabia, E. M. Ferreira, *Org. Lett.* **19**, 2865–2868 (2017).
38. F. J. Sarabia, Q. Li, E. M. Ferreira, *Angew. Chem. Int. Ed.* **57**, 11015–11019 (2018).
39. M. A. Ischay, M. S. Ament, T. P. Yoon, *Chem. Sci.* **3**, 2807–2811 (2012).
40. M. Riener, D. A. Nicewicz, *Chem. Sci.* **4**, 2625–2629 (2013).
41. S. Lin, M. A. Ischay, C. G. Fry, T. P. Yoon, *J. Am. Chem. Soc.* **133**, 19350–19353 (2011).
42. K. A. Margrey, D. A. Nicewicz, *Acc. Chem. Res.* **49**, 1997–2006 (2016).
43. H. Ohara, T. Itoh, M. Nakamura, E. Nakamura, *Chem. Lett.* **30**, 624–625 (2001).
44. J. Zuo *et al.*, *Molecules* **27**, 6102–6112 (2022).
45. S. M. Banik, A. Levina, A. M. Hyde, E. N. Jacobsen, *Science* **358**, 761–764 (2017).
46. J. M. Ovian, P. Vojáčková, E. N. Jacobsen, *Nature* **616**, 84–89 (2023).
47. R. R. Knowles, S. Lin, E. N. Jacobsen, *J. Am. Chem. Soc.* **132**, 5030–5032 (2010).
48. S. Lin, E. N. Jacobsen, *Nat. Chem.* **4**, 817–824 (2012).
49. E. Ronchi, S. M. Paradine, E. N. Jacobsen, *J. Am. Chem. Soc.* **143**, 7272–7278 (2021).
50. P. G. Gassman, D. A. Singleton, *J. Am. Chem. Soc.* **106**, 7993–7994 (1984).
51. S. Alvarez, *Chemistry* **26**, 4350–4377 (2020).
52. J. J. Koh *et al.*, *J. Mol. Struct.* **1171**, 458–465 (2018).
53. J. S. Renny, L. L. Tomasevich, E. H. Tallmadge, D. B. Collum, *Angew. Chem. Int. Ed.* **52**, 11998–12013 (2013).
54. N. P. Schepp, L. J. Johnston, *J. Am. Chem. Soc.* **118**, 2872–2881 (1996).
55. R. A. Davis *et al.*, *J. Nat. Prod.* **70**, 1118–1121 (2007).
56. Y. H. Cho, J. H. Kim, H. An, K.-H. Ahn, E. J. Kang, *Adv. Synth. Catal.* **362**, 2183–2188 (2020).
57. Y. Lian, H. M. L. Davies, *J. Am. Chem. Soc.* **132**, 440–441 (2010).
58. H. M. L. Davies, B. Xiang, N. Kong, D. G. Stafford, *J. Am. Chem. Soc.* **123**, 7461–7462 (2001).
59. J. F. Briones, H. M. L. Davies, *J. Am. Chem. Soc.* **135**, 13314–13317 (2013).
60. C. R. Kennedy *et al.*, *J. Am. Chem. Soc.* **138**, 13525–13528 (2016).
61. Q. Li, S. M. Levi, C. C. Wagen, A. E. Wendlandt, E. N. Jacobsen, *Nature* **608**, 74–79 (2022).

ACKNOWLEDGMENTS

We thank M. Baxter for experimental assistance and S.-L. Zheng for x-ray data collection and structure determination. We acknowledge the support to the x-ray core facility from the Major Research Instrumentation (MRI) Program of the NSF under award no. 2216066. **Funding:** This work was supported by NIH grant GM149244 (E.N.J.) and the Alfred Bader Fellowship in Chemistry (Harvard University) (P.V.). **Author contributions:** Conceptualization: P.V., E.N.J.; Funding acquisition: E.N.J.; Investigation: P.V.; Methodology: P.V.; Supervision: E.N.J.; Writing – original draft: P.V.; Writing – review & editing: P.V., E.N.J. **Competing interests:** The authors declare that they have no competing interests. **Data and materials availability:** Crystallographic data for compounds **2j**–NMe_4OTs and **8c** are available free of charge from the Cambridge Crystallographic Data Centre under references CCDC 2454561 and CCDC 2454562, respectively. All other data, as well as details for synthesizing the reported compounds, are available in the main text or the supplementary materials. **License information:** Copyright © 2025 the authors, some rights reserved; exclusive licensee American Association for the Advancement of Science. No claim to original US government works. https://www.science.org/about/science-licenses-journal-article-reuse

SUPPLEMENTARY MATERIALS

science.org/doi/10.1126/science.adz3362
Materials and Methods; Supplementary Text; Figs. S1 to S18; Tables S1 to S28; References (*62*–*98*)

Submitted 28 May 2025; accepted 30 September 2025

10.1126/science.adz3362

SOLAR CELLS

A cross-linked molecular contact for stable operation of perovskite/silicon tandem solar cells

Boxue Zhang[1,2]†, Junsheng Luo[1]†*, Haomiao Yin[1], Qing Li[3], Siqi Sun[4], Ningxuan Zhang[1], Nan Gan[2], Muhammad Azam[1], Tae Wan Park[5], Zhongquan Wan[1], Chunyang Jia[1]*, Mingyang Wei[4]*, So Min Park[2]*

Monolithic perovskite/silicon tandem solar cells surpass the power-conversion efficiency limits of single-junction solar cells but face challenges in operational stability. We identified fill factor diminution as a key performance-loss mode in the state-of-the-art tandem architecture. We reveal that widely used hole-selective molecular contacts, which enhance tandem cell performance, undergo thermal degradation that undermines charge transport. At elevated temperatures, the resistance of conventional monomeric contacts increases by about sixfold because of thermal-induced disorder. To stabilize interfacial structures, we introduce in situ synthesized cross-linked molecular contacts based on Schiff base linkages. One-square-centimeter perovskite/silicon tandem solar cells achieved power-conversion efficiencies exceeding 34% (33.61% certified), and three independent devices retained 96.2 ± 1.7% of their initial performance after about 1200-hour maximum power point operation under AM1.5G illumination at 65°C.

Monolithic tandem solar cells comprising a crystalline silicon (c-Si) bottom cell and a wide-bandgap (WBG; ~1.68 eV) perovskite top cell overcome the Shockley-Queisser limit of single-junction solar cells at a competitive cost (*1*–*5*). Certified power-conversion efficiencies (PCEs) of perovskite/Si tandems have reached 34.6%, but their limited operational stability presents an ongoing challenge (*6*–*9*). For example, the highest PCE devices reported (PCEs >33%) exhibit performance degradation under maximum-power-point (MPP) operation at room temperature (table S1) (*1*, *3*).

Intrinsic ion migration and light-induced phase segregation in WBG perovskites have been considered key factors limiting tandem cell stability (*10*–*12*). However, several single-junction WBG perovskite solar cells (PSCs) have demonstrated promising operational stability at elevated temperatures, in contrast to state-of-the-art tandem devices (*13*–*16*). These improvements primarily stem from enhanced bulk and interfacial properties in perovskite films achieved through compositional engineering, additive incorporation, and interface engineering (*17*, *18*).

We sought to understand how hole-selective contacts contribute to the stability limitations of perovskite/Si tandem solar cells. In recent years, self-assembled monolayers (SAMs) have driven breakthrough performance by accelerating hole extraction relative to conventional hole transport layers that limit fill factors (FFs) (*19*–*22*). Their ultrathin nature minimizes transport losses while providing uniform coverage and chemical passivation to reduce interfacial nonradiative recombination (*23*–*25*). Record-setting perovskite/Si tandems have used phosphonic acid–based SAMs to enhance hole selectivity (*4*). However, recent studies indicate that these SAMs suffer from stability issues because of chemical decomposition, desorption, and weak interfacial adhesion (*26*–*28*). The impact of SAM degradation on tandem cell stability will require further investigation.

In this study, we traced the current density–voltage (*J-V*) characteristics of state-of-the-art perovskite/Si tandems under accelerated aging conditions to elucidate their degradation mechanisms. Statistical analysis revealed that performance loss was largely associated with FF deterioration, indicating dominant transport degradation. We then measured charge transport through the hole-selective SAMs and observed a spatially uniform decline in conductivity upon heat exposure that correlated with contact failure. To reinforce labile monomeric SAMs, we exploited Schiff base chemistry to demonstrate in situ polymeric contacts from cross-linkable building blocks. This approach minimized the thermal degradation of hole-selective contacts, improved electrical properties, and suppressed nonradiative recombination, ultimately enabling stable operation of perovskite/Si tandem solar cells at an elevated temperature of 65°C.

Operational stability of perovskite/Si tandems

State-of-the-art perovskite/Si tandem solar cells use Si heterojunction solar cells as the bottom subcell built on double-sided, textured, n-type Czochralski wafers (*29*, *30*). To evaluate their operational stability, we replicated a high-efficiency inverted device structure previously described (*31*–*33*). A schematic of the tandem cell stack is shown in Fig. 1A. For compatibility with solution processing, we adopted chemically etched wafers featuring submicrometer random pyramid texturing on the front side (fig. S1). Cross-sectional scanning electron microscopy (SEM) measurements confirmed complete coverage of the WBG perovskite top cell (Fig. 1B). To ensure homogeneous SAM coverage, we used a 5-nm-thick indium zinc oxide (IZO) recombination layer as the anchoring oxide for 4-(9H-carbazol-9-yl)butyl phosphonic acid (4PACz)–based SAMs (*34*). Detailed processing procedures for the tandem cells are described in the supplementary materials and methods.

We studied the intrinsic operational stability of tandem cells using the International Summit on Organic Photovoltaic Stability (ISOS)-L-2 protocols (*35*). Accelerated aging tests of encapsulated devices were conducted under continuous light soaking, with concurrent MPP tracking and a heat sink maintained at 65°C. Performance degradation of three individual cells was characterized by periodic, in situ *J-V* measurements over the course of 1200 hours. The *J-V* curves retained exponential diode characteristics in both forward and reverse scans, albeit with enhanced hysteresis (Fig. 1C and fig. S2).

From the forward *J-V* scans, we recorded an average cumulative PCE decline of 5.1 ± 0.3% (absolute), corresponding to a relative efficiency loss of 19.5 ± 1.1% (table S2). Fig. 1D and fig. S3 show plotted normalized photovoltaic parameter changes from forward and reverse *J-V* sweeps, respectively. Data from the three replicate devices are presented as the average ± SD, revealing consistent loss modes. We also show raw photovoltaic parameter changes for individual devices in figs. S4 to S6. Here, the PCE reduction was predominantly driven by a decline in FF (relative loss of 13.7 ± 0.2%), whereas a moderate decrease in open-circuit voltage (V_{OC}; 4.7 ± 1.2%) and a minimal change in short-circuit current (J_{SC}) were also observed (2.2 ± 0.3%). Operational stability tests on single-junction WBG PSCs confirmed these findings (fig. S7). After ~790 hours of MPP operation at 65°C, an average PCE reduction of 15.7 ± 0.5% (relative) was recorded under reverse-scan conditions, dominated by a relative FF loss of 14.2 ± 0.3%. We hypothesized that contact failures constituted a major degradation pathway because bulk changes in the perovskite absorber (e.g., phase segregation and decomposition) typically led to severe J_{SC} losses (*36*, *37*).

[1]National Key Laboratory of Electronic Films and Integrated Devices, School of Integrated Circuit Science and Engineering, University of Electronic Science and Technology of China, Chengdu, P. R. China. [2]Department of Chemistry, National University of Singapore, Singapore, Singapore. [3]College of Chemistry and Materials Science, Sichuan Normal University, Chengdu, P. R. China. [4]Department of Materials Science and Engineering, National University of Singapore, Singapore, Singapore. [5]Querrey Simpson Institute for Bioelectronics, Northwestern University, Evanston, IL, USA. ***Corresponding author. Email: luojs@uestc.edu.cn (J.L.); cyjia@uestc.edu.cn (C.J.); weimingy@nus.edu.sg (M.W.); sompark@nus.edu.sg (S.M.P.)**; †These authors contributed equally to this work.

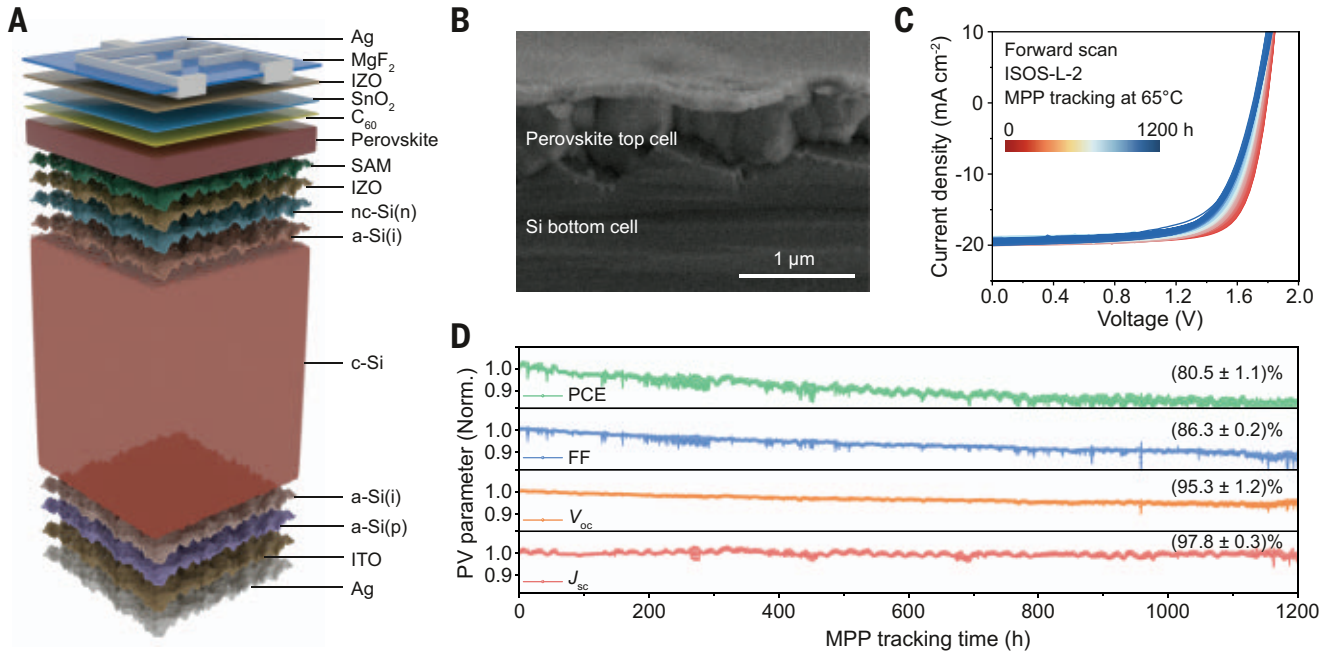

Fig. 1. Characterization of state-of-the-art perovskite/Si tandem solar cells. (**A**) Schematic illustration of the monolithic perovskite/Si tandem architecture with 4PACz SAMs (layer thicknesses are not to scale). (**B**) Cross-sectional SEM image of a completed tandem device showing the perovskite top cell conformally covering the textured Si bottom cell. (**C**) Forward-scan *J-V* curves (AM1.5G, 100 mW cm^{-2}) after successive periods of MPP tracking at 65°C following the ISOS-L-2 protocol. Color scale denotes the aging time from 0 to 1200 hours. (**D**) Temporal evolution of the normalized photovoltaic (PV) parameters PCE, FF, V_{OC}, and J_{SC} over 1200 hours of MPP tracking. Markers represent the normalized mean values among the three devices, and the connecting traces indicate the SD range.

Thermal degradation of hole-selective contacts

Hole-selective SAMs mitigate the FF bottleneck in inverted PSCs and corresponding tandems by reducing the transient time for hole extraction (*38*, *39*). Given the stability concerns with conventional phosphonic acid SAMs (*40*, *41*), we revisited their application in perovskite/Si tandem solar cells. Absolute-intensity photoluminescence (PL) measurements under 1-sun-equivalent excitation conditions confirmed effective interfacial passivation by 4PACz SAMs. We obtained a photoluminescence quantum yield (PLQY) of 0.59% for the as-prepared WBG perovskite/4PACz half-device stack on indium tin oxide (ITO) substrates, corresponding to an implied V_{OC} (iV_{OC}); that is, the quasi-Fermi level splitting (QFLS) normalized by the elementary charge of 1.226 V, a 58-mV enhancement over WBG perovskites deposited directly on ITO (table S3).

To distinguish between bulk and interfacial degradation, we thermally aged a half-device stack at 100°C for 500 hours while simultaneously aging bare 4PACz/ITO substrates (Fig. 2A) onto which WBG perovskite films were subsequently deposited. The degraded half-device stack showed a substantial iV_{OC} drop to 1.112 V, whereas the freshly prepared perovskite film retained a higher iV_{OC} of 1.181 V on aged 4PACz (Fig. 2B). We considered the observed iV_{OC} reduction (45 mV) in the latter scenario to be an upper limit because the subsequent perovskite deposition process may redissolve unbound phosphonic acids generated during thermal annealing (*26*, *42*). Indeed, x-ray photoelectron spectroscopy (XPS) showed that a dimethylformamide (DMF) rinse reduced the P:In atomic ratio by 81% for 4PACz SAMs aged at 65°C for 200 hours (fig. S8 and table S4). We reasoned that SAM degradation was not the primary mechanism underlying V_{OC} losses during tandem cell operation.

To investigate the impact of SAM degradation on charge transport, we used conductive atomic force microscopy (C-AFM) to measure the electrical resistance of 4PACz monolayers before and after thermal aging. Fig. 2C shows representative current-voltage (*I-V*) characteristics between ±0.2 V at an applied load of 1 nN to minimize damage to the monolayer surface (*43*). The *I-V* traces exhibited a linear response within the sweep range. From their slopes, we estimated a resistance of 1.4×10^9 Ω for the aged monolayer, a 5.6-fold increase relative to the fresh reference (2.5×10^8 Ω). These fall within the commonly reported range for conjugated molecular junctions (table S5). To directly probe interfacial charge-transfer kinetics, we performed time-resolved photoluminescence measurements on perovskite/4PACz half-device stacks at an excitation fluence of 27 nJ cm^{-2}. We extracted the differential lifetime (τ_{PL}) from the PL transients and found that hole injection into the underlying ITO was hindered after thermal aging (see supplementary text 1 in the supplementary materials) (*44*). These results were consistent with transport losses that dominate performance degradation in tandem cells.

Current maps acquired at an applied bias of +400 mV confirmed insulative degradation in the aged SAM (Fig. 2D). We measured the spatially averaged current as 1.6 ± 0.4 and 0.10 ± 0.02 nA for the fresh and aged samples, respectively (Fig. 2E). Kelvin probe force microscopy (KPFM) was further used to assess SAM uniformity. Contact potential difference (CPD) maps revealed spatial variations in the work function (WF) of the aged SAM (Fig. 2F), showing clusters of higher CPD (i.e., lower WF) even though the mean CPD value remained comparable to that of the fresh SAM (280 versus 277 mV). Thermal disordering was also evidenced by a broadened full-width at half-maximum (FWHM) of the CPD distribution (20 to 45 mV) (Fig. 2G). Given that the WF of SAM/ITO substrates scales with surface dipole density (*45*, *46*), these changes indicated that heat exposure induced restructuring of the SAM; x-ray diffraction (XRD) of densely packed 4PACz films revealed disrupted crystallinity after thermal aging (fig. S10). Combining XPS, C-AFM, KPFM, and XRD, we ascribed the reduced monolayer conductivity to partial molecular desorption and aggregation, which led to a disordered conjugated network. Supramolecular disorder weakens intermolecular coupling to enlarge the effective barrier height of the molecular junctions (see supplementary text 2 in the supplementary materials; fig. S11) (*47*–*49*). By contrast, cross-sectional SEM showed no morphological degradation (e.g., void or impurity formation) in the perovskite layer after similar aging conditions (fig. S12).

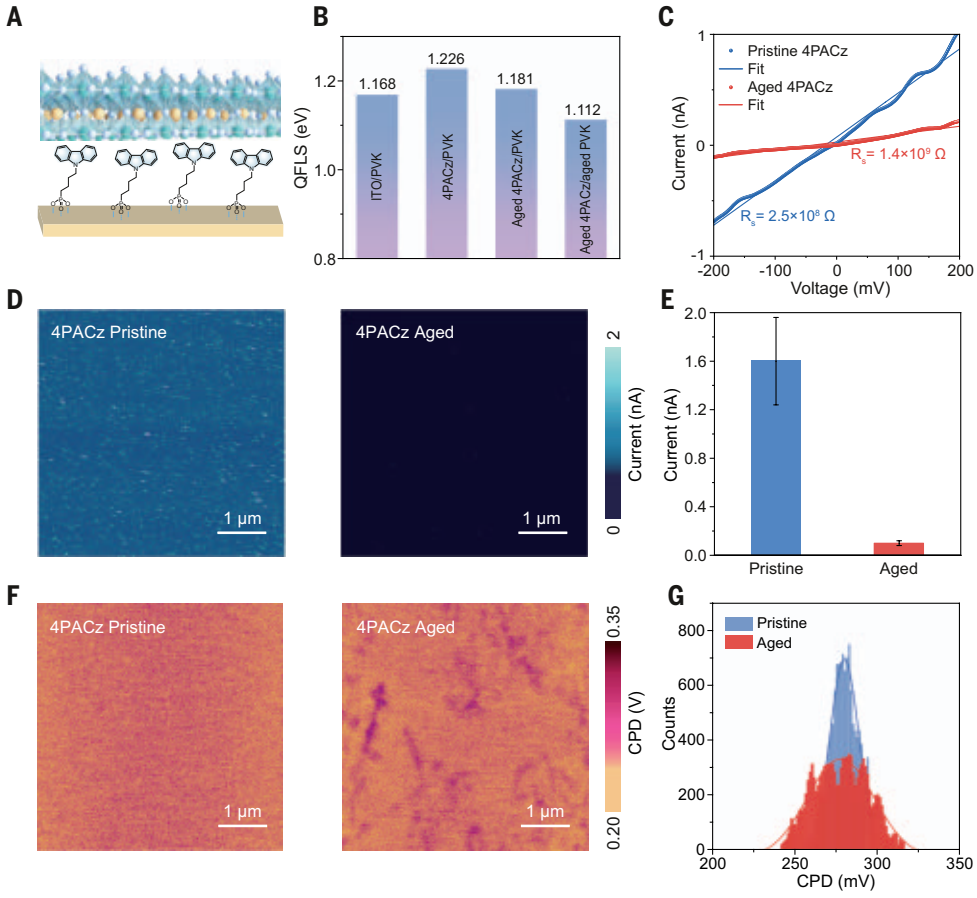

Fig. 2. Thermal aging degrades charge transport in monomeric 4PACz SAMs. (**A**) Schematic of the ITO/4PACz/perovskite (PVK) interface. 4PACz molecules chemisorb onto the ITO surface, forming a hole-selective contact beneath the perovskite absorber. (**B**) QFLS of perovskite films deposited on bare ITO, pristine 4PACz-modified ITO, the same substrate after 500 hours of thermal aging at 100°C, and a separately aged 4PACz/ITO substrate. (**C**) Point-contact *I-V* characteristics acquired by C-AFM on pristine and thermally aged 4PACz SAMs. Linear fit was used to determine monolayer resistance. (**D** and **E**) Corresponding C-AFM current maps (D) and spatially averaged current (E) of pristine and aged 4PACz SAMs. Error bars represent SD. (**F** and **G**) KPFM surface potential maps (F) and corresponding CPD histograms (G) of pristine and aged 4PACz SAMs. The distributions were fit using Gaussian functions.

Cross-linked molecular contacts for improved stability

Our investigations suggested that enhancing the rigidity of SAMs, and thereby reducing thermal-induced disorder, could address FF diminution in perovskite/Si tandems. We sought to cross-link monomeric hole-selective SAMs; however, activating their conjugated end groups typically requires catalysts (e.g., strong acids) (*50*, *51*). To enable the spontaneous binding of cross-linking agents, we introduced [4-(3,6-diamino-9H-carbazol-9-yl)butyl]phosphonic acid (4PACz-DM), which bears two amino groups that serve as reactive sites in the monolayer (see supplementary text 3 in the supplementary materials; figs. S13 to S23). The new molecule exhibited a dipole moment of 1.84 debye from electrostatic potential calculations (Fig. 3A), which is comparable to the 1.90 debye for 4PACz (fig. S24), thus indicating similar electrical properties.

Subsequently, a Schiff base condensation was performed between its primary amines and an aldehyde-functionalized bipyridine, 2,2′-bipyridine-4,4′-dicarboxaldehyde (BPDA) (Fig. 3B). We inferred high reactivity for this cross-linking route; simply mixing the two components in solution at 80°C or room temperature rapidly induced turbidity (figs. S25 and S26). Fourier transform infrared spectroscopy (FTIR) analysis verified Schiff base formation (Fig. 3C). In the mixed 4PACz-DM:BPDA spectrum, a new absorption band appeared at 1653 cm^{-1}, attributable to the C=N stretching vibration (i.e., imine bonds), whereas the C=O stretching band at 1703 cm^{-1} was reduced because of the consumption of aldehyde groups. The formation of a cross-linked network on IZO-coated, textured c-Si substrates was confirmed by XPS; after a DMF rinse, the P:In atomic ratio remained at 91% of its initial value, whereas the control monomeric SAM lost 41% of its molecular concentration (table S4). Alternatively, we constructed in situ polymeric contacts by exploiting N-hydroxysuccinimide chemistry to install amide linkages (fig. S27). We reasoned that the amino-terminated, highly nucleophilic 4PACz-DM would react with a plethora of electrophiles under mild, catalyst-free conditions, enabling tailored on-surface transformations beyond a recent cross-linking approach (see supplementary text 4 in the supplementary materials) (*26*).

The resultant cross-linked SAMs (CL-SAMs) incorporate multiple nitrogen donor sites at the film termini that could interact with undercoordinated Pb^{2+} ions. XPS confirmed this binding affinity by a 0.17-eV downward shift in the Pb $4f_{5/2}$ and $4f_{7/2}$ peaks upon treating perovskite surfaces with a mixed 4PACz-DM:BPDA solution (Fig. 3D). We then deposited WBG perovskite films on CL-SAM/ITO substrates. Absolute-intensity PL measurements revealed a high iV_{OC} of 1.299 V (Fig. 3E), corresponding to a relative improvement of 6% compared with the control half-device stack. We attributed the improved optoelectronic properties to synergistic bulk and interfacial effects. Dynamic contact angle measurements showed that the incorporation of bipyridine units enhanced substrate wettability (fig. S28), whereas pyridine moieties interacted with Pb^{2+} precursors to delay the growth kinetics of perovskite films (figs. S29 and S30). These effects led to uniform and compact perovskite films with an average domain size of 500 nm (fig. S31). Ultraviolet photoelectron spectroscopy measurements further revealed a larger vacuum-level shift at the perovskite/CL-SAM interface compared with the 4PACz reference (fig. S32), which in PSCs provides a stronger driving force for hole extraction.

We evaluated the thermal stability of the CL-SAMs and their corresponding half-device stacks. Annealing the CL-SAMs at 100°C for 500 hours resulted in no iV_{OC} drop for subsequently processed WBG perovskite films relative to the fresh reference, and the aged half-device stack exhibited a competitive iV_{OC} of 1.273 V (table S3), which is indicative of minimized recombination degradation. AFM current images of fresh CL-SAMs acquired under the same bias and load conditions as control SAMs revealed a 3.4-fold increase in mean current (5.5 versus 1.6 nA) (Fig. 3F and fig. S33). More encouragingly, aged CL-SAMs showed no conductivity degradation, maintaining a resistance of 9.2×10^7 Ω (fig. S34), which is comparable to that of fresh CL-SAMs (8.5×10^7 Ω), in stark contrast to the semi-insulating nature of aged control SAMs. As a result, aged perovskite/CL-SAM half-device stacks exhibited minor changes in τ_{PL} dynamics (fig. S9). We ascribed the higher stability to the presence of Schiff base linkages that largely suppress contact restructuring (*52*, *53*), as evidenced by only a slight increase in the FWHM of the CPD

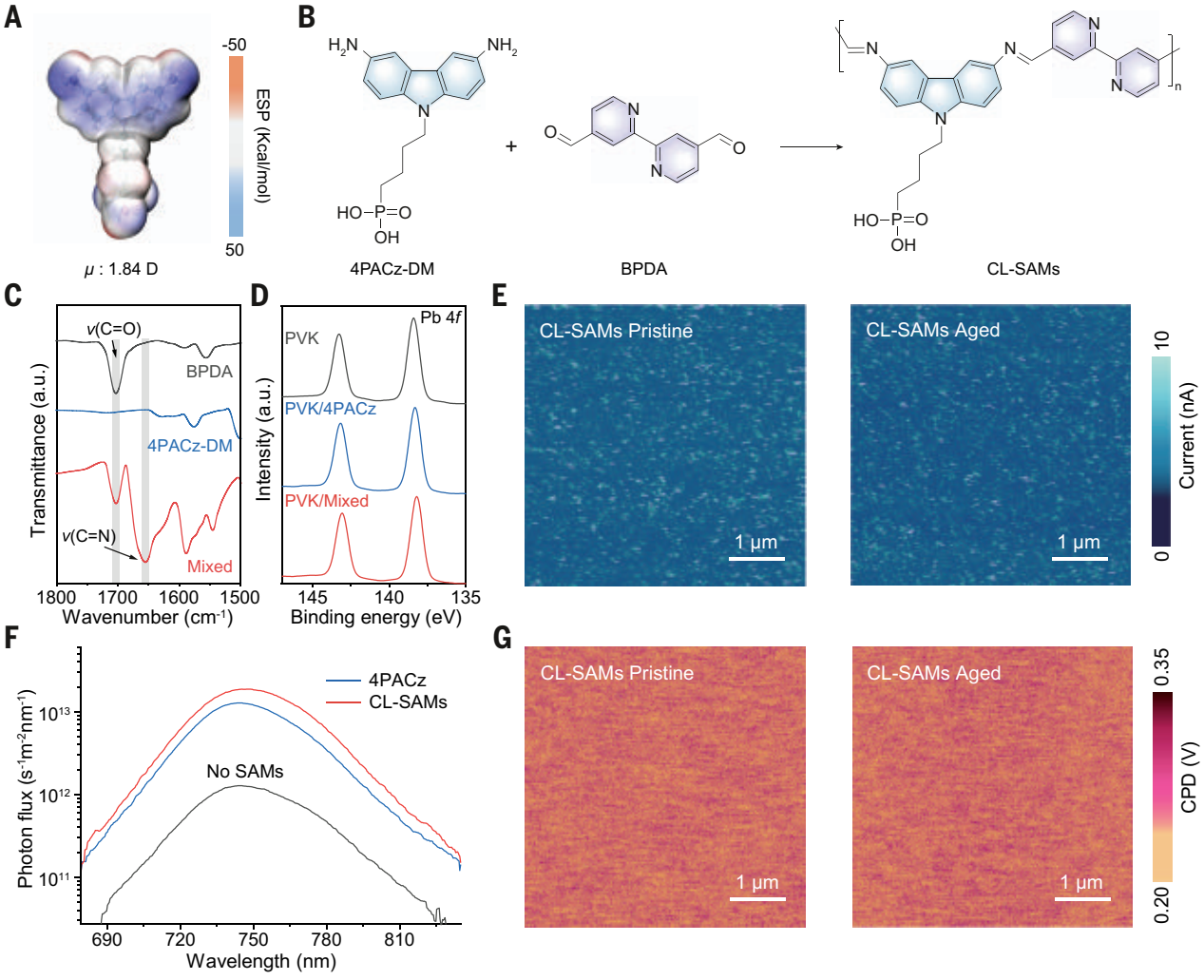

Fig. 3. Design and thermal robustness of polymeric CL-SAMs. (**A**) ESP map and calculated molecular dipole moment of the 4PACz-DM building block. (**B**) In situ cross-linking scheme: the aldehyde-containing linker BPDA (purple) condenses with amine-terminated 4PACz-DM to form an imine-bridged, cross-lined monolayer on ITO. (**C**) FTIR spectra of BPDA, 4PACz-DM, and their reaction mixture ("mixed"). BPDA shows the characteristic ν(C=O) band. After condensation, a new imine ν(C=N) band appears at 1653 cm^{-1}, confirming the formation of Schiff base linkages. (**D**) XPS Pb 4*f* spectra of the reference perovskite film and of films treated with 4PACz or with the 4PACz-DM/BPDA reaction mixture ("mixed"). (**E**) Absolute intensity PL spectra of perovskite films on bare ITO (no SAMs) and 4PACz and CL-SAMs. (**F** and **G**) C-AFM current maps (+400 mV bias) (F) and KPFM maps (G) of CL-SAMs before and after 500 hours of aging at 100°C showing negligible loss of nanoscale conductivity and structure changes.

distribution (11 to 12 mV) (Fig. 3G and fig. S35), minimal thermal-induced changes in the diffraction features for densely packed films (fig. S10), and the resistance of phosphonic acids to redissolution after thermal annealing (fig. S8 and table S4). Molecular dynamics simulations at a temperature of 373 K indicated the rapid reconstructions of monomeric phosphonic acid assemblies and confirmed that covalently connected networks suppressed enthalpy-driven agglomeration through enhanced rigidity (see supplementary text 5 in the supplementary materials; fig. S36).

Tandem solar cell performance and stability

To improve operational stability, we fabricated monolithic perovskite/Si tandem solar cells (aperture area of 1.05 cm^2) using CL-SAMs as the hole-selective contact (Fig. 4A and fig. S37). A batch of 20 devices had an average PCE of 33.7 ± 0.4% (fig. S38), demonstrating reproducible device performance. Fig. 4B shows the reverse- and forward-scan *J-V* curves of the best-performing tandem solar cell, exhibiting minor hysteresis. The device achieved a PCE of 34.1% from the reverse scan, with a V_{OC} of 1.98 V, a J_{SC} of 21.0 mA cm^{-2}, and an FF of 81.9%. These results were consistent with the steady-state power output measurement (PCE of 33.9%) recorded at a constant bias voltage of 1.70 V over 400 s (fig. S39). Furthermore, CL-SAMs established low-loss, hole-selective contacts with 1.53-, 1.68-, and 1.83-eV perovskite absorbers in single-junction PSCs, achieving PCEs of 26.7, 23.9, and 19.8%, respectively (fig. S40).

Integrated J_{SC} values of 20.8 and 20.9 mA cm^{-2}, derived from the external quantum efficiency (EQE) spectra (Fig. 4C) for the top and bottom subcells, respectively, matched well with the J_{SC} determined from the *J-V* sweep. For independent characterization, we sent a tandem solar cell to the National Photovoltaic Product Quality Inspection and Testing Center in China. The device delivered a certified PCE of 33.61% during 1200 s of MPP operation (fig. S41). We also anticipated further improvements in the PCE of perovskite/Si tandem solar cells; suns-V_{OC} measurements indicated a hypothetical, transport-limit *J-V* curve with a pseudo-FF of 85.2% and a pseudo-PCE of 35.4% (Fig. 4B), which were achievable after minimizing series resistance (*54*).

We subjected three independently fabricated tandem devices to operational stability tests using the same protocol as for the control 4PACz-based devices. In situ *J-V* measurements were performed every 15 min, and the cells were otherwise maintained at their maximum power point

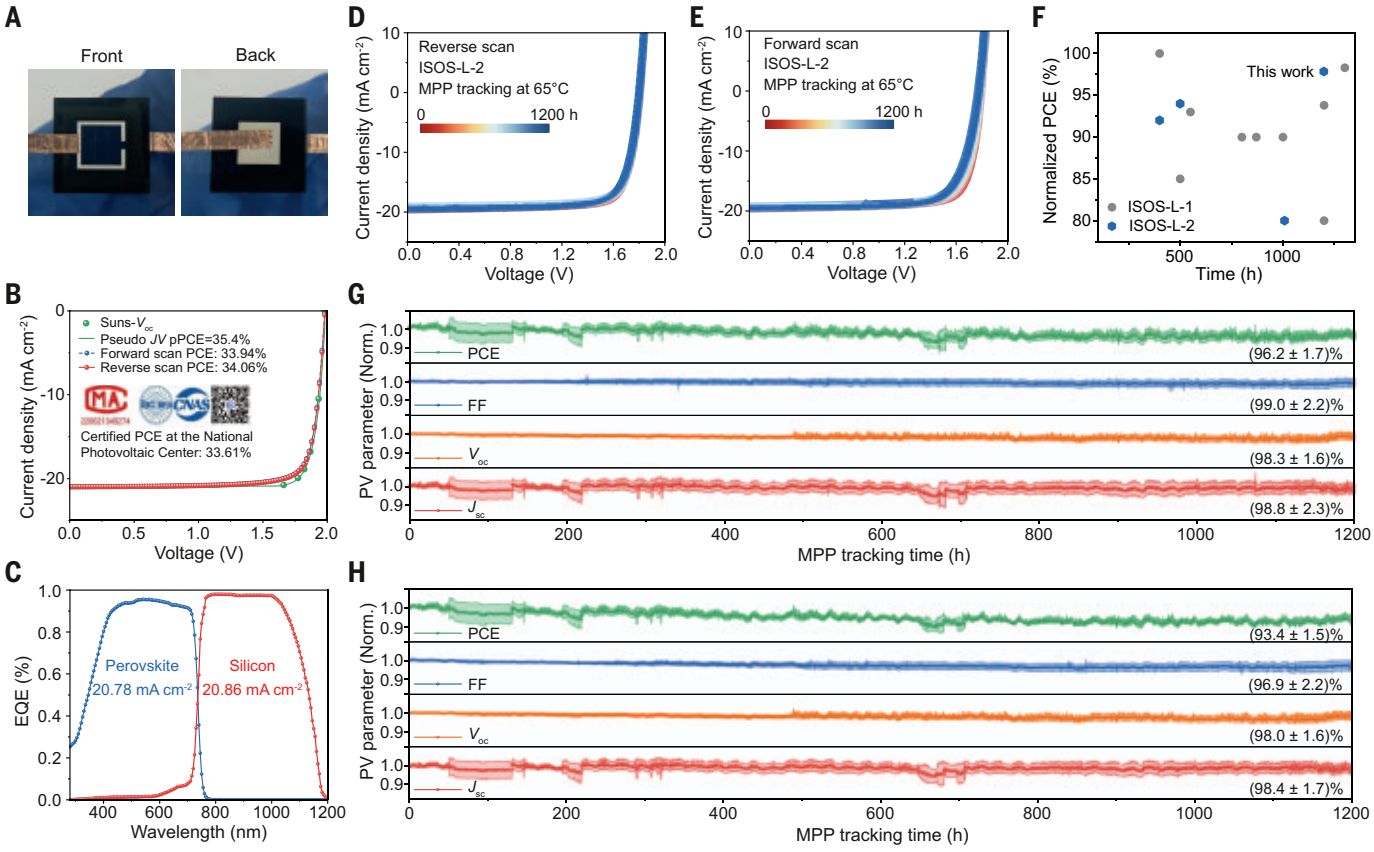

Fig. 4. Photovoltaic performance of perovskite/Si tandem solar cells with CL-SAMs. (**A**) Photographs of the encapsulated 1.05-cm^2 device showing the illuminated front surface and metal back contact. (**B**) *J-V* characteristics measured under AM1.5G illumination (100 mW cm^{-2}) at 25°C, along with the pseudo-*J-V* curves derived from suns-V_{OC} measurements. A certified PCE of 33.61% was obtained at the National Photovoltaic Center in China (inset stamp). (**C**) EQE spectra of the perovskite and silicon subcells. Their similar integrated current densities confirm nearly perfect current matching. (**D** and **E**) Reverse (D) and forward (E) *J-V* curves (AM1.5G, 100 mW cm^{-2}) after successive periods of MPP tracking at 65°C following the ISOS-L-2 protocol. Color scale denotes the aging time from 0 to 1200 hours. (**F**) Normalized PCE retention for perovskite/Si tandems tested under ISOS-L-1 (gray) and ISOS-L-2 (blue) conditions, comparing reported device properties with the most durable device presented in this work. (**G** and **H**) Temporal evolution of the normalized PV parameters PCE, FF, V_{OC}, and J_{SC} over 1200 hours of MPP tracking for three devices recorded with periodic reverse (G) and forward (H) scans under identical conditions. Markers represent the normalized mean values, and the connecting traces indicate the SD range.

under continuous AM1.5G illumination at 65°C. We noted lower initial PCEs (~27%) than those measured at room temperature on unencapsulated devices (table S7), which we ascribed to the intrinsic negative temperature coefficient (−0.3% per °C) and additional reflection losses at the front glass encapsulation (fig. S42). Here the temperature coefficient was set by the c-Si bottom cell, consistent with typical perovskite/Si tandems (fig. S43 and table S6); optical losses from the encapsulation stack were further supported by optical simulations (fig. S44). Representative *J-V* traces (Fig. 4, D and E) indicated a relative PCE reduction of ~2.1% at 1200 hours under reverse-scan conditions, accompanied by an increase in hysteresis (hysteresis index from 0.001 to 0.007). Forward-scan *J-V* measurements showed an average absolute PCE decrease of 1.8 ± 0.4%, corresponding to a relative efficiency loss of 6.6 ± 1.5% (table S7).

Statistical analyses of the photovoltaic parameters for the three devices are presented in Fig. 4, G and H, and the raw changes for individual cells are provided in figs. S45 to S47. We found that FF deterioration was no longer the dominant degradation pathway; instead, the observed PCE changes were ascribed to the superposition of multiple effects, including fluctuations in J_{SC} and modest declines in both V_{OC} and FF. After 1200-hour MPP operation, J_{SC}, V_{OC}, and FF retained 98.8 ± 2.3, 98.3 ± 1.6, and 99.0 ± 2.2% of their initial values, respectively, resulting in a relative PCE loss of 3.8 ± 1.7% determined from the reverse scan. Improved stability was further confirmed in single-junction PSCs (fig. S48), whereas 4PACz-DM–based devices still suffered from FF diminution (relative loss of 10.5 ± 1.2%) over 800 hours of MPP operation at 65°C (fig. S49). A comparison with previously reported operational stability of perovskite/Si tandem solar cells is provided in Fig. 4F and table S1.

Discussion

Perovskite/Si tandem solar cells using hole-selective SAMs achieve high performance, yet their operational stability at elevated temperatures requires further improvement. We investigated the status of long-term stability in these tandem architectures by correlating performance degradation with *J-V* characteristics. FF deterioration appeared to be the predominant mechanism, in contrast to the state of knowledge, which emphasizes bulk and interfacial degradation of WBG perovskites. We show here that monomeric SAMs, which improve hole selectivity, may evince thermal disordering that disrupts charge transport through the monolayer. We developed a cross-linking strategy using Schiff base linkages, stabilizing SAM structures while simultaneously improving interfacial passivation and perovskite film quality. We were able to achieve a certified PCE of 33.61% for perovskite/Si tandem solar cells with suppressed FF diminution and thereby moderate relative performance losses (3.8 ± 1.7%) among three individual cells after 1200 hours of MPP operation at 65°C.

REFERENCES AND NOTES

1. J. Liu *et al.*, *Nature* **635**, 596–603 (2024).
2. C. Kan *et al.*, *Nat. Photonics* **19**, 63–70 (2024).
3. E. Ugur *et al.*, *Science* **385**, 533–538 (2024).
4. E. Aydin *et al.*, *Nature* **623**, 732–738 (2023).
5. X. Y. Chin *et al.*, *Science* **381**, 59–63 (2023).
6. National Renewable Energy Laboratory, "Best research-cell efficiency chart" (NREL, 2025); https://www.nrel.gov/pv/cell-efficiency.
7. Y. Chen *et al.*, *Science* **385**, 554–560 (2024).
8. J. Liu *et al.*, *Science* **377**, 302–306 (2022).
9. E. Aydin *et al.*, *Nat. Energy* **5**, 851–859 (2020).
10. Z. Wang *et al.*, *Nature* **618**, 74–79 (2023).
11. S. Wu *et al.*, *Nat. Energy* **9**, 411–421 (2024).
12. Z. Zhang *et al.*, *Nat. Energy* **9**, 592–601 (2024).
13. Q. Jiang *et al.*, *Science* **378**, 1295–1300 (2022).
14. Q. Ye *et al.*, *Energy Environ. Sci.* **17**, 5866–5875 (2024).
15. Y. Luo *et al.*, *Adv. Energy Mater.* **14**, 2304429 (2024).
16. J. Wen *et al.*, *Nat. Commun.* **14**, 7118 (2023).
17. K. A. Bush *et al.*, *ACS Energy Lett.* **3**, 428–435 (2018).
18. S. Cho *et al.*, *Chem. Eng. J.* **446**, 137388 (2022).
19. Z. Dai *et al.*, *Science* **372**, 618–622 (2021).
20. M. Azam *et al.*, *Energy Environ. Sci.* **17**, 6974–7016 (2024).
21. S. Liu *et al.*, *Nature* **632**, 536–542 (2024).
22. K. Zhao *et al.*, *Nature* **632**, 301–306 (2024).
23. S. M. Park *et al.*, *Nature* **624**, 289–294 (2023).
24. X. Zheng *et al.*, *Nat. Energy* **8**, 462–472 (2023).
25. S. Zhang *et al.*, *Science* **380**, 404–409 (2023).
26. B. Dong *et al.*, *Nat. Energy* **10**, 342–353 (2025).
27. H. Anizelli, T. W. David, P. Tyagi, E. Laureto, J. Kettle, *Sol. Energy* **203**, 157–163 (2020).
28. E. Arkan *et al.*, *Mater. Chem. Phys.* **254**, 123435 (2020).
29. A. Harter *et al.*, *ACS Appl. Mater. Interfaces* **16**, 62817–62826 (2024).
30. Z. Liu *et al.*, *Joule* **8**, 2834–2850 (2024).
31. Q. Jiang *et al.*, *Nature* **611**, 278–283 (2022).
32. C. Li *et al.*, *Science* **379**, 690–694 (2023).
33. Y. Yang *et al.*, *Nat. Energy* **9**, 37–46 (2024).
34. C. Li *et al.*, *Adv. Funct. Mater.* **34**, 2407805 (2024).
35. M. V. Khenkin *et al.*, *Nat. Energy* **5**, 35–49 (2020).
36. S. Baumann *et al.*, *Energy Environ. Sci.* **17**, 7566–7599 (2024).
37. Y. Bai *et al.*, *Science* **378**, 747–754 (2022).
38. L. Li *et al.*, *Nat. Energy* **7**, 708–717 (2022).
39. C. Li *et al.*, *Angew. Chem. Int. Ed.* **64**, e202420585 (2025).
40. L. Liu *et al.*, *Adv. Energy Mater.* **15**, 2405675 (2025).
41. M. Wu *et al.*, *Adv. Funct. Mater.* **33**, 2304708 (2023).
42. A.-F. Castro-Méndez *et al.*, *J. Am. Chem. Soc.* **146**, 18459–18469 (2024).
43. T. Ishida *et al.*, *J. Phys. Chem. B* **106**, 5886–5892 (2002).
44. L. Krückemeier, B. Krogmeier, Z. Liu, U. Rau, T. Kirchartz, *Adv. Energy Mater.* **11**, 2003489 (2021).
45. N. Singh, A. Mohapatra, C.-W. Chu, Y.-T. Tao, *Org. Electron.* **98**, 106297 (2021).
46. G. Ligorio, N. Zorn Morales, E. J. W. List-Kratochvil, *Appl. Phys. Lett.* **116**, 241603 (2020).
47. J. Zhou *et al.*, *Nat. Chem.* **17**, 564–570 (2025).
48. S. Wang *et al.*, *ACS Appl. Mater. Interfaces* **12**, 53003–53011 (2020).
49. W. Azzam, *Colloids Surf. A Physicochem. Eng. Asp.* **698**, 134454 (2024).
50. R. Ruvalcaba *et al.*, *ACS Mater. Lett.* **7**, 1421–1430 (2025).
51. H. A. Hintz, C. S. Sevov, *Nat. Commun.* **13**, 1319 (2022).
52. J. Jang, G. D. Kong, H. J. Yoon, *Acc. Mater. Res.* **5**, 1251–1262 (2024).
53. J. Skolaut, J. Tepper, F. Galli, W. Wulfhekel, J. M. van Ruitenbeek, *Beilstein J. Nanotechnol.* **14**, 1169–1177 (2023).
54. N. Mundhaas *et al.*, *Sol. RRL* **3**, 1800378 (2019).

ACKNOWLEDGMENTS

We thank the Analysis and Testing Center, University of Electronic Science and Technology of China, for technical support. **Funding:** This work was supported by the National Natural Science Foundation of China (grants 62474033, 22175029, 62374029, and W2433038 to J.L., C.J., Z.W., and M.A.); the National Key Research and Development Program of China (grant 2023YFB4202501 to C.J.); the Young Elite Scientists Sponsorship Program by CAST (grant YESS20220550 to J.L.); the Sichuan Science and Technology Program (grant 2024NSFSC0250 to J.L.); the Fundamental Research Funds for the Central Universities of China (grant ZYGX2022J032 to J.L.); the Foundation of China Petroleum & Chemical Corporation (grants 30000000–23-ZC0607-0127 and 36850000-23-ZC0607-0045 to J.L.); the National University of Singapore Presidential Young Professorship (grants A-0010035-00-00 and A-0010035-01-00 to S.M.P.); the Ministry of Education, Singapore, under Academic Research Fund Tier 1 (grant A-8002904-00-00 to S.M.P.); and the National University of Singapore (Presidential Young Professorship grants A-0010046-00-00 and A-0010046-01-00 to M.W.). **Author contributions:** B.Z., J.L., C.J., and S.M.P. conceived the idea and designed the experiments. J.L., C.J., M.W., and S.M.P. supervised the project. B.Z. fabricated the devices and characterized device stability. H.Y. conducted C-AFM and KPFM characterizations. Q.L. performed the NMR, MS, and FTIR measurements. N.Z. performed the SEM measurements. Z.W. and M.A. conducted the XPS, PL, and contact angle measurements. B.Z., S.M.P., and M.W. wrote the manuscript. S.S., N.G., T.W.P., S.M.P., and C.J. edited the manuscript. All authors discussed the work. **Competing interests:** A Chinese patent application related to this article was submitted by the University of Electronic Science and Technology of China (2024112852595). **Data and materials availability:** All data are available in the main text or the supplementary materials. **License information:** Copyright © 2025 the authors, some rights reserved; exclusive licensee American Association for the Advancement of Science. No claim to original US government works. https://www.science.org/about/science-licenses-journal-article-reuse

SUPPLEMENTARY MATERIALS

science.org/doi/10.1126/science.ady6874
Materials and Methods; Supplementary Text; Figs. S1 to S49; Tables S1 to S7; References (*55*–*64*)

Submitted 2 May 2025; accepted 23 September 2025

10.1126/science.ady6874

PLANT SCIENCE

CRISPR-Cas–mediated heritable chromosome fusions in *Arabidopsis*

Michelle Rönspies[1], Solmaz Khosravi[2†], Ondřej Helia[3,4], Alessandro Valisi[1], Jiří Fajkus[3,4], Miloslava Fojtová[3,4], Andreas Houben[2], Holger Puchta[1*]

The genome of *Arabidopsis thaliana* consists of 10 chromosomes. By inducing CRISPR-Cas–mediated breaks at subcentromeric and subtelomeric sequences, we fused entire chromosome arms, obtaining two eight-chromosome lines. In one line, both arms of chromosome 3 were fused to chromosome 1. In another line, the arms were transferred to chromosomes 1 and 5. Both chromosome number–reduced lines were fertile. Phenotypic and transcriptional analyses revealed no differences compared with wild-type plants. After crossing with the wild type, the progeny showed reduced fertility. The meiotic recombination patterns of the transferred chromosome arms were substantially changed. Directed chromosome number changes in plants may enable new breeding strategies, redefining linkage groups and establishing genetic barriers. Moreover, our data indicate that plants are highly robust to engineered karyotype changes.

The emergence of the CRISPR–CRISPR-associated protein (CRISPR-Cas) system has allowed scientists to induce double-strand breaks (DSBs) at almost any predefined position in the genome (*1*). In plants, this technique can be used for crop improvement by manipulating agronomically important traits (*2*–*4*). However, in addition to gene modifications, larger structural changes can also be induced. Using the CRISPR-Cas–based chromosome engineering technique, large chromosomal rearrangements such as inversions can be induced in plants (*5*–*10*). Inversions are known to modulate the recombination landscape along a chromosome by suppressing crossovers (COs) in the rearranged area (*11*–*16*). We were able to show the potential of inducing inversions for changing recombination patterns by both restoring CO rates in a previously CO-dead region (*6*) and excluding a substantial part of the *Arabidopsis* genome from meiotic recombination by inverting almost an entire chromosome (*10*).

In addition to inversions, chromosome fusions are also implicated in speciation through reproductive isolation because of the production of inviable gametes (*17*). As a proof of concept, we aimed to artificially reduce chromosome numbers by inducing chromosome fusions. Thus far, chromosome number changes have been achieved in a targeted manner in only a few other nonplant organisms (*18*–*20*).

Our results demonstrate the resilience of the plant genome toward massive restructuring, and our approach provides a unique opportunity for gaining further insights into speciation, genome evolution, and potential biotechnological applications.

[1]Joseph Gottlieb Kölreuter Institute for Plant Sciences - Molecular Biology, Karlsruhe Institute of Technology, Karlsruhe, Germany. [2]Leibniz Institute of Plant Genetics and Crop Plant Research Gatersleben, Seeland, Germany. [3]Mendel Centre for Plant Genomics and Proteomics, Central European Institute of Technology (CEITEC), Masaryk University, Brno, Czech Republic. [4]National Centre for Biomolecular Research, Faculty of Science, Masaryk University, Brno, Czech Republic. ***Corresponding author. Email: holger.puchta@kit.edu**
†Present address: Julius Kühn-Institut (JKI), Quedlinburg, Germany.

Creation of the eight-chromosome lines

Our approach required the introduction of two consecutively induced chromosome (arm) fusions in the form of reciprocal translocations between both arms of chromosome 3 and the ends of one or two receiving chromosomes. To obtain these rare events, we used our protocol for inducing megabyte-sized chromosomal rearrangements in *Arabidopsis* (*21*). Either the wild-type (WT) Col-0 (for line F8) or the *ku70* mutant (for line T8) were used as the genetic background. The *ku70* mutant was chosen because we had observed increased rearrangement frequencies in this line compared with WT in previous experiments because of the absence of the classical nonhomologous end joining DSB repair pathway (*5*, *22*). To ensure the production of heritable events, we combined the *Staphylococcus aureus* ortholog of Cas9 and the *Lachnospiraceae bacterium* variants ttLbCas12a or ttLbCas12a-I (*23*, *24*), optimized for plant use, with an egg cell–specific promoter (*25*). Using this setup, two DSBs were induced at the borders of the core centromere of chromosome 3 and near the telomere repeats of the respective receiver chromosomes (table S1). To create line F8 (Fig. 1A), the short arm of chromosome 3 was first transferred onto the long arm of chromosome 1, creating a telocentric and elongated chromosome. In the second step, the remaining arm of the telocentric chromosome was transferred onto the short arm of chromosome 1, resulting in one very large fusion chromosome. Line T8 (Fig. 1B) was generated by first transferring the short arm of chromosome 3 onto the long arm of chromosome 5 and then transferring the remaining arm of chromosome 3 from the telocentric chromosome onto the long arm of chromosome 1 in the second step, generating two elongated fusion chromosomes in the process. As a by-product of these approaches, the generation of a minichromosome was expected, consisting of the functional centromere of chromosome 3 and two short (~10 kb) telomere ends of either chromosome 1 (line F8) or chromosomes 1 and 5 (line T8), respectively. However, because of its small size and lack of essential genetic information (table S2), we expected that the minichromosome might get lost in the progeny because of segregation problems.

We first screened for plants in which the short arm of chromosome 3 was either translocated onto the end of the long arm of chromosome 1 (line F8) or that of chromosome 5 (line T8). One plant of line T8 and two plants of line F8 were found to carry the translocation heterozygously (tables S3 and S4). The recombinant T8 plant and one of the two positively identified F8 plants were chosen for further experiments and establishment of homozygosity. Homozygous plants were then subjected to a second round of chromosome engineering to transfer the remaining long arm of chromosome 3 onto the short arm (line F8) or long arm (line T8) of chromosome 1. For line F8, five lines were found to carry independent arm transfers (tables S3 and S4). When screening line T8 for the second arm transfer, four lines with independent arm transfer events were identified (tables S3 and S4). In two of these lines, Mendelian segregation of the arm transfer junction was detected, yielding homozygous eight-chromosome lines in the T_2 generation. In line F8, but not line T8, a junction indicative of the presence of the minichromosome (in the heterozygous state) could be detected, and in only one of three minichromosome-positive lines was the minichromosome inherited. By screening three different seed batches of this line, the minichromosome junction could be detected in eight, 10, or 14 of 80 screened plants, respectively. This indicates that the minichromosome is rapidly lost during propagation because it apparently does not contain any essential genetic information (table S2). To establish lines F8 and T8, one minichromosome-negative line each was chosen for further experiments and homozygous mutants were propagated. All newly formed translocation junctions that were amplified by polymerase chain reaction and analyzed by Sanger sequencing exhibited InDels around the ligation sites (fig. S1). In line T8 (*ku70* genetic background), deletion repair patterns likely resulting from microhomology-mediated end joining repair could be observed. Furthermore, the translocation and fusion events generated in both

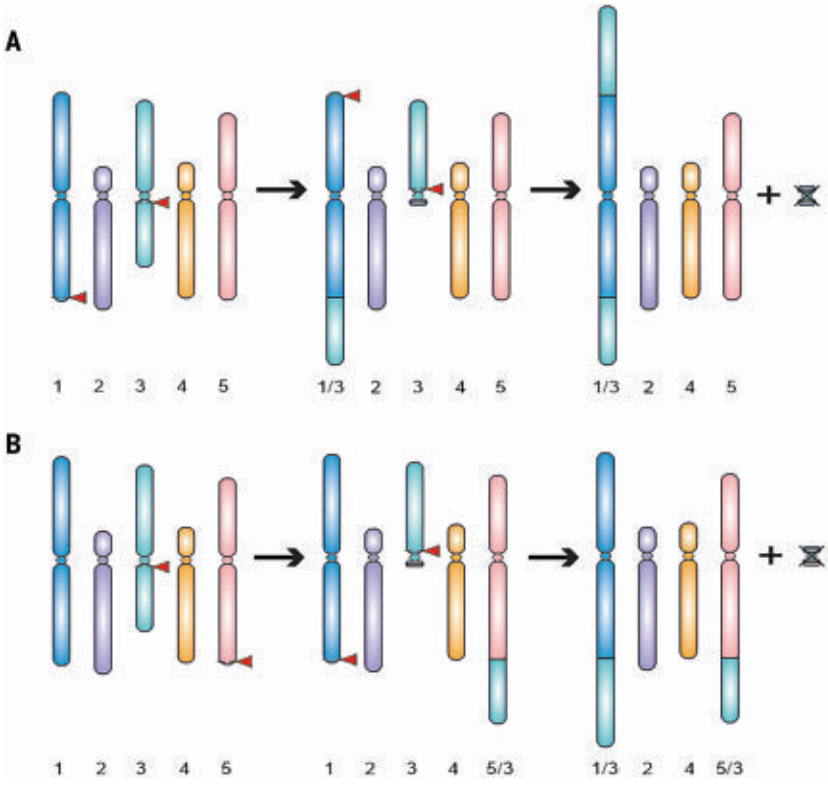

Fig. 1. Schematic overview of the generation of the two eight-chromosome lines F8 and T8. Schematic overview of the induced chromosome arm translocations of chromosome 3 in lines F8 and T8, leading to the creation of an eight-chromosome karyotype. As a by-product, the generation of a minichromosome was expected, consisting of the functional centromere of chromosome 3 and two short (~10 kb) telomere ends of chromosome 1 or chromosomes 1 and 5. However, because of its small size and lack of essential genetic information, we expected that the minichromosome might get lost in the progeny. Red triangles and dashed lines indicate the location of CRISPR-Cas–induced DSBs. (**A**) Schematic overview of the induced chromosome arm translocations of chromosome 3 in line F8. First, two DSBs were induced at the border of the core centromere of chromosome 3 and near the telomere sequences of chromosome 1. This resulted in the transfer of the short arm of chromosome 3 onto the long arm of chromosome 1, creating a telocentric and elongated chromosome through a reciprocal translocation in the process. Next, two DSBs were induced at the border of the core centromere of chromosome 3 on the remaining arm and near the remaining telomere sequences of chromosome 1. This resulted in the transfer of the remaining long arm of chromosome 3 onto the short arm of chromosome 1, creating a fusion chromosome of chromosomes 1 and 3. (**B**) Schematic overview of the induced chromosome arm translocations of chromosome 3 in line T8. First, two DSBs were induced at the border of the core centromere of chromosome 3 and near the telomere sequences of chromosome 5. This resulted in the transfer of the short arm of chromosome 3 onto the long arm of chromosome 5, creating a telocentric and elongated chromosome through a reciprocal translocation in the process. Next, two DSBs were induced at the border of the core centromere of chromosome 3 on the remaining arm and near the telomere sequences of chromosome 1. This resulted in the transfer of the remaining long arm of chromosome 3 onto the long arm of chromosome 1 in inverted orientation, creating another elongated chromosome in the process.

eight-chromosome lines were validated by fluorescence in situ hybridization (FISH) using chromosomal segment–specific probes (Fig. 2, A to D, and table S5). The loss of the centromeric minichromosomes formed from chromosome 3 and the reduction of the chromosome numbers to eight were confirmed in both lines by 4′,6-diamidino-2-phenylindole (DAPI) staining of mitotic chromosomes (Fig. 2E) and immunostaining of interphase nuclei with a centromere-specific CENH3 antibody (Fig. 2F). A maximum of eight CENH3 signals were detected in both engineered lines; by contrast, most nuclei showed up to 10 signals in WT Col-0 nuclei (Fig. 2F). To further confirm the genomic structure and to rule out the occurrence of major off-target rearrangements, both homozygous eight-chromosome lines were sequenced using the PacBio HiFi sequencing method. The expected junctions were verified, and no major off-target chromosomal rearrangements were detected (figs. S2 and S3 and data S1).

Gene expression and phenotype remain unaffected by the karyotype changes

Next, the effect of the chromosome fusions on gene expression was determined. Compared with WT Col-0, only 0.3% ($n = 88$) and 0.5% ($n = 151$) of total genes ($N =$ 27,000) in line F8 and line T8, respectively, displayed significant differential expression (fig. S4). In both lines, the differentially expressed genes (DEGs) were distributed over the entire genome and there was little overlap between them (fig. S4). Gene Ontology term analysis of the DEGs mostly showed their enrichment in metabolism pathways and no association with DNA repair mechanisms (fig. S5). The identified DEGs were not located near the chromosomal fusion sites, ruling out a chromosome position effect on gene expression.

In addition, the macroscopic effects of the chromosome number reductions were analyzed in lines T8 and F8. Phenotypes were monitored across multiple developmental stages, from late seedlings up to 22 days after sowing, with a total of seven scanning sessions (fig. S6A). The PlantScreen system measured 10 morphological parameters ranging from basic traits such as a raw area or perimeter to more complex traits such as compactness or slenderness of leaves (*26*). Phenotypic data from each scan were analyzed by principal components analysis (PCA) (fig. S7 and data S2). To enable an integrated comparison of developmental phenotypes, PCA was performed across all time points (Fig. 3A and data S2). The first two principal components (PC1 and PC2) explained 71.4 and 17.4% of the total variation, respectively. For a more comprehensive view of phenotypic variation, PCA results were visualized in three dimensions (3D) by including PC3, which accounted for 5.8% of the total variation (fig. S8 and data S2). Next, root morphology was assessed by measuring the primary root length of seedlings (fig. S6B and data S2), revealing no significant differences between the engineered and Col-0 lines. Seed phenotyping analysis further confirmed these results (fig. S9 and data S2). These data clearly demonstrate that the eight-chromosome plants retained a WT-like phenotype throughout all developmental phases.

Fertility of the eight-chromosome lines

We assessed the effect of the chromosome fusions on the fertility of homozygous and heterozygous mutant plants compared with WT Col-0 plants by counting the number of seeds per silique. In both lines, the total seed number did not differ significantly between homozygous mutant and WT plants, so haploid gametes of both eight-chromosome karyotypes seem to be fully fertile (Fig. 3, B and C, and data S2). In the case of line F8 (Fig. 3B), we detected a decrease in the seed number per silique by ~60% in heterozygous plants compared with WT plants and the homozygous mutant. In line T8, the seed number of heterozygous plants was reduced by ~75% compared with WT plants and the homozygous mutant (Fig. 3C). We speculated that meiotic pairing defects of the fusion chromosome with *Arabidopsis* WT chromosomes might lead to partial infertility. In line F8, both WT chromosomes 3 and 1 must pair simultaneously with the fused chromosome to enable proper

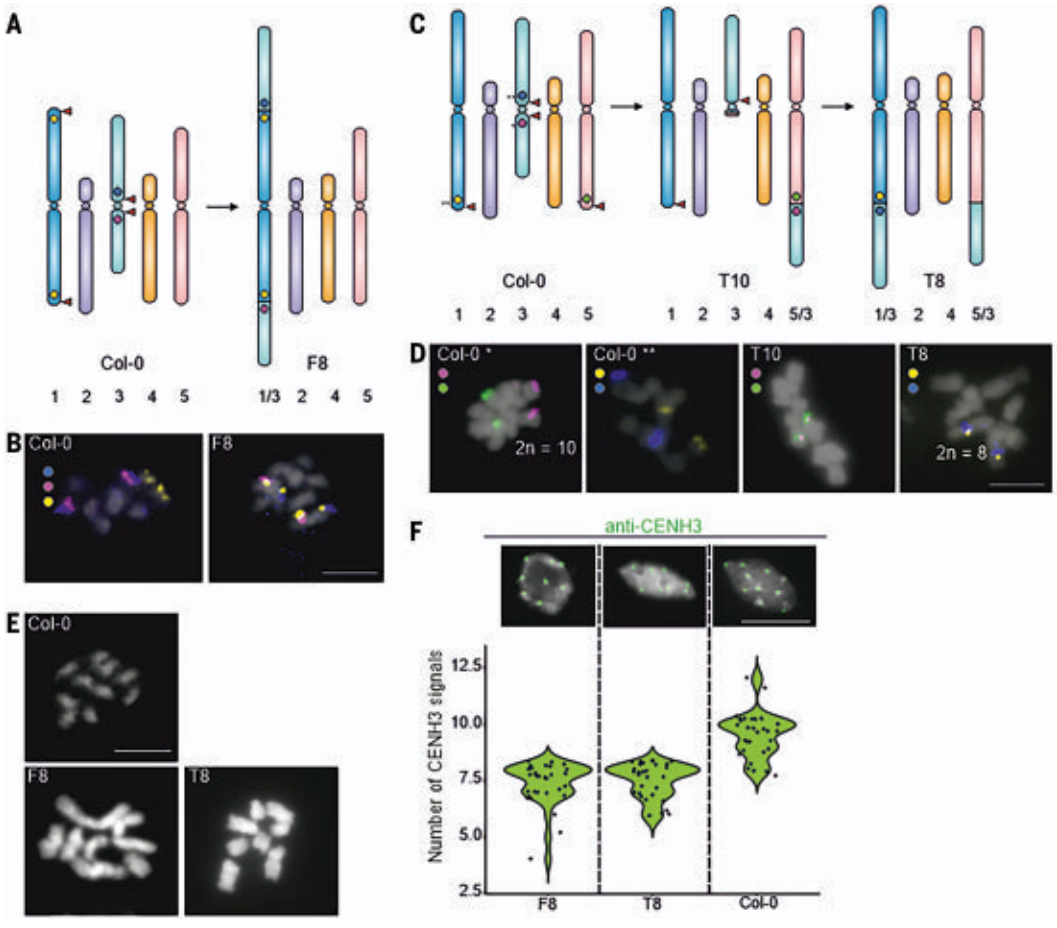

Fig. 2. Confirmation of the eight-chromosome lines by FISH, DAPI staining, and CENH3 immunostaining. (**A**) Schematic overview showing placement of the FISH probe combinations in WT Col-0 (left) and line F8 (right). Red triangles and dashed lines indicate the location of CRISPR-Cas–induced DSBs. The positions of FISH probes are indicated by colored circles. (**B**) FISH of mitotic Col-0 and F8 chromosomes with the probe combination of yellow, dark blue, and magenta (table S5). On Col-0 chromosomes, blue and magenta signals are located on chromosome 3 and the yellow signal is located on chromosome 1; in line F8, blue and magenta signals colocalize with yellow on the same fusion chromosome. Chromatin was counterstained with DAPI (gray). Scale bar, 10 μm. (**C**) Schematic overview showing placement of the FISH probe combinations in Col-0 (left), intermediate line T10 harboring the first chromosome arm translocation (middle), and line T8 (right). (**D**) FISH of mitotic Col-0, T10, and T8 mitotic chromosomes. In Col-0 (*), the probe combination magenta and green (table S5) is located on separate chromosomes 3 and 5, and in line T10, colocalization of the probes confirms the first translocation event between chromosomes 3 and 5. In Col-0 (**), the probe combination yellow and dark blue (table S5) is located on separate chromosomes 1 and the remaining arm of chromosome 3, and in line T8, colocalization of the probes confirms the second chromosome arm transfer. Chromatin was counterstained with DAPI (gray). Scale bar, 10 μm. (**E**) DAPI-stained mitotic chromosomes of lines F8, T8, and Col-0. Scale bar, 10 μm. (**F**) Anti-CENH3–labeled interphase nuclei of lines F8, T8, and Col-0. The rare occurrence of nuclei with CENH3 signals >10 is explained by the partial separation of sister chromatids (*46*). At least 30 nuclei were analyzed per line.

segregation and thus viable gametes. To visualize the meiotic behavior of line F8, DAPI staining was performed on meiotic metaphase I chromosome spreads prepared from the hybrid plants between line F8 and WT. As expected, we detected three bivalents and one trivalent. By contrast, WT plants formed five bivalents (Fig. 3, D to F).

Chromosome fusions change recombination patterns in hybrids

To elucidate how the chromosome fusions influence meiotic recombination in hybrids, both homozygous engineered eight-chromosome lines were crossed with the *Arabidopsis* ecotype Landsberg erecta (Ler-1) harboring the WT 10-chromosome set. Subsequently, F_1 seeds were harvested and propagated to obtain F_2 seeds. The recombination frequency was determined by analyzing 400 plants per line that were grown from the F_2 seeds. As a control, 400 plants of the progeny of crosses between WT Col-0 and Ler-1 (control for line F8) or *ku70* and Ler-1 (control for line T8), respectively, were analyzed. Using a TaqMan single-nucleotide polymorphism (SNP) genotyping assay, we selected SNP markers approximately every 2 Mb on the fused chromosomes to detect marker changes between Col-0 and Ler-1 alleles (tables S4 and S6). First, the presence or absence of a marker change was analyzed in each sample in each marker interval. Then, on the basis of the total number of marker changes in each marker interval, the recombination frequency was determined (Fig. 4 and data S2). In both lines, the chromosome fusion sites were depleted of COs compared with the respective chromosome areas in the control. At the same time, the recombination pattern detected in all translocated arms of chromosome 3 was inverted, shifting the COs from the fusion sites toward the telomeric ends. Conversely, the recombination pattern in the respective fusion partners, chromosome 1 or chromosome 5, was either unchanged or only slightly different from that in the corresponding WT control. In the long arm of chromosome 4, which was analyzed as another control, no difference in recombination pattern was observed between the engineered lines and the WT. Therefore, the chromosome arm transfers influenced the recombination landscape specifically at the fusion sites and in the fused arms.

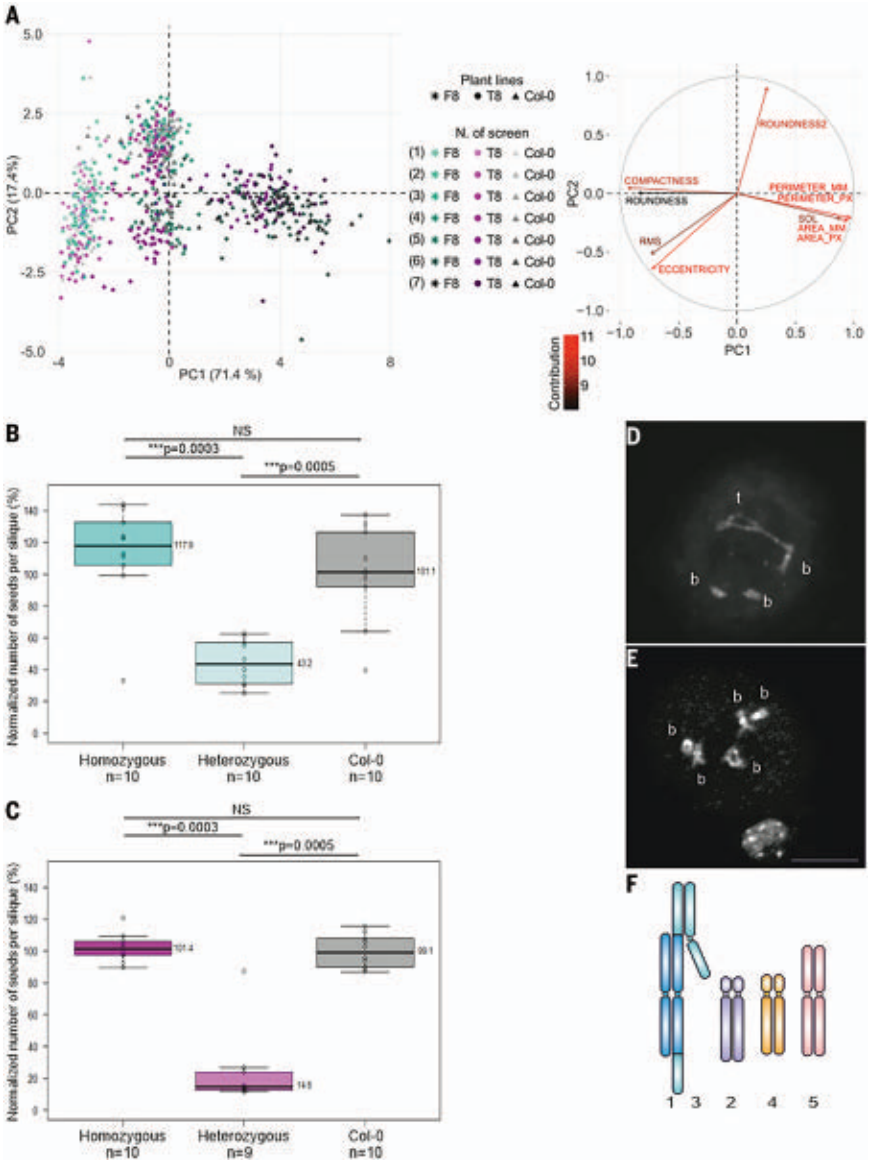

Fig. 3. Phenotypic and fertility analyses of lines F8 and T8 and meiotic chromosome Ppairing behavior of the eight-chromosome line F8. (**A**) PCA plot (left) and bi-plot (right) integrating phenotypic data of all seven scanned developmental stages. Arrows indicate the contribution of the individual morphological traits to the principal components (the longer the arrow, the higher the contribution). For each phenotype scan, $n \geq 30$ independent biological replicates for F8 and T8 and $n \geq 15$ for Col-0. For a more comprehensive view of phenotypic variation, PCA results were visualized in 3D by including PC3, which accounted for 5.8% of the total variation (fig. S8). (**B** and **C**) Homozygous, heterozygous, and Col-0 WT (Col) plants were randomly selected for fertility analysis ($n = 9$ or 10). Ten siliques per plant were randomly selected, and the number of seeds per silique was counted. The data were normalized to the mean seed count of Col-0, which was set to 100%. The boxplot shows the nine or 10 independent biological replicates for each genotype. The middle line represents the median, box edges represent the first and third quartiles, and whiskers extend to the minimum and maximum values. Individual data points are represented as open circles. The median values are indicated next to the middle line of each boxplot. *P* values were calculated using a two-sided Mann-Whitney *U* test (***$P < 0.001$; NS, not significant). (B) Fertility analysis of homozygous and heterozygous plants of line F8 and WT Col-0 plants. The seed number of the heterozygous plants was significantly reduced, by 56 and 61%, compared with Col-0 and homozygous plants, respectively. The seed number of homozygous and Col-0 plants did not differ significantly. (C) Fertility analysis of homozygous and heterozygous plants of line T8 and WT Col-0 plants. The seed number of the heterozygous plants was significantly reduced, by 76%, compared with Col-0 and homozygous plants. The seed number of homozygous and Col-0 plants did not differ significantly. (**D** and **E**) Meiotic chromosome pairing behavior of hybrids of the eight-chromosome line F8 and Col-0 (D) and Col-0 (E). The F8 × Col-0 hybrid shows the formation of one trivalent (marked by "t") plus three bivalents (marked by "b"). (E) Metaphase I cell of Col-0 showing five bivalents. Chromatin was counterstained with DAPI (gray). Scale bar, 10 μm. (**F**) Scheme of the formation of one trivalent plus three bivalents in the F8 × Col-0 hybrid plant.

Discussion

With the advance of large-scale sequencing and chromosome painting technologies, it has become clear that chromosome fusion events regularly take place in the course of genome evolution (*27*–*29*). The development of the CRISPR-Cas–mediated chromosome engineering technology has now allowed us to fuse chromosomes in a predefined way and thus to induce chromosome number reductions in plants in a targeted manner. The eight-chromosome *Arabidopsis* lines exhibited a completely WT-like phenotype during development and only minimal transcriptomic changes (*30*). Furthermore, the identified DEGs were not involved in DNA repair, indicating regular genome stability given that no persistent DNA damage signaling took place in these lines (*31*). These results also strongly resemble those obtained when analyzing two 5- and 7.5-Mb CRISPR-Cas–induced chromosomal inversions (*7*) and 0.5-Mb translocations (*30*) regarding their effect on epigenetic landscape and gene expression. Taken together, these results demonstrate the robustness of the plant genome toward substantial chromosomal restructuring.

However, chromosome fusions may have consequences for the evolution of species because they often coincide with reduced fertility in hybrids. Crossing with WT karyotypes results in heterozygotes that, because of disturbed meiotic pairing of the homologous chromosomes, display the generation of imbalanced gametes (*17*). We found a reduction in fertility of ~60% in line F8 and ~85% in line T8 compared with WT plants. We anticipate that with further structural chromosome changes, reproductive isolation between engineered and WT *Arabidopsis* plants will be achievable. In addition, using such a strategy, it should be possible to contain crops genetically and prevent outcrossing with wild relatives.

In two studies of haploid yeast, substantial chromosome number reductions were achieved by inducing consecutive chromosome fusions, leading to a reduction of the chromosome number from 16 to one and two chromosomes (*18*, *19*). In another study, the first chromosome fusions in mammals were achieved by editing haploid embryonic mice stem cells, resulting in the generation of animals with 19 instead of 20 pairs of chromosomes by fusing the two largest mouse chromosomes 1 and 2 as well as the two medium-sized chromosomes 4 and 5 (*20*). In all three studies, no major growth defects were detected; however, in contrast to our study, varying degrees of fertility impairments were observed.

In our experiments, the observed reduced fertility in heterozygotes indicated that meiotic segregation was affected by the presence of the chromosome fusions. Because successful chromosome pairing is a prerequisite for balanced segregation of the haploid chromosome sets during meiosis, aberrant gametes might have been produced due to the missegregation of the nonaligned engineered and WT chromosomes. In this situation, trivalents are likely to form, a complex and error-prone process, because the fused arms of chromosome 3 can pair with two different WT chromosomes at the same

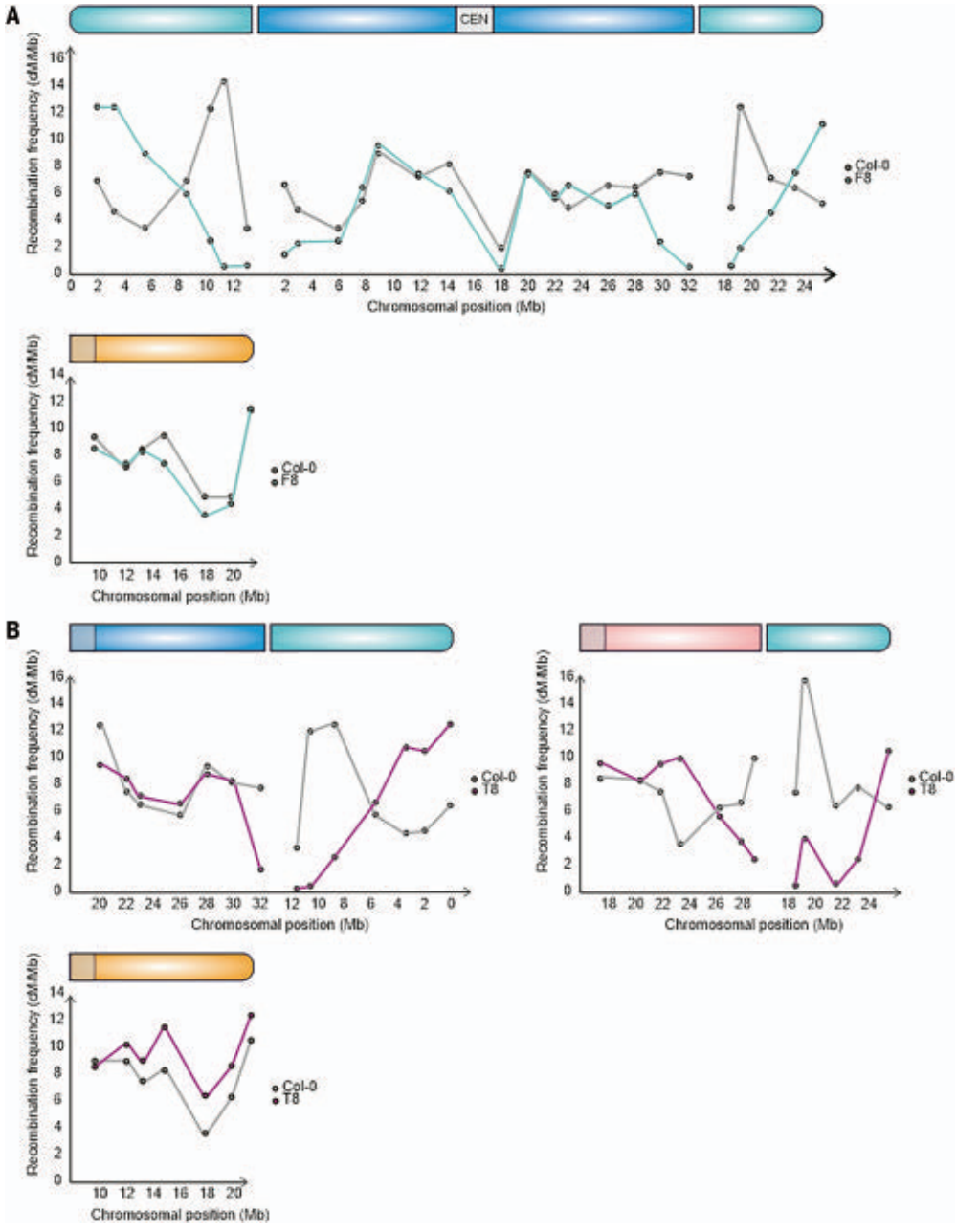

Fig. 4. Recombination frequency on the fusion chromosome arms and long arm of chromosome 4. (**A**) Recombination frequency on the fusion chromosome 1/3 (top) and the long arm of chromosome 4 (bottom) as a control in line F8 was determined by SNP-based genotyping of 400 plants (independent biological replicates) of the offspring of the F8 × Ler-1 line and the Col-0 × Ler-1 control. The recombination frequency is presented in cM/Mb. Chromosomal areas that were not analyzed are grayed out. (**B**) Recombination frequency on the arms of the fusion chromosome 1/3 (left) and 5/3 (right) and the long arm of chromosome 4 (bottom) as a control in line T8 was determined by SNP-based genotyping of 400 plants (independent biological replicates) of the offspring of the T8 × Ler-1 line and the *ku70* × Ler-1 control. Chromosomal areas that were not analyzed are grayed out. In both lines, we detected an inverted recombination pattern in the two translocated arms of chromosome 3, shifting the CO from the fusion sites toward the telomeric ends. At the same time, the chromosome fusions sites were depleted of COs compared with the respective chromosome areas in the control. The recombination pattern in the fusion partners, chromosome 1 and/or 5, did not differ from the pattern in the control.

time. Indeed, we were able to identify such a structure during meiosis (Fig. 4C). In addition to segregation, the natural recombination reaction itself might have also been influenced by the chromosome structure changes. In the offspring of crosses between the engineered eight-chromosome lines and Ler-1 (with a 10-chromosome set), we observed in both analyzed lines that the fusion sites were depleted of COs compared with the respective chromosome areas in the control, indicating impairments in homolog pairing close to the newly added heterologies. In both analyzed lines, the recombination pattern detected in all translocated arms of chromosome 3 was inverted, shifting the COs from the fusion sites toward the subtelomeric ends. These results could indicate that the complete formation of the synaptonemal complex during meiosis, a prerequisite for CO formation (*32*), was inhibited close to the fusion sites. The observed increase in CO frequencies toward the chromosome ends could be caused by a compensation mechanism, accounting for the reduced CO frequencies at the fusion sites to allow for the obligate CO necessary for proper segregation of the chromatids (*32*, *33*). For plant breeders, it will be of particular interest that by inducing large chromosomal translocations, the recombination landscape can be changed, both by reducing CO numbers near the newly brought-in heterologous regions and at the same time by enhancing COs in the subtelomeric parts of the elongated chromosome arms. Future application of the eight-chromosome lines in combination with meiotic mutants might be helpful to test the interplay between chromosome number reduction and interference-sensitive versus interference-insensitive CO pathways and also to test the coarsening model (*34*).

The applied chromosome fusion approach can also help to answer other basic research questions. For example, what are the minimum and maximum lengths of *Arabidopsis* chromosomes required to still be inherited? Minichromosomes are often lost during meiosis (*35*). In our lines, the minichromosomes were not carrying essential genes, so it is likely that there was no selective pressure to inherit them over several generations. However, we should soon be able to define the minimal size of functional *Arabidopsis* chromosomes by inducing translocations of different sizes (*36*). Generally, minichromosomes have considerable potential for breeding applications because they can be used as vectors for stacking and transferring many genes, such as genes associated with increased nutritional value, pest resistance, or tolerance to abiotic stress (*37*). Because they segregate independently of the other native chromosomes, linkage drag can be avoided. For the same reason, CRISPR-Cas

editing components could be placed on minichromosomes and later easily eliminated from the genome by back-crossing to achieve transgene-free lines (*38*).

An upper limit on chromosome size has been suggested by studying artificially increased chromosome arms in *Vicia faba* and barley (*39*, *40*). Those studies indicated that the chromosome arms must not exceed half of the average length of the spindle axis at telophase to avoid truncation of the nonseparated sister chromatids by the newly forming cell wall, causing a loss of genetic information. In our study, all obtained elongated chromosome arms still adhered to this proposed length limit. Future experiments using chromosome engineering could help to illuminate whether the proposed length limit can also be confirmed in *Arabidopsis*.

Artificially induced chromosome fission has been achieved in plants (*41*, *42*). A synthetic centromere was inserted into chromosome 4 of maize, making it a functional dicentric chromosome. Random chromosome breakage during segregation resulted in a line harboring a chromosome number of 22 instead of 20. The resulting plants showed no phenotypic deviation or growth defects and reproduced normally with 20-chromosome lines. By combining this approach with CRISPR-Cas–mediated chromosome engineering, one should be able to break up chromosomes at the desired position.

Our study demonstrates that by using CRISPR-Cas, we can now change the karyotype of plants in a predefined way. CRISPR-Cas–mediated chromosome number changes should be applicable to crops despite their larger and more complex genomes. In our experiments in *Arabidopsis*, we obtained translocation frequencies of complete chromosome arms of ~1 of 1000 tested plants (table S3). Because large intrachromosomal rearrangements have already been achieved in crops such as rice and maize (*8*, *9*) at frequencies similar to those observed in *Arabidopsis* (*6*, *10*), obtaining chromosome fusions in crops should not pose a significant obstacle if efficient plant transformation and screening protocols are used. Applying directed karyotype engineering will also allow us to mimic evolution, explore chromosome length limits, or achieve artificial reproductive isolation in the near future.

REFERENCES AND NOTES

1. J. Y. Wang, J. A. Doudna, *Science* **379**, eadd8643 (2023).
2. F. Wolter, P. Schindele, H. Puchta, *BMC Plant Biol.* **19**, 176 (2019).
3. B. Li, C. Sun, J. Li, C. Gao, *Nat. Rev. Genet.* **25**, 603–622 (2024).
4. A. Tuncel, C. Pan, J. S. Clem, D. Liu, Y. Qi, *Nat. Rev. Mol. Cell Biol.* **26**, 419–441 (2025).
5. N. Beying, C. Schmidt, M. Pacher, A. Houben, H. Puchta, *Nat. Plants* **6**, 638–645 (2020).
6. C. Schmidt *et al.*, *Nat. Commun.* **11**, 4418 (2020).
7. S. Khosravi *et al.*, *New Phytol.* **245**, 2527–2539 (2025).
8. C. Schwartz *et al.*, *Nat. Plants* **6**, 1427–1431 (2020).
9. Y. Lu *et al.*, *Nat. Plants* **7**, 1445–1452 (2021).
10. M. Rönspies *et al.*, *Nat. Plants* **8**, 1153–1159 (2022).
11. A. H. Sturtevant, *Proc. Natl. Acad. Sci. U.S.A.* **7**, 235–237 (1921).
12. K. N. Crown, D. E. Miller, J. Sekelsky, R. S. Hawley, *Curr. Biol.* **28**, 2984–2990.e3 (2018).
13. K. Huang, L. H. Rieseberg, *Front. Plant Sci.* **11**, 296 (2020).
14. M. Kirkpatrick, N. Barton, *Genetics* **173**, 419–434 (2006).
15. J. M. Coughlan, J. H. Willis, *Mol. Ecol.* **28**, 1343–1357 (2019).
16. D. E. Miller, K. R. Cook, R. S. Hawley, *PLOS Genet.* **15**, e1008421 (2019).
17. J. M. de Vos, H. Augustijnen, L. Bätscher, K. Lucek, *Philos. Trans. R. Soc. Lond. B Biol. Sci.* **375**, 20190539 (2020).
18. J. Luo, X. Sun, B. P. Cormack, J. D. Boeke, *Nature* **560**, 392–396 (2018).
19. Y. Shao *et al.*, *Nature* **560**, 331–335 (2018).
20. L.-B. Wang *et al.*, *Science* **377**, 967–975 (2022).
21. M. Rönspies, P. Schindele, R. Wetzel, H. Puchta, *Nat. Protoc.* **17**, 1332–1358 (2022).
22. C. Schmidt, M. Pacher, H. Puchta, *Plant J.* **98**, 577–589 (2019).
23. P. Schindele, H. Puchta, *Plant Biotechnol. J.* **18**, 1118–1120 (2020).
24. P. Schindele *et al.*, *Plant Biotechnol. J.* **21**, 457–459 (2023).
25. F. Wolter, J. Klemm, H. Puchta, *Plant J.* **94**, 735–746 (2018).
26. M. Pavicic *et al.*, *Front. Plant Sci.* **8**, 416 (2017).
27. F. Yu *et al.*, *New Phytol.* **233**, 1953–1965 (2022).
28. P. G. Hofstatter *et al.*, *Cell* **185**, 3153–3168.e18 (2022).
29. H. Lewis, *Evolution* **7**, 102–109 (1953).
30. O. Helia *et al.*, *Plant J.* **121**, e70024 (2025).
31. I.-P. Chen, U. Haehnel, L. Altschmied, I. Schubert, H. Puchta, *Plant J.* **35**, 771–786 (2003).
32. D. Zickler, N. Kleckner, *Cold Spring Harb. Perspect. Biol.* **7**, a016626 (2015).
33. N. M. Pazhayam, C. A. Turcotte, J. Sekelsky, *Front. Cell Dev. Biol.* **9**, 681123 (2021).
34. J. A. Fozard, C. Morgan, M. Howard, *eLife* **12**, e79408 (2023).
35. I. Schubert, *Cytogenet. Cell Genet.* **93**, 175–181 (2001).
36. H. Puchta, A. Houben, *New Phytol.* **241**, 541–552 (2024).
37. J. A. Birchler *et al.*, *Plant J.* **120**, 2356–2366 (2024).
38. J. A. Birchler, N. D. Graham, N. C. Swyers, J. P. Cody, M. E. McCaw, *Curr. Opin. Biotechnol.* **37**, 135–142 (2016).
39. I. Schubert, J. L. Oud, *Cell* **88**, 515–520 (1997).
40. S. Hudakova, G. Künzel, T. R. Endo, I. Schubert, *Cytogenet. Genome Res.* **98**, 101–107 (2002).
41. Y. Zeng, M. Wang, J. I. Gent, R. K. Dawe, *Sci. Adv.* **11**, eadw3433 (2025).
42. R. K. Dawe *et al.*, *Nat. Plants* **9**, 433–441 (2023).
43. European Molecular Biology Laboratory, "European Nucleotide Archive" (EMBL-EBI, 2025); https://www.ebi.ac.uk/ena/browser/view/PRJEB89813.
44. National Center for Biotechnology Information, "PacBio Hifi reads from Arabidopsis thaliana 8-chromosome line" (NCBI, 2011); https://www.ncbi.nlm.nih.gov/bioproject/PRJNA1267949/.
45. AVinJKIP, AVinJKIP/8-chromosome-lines-Arabidopsis-thaliana-: CRISPR/Cas-mediated heritable chromosome fusions in Arabidopsis, version #chromsome_engineering, Zenodo (2025); https://doi.org/10.5281/zenodo.17185110.
46. V. Schubert *et al.*, *Genetics* **172**, 467–475 (2006).

ACKNOWLEDGMENTS

We thank J. Baumann, N. Schäfter, L. E. Rothenberger, C. Brechtel, A. Hamidi, O. Weiss and K. Kumke for excellent technical assistance in performing experiments; M. Cuacos for support with microscopy; A. Fiebeg for data submission; and J. J. Szymanski for network analysis advice. Additionally, the authors acknowledge the support of the Freiburg Galaxy Team, Bioinformatics, University of Freiburg (Germany) funded by the German Federal Ministry of Education and Research BMBF grant 031 A538A de.NBI-RBC and the Ministry of Science, Research and the Arts Baden-Württemberg (MWK) within the framework of LIBIS/de.NBI Freiburg. The Core Facility Plant Sciences, CEITEC Masaryk University, and Labdeers company (www.labdeers.com) are gratefully acknowledged for the support in obtaining scientific data presented in this paper. **Funding:** This work was supported by Reinhard Koselleck Project Pu137/24-1, Deutsche Forschungsgemeinschaft (H.P.); EpiChrom (031B1220B), BMBF (H.P. and A.H.); Czech Science Foundation project 22-04364S (M.F. and O.H.); and Toward Next GENeration Crops, reg. no. CZ.02.01.01/00/22_008/0004581, ERDF Programme Johannes Amos Comenius (M.F. and J.F.). **Author contributions:** Conceptualization: M.R., S.K., O.H., J.F., M.F., A.H., H.P.; Funding acquisition: J.F., M.F., A.H., H.P.; Investigation: M.R., S.K., O.H., A.V.; Methodology: M.R., S.K., O.H., A.V.; Visualization: M.R., S.K., O.H., A.V.; Writing – original draft: M.R., S.K., O.H., A.V., J.F., M.F., A.H., H.P.; Writing – review & editing: M.R., S.K., O.H., A.V., J.F., M.F., A.H., H.P. **Competing interests:** The authors declare no competing interests. **Data and materials availability:** All data are available in the main text or the supplementary materials or have been deposited into the following repositories. RNA-sequencing raw sequence reads are available from the European Nucleotide Archive (ENA) under accession number PRJEB89813 (*43*). PacBio raw sequence reads and genome assemblies are available from the NCBI Sequence Read Archive (SRA) and NCBI GenBank under BioProject number PRJNA1267949 (*44*). Custom Python scripts are available through Zenodo (*45*). **License information:** Copyright © 2025 the authors, some rights reserved; exclusive licensee American Association for the Advancement of Science. No claim to original US government works. https://www.science.org/about/science-licenses-journal-article-reuse

SUPPLEMENTARY MATERIALS

science.org/doi/10.1126/science.adz8505
Materials and Methods; Figs. S1 to S9; Tables S1 to S6; References (*47*–*72*); MDAR Reproducibility Checklist; Data S1 to S4

Submitted 17 June 2025; accepted 29 September 2025

10.1126/science.adz8505

QUANTUM SIMULATION

Realization of a Rydberg-dressed extended Bose-Hubbard model

Pascal Weckesser[1,2], Kritsana Srakaew[1,2], Tizian Blatz[2,3], David Wei[1,2], Daniel Adler[1,2], Suchita Agrawal[1,2], Annabelle Bohrdt[2,3,4], Immanuel Bloch[1,2,5], Johannes Zeiher[1,2,5]*

The competition of different length scales in quantum many-body systems leads to phenomena such as correlated dynamics and nonlocal order. To investigate such effects in an itinerant lattice-based quantum simulator, it has been proposed to introduce tunable extended-range interactions using off-resonant optical coupling to Rydberg states, known as Rydberg dressing. In this work, we use this approach to realize an effective one-dimensional extended Bose-Hubbard model. Harnessing our quantum gas microscope, we probe the correlated out-of-equilibrium dynamics of extended-range repulsively bound pairs and "hard rods." By contrast, operating near equilibrium, we observe density ordering when adiabatically turning on the extended-range interactions. Our results pave the way to realizing light-controlled extended-range interacting quantum many-body systems.

Extended-range interactions between itinerant quantum particles give rise to a wealth of interesting phenomena in many-body systems, including, for example, the exotic properties of superfluid helium (*1*). When trapped in lattices, such systems with interactions that span at least the next-nearest-neighbor site are described by extended Hubbard models (eHMs), which feature a rich phenomenology arising from the extended-range interactions competing with the tunneling and local interaction energy scales (*2*). Near equilibrium, manifestations of this competition include the emergence of nonlocal order (*3*), lattice supersolids (*4*, *5*), and exotic cluster Luttinger liquid phases (*6*, *7*); out of equilibrium, the emergence of repulsively bound pairs has been predicted (*8*). Although ultracold atoms are an ideal platform to realize Hubbard systems (*9*, *10*), most work has focused on systems with on-site interactions (*11*). Over the past decade, much effort has been directed at overcoming this limitation and opening the stage for quantum simulations, including extended-range interactions. Experimentally, long-range interacting quantum simulators for itinerant particles have been realized using electric dipole interactions in molecules (*12*–*17*), magnetic dipole interactions in lanthanide atoms (*18*–*21*), and cavity-assisted all-to-all interactions (*22*–*24*). Furthermore, Rydberg quantum simulators, usually tailored to simulating spin models (*25*) or quantum computing (*26*, *27*), have been used to simulate itinerant hardcore interacting bosons through a spin-boson mapping (*28*). However, despite several notable advances, the microscopic control and readout of long-range interacting gases of itinerant particles have been limited, except for recently realized quantum gas microscopes for dilute molecular samples (*16*) and the observation of quantum solids in optical lattices with a tunable lattice constant (*21*). Harnessing the full set of capabilities of quantum gas microscopes, which includes both microscopic detection and single-particle control (*29*), has remained an outstanding experimental challenge in eHMs.

Off-resonant admixture of strongly interacting Rydberg states, or Rydberg dressing, offers an alternative pathway to realize extended-range interacting quantum gases that are compatible with in situ control over single atoms and provides flexible interaction control. Rydberg-dressed interactions emerge through the off-resonant coupling of short-range interacting ground-state atoms to a higher-lying, long-range interacting Rydberg state with Rabi frequency Ω and detuning Δ (*30*–*32*). In this case, the Rydberg blockade modifies the AC Stark shift experienced by two nearby ground-state atoms, which leads to a characteristic softcore-shaped potential with softcore height $V_0 = \Omega^4 / (8\Delta^3)$ and tunable interaction range $R_c = \left[|C_6|/(2\hbar|\Delta|)\right]^{1/6}$ of up to a few lattice sites, with an asymptotic van der Waals tail and coefficient C_6 (Fig. 1A) and the reduced Planck constant $\hbar$. The relatively large interaction range R_c easily spans micrometer-scale distances, making Rydberg dressing straightforwardly compatible with single-atom control and detection in quantum gas microscopes (*6*, *33*–*36*), without the need to dynamically adjust the lattice spacing (*21*). The optical coupling also provides a distinctive handle to control the interaction—for example, to realize sudden quenches of the interaction strength on submicrosecond timescales, periodically modulated interactions (*37*), or turning on the long-range interactions only after the system has been prepared. Furthermore, using blue- or red-detuned coupling enables the realization of either attractive or repulsive interactions (*38*), and changing the external field and polarization of the coupling light allows for controlling the isotropy of the interaction (*39*, *40*). So far, Rydberg-dressed interactions have been successfully implemented in different regimes for pinned atoms in the absence of motional dynamics to realize spin models (*39*–*45*). Although first steps toward using Rydberg-dressed interactions to realize itinerant fermionic systems have been taken (*46*), a widespread adoption of the technique has been hindered by the observation of strong collective losses (*39*, *47*). These can be attributed to off-resonant scattering, which can lead to the population of opposite-parity Rydberg states, whose interaction with the dressed state tunes the coupling light into resonance that can trigger an excitation avalanche (*39*, *47*, *48*). Thus, the feasibility of using Rydberg dressing to experimentally study such systems for tens of tunneling times or near equilibrium has been an open question.

In this work, we realize an effective one-dimensional (1D) extended Bose-Hubbard model (eBHM) using Rydberg-dressed ^{87}Rb atoms in an optical lattice. These results are enabled by a stroboscopic dressing sequence that leads to substantially increased lifetimes of more than 100 ms in our system, surpassing previous observations by two orders of magnitude (*42*, *46*). We use the excellent optical control over the extended interaction strength in combination with microscopic control over single atoms to study the eBHM in a number of interesting regimes both in and out of equilibrium.

In particular, our studies explore several regimes of interaction strength and thus highlight the impact of this energy scale on the emerging many-body physics. First, we observe the existence and dynamics of repulsively bound pairs of atoms occupying neighboring lattice sites stabilized by strong extended-range interactions. Second, increasing the filling, at large nearest-neighbor interaction, we realize a gas of "hard rods" and demonstrate the difference in the density relaxation of an initial charge density wave (CDW) of such hard rods compared with the case of hardcore bosons. Finally, we probe the nature of the low-energy states of the eBHM by slowly increasing the nearest-neighbor interaction and observing the emergence of density ordering into a state similar to the quantum solids that were recently observed in magnetic dipolar atoms (*21*).

[1]Max-Planck-Institut für Quantenoptik, Garching, Germany. [2]Munich Center for Quantum Science and Technology (MCQST), Munich, Germany. [3]Department of Physics and Arnold Sommerfeld Center for Theoretical Physics (ASC), Ludwig-Maximilians-Universität, München, Germany. [4]Institute of Theoretical Physics, University of Regensburg, Regensburg, Germany. [5]Fakultät für Physik, Ludwig-Maximilians-Universität, Munich, Germany. ***Corresponding author. Email: johannes.zeiher@mpq.mpg.de**

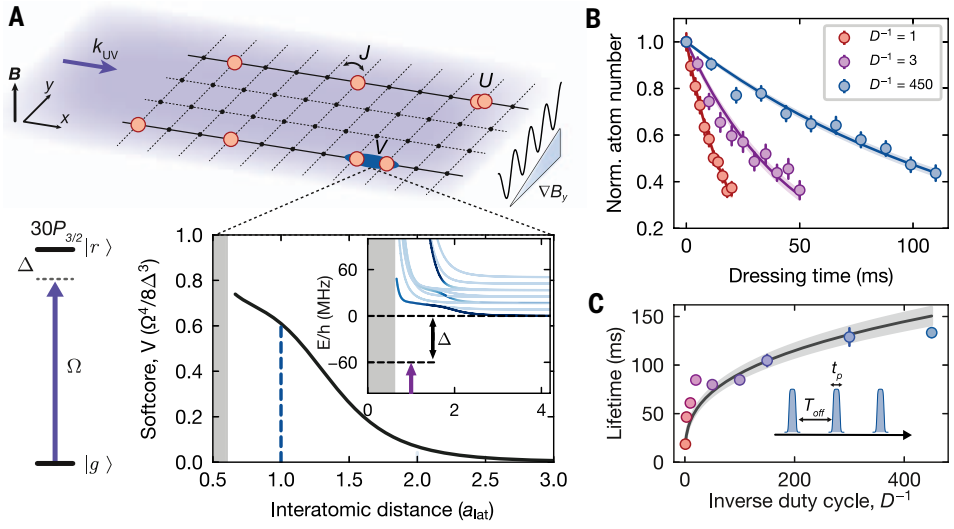

Fig. 1. Rydberg-dressed eBHM and Rydberg lifetimes. (**A**) Tilted lattice system and relevant energy scales. The atoms are allowed to tunnel along the chains with tunneling energy J and experience repulsive on-site interactions U. We engineer long-range, nearest-neighbor interactions V using off-resonant coupling to a Rydberg state $|r\rangle$, with Rabi frequency $\Omega = 2\pi \times 20$ MHz and detuning $\Delta = -2\pi \times 60$ to 400 MHz. The resulting softcore-shaped interaction is shown as the solid black line in the lower right panel and can be derived by adding the contributions of various interaction potentials (see blue-shaded lines in the inset). The relative optical coupling strength of the relevant Rydberg pair potentials is indicated by the intensity of the blue coloring. The purple arrow in the inset indicates the excitation laser with respect to the Rydberg states. (**B**) Duty cycle–dependent atomic lifetime for fixed $V/h =$ 114(4) Hz in a unity-filled 1D chain of 11 atoms. In this case, we apply stroboscopic, pulsed dressing for a total integrated dressing time, with pulse durations of $t_p = 0.5$ to 1 μs and tunable off times $T_{off} = 150$ to 300 μs [see inset of (C)]. The solid lines resemble the best-fit results of an exponential fit to the data. (**C**) Scanning the duty cycle $D = t_p/(t_p + T_{off})$, we improve the atom lifetime beyond 100 ms, following the expected scaling $\sqrt[3]{D^{-1}}$. Averaged over all measurements, our experimental lifetimes reach 54(3)% of their respective theoretical value. All error bars denote the SEMs.

Experimental system

In our experiment, we prepare up to 200 ^{87}Rb atoms in the $|g\rangle = |F = 2, m_F = +2\rangle$ ground state within a single plane of the vertical optical lattice (x-y plane). Here, F and m_F denote the hyperfine spin and its projection on the quantization axis. We realize a 2D Bose-Hubbard model using a folded lattice (*49*) with lattice spacing $a_{lat} = 752$ nm, tunable tunnel coupling J, and approximately fixed interaction strength $U/h = 225$ Hz set by the scattering properties of the ^{87}Rb atoms. Using single-site addressing (*50*, *51*), we prepare up to three parallel and independent 1D systems oriented along the x direction and separated by at least three lattice sites in the y direction. Each 1D system contains a variable and controllable number of atoms. Tunneling along the x direction is enabled at a rate J, whereas tunneling along the transverse y direction is inhibited by applying a magnetic field gradient $\nabla B_y \simeq 350(3)$ Hz / a_{lat} (Fig. 1A). In the following sections, all discussions refer to these equivalent 1D systems. We induce extended-range interactions up to two-lattice sites (Fig. 1A, inset) by off-resonantly coupling atoms from the ground state $|g\rangle$ to the $|r\rangle = |30P_{3/2}; m_j = +3/2\rangle$ Rydberg state with an ultraviolet laser at a wavelength of 297 nm, which propagates along the x direction. We calibrate the resulting time-averaged interaction strength V using a spectroscopic spin-echo sequence (*52*). Our system is described by the Hamiltonian

$$\hat{H} = -J\sum_{\langle i,j\rangle}\hat{a}_i^\dagger\hat{a}_j + \frac{U}{2}\sum_i \hat{n}_i(\hat{n}_i - 1) + V\sum_i \hat{n}_i\hat{n}_{i+1} \quad (1)$$

where $\hat{a}_i^\dagger$ and $\hat{a}_i$ are the raising and lowering operator and $\hat{n}_i$ is the number operator on site i. In this work, we focus on the 1D hardcore boson limit $U/J \gtrsim 11$, where doublon formation is strongly suppressed. To maximize the advantages of controlling the extended-range interaction V through the coupling light, we apply a stroboscopic pulse sequence with duty cycle $D < 1$. Compared with a continuous drive, our pulsed scheme requires us to operate at closer detuning ($\Delta_S < \Delta$) to compensate for the time-averaged reduction of the softcore ($V \propto D/\Delta_S^3$). This, however, is an advantage, because closer detunings improve the product of the time-averaged interaction times lifetime, as $V\tau \propto 1/\Delta_S$ (*53*, *54*), effectively scaling as $\sqrt[3]{D^{-1}}$ if the time-averaged softcore height is kept constant (*52*). Additionally, the pulsed scheme conveniently suppresses collective losses, which are normally observed for continuous dressing at closer detuning. Such collective losses are triggered by blackbody radiation–induced transitions to opposite-parity Rydberg states, whose interactions with the dressed states lead to additional resonant excitations to the Rydberg manifold (*39*, *47*). Operating in the most extreme case, where the laser is mostly off ($D \ll 1$), allows the opposite-parity Rydberg states to decay and the time-averaged physics of the eBHM to become accessible, provided that sufficiently many pulses are applied within one hopping event $\hbar/(2J)$. Applying stroboscopic dressing, we confirm the markedly increased lifetime that extends beyond 100 ms for $D \lesssim 1/150$, in agreement with the expected scaling (Fig. 1C). Such enhanced lifetimes exceed our typical tunneling times $\hbar/(2J) \simeq 4$ to 7 ms by at least an order of magnitude while reaching $V/J \simeq 6$ to 10. Reaching this long-pursued milestone puts us in place to probe microscopic features of the eBHM experimentally.

Repulsively bound pair states

We first focus on out-of-equilibrium dynamics by preparing two atoms on neighboring sites in the 1D chain and quenching the tunneling energy to finite values. In the eBHM, the interaction between atoms on adjacent sites has been predicted to result in the emergence of bound states when V exceeds the critical value $V_c = 2J$ (*8*). These bound states arise through the interplay of strong nearest-neighbor interactions and the bounded spectrum of extended states in the optical lattice, which have been analogously observed for atoms bound by the on-site Hubbard interaction before (*55*, *56*). In the center-of-mass frame, the energy of the bound-state solution is given by $E_B(K) = V + 4J^2/V\cos(Ka_{lat}/2)$, with K the center-of-mass quasimomentum (*8*). The bound state can thus be interpreted as an isolated state separated from the continuum of free single-particle states by the energy V and featuring a bandwidth set by the reduced tunneling energy J^2/V. This reduced tunneling energy of the bound pair can be intuitively understood as a hopping of the bound state occurring perturbatively in J/V through a second-order process coupling off-resonantly to the continuum of free states. In our experiment, we detect the presence of the bound state and measure its group velocity by monitoring the time evolution of an atom pair after a sudden quench of the tunnel coupling in the lattice (Fig. 2B). In the absence of Rydberg-dressed interactions ($V = 0$; case 1), we observe a characteristic light cone indicating the free expansion of the two particles expected for the hardcore boson limit (*56*–*58*). The expansion speed of the wavefront is consistent with the Lieb-Robinson bound given by $2Ja_{lat}/\hbar$ (Fig. 2B, black line). When introducing nearest-neighbor

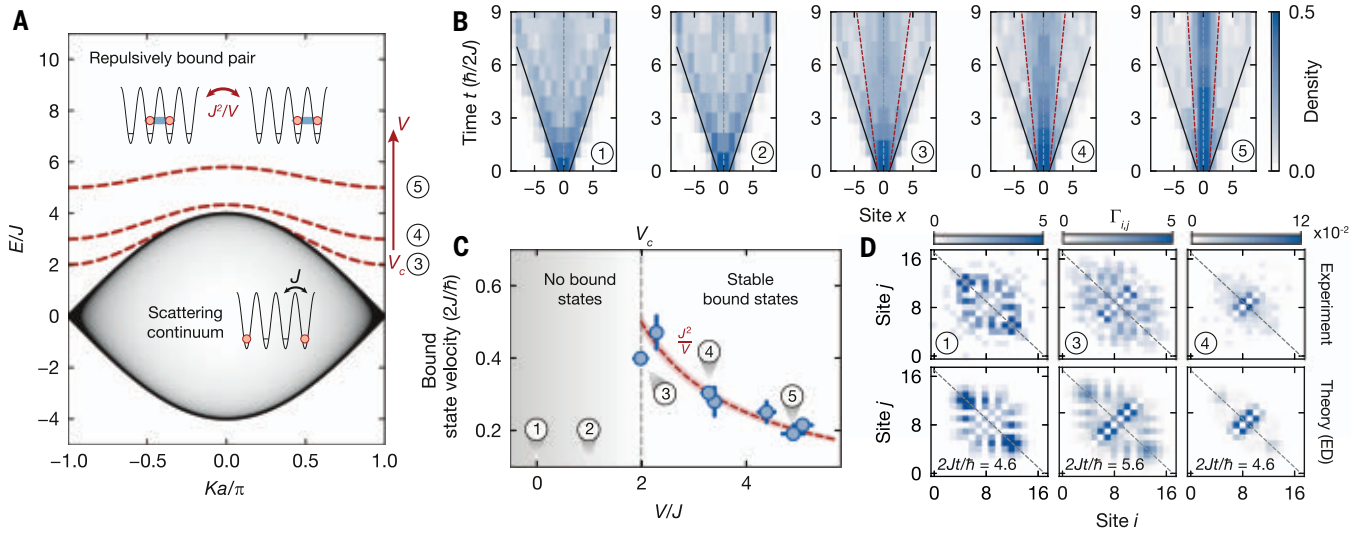

Fig. 2. Repulsively bound pair states in the eBHM. (**A**) Two-particle energy spectrum of the 1D eBHM as a function of center-of-mass quasimomentum K. For $V \geq V_c = 2J$, the spectrum features stable bound states, illustrated as red dashed lines, with reduced tunneling energy J^2/V. (**B**) Symmetrized two-particle density dynamics for $V/J = \{0, 1.0(1), 2.0(2), 3.3(1), 4.9(2)\}$ (cases 1 to 5, respectively) postselected on two particles being present. For $V < V_c$, the particles spread independently, following a ballistic light cone with group velocity $2Ja_{\mathrm{lat}}/\hbar$ until the system's boundary is reached (black lines). For $V \geq V_c$, we observe the additional emergence of an inner, slower light cone. The red dashed lines represent the best-fit result of the bound pair's expansion. (**C**) Extracted tunneling energy of the bound pair for variable V in units of the single-particle tunneling energy J. We find excellent agreement with the exact solution J^2/V derived by Valiente and Petrosyan (*8*), represented as the red dashed line. (**D**) Symmetrized two-particle correlator $\Gamma_{i,j}$ for variable V and time. The upper and lower rows show the measured correlator and the correlator calculated with ED, respectively (*52*). Without Rydberg-dressed interactions (case 1), we observe strong antibunching on the off-diagonal owing to the fermionization of the hardcore bosons. For $V \geq V_c$, we observe strong nearest-neighbor correlators on the diagonal, indicating correlated pair tunneling in good agreement with theory. The gray dashed lines in (B) and (D) show the symmetrization axis. All error bars denote the SEMs.

interactions $V \geq V_c$ (*8*), we observe the emergence of a second light cone with a lower expansion speed of the wavefront (cases 3 to 5). We determine the group velocities for the free and bound state by fitting an incoherent sum of four Bessel functions of the first kind to our experimental data (*52*) and find excellent agreement with the expected bound pair tunneling energy J^2/V (Fig. 2C). To prove the existence of the repulsively bound pairs microscopically, we evaluate the two-particle correlator $\Gamma_{i,j} = \left\langle a_i^\dagger a_j^\dagger a_i a_j \right\rangle$ (*56*). In the absence of long-range interactions, the hardcore bosons effectively behave as noninteracting spinless fermions and show long-range correlations on the antidiagonal (Fig. 2D). The latter is a direct consequence of Hanbury Brown and Twiss interference for fermions, resulting in pronounced antibunching (*56*). With nearest-neighbor interactions $V \geq V_c$, we observe correlated pair tunneling, resulting in strong nearest-neighbor correlations on the diagonal. In this case, we find an overall good agreement with exact diagonalization (ED).

Constrained hard rod dynamics

Proceeding from the two-atom initial state to larger fillings, we use single-site addressing to prepare an initial CDW with period $\lambda = 2a_{\mathrm{lat}}$ in the optical lattice and subsequently study its dynamics after a quench. We first investigate the many-body dynamics in the absence of Rydberg dressing. For hardcore bosons and fixed boundary walls, the CDW exhibits oscillatory dynamics while maintaining the crystalline-like order, with atoms either occupying the even or the odd sites (Fig. 3A). We quantify this oscillation by introducing the imbalance, defined as

$$\mathcal{I} = \frac{N_e - N_o}{N_e + N_o} \tag{2}$$

where N_e and N_o are the detected atom number on the even and odd sites, respectively. Comparing our data with ED calculations, including a reduced density $\overline{n} = 0.44$ to 0.50, we find excellent agreement (Fig. 3B). By contrast, operating in the strongly interacting regime $V/J \gg 1$, the hardcore bosons become hard rods, featuring an extended exclusion volume and thus inhibiting the occupation of neighboring sites (*59*). The latter can be explained by the energy gap induced by the bound pair, as discussed in Fig. 2A. The initially prepared CDW state is thus expected to be stabilized (*46*). Nevertheless, one can observe defect dynamics within the CDW if one edge site is unoccupied while the other is occupied (Fig. 3). In this configuration, the atom closest to the unoccupied left edge site is unimpeded by the extended interactions and can propagate freely through the system. This process can continue, and the hole defect initially localized on the left edge can ballistically propagate through the system, leaving behind a trace by shifting the entire CDW by one lattice site or, equivalently, flipping the sign of $\mathcal{I}$ in a small subsystem to the left of the defect. We quantify the different dynamics by evaluating the imbalance on two subsystems, labeled as "left" (sites < 7) and "right" (sites ≥ 7) region of interest (ROI). To the right, the imbalance remains positive as the CDW is preserved; whereas on the left, the imbalance undergoes a sign change, as the CDW is reordered by the defect motion. We find qualitative agreement with ED calculations (Fig. 3B) when including the nearest- and next-nearest-neighbor interactions (*52*). We attribute the remaining deviations to Rydberg decay, imperfect state preparation, and misalignment drifts of the projected repulsive walls, resulting in the loss of individual atoms on the right site.

Near-equilibrium density ordering

Finally, we aim to study the eBHM near equilibrium, where a wealth of interesting quantum phases intimately connected to extended-range interactions are expected (*21*). As a prerequisite, we first realize a 1D low-energy state near the many-body ground state at half-filling in absence of long-range interactions. We achieve this by preparing a 1D Mott insulator of 9 atoms on 9 sites and slowly reducing the lattice depth to enter the itinerant regime. Subsequently, we adiabatically expand the system into a 1D chain of 17 sites by lowering the external

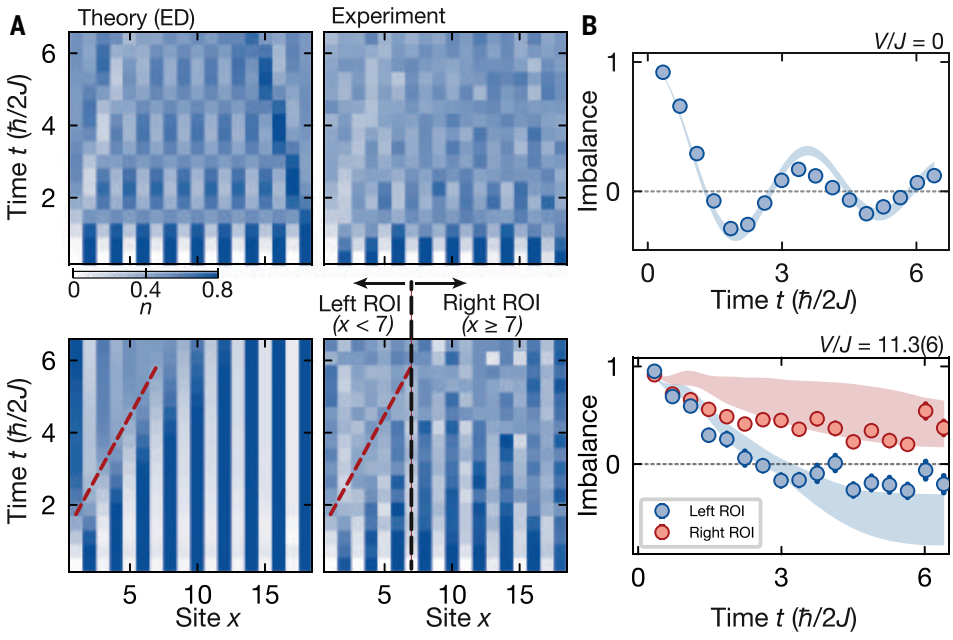

Fig. 3. Hard rod relaxation dynamics starting from a CDW. (**A**) Comparison of the many-body dynamics of a CDW in the hardcore boson (top row; $V/J = 0$) and the hard rod limit [bottom row; $V/J = 11.3(6)$] after a sudden quench of the tunneling energy. Here, we illustrate the density evolution calculated using ED ($\bar{n} = 0.5$) and the experimental result with postselected density $\bar{n} = 0.44$ to 0.50. For the hard rods, we consider nearest and next-nearest-neighbor interactions. Additionally, the red dashed line functions as a guide to the eye and highlights the ballistic spread of an edge defect through the stabilized CDW, leaving a trace by flipping the polarity of the CDW to its left. (**B**) Density imbalance of the system. In the hardcore boson limit, we observe the density oscillation of the CDW. For hard rods, we observe the stabilization of the CDW on the right indicated by the positive imbalance (red markers; sites ≥ 7), whereas we observe a sign change on the left (blue markers; sites < 7). The shaded areas show the expected results obtained by ED for $\bar{n} = 0.44$ to 0.50. All error bars denote the SEMs.

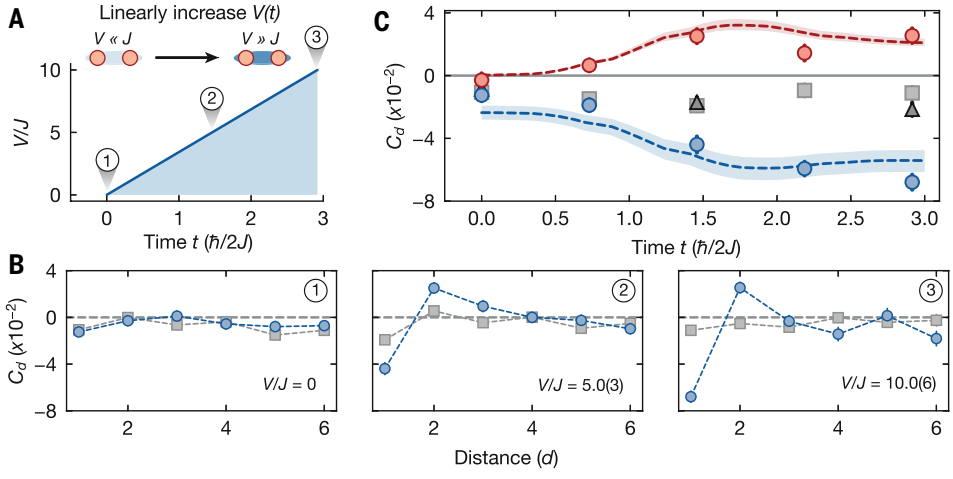

Fig. 4. Near-equilibrium density ordering through long-range interactions. (**A**) Illustration of the experimental protocol. Starting from a low-energy ensemble close to half filling, we linearly increase the nearest-neighbor repulsion up to $V/J = 10.0(6)$ within $2Jt/\hbar \sim 2.9$. Afterward, we freeze the dynamics and evaluate the density-density correlations. (**B**) Distance-dependent connected correlator C_d, evaluated at various points along the ramp and postselected for mean densities $\bar{n} = 0.35$ to 0.52. The blue points and gray squares show the respective correlation strength, comparing the cases where the ramp up of the Rydberg-dressed interaction is either applied or not applied. (**C**) Observed correlations for distances $d = 1$ (blue) and $d = 2$ (red) during the ramp. The dashed lines and shaded areas represent the theoretical correlations for $k_BT = 1.5J$ and $k_BT = 1.3$ to 1.7 J, respectively, derived by time-dependent MPS (*52*). The gray squares and black triangles correspond to two reference cases evaluated at $d = 1$, where we either apply no ramp of the interaction strength [gray squares from (B)] or prepare an initial high-energy ensemble before the ramp is applied (*52*).

confinement potential over a timescale of $\sim 60\hbar/J$ (*52*). As an upper bound, we estimate the ensemble to have an 88(2)% overlap with the initial many-body ground state (*52*). A similar overlap has been reported when adiabatically connecting individual atoms, localized in tweezer light, to the lattice ground state (*60*). After preparing this low-energy ensemble, we next linearly increase the nearest-neighbor interaction from $V = 0$ to $V = 10.0(6)J$ over a timescale corresponding to ~2.9 tunneling times. Matrix product state (MPS) simulations (*61*) predict that this short ramp already results in a substantial overlap with the final many-body ground state (~62%) if the system starts in the many-body ground state before the ramp. With increasing extended-range interaction strength, the buildup of nonlocal density-density correlations is expected because the strong nearest-neighbor repulsion results in crystalline-like structures (*52*). To probe this effect experimentally, we analyze the connected correlator $C_d = \langle \hat{n}_i \hat{n}_{i+d} \rangle - \langle \hat{n}_i \rangle \langle \hat{n}_{i+d} \rangle$ versus distance d for various points along the ramp (Fig. 4). We find that with increasing interaction V, the nearest-neighbor ($C_{d=1}$) and next-nearest-neighbor ($C_{d=2}$) correlation strengths decrease and increase, respectively, indicating the onset of density ordering in our system. We observe no detectable correlations for distances $d \gtrsim 3$, which is expected for our mean densities of $\bar{n} = 0.35$ to 0.52 (*52*). Comparing $C_{d=1}$ and $C_{d=2}$ with time-dependent MPS calculations at $k_BT = 1.5J$ (*52*), with k_B the Boltzmann constant, we find excellent agreement for most interaction strengths (Fig. 4C). In this case, the system's energy is limited by the initial state preparation, whose energy we independently estimate to be $k_BT \sim 2J$ (*52*). As a reference, when intentionally preparing a system at higher initial energy (*52*), we find that the correlations vanish (Fig. 4C, black triangles). Finally, when choosing longer ramp times up to ~8.7 tunneling times, we observe a slight decrease of the correlation strength, indicating that over longer timescales, the Rydberg-state decay and the corresponding heating rate may become relevant [fig. S9 (*52*)].

Discussion and outlook

Our experiments realize a Rydberg-dressed eBHM with lifetimes long enough to explore a number of intriguing many-body phenomena. Notably, the interaction strength and range are in a regime compatible with microscopic manipulation of atoms in an optical lattice through a quantum gas microscope, which was essential for all performed experiments. We anticipate various pathways to improving the coherence time of Rydberg-dressed systems even further,

including a cryogenic environment and larger-spaced lattices, which reduce collective losses while allowing us to work with longer-lived larger principal quantum numbers, and using alkaline-earth atoms, which feature intrinsically larger transition dipole moments between metastable and Rydberg states, resulting overall in an even more favorable figure of merit for limited laser power (*52*). Going forward, the demonstrated combination of local microscopic control for initial state preparation, the temporal control over extended-range interactions, and the flexibility in controlling Rydberg-dressed interactions through external fields open a number of perspectives that are not easily accessible on other platforms. Our work can, for example, straightforwardly be extended from 1D systems to ladder systems (*62*) and toward two-component mixtures with only one featuring long-range interactions (*63*). Similarly, it may be possible to leave the hard-core boson limit and explore the full $V/J - U/J$ phase diagram of the eBHM, which is expected to include the celebrated Haldane insulator (*3*, *64*). Exploring low-energy physics in extended-range interacting fermionic systems may be relevant to understanding 1D cuprate chains (*65*). Finally, the constrained dynamics of the hard rod model out of equilibrium realized in the presence of the extended interactions is an exciting frontier (*59*), and the arbitrary dynamic control of the interaction strength might open new avenues toward mixed analog-digital quantum simulation approaches (*27*, *36*).

REFERENCES AND NOTES

1. M. Boninsegni, N. V. Prokof'ev, *Rev. Mod. Phys.* **84**, 759–776 (2012).
2. N. Defenu *et al.*, *Rev. Mod. Phys.* **95**, 035002 (2023).
3. E. Berg, E. G. Dalla Torre, T. Giamarchi, E. Altman, *Phys. Rev. B* **77**, 245119 (2008).
4. F. Cinti, T. Macrì, W. Lechner, G. Pupillo, T. Pohl, *Nat. Commun.* **5**, 3235 (2014).
5. A. Geißler, I. Vasić, W. Hofstetter, *Phys. Rev. A* **95**, 063608 (2017).
6. M. Mattioli, M. Dalmonte, W. Lechner, G. Pupillo, *Phys. Rev. Lett.* **111**, 165302 (2013).
7. M. Dalmonte *et al.*, *Phys. Rev. B* **92**, 045106 (2015).
8. M. Valiente, D. Petrosyan, *J. Phys. At. Mol. Opt. Phys.* **42**, 121001 (2009).
9. I. Bloch, J. Dalibard, W. Zwerger, *Rev. Mod. Phys.* **80**, 885–964 (2008).
10. C. Gross, I. Bloch, *Science* **357**, 995–1001 (2017).
11. C. Chin, R. Grimm, P. Julienne, E. Tiesinga, *Rev. Mod. Phys.* **82**, 1225–1286 (2010).
12. B. Yan *et al.*, *Nature* **501**, 521–525 (2013).
13. S. A. Moses, J. P. Covey, M. T. Miecnikowski, D. S. Jin, J. Ye, *Nat. Phys.* **13**, 13–20 (2017).
14. N. Bigagli *et al.*, *Nature* **631**, 289–293 (2024).
15. J. S. Rosenberg, L. Christakis, E. Guardado-Sanchez, Z. Z. Yan, W. S. Bakr, *Nat. Phys.* **18**, 1062–1066 (2022).
16. L. Christakis *et al.*, *Nature* **614**, 64–69 (2023).
17. A. N. Carroll *et al.*, *Science* **388**, 381–386 (2025).
18. S. Baier *et al.*, *Science* **352**, 201–205 (2016).
19. H. Kadau *et al.*, *Nature* **530**, 194–197 (2016).
20. L. Chomaz *et al.*, *Rep. Prog. Phys.* **86**, 026401 (2022).
21. L. Su *et al.*, *Nature* **622**, 724–729 (2023).
22. R. Landig *et al.*, *Nature* **532**, 476–479 (2016).
23. J. Léonard, A. Morales, P. Zupancic, T. Esslinger, T. Donner, *Nature* **543**, 87–90 (2017).
24. V. Helson *et al.*, *Nature* **618**, 716–720 (2023).
25. A. Browaeys, T. Lahaye, *Nat. Phys.* **16**, 132–142 (2020).
26. M. Saffman, *J. Phys. At. Mol. Opt. Phys.* **49**, 202001 (2016).
27. M. Morgado, S. Whitlock, *AVS Quantum Sci.* **3**, 023501 (2021).
28. S. de Léséleuc *et al.*, *Science* **365**, 775–780 (2019).
29. C. Gross, W. S. Bakr, *Nat. Phys.* **17**, 1316–1323 (2021).
30. I. Bouchoule, K. Mølmer, *Phys. Rev. A* **65**, 041803 (2002).
31. N. Henkel, R. Nath, T. Pohl, *Phys. Rev. Lett.* **104**, 195302 (2010).
32. G. Pupillo, A. Micheli, M. Boninsegni, I. Lesanovsky, P. Zoller, *Phys. Rev. Lett.* **104**, 223002 (2010).
33. T. Macrì, T. Pohl, *Phys. Rev. A* **89**, 011402 (2014).
34. R. M. W. van Bijnen, T. Pohl, *Phys. Rev. Lett.* **114**, 243002 (2015).
35. Y. Zhou, Y. Li, R. Nath, W. Li, *Phys. Rev. A* **101**, 013427 (2020).
36. D. Malz, J. I. Cirac, *PRX Quantum* **4**, 020301 (2023).
37. Á. Rapp, X. Deng, L. Santos, *Phys. Rev. Lett.* **109**, 203005 (2012).
38. J. B. Balewski *et al.*, *New J. Phys.* **16**, 063012 (2014).
39. J. Zeiher *et al.*, *Nat. Phys.* **12**, 1095–1099 (2016).
40. L.-M. Steinert *et al.*, *Phys. Rev. Lett.* **130**, 243001 (2023).
41. Y.-Y. Jau, A. M. Hankin, T. Keating, I. H. Deutsch, G. W. Biedermann, *Nat. Phys.* **12**, 71–74 (2016).
42. J. Zeiher *et al.*, *Phys. Rev. X* **7**, 041063 (2017).
43. S. Hollerith *et al.*, *Phys. Rev. Lett.* **128**, 113602 (2022).
44. N. Schine, A. W. Young, W. J. Eckner, M. J. Martin, A. M. Kaufman, *Nat. Phys.* **18**, 1067–1073 (2022).
45. W. J. Eckner *et al.*, *Nature* **621**, 734–739 (2023).
46. E. Guardado-Sanchez *et al.*, *Phys. Rev. X* **11**, 021036 (2021).
47. E. A. Goldschmidt *et al.*, *Phys. Rev. Lett.* **116**, 113001 (2016).
48. L. Festa *et al.*, *Phys. Rev. A* **105**, 013109 (2022).
49. D. Wei *et al.*, *Phys. Rev. X* **13**, 021042 (2023).
50. C. Weitenberg *et al.*, *Nature* **471**, 319–324 (2011).
51. T. Fukuhara *et al.*, *Nature* **502**, 76–79 (2013).
52. See the supplementary materials.
53. J. Zeiher, thesis, Ludwig-Maximilians-Universität München (2017).
54. J. A. Hines *et al.*, *Phys. Rev. Lett.* **131**, 063401 (2023).
55. K. Winkler *et al.*, *Nature* **441**, 853–856 (2006).
56. P. M. Preiss *et al.*, *Science* **347**, 1229–1233 (2015).
57. M. Karski *et al.*, *Science* **325**, 174–177 (2009).
58. L. Sansoni *et al.*, *Phys. Rev. Lett.* **108**, 010502 (2012).
59. V. D. Naik, F. Ballar Trigueros, M. Heyl, *Phys. Rev. B* **110**, L220303 (2024).
60. A. W. Young, W. J. Eckner, N. Schine, A. M. Childs, A. M. Kaufman, *Science* **377**, 885–889 (2022).
61. U. Schollwöck, *Ann. Phys.* **326**, 96–192 (2011).
62. C. Kollath, J. S. Meyer, T. Giamarchi, *Phys. Rev. Lett.* **100**, 130403 (2008).
63. Y. Li, A. Geißler, W. Hofstetter, W. Li, *Phys. Rev. A* **97**, 023619 (2018).
64. E. G. Dalla Torre, E. Berg, E. Altman, *Phys. Rev. Lett.* **97**, 260401 (2006).
65. Z. Chen *et al.*, *Science* **373**, 1235–1239 (2021).
66. P. Weckesser *et al.*, Realization of a Rydberg-dressed extended Bose-Hubbard model, Edmond (2025).

ACKNOWLEDGMENTS

We gratefully acknowledge discussions with S. Hollerith, W. Bakr and his entire team, M. Eiles, M. Greiner, D. Malz, and M. Heyl. **Funding:** We acknowledge funding by the Max Planck Society (MPG), by the Deutsche Forschungsgemeinschaft (DFG, German Research Foundation) under Germany's Excellence Strategy–EXC-2111–390814868, and through the DFG Research Unit FOR 5522 (project ID 499180199) as well as project no. BL 574/15-1 within SPP 1929 (GiRyd). This publication has also received funding under the Horizon Europe program HORIZON-CL4-2022-QUANTUM-02-SGA through the project 101113690 (PASQuanS2.1). P.W. acknowledges funding through the Walter Benjamin program (DFG project 516136618). J.Z. acknowledges support from the BMBF through the program "Quantum technologies - from basic research to market" (grant no. 13N16265). K.S. and S.A. acknowledge funding from the International Max Planck Research School (IMPRS) for Quantum Science and Technology. **Author contributions:** All authors contributed to the work presented in this manuscript. P.W. and K.S. acquired the data and together with D.W., D.A., and S.A. maintained the experimental apparatus. P.W. and K.S. analyzed the data. P.W., K.S., T.B., and D.W. performed the numerical and analytical calculations. A.B., I.B., and J.Z. supervised the study. All authors worked on the interpretation of the data and contributed to writing the manuscript. **Competing interests:** The authors declare no competing interests. **Data and materials availability:** The data shown in the main text and extended data figures are available from the Edmond repository of the Max Planck Society (*66*).

License information: Copyright © 2025 the authors, some rights reserved; exclusive licensee American Association for the Advancement of Science. No claim to original US government works. https://www.science.org/about/science-licenses-journal-article-reuse

SUPPLEMENTARY MATERIALS

science.org/doi/10.1126/science.adq7082
Materials and Methods; Supplementary Text; Figs. S1 to S11; Table S1; References (*67*–*84*)

Submitted 3 June 2024; accepted 30 September 2025

10.1126/science.adq7082

Unite for a sustainable future: A call to all scientists

The Institute of Applied Ecology at the Chinese Academy of Sciences champions bold innovations in forestry, agriculture, and environmental science.

Established in 1954, IAE is China's premier institute of forestry, soil science, and ecology. From its inception, IAE has focused on studying and safeguarding the nation's rich, diverse forest and soil resources to enhance agricultural productivity.

Forests, farms, and the environment

Since the late 1970s, IAE has played a crucial role in the Three-North Protective Forest Program (TNP) to address China's high soil erosion rates. Often referred to as the "Green Great Wall," the TNP is China's largest ecological engineering project. Jiaojun Zhu, IAE president, member of the Chinese Academy of Engineering, and deputy chief of the advisory expert group for TNP, commented on TNP's successes and IAE's contribution in an article from Xinhua News. "This ambitious project has already increased the forest cover in the Three-North region of China from 5.05% in 1978 to 13.84% in 2024," says Zhu.

Forests are carbon sinks, natural systems that remove carbon dioxide from the atmosphere. Accurately measuring the carbon sink capacity of forests is of great significance in climate change research. Under Zhu's leadership, IAE established the Qingyuan Forest Ecosystem National Field Scientific Observation and Research Station, where scientists measure carbon dioxide emissions and sequestration to provide accurate, up-to-date analysis on changes in the carbon sink capacity of the forests of Northeast China.

Environmental challenges—especially pollution and restoring healthy ecosystems—have become a focus of the institute's modern era. To advance environmental studies, IAE developed the Center for Pollution Ecology and Environmental Ecological Engineering.

IAE researchers' studies illuminated the value of the Northeastern region's black soil through in-depth fieldwork and collaborations with agriculture, geography, forestry, and soil science. Their efforts were published in the book *Soil of Northeastern China*, a vital resource for soil researchers in China.

To continue its mission of sustainability, IAE has a strong need for researchers from across the globe to join its team of scientists working to make forests, farms, and the environment cleaner and smarter.

Climate-smart forestry

To address diverse environmental challenges, IAE's forestry research has identified climate-smart forestry as a key focus. Climate-smart forestry is a scientific framework that focuses on developing strategies to maximize forest carbon sequestration while leveraging data-driven decision-making to adapt to changing environmental conditions. Specifically, IAE researchers are using artificial intelligence (AI) to better understand complex interactions between forest ecosystems and climate change. In a paper titled "On the research of climate-smart forestry" published by *Scientia Silvae Sinicae,* IAE scientists identified carbon sink measurement, forest resilience processes, and intelligent data collection systems as key research directions. Zhu says, "By highlighting critical technologies for climate-smart forestry applications, such as Forest 3D observation,

PHOTO: © PROONTY/SHUTTERSTOCK.COM

Forestry Digital Twin, AI analysis, and human-machine decision-making systems, these climate-smart forestry research efforts can significantly reduce trial-and-error costs and transform traditional forestry research paradigms."

IAE invites passionate scientists to join the Climate-Smart Forestry Research Center to further investigate the following areas*:

- Forest carbon sink measurement and assessment
- Forest resilience under climate change
- Formation, sustainability, and enhancement of forest carbon sink
- Applications of big data and artificial intelligence in forestry
- Predictive modeling and expert-machine collaboration for decision making

Modern agriculture

The importance of food security can never be overemphasized for a populous country. Agricultural modernization and rural reforms are important tasks in China.

In the past 70 years, scientists from IAE have focused on soil nutrient cycling and soil microbial ecology. They developed new approaches and biomarker molecules for tracking soil-based microbial residues and metabolites in croplands and natural ecosystems. Their work also uncovered mechanisms underlying soil nutrient transformation, which guided the development of high-efficiency fertilizers.

To strengthen the position of IAE as an international leader in the research areas of soil ecology and agricultural engineering, the Soil Ecology and Agricultural Engineering Research Center offers research fellow positions in these areas*:

- Biogeochemistry
- Soil biology
- Soil health
- Sustainable agriculture
- Fertilizer design and management

Sustainable environmental solutions

Emerging pollutants are a group of harmful chemicals and biological agents that humans and the environment are exposed to on a daily basis, such as hormones, pesticides, heavy metals, and drugs. In recent years, IAE's Pollution Ecology and Environmental Ecological Engineering Research Center has been pushing forward technologies to address emerging pollutants, especially in drugs and personal care products that contain halogenated compounds.

To elevate IAE's research capacity and catalyze transformative scientific advancements, IAE invites passionate researchers to join the institute's Pollution Ecology and Environmental Ecological Engineering Research Center to further investigate the following areas*:

- Environmental biotechnology
- Ecotoxicology and health risk assessment
- Analytical chemistry
- Environmental big data
- Resource recovery from waste materials

*Available positions include **professor, associate professor, and postdoctoral fellow.**

Sponsored by

IAE

PHOTO: PROVIDED BY IAE, THE THOUSAND ACRE DEMONSTRATION ZONE IN CHANGTU, LIAONING PROVINCE 2022

Implementing "panda soil" protection has resulted in the autumn harvest corn yield reaching a level of "ton grain field."

ScienceCareers.org
Science Careers

myIDP Science Careers
INDIVIDUAL DEVELOPMENT PLAN

Features in myIDP include:

- Exercises to help you examine your skills, interests, and values.
- 20 career paths with a prediction of which ones best fit your skills and interests.
- A tool for setting strategic goals with optional reminders to keep you on track.
- Articles and resources to guide you through the process.
- Options to save materials online and print them for further review and discussion.
- A certificate of completion for users that finish myIDP.

Start planning your future today!
myIDP.sciencecareers.org

In partnership with:

FASEB Federation of American Societies for Experimental Biology
UMASS University of Massachusetts Medical School
UCSF University of California San Francisco
UIC
BURROUGHS WELLCOME FUND

What's Your Next Career Move?

From networking to mentoring to evaluating your skills, find answers to your career questions on *Science* Careers

To view the complete collection, visit **ScienceCareers.org/booklets**

ScienceCareers
FROM THE JOURNAL SCIENCE AAAS

MIT BE
BIOLOGICAL ENGINEERING

Biological Engineering and Data Science, Machine Learning and AI Tenure-Track

The Department of Biological Engineering (BE) and the Institute for Data, Systems, and Society (IDSS) at the Massachusetts Institute of Technology (Cambridge, Massachusetts) seek applicants for a tenure track position at the Assistant Professor level, effective July 1, 2026, or a mutually agreed-upon date. We welcome outstanding applicants developing novel methods in statistics, data science, machine learning, and AI to enable discovery and innovation in biological engineering.

Candidates are expected to have had formal graduate training and research focus in statistics, data science, machine learning or AI and hold a PhD (or equivalent terminal degree) in the field of biological engineering, statistics, or a related field by the start of employment.

The pay range for a 9-month academic appointment at the entry-level Assistant Professor rank (excluding summer salary): **$140,000 - $150,000**. Complete applications should be received by **15 December 2025**. For more information, please see: https://faculty-searches.mit.edu/idss-be/

Time to laugh

Lindsey Smith Taillie

"Come in," I said to the scientists at my doorstep, ushering them toward the kitchen. Our colorful tunics—not our typical work wear—rustled as we mixed that month's cocktail, a wintery take on an Aperol spritz. We bantered and laughed; one attendee asked which walkout song we would choose if we were professional mixed martial arts fighters. It was what I needed, and not just for relief after a long week in the lab. I've learned that levity helps me be a better scientist, mentor, and colleague. It is also what keeps me going during hard times—a lesson that was reinforced the very next month.

For much of my career, my fellow scientists only saw what I call my "resting science face," which conveys the part of me that's driven to spend hours obsessing over a conference talk or stay up all night putting the final touches on a grant. They didn't see the side of me that loves alien kidnapping skits on *Saturday Night Live*. As a woman and mother, I felt I needed to prove I was serious about the job, lest others view me as too distracted by my personal life to excel.

My serious face worked. I landed a job at a great university, recruited brilliant graduate students, and won tenure. But I felt I had to split myself in two—the serious scientist in public, the goofball in private. Only later did I realize how much stronger my science, and my relationships, could have been if I'd let both sides show sooner.

The first crack in my public persona came in 2024 when, on a whim, I participated in a local live storytelling show. I took a risk and described an embarrassing moment from a solo trip to Thailand. To my surprise, when people laughed it didn't feel bad or shameful. It felt like a hug.

The experience made me think I could start to experiment with being silly at work, too. So, when Halloween came around, I delivered a lecture dressed in a fuzzy pink axolotl costume. I began kicking off lab meetings by asking my graduate students what brings them joy or makes them laugh. And I started the monthly get together with colleagues. The idea was to get out of our usual professional mode by enjoying fancy cocktails and lighthearted conversation. Donning outlandish garments helped set the mood.

To my surprise, I found that injecting fun and humor into my work life didn't make me less effective or credible. Students seemed to find me more approachable. Humor also helped me open up with colleagues, which in turn led others to be more authentic and vulnerable with me, a key part of building trust. After one of my closest international collaborators and I discovered a shared love of humor, we began affectionately poking fun at each other. That brought us closer and made it easier for us to handle challenging issues.

But perhaps most importantly, humor has helped me be resilient. Not long after the gathering at my house last winter, my grant from the U.S. Environmental Protection Agency was abruptly terminated as part of the federal government's science cuts. After the shock and immediate grief wore off, I turned to my goofy side, writing several pieces of satire, making joke T-shirts, and letting colleagues distract me with discussions about the set design choices in Sir Mix-a-Lot's 1992 *Baby Got Back* music video.

That's not to say I was living in denial. I knew I needed to find new ways to pursue my goals in an increasingly complex funding environment. But that pressure could easily feel overwhelming. Making jokes and sharing laughter helped me stay present. It also served as a reminder of how much joy I get from interacting with the people I work with, whatever the circumstances.

In the end, I have come to realize that being authentic at work is not a weakness, but rather a strength. For other scientists, that may mean talking more about their hobbies or families, or showing off their other talents—whatever brings them joy and helps them connect with others. For me, that's humor.

So that's why, even as I reimagine my research plans, I'll be putting on a colorful outfit, calling up some friends, and cracking jokes. Now, more than ever, it's time to laugh. □

Lindsey Smith Taillie is a professor at the University of North Carolina at Chapel Hill. Send your career story to SciCareerEditor@aaas.org.

ILLUSTRATION: ROBERT NEUBECKER

Who's the Top Employer for 2025?

Science 2025
TOP EMPLOYERS

Science Careers' annual survey reveals the top companies in biotech & pharma voted on by *Science* readers.

Explore these highly-rated employers in our interactive experience:
sciencecareers.org/topemployers

TRILLIONS OF MICROBES ONE ESSAY

The NOSTER *Science* Microbiome Prize is an international prize that rewards innovative research by investigators who have completed their terminal degree in the last 10 years and are working on the functional attributes of microbiota. The research can include any organism with the potential to contribute to our understanding of human or veterinary health and disease, or to guide therapeutic interventions. The winner and finalists will be chosen by a committee of independent scientists chaired by a senior editor of *Science*. The top prize includes complimentary membership to AAAS, an online subscription to *Science*, and USD 25,000. Submit your research essay today.

Djenet Bousbaine, Ph.D.
2025 Winner

NOSTER | Science
MICROBIOME
PRIZE

Apply by 14 February 2026 at www.science.org/noster

Sponsored by Noster Inc.